Metal cluster aggregates of the composition $Nb_n^{+/-}$, $Co_n^{+/-}$ and $[Co_nPt_m]^{+/-}$ as model systems for catalytic C-H activation and structural determination of selected metal peptide complexes of the molecules aspartame (Asp-PheOMe) and Asp-Phe

Am Fachbereich Chemie der Technischen Universität Kaiserslautern zur Erlangung des akademischen Grades „Doktor der Naturwissenschaften" genehmigte

Dissertation
(D386)

vorgelegt von

Dipl.-Chem. Lars Barzen

Betreuer: Prof. Dr. G. Niedner-Schatteburg

Tag der wissenschaftlichen Aussprache: 11. Juni 2013
Technische Universität Kaiserslautern

Der experimentelle Teil der vorliegenden Arbeit wurde in der Zeit von Dezember 2006 bis Dezember 2012 im Fachbereich Chemie der Technischen Universität Kaiserslautern unter der Betreuung von Prof. Dr. G. Niedner-Schatteburg angefertigt.

Datum des Antrags der Eröffnung des Promotionsverfahrens: 27. Juni 2012

Tag der wissenschaftlichen Aussprache: 11. Juni 2013

Promotionskommission:

Vorsitzender: Prof. Dr. W. Thiel

1. Berichterstatter: Prof. Dr. G. Niedner-Schatteburg

2. Berichterstatter: Prof. Dr. M. Gerhards

I am among those who think that science has great beauty.

A scientist in his laboratory is not only a technician:

he is also a child placed before natural phenomena

which impress him like a fairy tale.

Marie Curie

Abbreviations

Asp	Aspartic acid
CID	Collision Induced Dissociation
CLIO	Centre Laser Infrarouge d'Orsay
DFT	Density Functional Theory
ESI	ElectroSpray Ionization
FEL	Free Electron Laser
FT-ICR	Fourier-Transform Ion-Cyclotron-Resonance
HP	HexaPole
IR-MPD	InfraRed MultiPhoton Dissociation
KTA	potassium titanyl arsenate
KTP	potassium titanyl phosphate
LVAP	Laser VAPorization
Me	Methyl
MP2	Møller-Plesset perturbation theory second order
MS	Mass Spectrometry
Nd:YAG	Neodymium-doped Yttrium Aluminum Garnet
OPO/OPA	Optical Parametric Oscillator / Amplifier
Phe	Phenylalanine
QIT	Quadrupole Ion Trap
QP	QuadruPole

Content   **Page**

1. Introduction, experimental setup and methods

1.1. General introduction

Characterization of unknown or newly synthesized molecules is often possible by standard analytical methods (e.g. elemental analysis, NMR spectroscopy, IR spectroscopy of solutions or KBr pellets, mass spectrometry etc.). Sometimes, we want to learn about a molecule's intrinsic structure and properties without the influence of surrounding solvents, surfaces or mutual self interactions. Then we have to investigate single molecules under isolating conditions. One way of doing so is to bring molecules into vacuum, alter them in some way and do mass detection. For these mass spectrometric investigations molecules either have to be ions from the beginning or have to be ionized before mass detection. As ions, they can be trapped and can be manipulated in many different ways. Within this thesis, chosen treatments of such ionic molecules will be kinetic investigations with reaction gases, collision induced dissociation (CID), or infrared multiphoton dissociation (IR-MPD). A wide range of molecules is accessible for these kinds of investigation.

Molecules containing transition metal atoms have often proven valuable in the catalytic synthesis of numerous compounds [1-5]. Hydrocarbon adsorption and subsequent C-H bond activation are amongst the most important steps in many catalyzed reactions [6-11]. Their exact mechanism is often not understood completely. The use of more than one metal atom (of the same type or even of different types of atoms) in the catalytic systems can improve the efficiency and yield of a catalytic cycle [12-15]. Of course single molecule gas phase reactions do not describe the synthetic processes of liquid or solid state chemistry, but in combination with quantum mechanical calculations they can serve as model systems to understand the catalytic processes in more detail. Transition metal cluster ions show a diverse behavior in reaction with gases depending on their size and their charge state, the appearance of chemisorption or physisorption being highly debated [16-35]. Amongst other adsorbate molecules the investigation of the interaction between metal atoms or clusters with organic systems containing π-electrons such as benzene has gained special interest in the literature [36-59]. In former kinetic investigations in our group niobium clusters $Nb_n^{+/-}$ have proven to yield reaction products of the compositions $[Nb_nC_6]^{+/-}$ and $[Nb_nC_6H_6]^{+/-}$, when trapping the metal clusters in a Fourier-Transform Ion-Cyclotron-Resonance (FT-ICR) mass spectrometer and reacting them with benzene [47, 50, 51]. Infrared spectroscopic investigations can help to understand the nature of these organo metallic complexes [60-99].

Chapter 2 of this thesis will present our modifications of a Fourier-Transform Ion-Cyclotron-Resonance (FT-ICR) mass spectrometer at the Free Electron Laser (FEL) facility CLIO in Paris, France, describing the installation of an ion bender and a Laser VAPorization (LVAP) source aiming to record

first IR-MPD spectra of the $[Nb_nC_6H_6]^{+/-}$ aggregates. It will further describe modifications made on the LVAP source for metal cluster aggregate production within the source. Investigation of hydrogen/deuterium isotope effects have helped to elucidate the origin of observable phenomena in hydrocarbon activation [100-104]. Chapter 3 will describe the extension of the kinetic investigations to cobalt complexes ($Co_n^{+/-}$) in their reaction with benzene (C_6H_6) and benzene-d6 (C_6D_6), determining the Kinetic and Dehydrogenation Isotope Effects (KIE and DIE), depending on their size and their charge state. In chapter 4 these investigations are extended to mixed cobalt platinum clusters ($[Co_nPt_m]^{+/-}$) focusing on the influence of the additional platinum atoms as compared to the findings of the pure cobalt clusters.

Not only transition metal cluster complexes are of interest for gas phase investigations. During the last years a rapid growth in understanding the influence of non-bonded, particularly hydrogen-bonded interactions, on the shapes and conformations of flexible molecules, including those of pharmacological or biological importance has come up (see e.g. an early review [105]). Structural investigations on peptides, esp. cationized with alkali metal ions, have gained large interest. Many single peptides have already been investigated finding two major structure types: The non-zwitterionic, charge-solvated (CS) type, where the alkali metal cation is often chelated in a tridentate type, and the zwitterionic, salt-bridge (SB) type [106-123]. Chapter 5 will focus on structure and reactivity studies of the dipeptide aspartame (Asp-Phe-OMe) and its unprotected analog Asp-Phe, revealing the influence of the additional methyl group on their protonated, deprotonated and cationized (Li^+ to Cs^+) species.

The following subchapters within this introduction will shortly present the experimental setup and the techniques that have been used. A more detailed description can be found in numerous text books [124, 125] and reviews.

1.2. Experimental setup

1.2.1. Quadrupole Ion Trap (QIT) mass spectrometry

A quadrupole ion trap, better known as Paul trap, uses oscillating electric fields to store ions in vacuum. A typical design of a QIT consists of a circular electrode and two ellipsoid caps perpendicular to the circular electrode. The idea of this kind of ion trap goes back to Paul and Steinwendel (1953) [126, 127]. The modification to a useful mass spectrometer was done by Stafford et al. (1984) [128] with a first review on the capabilities of this technique (1991) [129]. The overlapping of a direct potential with an alternating one creates a 3D quadrupole potential trapping the ions on 3D trajectories. The Mathieu equations as mathematical analysis give areas where certain masses have stable trajectories. Ions can either be created within the trap or transferred to it through a hole in one of the caps. A gas (typically helium), raising the pressure inside the trap to the range of 10^{-3} mbar helps in trapping the ions and reducing the amplitude of their trajectory. In most Paul trap mass spectrometers, mass detection is performed by ion ejection at the stability limit: Ions of all masses are trapped inside the cell. By stepwise changing the amplitude of either the direct or the alternating voltage the stability criteria of the ions are lost consecutively and they leave the trap through a hole in the second cap hitting a detector. This stability - ion signal relationship is then transferred into a mass spectrum.

Within this work, a Bruker Esquire 6000 instrument has been used to perform Collision Induced Dissociation (CID, see chapter 1.3.2.) experiments and a Bruker amaZon SL instrument to record InfraRed MultiPhoton Dissociation (IR-MPD, see chapter 1.3.3.) spectra in Kaiserslautern and a Bruker Esquire 3000+ instrument to record IR-MPD spectra at the Free Electron Laser CLIO in Orsay, Prais, France. For the IR-MPD measurements, the cylindrical electrodes of the traps within the Esquire and the amaZon SL instruments had been modified with one hole allowing the IR beam to enter and - in the case of the amaZon SL - a second hole to leave the center of the trap.

1.2.2. Fourier-Transform Ion-Cyclotron-Resonance (FT-ICR) mass spectrometry

In contrast to the trapping with electric fields in the QIT (Paul trap), an FT-ICR mass spectrometer uses a magnetic field to trap the ions on circular orbits. Therefore, the part of the vacuum chamber containing the ICR cell (Penning trap) has to be located within the center of a strong magnet (typical magnetic fields between 3 and 15 T). For the concept of *cyclotron* (see Ref. [130]) the Nobel Prize of Physics was awarded to Ernest Lawrence in 1939. Fourier transform mass spectrometry (FTMS) was first described by Comisarow and Marshall (1974) [131, 132] and reviewed by Amster (1996) [133] and Marshall et al. (1998) [134].

Ions on circular orbits experience two different forces:

$$\text{Lorentz force:} \quad F = qv_{xy}B \qquad (1.1a)$$

$$\text{Centrifugal force:} \quad F' = \frac{mv_{xy}^2}{r} \qquad (1.1b)$$

$q = z \cdot e$: charge of the ion

z: charge number

e: elementary charge

v_{xy}: velocity of the ion in the xy plane

B: magnetic field strength

m: mass of the ion

r: radius of the ion's orbit

Ions on trajectories within the balance of these forces possess an angular velocity ω_c:

$$\omega_c = 2\pi\nu = \frac{v_{xy}}{r} = \frac{q}{m}B \qquad (1.2)$$

ν: frequency of the ion

which is independent of the velocity of the ions. This converts mass detection into a frequency measurement which can be done very precisely.

A typical ICR cell (in our instruments of the "infinity cell" type [135]) consists of at least six plates, four of them for ion excitation and detection, being located in the xy plane (z being the axis of the magnetic field). Ions entering the cell along the z axis through a hole in the front plate are trapped along the axis by an electrostatic field and start their circular motion within the xy plane. If the vacuum is good enough (10^{-10} mbar and better) ions can be stored within the cell for minutes over hours or even days. For mass detection, all ions on their orbits are simultaneously excited by a rapid scan of a large frequency range applied over the two excitation plates. On their higher orbits, they induce an image current on the detection plates giving a signal as a function of time. This signal is Fourier-transformed resulting in a graph which plots intensity as a function of frequency. With the above relations this is recalculated into a graph showing intensity as a function of mass-to-charge ratio m/z. Ions do not only have this cyclotron motion that is measured in the FT-ICR-MS process. The

whole motion of the ion [136] results from an axial oscillation due to the trapping voltage with frequency ω_z, a cyclotron motion with frequency ω_c and a magnetron motion with frequency $\omega_m = \omega_z^2/2\omega_c$.

Within this work, the FT-ICR technique has been used to perform kinetic investigations with neutral reaction gases (see chapter 1.3.1.) and to record IR-MPD spectra (see chapter 1.3.3.) with three different mass spectrometers: A modified Bruker 7 T FT-ICR Apex Qe instrument near the FEL CLIO, Orsay, Paris, France and a modified Bruker 7 T FT-ICR Apex III instrument in Kaiserslautern for all investigations regarding metal clusters (see chapters 2 - 4) and an unmodified Bruker 7 T Apex-Ultra instrument in Kaiserslautern for part of the investigations regarding peptide alkali metal complexes (see chapter 5). Main part of the modifications was the installation of a Laser VAPorization (LVAP) ion source (1.2.4.) together with an ion bender, so that switching between the originally installed ElectroSpray Ionization (ESI) sources (see chapter 1.2.3.) and the LVAP sources could be performed very easily. As especially the installation of the Orsay-FT-ICR instrument was part of this work, a detailed description of the modifications is given in chapter 2.

1.2.3. ElectroSpray Ionization (ESI) source

The ESI source allows for the transfer of dissolved ions into vacuum. Since its first application by Fenn et al. [137-140] (1984, noble prize 2002), ESI principles and mostly biological applications [141-144] have been extensively reviewed [145-147] and the subject has been topic of several books [148-150] (beginning from 1996). Within the ESI process, a field gradient (several kV) between a capillary tube (comprising the solvated ions) and the entrance of the mass spectrometer allows for a charge accumulation at the liquid surface at the end of the tube. A nebulizing gas (here: nitrogen) flowing along the tube helps in creating a stream of very small droplets. Removal of the remaining solvent molecules is performed by a heated drying gas (here: nitrogen) flowing against the stream of droplets releasing naked ions which then enter the vacuum of the mass spectrometer. In all instruments used in this work the entrance consists of a glass capillary (diameter 0.5 mm, length between 15 and 20 cm) which is coated with platinum at both ends. The exact mechanism of ion release and solvent removing is still debated [151, 152]. Solvents best suitable for the ESI process are water, methanol, acetonitrile and dimethylsulfoxide. All molecules (up to a molecular weight of several 10,000 Da) that are soluble within these substances are easily accessible to the ESI process. Molecules with higher molecular weight are typically multiply charged.

1.2.4. Laser VAPorization (LVAP) source

A homebuilt Laser VAPorization source (LVAP) serves to generate metal cluster ions [153-155] (for a more detailed description, drawings and pictures of the complete source see chapter 2.2). The second harmonic (λ = 532 nm) of a pulsed Continuum Surelite II neodymium-doped yttrium aluminum garnet (Nd:YAG) laser (Kaiserslautern) or an Innolas Spit Light 300 Nd:YAG laser (Orsay, Paris, France) is used to evaporate metal atoms from a 0.4 - 1.0 mm thick rotating metal foil (usage of alloys for mixed clusters). The emerging metal plasma is cooled and made to yield clusters by a short transverse gas pulse (40 µs, helium, 8 - 15 bar) from a homebuilt piezoelectric valve [156]. Further cooling arises from the subsequent supersonic nozzle expansion through a 20 mm long channel (diameter of 2 mm) into vacuum (10^{-6} mbar). No additional ionization step is needed. All investigated ions are generated within the laser induced plasma. Past a 1.4 mm diameter skimmer the cold cluster ions are accelerated, fed into a quadrupole ion bender (90^0) and steered by electrostatic lenses into the FT-ICR cell within the high field region of the superconducting magnet of the originally installed FT-ICR mass spectrometer.

Part of this work was the modification of the source by adding a "pick up unit" (see chapter 2.7). Subsequent to the expansion channel, the pick up block with a gas inlet was installed (diameter of 10 mm, length of up to 30 mm). This allows for the adsorption (or even reaction) of gases to / with the metal clusters during their formation.

1.2.5. Free Electron Laser (FEL)

The "classical" way of generating laser light has long time been the usage of atoms or molecules (e.g. crystals) as active medium (for an overview on light and lasers see Ref. [157]). Madey et al. established a new concept of a widely tunable laser using electrons of high energy as active medium (Free Electron Laser (FEL), 1977, Ref. [158]): An electron beam is accelerated and sent through alternating magnetic fields (undulator). Whenever the electron beam changes its direction, it releases the so called bremsstrahlung. The energy range of this radiation is determined by the kinetic energy of the electrons and fine tuning within one range is established by changing the magnetic field strength of the undulator magnets. In most cases this is simply done by opening or closing of the gap between a pair of north and south pole magnets. A review giving more details on the characteristics of infrared (IR) to ultraviolet (UV) FELs was written in 2000 by Couprie and Ortega [159]. For our purposes of gaining structural information of molecules, the use of IR FELs is suitable. In Europe, this can be done at the two facilities FELIX (Free Electron Laser for Infrared eXperiments, [160, 161]), located at the university of Nijmegen, Netherlands, providing tunable radiation in the spectral range of 40 - 2500 cm^{-1}, and CLIO (Centre Laser Infrarouge d'Orsay, [159, 162, 163]), located

at the university Paris-Sud in Orsay, Paris, France, providing laser light in the range of 67 - 3333 cm^{-1} (maximum average power of 40 mJ). Within our European cooperation project EPITOPES (Electrons Plus Ions TO Probe and Elucidate Structure, see Chapter 2) all measurements using FEL technology have been performed at CLIO in the wavelength range of 600 - 1800 cm^{-1}.

1.2.6. Optical Parametrical Oscillator / Amplifier (OPO/OPA)

Free Electron Lasers (as mentioned in Chapter 1.2.5.) can be sources of infrared light with high intensity. These systems are huge machines with installation and maintenance costs of many millions of Euro. Access to these rare setups has to be limited for each working group to few weeks per year according to the number of scientific proposals handed in. During the last years (first mentioned in 1967, Ref. [164], and first reported in an edited book 1977, Ref. [165]) another much smaller solution of generating tunable light has been established: The Optical Parametric Oscillator / Amplifier (OPO/OPA, with space requirements below 1 m^2). Polarized laser light of a fixed frequency pump laser is split into a signal wave and an idler wave within a nonlinear crystal. The wavelengths of these new waves depend on the refraction index of the crystal. This refraction index can be influenced either by heat or by the angle of the crystal according to the axis of the intruding light. In order to obtain high resolution (in our cases for InfraRed MultiPhoton Dissociation, IR-MPD, see chapter 1.3.3.), the laser light emitting from the OPO should have a bandwidth as small as possible. Therefore, two things have to be considered: On the one hand, the bandwidth of the pump laser should be as small as possible. This can be established by using seeded lasers (Ref. [166]) where the oscillation build-up of only one mode within the laser is favored. On the other hand, the usage of a grating within the OPO setup can also reduce the bandwidth of the laser light within the OPO cavity.

Within this work OPO/OPA systems of Dean Guyer's company Laservision have been used:
The original infrared light pulses are generated by Nd:YAG lasers with an output wavelength of 1064 nm. When entering the OPO, the laser beam is splitted into two separate beam lines. One third of the original intensity is frequency doubled to green light (532 nm). This beam is coupled into the OPO resonator, which is equipped with a converging potassium titanyl phosphate (KTP) crystal. According to the angle between the light and the crystal, each photon is converted into one signal (signal 1) and one idler photon (idler 1). The idler 1 photon is coupled out into four OPA potassium titanyl arsenate (KTA) crystals, where they are recombined with the residuing two thirds of the original 1064 nm light. This process produces once again a signal (signal 2) and an idler beam (idler 2), signal 2 having the same wavelength as idler 1. As these two beams have different polarization, a suitable filter can separate them. Idler 2 hereby gives a wavelength of about 2200 - 4700 cm^{-1}, signal 2 has a wavelength of about 4700 - 7400 cm^{-1}. If those two beams are recombined within a

Difference Frequency Mixing (DFM) crystal (AgGaSe$_2$), a wavelength range from 800 - 2200 cm^{-1} is also accessible. In the range of a molecule's OH and NH stretching vibrations (around 2700 - 3700 cm^{-1}), the laser power (up to 15 mJ) is nearly comparable to the one of FELs, but especially when using the DFM stage, the power is quite low (approx. 2 - 3 mJ). The intensity output of the OPO / OPA system is controlled by a variable attenuator in the light path of the linear polarized 1064 nm beam which is coupled into the OPA crystals. This filter blocks the beam at an adjustment angle of 0° and allows for maximum intensity at a position of 45°.

In this work, three different combinations of Nd:YAG pump lasers and Dean Guyer OPO/OPA systems were used: In Orsay, Paris, France a seeded Innolas Spit Light 600 laser with a broadband OPO/OPA system, in Kaiserslautern a Continuum PowerLite 8000 with a narrowband OPO/OPA system and a seeded Continuum PowerLite 8000 laser with a broadband OPO/OPA system.

1.3.   Methods

1.3.1.   Kinetic investigations with neutral reaction gases

A series of molecules with only slightly different composition can have distinctly different properties. One part of these differences can be their reactivity with neutral gas molecules. As mentioned in chapter 1.1., we are using mass spectrometry to investigate separated ions that are neither influenced by solvent molecules nor by other molecules of the same kind. These ions that either have been transferred into the vacuum out of a solution by an ESI source (see chapter 1.2.3.) or have been created in vacuum by an LVAP source (see chapter 1.2.4.) are transferred into the ICR cell within the highfield region of an FT-ICR magnet where they can be stored before mass detection (see chapter 1.2.2.). If we want to learn about the reactivity of these ions, we can add a distinct amount of gas into the vacuum chamber of the ICR cell. A reaction of any kind can be proven by the appearance of additional *daughter* masses in the mass spectrum and simultaneous decrease of the intensity signal of the former *parent* ion. By recording multiple mass spectra while varying the *reaction delay* between entering of the ions into the ICR cell region and their mass detection, one can perform a kinetic investigation. As the reaction gas as one of the two reaction partners is apparent in excess, the relative intensities of the mass peaks can be plotted and fitted as pseudo-first-order kinetics:

$$v = -\frac{d[Int]}{dt} = k \cdot [Int] \qquad (1.3)$$

The resulting rate constants of different molecules and thus their reactivity against distinct gases can be interpreted by comparing these values. The applications of this technique reach from investigations on biologically relevant molecules by performing H-/D-exchange experiments with

deuterated gases (e.g. D_2O, ND_3, see chapter 5) up to complex gas activation mechanisms on size selected pure or mixed metal clusters (see chapters 2 - 4).

1.3.2. Collision Induced Dissociation (CID)

When trying to characterize a molecule, its mass can give information on its composition, but does not reveal any structural feature. Especially the identification of biomolecules with large sequences can not only be done by the mass of the intact molecule. One possible technique of gaining structural information is Collision Induced Dissociation (CID) where ions are fragmented and remaining species are mass detected. This does not only reveal characteristic fragment patterns but also can give hints on the stability of the original parent ions. After the first mention of its importance by McLafferty et al. in 1972[167] it has become a widely used and reviewed technique [168-174].

Within this work CID was performed in our Bruker Esqiure 6000 quadrupole ion trap mass spectrometer. Ions are stored in an electronic Paul trap (see chapter 1.2.1.). They are given kinetic energy by applying appropriate voltages. Thus they collide with helium atoms that are present inside the Paul trap (helium does not only allow for the trapping but also for the collisions). A higher voltage corresponds to higher kinetic energy. When colliding, this kinetic energy is transferred into internal energy of the ions. If this additional energy is high enough, these parent ions undergo fragmentation. Therefore the intensity of the parent ions decreases, while the intensity of the fragment ions increases. The applied collision voltage thereby is proportional to an energy value E_{LAB}. As the kinetic energy depends on the masses of the ions, one has to do a center-of-mass-transformation of the collision energy when comparing the values of molecules with different masses:

$$E_{COM} = E_{LAB} \frac{M_{gas}}{M_{ion}+M_{gas}} \qquad (1.4)$$

M_{gas}: molecular mass of the gas
M_{ion}: molecular mass of the parent ion

When scanning the collision voltage, for every voltage step the relative intensities of parent and fragment ions of a distinct number of mass spectra is averaged resulting in a curve of sigmoidal shape (see Fig. 1).
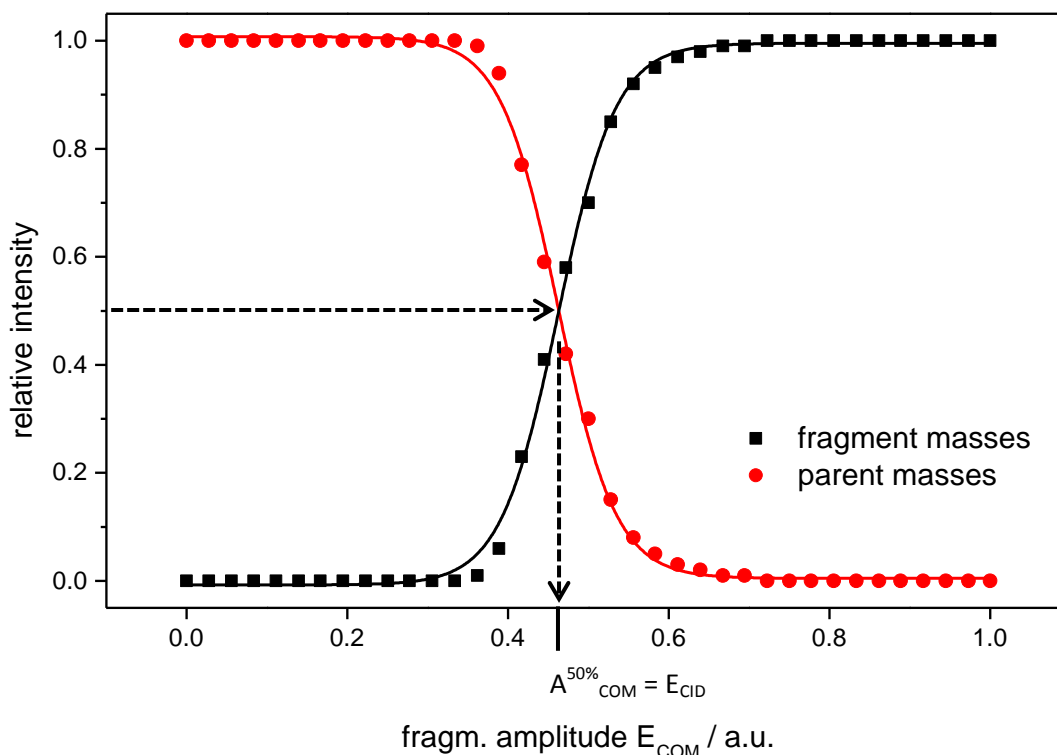
Fig. 1: *Example of CID sigmoidal curve fits: Relative intensities of the occurring masses against fragmentation amplitude E_{COM}; red: sum of parent masses, black: sum of fragment masses.*

When fragmentation does not only result in a simple "one parent ion decays into one fragment ion" behavior, the definition of a fragmentation efficiency including the intensities of all parent and fragment ions has proven to be necessary:

$$\text{fragm. eff.} = \frac{\sum Int_{fragments}}{\sum Int_{fragments} + \sum Int_{parents}} \qquad (1.5)$$

If the fragmentation process does not produce any ions or if the mass to charge ratio of the fragment ions is out of mass range of the mass spectrometer, the definition of the fragmentation efficiency has to be modified slightly so that only the intensities of the parent mass peaks is used:

$$\text{fragm. eff. par.} = 1 - \frac{\sum Int_{parents}}{\sum Int_{parents,av.1-10}} \qquad (1.6)$$

For our experiments it has proven useful to average the not activated parent ion intensities of 10 mass spectra before starting the stepwise rising of the fragmentation amplitude.

One way of comparing CID curves and thus the stability behavior of different molecules is the fragmentation amplitude value that has to be used to yield a fragmentation efficiency of 50 %.

Within this thesis this value will be referred to as $A^{50\%}_{COM}$ (Center-Of-Mass transformed fragmentation Amplitude to reach a fragmentation efficiency of 50 %) or for simpler understanding just as E_{CID}. In general the meaning of this is as follows: The higher this value, the more stable is the parent ion.

1.3.3. InfraRed MultiPhoton Dissociation (IR-MPD)

As already mentioned in chapter 1.3.2., dissociation of ions and mass detection of the fragments can help in gathering structural information of a molecule. In CID experiments fragmentation is performed by collisions of the ions with neutral gases. Another idea that was first described by Lee et al. in 1977 [175, 176] and came up for biologically relevant molecules by Beauchamp et al. in 1978 [177] is to induce the fragmentation by irradiating and thus heating the trapped ions with infrared light. This idea was especially useful for the application of dissociation experiments within FT-ICR mass spectrometers (see chapter 1.2.2.), as in general these instruments do give highest resolution with a minimum of gas load within the ICR cell. One possibility of investigating the interaction between infrared light and ions trapped in these cells is the monitoring of Blackbody Infrared Radiative Dissociation (BIRD) [178] which occurs by ambient radiation and does not include any laser. But being more effective the use of CO_2 lasers in combination with FT-ICR instruments to perform InfraRed MultiPhoton Dissociation (IR-MPD) especially for biological sequencing [179] became a widely used technique. Its application to QIT instruments (see chapter 1.2.1.) with their high gas load and thus re-thermalizing of the irradiated ions was established shortly after (review see Ref. [180]), especially with their modification of dynamic control of the bath gas [181]. Investigations on large proteins in Dual Pressure Linear Ion Trap Mass Spectrometers revealed distinct differences in the fragmentation behavior of molecules treated with IR-MPD or CID: IR-MPD yielded product ions in significantly lower charge states as compared to CID [182, 183]. Quite recently the combination of IR-MPD with Electron Capture Dissociation (ECD) has extended the usage of the IR-MPD technique [184-186]. As in the early years of IR-MPD only the use of fixed frequency lasers has been described, it is nowadays also possible to record complete IR-MPD spectra when using tunable lasers as light source (e.g. FELs or OPO/OPA systems, see chapters 1.2.5. and 1.2.6.): The laser is scanned and for every mass spectrum the fragmentation efficiency is calculated (see chapter 1.3.2.) and drawn in dependence of the photon energy. When the laser frequency equals a vibrational mode, energy is transferred into this mode and by repeatedly photon absorption the molecule is heated, until the energy is high enough to break a bond and cause fragmentation. Two models have been highly debated: One idea was that dissociation occurs by absorption of multiple photons adding their energy into one mode and ladder-climbing in this mode. The second model assumes energy pumping of photons into the ground state of one mode, redistribution of the energy into the rest of the

molecule (IVR: intramolecular vibrational redistribution) and thus repeatedly pumping the ground state. Depending on the photon energy the absorption of up to 100 photons can be necessary before bond breaking [187]. The second model appears much more reasonable, as experimentally observed fragmentation does not always occur in the mode which is pumped, but often in the path that needs lowest energy for bond breaking. Many articles have been dealing with the dynamics of the energy transfer and fragmentation process of CID [188] and IR-MPD [189, 190], often combining theoretical investigations of the RRKM (Rice-Ramsberger-Kassel-Markus) theory of collisionless dissociation [191-198]. According to this latter model the usage of the term *MultiplePhoton Dissociation* instead of *MultiPhoton Dissociation* is preferred in several literature articles.

As mentioned in chapter 1.2.6. energy output of an OPO / OPA system is low when using the DFM stage. So when trying to record IR spectra in this energy range, it might happen that repeated photon absorption into a vibrational mode is too weak to cause fragmentation. This can be overcome by postheating an irradiated molecule with a second laser pulse, whose wavelength is set to a known band of the system, e.g. in the OH/NH stretching vibrations region. The scanning laser is referred to as pump laser and the fixed frequency laser used for postheating as probe laser.

This two-color scheme is not only useful for additional heating of the molecule. It is currently used in our group for investigations regarding the mechanism of energy redistribution within one molecule. Within the two-color investigations reported in this thesis, the broadband system was used for scanning and the narrowband system for probing.

1.3.4. Computational Methods

Much effort has been spent during the last years in the computational prediction of molecular properties. Especially the ongoing improvements in computer hardware allow for more and more exact treatment of the molecules' intrinsic forces. Besides others the Density Functional Theory (DFT) has become a method for determining a molecule's ground state energy by performing calculations using the electron density (short lecture see Ref. [199]): During the calculations a molecule's geometry is energy optimized until within given convergence criteria the lowest energy is reached. As this method will only find the minimum geometry similar to the start one, for each molecule a large number of calculations with differing possible start geometries have to be performed. Comparing the final energy values will give the global minimum. Not only characteristic atom-atom bond lengths and angles can easily be extracted out of the geometry, but also vibrational spectra can be predicted by calculating the forces onto the atoms after displacement out of their minimum geometry.

The idea of electron density goes back to the Hohenberg-Kohn-Theorem[200]. It claims that the ground state of a system of N electrons does have a unique position dependent electron density. All molecular properties are functionals of this electron density. Instead of solving the Schrödinger equation for the whole system, the Kohn-Sham equations[201] treat all N electrons separately generating the same density as the complete molecule with interacting electrons. Therefore the Kohn-Sham wavefunction is a single Slater determinant constructed from a set of orbitals that are the lowest energy solution to

$$\left(-\frac{\hbar^2}{2m}\nabla^2 + v_{eff}(\boldsymbol{r}) \right)\Phi_i(\boldsymbol{r}) = \epsilon_i\Phi_i(\boldsymbol{r}) \qquad (1.7)$$

with ε_i being the orbital energy of the corresponding Kohn-Sham orbital.

The density of the whole system then is

$$\rho(\boldsymbol{r}) = \Sigma_i^N |\Phi_i(\boldsymbol{r})|^2 \qquad (1.8)$$

In DFT the total energy of a system is

$$E[\rho] = T_s[\rho] + \int d\boldsymbol{r}\, v_{ext}(\boldsymbol{r})\rho(\boldsymbol{r}) + V_H[\rho] + E_{XC}[\rho] \qquad (1.9)$$

with $T_s[\rho]$ being the Kohn-Sham kinetic energy, v_{ext} an external potential (electron-nuclei interaction), $V_H[\rho]$ the Coulomb energy and $E_{xc}[\rho]$ the exchange-correlation (XC) energy.

The huge variety of DFT calculations originates, on the one hand, from the choice of the basis set and, on the other hand, from the functionals used in the term of the exchange-correlation energy. This latter XC term can e.g. be approached by either local density approximations (LDA) or by generalized gradient approximation (GGA). The use of hybrid methods combining GGA methods with partially calculating exchange energy according to the Hartree-Fock-method has become very popular, as despite the longer calculation effort the results are more precise (e.g. see Ref. [202-204]). Most of these XC functionals are named by their inventors.

Within this work, nearly all energetic and structural calculations have been performed on DFT level. For comparison reason several few calculations were also made with MP2 Møller-Plesset

perturbation theory second order [205-209], which is a standard post-Hartree-Fock ab initio method improving the Hartree-Fock method by adding electron correlation effects. All calculations were performed using the ECCE (Extensible Computational Chemistry Environment) interface (Ref. [210]) to submit and monitor calculations running with the program packages Gaussian 03 (Ref. [211]) and Gaussian 09 (Ref. [212]). The specific use of basis sets and functionals will be indicated within the according chapters. Calculations were gratefully run on the computing clusters of the university of technology Kaiserslautern which are under the supervision of the group of Prof. Ch. vanWüllen.

1.4. References

[1]   M.J. Wilkinson, P. van Leeuwen, J.N.H. Reek, *New directions in supramolecular transition metal catalysis*, Organic & Biomolecular Chemistry, **3** (2005) 2371-2383.

[2]   A. Behr, P. Neubert, *Applied Homogeneous Catalysis*, Wiley, 2012.

[3]   P.A. Evans, J. Tsuji, *Modern Rhodium-Catalyzed Organic Reactions*, Wiley, 2006.

[4]   B. Breit, *Supramolecular approaches to generate libraries of chelating bidentate ligands for homogeneous catalysis*, Angewandte Chemie-International Edition, **44** (2005) 6816-6825.

[5]   A.J. Sandee, J.N.H. Reek, *Bidentate ligands by supramolecular chemistry - the future for catalysis?*, Dalton Transactions, (2006) 3385-3391.

[6]   F.W. Patureau, T. Besset, R. Froehlich, F. Glorius, *On the selectivity in some Rh(III) catalyzed C-H activation cross-couplings*, Comptes Rendus Chimie, **15** (2012) 1081-1085.

[7]   F.W. Patureau, J. Wencel-Delord, F. Glorius, *Cp*Rh-Catalyzed C-H Activations: Versatile Dehydrogenative Cross-CoupHngs of C-sp2 C-H Positions with Olefins, Alkynes, and Arenes*, Aldrichimica Acta, **45** (2012) 31-41.

[8]   J. Wencel-Delord, C. Nimphius, F.W. Patureau, F. Glorius, *Undirected Arene and Chelate-Assisted Olefin C-H Bond Activation: RhIIICp* -Catalyzed Dehydrogenative Alkene-Arene Coupling as a New Pathway for the Selective Synthesis of Highly Substituted Z Olefins*, Chemistry-an Asian Journal, **7** (2012) 1208-1212.

[9]   J. Wencel-Delord, C. Nimphius, F.W. Patureau, F. Glorius, *RhIIICp* -Catalyzed Dehydrogenative Aryl?Aryl Bond Formation*, Angewandte Chemie-International Edition, **51** (2012) 2247-2251.

[10]   G. Altenhoff, R. Goddard, C.W. Lehmann, F. Glorius, *An N-heterocyclic carbene ligand with flexible steric bulk allows Suzuki cross-coupling of sterically hindered aryl chlorides at room temperature*, Angewandte Chemie-International Edition, **42** (2003) 3690-3693.

[11]   S. Wuertz, C. Lohre, R. Froehlich, K. Bergander, F. Glorius, *IBiox (-)-menthyl : A Sterically Demanding Chiral NHC Ligand*, Journal of the American Chemical Society, **131** (2009) 8344-+.

[12]   R.D. Adams, F.A. Cotton, *Catalysis by di- and polynuclear metal cluster complexes*, Wiley-VCH, 1998.

[13]   M.-L. Louillat, F.W. Patureau, *Toward Polynuclear Ru-Cu Catalytic Dehydrogenative C-N Bond Formation, on the Reactivity of Carbazoles*, Organic Letters, **15** (2013) 164-167.

[14]   H.M.L. Davies, J.R. Manning, *Catalytic C-H functionalization by metal carbenoid and nitrenoid insertion*, Nature, **451** (2008) 417-424.

[15]   G.M. Sammis, H. Danjo, E.N. Jacobsen, *Cooperative dual catalysis: Application to the highly enantioselective conjugate cyanation of unsaturated imides*, Journal of the American Chemical Society, **126** (2004) 9928-9929.

[16]   C.S. Yeh, Y.G. Byun, S. Afzaal, S.Z. Kan, S. Lee, B.S. Freiser, P.J. Hay, *Experimental and theoretical-studies on Nb4C40/+ - reactivity and structure of the smallest cubic niobium-carbon cluster*, Journal of the American Chemical Society, **117** (1995) 4042-4048.

[17]   Y.G. Byun, S.Z. Kan, S.A. Lee, Y.H. Kim, M. Miletic, R.E. Bleil, S. Kais, B.S. Freiser, *Experimental and theoretical studies of Nb6C7(0/+)*, Journal of Physical Chemistry, **100** (1996) 6336-6341.

[18]   M.R. Zakin, R.O. Brickman, D.M. Cox, A. Kaldor, *Dependence of metal cluster reaction-kinetics on charge state .2. Chemisorption of hydrogen by neutral and positively charged iron clusters*, Journal of Chemical Physics, **88** (1988) 6605-6610.

[19]   J.L. Elkind, F.D. Weiss, J.M. Alford, R.T. Laaksonen, R.E. Smalley, *Fourier-Transform Ion Cyclotron Resonance studies of H-2 chemisorption on niobium cluster cations*, Journal of Chemical Physics, **88** (1988) 5215-5224.

[20]   R.S. Walters, T.D. Jaeger, M.A. Duncan, *Infrared Spectroscopy of Ni+(C2H2)(n) complexes: Evidence for intracluster cyclization reactions*, Journal of Physical Chemistry A, **106** (2002) 10482-10487.

[21]   P.J. Brucat, C.L. Pettiette, S. Yang, L.S. Zheng, M.J. Craycraft, R.E. Smalley, *Charge dependence of chemisorption patterns for transition-metal clusters*, Journal of Chemical Physics, **85** (1986) 4747-4748.

[22]   M.P. Irion, *Size effects in metal cluster-ion chemistry*, International Journal of Mass Spectrometry and Ion Processes, **121** (1992) 1-47.

[23]   P.B. Armentrout, *Reactions and thermochemistry of small transition metal cluster ions*, Annual Review of Physical Chemistry, **52** (2001) 423-461.

[24]   M.B. Knickelbein, *Reactions of transition metal clusters with small molecules*, Annual Review of Physical Chemistry, **50** (1999) 79-115.

[25]   S. Wei, B.C. Guo, H.T. Deng, K. Kerns, J. Purnell, S.A. Buzza, A.W. Castleman, *Formation of Met-cars and face-centered-cubic structures - thermodynamically or kinetically controlled*, Journal of the American Chemical Society, **116** (1994) 4475-4476.

[26]   J. Harris, S. Andersson, *H-2 dissociation at metal-surfaces*, Physical Review Letters, **55** (1985) 1583-1586.

[27]   J.S. Pilgrim, L.R. Brock, M.A. Duncan, *Photodissociation of niobium - carbon clusters and nanocrystals*, Journal of Physical Chemistry, **99** (1995) 544-550.

[28]   M.R. Zakin, R.O. Brickman, D.M. Cox, A. Kaldor, *Dependence of metal cluster reaction-kinetics on charge state .1. Reaction of neutral (Nbx) and ionic (Nbx+, Nbx-) niobium clusters with D2*, Journal of Chemical Physics, **88** (1988) 3555-3560.

[29]   A. Berces, P.A. Hackett, L. Lian, S.A. Mitchell, D.M. Rayner, *Reactivity of niobium clusters with nitrogen and deuterium*, Journal of Chemical Physics, **108** (1998) 5476-5490.

[30]   D.C. Parent, S.L. Anderson, *Chemistry of metal and semimetal cluster ions*, Chemical Reviews, **92** (1992) 1541-1565.

[31]   K. Eller, H. Schwarz, *Organometallic chemistry in the gas-phase*, Chemical Reviews, **91** (1991) 1121-1177.

[32]   U. Achatz, C. Berg, S. Joos, B.S. Fox, M.K. Beyer, G. Niedner-Schatteburg, V.E. Bondybey, *Methane activation by platinum cluster ions in the gas phase: effects of cluster charge on the Pt-4 tetramer*, Chemical Physics Letters, **320** (2000) 53-58.

[33]   G. Albert, C. Berg, M. Beyer, U. Achatz, S. Joos, G. NiednerSchatteburg, V.E. Bondybey, *Methane activation by rhodium cluster argon complexes*, Chemical Physics Letters, **268** (1997) 235-241.

[34]   R.L. Whetten, D.M. Cox, D.J. Trevor, A. Kaldor, *Correspondence between electron-binding energy and chemisorption reactivity of iron clusters*, Physical Review Letters, **54** (1985) 1494-1497.

[35]   J. Ho, L. Zhu, E.K. Parks, S.J. Riley, *Temperature-dependence of the reactions of small cobalt clusters with deuterium*, Journal of Chemical Physics, **99** (1993) 140-147.

[36]   R.C. Dunbar, *Photodissociation of trapped ions*, International Journal of Mass Spectrometry, **200** (2000) 571-589.

[37]   T.D. Jaeger, M.A. Duncan, *Vibrational spectroscopy of Ni+(benzene)(n) complexes in the gas phase*, Journal of Physical Chemistry A, **109** (2005) 3311-3317.

[38]   T.D. Jaeger, D. van Heijnsbergen, S.J. Klippenstein, G. von Helden, G. Meijer, M.A. Duncan, *Vibrational spectroscopy and density functional theory of transition-metal ion-benzene and dibenzene complexes in the gas phase*, Journal of the American Chemical Society, **126** (2004) 10981-10991.

[39]   D. van Heijnsbergen, T.D. Jaeger, G. von Helden, G. Meijer, M.A. Duncan, *The infrared spectrum of Al+-benzene in the gas phase*, Chemical Physics Letters, **364** (2002) 345-351.

[40]   H.P. Fritz, W. Luttke, H. Stammreich, R. Forneris, *IR-Untersuchungen und Ramen-Untersuchungen zur Struktur des Di-Benzol-Chroms, seines Kations sowie verwandter Verbindungen*, Spectrochimica Acta, **17** (1961) 1068-1091.

[41]   G.M. Koretsky, M.B. Knickelbein, *Infrared photodissociation spectroscopy of Ag-n(C6H6)(m) and Ag-n(C6D6)(m) clusters: Evidence of adsorption-induced symmetry reduction in benzene*, Chemical Physics Letters, **267** (1997) 485-490.

[42]   N.R. Walker, R.S. Walters, M.A. Duncan, *Frontiers in the infrared spectroscopy of gas phase metal ion complexes*, New Journal of Chemistry, **29** (2005) 1495-1503.

[43]   M.R. Zakin, D.M. Cox, A. Kaldor, *Reaction of niobium clusters with benzene-H6 and benzene-D6 - evidence for cluster-induced dehydrogenation*, Journal of Physical Chemistry, **91** (1987) 5224-5228.

[44]   C. Berg, T. Schindler, A. Lammers, G. Niednerschatteburg, V.E. Bondybey, *Dehydrogenation of xylene isomers on niobium cluster cations Nb-n(+) (n=2-26)*, Journal of Physical Chemistry, **99** (1995) 15497-15501.

[45]   M.R. Zakin, R.O. Brickman, D.M. Cox, A. Kaldor, *Size-selective dehydrogenation of benzene by gas-phase niobium cluster ions (Nbx+)*, Journal of Chemical Physics, **88** (1988) 5943-5947.

[46]   G.M. Koretsky, M.B. Knickelbein, *The reactions of silver clusters with ethylene and ethylene oxide: Infrared and photoionization studies of Agn(C2H4)(m), Ag-n(C2H4O)(m) and their deuterated analogs*, Journal of Chemical Physics, **107** (1997) 10555-10566.

[47]   C. Berg, M. Beyer, U. Achatz, S. Joos, G. Niedner-Schatteburg, V.E. Bondybey, *Effect of charge upon metal cluster chemistry: Reactions of Nb-n and Rh-n anions and cations with benzene*, Journal of Chemical Physics, **108** (1998) 5398-5403.

[48]   C. Berg, M. Beyer, T. Schindler, G. NiednerSchatteburg, V.E. Bondybey, *Reactions of benzene with rhodium cluster cations: Competition between chemisorption and physisorption*, Journal of Chemical Physics, **104** (1996) 7940-7946.

[49]   C. Berg, T. Schindler, M. Kantlehner, G. Niedner-Schatteburg, V.E. Bondybey, *Reactions of homonuclear and heteronuclear group Vb clusters with ethylene: evidence for structural isomers*, Chemical Physics, **262** (2000) 143-149.

[50]   C. Berg, T. Schindler, G. Niednerschatteburg, V.E. Bondybey, *Reactions of simple hydrocarbons with Nb-n(+) - chemisorption and physisorption on ionized niobium clusters*, Journal of Chemical Physics, **102** (1995) 4870-4884.

[51]   B. Pfeffer, S. Jaberg, G. Niedner-Schatteburg, *Reactions of simple aromatic heterocycles with niobium cluster ions (n < 30)*, Journal of Chemical Physics, **131** (2009).

[52]   M. Gerhards, O.C. Thomas, J.M. Nilles, W.J. Zheng, K.H. Bowen, *Cobalt-benzene cluster anions: Mass spectrometry and negative ion photoelectron spectroscopy*, Journal of Chemical Physics, **116** (2002) 10247-10252.

[53]   S. Jaberg, *Reaktivitätsstudien von Übergangsmetallclustern in der Gasphase mittels Fourier-Transformation-Ionen-Zyklotron-Resonanz-Massenspektrometrie und Infrarot-Multiphotonen-Dissoziation von Adipinsäure*, Doktorarbeit, Fachbereich Chemie, Technische Universität, 2008, Kaiserslautern.

[54]   B. Pfeffer, *Reaktivitätsstudien zur Aktivierung kleiner Kohlenwasserstoffe an Übergangsmetallclustern*, Doktorarbeit, Fachbereich Chemie, Technische Universität, 2008, Kaiserslautern.

[55]   V.E. Bondybey, M.K. Beyer, *Temperature effects in transition metal ion and cluster ion reactions*, Journal of Physical Chemistry A, **105** (2001) 951-960.

[56]   E.R. Fisher, P.B. Armentrout, *Reactions of Co+, Ni+, and Cu+ with cyclopropane and ethylene-oxide - metal methylidene ion bond-energies*, Journal of Physical Chemistry, **94** (1990) 1674-1683.

[57]   H.T. Liu, S.T. Sun, X.P. Xing, Z.C. Tang, *Reactions of platinum cluster ions with benzene*, Rapid Communications in Mass Spectrometry, **20** (2006) 1899-1904.

[58]   D. Majumdar, S. Roszak, K. Balasubramanian, *Interaction of benzene (Bz) with Pt and Pt-2: A theoretical study on Bz-Pt-2, Bz(2)-Pt-2, and Bz(3)-Pt-2 clusters*, Journal of Chemical Physics, **114** (2001) 10300-10310.

[59]   K. Bechamp, M. Levesque, H. Joly, L. Manceron, *A combined electron paramagnetic resonance and Fourier transform infrared study of the Co(C6H6)(1,2) complexes isolated in neat benzene or in cryogenic matrixes*, Journal of Physical Chemistry A, **110** (2006) 6023-6031.

[60]   D. van Heijnsbergen, G. von Helden, M.A. Duncan, A.J.A. van Roij, G. Meijer, *Vibrational spectroscopy of gas-phase metal-carbide clusters and nanocrystals*, Physical Review Letters, **83** (1999) 4983-4986.

[61]   H. Harris, I. Dance, *The geometric and electronic structures of niobium carbon clusters*, Journal of Physical Chemistry A, **105** (2001) 3340-3358.

[62]   I. Swart, F.M.F. de Groot, B.M. Weckhuysen, P. Gruene, G. Meijer, A. Fielicke, *H-2 adsorption on 3d transition metal clusters: A combined infrared spectroscopy and density functional study*, Journal of Physical Chemistry A, **112** (2008) 1139-1149.

[63]   I. Swart, P. Gruene, A. Fielicke, G. Meijer, B.M. Weckhuysen, F.M.F. de Groot, *Molecular adsorption of H(2) on small cationic nickel clusters*, Physical Chemistry Chemical Physics, **10** (2008) 5743-5745.

[64]   I. Swart, F.M.F. de Groot, B.M. Weckhuysen, D.M. Rayner, G. Meijer, A. Fielicke, *The effect of charge on CO binding in rhodium carbonyls: From bridging to terminal CO*, Journal of the American Chemical Society, **130** (2008) 2126-+.

[65]   V. Dryza, E.J. Bieske, *Infrared Spectroscopy of the Ag+-H-2 Complex: Exploring the Connection Between Vibrational Band-Shifts and Binding Energies*, Journal of Physical Chemistry Letters, **2** (2011) 719-724.

[66]   M.B. Knickelbein, G.M. Koretsky, *Infrared studies of the interaction of methanol with Cu-n, Ag-n, and Au-n*, Journal of Physical Chemistry A, **102** (1998) 580-586.

[67]   R. Rousseau, G. Dietrich, S. Kruckeberg, K. Lutzenkirchen, D. Marx, L. Schweikhard, C. Walther, *Probing cluster structures with sensor molecules: methanol adsorbed onto gold clusters*, Chemical Physics Letters, **295** (1998) 41-46.

[68]   G. Dietrich, K. Dasgupta, S. Kruckeberg, K. Lutzenkirchen, L. Schweikhard, C. Walther, J. Ziegler, *Infrared photodesorption of methanol molecules adsorbed on a Au-4(+) cluster*, Chemical Physics Letters, **259** (1996) 397-402.

[69]   E.D. Pillai, T.D. Jaeger, M.A. Duncan, *IR spectroscopy of Nb+(N-2)(n) complexes: Coordination, structures, and spin states*, Journal of the American Chemical Society, **129** (2007) 2297-2307.

[70]   D. van Heijnsbergen, A. Fielicke, G. Meijer, G. von Helden, *Structure determination of gas-phase niobium and tantalum carbide nanocrystals via infrared spectroscopy*, Physical Review Letters, **89** (2002) 013401-013401.

[71]   H. Kietzmann, J. Morenzin, P.S. Bechthold, G. Gantefor, W. Eberhardt, D.S. Yang, P.A. Hackett, R. Fournier, T. Pang, C.F. Chen, *Photoelectron spectra and geometric structures of small niobium cluster anions*, Physical Review Letters, **77** (1996) 4528-4531.

[72]   I. Swart, A. Fielicke, B. Redlich, G. Meijer, B.M. Weckhuysen, F.M.F. de Groot, *Hydrogen-induced transition from dissociative to molecular chemisorption of CO on vanadium clusters*, Journal of the American Chemical Society, **129** (2007) 2516-2520.

[73]   A. Fielicke, G. von Helden, G. Meijer, D.B. Pedersen, B. Simard, D.M. Rayner, *Size and charge effects on the binding of CO to small isolated rhodium clusters*, Journal of Physical Chemistry B, **108** (2004) 14591-14598.

[74]   M.R. Zakin, R.O. Brickman, D.M. Cox, K.C. Reichmann, D.J. Trevor, A. Kaldor, *Infrared-spectroscopy of unsupported metal cluster complexes using multiple photon dissociation*, Journal of Chemical Physics, **85** (1986) 1198-1199.

[75]   M.B. Knickelbein, *Infrared-spectroscopy of metal cluster-adsorbate complexes - Fe-n(CH3OH)(m) revisited*, Chemical Physics Letters, **239** (1995) 11-17.

[76]   U. Frenzel, A. Roggenkamp, D. Kreisle, *Black-body radiation of free niobium clusters heated by oxidation*, Chemical Physics Letters, **240** (1995) 109-113.

[77]   M.B. Knickelbein, *The infrared photodissociation spectra of Fe-n(CH3OH)(m) complexes and their deuterated analogs near 10 mu*, Journal of Chemical Physics, **104** (1996) 3517-3525.

[78]   B.M. Reinhard, A. Lagutschenkov, J. Lemaire, P. Maitre, P. Boissel, G. Niedner-Schatteburg, *Reductive nitrile coupling in niobium-acetonitrile complexes probed by free electron laser IR multiphoton dissociation spectroscopy*, Journal of Physical Chemistry A, **108** (2004) 3350-3355.

[79]   S. Hirabayashi, R. Okawa, M. Ichihashi, Y. Kawazoe, T. Kondow, *Structures and reactions of methanol molecules on cobalt cluster ions studied by infrared photodissociation spectroscopy*, Journal of Chemical Physics, **130** (2009).

[80]   S. Minemoto, A. Terasaki, T. Kondow, *Electronic and geometric structures of vanadium cluster ions; V-n(+) (n=3-5), studied by optical absorption spectroscopy*, Journal of Electron Spectroscopy and Related Phenomena, **106** (2000) 171-178.

[81]   D.G. Leopold, W.C. Lineberger, *A study of the low-lying electronic states of Fe2 and Co2 by negative-ion photoelectron-spectroscopy*, Journal of Chemical Physics, **85** (1986) 51-55.

[82]   D. Schooss, S. Gilb, J. Kaller, M.M. Kappes, F. Furche, A. Kohn, K. May, R. Ahlrichs, *Photodissociation spectroscopy of Ag-4(+)(N-2)(m), m=0-4*, Journal of Chemical Physics, **113** (2000) 5361-5371.

[83]   R.L. Whetten, M.R. Zakin, D.M. Cox, D.J. Trevor, A. Kaldor, *Electron-binding and chemical inertness of specific Nbx clusters*, Journal of Chemical Physics, **85** (1986) 1697-1698.

[84]   H. Kietzmann, J. Morenzin, P.S. Bechthold, G. Gantefor, W. Eberhardt, *Photoelectron spectra of Nb-n(-) clusters: Correlation between electronic structure and hydrogen chemisorption*, Journal of Chemical Physics, **109** (1998) 2275-2278.

[85]   M. Ichihashi, C.A. Corbett, T. Hanmura, J.M. Lisy, T. Kondow, *Size-specific reactions of copper cluster ions with a methanol molecule*, Journal of Physical Chemistry A, **109** (2005) 7872-7880.

[86]   J. Conceicao, R.T. Laaksonen, L.S. Wang, T. Guo, P. Nordlander, R.E. Smalley, *Photoelectron-spectroscopy of transition-metal clusters - correlation of valence electronic-structure to reactivity*, Physical Review B, **51** (1995) 4668-4671.

[87]   S. Hirabayashi, R. Okawa, M. Ichihashi, T. Kondow, *Detection of OH stretching mode of CH3OH chemisorbed on Ni-3(+) and Ni-4(+) by infrared photodissociation Spectroscopy*, Journal of Physical Chemistry A, **111** (2007) 7664-7669.

[88]   P.M. Bialach, M. Braun, A. Luechow, M. Gerhards, *Structures of isolated Co-2(alcohol)(1) cluster anions*, Physical Chemistry Chemical Physics, **11** (2009) 10403-10408.

[89]   P.M. Bialach, A. Funk, M. Weiler, M. Gerhards, *IR spectroscopy on isolated Co-n(alcohol)(m) cluster anions (n=1-4, m=1-3): Structures and spin states*, Journal of Chemical Physics, **133** (2010).

[90]   A. Fielicke, A. Kirilyuk, C. Ratsch, J. Behler, M. Scheffler, G. von Helden, G. Meijer, *Structure determination of isolated metal clusters via far-infrared spectroscopy*, Physical Review Letters, **93** (2004).

[91]   A. Fielicke, C. Ratsch, G. von Helden, G. Meijer, *Isomer selective infrared spectroscopy of neutral metal clusters*, Journal of Chemical Physics, **122** (2005).

[92]   A. Fielicke, C. Ratsch, G. von Helden, G. Meijer, *The far-infrared spectra of neutral and cationic niobium clusters: Nb(5)(0/+) to Nb(9)(0/+)*, Journal of Chemical Physics, **127** (2007).

[93]   C. Ratsch, A. Fielicke, A. Kirilyuk, J. Behler, G. von Helden, G. Meijer, M. Scheffler, *Structure determination of small vanadium clusters by density-functional theory in comparison with experimental far-infrared spectra*, Journal of Chemical Physics, **122** (2005).

[94]   B.A. Collings, K. Athanassenas, D. Lacombe, D.M. Rayner, P.A. Hackett, *Optical-absorption spectra of Au-7, Au-9, Au-11 and Au-13 and their cations - gold clusters with 6, 7, 8, 9, 10, 11, 12, and 13 s-electrons*, Journal of Chemical Physics, **101** (1994) 3506-3513.

[95]   B.A. Collings, K. Athanassenas, D.M. Rayner, P.A. Hackett, *Absorption-spectra of small niobium and gold clusters measured by photodepletion of their rare-gas van-der-Waals complexes - some preliminary experiments*, Zeitschrift Fur Physik D-Atoms Molecules and Clusters, **26** (1993) 36-40.

[96]   B.A. Collings, K. Athanassenas, D.M. Rayner, P.A. Hackett, *Optical spectroscopy of Ag7, Ag-9+, and Ag9 - a test of the photodepletion method*, Chemical Physics Letters, **227** (1994) 490-495.

[97]   M.B. Knickelbein, *The absorption spectra of small nickel clusters via photodissociation - NinArm- Nin+mAr*, Journal of Chemical Physics, **99** (1993) 2377-2382.

[98]   M.B. Knickelbein, W.J.C. Menezes, *Optical-response of small niobium clusters*, Physical Review Letters, **69** (1992) 1046-1049.

[99]   W.J.C. Menezes, M.B. Knickelbein, *Photodissociation spectroscopy of NbnArm complexes*, Journal of Chemical Physics, **98** (1993) 1856-1866.

[100]   E.V. Anslyn, D.A. Dougherty, *Modern Physical Organic Chemistry*, University Science Books, Sausalito, 2006.

[101]   A. Kohen, H.-H. Limbach, *Isotope Effects in Chemistry and Biology*, CRC Press, Boca Raton, 2006.

[102]   H.S. Johnston, *Gas Phase Reaction State Theory*, The Ronald Press Company, New York, 1966.

[103]   L. Melander, W.A. Saunders Jr., *Reaction Rates of Isotopic Molecules*, Wiley, New York, 1980.

[104]   K.B. Wiberg, *The deuterium isotope effect*, Chemical Reviews, **55** (1955) 713-743.

[105]   E.G. Robertson, J.P. Simons, *Getting into shape: Conformational and supramolecular landscapes in small biomolecules and their hydrated clusters*, Physical Chemistry Chemical Physics, **3** (2001) 1-18.

[106]   S. Hoyau, G. Ohanessian, *Interaction of alkali metal cations (Li+-Cs+) with glycine in the gas phase: A theoretical study*, Chemistry-a European Journal, **4** (1998) 1561-1569.

[107]   C. Kapota, J. Lemaire, P. Maitre, G. Ohanessian, *Vibrational signature of charge solvation vs salt bridge isomers of sodiated amino acids in the gas phase*, Journal of the American Chemical Society, **126** (2004) 1836-1842.

[108]   N.C. Polfer, B. Paizs, L.C. Snoek, I. Compagnon, S. Suhai, G. Meijer, G. von Helden, J. Oomens, *Infrared fingerprint spectroscopy and theoretical studies of potassium ion tagged amino acids and peptides in the gas phase*, Journal of the American Chemical Society, **127** (2005) 8571-8579.

[109]   M.W. Forbes, M.F. Bush, N.C. Polfer, J. Oomens, R.C. Dunbar, E.R. Williams, R.A. Jockusch, *Infrared spectroscopy of arginine cation complexes: Direct observation of gas-phase zwitterions*, Journal of Physical Chemistry A, **111** (2007) 11759-11770.

[110]   M.F. Bush, J.T. O'Brien, J.S. Prell, R.J. Saykally, E.R. Williams, *Infrared spectroscopy of cationized arginine in the gas phase: Direct evidence for the transition from nonzwitterionic to zwitterionic structure*, Journal of the American Chemical Society, **129** (2007) 1612-1622.

[111]   M.F. Bush, M.W. Forbes, R.A. Jockusch, J. Oomens, N.C. Polfer, R.J. Saykally, E.R. Williams, *Infrared spectroscopy of cationized lysine and epsilon-N-methyllysine in the gas phase: Effects of alkali-metal ion size and proton affinity on zwitterion stability*, Journal of Physical Chemistry A, **111** (2007) 7753-7760.

[112]   M.F. Bush, J. Oomens, E.R. Williams, *Proton Affinity and Zwitterion Stability: New Results from Infrared Spectroscopy and Theory of Cationized Lysine and Analogues in the Gas Phase*, Journal of Physical Chemistry A, **113** (2009) 431-438.

[113]   M.K. Drayss, D. Blunk, J. Oomens, M. Schaefer, *Infrared Multiple Photon Dissociation Spectroscopy of Potassiated Proline*, Journal of Physical Chemistry A, **112** (2008) 11972-11974.

[114]   P.B. Armentrout, M.T. Rodgers, J. Oomens, J.D. Steill, *Infrared multiphoton dissociation spectroscopy of cationized serine: Effects of alkali-metal cation size on gas-phase conformation*, Journal of Physical Chemistry A, **112** (2008) 2248-2257.

[115]   M.F. Bush, J. Oomens, R.J. Saykally, E.R. Williams, *Alkali metal ion binding to glutamine and glutamine derivatives investigated by infrared action spectroscopy and theory*, Journal of Physical Chemistry A, **112** (2008) 8578-8584.

[116]   M.T. Rodgers, P.B. Armentrout, J. Oomens, J.D. Steill, *Infrared multiphoton dissociation spectroscopy of cationized threonine: Effects of alkali-metal cation size on gas-phase conformation*, Journal of Physical Chemistry A, **112** (2008) 2258-2267.

[117]   A.L. Heaton, V.N. Bowman, J. Oomens, J.D. Steill, P.B. Armentrout, *Infrared Multiple Photon Dissociation Spectroscopy of Cationized Asparagine: Effects of Metal Cation Size on Gas-Phase Conformation*, Journal of Physical Chemistry A, **113** (2009) 5519-5530.

[118]   M.K. Drayss, P.B. Armentrout, J. Oomens, M. Schaefer, *IR spectroscopy of cationized aliphatic amino acids: Stability of charge-solvated structure increases with metal cation size*, International Journal of Mass Spectrometry, **297** (2010) 18-27.

[119]   D.R. Carl, T.E. Cooper, J. Oomens, J.D. Steill, P.B. Armentrout, *Infrared multiple photon dissociation spectroscopy of cationized methionine: effects of alkali-metal cation size on gas-phase conformation*, Physical Chemistry Chemical Physics, **12** (2010) 3384-3398.

[120]   M. Citir, E.M.S. Stennett, J. Oomens, J.D. Steill, M.T. Rodgers, P.B. Armentrout, *Infrared multiple photon dissociation spectroscopy of cationized cysteine: Effects of metal cation size on gas-phase conformation*, International Journal of Mass Spectrometry, **297** (2010) 9-17.

[121]   R.C. Dunbar, J.D. Steill, J. Oomens, *Cationized phenylalanine conformations characterized by IRMPD and computation for singly and doubly charged ions*, Physical Chemistry Chemical Physics, **12** (2010) 13383-13393.

[122]   M. Citir, C.S. Hinton, J. Oomens, J.D. Steill, P.B. Armentrout, *Infrared Multiple Photon Dissociation Spectroscopy of Cationized Histidine: Effects of Metal Cation Size on Gas-Phase Conformation*, Journal of Physical Chemistry A, **116** (2012) 1532-1541.

[123]   J.T. O'Brien, J.S. Prell, J.D. Steill, J. Oomens, E.R. Williams, *Interactions of mono- and divalent metal ions with Aspartic and Glutamic acid investigated with IR photodissociation spectroscopy and theory*, Journal of Physical Chemistry A, **112** (2008) 10823-10830.

[124]   E. deHoffmann, V. Stroobant, *Mass Spectrometry: Principles and Applications*, Third ed., John Wiley & Sons Ltd., Chichester, West Sussex, England, 2007.

[125]   J.H. Gross, *Massenspektrometrie: Ein Lehrbuch*, Springer Spektrum, Berlin Heidelberg, 2013.

[126]   W. Paul, H. Steinwedel, *Ein neues Massenspektrometer ohne Magnetfeld*, Zeitschrift Fur Naturforschung Section a-a Journal of Physical Sciences, **8** (1953) 448-450.

[127]   W. Paul, H. Steinwedel, *Apparatus for separating charged particles of different specific charges, US patent 2939952*, in: US patent, 1960.

[128]   G.C. Stafford, P.E. Kelley, J.E.P. Syka, W.E. Reynolds, J.F.J. Todd, *Recent improvements in and analytical applications of advanced ion trap technology*, International Journal of Mass Spectrometry and Ion Processes, **60** (1984) 85-98.

[129]   J.F.J. Todd, *Ion trap mass-spectrometer - past, present, and future*, Mass Spectrometry Reviews, **10** (1991) 3-52.

[130]   E.O. Lawrence, D. Cooksey, *On the Apparatus for the Multiple Acceleration of Light Ions to High Speeds*, Physical Review, **50** (1936) 1131-1140.

[131]   Comisaro.Mb, A.G. Marshall, *Fourier-Transform Ion-Cyclotron Resonance spectroscopy*, Chemical Physics Letters, **25** (1974) 282-283.

[132]   Comisaro.Mb, A.G. Marshall, *Frequency-sweep Fourier-Transform Ion-Cyclotron Resonance spectroscopy*, Chemical Physics Letters, **26** (1974) 489-490.

[133]   I.J. Amster, *Fourier transform mass spectrometry*, Journal of Mass Spectrometry, **31** (1996) 1325-1337.

[134]   A.G. Marshall, C.L. Hendrickson, G.S. Jackson, *Fourier transform ion cyclotron resonance mass spectrometry: A primer*, Mass Spectrometry Reviews, **17** (1998) 1-35.

[135]   P. Caravatti, M. Allemann, *The infinity cell - a new trapped-ion cell with radiofrequency covered trapping electrodes for Fourier-Transform Ion-Cyclotron Resonance mass-spectrometry*, Organic Mass Spectrometry, **26** (1991) 514-518.

[136]   L.S. Brown, G. Gabrielse, *Geonium theory - physics of a single electron or ion in a Penning trap*, Reviews of Modern Physics, **58** (1986) 233-311.

[137]   J.B. Fenn, M. Mann, C.K. Meng, S.F. Wong, C.M. Whitehouse, *Electrospray ionization for mass-spectrometry of large biomolecules*, Science, **246** (1989) 64-71.

[138]   M. Mann, C.K. Meng, J.B. Fenn, *Interpreting mass-spectra of multiply charged ions*, Analytical Chemistry, **61** (1989) 1702-1708.

[139] M. Yamashita, J.B. Fenn, *Electrospray ion-source - another variation on the free-jet theme*, Journal of Physical Chemistry, **88** (1984) 4451-4459.

[140] M. Yamashita, J.B. Fenn, *Negative-ion production with the electrospray ion-source*, Journal of Physical Chemistry, **88** (1984) 4671-4675.

[141] J.A. Loo, H.R. Udseth, R.D. Smith, *Peptide and protein-analysis by electrospray ionization mass-spectrometry and capillary electrophoresis mass-spectrometry*, Analytical Biochemistry, **179** (1989) 404-412.

[142] M.G. Ikonomou, A.T. Blades, P. Kebarle, *Investigations of the electrospray interface for liquid-chromatography mass-spectrometry*, Analytical Chemistry, **62** (1990) 957-967.

[143] R.D. Smith, J.A. Loo, C.G. Edmonds, C.J. Barinaga, H.R. Udseth, *New developments in biochemical mass-spectrometry - electrospray ionization*, Analytical Chemistry, **62** (1990) 882-899.

[144] M. Mann, *Electrospray - its potential and limitations as an ionization method for biomolecules*, Organic Mass Spectrometry, **25** (1990) 575-587.

[145] J.F. de la Mora, G.J. Van Berkel, C.G. Enke, R.B. Cole, M. Martinez-Sanchez, J.B. Fenn, *Electrochemical processes in electrospray ionization mass spectrometry - Discussion*, Journal of Mass Spectrometry, **35** (2000) 939-952.

[146] N.B. Cech, C.G. Enke, *Practical implications of some recent studies in electrospray ionization fundamentals*, Mass Spectrometry Reviews, **20** (2001) 362-387.

[147] T.C. Rohner, N. Lion, H.H. Girault, *Electrochemical and theoretical aspects of electrospray ionisation*, Physical Chemistry Chemical Physics, **6** (2004) 3056-3068.

[148] A.P. Snyder, A.C.S.D.o.A. Chemistry, A.C.S. Meeting, *Biochemical and biotechnological applications of electrospray ionization mass spectrometry*, American Chemical Society, 1996.

[149] R.B. Cole, *Electrospray ionization mass spectrometry: fundamentals, instrumentation, and applications*, Wiley, 1997.

[150] R.B. Cole, *Electrospray and MALDI Mass Spectrometry: Fundamentals, Instrumentation, Practicalities, and Biological Applications*, Wiley, 2011.

[151] A. Gomez, K.Q. Tang, *Charge and fission of droplets in eletcrostatic sprays*, Physics of Fluids, **6** (1994) 404-414.

[152] P. Kebarle, L. Tang, *From ions in solution to ions in the gas-phase - the mechanism of electrospray mass-spectrometry*, Analytical Chemistry, **65** (1993) A972-A986.

[153] C. Berg, T. Schindler, G. Niednerschatteburg, V.E. Bondybey, *Reactions of simple Hydrocarbons with Nb_n^+ - Chemisorption and Physisorption on Ionized Niobium Clusters*, Journal of Chemical Physics, **102** (1995) 4870-4884.

[154] S. Maruyama, L.R. Anderson, R.E. Smalley, *Direct injection supersonic cluster beam source for FT-ICR studies of clusters*, Review of Scientific Instruments, **61** (1990) 3686-3693.

[155] T.G. Dietz, M.A. Duncan, D.E. Powers, R.E. Smalley, *Laser production of supersonic metal cluster beams*, Journal of Chemical Physics, **74** (1981) 6511-6512.

[156] D. Proch, T. Trickl, *A high-intensity multi-purpose piezoelectric pulsed molecular-beam source*, Review of Scientific Instruments, **60** (1989) 713-716.

[157] W. Demtröder, *Laserspektroskopie 1: Grundlagen*, Springer, 2011.

[158] D.A.G. Deacon, L.R. Elias, J.M.J. Madey, G.J. Ramian, H.A. Schwettman, T.I. Smith, *1st operation of a Free-Electron Laser*, Physical Review Letters, **38** (1977) 892-894.

[159] M.E. Couprie, J.M. Ortega, *Free-electron lasers sources for scientific applications*, Analusis, **28** (2000) 725-736.

[160] D. Oepts, A.F.G. Vandermeer, P.W. Vanamersfoort, *The Free-Electron-Laser user facility FELIX*, Infrared Physics & Technology, **36** (1995) 297-308.

[161] J.J. Valle, J.R. Eyler, J. Oomens, D.T. Moore, A.F.G. van der Meer, G. von Helden, G. Meijer, C.L. Hendrickson, A.G. Marshall, G.T. Blakney, *Free electron laser-Fourier transform ion cyclotron resonance mass spectrometry facility for obtaining infrared multiphoton dissociation spectra of gaseous ions*, Review of Scientific Instruments, **76** (2005).

[162] R. Prazeres, F. Glotin, J.M. Ortega, C. Rippon, R. Andouart, J.M. Berset, E. Arnaud, R. Chaput, *Study of the "CLIO" FEL properties at long wavelengths*, Nuclear Instruments and Methods in

Physics Research Section A: Accelerators, Spectrometers, Detectors and Associated Equipment, **445** (2000) 204-207.

[163] J.M. Ortega, J.M. Berset, R. Chaput, F. Glotin, G. Humbert, D. Jaroszynski, P. Joly, B. Kergosien, J. Lesrel, O. Marcouillé, A. Peremans, R. Prazeres, A. Tadjeddine, *Activities of the CLIO infrared facility*, Nuclear Instruments and Methods in Physics Research Section A: Accelerators, Spectrometers, Detectors and Associated Equipment, **375** (1996) 618-625.

[164] S.E. Harris, M.K. Oshman, R.L. Byer, *Observation of tunable optical parametric fluorescence*, Physical Review Letters, **18** (1967) 732-&.

[165] R.L. Byer, *Parametric oscillators and nonlinear materials*, in: P.G. Harper, B.S. Wherret (Eds.) *Nonlinear Optics*, Academic, London, 1977.

[166] J.G. Haub, M.J. Johnson, B.J. Orr, R. Wallenstein, *Continuously tunable, injection-seeded beta-barium borate optical parametric oscillator - spectroscopic applications*, Applied Physics Letters, **58** (1991) 1718-1720.

[167] F.W. McLafferty, P.F. Bente, R. Kornfeld, S.-C. Tsai, I. Howe, *Metastable ion characteristics. XXII. Collisional activation spectra of organic ions*, Journal of the American Chemical Society, **95** (1973) 2120-2129.

[168] K. Levsen, H. Schwarz, *Stoßaktivierungsmassenspektrometrie - eine neue Sonde zur Strukturbestimmung von Ionen in der Gasphase*, Angewandte Chemie, **88** (1976) 589-599.

[169] R.G. Cooks, *Collision-induced dissociation - readings and commentary*, Journal of Mass Spectrometry, **30** (1995) 1215-1221.

[170] E. deHoffmann, *Tandem mass spectrometry: A primer*, Journal of Mass Spectrometry, **31** (1996) 129-137.

[171] A.K. Shukla, J.H. Futrell, *Tandem mass spectrometry: dissociation of ions by collisional activation*, Journal of Mass Spectrometry, **35** (2000) 1069-1090.

[172] K.R. Jennings, *The changing impact of the collision-induced decomposition of ions on mass spectrometry*, International Journal of Mass Spectrometry, **200** (2000) 479-493.

[173] J. Laskin, J.H. Futrell, *Activation of large ions in FT-ICR mass spectrometry*, Mass Spectrometry Reviews, **24** (2005) 135-167.

[174] H. Zhao, J. Adams, *Mechanisms of fragmentation of cationic peptide ions*, International Journal of Mass Spectrometry and Ion Processes, **125** (1993) 195-205.

[175] M.J. Coggiola, P.A. Schulz, Y.T. Lee, Y.R. Shen, *Molecular-beam study of multiphoton dissociation of SF6*, Physical Review Letters, **38** (1977) 17-20.

[176] E.R. Grant, P.A. Schulz, A.S. Sudbo, Y.R. Shen, Y.T. Lee, *Is multiphoton dissociation of molecules a statistical thermal process*, Physical Review Letters, **40** (1978) 115-118.

[177] R.L. Woodin, D.S. Bomse, J.L. Beauchamp, *Multi-phoon dissociation of molecules with low-power continuous wave infrared-laser radiation*, Journal of the American Chemical Society, **100** (1978) 3248-3250.

[178] R.C. Dunbar, *BIRD (blackbody infrared radiative dissociation): Evolution, principles, and applications*, Mass Spectrometry Reviews, **23** (2004) 127-158.

[179] D.P. Little, J.P. Speir, M.W. Senko, P.B. Oconnor, F.W. McLafferty, *Infrared multiphoton dissociation of large multiply-charged ions for biomolecule sequencing*, Analytical Chemistry, **66** (1994) 2809-2815.

[180] J.S. Brodbelt, J.J. Wilson, *Infrared multiphoton dissociation in quadrupole ion traps*, Mass Spectrometry Reviews, **28** (2009) 390-424.

[181] Y. Hashimoto, H. Hasegawa, L. Waki, *High sensitivity and broad dynamic range infrared multiphoton dissociation for a quadrupole ion trap*, Rapid Communications in Mass Spectrometry, **18** (2004) 2255-2259.

[182] M.W. Gardner, S.I. Smith, A.R. Ledvina, J.A. Madsen, J.J. Coon, J.C. Schwartz, G.C. Stafford, Jr., J.S. Brodbelt, *Infrared Multiphoton Dissociation of Peptide Cations in a Dual Pressure Linear Ion Trap Mass Spectrometer*, Analytical Chemistry, **81** (2009) 8109-8118.

[183] J.A. Madsen, M.W. Gardner, S.I. Smith, A.R. Ledvina, J.J. Coon, J.C. Schwartz, G.C. Stafford, Jr., J.S. Brodbelt, *Top-down protein fragmentation by Infrared Multiphoton Dissociation in a dual pressure linear ion trap*, Analytical Chemistry, **81** (2009) 8677-8686.

[184] K. Hakansson, H.J. Cooper, M.R. Emmett, C.E. Costello, A.G. Marshall, C.L. Nilsson, *Electron capture dissociation and infrared multiphoton dissociation MS/MS of an N-glycosylated tryptic peptide to yield complementary sequence information*, Analytical Chemistry, **73** (2001) 4530-4536.

[185] Y.O. Tsybin, M. Witt, G. Baykut, F. Kjeldsen, P. Hakansson, *Combined infrared multiphoton dissociation and electron capture dissociation with a hollow electron beam in Fourier transform ion cyclotron resonance mass spectrometry*, Rapid Communications in Mass Spectrometry, **17** (2003) 1759-1768.

[186] Y.O. Tsybin, M. Ramstrom, M. Witt, G. Baykut, P. Hakansson, *Peptide and protein characterization by high-rate electron capture dissociation Fourier transform ion cyclotron resonance mass spectrometry*, Journal of Mass Spectrometry, **39** (2004) 719-729.

[187] J. Oomens, A.J.A. van Roij, G. Meijer, G. von Helden, *Gas-phase infrared photodissociation spectroscopy of cationic polyaromatic hydrocarbons*, Astrophysical Journal, **542** (2000) 404-410.

[188] J. Laskin, J.H. Futrell, *Collisional activation of peptide ions in FT-ICR mass spectrometry*, Mass Spectrometry Reviews, **22** (2003) 158-181.

[189] J. Roithova, *Characterization of reaction intermediates by ion spectroscopy*, Chemical Society Reviews, **41** (2012) 547-559.

[190] J. Oomens, B.G. Sartakov, G. Meijer, G. von Helden, *Gas-phase infrared multiple photon dissociation spectroscopy of mass-selected molecular ions*, International Journal of Mass Spectrometry, **254** (2006) 1-19.

[191] J.G. Black, E. Yablonovitch, N. Bloembergen, S. Mukamel, *Collisonless multiphoton dissociation of SF6 - statistical thermodynamic process*, Physical Review Letters, **38** (1977) 1131-1134.

[192] W.H. Green, C.B. Moore, W.F. Polik, *Transition-states and rate constants for unimolecular reactions*, Annual Review of Physical Chemistry, **43** (1992) 591-626.

[193] K.K. Lehmann, G. Scoles, B.H. Pate, *Intramolecular dynamics from Eigenstate-resolved infrared-spectra*, Annual Review of Physical Chemistry, **45** (1994) 241-274.

[194] Rynbrand.Jd, Rabinovi.Bs, *Intramolecular energy relaxation - nonrandom decomposition of hexafluorobicyclopropyl*, Journal of Physical Chemistry, **75** (1971) 2164-&.

[195] S.H.P. Bly, L.W. Dickson, Y. Nomura, J.C. Polanyi, I.W.M. Smith, P.N. Clough, M. Kneba, U. Wellhausen, J. Wolfrum, P.E. Siska, R.J. Wolf, C.S. Sloane, W.L. Hase, L. Holmlid, K. Rynefors, K. Luther, M. Quack, K. Freed, W.M. Jackson, R. Naaman, R.N. Zare, G. Hancock, R. Walsh, J. Troe, D.M. Lubman, G. Atkinson, D.W. Setser, M.R. Levy, M. Mangir, H. Reisler, M.H. Yu, C. Wittig, C.M. Miller, F.M.G. Tablas, M.N.R. Ashfold, A.J. Roberts, I. Veltman, A. Durkin, D.J. Smith, R. Grice, D.R. Herschbach, G.M. McClelland, K.L. Kompa, *General discussion*, Faraday Discussions of the Chemical Society, **67** (1979) 221-254.

[196] O.K. Rice, H.C. Ramsperger, *Theories of unimolecular gas reactions at low pressures*, Journal of the American Chemical Society, **49** (1927) 1617-1629.

[197] L.S. Kassel, *Studies in homogeneous gas reactions I*, Journal of Physical Chemistry, **32** (1928) 225-242.

[198] L.S. Kassel, *Studies in homogeneous gas reactions II Introduction of quantum theory*, Journal of Physical Chemistry, **32** (1928) 1065-1079.

[199] K. Capelle, *A bird's-eye view of density-functional theory*, Brazilian Journal of Physics, **36** (2006) 1318-1343.

[200] P. Hohenberg, W. Kohn, *Inhomogeneous Electron Gas*, Physical Review, **136** (1964) B864-B871.

[201] W. Kohn, L.J. Sham, *Self-Consistent Equations Including Exchange and Correlation Effects*, Physical Review, **140** (1965) A1133-A1138.

[202] S. Grimme, *Accurate description of van der Waals complexes by density functional theory including empirical corrections*, Journal of Computational Chemistry, **25** (2004) 1463-1473.

[203] S. Grimme, *Semiempirical GGA-type density functional constructed with a long-range dispersion correction*, Journal of Computational Chemistry, **27** (2006) 1787-1799.

[204]   S. Grimme, *Semiempirical hybrid density functional with perturbative second-order correlation*, The Journal of Chemical Physics, **124** (2006) 034108.

[205]   M.J. Frisch, M. Headgordon, J.A. Pople, *A direct MP2 gradient-method*, Chemical Physics Letters, **166** (1990) 275-280.

[206]   M.J. Frisch, M. Headgordon, J.A. Pople, *Semidirect algorithms for the MP2 energy and gradient*, Chemical Physics Letters, **166** (1990) 281-289.

[207]   M. Headgordon, T. Headgordon, *Analytical MP2 frequencies without 5th-order storage - theory and application to bifurcated hydrogen-bonds in the water hexamer*, Chemical Physics Letters, **220** (1994) 122-128.

[208]   M. Headgordon, J.A. Pople, M.J. Frisch, *MP2 energy evaluation by direct methods*, Chemical Physics Letters, **153** (1988) 503-506.

[209]   S. Saebo, J. Almlof, *Avoiding the integral storage bottleneck in LCAO calculations of electron correlation*, Chemical Physics Letters, **154** (1989) 83-89.

[210]   K. Schuchardt, B. Didier, G. Black, *Ecce—a problem-solving environment's evolution toward Grid services and a Web architecture*, Concurrency and Computation: Practice and Experience, **14** (2002) 1221-1239.

[211]   M.J. Frisch, G.W. Trucks, H.B. Schlegel, G.E. Scuseria, M.A. Robb, J.R. Cheeseman, J. Montgomery, J. A., T. Vreven, K.N. Kudin, J.C. Burant, J.M. Millam, S.S. Iyengar, J. Tomasi, V. Barone, B. Mennucci, M. Cossi, G. Scalmani, N. Rega, G.A. Petersson, H. Nakatsuji, M. Hada, M. Ehara, K. Toyota, R. Fukuda, J. Hasegawa, M. Ishida, T. Nakajima, Y. Honda, O. Kitao, H. Nakai, M. Klene, X. Li, J.E. Knox, H.P. Hratchian, J.B. Cross, V. Bakken, C. Adamo, J. Jaramillo, R. Gomperts, R.E. Stratmann, O. Yazyev, A.J. Austin, R. Cammi, C. Pomelli, J.W. Ochterski, P.Y. Ayala, K. Morokuma, G.A. Voth, P. Salvador, J.J. Dannenberg, V.G. Zakrzewski, S. Dapprich, A.D. Daniels, M.C. Strain, O. Farkas, D.K. Malick, A.D. Rabuck, K. Raghavachari, J.B. Foresman, J.V. Ortiz, Q. Cui, A.G. Baboul, S. Clifford, J. Cioslowski, B.B. Stefanov, G. Liu, A. Liashenko, P. Piskorz, I. Komaromi, R.L. Martin, D.J. Fox, T. Keith, M.A. Al-Laham, C.Y. Peng, A. Nanayakkara, M. Challacombe, P.M.W. Gill, B. Johnson, W. Chen, M.W. Wong, C. Gonzalez, J.A. Pople, *Gaussian 03*, in, Gaussian, Inc., Wallingford CT, 2004.

[212]   M.J. Frisch, G.W. Trucks, H.B. Schlegel, G.E. Scuseria, M.A. Robb, J.R. Cheeseman, G. Scalmani, V. Barone, B. Mennucci, G.A. Petersson, H. Nakatsuji, M. Caricato, X. Li, H.P. Hratchian, A.F. Izmaylov, J. Bloino, G. Zheng, J.L. Sonnenberg, M. Hada, M. Ehara, K. Toyota, R. Fukuda, J. Hasegawa, M. Ishida, T. Nakajima, Y. Honda, O. Kitao, H. Nakai, T. Vreven, J. Montgomery, J. A., J.E. Peralta, F. Ogliaro, M. Bearpark, J.J. Heyd, E. Brothers, K.N. Kudin, V.N. Staroverov, R. Kobayashi, J. Normand, K. Raghavachari, A. Rendell, J.C. Burant, S.S. Iyengar, J. Tomasi, M. Cossi, N. Rega, J.M. Millam, M. Klene, J.E. Knox, J.B. Cross, V. Bakken, C. Adamo, J. Jaramillo, R. Gomperts, R.E. Stratmann, O. Yazyev, A.J. Austin, R. Cammi, C. Pomelli, J.W. Ochterski, R.L. Martin, K. Morokuma, V.G. Zakrzewski, G.A. Voth, P. Salvador, J.J. Dannenberg, S. Dapprich, A.D. Daniels, Ö. Farkas, J.B. Foresman, J.V. Ortiz, J. Cioslowski, D.J. Fox, *Gaussian 09*, in, Gaussian, Inc., Wallingford CT, 2009.

2.   The EPITOPES project: Infrared structural investigations on metal cluster adsorbate complexes

2.1.   Introduction

In gas phase experiments transition metal cluster ions show diverse behavior in reactions with gases depending on their size and their charge state. Especially the appearance of chemisorption or physisorption is highly debated [1-20]. Infrared (and photoelectronic) spectroscopic techniques can be an instrument to help determining the structure of both transition metal clusters and of transition metal cluster adsorbate complexes that form within these reactions [21-60]. Amongst other adsorbate molecules the investigation of the interaction between metal atoms or clusters with organic systems containing π-electrons like benzene has gained special interest in literature [61-84].

For applying InfraRed Multiphoton Dissociation spectroscopy (IR-MPD, see chapter 1.3.3.) to metal clusters a Bruker Apex Qe 7 T Fourier-Transform Ion-Cyclotron Resonance mass spectrometer instrument (FT-ICR, see chapter 1.2.2.) was installed at the Free Electron Laser (FEL) facility CLIO (Centre Laser Infrarouge d'Orsay) in Paris within the EPITOPES project (Electrons Plus Infrared TO Probe and Elucidate Structure) of the 6th European Framework Program NEST (New and Emerging Science and Technologies). Its aim was to set up a gas phase mass spectrometer instrument that would be capable of combining different ion sources (at least ElectroSpray Ionization (ESI, see chapter 1.2.3.) and Laser VAPorization (LVAP, see chapter 1.2.4.)) with the techniques of Electron Capture Dissociation (ECD) and IR-MPD spectroscopy. An excerpt of the project description reads as follows: "The EPITOPES setup is based on high performance Mass Spectrometry (MS) with high power tunable mid InfraRed (IR) spectroscopy and with Electron Capture Dissociation (ECD). This shall allow to achieve structural characterisation of isolated peptides, specifically non covalent bound complexes, and of catalytically active transition metal complexes and clusters in the gas phase."

2.2.   Experimental setup: Modifications on the commercial FT-ICR mass spectrometer

The commercial spectrometer, which is equipped with a standard ESI source, has been modified with an ion bender that allows for any type of ion source to be installed to the system. For the production of metal cluster ions an LVAP source has been connected to this ion bender.

In detail, this installation was performed as follows:
The commercial Bruker Apex Qe FT-ICR mass spectrometer (equipped with a 7 T superconducting Magnex magnet, Fig. 1) was installed into a small room on the first floor inside the building where the FEL CLIO is located at ground floor level.

The commercial ICR setup in principle consists of (Fig. 1b)

1) an electrospray ionization source that brings ions out of solutions into the gas phase

2) a quadrupole mass filter for mass selection of the ions

3) a hexapole collision cell for fragmentation of the ions

4) the transfer ion optics that lead the ions into the magnetic field of the superconducting magnet
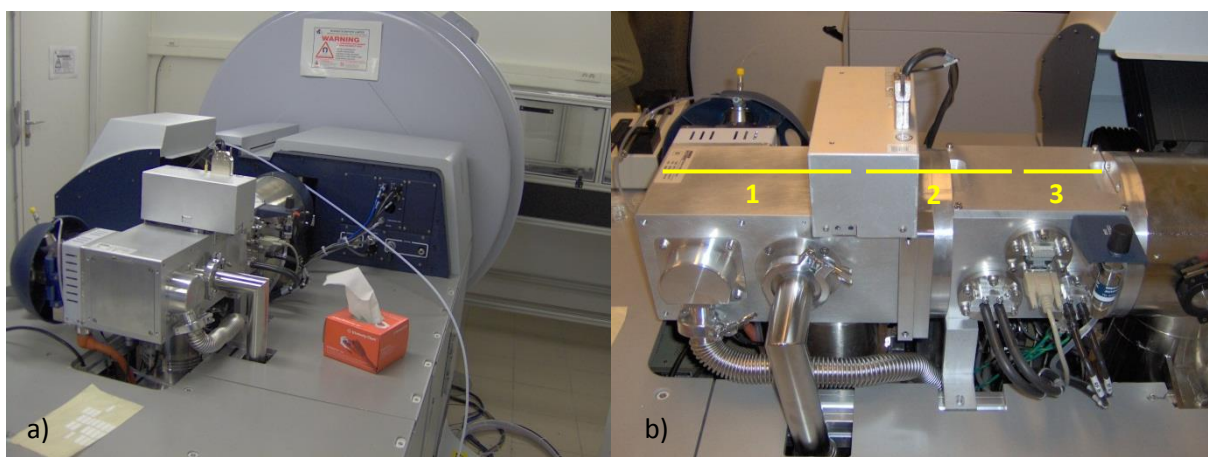
5) the ICR cell inside the magnet

Fig. 1: *a) The Bruker Apex Qe FT-ICR-MS after installation of the manufacturer; b) a closer look to the source part (parts inside the vacuum chamber: 1) ESI source, 2) quadrupole mass filter, 3) hexapole collision cell).*

The assembling of parts 1) - 3) had been constructed by the manufacturer in two vacuum chamber parts with the mass filter being part of both chambers. A splitting of the instrument between these two chambers would have lead into a complete rebuilt of the instrument. Therefore, we decided to split the instrument after the collision cell and before the transfer ion optics for the installation of the ion bender. Fig. 2a shows the disassembled machine with the mechanical IR light safety shutter being visible.
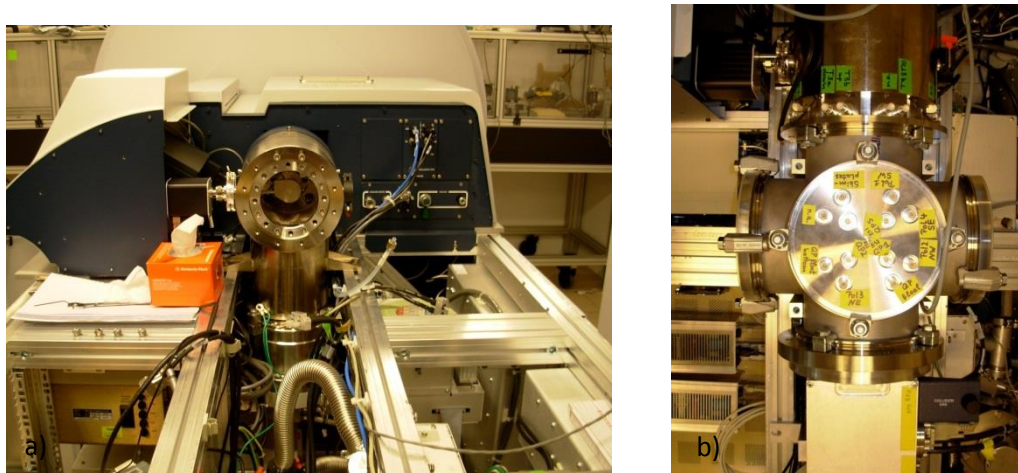
Fig. 2: *a) Disassembled ICR machine with IR light safety shutter visible (front view), b) reassembled machine with six-way-cross (ion bender inside), accelerating ion optics flange and ESI source - quadrupole - hexapole unit attached (top view).*

The ion bender (Fig. 3) was installed into a six-way-cross. As the ions have to be accelerated before entering the bender, they do not have energies appropriate for the transfer ion optics of the manufacturer's electronics. Therefore, a new set of accelerating and steering ion optics had to be installed between the ion bender and the transfer optics of the original setup. These original elements were then wired not for accelerating but only for conducting of the ions.
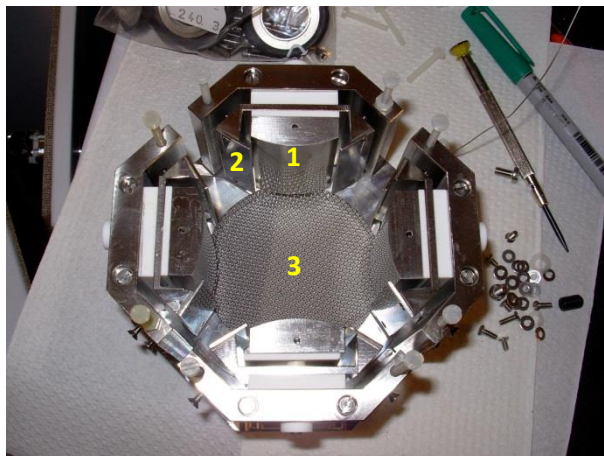

Fig. 3: *Ion bender with 1) pole electrodes, 2) skim plates, 3) mesh for up/down correction.*

The connection to the six-way-cross of the laser vaporization source chamber was established by a flange containing a mechanical shutter (Fig. 4a, front view) and a set of accelerating and steering ion optics (Fig. 4b, rear view).
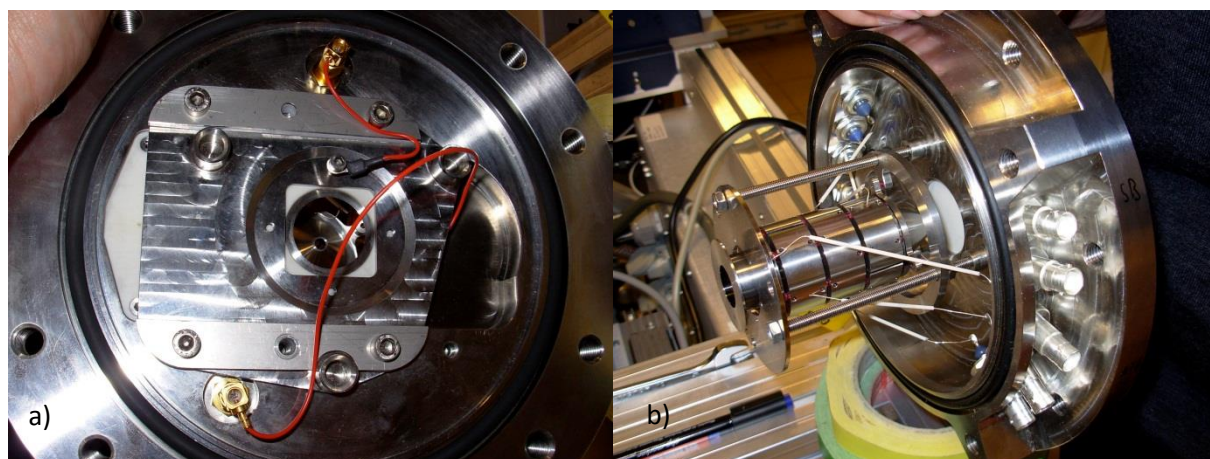
Fig. 4: *Flange between LVAP and ion bender chamber; a) mechanical shutter (front view), b) ion optics (rear view).*

Fig. 5 shows the whole setup after installation of additional vacuum pumps and wiring.
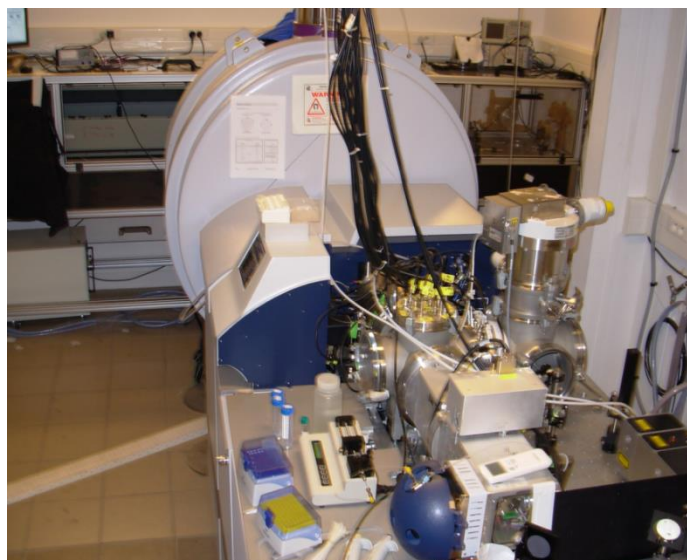
Fig. 5: *New setup after installation of ion bender and laser vaporization source.*

After completion of these changes and with that fulfilling of work package 1 "instrumentation" within the EPITOPES project, we started the scientific investigations:

Our aim was to record IR-MPD spectra of metal adsorbate complexes. Therefore we generated ionic metal clusters within our laser vaporization source. Fig. 6 gives a drawing and a picture of this source:
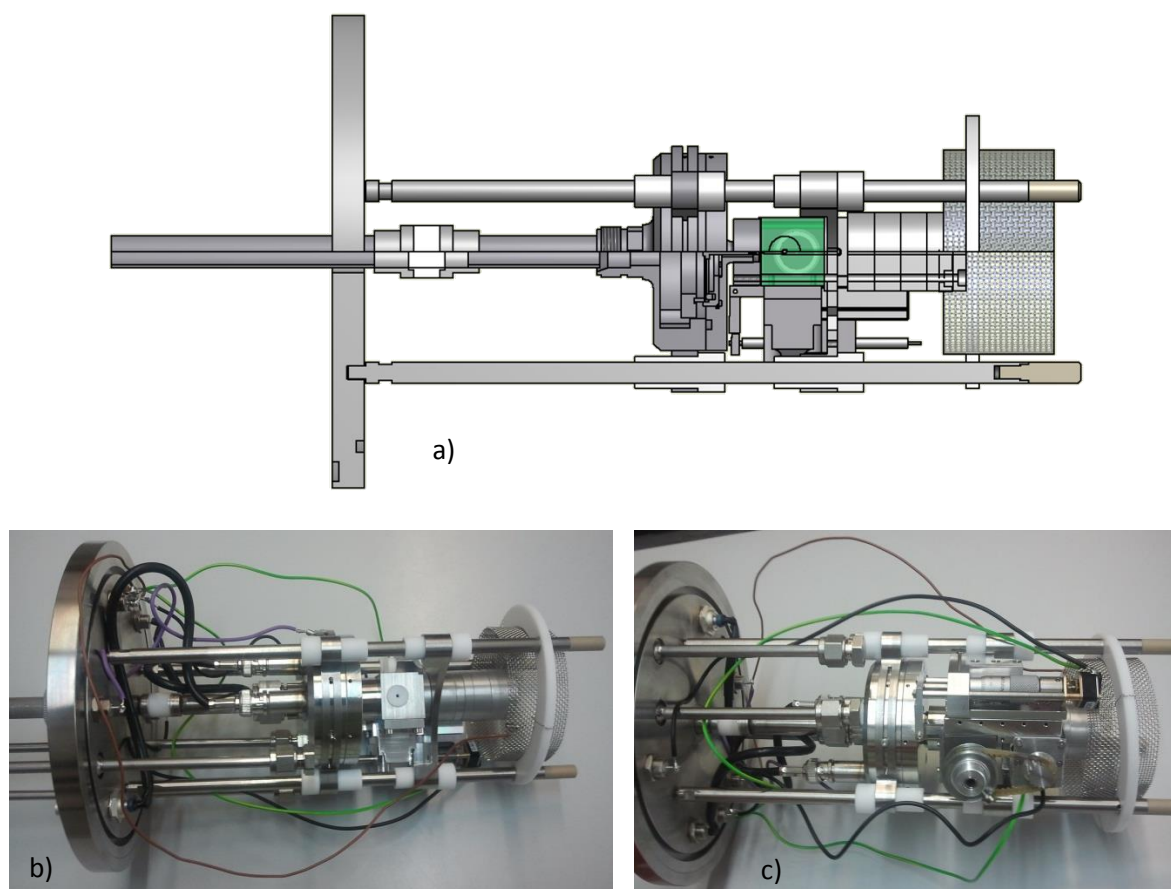

a)

b)

c)

Fig. 6: *The laser vaporization source; a) schematic drawing, b) photograph laser entrance side, c) photograph target side.*

The main part of the source is the evaporation chamber which is a nearly cubic metal block with two drilled holes that are perpendicular to each other and go completely from one side to the opposite site. Behind the one end, a metal cluster target (diameter approx. 12 mm, thickness approx. 0.5 mm) is fixed in a manner that it can be rotated and moved. Through the hole this target is hit by a pulsed laser beam of the frequency doubled laser light (532 nm) of a Nd:YAG laser (Innolas Spit Light 300). The so created metal plasma is cooled down within the supersonic expansion of a helium gas pulse through the perpendicular drill hole within the evaporation block. This helium pulse is created by a homebuilt piezoelectric valve. It allows for the creation of very short and sharp helium pulses with the helium expanding from 10 - 15 bar into the background pressure within the LVAP chamber of about $1 \cdot 10^{-6}$ mbar. The supersonic expansion cools down the metal plasma. Within the expansion channel neutral and ionic metal clusters with atom numbers from 2 - approx. 40 form. The whole source part is insulated against ground so that a small voltage (normally up to 10 V) can be applied. The resulting ionic part of the clusters is skimmed, accelerated to the ion bender and transferred into the ICR cell. Ions are stored within this cell and exposed to a reaction gas. Reaction products can then be mass detected, or they can be irradiated with IR light through the entrance within the rear side of the ICR cell before mass detection. In addition to the IR light of the FEL CLIO (according to specifications 67 - 3333 cm^{-1}, experimentally available during our time 600 - 1800 cm^{-1}; see chapter 1.2.5.) the range of higher frequencies (2500 - 4000 cm^{-1}) is accessible by a table top Dean Guyer Laservision Optical Parametric Oscillator / Amplifier system (OPO/OPA, see chapter 1.2.6.). Both systems are used with a repetition rate of 25 Hz. In the case of CLIO one "shot" has a length of approx. 10 μs, each consisting of several bunches of 1 ps with a distance of 16 ns. The length of one OPO/OPA laser shot is about 8 ns.

2.3.   Mass spectra of $Nb_n^{+/-}$ metal clusters and $[Nb_nC_6H_x]^{+/-}$ metal cluster adsorbate complexes

In the reaction with benzene (C_6H_6) niobium cluster ions either yield products with formal intact adsorption of a complete C_6H_6 unit or they lose all H atoms resulting in formal adsorption of C_6. In Fourier-Transform Ion-Cyclotron-Resonance Mass Spectrometry (FT-ICR-MS) experiments, $[Nb_{19}]^+$ showed to be the only cluster which leads to C_6H_6 addition to nearly 100 % [73-75].

The aim of this work was to find evidence for either aromatic, acetylene type or any other structural motive of the C_6H_6 unit of the $[Nb_{19}C_6H_6]^+$ complex by applying IR-MPD spectroscopy. Activating this $[Nb_{19}C_6H_6]^+$ complex by Collision Induced Dissociation leads to a complete loss of all 6 H atoms in only one visible reaction step resulting in the product $[Nb_{19}C_6]^+$.

We experienced several throwbacks during the installation of the LVAP source. One was the complete destruction of our source by subsequent applications of water vapor and NO gas applied to our LVAP chamber accidentally by another group. This resulted in the corroding of every part that was not built of stainless steel or aluminum. The destruction is visible quite well in Fig. 7 with the complete disappearance of the tooth belt leaving its wire as residue behind.
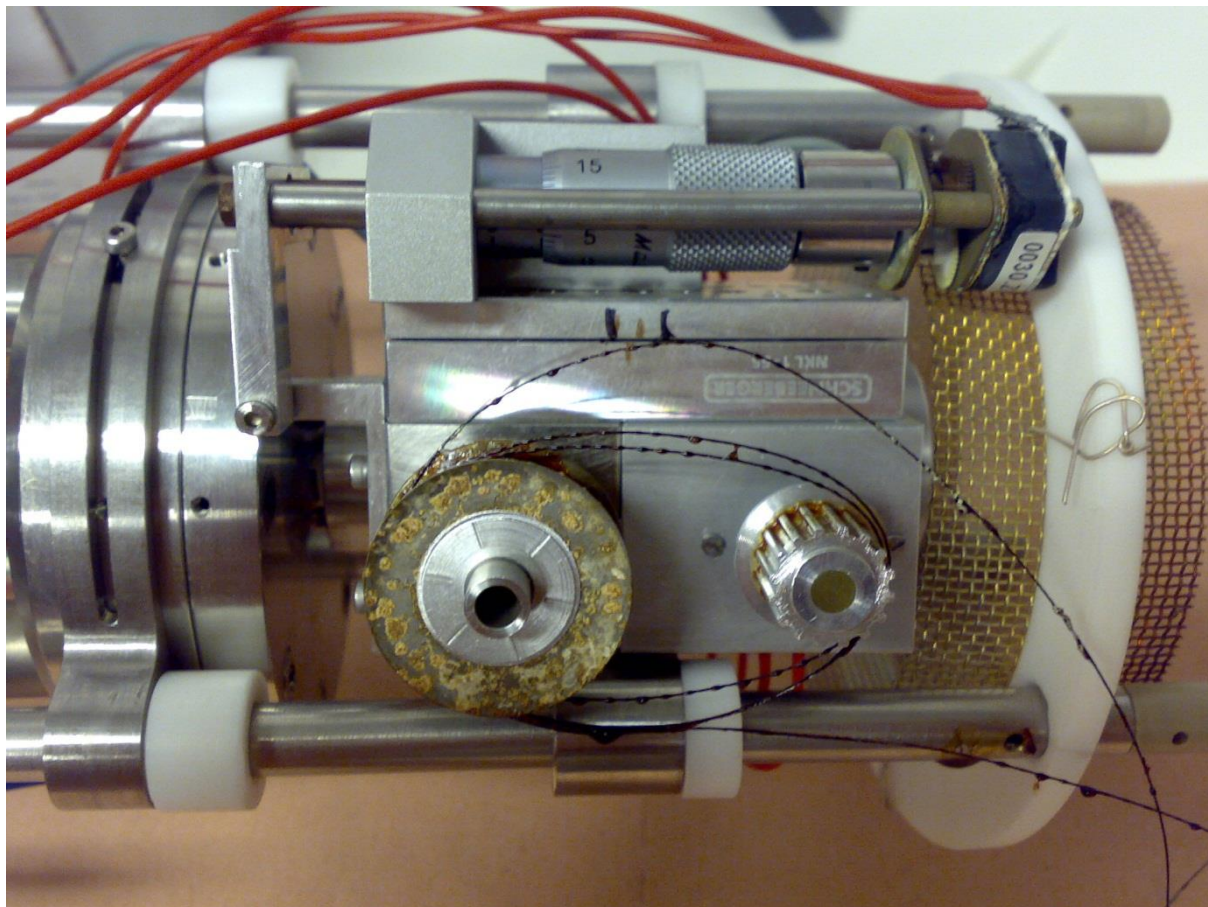

Fig. 7: *Destruction of the LVAP source by water vapor and NO gas. The black wire and yellowish deposits in the front stem from a prior tooth belt that completely disintegrated through Xanthoprotein reaction.*

Eventually we succeeded to completely reinstall LVAP source, gas tubes, pressure reducer, helium gas bottle etc. The first step was to achieve a mass spectrum of niobium metal clusters (Fig. 8). The niobium metal cluster ions were then reacted with the continuously injected benzene gas (reaction gas pressure within the cell: $1.0 \cdot 10^{-8}$ mbar). Applying a very short (0 s, Fig. 9a) or a longer reaction time (1 s, Fig. 9b) introduces the product formation of $[Nb_nC_6]^+$ and $[Nb_nC_6H_6]^+$.
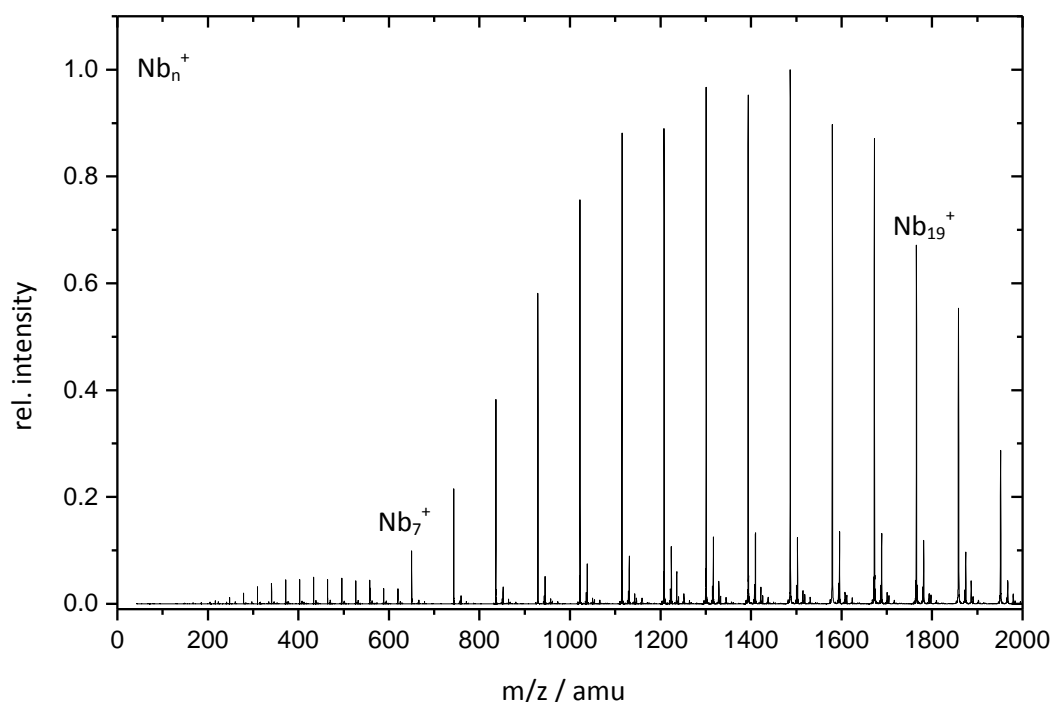
Fig. 8: *First mass spectrum of cationic niobium metal clusters at the EPITOPES instrument: Mass peaks could be assigned to Nb$_n^+$ (n = 7 - 21). Smaller peaks on the right side of the cluster peaks stem from oxygen and water impurities. Peaks in the region between 200 and 600 m/z are a result of the Fourier Transformation as the third harmonics of the original mass peaks.*
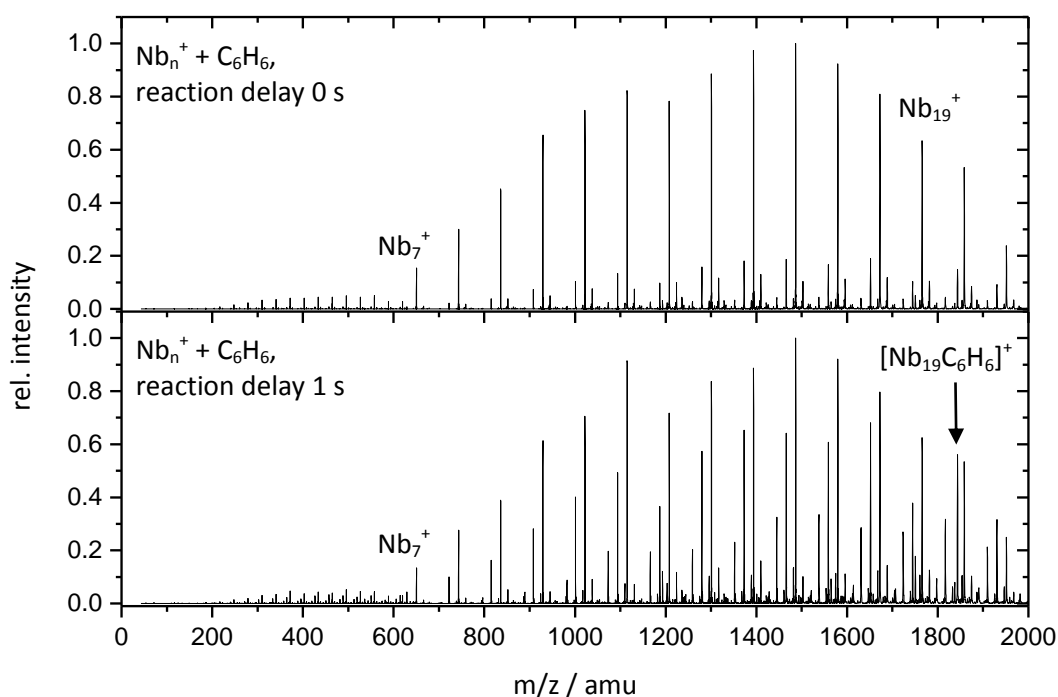

Fig. 9: *Mass spectra of the reaction of Nb$_n^+$ with benzene; a) reaction delay 0 s, b) reaction delay 1 s. New peaks [Nb$_n$C$_6$]$^+$ and [Nb$_n$C$_6$H$_6$]$^+$ appear with different intensity distributions depending on the cluster size.*

2.4. First prove of IR induced H atom loss

For the Nb_{19}^+ cluster this leads to a $[Nb_{19}C_6]^+$ / $[Nb_{19}C_6H_6]^+$ product ratio of approx. 1 / 7 (see Fig. 10a and b). Applying infrared radiation (Fig. 10c, frequency of 3620 cm^{-1}) induces the simultaneous loss of all 6 H atoms resulting in a raise of this ratio.
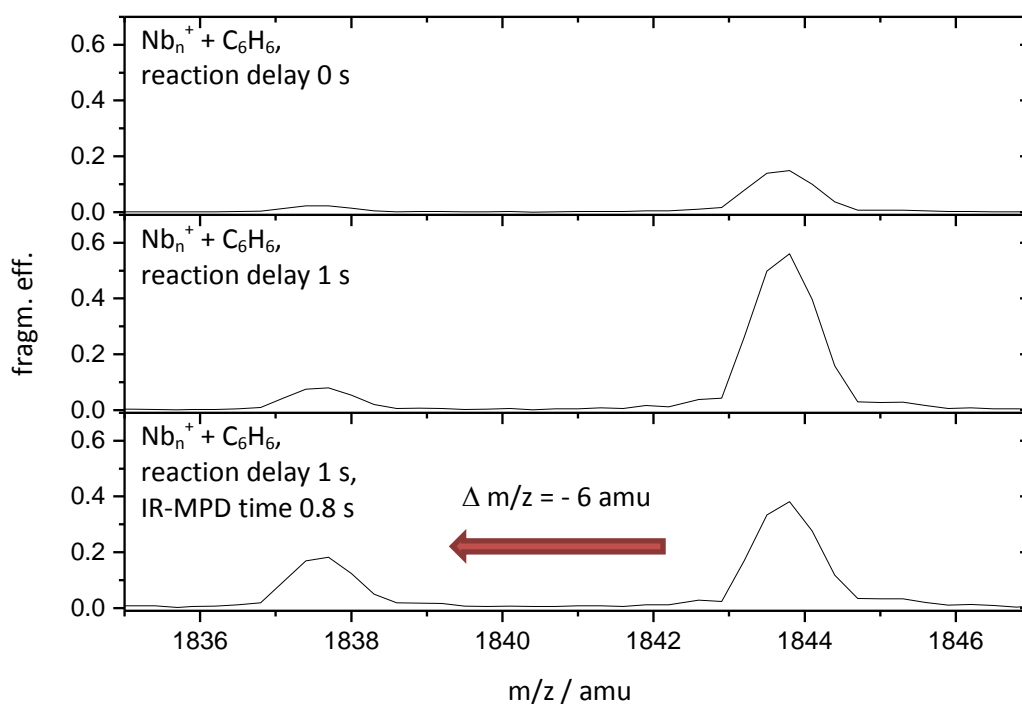

Fig. 10: *Mass spectra of Nb_n^+ + C_6H_6 (m/z 1837.2: $[Nb_{19}C_6]^+$, m/z 1843.3: $[Nb_{19}C_6H_6]^+$): a) reaction delay 0 s, b) reaction delay 1 s, c) irradiation time (IR-MPD time) 800 ms (3620 cm^{-1}). Irradiation with IR light induces a decrease in the intensity of the mass peak assigned to $[Nb_{19}C_6H_6]^+$ and an increase of the mass peak for $[Nb_{19}C_6]^+$ and thus inducing the simultaneous loss of 6 H atoms.*

As IR-MPD spectroscopy is a consequence spectroscopy the intensity of absorption is expressed by the fragmentation efficiency:

$$\text{fragm. eff.} = \frac{\sum Int_{[Nb_nC_6]^{+/-}}}{\sum Int_{[Nb_nC_6H_6]^{+/-}} + \sum Int_{[Nb_nC_6]^{+/-}}} \qquad (2.1)$$

In the case of the Nb_{19}^+ cluster all isotopes of $[Nb_{19}C_6H_6]^+$ are regarded as parent ions and of $[Nb_{19}C_6]^+$ as fragment ions.

For determination of the best overlap between IR beam and the ion cloud, one has not only to align the IR laser beam through the instrument, but can also influence the location of the ion cloud. Therefore, one can change the side kick potential that moves the ion off the magnet filed axis when flying into the ICR cell. We did so (Fig. 11) and found a potential difference of 0 V to be best suitable for our purposes.
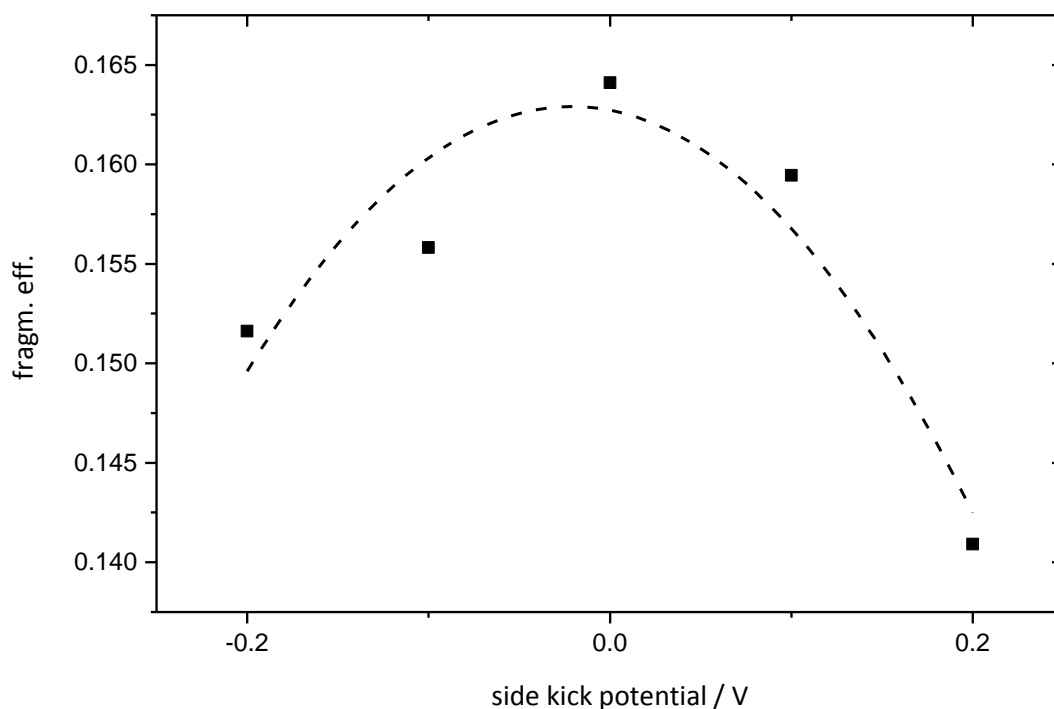

Fig. 11: *Dependence of fragmentation efficiency on the side kick potential of the ICR trap. The dashed line results of a quadratic fit.*

After having the best overlap, we now recorded several IR-MPD spectra. When scanning with the FEL CLIO, the laser was set to one frequency, and for every frequency the sum of eight individual mass spectra has been recorded. After that CLIO was set to the next frequency and another sum of eight mass spectra was recorded. Here changing of the frequency is achieved by changing the undulator gap, that can be changed stepwise. The peakwidth of the laser at one data point is given as FWHM of 0.2 - 2 % (e.g. for 1000 cm^{-1} resulting in 2 - 20 cm^{-1}). The spectra with the OPO laser are recorded in a different way: The OPO laser is set to the start frequency and then continuously tuned to the end frequency. Therefore a set of eight individual mass spectra that are summed up as one spectrum always has a certain uncertainty due to the continuous scanning of the laser. As the recording of an individual spectrum lasts at about 2.5 s a complete eighth fold scan is about 20 s. The laser is scanned with 0.2 cm^{-1}/s at a FWHM of approx. 3 cm^{-1} what gives an uncertainty of 7 cm^{-1} in the frequency data points.

2.5. IR-MPD spectra of $[Nb_{19}C_6H_6]^+$

Fig. 12 shows measurements of the fragmentation efficiency of the IR induced reaction $[Nb_{19}C_6H_6]^+$ -> $[Nb_{19}C_6]^+$ in the CLIO (600 - 1600 cm^{-1}) and in the OPO region (2500 - 4000 cm^{-1}). Black curves show the fragmentation efficiency (left axis), grey curves give the laser power (right axis). For comparison reason the gas phase IR spectrum of benzene (red curve, digitized by Ref. [85]) and the electronic transitions (values from Ref. [86]) of the neutral Nb^0 atom (blue sticks) and of the Nb^+ cation (green sticks) are also plotted.
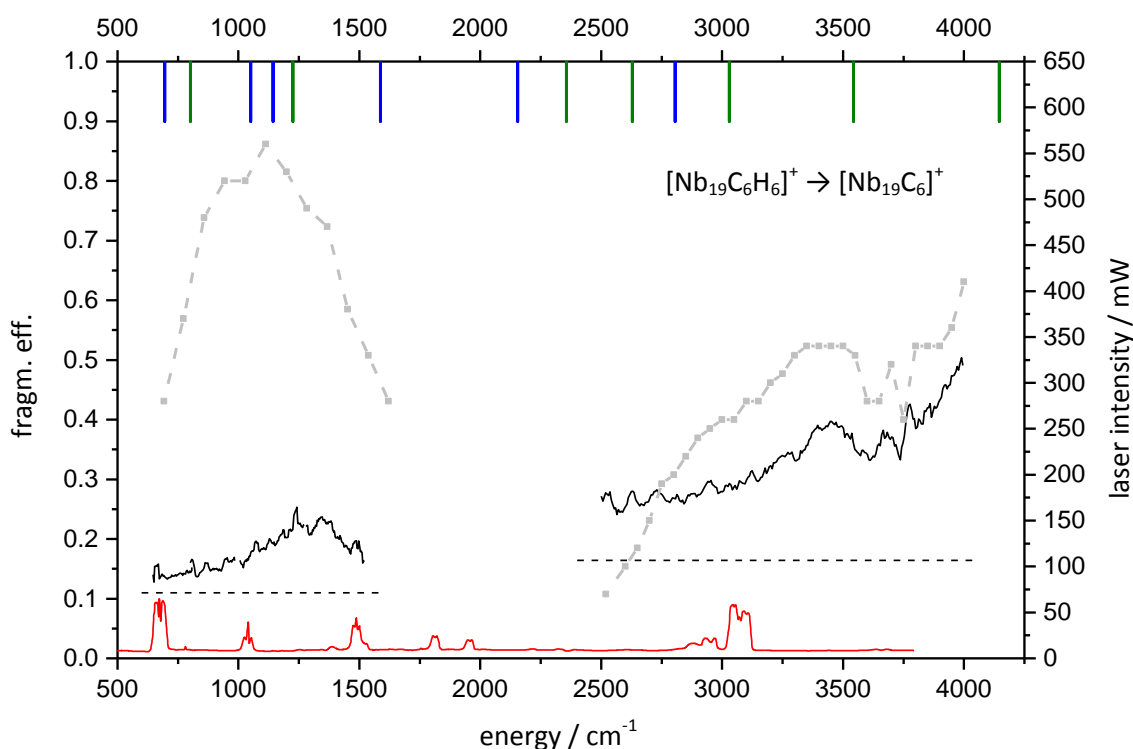

Fig. 12: *Spectra of the IR light induced reaction $[Nb_{19}C_6H_6]^+$ -> $[Nb_{19}C_6]^+$ (black curves); grey curves show the corresponding laser power; red curve displays the gas phase IR spectrum of benzene; sticks indicate electronic transitions of Nb^0 (blue) and Nb^+ (green). Black dashed lines show the base line of the $[Nb_{19}C_6]^+/[Nb_{19}C_6H_6]^+$ ratio without irradiation. IR light induced fragmentation is present over the whole measured range. No specific features were found. The IR-MPD efficiency follows the general trend of the laser intensity.*

In the CLIO region, fragmentation is dependent on the laser power. Therefore, we do not assign any special feature to the top peak around 1200 cm^{-1} and the decay to lower and higher energies. In the OPO region, fragmentation efficiency also does not show any significant peak: Starting from 2500 cm^{-1}, the fragmentation efficiency rises up to the end of the measured range of 4000 cm^{-1}. Same holds for the laser power. The dip around 3500 - 3800 cm^{-1} originates from partial absorption of the IR laser light by water. Unfortunately the humidity of the air could not be reduced to values lower than 20 %. During the whole scan range no significant features according to the gas phase

spectrum of benzene or similar to electronic transitions of Nb^0 or Nb^+ were obtained. When scanning the IR laser from 2500 - 4000 cm^{-1}, the rise in fragmentation efficiency follows the same trend as the laser intensity. This indicates that we do introduce splitting off of the H atoms by laser light, but so far apparently without resonant absorption. According to literature, absorption of radiation above 3000 cm^{-1} has been found already at smaller metal cluster systems and has been assigned to vibronic couplings: Vibrational spectra of $[Co_n(CH_3OH)_3]^+$ (n = 1 - 3) show an increasing IR induced fragmentation when scanning from 3000 to 7000 cm^{-1} for n = 2 and 3 [87]. Infrared spectra of the cobalt dimer Co_2 isolated in neon matrices reveal a broad range of isolated peaks between approx. 3000 - 9000 cm^{-1}. They could be calculated to originate from electronic transitions. Photodissociation spectroscopy of $[Co_nAr]^+$ (n = 3 – 5) reveals a very broad absorption band between approx. 6000 and 12000 cm^{-1} [88]. According to the findings of Co_2, this result has been explained by theoretical calculations to originate from a contribution of electronic transitions [89]. The underlying rise of laser intensity makes it difficult to distinguish any remarkable peaks explaining the structure of the C_6H_6 unit. To extend this examination, we measured the dependence of the fragmentation efficiency on the IR-MPD time and therefore the number of laser bunches (Laser 25 Hz = one bunch per 40 ms) at different frequencies: 3200 and 3723 cm^{-1} in some tops and 3500 and 3776 cm^{-1} in some dips of the fragmentation efficiency curve (Fig. 13).
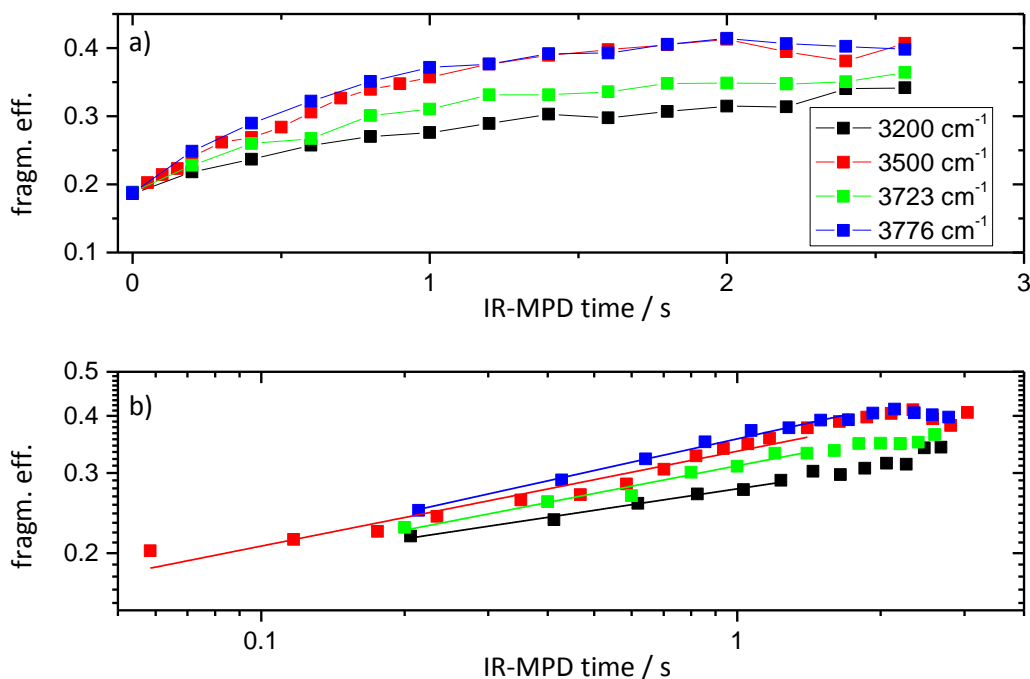

Fig. 13: *Fragmentation efficiency as function of IR-MPD time at four frequencies; a) normal plots, b) log-log plots with linear fits (IR-MPD time corrected for laser power).*

Corrected for the laser power in those peaks and drawn as a log-log plot the slope of the resulting curve gives a hint for the effectiveness of fragmentation in these cases.

Table 1: *Characteristic data of the log/log plot "fragmentation efficiency as function of IR-MPD time" (see* **Fig. 13** *b).*

Energy / cm^{-1}	Approx. laser power / mW	Correction factor for IR-MPD time	Slope of log/log plot	Intercept
3200	300	1.03	0.15702	-0.55751
3500	340	1.17	0.208	-0.47509
3723	290	1.00	0.20205	-0.50702
3776	310	1.07	0.24314	-0.44372

The general trend arises that higher photon energies are more effective in causing fragmentation.

2.6. IR-MPD spectra of [Nb$_{18}$C$_6$H$_6$]$^+$, [Nb$_{19}$C$_6$H$_6$]$^-$ and [Nb$_{18}$C$_6$H$_6$]$^-$

A similar result for the IR-MPD spectrum can be found for Nb$_{18}$$^+$ (Fig. 14). But as the ratio of [Nb$_{18}$C$_6$]$^+$ to [Nb$_{18}$C$_6$H$_6$]$^+$ even without IR-irradiation is already approx. 1 : 1; the initial fragmentation efficiency is already higher than 50 % and therefore the IR-MPD spectra are not as significant:
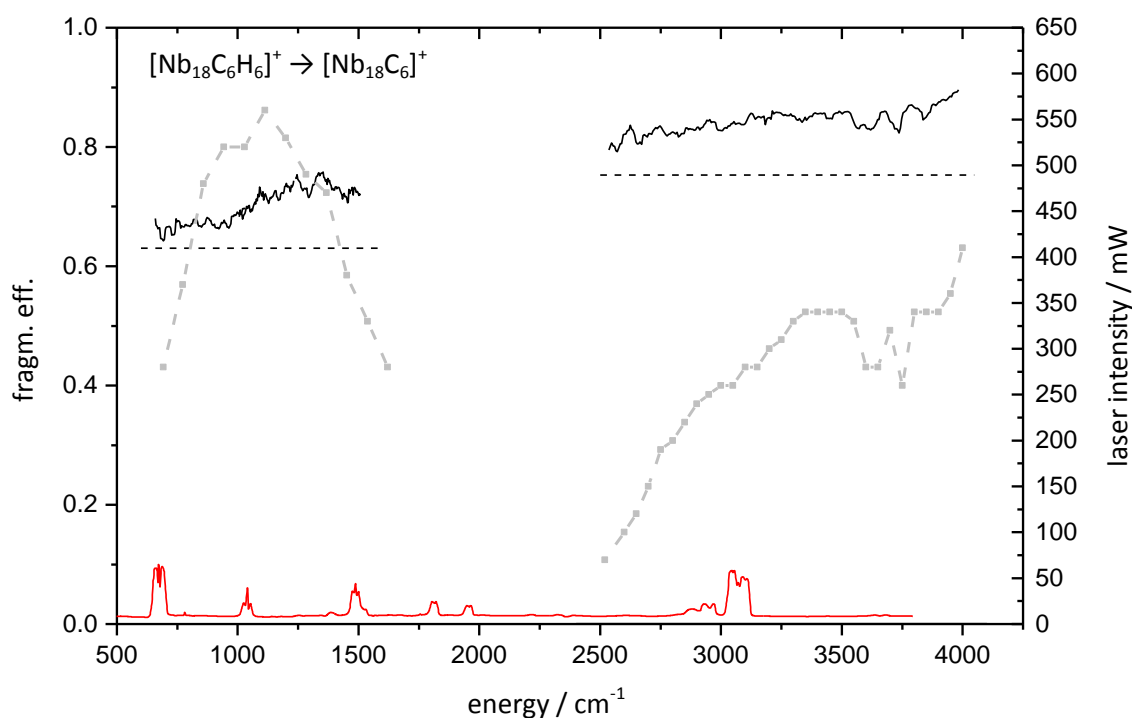

Fig. 14: *Spectra of the IR light induced reaction [Nb$_{18}$C$_6$H$_6$]$^+$ -> [Nb$_{18}$C$_6$]$^+$ (black curves); grey curves show the corresponding laser power; red curve displays the gas phase IR spectrum of benzene. Black dashed lines show the base line of the [Nb$_{18}$C$_6$]$^+$/[Nb$_{18}$C$_6$H$_6$]$^+$ ratio without irradiation. IR light induced fragmentation is present over the whole measured range. No specific features were found. The IR-MPD efficiency follows the general trend of the laser intensity.*

The anionic equivalent clusters Nb$_{18}^-$ and Nb$_{19}^-$ show a similar but not as intensive rise in the OPO region (Fig. 15). This is due to the much higher [Nb$_n$C$_6$]$^-$ / [Nb$_n$C$_6$H$_6$]$^-$ ratio even without irradiation by the IR laser light. Especially for n = 18 the H atom loss is nearly complete even without IR laser light.
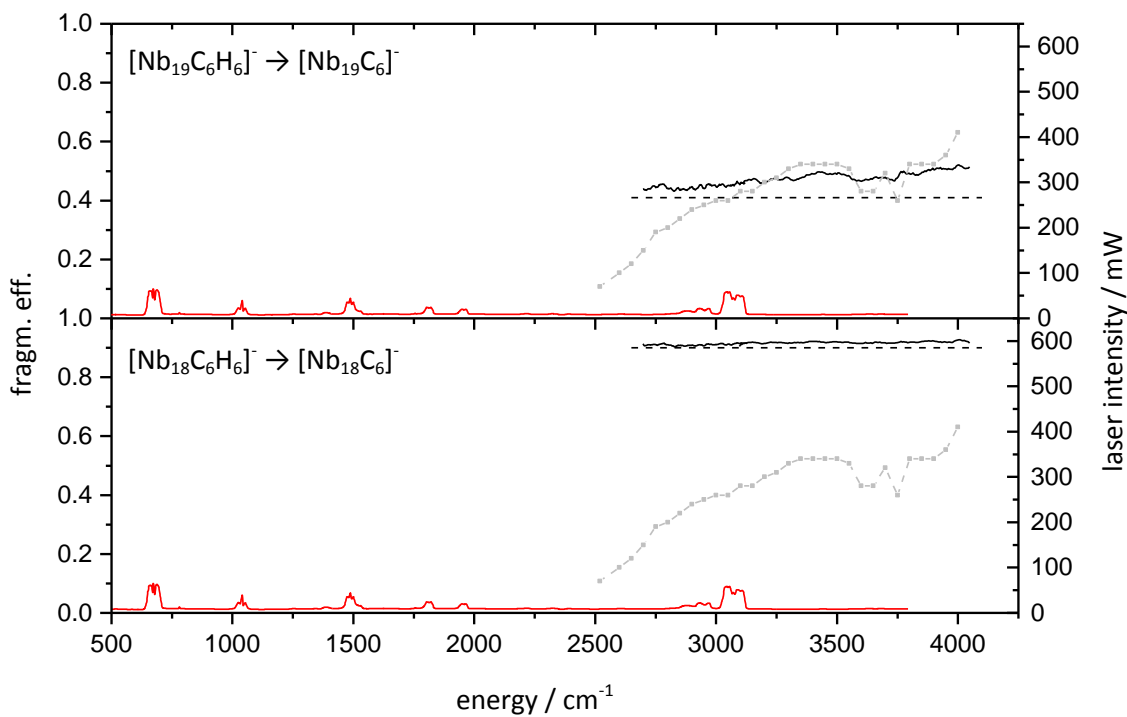

Fig. 15: *Spectra of the IR light induced reaction [Nb$_n$C$_6$H$_6$]$^-$ -> [Nb$_n$C$_6$]$^-$ (black curves); a) n = 19, b) n = 18; grey curves show the corresponding laser power; red curves display the gas phase IR spectrum of benzene. Black dashed lines show the base line of the intensity relation [Nb$_n$C$_6$]$^-$/[Nb$_n$C$_6$H$_6$]$^-$ without irradiation. IR light induced fragmentation is present over the whole measured range. No specific features were found. The IR-MPD efficiency follows the general trend of the laser intensity.*

When trying to reduce base line fragmentation by isolating the [Nb$_n$C$_6$H$_6$]$^{+/-}$ species in the ICR cell prior to the reaction time, isolation could only be achieved by using a quite high isolation power. This high power not only removes the unwanted species but also transfers energy into the molecule, which should be isolated. This caused an additional fragmentation in our case. So isolation inside the ICR cell did not yield an improvement in this experiment.

2.7. Installation of pick up source and first Nb$_n^{+/-}$ metal cluster mass spectra

One possibility of improving the experiment is the concept of forming the metal adsorbate clusters not in the ICR cell, but even before. The following experiments were all performed at the Bruker Apex III FT-ICR instrument in Kaiserslautern which - regarding the part of the LVAP source, the ion bender and the ICR cell - had an identical setup.

As one of the easiest ways of preforming metal cluster adsorbate complexes, we modified the LVAP source by adding a so called "pick up unit" into the area of the expansion channel. This unit is a metal block with an inner diameter of 10 mm. The block itself is hollow with a 6 mm Swagelok connection on the outside and several little holes in the inner wall. Through an additional 6 mm tube in the LVAP flange, the adsorbate gas pressure can be controlled outside the vacuum. With this pick up design the metal clusters undergo some kind of shower of the adsorbate gas when flying through the expansion channel. Fig. 16 shows a schematic drawing and a photograph of the LVAP source with the pickup unit built in.
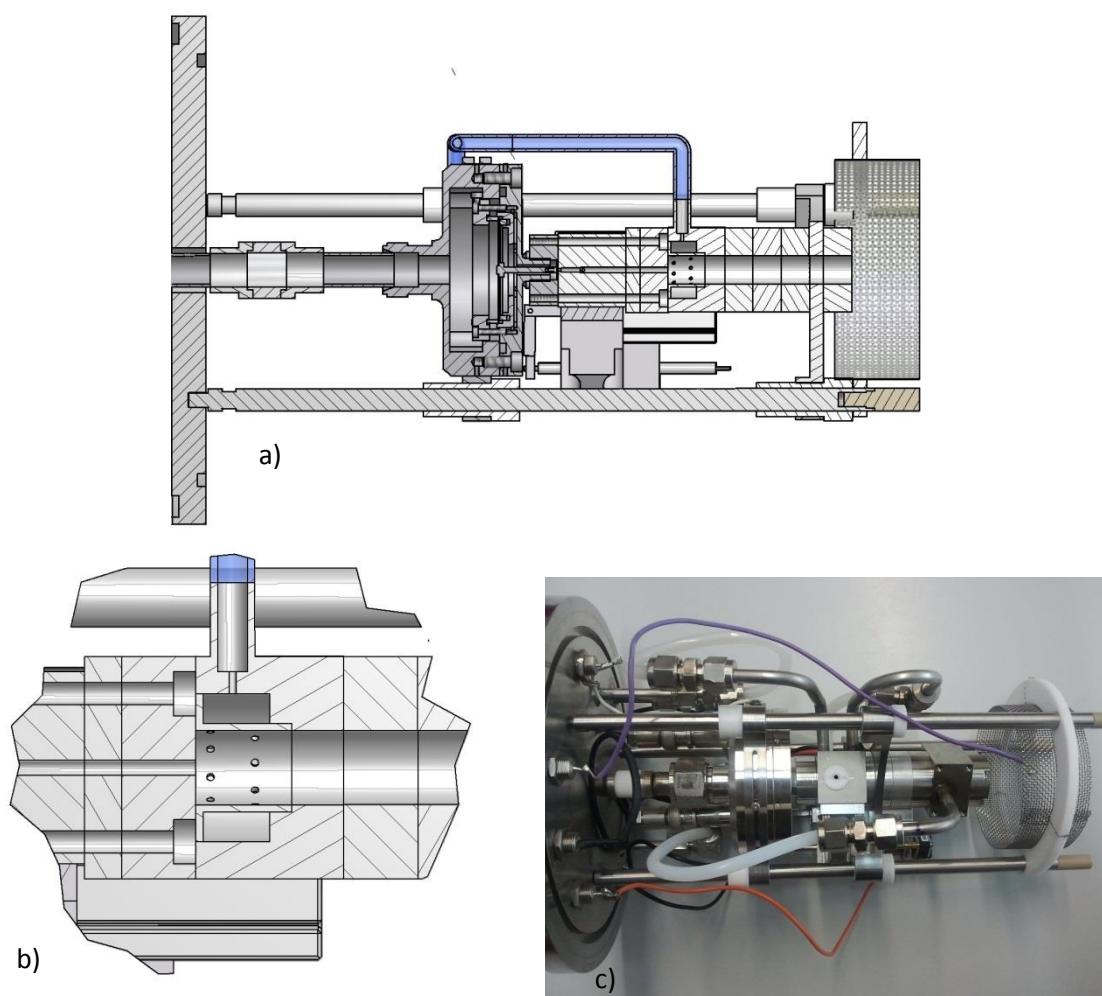

Fig. 16: *Laser vaporization source with pick up unit; a) schematic drawing of the whole source, b) schematic drawing of the pick up part, c) photograph with view from laser entrance side (drawings: Heinrich Kampschulte, Thomas Kolling).*

As an additional option, the evaporation block was modified with a tubing system that allows for liquids to flow through the block and enter/leave the LVAP chamber through two 6 mm tubes in the LVAP flange. That way a temperature control of the block from the outside is possible.

Fig. 17 shows the first metal cluster spectrum of cationic niobium metal clusters after installation of the LVAP with pick up source without the addition of any adsorbate gas. These side peaks always arise when the mass spectrum is recorded shortly after introduction of the metal target into the vacuum and vanish after ablating its top layer.
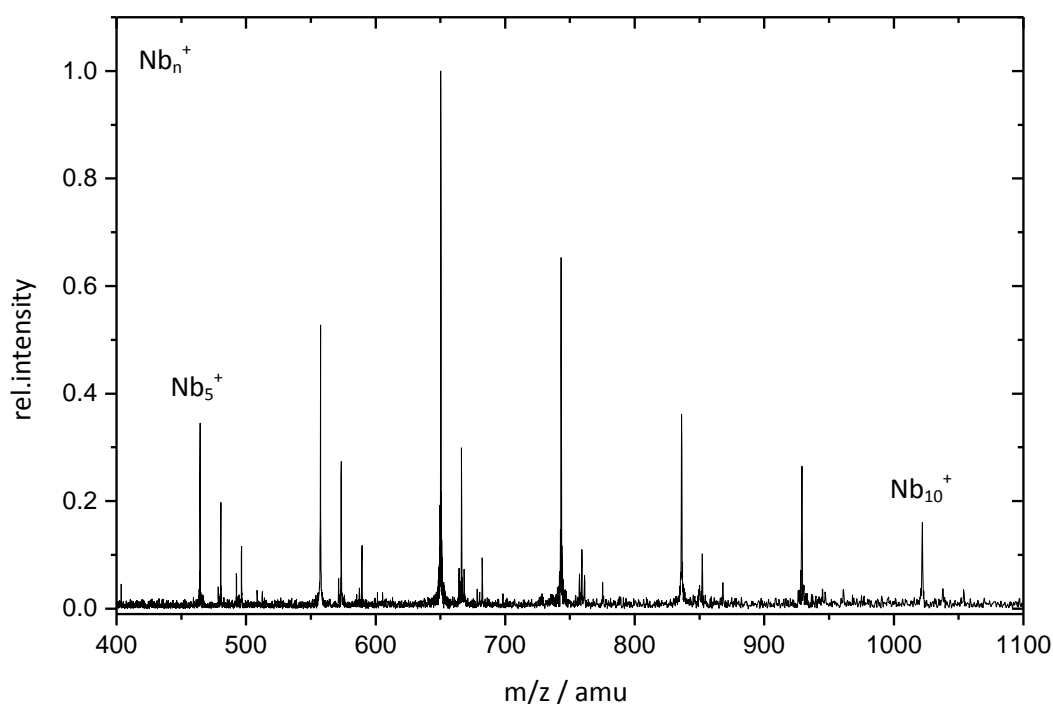

Fig. 17: *Mass spectrum of cationic niobium clusters generated by LVAP source with pick up unit. Mass peaks could be assigned to Nb_n^+ (n = 5 - 10). Smaller peaks on the right side of the cluster peaks stem from oxygen and water impurities.*

2.8. Mass spectra of $Nb_n^{+/-}$ clusters plus benzene introduced through pick up unit

After the verification of the general functionality of this modification to the LVAP source, we introduced benzene gas into the pick up unit, raising the background pressure within the LVAP six-way-cross vacuum chamber from $1.0 \cdot 10^{-6}$ mbar to $5.0 \cdot 10^{-6}$ - $3.0 \cdot 10^{-5}$ mbar. With rising benzene gas pressure, the overall signal decreases until with pressures larger than $5.0 \cdot 10^{-5}$ mbar it vanishes completely. Fig. 18 shows the resulting mass spectrum recorded at a vacuum chamber pressure of $1.0 \cdot 10^{-5}$ mbar.

Addition of benzene gas to the small cationic clusters shows additional peaks arising. They have a spacing of multiple times 12 m/z to the pure metal cluster peak. The enlargement in Fig. 18 shows not only the occurrence of Nb_7^+, $[Nb_7C_1]^+$ and of $[Nb_7C_2]^+$ but also of $[Nb_7C_6]^+$. This indicates not only the adsorption of the C_6 unit to the cluster but also partial fragmentation of benzene gas into its

atoms. Two points might contribute to this fragmentation. First, the metal clusters that are generated in the plasma of a laser shot have high temperatures when entering the pick up zone and the benzene breaks when coming into contact with the clusters. Second, the benzene gas is present all over the LVAP chamber. In particular, it is the evaporation chamber, where the hot metal plasma can cause benzene fragmentation. The most abundant adsorbate peaks arise from carbide formation of either one or six C atoms (see Table 2).
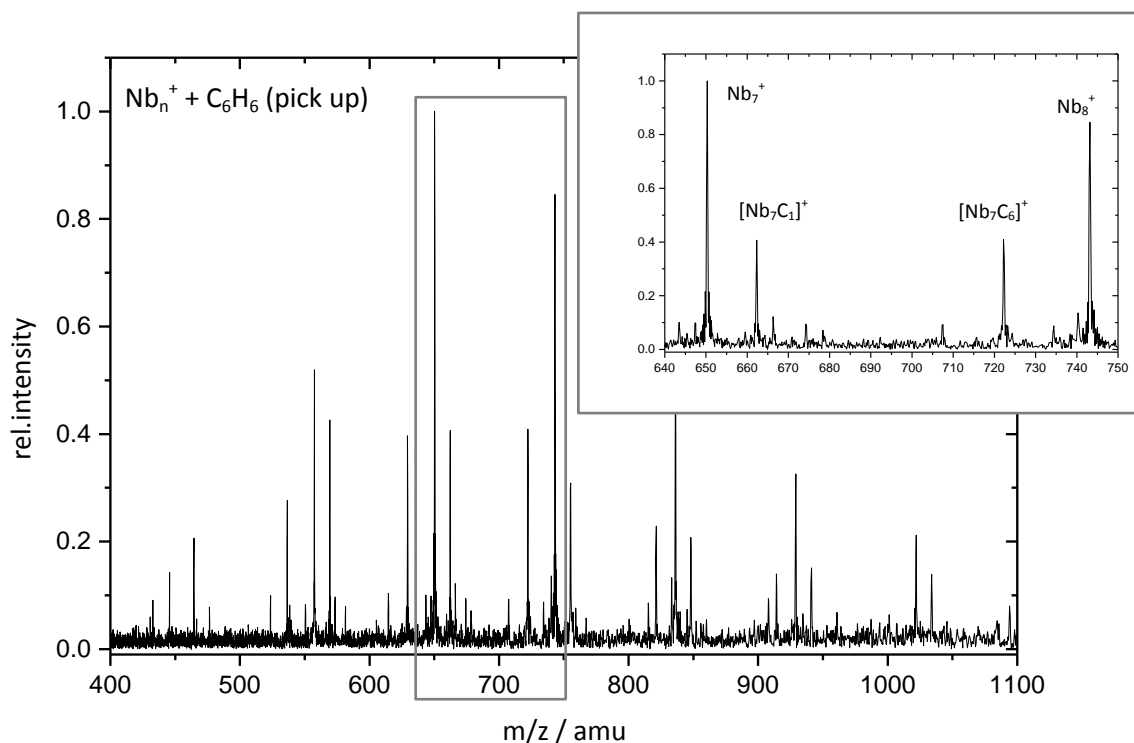

Fig. 18: *Mass spectrum of cationic niobium clusters generated by LVAP source with pick up unit; addition of benzene gas raising the pressure to $1.0 \cdot 10^{-5}$ mbar. (Partial) fragmentation of benzene gas into its atoms leads to cluster adsorbate peaks of the predominant composition $[Nb_nC_m]^+$.*

Table 2: *Observed intensities of Nb_n^+ clusters and products as generated by the LVAP / C_6H_6 added via pick up combination.*

Cluster size n	Nb_n^+	$+ C_1$	$+ C_2$	$+ C_6$	$+ C_6H_6$
5	36.8	13.9		49.3	
6	36.5	30.0	5.6	27.9	
7	52.3	21.3	5.0	21.4	
8	55.4	20.2	3.8	5.6	15.0
9	52.0	20.1	5.3	9.1	13.5
10	55.7	25.8	7.6	11.0	
11	43.9	28.9	10.7	16.6	
12	36.8	13.9		49.3	

Unfortunately the cluster $[Nb_{19}]^+$ which showed a formally intact adsorption of benzene in high vacuum kinetic experiments (see chapter 2.3.) could not be obtained experimentally in cationic mode. Presumably the cooling effect of the helium expansion out of the current piezo valve was not good enough to produce large cationic metal clusters. We changed polarity and continued with the investigation of anionic clusters. Without introducing any reaction gas we could achieve a much broader metal cluster distribution at once (Fig. 19), assuming that the formation of large anionic clusters can take place at higher expansion gas temperatures than it is the case for cationic clusters.
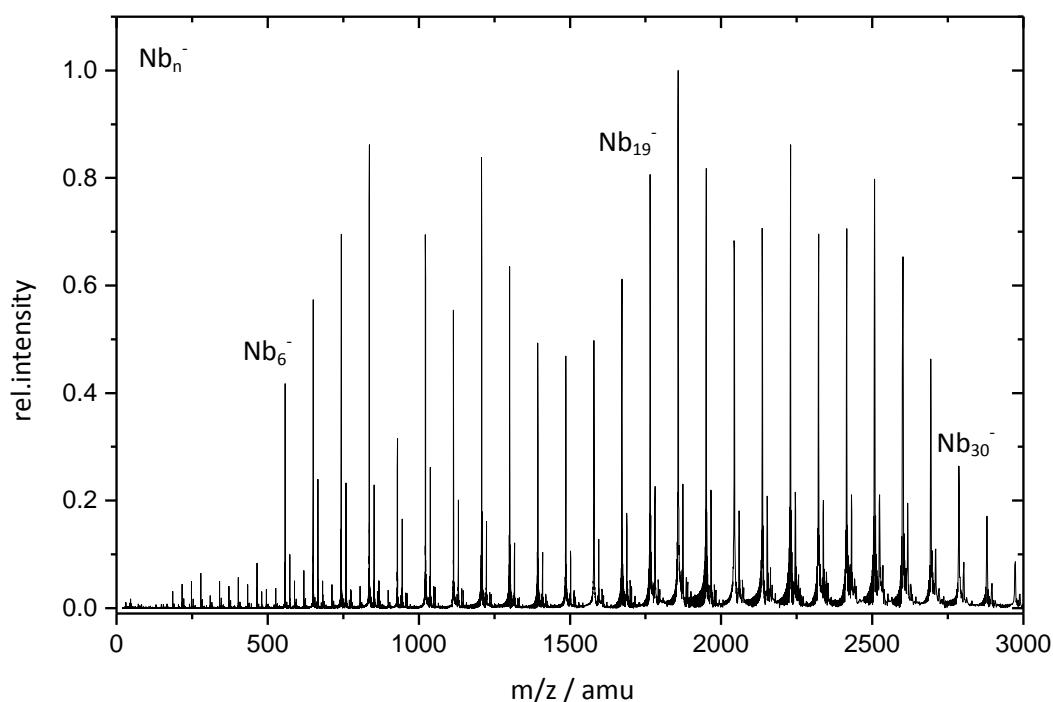

Fig. 19: *Mass spectrum of anionic niobium clusters generated by LVAP source with pick up unit. Mass peaks could be assigned to Nb_n^- (n = 5 - 32). Smaller peaks on the right side of the cluster peaks stem from oxygen and water impurities. Small peaks in the region between 200 and 1000 m/z are a result of the Fourier Transformation as the third harmonics of the original mass peaks.*

When introducing benzene into the pick up unit (LVAP chamber pressure $1.0 \cdot 10^{-5}$ mbar), a result similar to the one of cationic clusters could be found (Fig. 20): The benzene breaks within the LVAP source resulting in metal cluster peaks and adsorbate complexes with a distance of 12 m/z. The most abundant peaks originate from carbide formation with a single or multiple carbon atoms. Hydride formation can also be found, but merely in the addition of one or two H atoms to a cluster size (see Table 3). For medium cluster sizes even the addition of formally intact C_6H_6 to some clusters can be found. The peak of Nb_{19}^- does neither show the addition of C_6H_6 (+ 78 m/z) nor the one of C_6 (+ 72 m/z).
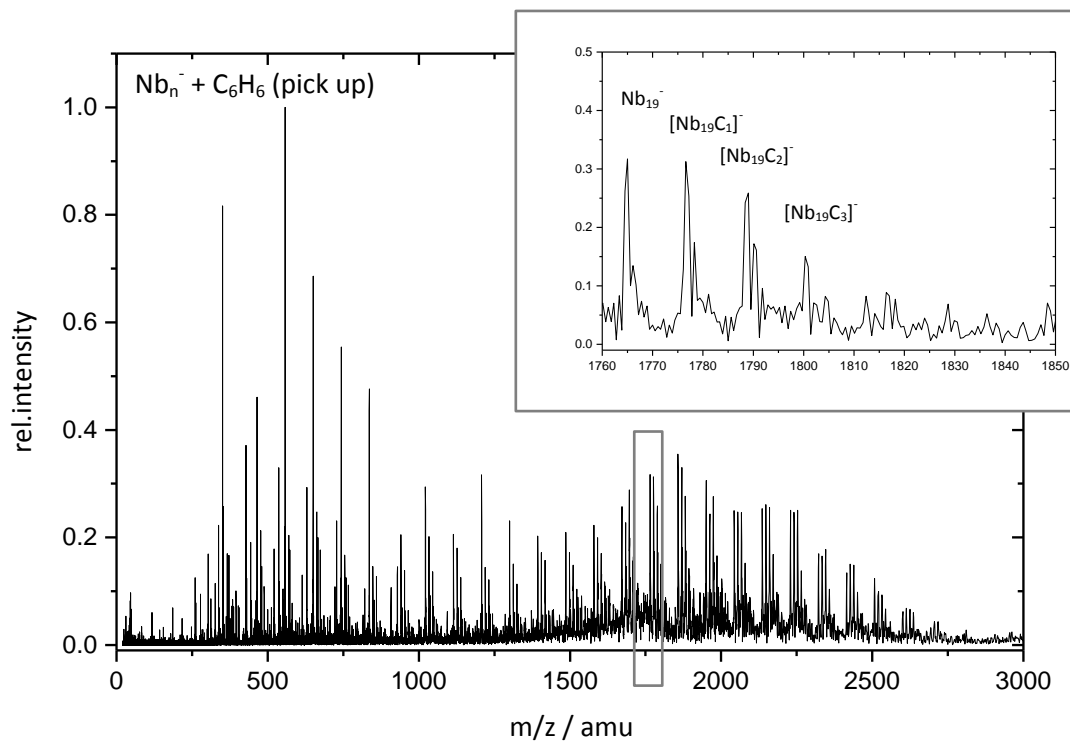
Fig. 20: *Mass spectrum of anionic niobium clusters generated by LVAP source with pick up unit; addition of benzene gas raising the pressure to $1.0 \cdot 10^{-5}$ mbar. (Partial) fragmentation of benzene gas into its atoms leads to cluster adsorbate peaks of the composition $[Nb_nC_mH_l]^-$.*

Table 3: *Observed intensities of Nb_n^- clusters and products as generated by the LVAP / C_6H_6 added via pick up combination.*

Cluster size n	Nb_n^-	+ H	+ C_1	+ C_1H_1	+ C_2	+ C_2H_1	+ C_3	+ C_3H_1	+ C_4	+ C_4H_1	+ C_5	+ C_6	+ C_6H_1	+ C_6H_2	+ C_6H_6
2	60.0				16.5				15.2			8.4			
3	1.8		1.4		10.4		1.9		7.1		2.2	50.4	8.9	15.9	
4	22.6		11.5		13.7		0.0		3.5		3.4	26.0	8.1	11.2	
5	31.8		14.7		7.5		4.5		4.8		1.4	22.7	4.4	8.1	
6	55.9		11.4		4.3		2.5		2.8			16.3	2.5	2.1	2.1
7	41.9		15.1		10.8		3.3		3.1		1.3	6.6	2.1	1.7	14.1
8	47.3		14.3		9.5		3.1	2.1	3.4	2.3	1.5	4.8	2.8		8.9
9	43.5		13.4		11.7	3.9	4.1	2.5	2.1		1.4	9.8	3.2	2.0	2.5
10	18.1		25.5		17.2	7.9	7.9	4.4	4.1		1.7	5.8	3.3		4.2
11	27.6	8.2	18.9	6.4	12.8	6.7	4.5	2.9	2.0	1.4		5.8	2.7		
12	21.2	7.0	18.6	6.1	12.9	6.5	5.1	3.4	3.3	2.7	1.5	4.0	2.8		4.8
13	30.2	7.2	13.8	6.2	11.6	6.9	5.5	3.6	3.2	3.0		3.3			5.5
14	24.3	5.8	15.8	5.7	11.9	5.1	5.4	4.1	4.4	3.2	2.6	6.7			5.1
15	21.4		18.1	5.3	16.6		6.7	5.8	6.8	5.3	3.4	5.9			4.7
16	17.4	4.0	14.3	7.1	12.4	9.3	8.6	6.3	5.7	5.6	3.8	5.6			
17	14.9	5.5	13.3	7.7	11.3	8.8	7.8	7.3	6.1	5.5	3.0	4.5			4.3
18	12.9	6.0	11.4	7.3	14.4	9.9	7.8	8.2	4.9	5.1	2.8	4.9			4.6
19	20.9	8.9	20.6	11.4	17.0	11.3	9.9								
20	26.0		24.2		20.3		10.4		5.1		3.7	7.2			3.1
21	26.2		20.8		23.6		14.2		8.3			6.9			
22	38.3		38.0				23.6								
23	27.0		27.8		27.2		17.9								
24	25.8		25.4		25.8		14.2		8.8						
25	27.5		26.8		28.8		16.9								
26	25.2		28.3		27.9		18.5								
27	32.3		25.9		24.4		17.4								
28	24.1		26.5		26.0		23.4								

2.9. Mass spectra of $Nb_n^{+/-}$ clusters plus carbon monoxide introduced through pick up unit

To compare the behavior of benzene with the one of other gases, we introduced carbon monoxide into the pick up unit and recorded the resulting metal cluster + CO complexes mass spectra. Fig. 21 shows the result of cationic clusters (LVAP chamber pressure $8.0 \cdot 10^{-5}$ mbar).
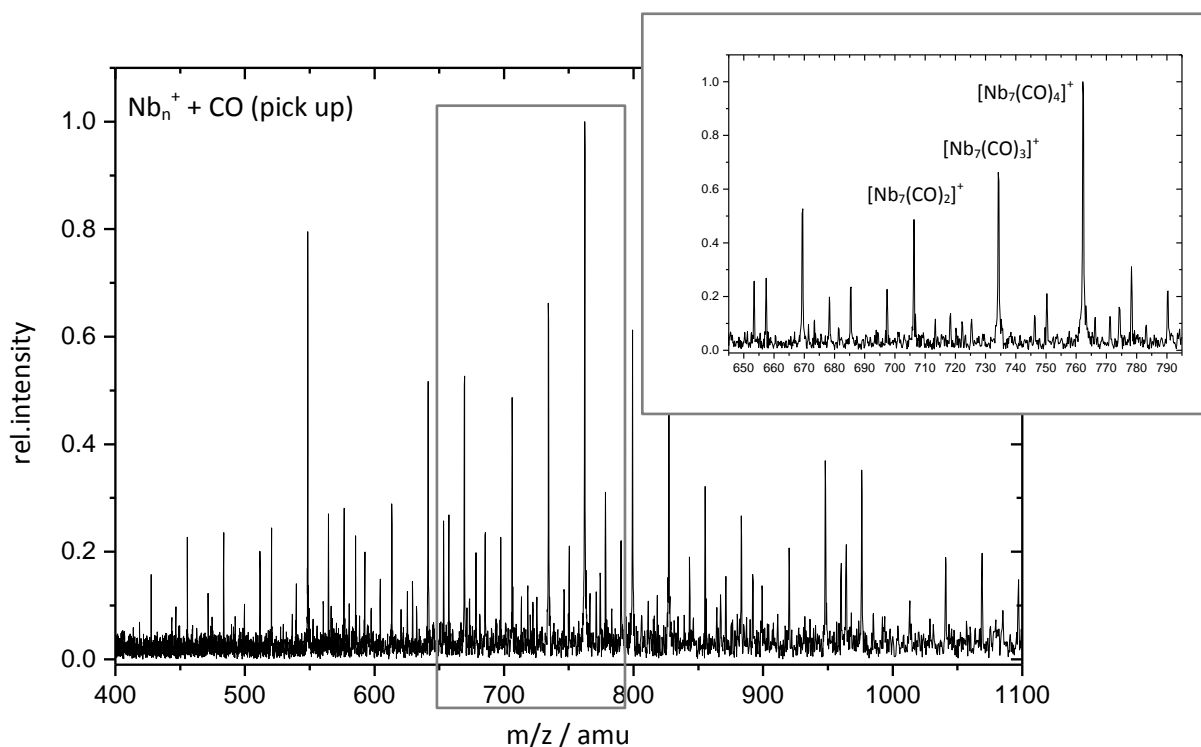

Fig. 21: *Mass spectrum of cationic niobium clusters generated by LVAP source with pick up unit; addition of CO gas raising the pressure to $8.0 \cdot 10^{-5}$ mbar. Predominant complexes are of the type $[Nb_n(CO)_m]^+$ (with oxygen impurities $[Nb_nO(CO)_m]^+$), pure metal clusters are no longer visible.*

The enlarged part of the mass spectrum in Fig. 21 shows the behavior of the Nb_7^+ cluster as an example: The cluster itself is not visible any more, but the addition of up to five CO units (+ 5 · 28 m/z) to the metal cluster or to the metal cluster oxide complexes (the oxygen origins from impurities in first layers of the metal cluster target). Table 4 provides a complete list of all recorded metal cluster adsorbate peaks.

Table 4: *Observed intensities of Nb_n^+ clusters and products as generated by the LVAP / CO added via pick up combination.*

Cluster size n	Nb_n^+	+ (CO)	+ O(CO)	+ (CO)$_2$	+ O(CO)$_2$	+ (CO)$_3$	+ O(CO)$_3$	+ (CO)$_4$	+ O(CO)$_4$	+ (CO)$_5$
4				19.2	9.4	27.7	15.0	28.7		
5				14.6	5.0	47.5	16.1	16.8		
6		10.4		13.1	6.6	23.5	12.2	23.9		10.3
7		1.6	0.5	4.0	0.9	5.4	1.7	81.6	2.5	1.8
8		5.4		26.5		27.8	8.2	13.9	6.7	11.6
9		6.0	5.2	9.7	4.2	12.8	4.6	22.8	13.1	21.7
10				14.7		18.7		32.6		34.0

Anionic clusters (Fig. 22) show a much slower reactivity[78]. The enlarged part shows the behavior of the Nb_7^- cluster: The cluster itself still occurs with highest intensity. Beside the addition of up to a maximum of three formal intact CO units, the addition of C (+12 m/z) and O (+ 16 m/z) fragment atoms is remarkably high.
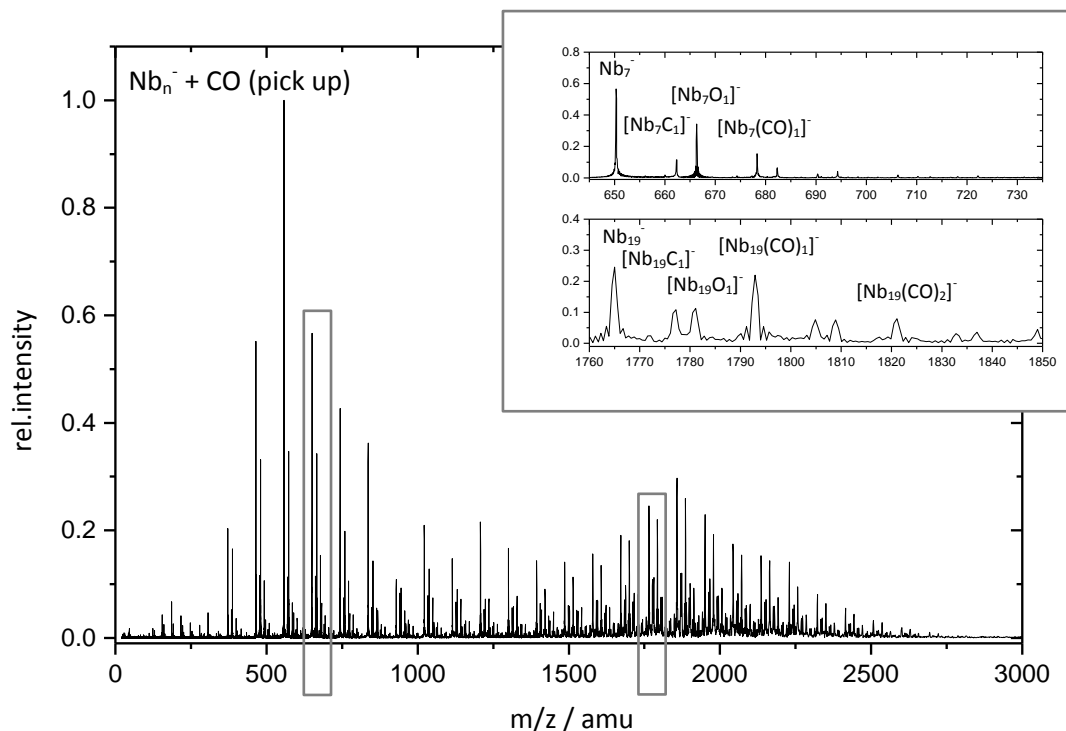

Fig. 22: *Mass spectrum of anionic niobium clusters generated by LVAP source with pick up unit; addition of CO gas raising the pressure to $6.0 \cdot 10^{-6}$ mbar. Complexes are of the type $[Nb_nC_mO_i]^-$, indicating the at least partial activation of CO molecules.*

Table 5 gives the relative abundance of each peak. As the addition of 28 m/z is only the formal addition of a complete CO molecule, IR-MPD spectroscopy might help determining whether the molecule is still bound intact to the cluster or already broken into the two atoms.

Table 5: *Observed intensities of Nb$_n^-$ clusters and products as generated by the LVAP / CO added via pick up combination.*

Cluster size n	Nb$_n^-$	+ C	+ O	+ C$_2$	+ (CO)	+ O$_2$	+ C(CO)	+ O(CO)	+ C$_2$(CO)	+ (CO)$_2$	+O$_2$(CO)	+ C(CO)$_2$	+ O(CO)$_2$	+ (CO)$_3$
4	41.1	10.6	33.4	0.8	7.3	1.7	1.1	3.4		0.7				
5	45.8	9.6	27.5	0.5	8.8	2.8	1.3	2.3		0.7	0.4		0.3	
6	60.6	6.9	21.0	0.3	3.9	2.8	0.9	2.2		0.8	0.5			
7	41.4	8.4	25.0	1.0	11.2	4.7	1.8	3.0	0.4	1.4	0.6		1.0	
8	44.2	7.7	20.6	1.1	10.9	4.7	1.4	4.5	0.7	1.8	1.1	0.5	0.8	
9	47.5	7.4	18.7	1.3	7.3	6.7	1.9	3.3	0.7	2.6	0.6	0.8	1.2	
10	22.6	17.4	19.3	2.3	10.4	5.5	6.9	5.3	1.1	4.5	1.2	1.6	1.9	
11	33.1	12.4	20.3	1.4	11.8	4.6	3.1	4.5	0.9	3.0	1.0	1.2	1.7	1.1
12	27.7	12.4	16.9	1.6	13.6	4.0	4.7	5.9	0.8	5.7	1.8	1.3	2.4	1.0
13	37.9	9.3	12.6	2.4	12.8	3.3	3.8	5.0	1.4	4.5	1.8	1.6	1.8	1.8
14	32.0	10.8	11.2	2.5	14.9	4.0	4.8	4.8	1.6	4.9	1.6	2.3	2.0	2.6
15	24.8	11.0	9.0	2.8	15.7	2.6	7.1	5.5	2.3	8.4	2.1	3.4	2.5	2.6
16	20.9	8.9	8.8	2.9	16.8	3.2	7.7	7.4	2.8	8.4	2.1	3.2	3.4	3.5
17	21.1	9.4	9.4	1.9	18.2	2.5	6.2	8.2	2.2	7.7	2.2	3.8	3.6	3.6
18	19.6	7.3	10.0	2.1	18.5	3.8	6.9	8.5	2.2	8.2	2.6	2.8	3.5	4.0
19	23.9	10.5	10.9		21.4		7.4	7.4		7.7		3.1	3.5	4.3
20	24.5	9.9	9.9		21.4		6.2	8.4		7.6	2.3	2.3	3.4	4.0
21	20.8	7.7	10.0	2.7	17.4	3.1	7.0	7.1	2.4	8.4	2.0	4.1	3.5	3.8
22	23.3	9.1	11.0		20.5		7.3	8.0		8.4		4.1	3.8	4.6
23	21.8	9.4	10.1		20.4		8.3	8.4		10.7		3.4	4.2	3.4
24	27.3	10.5	11.8		18.4		7.0	8.0		6.9		3.3	3.3	3.6
25	24.9	10.6	11.4		19.6		6.5	7.5		8.6		4.5	4.1	2.3

2.10. Mass spectra of $Nb_n^{+/-}$ clusters with argon as expansion gas

In many IR-MPD experiments of other groups, noble gases are used as messenger molecules: This atom is bound very weakly to the transition metal cluster or transition metal - adsorbate complex and thus does not change its structural motif. As it is bound very weakly, a resonant absorption of (infrared) light to a cluster mode can easily lead to the splitting-off of this tagged atom [51-60]. For the sake of completeness is has to be mentioned that whether the addition of such a tagged molecule does or does not affect the original structure in a significant manner is in doubt. New investigations varying the nature of tagged atoms/molecules or their number systematically do show an influence of the messenger molecule at least on small systems [90, 91]. Nevertheless we made several attempts to attach argon to metal clusters when introducing it into the pick up source. But no metal cluster argon complex could be confirmed.

In former experiments of our group [18] changing the expansion gas from helium to argon in the LVAP source had already proven useful for attaching argon atoms to the clusters. In our recent experimental setup most abundantly the Nb_1^+ cluster with multiple argon atoms and very small amounts of Nb_2^+ and Nb_3^+ with argon atoms could be obtained (Fig. 23). Attaching multiple argon atoms to larger clusters did not succeed with the current valve. In former experiments in our group the characteristic of the piezo valve has proven to be crucial on the production of metal cluster argon complexes: One valve might produce only very small clusters with many argon atoms attached, the other might produce higher clusters with smaller amounts of argon atoms attached [92].
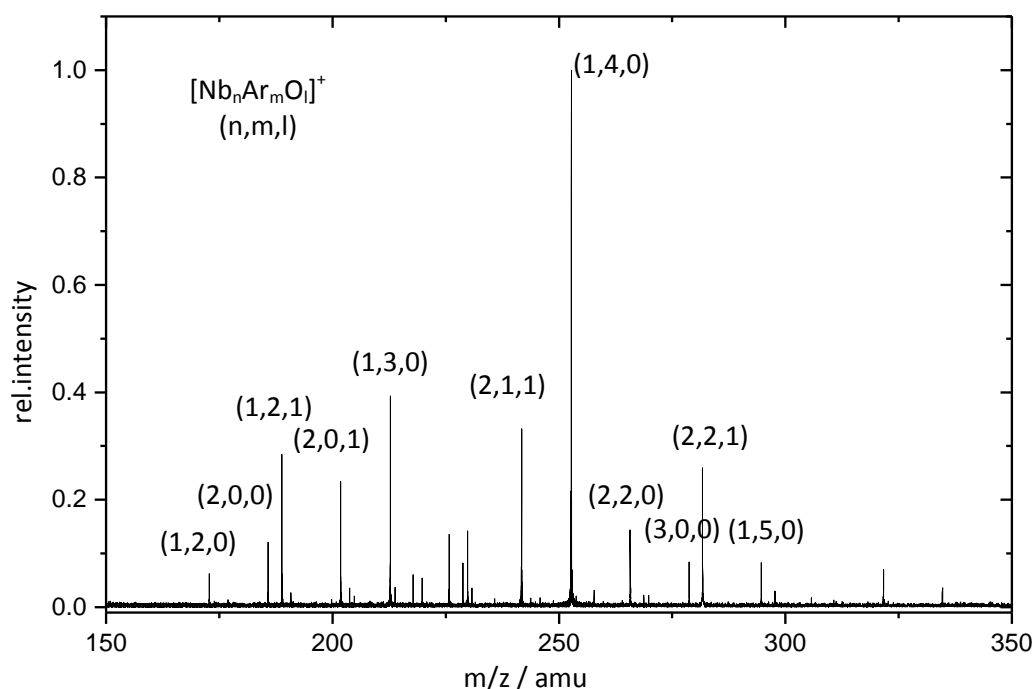

Fig. 23: *Mass spectrum of Nb_n^+ with argon as expansion gas. Multiple addition of argon atoms to the Nb_1^+ atom is present.*

2.11. Adsorbate gas tagging in a multipole: Planned modifications on Kaiserslautern FT-ICR

As the idea of tagging molecules onto the metal clusters by introducing the gases through the pick up unit of the LVAP source did not completely succeed, two different ideas have to be considered. The first idea is to introduce the tagging gas already within the expansion gas. This has proven useful in the experiments of other groups (e.g. Ref. [49, 50, 77]). A second idea is to modify the recently delivered Kaiserslautern Apex Ultra FT-ICR (see Fig. 24). As mentioned in chapter 2.2. installation of an ion bender within the Paris-instrument was only possible after the combined unit of ESI source, quadrupole (QP) mass filter and hexapole (HP) collision cell. This is different at the new Kaiserslautern Bruker Apex Ultra FT-ICR mass spectrometer. Here, we can install an ion bender (with smaller dimensions to bend the ions with lower voltages) directly after the ESI source and in front of the QP/HP part and use the quadrupole to mass select ions from any ion source and store them afterwards in the HP. Here, the addition of gases is accessible. To improve the capabilities of the new FT-ICR this HP will also be installed on a helium cryostat that will allow for the cooling of the HP and thus the gases within the HP down to 10 K. Together with the already installed modifications developed by Heinrich Kampschulte [93] (installation of three passively and two actively cooling copper shields), which allow for the cooling of the ICR cell region down to approx. 10 K this will open the options for temperature controlled kinetic and high resolution IR investigations in two ways (the cooling reduces the thermally induced population of higher rotational states and thus reduces the bandwidth of the peaks in the IR-MPD spectra):

a) Ions are produced in any source and cooled in the high pressure HP. This allows for fast FT-ICR-MS detection. The investigation of metal cluster adsorbate complexes is achievable for complexes that already form in the LVAP source (with or without pick up unit).

b) Metal clusters are generated in the LVAP source, adsorbate complexes are formed in the HP and transferred into and cooled down in the ICR cell region by collisional cooling with cold helium gas. As the gas has to be pumped before ICR mass detection, this method will be the slower one, but allows for the formation of any metal cluster adsorbate complex.

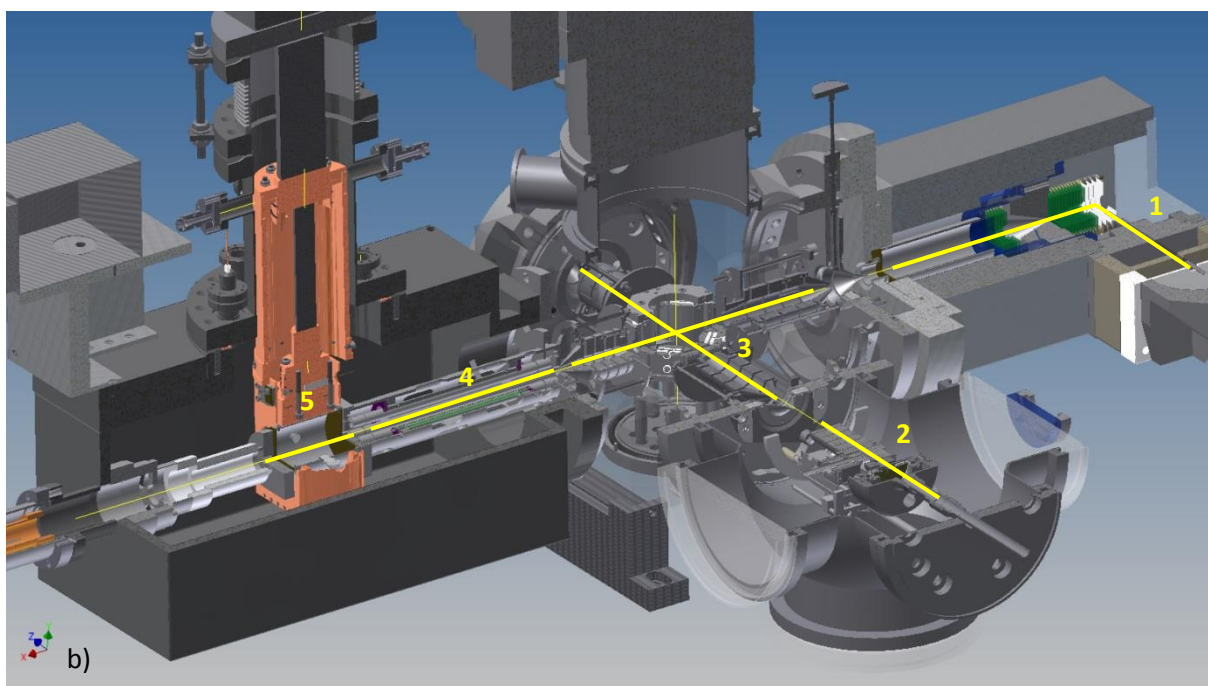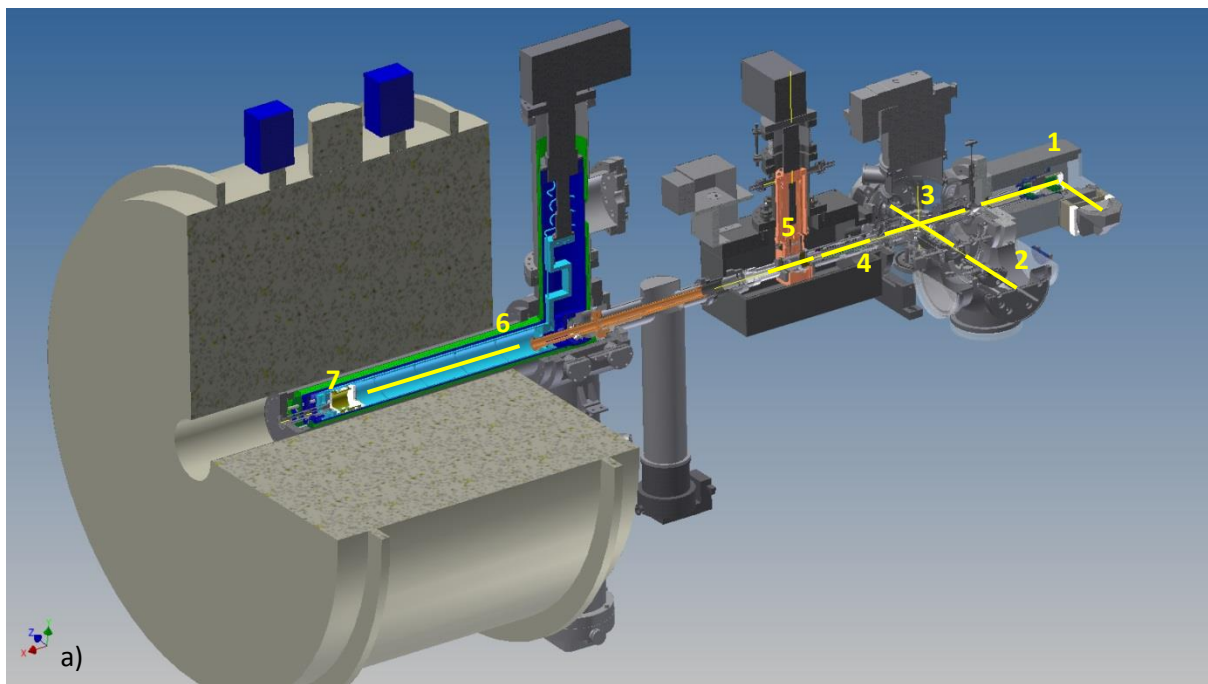A schematic drawing of the new concept is given in detail in Fig. 24.

Fig. 24: *Plan of modified Apex Ultra setup of the Kaiserslautern FT-ICR: a) complete scheme; b) source part. 1) ESI source unit with ion funnels, 2) LVAP source, 3) ion bender with transfer optics, 4) quadrupole mass filter, 5) hexapole collision cell with helium cryostat, 6) copper shields with helium cryostat, 7) ICR cell (drawings: Thomas Kolling).*

2.12. Summary and conclusions

At the Paris CLIO facility a newly installed Bruker Apex Qe FT-ICR mass spectrometer has been modified with an ion bender that allows for the usage of any ion source in addition to the manufacturer installed ESI source. We installed an LVAP source to produce metal cluster adsorbate complex ions of the type $[Nb_n(C_6H_6)]^{+/-}$. IR-MPD of the complexes $[Nb_nC_6H_6]^{+/-}$ (n = 18, 19) resulting in the fragments of $[Nb_nC_6]^{+/-}$ succeeded, obviously nonresonant, possibly because of vibronic / electronic transitions. In Kaiserslautern we extended the capabilities of the LVAP by adding a gas pick up unit with partial success: Complex gases containing C-H bonds break within the plasma of the cluster formation, but more stable gases like CO seem to attach at least partially intactly to the metal clusters. Metal cluster production with argon tagged onto the cluster failed when introducing argon through the pick up source, but succeeded when using argon as expansion gas.

A new mass spectrometer concept of an additional multipole collision cell for metal cluster adsorbate formation and subsequent cooling and with that achieving high resolution IR-MPD of the transition metal cluster adsorbate complexes is currently under construction.

2.13. References

[1]   C.S. Yeh, Y.G. Byun, S. Afzaal, S.Z. Kan, S. Lee, B.S. Freiser, P.J. Hay, *Experimental and theoretical-studies on Nb4C40/+ - reactivity and structure of the smallest cubic niobium-carbon cluster*, Journal of the American Chemical Society, **117** (1995) 4042-4048.

[2]   Y.G. Byun, S.Z. Kan, S.A. Lee, Y.H. Kim, M. Miletic, R.E. Bleil, S. Kais, B.S. Freiser, *Experimental and theoretical studies of Nb6C7(0/+)*, Journal of Physical Chemistry, **100** (1996) 6336-6341.

[3]   M.R. Zakin, R.O. Brickman, D.M. Cox, A. Kaldor, *Dependence of metal cluster reaction-kinetics on charge state .2. Chemisorption of hydrogen by neutral and positively charged iron clusters*, Journal of Chemical Physics, **88** (1988) 6605-6610.

[4]   J.L. Elkind, F.D. Weiss, J.M. Alford, R.T. Laaksonen, R.E. Smalley, *Fourier-Transform Ion Cyclotron Resonance studies of H-2 chemisorption on niobium cluster cations*, Journal of Chemical Physics, **88** (1988) 5215-5224.

[5]   R.S. Walters, T.D. Jaeger, M.A. Duncan, *Infrared Spectroscopy of Ni+(C2H2)(n) complexes: Evidence for intracluster cyclization reactions*, Journal of Physical Chemistry A, **106** (2002) 10482-10487.

[6]   P.J. Brucat, C.L. Pettiette, S. Yang, L.S. Zheng, M.J. Craycraft, R.E. Smalley, *Charge dependence of chemisorption patterns for transition-metal clusters*, Journal of Chemical Physics, **85** (1986) 4747-4748.

[7]   M.P. Irion, *Size effects in metal cluster-ion chemistry*, International Journal of Mass Spectrometry and Ion Processes, **121** (1992) 1-47.

[8]   P.B. Armentrout, *Reactions and thermochemistry of small transition metal cluster ions*, Annual Review of Physical Chemistry, **52** (2001) 423-461.

[9]   M.B. Knickelbein, *Reactions of transition metal clusters with small molecules*, Annual Review of Physical Chemistry, **50** (1999) 79-115.

[10]   S. Wei, B.C. Guo, H.T. Deng, K. Kerns, J. Purnell, S.A. Buzza, A.W. Castleman, *Formation of Met-cars and face-centered-cubic structures - thermodynamically or kinetically controlled*, Journal of the American Chemical Society, **116** (1994) 4475-4476.

[11]   J. Harris, S. Andersson, *H-2 dissociation at metal-surfaces*, Physical Review Letters, **55** (1985) 1583-1586.

[12]   J.S. Pilgrim, L.R. Brock, M.A. Duncan, *Photodissociation of niobium - carbon clusters and nanocrystals*, Journal of Physical Chemistry, **99** (1995) 544-550.

[13]   M.R. Zakin, R.O. Brickman, D.M. Cox, A. Kaldor, *Dependence of metal cluster reaction-kinetics on charge state .1. Reaction of neutral (Nbx) and ionic (Nbx+, Nbx-) niobium clusters with D2*, Journal of Chemical Physics, **88** (1988) 3555-3560.

[14]   A. Berces, P.A. Hackett, L. Lian, S.A. Mitchell, D.M. Rayner, *Reactivity of niobium clusters with nitrogen and deuterium*, Journal of Chemical Physics, **108** (1998) 5476-5490.

[15]   D.C. Parent, S.L. Anderson, *Chemistry of metal and semimetal cluster ions*, Chemical Reviews, **92** (1992) 1541-1565.

[16]   K. Eller, H. Schwarz, *Organometallic chemistry in the gas-phase*, Chemical Reviews, **91** (1991) 1121-1177.

[17]   U. Achatz, C. Berg, S. Joos, B.S. Fox, M.K. Beyer, G. Niedner-Schatteburg, V.E. Bondybey, *Methane activation by platinum cluster ions in the gas phase: effects of cluster charge on the Pt-4 tetramer*, Chemical Physics Letters, **320** (2000) 53-58.

[18]   G. Albert, C. Berg, M. Beyer, U. Achatz, S. Joos, G. NiednerSchatteburg, V.E. Bondybey, *Methane activation by rhodium cluster argon complexes*, Chemical Physics Letters, **268** (1997) 235-241.

[19]   R.L. Whetten, D.M. Cox, D.J. Trevor, A. Kaldor, *Correspondence between electron-binding energy and chemisorption reactivity of iron clusters*, Physical Review Letters, **54** (1985) 1494-1497.

[20]   J. Ho, L. Zhu, E.K. Parks, S.J. Riley, *Temperature-dependence of the reactions of small cobalt clusters with deuterium*, Journal of Chemical Physics, **99** (1993) 140-147.

[21]   D. van Heijnsbergen, G. von Helden, M.A. Duncan, A.J.A. van Roij, G. Meijer, *Vibrational spectroscopy of gas-phase metal-carbide clusters and nanocrystals*, Physical Review Letters, **83** (1999) 4983-4986.

[22]   H. Harris, I. Dance, *The geometric and electronic structures of niobium carbon clusters*, Journal of Physical Chemistry A, **105** (2001) 3340-3358.

[23]   I. Swart, P. Gruene, A. Fielicke, G. Meijer, B.M. Weckhuysen, F.M.F. de Groot, *Molecular adsorption of H(2) on small cationic nickel clusters*, Physical Chemistry Chemical Physics, **10** (2008) 5743-5745.

[24]   I. Swart, F.M.F. de Groot, B.M. Weckhuysen, P. Gruene, G. Meijer, A. Fielicke, *H-2 adsorption on 3d transition metal clusters: A combined infrared spectroscopy and density functional study*, Journal of Physical Chemistry A, **112** (2008) 1139-1149.

[25]   V. Dryza, E.J. Bieske, *Infrared Spectroscopy of the Ag+-H-2 Complex: Exploring the Connection Between Vibrational Band-Shifts and Binding Energies*, Journal of Physical Chemistry Letters, **2** (2011) 719-724.

[26]   I. Swart, F.M.F. de Groot, B.M. Weckhuysen, D.M. Rayner, G. Meijer, A. Fielicke, *The effect of charge on CO binding in rhodium carbonyls: From bridging to terminal CO*, Journal of the American Chemical Society, **130** (2008) 2126-+.

[27]   M.B. Knickelbein, G.M. Koretsky, *Infrared studies of the interaction of methanol with Cu-n, Ag-n, and Au-n*, Journal of Physical Chemistry A, **102** (1998) 580-586.

[28]   R. Rousseau, G. Dietrich, S. Kruckeberg, K. Lutzenkirchen, D. Marx, L. Schweikhard, C. Walther, *Probing cluster structures with sensor molecules: methanol adsorbed onto gold clusters*, Chemical Physics Letters, **295** (1998) 41-46.

[29]   G. Dietrich, K. Dasgupta, S. Kruckeberg, K. Lutzenkirchen, L. Schweikhard, C. Walther, J. Ziegler, *Infrared photodesorption of methanol molecules adsorbed on a Au-4(+) cluster*, Chemical Physics Letters, **259** (1996) 397-402.

[30]   E.D. Pillai, T.D. Jaeger, M.A. Duncan, *IR spectroscopy of Nb+(N-2)(n) complexes: Coordination, structures, and spin states*, Journal of the American Chemical Society, **129** (2007) 2297-2307.

[31]   D. van Heijnsbergen, A. Fielicke, G. Meijer, G. von Helden, *Structure determination of gas-phase niobium and tantalum carbide nanocrystals via infrared spectroscopy*, Physical Review Letters, **89** (2002) 013401-013401.

[32]   H. Kietzmann, J. Morenzin, P.S. Bechthold, G. Gantefor, W. Eberhardt, D.S. Yang, P.A. Hackett, R. Fournier, T. Pang, C.F. Chen, *Photoelectron spectra and geometric structures of small niobium cluster anions*, Physical Review Letters, **77** (1996) 4528-4531.

[33]   I. Swart, A. Fielicke, B. Redlich, G. Meijer, B.M. Weckhuysen, F.M.F. de Groot, *Hydrogen-induced transition from dissociative to molecular chemisorption of CO on vanadium clusters*, Journal of the American Chemical Society, **129** (2007) 2516-2520.

[34]   A. Fielicke, G. von Helden, G. Meijer, D.B. Pedersen, B. Simard, D.M. Rayner, *Size and charge effects on the binding of CO to small isolated rhodium clusters*, Journal of Physical Chemistry B, **108** (2004) 14591-14598.

[35]   M.R. Zakin, R.O. Brickman, D.M. Cox, K.C. Reichmann, D.J. Trevor, A. Kaldor, *Infrared-spectroscopy of unsupported metal cluster complexes using multiple photon dissociation*, Journal of Chemical Physics, **85** (1986) 1198-1199.

[36]   M.B. Knickelbein, *Infrared-spectroscopy of metal cluster-adsorbate complexes - Fe-n(CH3OH)(m) revisited*, Chemical Physics Letters, **239** (1995) 11-17.

[37]   U. Frenzel, A. Roggenkamp, D. Kreisle, *Black-body radiation of free niobium clusters heated by oxidation*, Chemical Physics Letters, **240** (1995) 109-113.

[38]   M.B. Knickelbein, *The infrared photodissociation spectra of Fe-n(CH3OH)(m) complexes and their deuterated analogs near 10 mu*, Journal of Chemical Physics, **104** (1996) 3517-3525.

[39]   B.M. Reinhard, A. Lagutschenkov, J. Lemaire, P. Maitre, P. Boissel, G. Niedner-Schatteburg, *Reductive nitrile coupling in niobium-acetonitrile complexes probed by free electron laser IR multiphoton dissociation spectroscopy*, Journal of Physical Chemistry A, **108** (2004) 3350-3355.

[40]   S. Hirabayashi, R. Okawa, M. Ichihashi, Y. Kawazoe, T. Kondow, *Structures and reactions of methanol molecules on cobalt cluster ions studied by infrared photodissociation spectroscopy*, Journal of Chemical Physics, **130** (2009).

[41]   S. Minemoto, A. Terasaki, T. Kondow, *Electronic and geometric structures of vanadium cluster ions; V-n(+) (n=3-5), studied by optical absorption spectroscopy*, Journal of Electron Spectroscopy and Related Phenomena, **106** (2000) 171-178.

[42]   D.G. Leopold, W.C. Lineberger, *A study of the low-lying electronic states of Fe2 and Co2 by negative-ion photoelectron-spectroscopy*, Journal of Chemical Physics, **85** (1986) 51-55.

[43]   D. Schooss, S. Gilb, J. Kaller, M.M. Kappes, F. Furche, A. Kohn, K. May, R. Ahlrichs, *Photodissociation spectroscopy of Ag-4(+)(N-2)(m), m=0-4*, Journal of Chemical Physics, **113** (2000) 5361-5371.

[44]   R.L. Whetten, M.R. Zakin, D.M. Cox, D.J. Trevor, A. Kaldor, *Electron-binding and chemical inertness of specific Nbx clusters*, Journal of Chemical Physics, **85** (1986) 1697-1698.

[45]   H. Kietzmann, J. Morenzin, P.S. Bechthold, G. Gantefor, W. Eberhardt, *Photoelectron spectra of Nb-n(-) clusters: Correlation between electronic structure and hydrogen chemisorption*, Journal of Chemical Physics, **109** (1998) 2275-2278.

[46]   M. Ichihashi, C.A. Corbett, T. Hanmura, J.M. Lisy, T. Kondow, *Size-specific reactions of copper cluster ions with a methanol molecule*, Journal of Physical Chemistry A, **109** (2005) 7872-7880.

[47]   J. Conceicao, R.T. Laaksonen, L.S. Wang, T. Guo, P. Nordlander, R.E. Smalley, *Photoelectron-spectroscopy of transition-metal clusters - correlation of valence electronic-structure to reactivity*, Physical Review B, **51** (1995) 4668-4671.

[48]   S. Hirabayashi, R. Okawa, M. Ichihashi, T. Kondow, *Detection of OH stretching mode of CH3OH chemisorbed on Ni-3(+) and Ni-4(+) by infrared photodissociation Spectroscopy*, Journal of Physical Chemistry A, **111** (2007) 7664-7669.

[49]   P.M. Bialach, M. Braun, A. Luechow, M. Gerhards, *Structures of isolated Co-2(alcohol)(1) cluster anions*, Physical Chemistry Chemical Physics, **11** (2009) 10403-10408.

[50]   P.M. Bialach, A. Funk, M. Weiler, M. Gerhards, *IR spectroscopy on isolated Co-n(alcohol)(m) cluster anions (n=1-4, m=1-3): Structures and spin states*, Journal of Chemical Physics, **133** (2010).

[51]   A. Fielicke, A. Kirilyuk, C. Ratsch, J. Behler, M. Scheffler, G. von Helden, G. Meijer, *Structure determination of isolated metal clusters via far-infrared spectroscopy*, Physical Review Letters, **93** (2004).

[52]   A. Fielicke, C. Ratsch, G. von Helden, G. Meijer, *Isomer selective infrared spectroscopy of neutral metal clusters*, Journal of Chemical Physics, **122** (2005).

[53]   A. Fielicke, C. Ratsch, G. von Helden, G. Meijer, *The far-infrared spectra of neutral and cationic niobium clusters: Nb(5)(0/+) to Nb(9)(0/+)*, Journal of Chemical Physics, **127** (2007).

[54]   C. Ratsch, A. Fielicke, A. Kirilyuk, J. Behler, G. von Helden, G. Meijer, M. Scheffler, *Structure determination of small vanadium clusters by density-functional theory in comparison with experimental far-infrared spectra*, Journal of Chemical Physics, **122** (2005).

[55]   B.A. Collings, K. Athanassenas, D. Lacombe, D.M. Rayner, P.A. Hackett, *Optical-absorption spectra of Au-7, Au-9, Au-11 and Au-13 and their cations - gold clusters with 6, 7, 8, 9, 10, 11, 12, and 13 s-electrons*, Journal of Chemical Physics, **101** (1994) 3506-3513.

[56]   B.A. Collings, K. Athanassenas, D.M. Rayner, P.A. Hackett, *Optical spectroscopy of Ag7, Ag-9+, and Ag9 - a test of the photodepletion method*, Chemical Physics Letters, **227** (1994) 490-495.

[57]   B.A. Collings, K. Athanassenas, D.M. Rayner, P.A. Hackett, *Absorption-spectra of small niobium and gold clusters measured by photodepletion of their rare-gas van-der-Waals complexes - some preliminary experiments*, Zeitschrift Fur Physik D-Atoms Molecules and Clusters, **26** (1993) 36-40.

[58]   M.B. Knickelbein, *The absorption spectra of small nickel clusters via photodissociation - NinArm- Nin+mAr*, Journal of Chemical Physics, **99** (1993) 2377-2382.

[59]   M.B. Knickelbein, W.J.C. Menezes, *Optical-response of small niobium clusters*, Physical Review Letters, **69** (1992) 1046-1049.

[60]   W.J.C. Menezes, M.B. Knickelbein, *Photodissociation spectroscopy of NbnArm complexes*, Journal of Chemical Physics, **98** (1993) 1856-1866.

[61]   R.C. Dunbar, *Photodissociation of trapped ions*, International Journal of Mass Spectrometry, **200** (2000) 571-589.

[62]   T.D. Jaeger, M.A. Duncan, *Vibrational spectroscopy of Ni+(benzene)(n) complexes in the gas phase*, Journal of Physical Chemistry A, **109** (2005) 3311-3317.

[63]   T.D. Jaeger, D. van Heijnsbergen, S.J. Klippenstein, G. von Helden, G. Meijer, M.A. Duncan, *Vibrational spectroscopy and density functional theory of transition-metal ion-benzene and dibenzene complexes in the gas phase*, Journal of the American Chemical Society, **126** (2004) 10981-10991.

[64]   D. van Heijnsbergen, T.D. Jaeger, G. von Helden, G. Meijer, M.A. Duncan, *The infrared spectrum of Al+-benzene in the gas phase*, Chemical Physics Letters, **364** (2002) 345-351.

[65]   H.P. Fritz, W. Luttke, H. Stammreich, R. Forneris, *IR-Untersuchungen und Ramen-Untersuchungen zur Struktur des Di-Benzol-Chroms, seines Kations sowie verwandter Verbindungen*, Spectrochimica Acta, **17** (1961) 1068-1091.

[66]   G.M. Koretsky, M.B. Knickelbein, *Infrared photodissociation spectroscopy of Ag-n(C6H6)(m) and Ag-n(C6D6)(m) clusters: Evidence of adsorption-induced symmetry reduction in benzene*, Chemical Physics Letters, **267** (1997) 485-490.

[67]   N.R. Walker, R.S. Walters, M.A. Duncan, *Frontiers in the infrared spectroscopy of gas phase metal ion complexes*, New Journal of Chemistry, **29** (2005) 1495-1503.

[68]   M.R. Zakin, D.M. Cox, A. Kaldor, *Reaction of niobium clusters with benzene-H6 and benzene-D6 - evidence for cluster-induced dehydrogenation*, Journal of Physical Chemistry, **91** (1987) 5224-5228.

[69]   C. Berg, T. Schindler, A. Lammers, G. Niednerschatteburg, V.E. Bondybey, *Dehydrogenation of xylene isomers on niobium cluster cations Nb-n(+) (n=2-26)*, Journal of Physical Chemistry, **99** (1995) 15497-15501.

[70]   M.R. Zakin, R.O. Brickman, D.M. Cox, A. Kaldor, *Size-selective dehydrogenation of benzene by gas-phase niobium cluster ions (Nbx+)*, Journal of Chemical Physics, **88** (1988) 5943-5947.

[71]   G.M. Koretsky, M.B. Knickelbein, *The reactions of silver clusters with ethylene and ethylene oxide: Infrared and photoionization studies of Agn(C2H4)(m), Ag-n(C2H4O)(m) and their deuterated analogs*, Journal of Chemical Physics, **107** (1997) 10555-10566.

[72]   C. Berg, M. Beyer, T. Schindler, G. NiednerSchatteburg, V.E. Bondybey, *Reactions of benzene with rhodium cluster cations: Competition between chemisorption and physisorption*, Journal of Chemical Physics, **104** (1996) 7940-7946.

[73]   C. Berg, T. Schindler, G. Niednerschatteburg, V.E. Bondybey, *Reactions of simple hydrocarbons with Nb-n(+) - chemisorption and physisorption on ionized niobium clusters*, Journal of Chemical Physics, **102** (1995) 4870-4884.

[74]   B. Pfeffer, S. Jaberg, G. Niedner-Schatteburg, *Reactions of simple aromatic heterocycles with niobium cluster ions (n < 30)*, Journal of Chemical Physics, **131** (2009).

[75]   C. Berg, M. Beyer, U. Achatz, S. Joos, G. Niedner-Schatteburg, V.E. Bondybey, *Effect of charge upon metal cluster chemistry: Reactions of Nb-n and Rh-n anions and cations with benzene*, Journal of Chemical Physics, **108** (1998) 5398-5403.

[76]   C. Berg, T. Schindler, M. Kantlehner, G. Niedner-Schatteburg, V.E. Bondybey, *Reactions of homonuclear and heteronuclear group Vb clusters with ethylene: evidence for structural isomers*, Chemical Physics, **262** (2000) 143-149.

[77]   M. Gerhards, O.C. Thomas, J.M. Nilles, W.J. Zheng, K.H. Bowen, *Cobalt-benzene cluster anions: Mass spectrometry and negative ion photoelectron spectroscopy*, Journal of Chemical Physics, **116** (2002) 10247-10252.

[78]   S. Jaberg, *Reaktivitätsstudien von Übergangsmetallclustern in der Gasphase mittels Fourier-Transformation-Ionen-Zyklotron-Resonanz-Massenspektrometrie und Infrarot-Multiphotonen-Dissoziation von Adipinsäure*, Doktorarbeit, Fachbereich Chemie, Technische Universität, 2008, Kaiserslautern.

[79]   B. Pfeffer, *Reaktivitätsstudien zur Aktivierung kleiner Kohlenwasserstoffe an Übergangsmetallclustern*, Doktorarbeit, Fachbereich Chemie, Technische Universität, 2008, Kaiserslautern.

[80]   V.E. Bondybey, M.K. Beyer, *Temperature effects in transition metal ion and cluster ion reactions*, Journal of Physical Chemistry A, **105** (2001) 951-960.

[81]   E.R. Fisher, P.B. Armentrout, *Reactions of Co+, Ni+, and Cu+ with cyclopropane and ethylene-oxide - metal methylidene ion bond-energies*, Journal of Physical Chemistry, **94** (1990) 1674-1683.

[82]   H.T. Liu, S.T. Sun, X.P. Xing, Z.C. Tang, *Reactions of platinum cluster ions with benzene*, Rapid Communications in Mass Spectrometry, **20** (2006) 1899-1904.

[83]   D. Majumdar, S. Roszak, K. Balasubramanian, *Interaction of benzene (Bz) with Pt and Pt-2: A theoretical study on Bz-Pt-2, Bz(2)-Pt-2, and Bz(3)-Pt-2 clusters*, Journal of Chemical Physics, **114** (2001) 10300-10310.

[84]   K. Bechamp, M. Levesque, H. Joly, L. Manceron, *A combined electron paramagnetic resonance and Fourier transform infrared study of the Co(C6H6)(1,2) complexes isolated in neat benzene or in cryogenic matrixes*, Journal of Physical Chemistry A, **110** (2006) 6023-6031.

[85]   C.D. Carver, *The Coblentz Society Desk Book of Infrared Spectra*, The Coblentz Society, Kirkwood, MO, 1982.

[86]   A.A. Radzig, B.M. Smirnov, *Reference Data on Atoms, Molecules, and Ions*, in: V.I. Goldanskii, R. Gomer, F.P. Schäfer, J.P. Toennies (Eds.) Springer Series in Chemical Physics, Springer-Verlag, Berlin, Heidlerberg, New York, Tokyo, 1985.

[87]   S. Hirabayashi, M. Ichihashi, Y. Kawazoe, T. Kondow, *Vibrational and electronic spectra of Con+(CH3OH)3 (n=1–3) measured by infrared photodissociation spectroscopy*, Chemical Physics Letters, **490** (2010) 19-23.

[88]   S. Minemoto, A. Terasaki, T. Kondow, *Electronic structures of cobalt cluster cations: Photodissociation spectroscopy of Con+Ar (n=3-5) in the visible to near-infrared range*, Journal of Chemical Physics, **104** (1996) 5770-5775.

[89]   S. Minemoto, K. Takahashi, J. Matsumoto, M. Iseda, A. Terasaki, H. Imoto, T. Kondow, *Analysis of optical absorption spectra of transition metal cluster ions by the spin-polarized DV-X alpha method*, Zeitschrift Fur Physik D-Atoms Molecules and Clusters, **40** (1997) 13-16.

[90]   R. Gehrke, P. Gruene, A. Fielicke, G. Meijer, K. Reuter, *Nature of Ar bonding to small Co[sub n][sup +] clusters and its effect on the structure determination by far-infrared absorption spectroscopy*, The Journal of Chemical Physics, **130** (2009) 034306.

[91]   K. Mizuse, A. Fujii, *Infrared photodissociation spectroscopy of H+(H2O)6[middle dot]Mm (M = Ne, Ar, Kr, Xe, H2, N2, and CH4): messenger-dependent balance between H3O+ and H5O2+ core isomers*, Physical Chemistry Chemical Physics, **13** (2011) 7129-7135.

[92]   J. Meyer, *Isolierte Übergangsmetallcluster-Edelgas-Komplexe: Erzeugung und Charakterisierung*, Diplomarbeit, Fachbereich Chemie, Technische Universität, 2009, Kaiserslautern.

[93]   H. Kampschulte, *Entwicklung einer Tieftemperatur-FT-ICR Zelle und ihre Charakterisierung mittels Reaktionskinetiken und Synchrotron-Spektroskopie*, Doktorarbeit, Fachbereich Chemie, Technische Universität, 2011, Kaiserslautern.

3. Inverse H/D isotope effects in benzene activation by cationic and anionic cobalt clusters

Abstract

Reactions under single collision conditions with benzene C_6H_6 and with benzene-d₆ C_6D_6 of size selected cationic cobalt clusters $Co_n{}^+$ and of anionic cobalt clusters $Co_n{}^-$ in the cluster size range $n = 3 - 28$ revealed that dehydrogenation by cationic clusters is sparse, while it is ubiquitous in reactions by anionic clusters. Kinetic Isotope Effects (KIE) in total reaction rates are inverse and − in part − large. Dehydrogenation Isotope Effects (DIE) are normal. A multistep model of adsorption and stepwise dehydrogenation from the precursor adsorbate unravels a possible origin of the inverse KIE: Single step C-H bond activation is swift (no KIE in forward direction) and largely reversible (normal KIE backwards) while H/D tunneling is likely to contribute (backwards). DFT calculations of the structures and energetics along the reaction path in $[Co_{13}C_6H_6]^+$ lend support to the proposed multistep model. The observed effects on rates and KIEs of cluster charges and of cluster sizes are to elucidate further.

Keywords: transition metal cluster, benzene activation, inverse kinetic isotope effect, kinetic multistep modeling, DFT calculations

3.1. Introduction

Transition metal clusters may serve as model systems for the elucidation of elementary processes in heterogeneous catalysis. Hydrocarbon adsorption and subsequent C-H bond activation are amongst the most important steps in many catalyzed reactions, and either of both is often rate limiting.

Investigations of hydrogen/deuterium (H/D) isotope effects have helped to elucidate the origin of observable phenomena in hydrocarbon activation[1-5]. Cobalt has proven valuable in numerous catalytical applications, in particular as an important metal component in the benzene hydrogenation at low temperatures[6]. Fischer Tropsch conversion of CO by cobalt nano particles showed an inverse H/D kinetic isotope effect with a mechanistic interpretation pending[7]. The significance of H/D atom tunneling in homogeneous organic transformations was recently highlighted[8]. In the particular case of C-H bond cleavage by oxoiron(IV) complexes it was concluded, however, that multiple spin state surfaces may give rise to possible spin crossover issues that enhance KIEs to such large values that resemble a tunneling like behavior[9]. The investigation of C-H bond reductive elimination of benzene from phenyl metal hydrides revealed a normal kinetic isotope effect (KIE) in the case of molybdenocene and an inverse KIE in the case of tungstenocene[10]. It was concluded that relative

barrier heights determine the kinetics and suffice to switch observable KIEs. Similar interpretations arose from the study of temperature dependent alkane reductive elimination from alkyl metal hydrides[11,12]. The lack of H/D isotope effects in the gas phase reactions of neutral zirconium atoms with small olefins was interpreted in terms of a stepwise association – activation mechanism[13].

Prior gas phase studies of benzene adsorption and activation focused on niobium and rhodium clusters[14-16]. Ubiquitous dehydrogenation through niobium cluster cations and anions alike contrast to mere adsorption by $Rh_n^\pm$. Little to no observable isotope effects prevailed in either cases. Through methane activation by cobalt cluster cations Armentrout et al.[17] determined their bond energies to D, C, CD, CD_2 and CD_3. Moreover, Armentrout et al. determined the bond energies (BDE) of cobalt-benzene and cobalt-dimer-benzene cations (2.65(11) and 1.73(14) eV, respectively) by meticulous analysis of thermochemical modeling of high precision flow reactor MS experiments[18]. Dissociative nitrogen interaction with cationic cobalt clusters is endoergic[19], nitrogen association to anionic clusters Co_n^- under flow tube conditions only takes place slowly beyond a size threshold of $n \geq 7$ [20]. Another flow tube study of photoionization efficiencies of $Co_n(C_6H_6)_m$ clusters focused onto species with multiple benzene adsorbates[21,22]. Negative ion photoelectron spectra of cobalt benzene anions revealed sandwich like structures[23]. Photoionization efficiency (PIE) spectra of cold cobalt clusters ($Co_3, Co_7 - Co_{92}$) revealed vertical ionization potentials (IPs) that decreased rapidly up to n ≈ 20, beyond which IPs evolve more slowly and smoothly. No particular cluster size sticks out significantly[24]. Insight into the electronic structure of cobalt clusters and of cobalt cluster benzene complexes arose from multiple Stern-Gerlach experiments[25-28]. Advanced synchrotron ionization studies of cationic cobalt clusters revealed significant magnetization by spins and by orbital angular moments with little cluster size dependence [29].

Plane wave density functional calculations with PBE exchange correlation functional have revealed a preference of hcp-structures in neutral high spin Co clusters[30] over icosahedral motifs which in turn had been predicted previously by application of the BLYP functional in conjunction with atom centered basis functions of double zeta plus polarization quality[31].

We chose to record the reaction kinetics and H/D isotope effects of size selected cobalt clusters with benzene in the dilute gas phase (under single collision conditions) as enabled by application of Fourier-Transform Ion-Cyclotron-Resonance (FT-ICR) mass spectrometry[32] in conjunction with the concomitant ion trapping. In this report, we investigated the difference in the reaction of ionic cobalt clusters with benzene (C_6H_6) and benzene-d_6 (C_6D_6).

3.2. Experimental and theoretical methods

3.2.1. Experimental methods

The experiments were performed with a modified Fourier-Transform Ion-Cyclotron-Resonance (FT-ICR) mass spectrometer (Bruker Apex III). We generated the cobalt clusters with a homebuilt laser vaporization source (LVAP) as described before[16,33]. The second harmonic of a pulsed Continuum Nd-YAG laser is used to evaporate cobalt atoms from a 0.4 – 1.0 mm thick rotating cobalt foil (Alpha Aesar, purity ≥ 99.95%). The emerging metal plasma is cooled and made to yield clusters by a short transverse pulse (40 μs, Helium, 8-15 bar) from a homebuilt piezoelectric valve[34]. Further cooling arises from the subsequent supersonic nozzle expansion through a 20 mm long channel (diameter of 2 mm) into vacuum (10^{-6} mbar). There is no additional ionization step. All investigated ions are generated within the laser induced plasma. Past a 1.4 mm diameter skimmer the cold cluster ions are accelerated, fed into a quadrupole ion bender (90^0) and steered by electrostatic lenses into the high field region of a superconducting magnet (7.05 Tesla, actively shielded) while appropriately decelerated. Eventually, the cluster ions are trapped for reaction and/or detection within the FT-ICR cell of so called "infinity" type[35].

In order to pursue the reactivity studies with benzene (C_6H_6) / benzene-d_6 (C_6D_6) we permitted the controlled admission of a reaction gas in order to raise the pressure in the ultrahigh vacuum chamber of the FT-ICR mass spectrometer, where the ICR trapping cell is located, from ~ 3 x 10^{-10} to typically 1-5 x 10^{-9} mbar such that a single bimolecular reactant collision per cluster per second takes place (single collision conditions). A commercial ultrahigh vacuum gauge (cold cathode gas discharge, calibrated for N_2) provides for a nominal pressure reading. There is a pressure gradient between the gauge and ICR cell of about a factor of 4, the exact value not being known. Commercially available benzene/benzene-d_6 (Sigma-Aldrich, purity ≥ 99.6 %) was applied after degassing by multiple "pump and freeze" cycles. Kinetic curves of reactant and product ions extracted from mass spectra of trapped cluster ions while exposed to the continuously admitted reactant gases and under variation of reaction delays between cluster ion admission and detection. Fits to pseudo-first-order-kinetics arise through a genetic algorithm ("evofit" program[36]).

3.2.2. Theoretical methods

Preliminary density functional calculations were performed by standard programs[37] and by applying the PBE0 exchange correlation functional[38]. Carbon and hydrogen atoms were represented by aug-cc-pVTZ basis sets, cobalt atoms by effective core potentials of double zeta quality[39-40]. The SCF density convergence criterion needed to relax to 10^{-4}. In this way, it became possible to pursue full geometry optimization and subsequent frequency calculations at an approximate level. Found minimum structures revealed either no or a single imaginary frequency that corresponds to some

large amplitude motion with a small force constant. Systematic screening for an optimum functional and for usage of advanced basis sets was beyond the scope of this study. Instead, we refer to a recent benchmark study that revealed about equal performance of several DFT functionals (PBE0, B1B95, PW6B95, and TPSS25B95) when computing reactions of late transition metal clusters[41]. The present study focusses on structures, spin states and energetics along the reaction path in $[Co_{13}C_6H_6]^+$. Systematic variation of cluster size and cluster charge remains for further studies.

Kinetic modeling took place by customized code for the *Mathematica 8* program package running on standard PC hardware. In particular the numerical integration of differential rate equations through the *NDSolve* command proved helpful.

3.3. Results and discussion

3.3.1. Experimental results
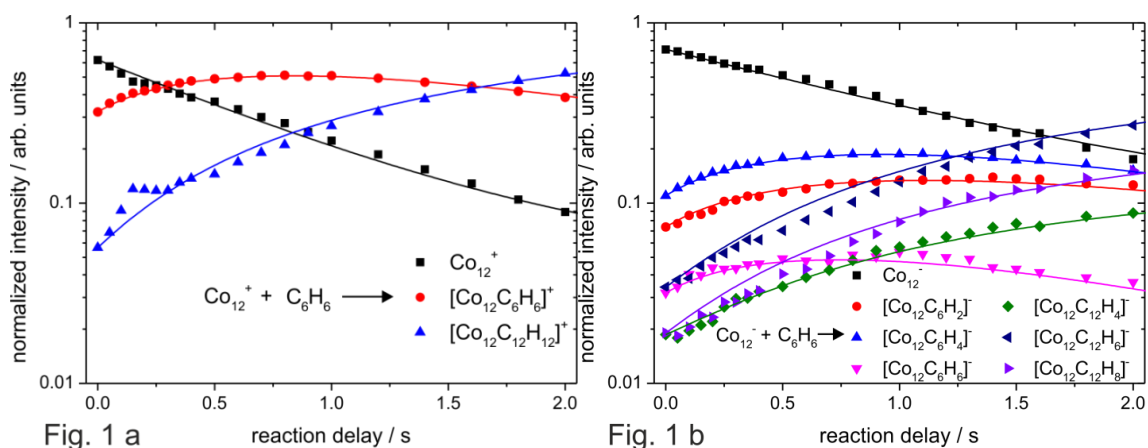
Fig. 1: *Normalized reactant and product intensities in the reactions **(a)** of cationic cobalt clusters Co_{12}^+ and **(b)** of anionic cobalt clusters Co_{12}^- with benzene C_6H_6. The temporal evolution of the experimental data points (symbols) is fitted to pseudo first order kinetics (solid lines) which provides for relative partial rate constants.*

The reaction of cationic cobalt clusters Co_n^+ with benzene (C_6H_6) and benzene-d_6 (C_6D_6) proceeds towards a single class of primary products (cf. Fig. 1a in the case of $n = 12$):

$$Co_n^+ + C_6(H,D)_6 \rightarrow [Co_n C_6(H,D)_6]^+ \qquad (3.1)$$
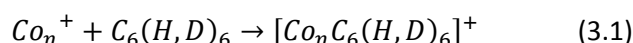
The addition resembles a seemingly intact adsorption of the reactant to the cluster surface. Structural information, however, is not retrieved through this observation. In particular, C-H bond activation with the formation of hydrido-phenylic cobalt clusters $Co_n(H)C_6H_5^+$ is conceivable. In order to account for the concomitant structural ambiguity we designate such observed products with

chemical formulas in square brackets as above. Secondary reactions with further C_6H_6 molecules – although well observable (cf. $Co_{12}C_{12}H_{12}^+$ and other "C_{12}" products in Figs. 1a and 1b) – are not subject of further inspection as of now. Within the limit of detection the cobalt cluster Co_{13}^+ is the only cationic cluster that proceeds towards a second product channel. It does so through molecular dehydrogenation and much more effectively when reacting with benzene (C_6H_6):

$$Co_{13}^+ + C_6H_6 \rightarrow [Co_{13}C_6H_6]^+$$
$$\rightarrow [Co_{13}C_6H_4]^+ + H_2 \qquad (3.2)$$
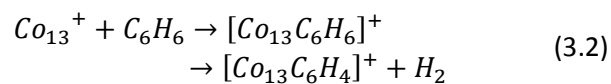
Products from dehydrogenation of perdeuterated benzene (C_6D_6) are barely detectable.

Anionic cobalt clusters such as e.g. Co_{12}^- (cf. Fig. 1b) react efficiently into multiple observable product channels in parallel:

$$Co_n^- + C_6H_6 \rightarrow [Co_nC_6H_6]^- \qquad (3.3)$$
$$\rightarrow [Co_nC_6H_4]^- + H_2$$
$$\rightarrow [Co_nC_6H_2]^- + 2H_2$$
$$\rightarrow Co_nC_6^- \quad + 3H_2$$
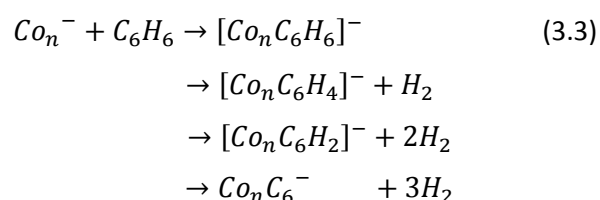
We label the overall reaction processes as adsorption, dehydrogenation, twofold dehydrogenation and total dehydrogenation, respectively. Once more, the particular structures of the observed products remain ambiguous as of now. The hydrido-phenylic cobalt cluster motif $Co_n(H)C_6H_5^-$ is a conceivable structure in the case of adsorption onto anionic clusters as well. In particular, the observation of strong dehydrogenation lends evidence to a likely C-H bond activation in general.

Kinetic information arises from the temporal evolution of the reactions (Fig. 1a and 1b). The fits of the experimental data (points) to pseudo first order kinetics (curves) determine partial and total relative rate constants and branching ratios amongst competing reaction channels. When assuming the fastest observed reaction to proceed with collision rate the obtained experimental rates would convert into reaction efficiencies per single collision event. In ionic metal cluster molecule collisions, rates may enhance somewhat through a conducting sphere effect[42]. The provided plots of Fig. 2a and 2b leave the obtained data in the form of relative rate constants, however. Otherwise, there would be exceedingly large uncertainties in the absolute reaction rate values. A quantitative determination of reactant gas densities within the ICR trap is pending.
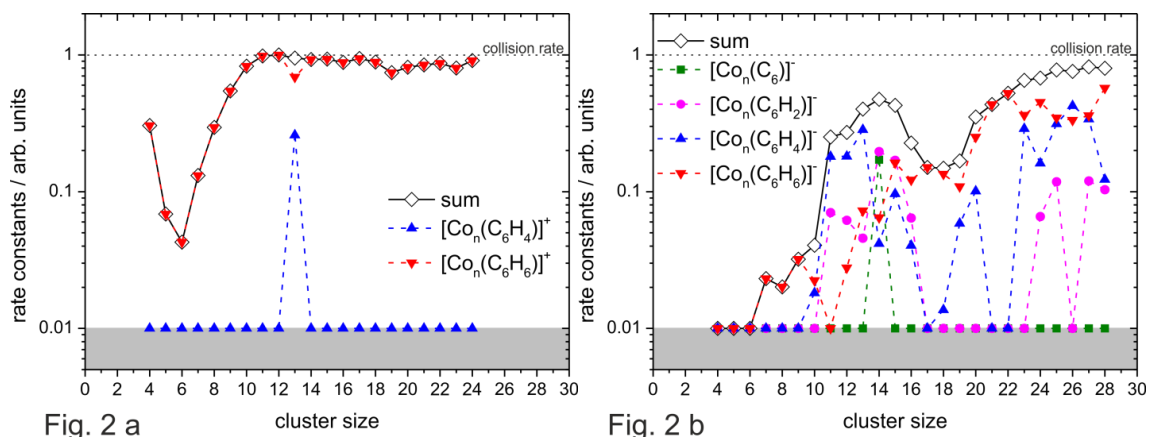
Fig. 2: *Relative partial rate constants for the reaction (a) of Co_n^+ and (b) of Co_n^- with benzene. All values were normalized to the highest rate constant. Total rate constants are provided as well. The shaded areas indicate the background noise level.*

Cationic cobalt clusters Co_n^+ with $n \geq 10$ adsorb benzene with unit efficiency per collision and without dehydrogenation (Fig. 2a). As a sole exemption, Co_{13}^+ does cause some dehydrogenation. This may relate to a conceivable icosahedral structure. At $n = 13$ it would provide for a closed geometric shell (an icosahedron of 12 surface atoms and a single volume atom at the center) with high and equal coordination of all Cobalt surface atoms. Lack of surface defects – adatoms and/or kinks – would allow for high mobility of activated species and possible pairwise recombination of H atoms at the cluster surface. Presence of surface defects might enhance the risk of pinning, reduces mobility on the surface and thereby may suppress H₂ desorption. Seemingly this scenario holds in the case of cationic clusters while it is of less to no importance in anionic clusters (cf. below).

The smaller cationic clusters provide for an adsorption efficiency that is reduced by up to a factor of five resembling a typical behavior of metal cluster reactions under single collision conditions as observed several times before [14,15,16] and attributed to microscopic reversibility within a cluster size dependent, finite heat bath.

Anionic cobalt clusters Co_n^- with $n \leq 6$ do not yield observable products while collisions with benzene inevitably take place at collision rates that are high enough to allow for detection of products down to 1% collision efficiency. The intermediate collision complex $[Co_n C_6 H_6]^-$ may in principle decay into some charged products that are outside the mass range of detection in the present experiment, e.g. by electron detachment according to:

$$Co_n^- + C_6 H_6 \rightarrow [Co_n C_6 H_6]^{*-} \rightarrow Co_n C_6 H_6 + e^- \qquad (3.4)$$
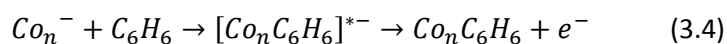
Our recorded data, however, do not provide evidence for a seeming loss of charges such that a "dark" reaction channel by electron detachment is presently ruled out to contribute significantly. Further insight could arise from the inspection of size dependencies in heats of adsorption $\Delta_{ads}H(Co_n{}^- - C_6H_6)$ and in electron detachment enthalpies $\Delta_{detach}H([Co_nC_6H_6]^-)$ of all conceivable isomers, none of which is known as of now.

Instead, basic thermodynamics regards the cluster as a finite heat bath that serves to dissipate the heat of adsorption. The more effective the dissipation the less probable becomes the benzene eventually evaporating off the cluster. With increasing cluster size the total adsorption efficiency rises, as apparent in the rate constants of cationic clusters $Co_n{}^+, n = 6 - 10$, and of anionic clusters $Co_n{}^-, n = 7 - 28$, with some modulation in between.

The size range $n = 11,..,15$ of anionic clusters is most reactive in terms of dehydrogenation, and it provides for a somewhat larger total reaction efficiency with respect to the general trend. In particular, the cluster anions $Co_n{}^-, n = 10 - 16$, form products of single, double and triple dehydrogenation at enhanced yields as compared to either smaller or larger clusters. These enhanced dehydrogenation reactivities correspond well to the increase of the total rate constant. Other than in the case of cationic clusters (the exceptional $Co_{13}{}^+$) there is no exceptional enhancement or reduction of dehydrogenation efficiency of anionic clusters (an ordinary $Co_{13}{}^-$). This may relate to enthalpic details that are not retrieved at present.

All experiments on benzene reactions with cationic and anionic cobalt clusters have been duplicated with perdeuterated benzene (C_6D_6) as well. Plots of these results are provided in the supplement, Fig. S1a and S1b. The thereby recorded findings are in qualitative agreement with those of benzene (C_6H_6). Differences arise in terms of a quantitative comparison. The many parallel reaction channels of anionic clusters however cause a risk of blurring the overall picture. We therefore introduce some scheme of further data evaluation before commencing with further interpretation.

3.3.2. Data evaluation

In order to take the degree of activation into account and to provide for further data evaluation, we define a so called average degree of dehydrogenation $\langle \chi_n \rangle$ as before[43]

$$\langle \chi_n \rangle = \frac{1}{m} \frac{1}{k_n^{tot}} \sum_{m_i=1}^{m} m_i k_n(m_i) \qquad (3.5)$$

with

$$k_n^{tot} = \sum_i k_n(m_i) \tag{3.6}$$

Here, m indicates the total amount of hydrogen or deuterium atoms as available from the reactant ($m=6$ in the present case). The partial reaction rate $k_n(m_i)$ corresponds to the cluster size n and the loss of hydrogen or deuterium atoms m_i in the observed product. $\langle \chi_n \rangle = 1$ indicates complete dehydrogenation, $\langle \chi_n \rangle = 0$ indicates adsorption without any dehydrogenation.
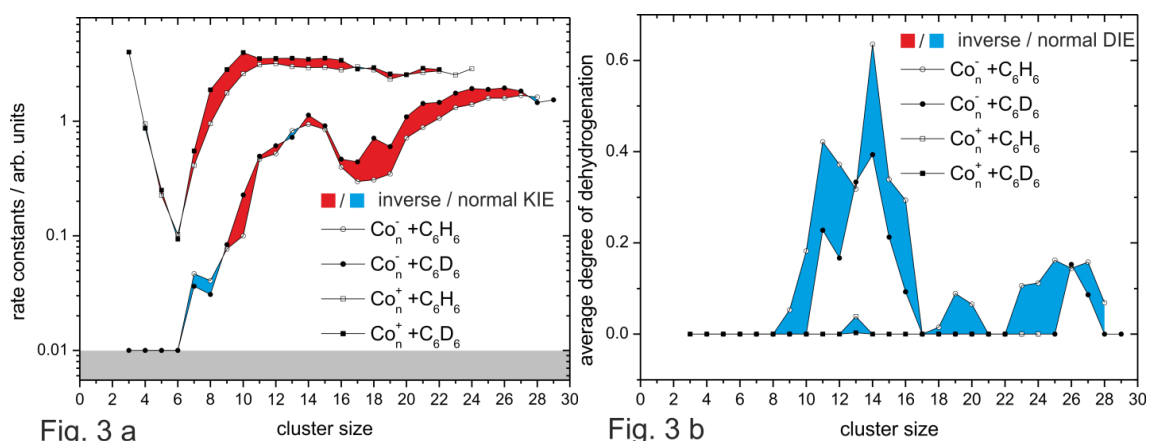

Fig. 3: (a) *Total rate constants of anionic cobalt clusters (circles) and of cationic cobalt clusters (squares) reacting with benzene (open symbols) and benzene-d_6 (filled symbols). Blue and red shadings emphasize normal and inverse kinetic isotope effects KIE(n), respectively. Gray shading indicates the background noise level.* **(b)** *Average degrees of dehydrogenation (see text for definition) of benzene (open symbols) and benzene-d_6 (filled symbols) when reacted by cationic cobalt clusters (squares) and by anionic cobalt clusters (circles). Blue shadings emphasize the prevailing normal Dehydrogenation Isotope Effect (DIE) with no inverse DIE (red) occurring - Co_{13}^- being exempt.*

A convenient way to present the results for further discussion is the combination of total reaction rates with normal benzene and with perdeuterated benzene in a single plot (Fig. 3a) and of average degrees of dehydrogenation of benzene and of perdeuterated benzene in another plot (Fig. 3b). The isotopic effects are indicated by coloring the area between related curves such that a cluster size dependent kinetic isotope effect KIE(n)

$$KIE(n) := \frac{k_{tot}^{(H)}(n)}{k_{tot}^{(D)}(n)} \tag{3.7}$$

is indicated as normal ($KIE(n) > 1$) by blue shading and as inverse ($KIE(n) < 1$) by red shading (Fig. 3a). The diagram provides a set of data for cationic cobalt clusters and a set of data for anionic cobalt clusters. $KIE(n)$ is inverse in the case of cationic clusters throughout all n values and it is

inverse in the case of most anionic clusters. Anionic clusters Co_n^- with either $n \leq 9$ or $n \geq 26$ are exemptions and reveal a normal isotope effect. While we can observe the C_6D_6 rate constants of anionic and cationic clusters revealing all of the gross features as in the C_6H_6 case before, the merging point of anionic and cationic rate constants with C_6D_6 is shifted to lower cluster sizes. The rate constants of Co_{4-8}^+ with C_6D_6 and C_6H_6 diminish by up to one order of magnitude (at $n = 6$) with respect to those of larger clusters where the total reaction rate k_n^{tot} approaches the collision rate k_{coll}. This limiting case, $k_n^{tot} \approx k_{coll}$, corresponds in the terminology of surface science to a sticking probability of unity.

Correspondingly the cluster size dependent dehydrogenation isotope effect $DIE(n)$

$$DIE(n) := \frac{<\chi_n^{(H)}>}{<\chi_n^{(D)}>} \qquad (3.8)$$

is indicated as normal ($DIE(n) > 1$) in blue and as inverse ($DIE(n) < 1$) in red (Fig. 3b). Normal $DIE(n)$ prevails in all cases investigated, namely cationic clusters $3 \leq n \leq 24$ and anionic clusters $4 \leq n \leq 29$. A very small inverse DIE for Co_{13}^- (hardly visible in Fig. 3b) is a possible exemption within combined uncertainties, however. The average degree of dehydrogenation decreases if we exchange C_6H_6 for C_6D_6 to react either with cationic clusters or with anionic clusters. The overall observable activation of C-H/C-D bonds by cationic clusters is negligible and the concomitant DIE vanishes except at Co_{13}^+ where some normal DIE persists. Effective benzene activation and product formation through anionic clusters $Co_n^-, n \geq 9$, leads to considerable dehydrogenation with normal DIE throughout. Dehydrogenation of benzene-d$_6$ takes place by Co_{11-16}^-, (as compared to Co_{9-16}^-, with benzene) and by $Co_{26,27}^-$ (as compared to Co_{18-20}^- and Co_{23-28}^- with benzene). Overall, the dehydrogenation of benzene-d$_6$ by cobalt cluster anions diminishes with respect to the one of benzene.

Numerical values of the KIE(n) derive from the data sets of Fig. 3a through eq. (3.7) and as displayed in Fig 4a and 4b.
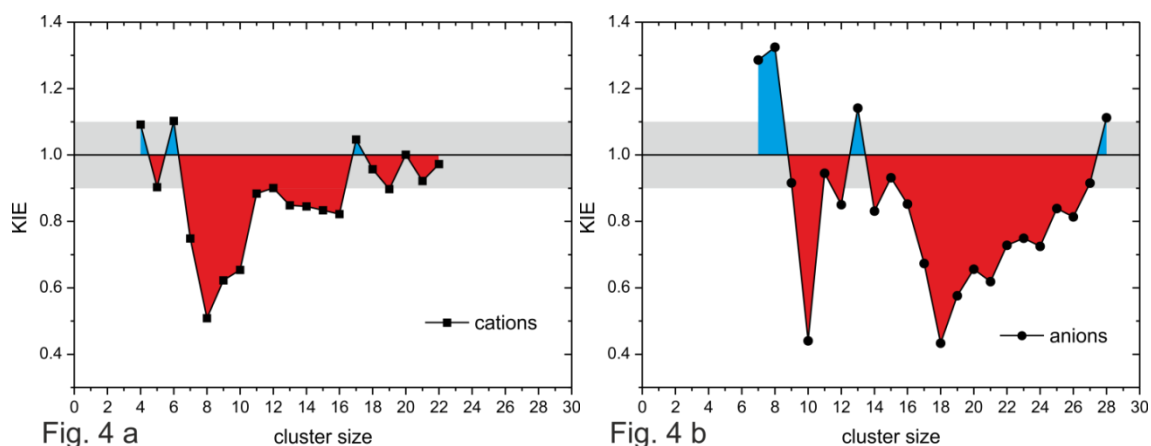
Fig. 4: *Kinetic Isotope Effects (KIE) as function of cluster size in the reactions of C_6H_6 / C_6D_6 (a) with cationic cobalt clusters and (b) with anionic cobalt clusters. Blue shadings indicate normal KIEs and red shadings indicate inverse KIEs. Gray shading indicate the estimated uncertainty.*

The reaction with benzene-d_6 for cationic clusters is up to 5 times faster than the reaction with benzene for e.g. KIE(Co_8^+).

3.3.3. Kinetic interpretation of the inverse Kinetic Isotope Effect (KIE) in terms of consecutive elementary processes

The found isotope effects on rate constants (Kinetic Isotope Effect $KIE(n)$ is inverse) and on the dehydrogenation efficiency (Dehydrogenation Isotope Effect $DIE(n)$ is normal) ask for a kinetic interpretation in terms of a model that comprises of consecutive elementary processes. While it is not possible to obtain definite answers at present state of investigations, it is mandatory to evaluate possible and likely effects.

The energetics of benzene adsorption and activation through ionic cobalt clusters are largely unknown. Some insight arises from the inspection of atomic cobalt ion complexes and of energetics from cobalt surface studies[18,44-53]. It shows that some independent cluster calculations are mandatory.

We devise a scheme of consecutive elementary processes as follows:

$$
\begin{array}{|c|}
\hline
Co_n^{\pm} + C_6H_6 \quad (\mathbf{1}^{\pm}) \\
k_1 \downarrow \quad \uparrow k_{-1} \\
\hline
Co_n(C_6H_6)^{\pm} \quad (\mathbf{2}^{\pm}) \\
k_2 \downarrow \quad \uparrow k_{-2} \\
Co_n(H)(C_6H_5)^{\pm} \quad (\mathbf{3}^{\pm}) \\
k_3 \downarrow \quad \uparrow k_{-3} \\
Co_n(H)(H)(C_6H_4)^{\pm} \quad (\mathbf{4}^{\pm}) \\
k_4 \downarrow \\
Co_n(C_6H_4)^{\pm} + H_2 \quad (\mathbf{5}^{\pm}) \\
\hline
\end{array}
$$

KIE =
$k_{tot}^{(H)} / k_{tot}^{(D)}$
< 1

DIE =
$\langle \chi_n^{(H)} \rangle / \langle \chi_n^{(D)} \rangle$
> 1

(3.9)
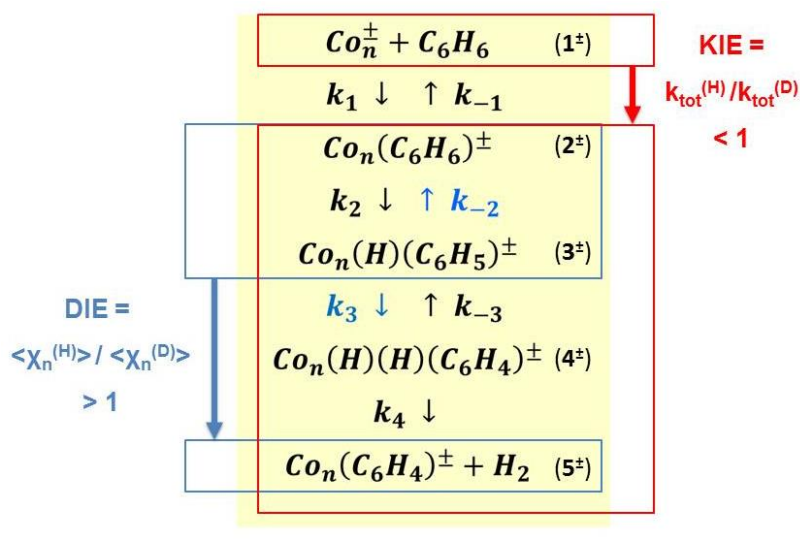
Note, that the magnitude of each rate constant k_i actually depends on the cluster size n, charge state +/-, forward or reverse direction, and isotope H or D, thus $k_i = k_{\pm i}^{\pm,(H/D)}(n)$. The rate constants k_1 and k_{-1} designate the elementary processes of adsorption and desorption, k_2 and k_{-2} those of a C-H bond activation and of its recombination, k_3 and k_{-3} those of a second C-H bond activation and of its recombination, and k_4 designates molecular desorption of H$_2$. The reverse process (k_{-4}) does not occur because of the experimental conditions of extreme dilution in ultra high vacuum in conjunction with ion cloud trapping at sparse number densities. The kinetic isotope effect KIE on each of these elementary processes is discussed below:

1.   Adsorption of C_6H_6 or of C_6D_6 onto $Co_n^{\pm}$ (rate constant k_1). The initial adsorption of benzene or benzene-d$_6$ leads to an almost complete loss of its translational entropy. An ideal gas estimate according to Sackur and Tetrode yields a normal KIE ≤ 1.13 . This KIE is independent of cobalt cluster size and holds for cationic and anionic clusters as well.

2.   Desorption of C_6H_6 from $Co_nC_6H_6^{\pm}$ or of C_6D_6 from $Co_nC_6D_6^{\pm}$ (rate constant k_{-1}). The vibrational mode within the complex $\mathbf{2}^{\pm}$, that corresponds to the reaction coordinate of desorption, is $\nu(Co_n^{\pm} - C_6H_6)$ or $\nu(Co_n^{\pm} - C_6D_6)$, respectively. Our DFT calculations estimate these frequencies to 324 cm^{-1} and 211 cm^{-1}, respectively. The difference of ~ 0.05 kJ/mol in zero point energy is vanishingly small. The related KIE is negligible.

3.   C-H bond or C-D bond activation (rate constant k_2). When taking place in the course of adsorption or swiftly afterwards, the adsorbate C_6H_6 or C_6D_6 is energized through the released heat of adsorption. The prevailing C-H activation barriers are not known. Most likely they depend on the size, on the net charge and on the spin state of the clusters. In the present case of cobalt clusters the C-H activation k_2 likely is somewhat endoergic (cf. Fig. S3 in the supplement) and it cools the cluster adiabatically. The KIE diminishes because of the hot starting point.

The significance (or insignificance) of tunneling contributions to k_2 was addressed before e.g. in the quantum dynamic modeling of CH_4 dissociation on metal surfaces[54]. It revealed the sensitivity of kinetic isotope effects on the location of the activation barrier. Entrance channel barriers (when the molecule vibrates towards the surface) show little to no KIE by tunneling. Exit channel barriers (when H/D moves away from the C-H or C-D bond) are prone to large tunneling KIEs. For the time being we assume the former case valid in C-H and C-D activation within $Co_n C_6 H_6^{\pm}$ and $Co_n C_6 D_6^{\pm}$. Thus KIEs in k_2 may well be small to negligible – and with a tendency towards normal KIE , if any.

4.   Recombination (rate constant k_{-2}), with a significant normal KIE(n)). The reverse exoergic C-H recombination starts from a hydrido-phenylic cluster structure **3$^{\pm}$**. This complex had cooled significantly by having spent the endoergic heat of formation of about 100 kJ/mol in the course of formation from the prior adsorption complex **2$^{\pm}$** . The hydrido-phenylic cluster complex **3$^{\pm}$** is thus cold. Zero point energy of the cobalt hydrid bond is lowered by isotopic substitution and the activation barrier towards recombination accordingly enhanced. Because of the cold conditions at this stage a significant normal KIE results. It is likely that H/D-atom tunneling adds on top and significantly increases the normal KIE. A normal KIE (without tunneling contributions) of up to 7 (by zero point effects ZPE) would not suffice to drive the overall (inverse) KIE below 0.95. It would take much higher values of KIE > 10 in k_{-2} in order to rationalize an overall observable KIE < 0.5. Such high KIE values for k_{-2} are likely caused by H/D tunneling. Taking all elementary process up to here together (k_1, k_{-1}, k_2, and k_{-2}), a significant normal KIE in k_{-2} may occur in backwards direction towards reactants. The other three rate constants reveal no or little KIE. The first part of Scheme (3.9) (up to here) thus predicts an inverse KIE in the total observable rate constant for adsorption $k_{obs}{}^{adsorb}$– as is indeed observed in the recorded experimental data.

5.   Second C-H bond activation (rate constant k_3). It is possible that a second C-H bond is activated without releasing molecular hydrogen from the cluster adsorbate complex. In this case the second activation stays "invisible" as compared to the prior activation k_2 . In the case of clusters that do yield efficient dehydrogenation, however, its presumed normal KIE (both by ZPE and by tunneling) induces a normal KIE in dehydrogenation (next step). The order of magnitude in the normal KIE of k_3 may be comparable to the normal KIE in k_{-2}.

6.   Recombination (rate constant k_{-3}). Recombination of the second activated C-H bond is conceivable. It is in competition to the presumably swift desorption (next step), however. Therefore, it is assumed to be negligible. Some normal KIE in backwards direction is conceivable, it would add to the previous KIEs in backward direction without altering observable KIE effects.

7.   Molecular desorption of H_2 (rate constant k_4). The molecular desorption is subject of a small normal KIE that adds on top of the larger normal KIE in k_3.

The combination of the first four listed elementary processes is thus expected to describe the product yields of adsorption. When adding the subsequent three processes a qualitative description of the observable dehydrogenation is expected. The KIEs in both processes – inverse KIE in adsorption and normal DIE in dehydrogenation - should emerge.

In order to corroborate this hypothesis we undertook extended kinetic modeling by solving the kinetic differential equations that resemble Scheme (3.9). We proceeded by variation of normal KIEs in the rate constants k_{-2} and k_3 while keeping all other seven rate constants neutral (KIE = 1). It showed that ZPEs in C-H and Co-H bonds are far too small to model overall inverse KIEs of up to 0.4. Instead, the assumption of contributions to k_{-2} and k_3 from hydrogen/deuterium tunneling (large normal KIEs) sufficed to model an inverse KIE in adsorption of up to 0.4 and below, and a normal KIE in dehydrogenation (DIE > 1). Both effects are stable against a wide variation of 10 < KIE < 100 in k_{-2} and k_3 .

In principle successful – the kinetic modeling of Scheme (3.9) falls short to elucidate dependencies on cluster size and on cluster charge of KIEs and DIEs. Such a large scale endeavor takes additional insight into the enthalpies and entropies of the stationary points and barriers along the dehydrogenation reaction path. On a much smaller scale our own computations reveal some energetics of stationary points along the reaction coordinate of a single combination of cluster size and cluster charge assuming icosahedral (though relaxing) cluster geometries (cf. Fig. S3 in the supplementary material). The found values lend support to the kinetic model in general while the lack of reliable transition state information is to acknowledge.

Despite all efforts, it remains an open question why dehydrogenation is strongly sustained by an intermediate size range of anionic clusters while it is sparse by cationic clusters of all sizes – n=13 exempt. Hidden electronic effects seem likely. The anticorrelation of high dehydrogenation yields (with concomitant large DIE) and reduced KIE in total yields is obvious as a phenomenon. It takes further effort to elucidate.

3.4. Summary and conclusions

We investigated the reaction with benzene and benzene-d_6 of size selected cationic cobalt clusters $Co_n{}^+$ and of anionic cobalt clusters $Co_n{}^-$ in the size range n = 3 - 28 in extension of prior work on reaction of transition metal clusters with benzene[14,15]. Dehydrogenation by cationic clusters is sparse, it is ubiquitous in reactions by anionic clusters. Kinetic isotope effects KIE(n) in total reaction rates are inverse and – in part - large, dehydrogenation isotope effects DIE(n) are normal. A multistep model of adsorption and stepwise dehydrogenation from the precursor adsorbate proves suitable to

rationalize the found KIEs and DIEs in principle. Some DFT calculations – though preliminary – lend strong support to the otherwise assumed structures and enthalpies. Particular insights into the effects of charge and of cluster size are largely beyond this model. It is mandatory to spend further efforts in experiment, in modeling and in high level ab initio calculations in order to fully elucidate the Cobalt-benzene model system. Comparison to other transition metal clusters would be beneficial. Such experiments are under way.

Acknowledgment

Associated Content

Supporting Information (see chapter 3.6.):

Figures showing relative partial rate constants for the reaction of Co_n^+ and of Co_n^- with perdeutero-benzene. A scheme for energetics of the benzene cobalt interaction as a function of cobalt sample size. A qualitative scheme of the energetics along the reaction coordinate of C-H bond activations in $Co_n^{\pm} + C_6H_6$ as compared to $Nb_n^{\pm} + C_6H_6$ and $Rh_n^{\pm} + C_6H_6$. Figures of calculated structure of $Co_{13}(C_6H_6)^+$, $Co_{13}(H)(C_6H_5)^+$ and $Co_{13}(H)(H)(C_6H_4)^+$. And the full reference to the Gaussian program package.

3.5. References

(1) Anslyn, E. V.; Dougherty, D. A. *Modern Physical Organic Chemistry*; University Science Books: Sausalito, 2006.
(2) Kohen, A.; Limbach, H.-H. *Isotope Effects in Chemistry and Biology*; CRC Press: Boca Raton, 2006.
(3) Johnston, H. S. *Gas Phase Reaction State Theory*; The Ronald Press Company: New York, 1966.
(4) Wiberg, K. B. *Chem. Rev.* **1955**, *55*, 713-743.
(5) Melander, L.; Saunders Jr., W. A. *Reaction Rates of Isotopic Molecules*; Wiley: New York, 1980.

(6)   Lu, S.; Lonergan, W. W.; Bosco, J. P.; Wang, S.; Zhu, Y.; Xie, Y.; Chen, J. G. *J. Catalysis* **2008**, *259*, 260-268.

(7)   Yang, J.; Tveten, E. Z.; Chen, D.; Holmen, A. *Langmuir* **2010**, *26*, 16558-16567.

(8)   Patureau, F. W. *Angewandte Chemie - Intern. Ed.* **2012**, *51*, 4784-4786.

(9)   Klinker, E. J.; Shaik, S.; Hirao, H.; Que, L. *Angewandte Chemie – Intern. Ed.* **2009**, *48*, 1291-1295.

(10)   Churchill, D. G.; Janak, K. E.; Wittenberg, J. S.; Parkin, G. *J. Am. Chem. Soc.* **2003**, *125*, 1403-1420.

(11)   (a) Northcutt, T. O.; Wick, D. D.; Vetter, A. J.; Jones, W. D. *J. Am. Chem. Soc.* **2001**, *123*, 7257-7270. (b) Jones, W. D. *Acc. Chem. Res.* **2003**, *36*, 140-146.

(12)   (a) Janak, K. E.; Parkin, G. *J. Am. Chem. Soc.* **2003**, *125*, 6889-6891. (b) Janak, K. E.; Churchill, D. G.; Parkin, G. *ACS Symposium Series* **2004**, *885*, 86-104.

(13)   Porembski, M.; Weisshaar, J. C. *J. Phys. Chem. A* **2000**, *104*, 1524-1531.

(14)   Berg, C.; Beyer, M.; Achatz, U.; Joos, S.; Niedner-Schatteburg, G.; Bondybey, V. E. *J. Chem. Phys.* **1998**, *108*, 5398-5403.

(15)   Pfeffer, B.; Jaberg, S.; Niedner-Schatteburg, G. *J. Chem. Phys.* **2009**, *131*, 194305/1-12.

(16)   Berg, C.; Schindler, T.; Niedner-Schatteburg, G.; Bondybey, V. E. *J. Chem. Phys.* **1995**, *102*, 4870-4884.

(17)   Citir, M.; Liu, F.; Armentrout, P. B. *J. Chem. Phys.* **2009**, *130,054309/1-16*.

(18)   Meyer, F.; Khan, F. A.; Armentrout, P. B. *J. Am. Chem. Soc.* **1995**, *117*, 9740-9748.

(19)   Liu, F. Y.; Li, M.; Tan, L.; Armentrout, P. B. *J. Chem. Phys.* **2008**, *128,194313/1-12*.

(20)   Kapiloff, E.; Ervin, K. M. *J. Phys. Chem. A* **1997**, *101*, 8460-8469.

(21)   Kurikawa, T.; Hirano, M.; Takeda, H.; Yagi, K.; Hoshino, K.; Nakajima, A.; Kaya, K. *J. Phys. Chem.* **1995**, *99*, 16248-16252.

(22)   Xiuyun, Z.; Jinlan, W. *J. Phys. Chem. A* **2008**, *112*, 296-304.

(23)   Gerhards, M.; Thomas, O. C.; Nilles, J. M.; Zheng, W. J.; Bowen, K. H. *J. Chem. Phys.* **2002**, *116*, 10247-10253.

(24)   Yang, S.; Knickelbein, M. B. *J. Chem. Phys.* **1990**, *93*, 1533-1540.

(25)   Billas, I. M. L.; Chatelain, A.; De Heer, W. A. *Science* **1994**, *265*, 1682-1684.

(26)   Xu, X.; Yin, S.; Moro, R.; de, H. W. A. *Phys. Rev. Lett.* **2005**, *95*, 237209/1-4.

(27)   Knickelbein, M. B. *J. Chem. Phys.* **2006**, *125,044308/1-7*.

(28)   Payne, F. W.; Jiang, W.; Emmert, J. W.; Deng, J.; Bloomfield, L. A. *Phys. Rev. B: Condens. Matter Mater. Phys.* **2007**, *75*, 094431/1-10.

(29)   Peredkov, S.; Neeb, M.; Eberhardt, W.; Meyer, J.; Tombers, M.; Kampschulte, H.; Niedner-Schatteburg, G. *Phys. Rev. Lett.* **2011**, *107,233401/1-5*.

(30)   Datta, S.; Kabir, M.; Ganguly, S.; Sanyal, B.; Saha-Dasgupta, T.; Mookerjee, A. *Phys. Rev. B: Condens. Matter Mater. Phys.* **2007**, *76*, 014429/1-11.

(31)   Ma, Q. M.; Liu, Y.; Xie, Z.; Wang, J. *J. Phys.: Conf. Ser.* **2006**, *29*, 163-166.

(32)   Marshall, A. G.; Hendrickson, C. L.; Jackson, G. S. *Mass Spectrom. Rev.* **1998**, *17*, 1-35.

(33)   Maruyama, S.; Anderson, L. R.; Smalley, R. E. *Rev. Sci. Instr.* **1990**, *61*, 3686-3693.

(34)   Proch, D.; Trickl, T. *Rev. Sci. Instr.* **1989**, *60*, 713-716.

(35)   Caravatti, P.; Allemann, M. *Org. Mass Spectrom.* **1991**, *26*, 514-518.

(36)   Graf, M., Diploma Thesis, TU Kaiserslautern, 2006 (unpublished).

(37)   Frisch, M. J.; Trucks, G. W.; Schlegel, H. B. ; Scuseria, G.E.; Robb, M. A.; Cheeseman, J. R.; Scalmani, G.; Barone, V.; Mennucci, B.; Petersson, G.A., *et al,* Gaussian 09, Rev. B.01, Gaussian, Inc., Wallingford CT, 2009

(38)   Adamo, C.; Barone, V. *J. Chem. Phys.* **1999**, *110*, 6158-6170.

(39)   Kaupp, M.; Schleyer, P. V.; Stoll, H.; Preuss, H. *J. Chem. Phys.* **1991**, *94*, 1360-1366.

(40)   (a) Bergner, A.; Dolg, M.; Kuchle, W.; Stoll, H.; Preuss, H. *Mol. Phys.* **1993**, *80*, 1431-141. (b) Dolg, M.; Stoll, H.; Preuss, H.; Pitzer, R. M. *J. Phys. Chem.* **1993**, *97*, 5852-5859.

(41) Quintal, M. M.; Karton, A.; Iron, M. A.; Boese, A. D.; Martin J. M. L. *J. Phys. Chem. A* **2006**, *110*, 709-716.
(42) Kummerlöwe, G.; Beyer, M. K. *Int. J. Mass Spectrom.* **2005**, *244*, 84-90.
(43) Niedner-Schatteburg, G., Habilitation Thesis, TU München, 1996.
(44) Georgiadis, R.; Fisher, E. R.; Armentrout, P. B. *J. Am. Chem. Soc.* **1989**, *111*, 4251-4262.
(45) Fisher, E. R.; Armentrout, P. B. *J. Phys. Chem.* **1990**, *94*, 1674-1683.
(46) Sallans, L.; Lane, K. R.; Squires, R. R.; Freiser, B. S. *J. Am. Chem. Soc.* **1985**, *107*, 4379-4385.
(47) Elkind, J. L.; Armentrout, P. B. *J. Phys. Chem.* **1986**, *90*, 5736-5745.
(48) Cassady, C. J.; Freiser, B. S. *J. Am. Chem. Soc.* **1985**, *107*, 1566-1573.
(49) Allison, J.; Ridge, D. P. *J. Am. Chem. Soc.* **1979**, *101*, 4998-5009.
(50) Kemper, P. R.; Bushnell, J.; von Helden, G.; Bowers, M. T. *J. Phys.Chem.* **1993**, *97*, 52-58.
(51) Kemper, P. R.; Bushnell, J.; van Koppen, P.; Bowers, M. T. *J. Phys. Chem.* **1993**, *97*, 1810-1817.
(52) Hettich, R. L.; Jackson, T. C.; Stanko, E. M.; Freiser, B. S. *J. Am. Chem. Soc.* **1986**, *108*, 5086-5093.
(53) Vankoppen, P. A. M.; Kemper, P. R.; Bowers, M. T. *J. Am. Chem. Soc.* **1993**, *115*, 5616-5623.
(54) Luntz, A. C.; Harris, J. *Surface Science* **1991**, *258*, 397-426.

3.6.   Supplementary material

Fig. S1: Relative partial rate constants for the reaction **(a)** of Co_n^+ and **(b)** of Co_n^- with perdeutero-benzene.

Fig. S2: Energetics of the benzene cobalt interaction as a function of cobalt sample size.

Fig. S3: Qualitative scheme of the energetics along the reaction coordinate of C-H bond activations in $Co_n^{\pm} + C_6H_6$ as compared to $Nb_n^{\pm} + C_6H_6$ and $Rh_n^{\pm} + C_6H_6$.

Fig. S4(a): Calculated structure of $Co_{13}(C_6H_6)^+$.

Fig. S4(b): Calculated structure of $Co_{13}(H)(C_6H_5)^+$.

Fig. S4(c): Calculated structure of $Co_{13}(H)(H)(C_6H_4)^+$.

Full reference to the Gaussian program package
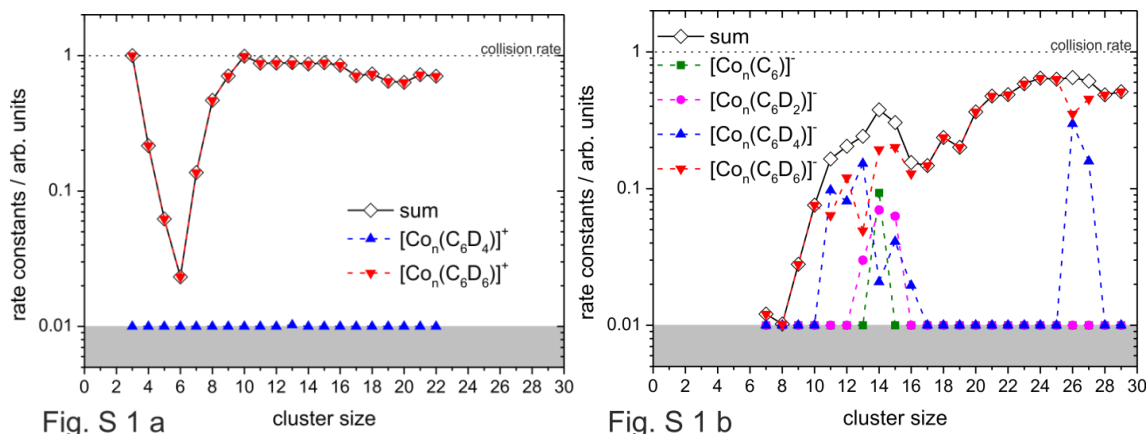
Fig. S 1 a

Fig. S 1 b

Fig. S1: Relative partial rate constants for the reaction **(a)** of Co_n^+ and **(b)** of Co_n^- with perdeutero-benzene. All values were normalized to the highest rate constant. Total rate constants are provided as well. The shaded areas indicate the background noise level.
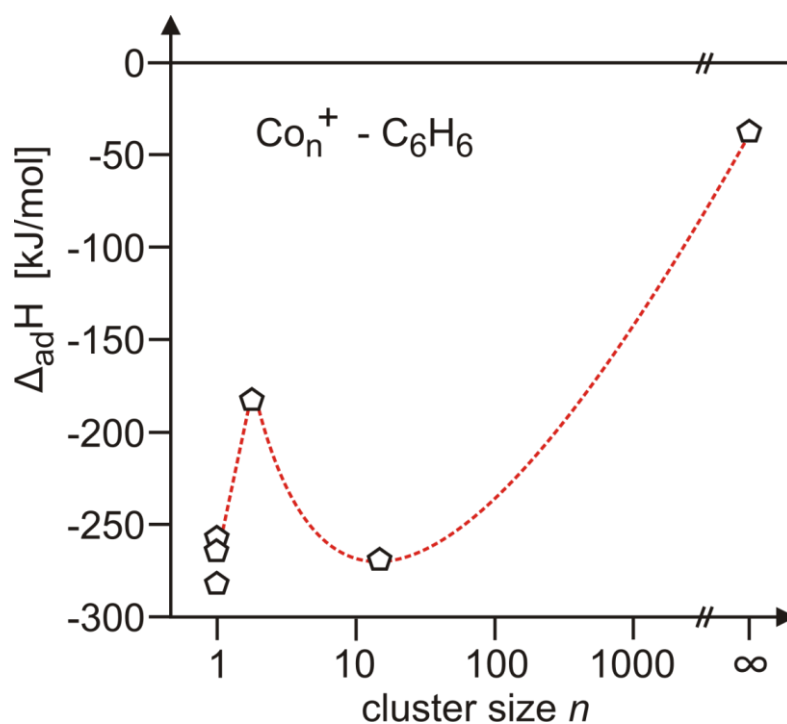
Fig. S2: Energetics of the benzene cobalt interaction as a function of cobalt sample size. Indicated value at n=1 see: B. Freiser: *Organometallic Ion Chemistry*, Kluwer Academic Publishers, Dodrecht 1996; at n=2: F. Meyer, F. Khan, and P. Armentrout, J. Am. Chem. Soc. **117**, 9740 (1995); at n=13: this work (DFT calc.) ; at n=∞ see: S. Lu, C. A. Menning, Y. Zu, and J. G. Chen, Chem. Phys .Chem. **10**, 1763 (2009)
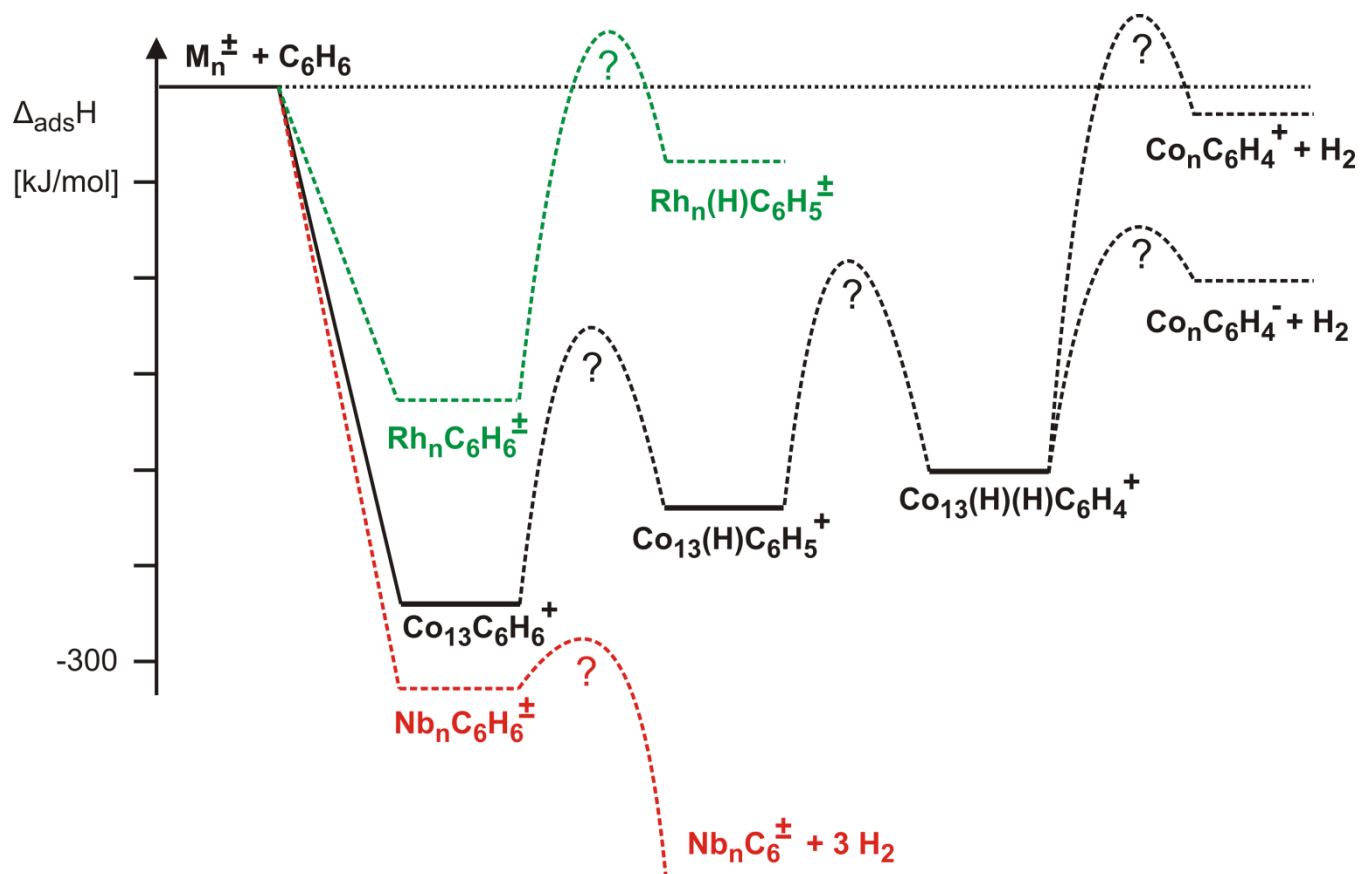
Fig. S3: Qualitative scheme of the energetics along the reaction coordinate of C-H bond activations in $Co_n^\pm$ + C_6H_6 (black line) as compared to $Nb_n^\pm$ + C_6H_6 (dashed red line) and $Rh_n^\pm$ + C_6H_6 (dashed green line). Niobium readily activates benzene while Rhodium adsorbs without activation. Neither of both reveals considerable KIEs – irrespective of charge or cluster size. Benzene activation by Cobalt clusters is in between and gives rise to KIEs – largely independent of charge and across an intermediate range of cluster sizes. Calculated enthalpies of intermediates along the reaction coordinate of dehydrogenation in $[Co_{13}, C_6H_6]^+$ are indicated in bold – no corresponding values known in the cases of Rhodium or Niobium. Other charge states and other cluster sizes of $Co_n^\pm$ may possess shift values of these enthalpies. The Cobalt related part of the diagram closely resembles Scheme (9) within the text body of the publication.
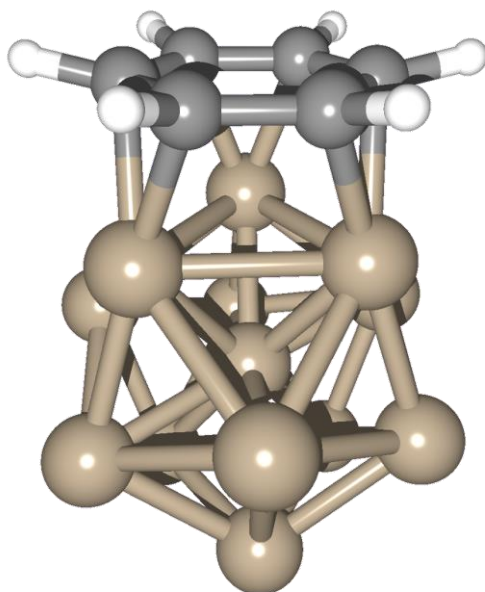
Fig. S4(a): Calculated structure of $Co_{13}(C_6H_6)^+$. All structures are predicted to possess likely high spin ground electronic states that comprise 14 unpaired electrons. Calculations are preliminary, and a systematic verification is pending.
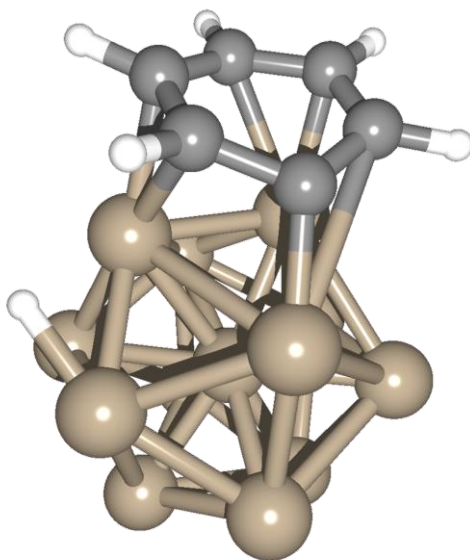
Fig. S4(b): Calculated structure of $Co_{13}(H)(C_6H_5)^+$. All structures are predicted to possess likely high spin ground electronic states that comprise 14 unpaired electrons. Calculations are preliminary, and a systematic verification is pending.
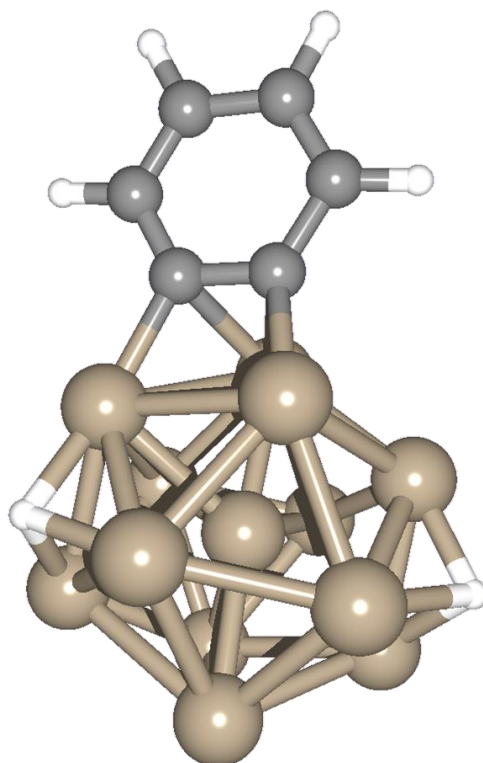
Fig. S4(c): Calculated structure of $Co_{13}(H)(H)(C_6H_4)^+$. All structures are predicted to possess likely high spin ground electronic states that comprise 14 unpaired electrons. Calculations are preliminary, and a systematic verification is pending.

Full reference to the Gaussian program package:

Gaussian 09, Revision **B.01**, Frisch, M. J.; Trucks, G. W.; Schlegel, H. B.; Scuseria, G. E.; Robb, M. A.; Cheeseman, J. R.; Scalmani, G.; Barone, V.; Mennucci, B.; Petersson, G. A.; Nakatsuji, H.; Caricato, M.; Li, X.; Hratchian, H. P.; Izmaylov, A. F.; Bloino, J.; Zheng, G.; Sonnenberg, J. L.; Hada, M.; Ehara, M.; Toyota, K.; Fukuda, R.; Hasegawa, J.; Ishida, M.; Nakajima, T.; Honda, Y.; Kitao, O.; Nakai, H.; Vreven, T.; Montgomery, Jr., J. A.; Peralta, J. E.; Ogliaro, F.; Bearpark, M.; Heyd, J. J.; Brothers, E.; Kudin, K. N.; Staroverov, V. N.; Kobayashi, R.; Normand, J.; Raghavachari, K.; Rendell, A.; Burant, J. C.; Iyengar, S. S.; Tomasi, J.; Cossi, M.; Rega, N.; Millam, J. M.; Klene, M.; Knox, J. E.; Cross, J. B.; Bakken, V.; Adamo, C.; Jaramillo, J.; Gomperts, R.; Stratmann, R. E.; Yazyev, O.; Austin, A. J.; Cammi, R.; Pomelli, C.; Ochterski, J. W.; Martin, R. L.; Morokuma, K.; Zakrzewski, V. G.; Voth, G. A.; Salvador, P.; Dannenberg, J. J.; Dapprich, S.; Daniels, A. D.; Farkas, Ö.; Foresman, J. B.; Ortiz, J. V.; Cioslowski, J.; Fox, D. J. Gaussian, Inc., Wallingford CT, 2009.

3.7. Publication

The above work has been accepted for publication in a slightly different way at *The Journal of Physical Chemistry A* with the title: *"Inverse H/D Isotope Effects in Benzene Activation by Cationic and Anionic Cobalt Clusters"* within the special issue dedicated to Peter B. Armentrout on the occasion of his 60th birthday. The text of the publication was mainly written by Matthias Tombers on behalf of his diploma thesis. His introduction into the research field and training on the machine was done by me. Measurements and data evaluation were done by Matthias Tombers and me / under my supervision. Structural and energetic calculations were made by Gereon Niedner-Schatteburg.

Full reference to the publication:

M. Tombers, L. Barzen, G. Niedner-Schatteburg, Inverse h/d isotope effects in benzene activation by cationic and anionic cobalt clusters, The journal of physical chemistry. A, 117 (2013) 1197-1203.

4. Benzene activation and H/D isotope effects in reactions of mixed cobalt platinum clusters: the influence of charge and of composition

Abstract

A dedicated ion trap served to investigate the reaction with benzene and benzene-d$_6$ under single collision conditions of size selected bimetallic cobalt platinum clusters $Co_nPt_m^{\pm}$ in the size range n + m ≤ 8. Dehydrogenation by cationic cobalt clusters Co$_n^+$ is sparse, it is effective in small bimetallic clusters $Co_nPt_m^+$, n + m ≤ 3. Single platinum atoms promote benzene dehydrogenation while further cobalt atoms quench it. Mixed triatomic clusters $Co_2Pt_1^-$ and $Co_1Pt_2^-$ are special in causing effective reactions in a cooperative way. Kinetic Isotope Effects KIE(n) in total reaction rates are inverse and – in part – large, Dehydrogenation Isotope Effects DIE(n) are normal. A multistep model of adsorption and stepwise dehydrogenation from the precursor adsorbate proves suitable to rationalize the found KIEs and DIEs in principle. The pronounced influence of cluster charge and of cluster composition demands for further investigation.

4.1. Introduction

Bimetallic transition metal clusters may serve as model systems for the elucidation of elementary processes in heterogeneous catalysis. Hydrocarbon adsorption and subsequent C-H bond activation are amongst the most important steps in many catalyzed reactions, and either is often rate limiting. Cobalt has numerous applications as heterogeneous catalyst based on its redox properties that allow for ease of electron transfer via unstable intermediates [1]. Platinum is well known for its capability to cause catalytic hydrogenation and/or dehydrogenation of many functional groups at low temperature [1]. In batch and flow reactor studies bimetallic PtCo catalysts are more active in benzene hydrogenation than monometallic Co and Pt catalysts [2]. The activity showed to follow the trend: PtCo >> PdCo > RuCo ~ Pt ~ Co ~ Ru ~ Pd [3]. Cobalt monolayers on bulk platinum exhibited low temperature hydrogenation properties e.g. on cyclohexene [4]. Transition metal cluster alloys have found application as oxygen-reduction catalyst in the polymer electrolyte membrane of fuel-cells to improve and reduce platinum loading [5-7]. Magnetic cobalt platinum nanoparticles are considered suitable media for ultra-high density magnetic recording [8]. An introductory overview over recent work on cobalt platinum nano particles can be found elsewhere [9].

Prior gas phase studies of benzene adsorption and activation focused on niobium and rhodium clusters [10-12]. Vivid dehydrogenation through niobium cluster cations and anions alike contrast to

mere adsorption by $Rh_n^{\pm}$. Little to no observable isotope effects prevailed in either cases. Prior ion trap investigations revealed catalytic dehydrogenation of saturated and aromatic cyclic hydrocarbons by small platinum clusters Pt_n^+, n ≤ 4 [13]. Methane activation through platinum clusters proved sensitive to their charge states and/or structures with n = 4 behaving special [14], and a normal H/D isotope effect in dehydrogenation was found subsequently [15].

The relative scale of binding strength in complexes of atomic transition metal is established well. Armentrout et al. have conducted multiple guided ion beam studies and found the following trends in binding energies: $[Pt-CH_3]^+$ > $[Co-CH_3]^+$ > $[Rh-CH_3]^+$ and $[Pt-H]^+$ > $[Co-H]^+$ > $[Rh-H]^+$ [16-22]. In a recent study with complexed platinum cations they found the thermal C-H bond activation of benzene reversible [23]. By guided beam studies of cobalt cluster cations Armentrout et al. obtained cluster binding energies [24], deuteride - cluster binding energies [25] and methyl - cluster binding energies [26].

Density functional theory showed capable to allow for structural predictions on small neutral and anionic cobalt clusters $Co_n^{0,-}$, n ≤ 6 [27] and of neutral cobalt-platinum "nanoalloy" clusters Co_nPt_m, n + m ≤ 5 [9]. Triangular, rhombic and trapezoidal structures prevailed.

Our present study serves to investigate the reactions of benzene C_6H_6 and perdeutero benzene C_6D_6 under single collision conditions with isolated bimetallic cobalt platinum clusters $Co_nPt_m^{\pm}$, n + m ≤ 8, by application of Fourier-Transform Ion-Cyclotron-Resonance (FT-ICR) mass spectrometry.

4.2. Material and methods

The experiments were performed with a modified Fourier-Transform Ion-Cyclotron-Resonance (FT-ICR) mass spectrometer (Bruker Apex III). We generated the mixed cobalt platinum clusters with a homebuilt laser vaporization source (LVAP) as described before[12, 28]. The second harmonic of a pulsed Continuum Nd-YAG laser is used to evaporate off atoms from a 0.4 – 1.0 mm thick rotating Cobalt Platinum alloy target (HMW Hauner, Co:Pt molar ratio of 2:1). The emerging metal plasma is cooled and made to yield clusters by a short transverse pulse (40 μs, Helium, 8-15 bar) from a homebuilt piezoelectric valve[29]. Further cooling arises from the subsequent supersonic nozzle expansion through a 20 mm long channel (diameter of 2 mm) into vacuum (10^{-6} mbar). There is no further ionization step in addition. All investigated ions are generated within the laser induced plasma. Unfortunately, the current ion source yielded neither Pt_2^+ nor Pt_3^+ clusters while utilizing the present mixed metal target. Future experiments with a pure platinum target will help this.

Past a 1.4 mm diameter skimmer the cold cluster ions are accelerated, fed into a cw quadrupole ion bender (90^0) and steered by electrostatic lenses into the high field region of a superconducting magnet (7.05 Tesla, actively shielded) while appropriately decelerated. Eventually, the cluster ions are trapped for reaction and/or detection within the FT-ICR cell of so called "infinity" type [30].

Internal degrees of freedom of the cluster ions are relaxed to sub thermal energies through the supersonic expansion in the cluster source. Kinetic energies of the heavy cluster ions is limited by the storage in the ion trap to $E_{kin,lab}$ < 0.5 eV (laboratory frame value). In collisions with light neutral gases the collision energies in the center of mass frame amount to quasi thermal values $E_{kin,cm}$ ~ 0.1 eV and below.

In order to pursue the reactivity studies with benzene (C_6H_6) / benzene-d$_6$ (C_6D_6) we permitted the controlled admission of a reaction gas in order to raise the pressure in the ultrahigh vacuum chamber of the FT-ICR mass spectrometer, where the ICR trapping cell is located, from ~ 3×10^{-10} to typically 1-5×10^{-9} mbar such that a single bimolecular reactant collision per cluster per second takes place (single collision conditions). A commercial ultrahigh vacuum gauge (cold cathode gas discharge, calibrated for N$_2$) provides for a nominal pressure reading. Commercially available benzene/benzene-d$_6$ (Sigma-Aldrich, purity ≥ 99.6 %) was applied after degassing by multiple "pump and freeze" cycles. Kinetic curves of reactant and product ions extract from mass spectra of trapped cluster ions while exposed to the cw admitted reactant gases and under variation of reaction delays between cluster ion admission and detection. Fits to pseudo-first-order-kinetics arise through a genetic algorithm ("evofit" program [31]).

An exact absolute calibration of the reactant gas pressure at the location of the ICR cell is at present not possible. There is a pressure gradient between gauge and ICR cell of about a factor of 4, the exact value not being known, and most likely depending on the chemical nature of the prevailing neutral gas. Gauging against known reactions is conceivable, in principle, and tedious, in practice. There are few absolute rate constants of bimolecular reactions of small molecular ions with neutral benzene published. None of these ions is accessible with the current ICR setup for technical reasons, however. Reactions of benzene cations with benzene and other hydrocarbon molecules were shown to vary largely depending on the ion precursor [32]. Future attempts in gauging the absolute reactant gas density of the present ICR setup are pending. For the time being we rely on the evaluation of relative rate constants that compare against each other. From studies of large cobalt clusters up to Co$_{28}^+$ with benzene it may be concluded that the fastet observed reaction rates come close to collision rate. This would relate to a benzene to cobalt surface sticking coefficient of unity, and we have normalized the recorded relative rate constants accordingly. The noise equivalent detection limit of the relative rate constants amounts to k ≈ 0.0025.

We pursued accompanying *ab initio* modeling of clusters and products by density functional theory (DFT). We utilize a level of theory that is similar to our study on pure cobalt clusters. A combination of the Stuttgart relativistic effective core potentials for Co and Pt with cc-pVDZ basis sets for carbon and hydrogen [33-35] proved appropriate in conjunction with the PBE0 hybrid exchange correlation functional [36] as implemented in the Gaussian 09 program suite [37]. No effort was made to cover all cluster sizes. Instead we focused onto stationary points of the $^{M}[Co_nPt_m, C_6H_6]^+$ potential hypersurfaces with n + m = 3 and variation of the spin state multiplicity M. Full coverage of these investigations remains to a future publication[38] while some preliminary results will be discussed here as needed.

4.3. Results and discussion

The recorded kinetics reveal that pure cobalt clusters $Co_nPt_m^{\pm}$, m = 0, react with benzene to form a single type of products:

$$Co_n^{\pm} + C_6(H,D)_6 \rightarrow [Co_nC_6(H,D)_6]^{\pm} \qquad (4.1)$$

This holds both for cationic clusters as well as for anionic clusters, and for reactions with benzene C_6H_6 and perdeutero benzene C_6D_6 alike. Dehydrogenation does not take place up to the limit of sensitivity of this experiment in the range of n = 3 - 10 – with the $Co_{9,10}^{-} + C_6H_6$ cases exempt, where some additional products form ($[Co_{9,10}C_6H_4]^{-}$, see eq. 4.2b below). Indication of the product species in (4.1) in square parenthesis shall indicate the ambiguity in its molecular structure. While the sum formula is well determined through the high resolution mass detection its structure, of course, is not. It is well conceivable, that benzene does react beyond mere attachment to the cobalt cluster. It may well have experienced activation of some C-H bond thereby forming a hydrido phenylic complex of the form $Co_n(H)C_6H_5^{\pm}$. Activation of multiple C-H bonds would induce a subsequent pair wise recombination of the hydridic H-atoms and desorption of molecular H_2. While this is not observed either the benzene adsorbate cluster complex or the hydrido phenylic complex stabilize radiatively on the long run. Anionic cobalt cluster cations may stabilize by electron detachment, in addition. As of now, we do not have evidence for such processes in the current case.

Mixed cationic and anionic clusters $Co_nPt_m^{\pm}$, n,m ≥ 1, react with benzene C_6H_6 and with perdeutero benzene C_6D_6 either through association (4.2a) or through dehydrogenation (4.2b):

$$Co_nPt_m^{\pm} + C_6(H,D)_6 \rightarrow [Co_nPt_mC_6(H,D)_6]^{\pm} \qquad (4.2a)$$

$$\rightarrow [Co_nPt_mC_6(H,D)_4]^{\pm} + (H,D)_2 \qquad (4.2b)$$
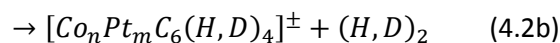
The ratio of both varies with cluster size, with cluster charge and somewhat with the reactant. No products of reactions were observed that would proceed beyond single dehydrogenation (4.2b). In particular, there was no evidence for loss of odd numbers of H-atoms or for loss of more than a single molecule of H_2. It is therefore most likely that a single molecular hydrogen evolves per encounter of cluster and reactant. Seemingly, C-H and C-D bond activation ceases after two instances per benzene molecule at most.
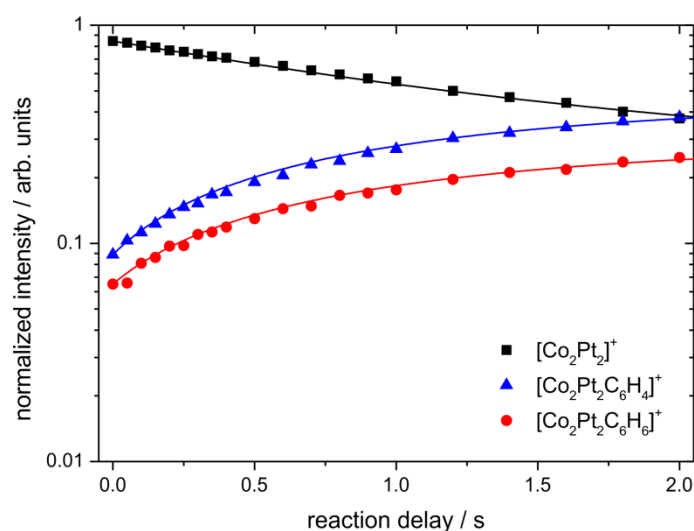
Fig. 1: *An example for the reaction kinetics of $Co_2Pt_2^+$ (black, squares) with C_6H_6. Symbols represent experimental data, solid lines represent numerical fits by a genetic algorithm to pseudo first order kinetics. Association (red, circles) and dehydrogenation (blue, triangles) take place in parallel.*

Fitting the recorded kinetics (cf. e.g. in the case of $Co_2Pt_2^+$ + C_6H_6 at Fig. 1) yields relative partial rate constants for association and for dehydrogenation, and the relative total rate constants.
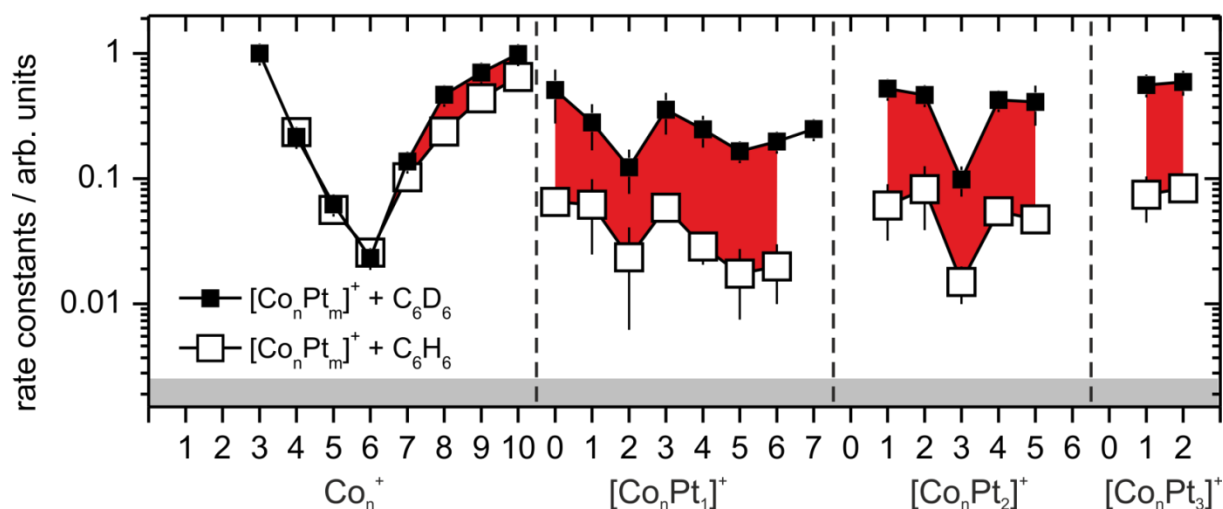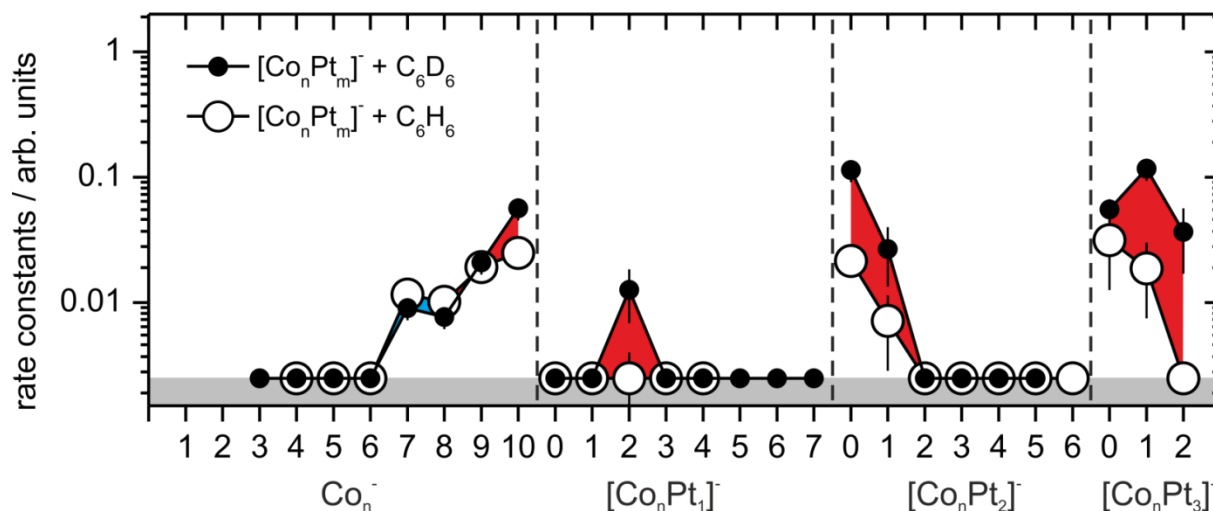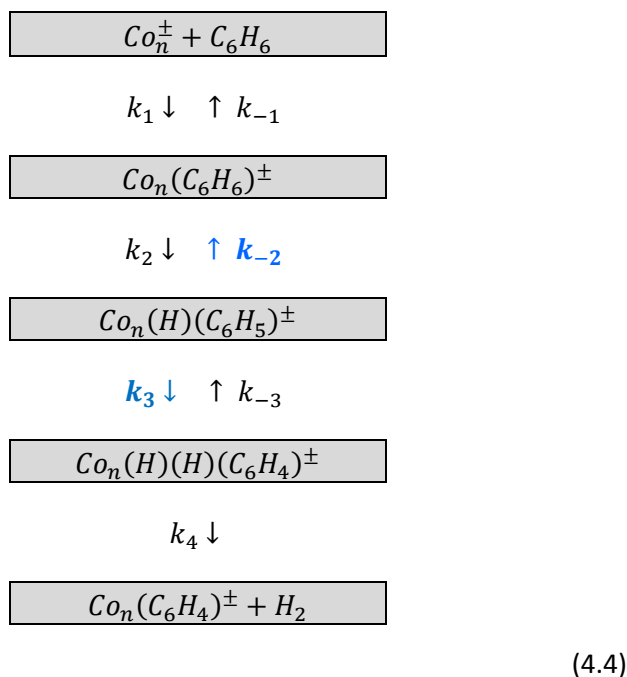
Fig. 2: *Total rate constants for the reaction of $Co_nPt_m^+$ with benzene (open symbols) and perdeutero benzene (solid symbols). The observed inverse Kinetic Isotope Effect (KIE) is emphasized by red shading of the areas in between of the corresponding rate constants. The noise equivalent level of the present experiments is indicated by grey shading.*

Total reaction rates with benzene and with perdeutero benzene of pure cationic cobalt clusters Co_n^+ reveal a pronounced size dependence. The rates of Co_6^+ diminish by a factor of 40 with respect to larger and smaller clusters. The very cause is unknown while numerous speculations arise. A drop with cluster size in the total association rate of alkanes on small niobium cluster cations was attributed before to an increase of coordinative saturation and a concomittant drop of reactivity [10]. In principle such an argument might hold for the case of cobalt as well. In reactions with benzene the same study found a rise in total reaction rate upon increase of the size of these clusters, possibly due to the rise in heat capacity that helps to dissipate the released heat of adsorption. A combination of both counteracting effects, however, was not observed up to now in the reactions of transition metal clusters.

Notably there is little difference whether reacting benzene C_6H_6 or perdeutero benzene C_6D_6. It is common practice to discuss such differences in terms of a Kinetic Isotope Effect (KIE) defined as the ratio of hydrogenic rate constant $k_{tot}^{(H)}(n)$ and perdeutero rate constant $k_{tot}^{(D)}(n)$:

$$KIE(n) = \frac{k_{tot}^{(H)}(n)}{k_{tot}^{(D)}(n)} \qquad (4.3)$$

Normal KIE > 1 or inverse KIE < 1 elucidate indirectly the underlying micro kinetics. (Throughout all of this paper blue and red colors code for normal and inverse KIEs). In the present case of Co_n^+ + C_6H_6/C_6D_6 reactions, the KIE is small (< 0.5) and inverse.

Fig. 3: *Total rate constants for the reaction of $Co_nPt_m^-$ with benzene (open symbols) and perdeutero benzene (solid symbols). The observed inverse Kinetic Isotope Effect (KIE) is emphasized by red shading of the areas in between of the corresponding rate constants. Some normal KIE is signified by blue shading. The noise equivalent level of the present experiments is indicated by grey shading.*

Anionic cobalt clusters Co_n^- with n ≤ 6 do not yield observable products while collisions with benzene inevitably take place at collision rates that are high enough to allow for detection of products down to 1% collision efficiency. Adsorption induced electron detachment is a conceivable reason, while our recorded data do not provide evidence for such a "dark" reaction channel. Further insight could arise from the inspection of size dependencies in heats of adsorption $\Delta_{ads}H(Co_n^- - C_6H_6)$ and in electron detachment enthalpies $\Delta_{detach}H([Co_nC_6H_6]^-)$ of all conceivable isomers, none of which is known as of now. Instead, basic thermodynamics regards the cluster as a finite heat bath that serves to dissipate the heat of adsorption. The more effective the dissipation the less probable becomes the benzene eventually evaporating off the cluster. With increasing cluster size the total adsorption efficiency improves. The rises in adsorption efficiency are apparent in the rate constants of anionic clusters Co_n^-, n ≥ 7. The according reactions of Co_n^- with C_6D_6 reveal a small inverse KIE (< 0.5) with n = 7,8 exempt (normal KIE).

4. Benzene activation and H/D isotope effects in reactions of mixed cobalt platinum clusters: the influence of charge and of composition

We have most recently undertaken a systematic evaluation of KIEs in cobalt cluster reactions with benzene and worked out a multi step reaction model (4.4) that managed to explain this somewhat surprising finding [39]. The argumentation runs – in short – as follows:

$$Co_n^\pm + C_6H_6$$

$$k_1 \downarrow \quad \uparrow k_{-1}$$

$$Co_n(C_6H_6)^\pm$$

$$k_2 \downarrow \quad \uparrow \boldsymbol{k_{-2}}$$

$$Co_n(H)(C_6H_5)^\pm$$

$$\boldsymbol{k_3} \downarrow \quad \uparrow k_{-3}$$

$$Co_n(H)(H)(C_6H_4)^\pm$$

$$k_4 \downarrow$$

$$Co_n(C_6H_4)^\pm + H_2$$

(4.4)

Scheme (4) equally holds for reactions with C_6D_6. The observable reactions of association and of dehydrogenation comprise the consecutive elementary processes: adsorption and desorption (k_1 and k_{-1}), C-H bond activation and its recombination (k_2 and k_{-2}), second C-H bond activation and its recombination (k_3 and k_{-3}), and molecular desorption of H_2 (k_4). Most of these processes provide for little to no KIE (for more detail see [39]). Merely the C-H recombination (k_{-2}) and the second C-H activation (k_3) provide for a normal KIE, in part due to zero point effects and mostly due to strong mass effects in H/D tunneling. Altogether the combination of KIEs from these seven elementary processes results in an observable inverse KIE for association and in a normal KIE for dehydrogenation – as indeed observed in the experiments with pure cobalt clusters up to n = 27 [39].

When doping cobalt clusters with a single platinum atom or with a few platinum atoms one obtains mixed clusters $Co_nPt_m^\pm$, at present with n ≤ 7 and m ≤ 3. These mixed clusters undergo – in principle – the same reactions (4.2a,b) as pure cobalt clusters.

Once more, there is no reaction observed that would go beyond single dehydrogenation (4.2b). Differences with respect to the pure clusters arise as follows: The remarkable size dependence of cationic rates diminishes in the reactions of mixed clusters. The inverse KIE persists in the mixed clusters, and it increases significantly as compared to the inverse KIE of pure cobalt clusters. Anionic mixed clusters are less reactive by more than an order of magnitude (cf. Figs 2 and 3). While pure

anionic cobalt clusters set in to react at n = 7 and beyond, only small mixed clusters of five atoms at most react at all. These are namely $Co_2Pt_1^-$, $Co_1Pt_2^-$, $Co_1Pt_3^-$, $Co_2Pt_3^-$, and the pure platinum clusters Pt_2^- and Pt_3^-. Inverse KIEs prevail throughout, and they are larger in anionic mixed clusters than in pure cobalt clusters.

It is worthwhile to deliberate on the likely origin of the enhanced inverse KIEs in heterogeneous clusters. As a starting point one may assume the previous micro kinetic model of scheme (4.4) valid for heterogeneous clusters as well. If so then it is once more the recombination of the hydridic hydrogen atom with the phenyl ligand (microscopic rate constant k_{-2} in scheme (4.4)) which is subject to a normal KIE (in backwards direction). The platinum heteroatom would enhance this KIE which implies that platinum would drive hydrogenation more efficiently than cobalt – as is anticipated by prior studies (cf. introduction). Moreover the experiments with pure anionic platinum clusters show efficient dehydrogenation of benzene (4.2b). Namely Pt_2^- reacts efficiently with either benzene or perdeutero benzene as compared to CoPt$^-$ which does not provide for any reaction rate within our experimental uncertainties. Similarly, Pt_3^- readily reacts effectively with either benzene or perdeutero benzene while $CoPt_2^-$ does so slowly if at all. The thus emerging picture of a more efficient hydrogen release from heterogeneous clusters – in conjunction with the inverse KIE in the total overall reaction rates – furthermore implies large tunneling contributions to k_{-2}. This is the major cause of the normal KIE > 7 in k_{-2} which in turn explains the inverse KIE in the overall reaction. $Co_nPt_2^-$ only reacts as long as n ≤ 1. This particular cooperativity of small heterogeneous metal clusters of at most three atoms is noteworthy.

Association (4.2a) and dehydrogenation (4.2b) are competing parallel reactions. The branching ratio amongst both varies with size, charge and composition of clusters, and with the deuteration of benzene. In order to discuss the degree of activation and to provide for some data reduction, we define a so called "average degree of dehydrogenation" $\langle \chi_n \rangle$ as before [40]:

$$\langle \chi_n \rangle = \frac{1}{m} \frac{1}{k_n^{tot}} \sum_{m_i=1}^{m} m_i k_n(m_i) \qquad (4.5)$$

with

$$k_n^{tot} = \sum_i k_n(m_i) \qquad (4.6)$$

Here, *m* (= 6 in the present case) indicates the total amount of hydrogen or deuterium atoms as available from C$_6$H$_6$/C$_6$D$_6$. The partial reaction rate $k_n(m_i)$ classifies according to the cluster size *n* and the loss of hydrogen or deuterium atoms m_i in the observed product. $\langle \chi_n \rangle = 1$ would indicate complete dehydrogenation, $\langle \chi_n \rangle = 0$ would indicate adsorption without any dehydrogenation.
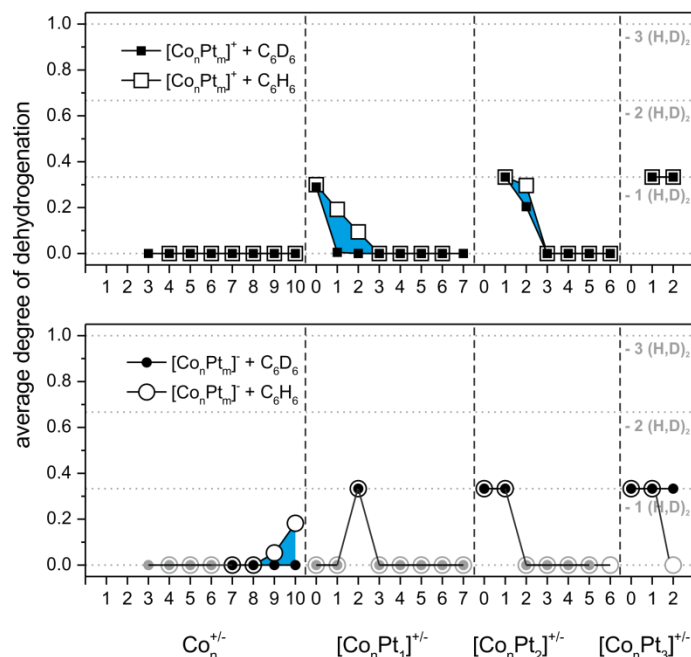
Fig. 4: *Average degree of dehydrogenation $\langle \chi_n \rangle$ (a) by pure and mixed cationic clusters and (b) by pure and mixed anionic clusters. Blue areas indicate a normal Dehydrogenation Isotope Effect (DIE > 1). Those $\langle \chi_n \rangle = 0$ values that are indicated in grey arise from vanishing total reaction rates $k_{tot}(n) = 0$. Solid symbols represent reaction with C_6D_6, open symbols with C_6H_6. Uncertainties are within the size of the symbols.*

The thus obtained values of $\langle \chi_n \rangle$ range between 0 and 1/3. The latter signifies a branching ratio of (4.2a) : (4.2b) of 0 : 1, in other words: single dehydrogenation only. The observable influence of deuteration is small. We label the kinetic isotope effect on $\langle \chi_n \rangle$ as a Dehydrogenation Isotope Effect (DIE):

$$DIE(n) = \frac{\langle \chi_n^{(H)} \rangle}{\langle \chi_n^{(D)} \rangle} \qquad (4.7)$$

The (few) cases where $DIE(n) \neq 1$ are: $Co_1Pt_2^+$, $Co_2Pt_1^+$, $Co_2Pt_2^+$, Co_9^-, and Co_{10}^-. All of these reveal a normal DIE. From our micro kinetic model of consecutive elementary steps (scheme (4.4)) we recall likely tunneling contributions in hydrogen migration steps k_{-2} (C-H recombination) and k_3 (second C-H activation). The former served to rationalize the inverse KIE in the observed total rates, the latter explains the observation of a normal DIE.

The observed isotope effects, both KIEs and DIEs, are thereby well interpreted - the observed effects of cluster size and of composition remain to discuss. The most pronounced size effects are: (1) the quenching of the total reactivity in anionic cobalt clusters through addition of a single or a few platinum atoms (cf. Fig. 3); (2) the quenching of the average degree of dehydrogenation in small mixed cationic clusters $Co_{1,2}Pt_{1,2}^+$ through addition for single further cobalt atoms (cf. Fig. 4a) ; and (3) the almost "magic" size dependence of the average degree of dehydrogenation in mixed anionic clusters with e.g. $Co_2Pt_1^-$ and $Co_1Pt_2^-$ sticking out as compared to others (cf. Fig. 4b). None of these three effects is accessible to an unambiguous interpretation. They challenge further investigations.
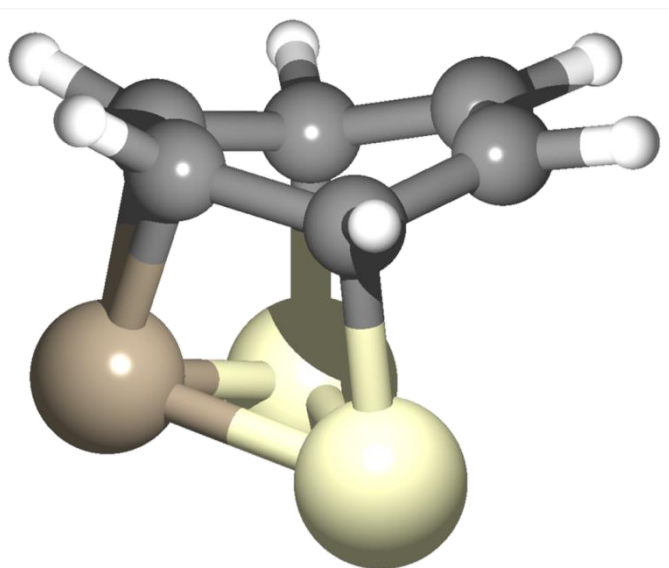
Fig. 5: *A calculated (PBE0/Stuttgart ECP; cc-pVDZ) association complex by example: $Co_1Pt_2(C_6H_6)^-$ in singlet spin state. The cobalt atoms favor η_2 coordination ("on bridge") towards two carbon atoms within the benzene ring. The two platinum atoms favor η_1 coordination ("on top") to single carbon atoms. Some aromaticity is lost by forcing the ring into a non planar geometry (further discussion see text).*

We have started a systematic *ab initio* approach on structures and energetic of the seemingly "magic" $Co_nPt_m^+$, n + m = 3 case [33-37]. This investigation is still in progress. Some preliminary – yet robust – findings help to elucidate the interaction of these clusters with benzene at this stage: All clusters with cobalt favor high spin states. Cobalt atoms favor η_2 coordination ("on bridge") towards C_2 units in benzene. The coordination and hybridization at the carbon center remains constant before and after coordination, i.e., the C-C π bond is replaced by a metallacycle. Platinum atoms favor η_1 coordination ("on top") to single carbon atoms in benzene. The coordinating C becomes sp³

hybridized instead of sp^2, which results in the puckering of the ring. This clearly weakens the π bond, creating a radical center at the adjacent carbon atom. The ability to activate a C-H bond in proximity follows. In all cases investigated thus far the side on coordination of a triangular metal cluster with maximum hapticity towards benzene proved most stable (cf. Fig. 5). Single or twofold C-H bond activation with migration of the activated hydrogen onto the metal cluster leads to a tilt of the benzene plane with respect to the metal triangle. It is open as of now whether benzene adsorption induces structural changes of the mixed clusters.

Further support of the experimental findings arise from computed (yet preliminary) enthalpies, confirmation pending. - Benzene dehydrogenation by homogeneous Cobalt cluster cations Co_3^+ seems endoergic, and it is predicted exoergic for mixed cluster cations $Co_2Pt_1^+$ and $Co_1Pt_2^+$:

$$^7Co_3^+ + C_6H_6 \rightarrow {}^7[Co_3C_6H_4]^+ + H_2 \qquad \Delta_rH = +67 \frac{kJ}{mol} \qquad (4.8a)$$

$$^6Co_2Pt_1^+ + C_6H_6 \rightarrow {}^6[Co_2Pt_1C_6H_4]^+ + H_2 \qquad \Delta_rH = -6 \frac{kJ}{mol} \qquad (4.8b)$$

$$^5Co_1Pt_2^+ + C_6H_6 \rightarrow {}^5[Co_1Pt_2C_6H_4]^+ + H_2 \qquad \Delta_rH = -48 \frac{kJ}{mol} \qquad (4.8c)$$
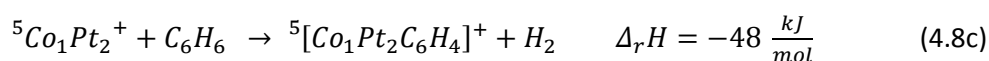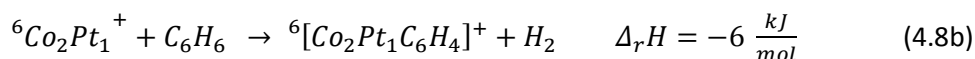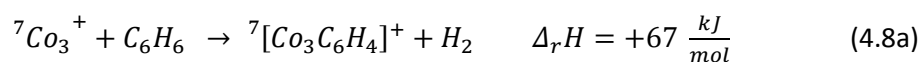
The same high spin multiplicities prevail in reactants and products while other spin states may get involved in the course of the reaction. The influence of spin orbit coupling may be significant in the mixed clusters as induced by the high nuclear charge of platinum. The present level of DFT does not cover this, however. The experimentally observed rise in dehydrogenation efficiency upon replacement of cobalt for platinum is well in agreement with the calculated ergicities at the present – albeit limited – level of theory. A complete documentation and discussion of the ongoing computations remains to a future publication in due time [38].

4.4. Summary and conclusions

We investigated the reaction with benzene and benzene-d$_6$ of size selected bimetallic cobalt platinum clusters $Co_nPt_m^\pm$ in the size range n + m ≤ 8 in extension of prior work on reaction of transition metal clusters with benzene [14, 15]. Dehydrogenation by cationic cobalt clusters Co_n^+ is sparse, it is effective in small bimetallic clusters $Co_nPt_m^+$, n + m ≤ 3. Thus single platinum atoms promote benzene dehydrogenation while further cobalt atoms quench it. Mixed triatomic clusters $Co_2Pt_1^-$ and $Co_1Pt_2^-$ are special in causing effective reactions and single dehydrogenation through some kind of cooperativity while $Co_nPt_{1,2}^-$, n ≥ 3 do not react at all.

Kinetic Isotope Effects KIE(n) in total reaction rates are inverse and – in part - large, Dehydrogenation Isotope Effects DIE(n) are normal. A multistep model of adsorption and stepwise dehydrogenation from the precursor adsorbate proves suitable to rationalize the found KIEs and DIEs in principle. Particular insights into the cause of the found effects of charge, size and composition of mixed clusters shall arise from ongoing ab initio modeling of especially the $n + m = 3$ case. Further experiments are under way as well.

Acknowledgement

4.5.   References

[1] B. Cornils, W.A. Hermann, R. Schlögl, C.-H. Wong, Catalysis from A to Z, Wiley-VCH, Weinheim, 2000.
[2] S. Lu, W.W. Lonergan, J.P. Bosco, S. Wang, Y. Zhu, Y. Xie, J.G. Chen, Low temperature hydrogenation of benzene and cyclohexene: A comparative study between γ-Al2O3 supported PtCo and PtNi bimetallic catalysts, Journal of Catalysis, 259 (2008) 260-268.
[3] S. Lu, C.A. Menning, Y. Zhu, J.G. Chen, Correlating Benzene Hydrogenation Activity with Binding Energies of Hydrogen and Benzene on Co-Based Bimetallic Catalysts, Chemphyschem, 10 (2009) 1763-1765.
[4] N.A. Khan, L.E. Murillo, J.G. Chen, Observation of novel low-temperature hydrogenation activity on Co/Pt(III) surfaces, Journal of Physical Chemistry B, 108 (2004) 15748-15754.
[5] V.R. Stamenkovic, B.S. Mun, M. Arenz, K.J.J. Mayrhofer, C.A. Lucas, G. Wang, P.N. Ross, N.M. Markovic, Trends in electrocatalysis on extended and nanoscale Pt-bimetallic alloy surfaces, Nat Mater, 6 (2007) 241-247.
[6] Y. Bing, H. Liu, L. Zhang, D. Ghosh, J. Zhang, Nanostructured Pt-alloy electrocatalysts for PEM fuel cell oxygen reduction reaction, Chemical Society Reviews, 39 (2010) 2184-2202.
[7] S. Mukerjee, S. Srinivasan, Enhanced electrocatalysis of oxygen reduction on platinum alloys in proton-exchange membrane fuel-cells, Journal of Electroanalytical Chemistry, 357 (1993) 201-224.
[8] M.N. Dave, M.L. Wears, J. Michael, C. Desmond, Fabrication and characterization of nano-particulate PtCo media for ultra-high density perpendicular magnetic recording, Nanotechnology, 18 (2007) 205301.
[9] A. Sebetci, Density functional study of small cobalt-platinum nanoalloy clusters, Journal of Magnetism and Magnetic Materials, 324 (2012) 588-594.
[10] C. Berg, M. Beyer, U. Achatz, S. Joos, G. Niedner-Schatteburg, V.E. Bondybey, Effect of charge upon metal cluster chemistry: Reactions of Nb-n and Rh-n anions and cations with benzene, Journal of Chemical Physics, 108 (1998) 5398-5403.

[11] B. Pfeffer, S. Jaberg, G. Niedner-Schatteburg, Reactions of simple aromatic heterocycles with niobium cluster ions (n < 30), Journal of Chemical Physics, 131 (2009).

[12] C. Berg, T. Schindler, G. Niednerschatteburg, V.E. Bondybey, Reactions of simple Hydrocarbons with Nb_n^+ - Chemisorption and Physisorption on Ionized Niobium Clusters, Journal of Chemical Physics, 102 (1995) 4870-4884.

[13] G.S. Jackson, F.M. White, C.L. Hammill, R.J. Clark, A.G. Marshall, Gas-phase dehydrogenation of saturated and aromatic cyclic hydrocarbons by Pt-n(+) (n=1-4), Journal of the American Chemical Society, 119 (1997) 7567-7572.

[14] U. Achatz, C. Berg, S. Joos, B.S. Fox, M.K. Beyer, G. Niedner-Schatteburg, V.E. Bondybey, Methane activation by platinum cluster ions in the gas phase: effects of cluster charge on the Pt-4 tetramer, Chemical Physics Letters, 320 (2000) 53-58.

[15] M.K. Beyer, G. Kummerlowe, I. Balteanu, S. Zheng, O.P. Balaj, V.E. Bondybey, Activation of methane and methane-d 4 by ionic platinum clusters, International Journal of Mass Spectrometry, 254 (2006).

[16] Y.M. Chen, P.B. Armentrout, Activation of C2H6, C3H8, and C-C3H6 by gas-phase Rh+ and the thermochemistry of Rh-ligand complexes, Journal of the American Chemical Society, 117 (1995) 9291-9304.

[17] Y.M. Chen, J.L. Elkind, P.B. Armentrout, Reactions of Ru+, Rh+, Pd+, and Ag+ with H-2, HD, and D-2, Journal of Physical Chemistry, 99 (1995) 10438-10445.

[18] R. Georgiadis, E.R. Fisher, P.B. Armentrout, Neutral and ionic metal hydrogen and metal-carbon bond-energies - reactions of Co+, Ni+, and Cu+ with ethane, propane, methylpropane, and dimethylpropane, Journal of the American Chemical Society, 111 (1989) 4251-4262.

[19] E.R. Fisher, L.S. Sunderlin, P.B. Armentrout, Guided ion-beam studies of the reactions of Co+ and Ni+ with CH3Cl, CH3Br, CH3I - implications for the metal-methyl ion bond-energies, Journal of Physical Chemistry, 93 (1989) 7375-7382.

[20] Y.M. Chen, D.E. Clemmer, P.B. Armentrout, Conversion of CH4 to CH3OH - reactions of CoO+ WITH CH4 and D-2, Co+ with CH3OD and D2O, and Co+(CH3OD) with Xe, Journal of the American Chemical Society, 116 (1994) 7815-7826.

[21] X.G. Zhang, R. Liyanage, P.B. Armentrout, Potential energy surface for activation of methane by Pt+: A combined guided ion beam and DFT study, Journal of the American Chemical Society, 123 (2001) 5563-5575.

[22] J.L. Elkind, P.B. Armentrout, Effect of kinetic and electronic-energy on the reactions of Co+, Ni+, and Cu+ with H-2, HD, and D2, Journal of Physical Chemistry, 90 (1986) 6576-6586.

[23] B. Butschke, D. Schroeder, H. Schwarz, Thermal C-H Bond Activation of Benzene with Cationic Pt(CX3(L) (+) Complexes in the Gas Phase: A Combined Experimental/Theoretical Study (X = H, D; L=1,10-Phenanthroline, 2,2 '-Bipyrimidine, 2,2 '-Bipyridine, and (o,o '-Cl2C6H3)N=C(CH3)-C(CH3)=N(o,o '-Cl2C6H3)), Organometallics, 28 (2009) 4340-4349.

[24] S. Goebel, C.L. Haynes, F.A. Khan, P.B. Armentrout, Collision-induced dissociation studies of Co(CO)(X)(+), X=1-5 - sequential bond-energies and the heat of formation of Co(CO)(4), Journal of the American Chemical Society, 117 (1995) 6994-7002.

[25] F.Y. Liu, P.B. Armentrout, Guided ion-beam studies of the kinetic-energy-dependent reactions of Co-n(+) (n=2-16) with D-2: Cobalt cluster-deuteride bond energies, Journal of Chemical Physics, 122 (2005).

[26] M. Citir, F. Liu, P.B. Armentrout, Methane activation by cobalt cluster cations, Co-n(+) (n=2-16): Reaction mechanisms and thermochemistry of cluster-CHx (x=0-3) complexes, Journal of Chemical Physics, 130 (2009).

[27] A. Sebetci, Cobalt clusters (Co(n), n <= 6) and their anions, Chemical Physics, 354 (2008) 196-201.

[28] S. Maruyama, L.R. Anderson, R.E. Smalley, Direct injection supersonic cluster beam source for FT-ICR studies of clusters, Review of Scientific Instruments, 61 (1990) 3686-3693.

[29] D. Proch, T. Trickl, A high-intensity multi-purpose piezoelectric pulsed molecular-beam source, Review of Scientific Instruments, 60 (1989) 713-716.

[30] P. Caravatti, M. Allemann, The infinity cell - a new trapped-ion cell with radiofrequency covered trapping electrodes for Fourier-Transform Ion-Cyclotron Resonance mass-spectrometry, Organic Mass Spectrometry, 26 (1991) 514-518.

[31] M. Graf, Habilitation Thesis, TU Kaiserslautern, Kaiserslautern, 2006

[32] M.L. Gross, D.H. Russell, R.J. Aerni, S.A. Bronczyk, Ion-molecule reaction chemistry of various gas-phase C6H6 radical cations, Journal of the American Chemical Society, 99 (1977) 3603-3609.

[33] M. Kaupp, P.V. Schleyer, H. Stoll, H. Preuss, Pseudopotential approaches to Ca, Sr, and Ba hydrides - why are some alkaline-earth MX2 compounds bent, Journal of Chemical Physics, 94 (1991) 1360-1366.

[34] A. Bergner, M. Dolg, W. Kuchle, H. Stoll, H. Preuss, Ab-initio energy-adjusted pseudopotentials for elements of groups 13-17, Molecular Physics, 80 (1993) 1431-1441.

[35] M. Dolg, H. Stoll, H. Preuss, R.M. Pitzer, Relativistic and correlation-effects for element 105 (Hahnium, Ha) - a comparative-study of M and MO (M=Nb, Ta, Ha) using energy-adjusted abinitio pseudopotentials, Journal of Physical Chemistry, 97 (1993) 5852-5859.

[36] C. Adamo, V. Barone, Toward reliable density functional methods without adjustable parameters: The PBE0 model, Journal of Chemical Physics, 110 (1999) 6158-6170.

[37] M.J. Frisch, G.W. Trucks, H.B. Schlegel, Gaussian 09, in, Gaussian, Inc., Wallingford CT, 2009.

[38] G. Niedner-Schatteburg, unpublished results and work in progress

[39] M. Tombers, L. Barzen, G. Niedner-Schatteburg, Inverse H/D isotope effects in benzene activation by cationic and anionic cobalt clusters, submitted to Journal of Physical Chemistry.

[40] G. Niedner-Schatteburg, Habilitation Thesis, TU München, Garching, 1996

4.6. Publication

The above work has been accepted for publication in a slightly different way at *The International Journal of Mass Spectrometry* with the title: *"Benzene activation and H/D isotope effects in reactions of mixed cobalt platinum clusters: The influence of charge and of composition"* within the special issue dedicated to Peter B. Armentrout on the occasion of his 60th birthday. The text of the publication was mainly written by me. Measurements and data evaluation were done by Matthias Tombers, Christine Merkert, Joachim Hewer and me / under my supervision. Structural and energetic calculations were made by Gereon Niedner-Schatteburg.

Full reference to the publication:

L. Barzen, M. Tombers, C. Merkert, J. Hewer, G. Niedner-Schatteburg, Benzene activation and H/D isotope effects in reactions of mixed cobalt platinum clusters: The influence of charge and of composition, International Journal of Mass Spectrometry, 330 (2012) 271-276.

5. Aspartame (Asp-PheOMe) and Asp-Phe:

Structural investigations on their isolated protonated, deprotonated and alkali metal ion attached species

5.1. Introduction

During the last years a rapid growth in understanding the influence of non-bonded, particularly hydrogen-bonded interactions, on the shapes and conformations of flexible molecules, including those of pharmacological or biological importance has come up (see a review already in 2000 [1]). Large interest arose in the structural investigations on peptides, esp. when cationized with alkali metal ions. Many single peptides have already been investigated finding two major structure types: The non-zwitterionic, charge-solvated (CS) type, where the alkali metal cation is often chelated in a tridentate type, and the zwitterionic, salt-bridge (SB) type. Four major tasks can be performed to help determining a gas phase molecule's structure: H/D exchange to determine the number of acidic H atoms, CID measurements to determine the stability and fragmentation pattern of a complex, record IR-MPD to obtain characteristic vibrational modes and quantum mechanical calculations to compare with the IR-MPD spectra. All these types of investigations have become accessible by the widely spreading of useful instruments, such as ion traps, spectroscopic, mostly laser-based techniques, and with the increasing hardware capabilities of computing clusters.

Regarding the topic of H-/D-exchange, multiple reviews illustrate its importance for studying protein structure and dynamics [2-4]. Deuterium exchange rates k_{ex} show a general trend with the reagents: $k_{ex}(D_2O) < k_{ex}(CD_3OD) < k_{ex}(CD_3CO_2D) < k_{ex}(ND_3)$ [5]. Especially for ND_3 the role of multiple exchanges is present [6]. For some molecules site-specific rate constants of H-/D-exchange could be calculated [7-9] finding the general trend of k_{ex}(amine terminus) > k_{ex}(carboxyl terminus) > k_{ex}(NH,OH) [10, 11]. The deuteration agent may cause a perturbation of the molecule's structure before the exchange takes place [12-14]. Theoretical calculations on gaseous glycine and derivatives have proven that proton exchange with NH_3 is best modeled not with Hartree-Fock based methods, but with DFT (functional B3LYP [15]).

CID has helped determining binding energies and fragmentation pathways of many peptides [16-21]. The binding energies of carnosine alkali complexes correspond to CID values as verified by H-/D-exchange, CID experiments and QM calculations. The calculations suggest charge-solvated (CS) type for all alkali metal atoms. Fragmentation is versatile for small alkali metal ions. For large alkali metal ions the loss of the metal atom becomes the most prominent fragmentation pathway [22].

5. Aspartame (Asp-PheOMe) and Asp-Phe: Structural investigations on their isolated protonated, deprotonated and alkali metal ion attached species

IR-MPD spectroscopy was used to detect the H-/D-exchange of model gas-phase peptide ions [23] and phenylalanine analogs [24]. Several IR-MPD and theoretical investigations on alkali metal ions attached to amino acids and peptides reveal the general trend of a CS type, tridentate structure for Li^+ and in most cases also Na^+, where the alkali metal atom is chelated by the molecule (N,CO,CO). For the larger alkali metal atoms a growing percentage of a CS, tridentate structure at the end of the molecule (CO,COOH) or even a zwitterionic, salt bridge bidentate type occurs [25-42]. A difference in fragment types is reported in cationized arginine (blackbody infrared radiative dissociation (BIRD) 200 °C): Li^+ and Na^+ attached arginine (CS type) shows loss of H_2O, K^+, Rb^+ and CS^+ attached (salt-bridge (SB) type) loses NH_3 [43]. In several small molecules motifs of proton bridges were found. In more complex ones they are hardly describable due to mode coupling [44, 45]. Isomer specific IR-IR double resonance spectroscopy (D_2-tagged protonated dipeptides; isomer separation by hole-burning technique) [46]. Molecules containing phenylalanine have gained considerable interest. Gas-phase IR spectra of the protonated dipeptides [Phe-Ala H]$^+$ and [Ala-Phe]$^+$ were compared to condensed-phase results [47]. Structural information of neutral phenylalanine arose from IR/UV double resonance spectra of the neutral protected amino acid AcPheOMe, of its dimer and of its water clusters [48-51]. Whenever ring π-electrons are present their interaction with cations has to be taken into account, e.g. in benzene / water mixtures [52]. Of course, such interactions are also significant in peptides. Their attraction to positive charges of a hydrogen atom and of alkali metal atoms can stabilize particular structural conformations [53-60].

Our investigations in this chapter focus on structure and reactivity of the isolated molecule aspartame (Asp-Phe-OMe) and of its unprotected analog Asp-Phe in protonated, deprotonated or alkalated (with alkali metal ions attached) form (schematic drawing see Fig. 1).
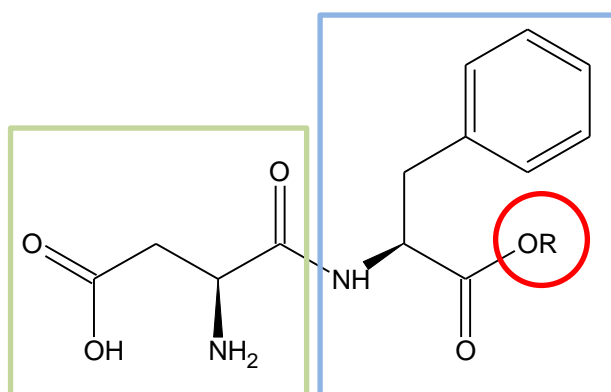
Fig. 1: *Schematic drawing of N-(L-α-Aspartyl)- L-phenylalanin (Asp-Phe; R = H) and N-(L-α-Aspartyl)- L-phenylalanin- methylester (Asp-PheOMe; trivial name: aspartame; R = CH₃); green frame: aspartic acid residue; blue frame: phenylalanine residue.*

Aspartame is known as a sweetener with a sweetness of 200 times that of saccharose. It has been discovered in 1965 and was patented in 1970 [61]. Today it is widely used as additive in many kinds of food and it is traded under the names "Canderel", "Equal", "Nutrasweet" and "AminoSweet". In the human body, most substances are not neutral, but more likely protonated, deprotonated or complexed with Na^+ or K^+. Therefore, we chose to investigate these ionic species. As aspartame is the methyl ester of the dipeptide Asp-Phe we extended our investigations on the unprotected species to gain information about the influence of the additional methyl group. The addition of alkali metal atoms was extended to all ions from Li^+ to Cs^+.

5.2. Methods and experimental setup

We performed mass spectrometric H-/D-exchange, CID and IR-(MPD) studies. We utilized solutions (10^{-4} - 10^{-3} mol / L) of aspartame or Asp-Phe in a water / methanol mixture (1:1). Dipeptide alkalates were obtained by mixing those stock solutions with alkali metal chloride solutions. No addition of bases or acids was necessary in order to obtain protonated or deprotonated species. Both ionic forms are seemingly produced and obtained in the course of the ESI process. H-/D-exchange reactions with D_2O and ND_3 were recorded at a Bruker 7 T Apex Ultra FT-ICR mass spectrometer in Kaiserslautern: The solutions are sprayed and released into the vacuum by an ESI source. Ions are transferred into and stored in a Penning Trap (see chapter 1.2.2.). Deuteration agents were continuously admitted via a leak valve. Reaction kinetics were obtained by variation of a reaction delay between trapping of the ions and mass detection of the deuteration products. The recorded intensity patterns are fitted to pseudo-first-order-kinetics (see chapter 1.3.1.). This yields partial and total rate constants. CID experiments took place in a Bruker Esquire 6000 QIT instrument in Kaiserslautern (see chapter 1.2.1.). Fragmentation patterns of protonated aspartame and Asp-Phe are known from prior CID experiments [62]. Our studies extend these experiments to deprotonated and alkalated specie, not only to identify the fragments qualitatively, but also to gain stability data by varying the fragmentation amplitude (see chapter 1.3.2.). IR-MPD spectra (see chapter 1.3.3.) were recorded at multiple instruments. IR spectra of protonated and deprotonated aspartame in the frequency range of 1000 - 2200 cm^{-1} were recorded by use of the high intensity laser light output of the Free Electron Laser CLIO(see chapter 1.2.5.) in Orsay, Paris, in combination with a Bruker Esquire 3000+ QIT instrument (see chapter 1.2.1.). IR spectra (2500 - 4000 cm^{-1} and 1000 - 2200 cm^{-1}) of all protonated, deprotonated and alkalated complexes were recorded by two Dean Guyer OPO/OPA systems (see chapter 1.2.6.) in Kaiserslautern in combination with a Bruker amaZon SL QIT instrument (see chapter 1.2.1.). Structures, energetics and vibrational spectra were calculated by quantum mechanical calculations(see chapter 1.3.4.) and compared to measured IR-MPD spectra for all protonated, deprotonated and alkalated aspartame and Asp-Phe species. We combined a

correlation treatment by the MP2 method and by various DFT functionals with a variation of basis sets.

5.3. Results and discussion

5.3.1. H-/D- gas phase exchange

We utilized ND_3 as deuteration agent. It provides for a higher proton affinity than D_2O, and it is known to drive H-/D-exchange efficiently.

All species exchange up to the anticipated number of acidic protons available.. According to "paper chemistry" neutral aspartame provides four acidic protons: one from the NH group in the peptide bond, two from the NH_2 group of the Asp residue and one from the COOH group of the Asp residue. Asp-Phe provides an additional proton by the COOH group of the Phe part, conceivable proton migration in protonated and deprotonated ions not withstanding. H-/D-exchange experiments on protonated aspartame reveals a maximum of five H-/D-exchanges. Aspartame with alkali metal ions attached shows the maximum exchange of four protons. Protonated Asp-Phe accordingly reveals the maximum exchange of six and with alkali metal ions attached five protons (For an example of mass spectra of Asp-Phe plus ND_3 recorded during deuteration see Fig. 2).

Beyond the total number of exchangeable protons, we have the rate constants of the first H-/D-exchange steps. For each delay between ion storage and mass detection within the ICR cell the according mass spectra were recorded, the intensities of the ions extracted and plotted. Assuming a pseudo-first-order kinetics an exponential decay of the mother peaks was fitted. The according rate constants are listed in Table 1, normalized to the number of maximum exchangeable H atoms (see Fig. 4).
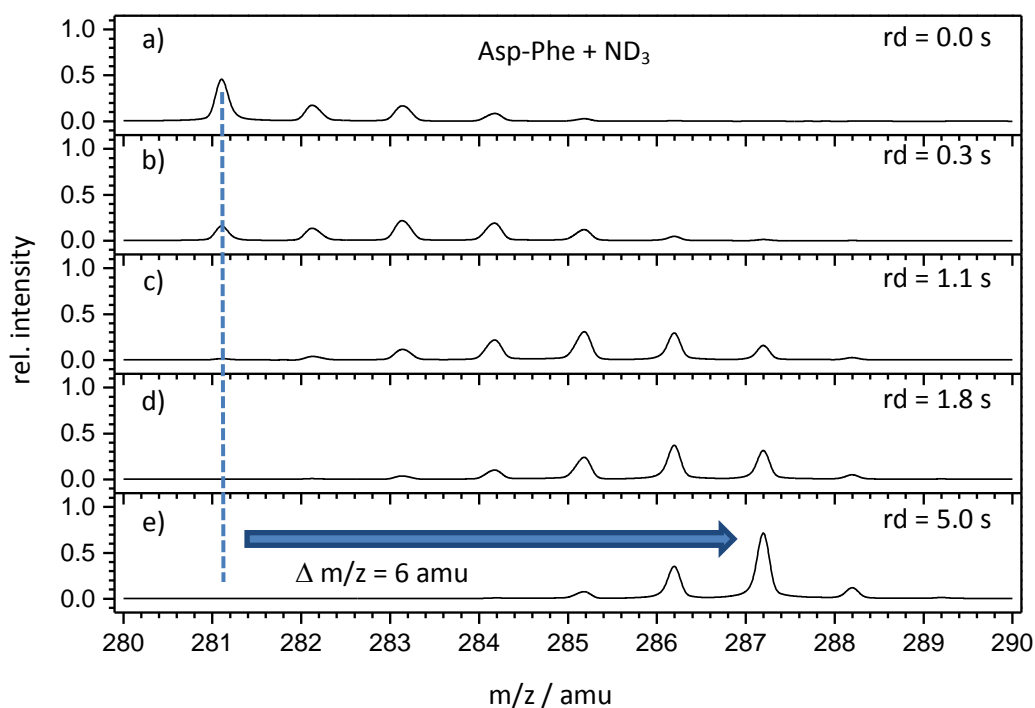
Fig. 2: *Mass spectra of the gas phase H/D exchange reaction of Asp-Phe + H^{+} with ND$_3$ (gas phase pressure 2.0 x 10^{-9} mbar); reaction delay (rd): a) 0.0 s, b) 0.3 s, c) 1.1 s, d) 1.8 s, e) 5.0 s; exchange of up to 6 H atoms. Mass peaks equal to or higher than m/z 288 arise from* ^{13}*C isotopic distribution.*

The normalized rate constants of protonated Asp-Phe is higher than the one of protonated aspartame. This indicates that not all positions are equal, but that the H atom of the additional OH group exchanges faster than the ones of the other acidic places. The values of the rate constant decrease with increasing size of the alkali metal ion attached. The offset in the rate constants for Asp-Phe prevails constant. This reveals that the additional OH group is not involved in the binding of the alkali metal ions.

As already mentioned the rate constants drawn above are only considering the decreasing of the undeuterated mother signal. A complete description of the complex deuteration reaction is very difficult, as in some reaction steps double and triple exchange might occur. An example of this complexity is given in Fig. 3: The relative intensity of the ions is fitted allowing a) only single H-/D-exchange, b) double H-/D-exchange and c) even triple H-/D-exchange out of each consecutive step. Comparison of experimental data points and fitting curves reveals evidence for contributions by double exchange (> 50%). Assumption of triple exchange does not increase the quality of the fits.
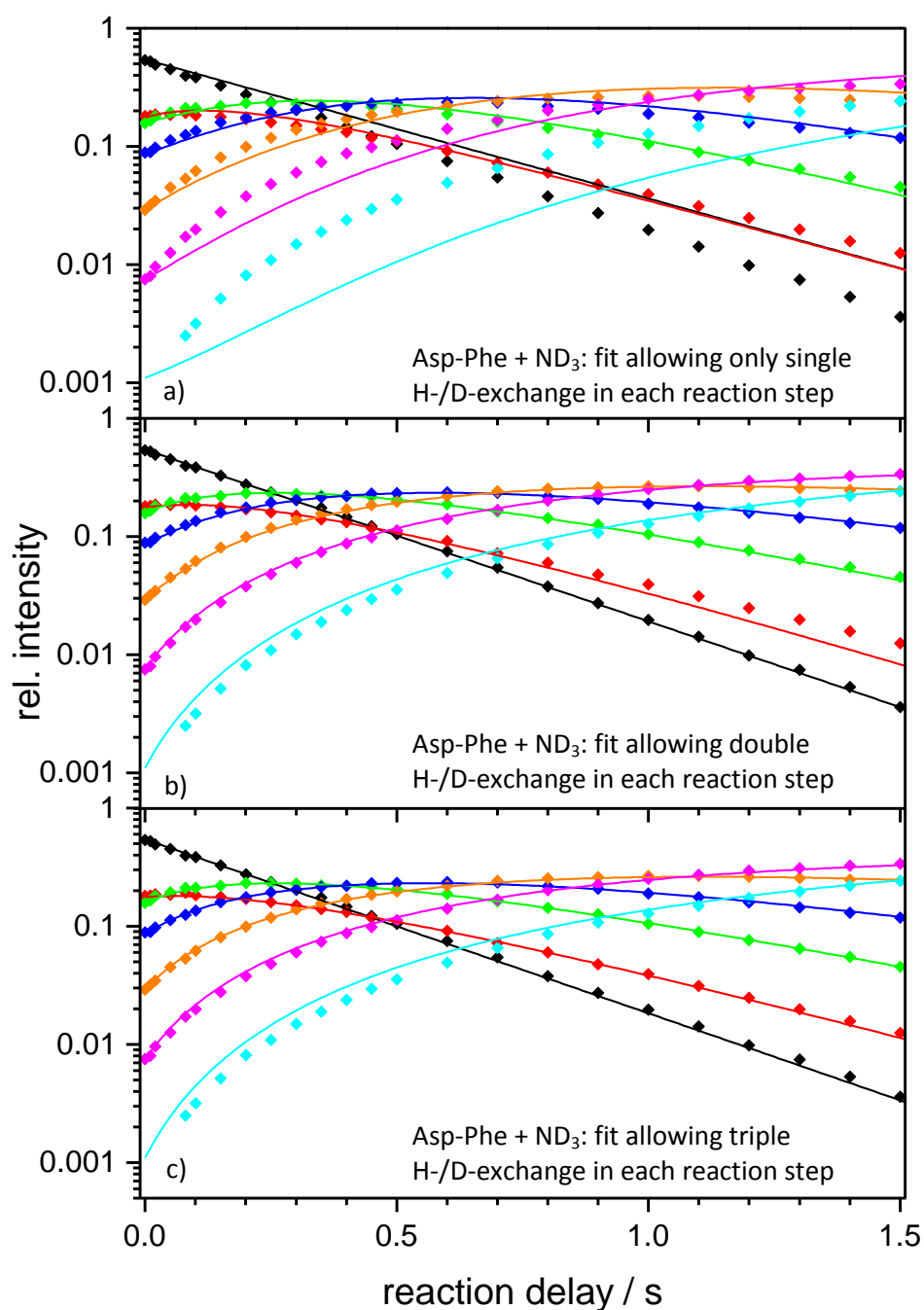
Fig. 3: *Relative intensities of abundant mass peaks of the reaction Asp-Phe + ND$_3$; a) single, b) double, c) triple H-/D-exchange allowed for each consecutive step: $[C_{14}H_{19}N_2O_5]^+$ (black), $[C_{14}H_{18}D_1N_2O_5]^+$ (red), $[C_{14}H_{17}D_2N_2O_5]^+$ (green), $[C_{14}H_{16}D_3N_2O_5]^+$ (blue), $[C_{14}H_{15}D_4N_2O_5]^+$ (orange), $[C_{14}H_{14}D_5N_2O_5]^+$ (magenta), $[C_{14}H_{13}D_6N_2O_5]^+$ (cyan). Single exchange is not sufficient, at least double exchange has to be considered (> 50%).*
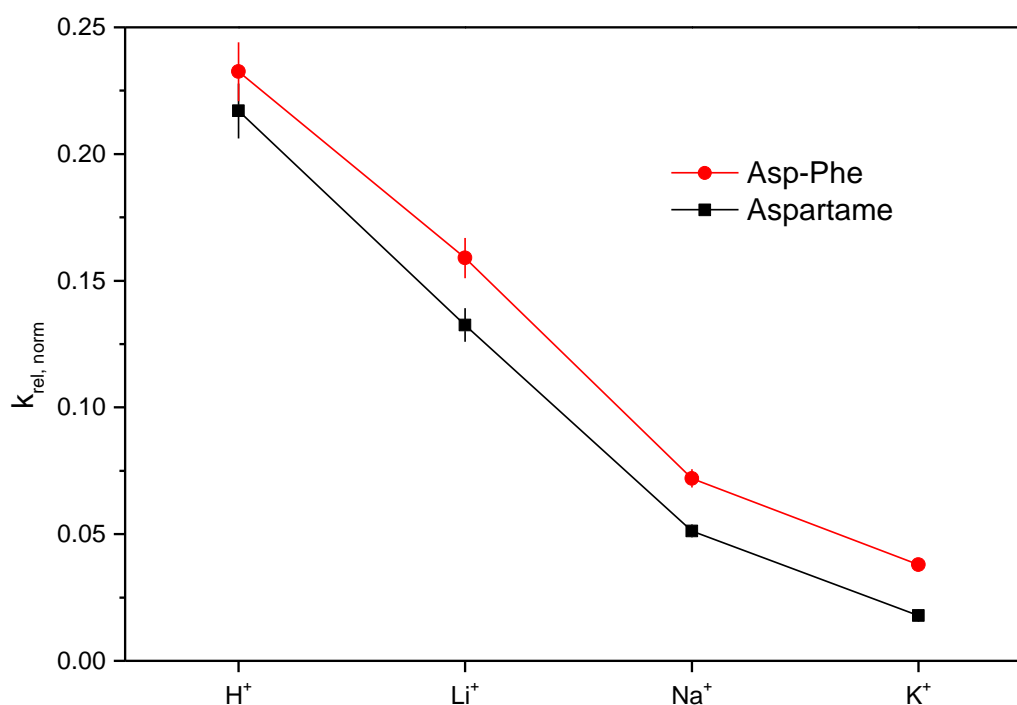
Fig. 4: *Relative rate constants of first H-/D-exchange step (decreasing of the mother intensity signal), normalized to the number of exchangeable protons n_p for protonated ($n_p = 5$) and alkalated ($n_p = 4$) aspartame and for protonated ($n_p = 6$) and alkalated ($n_p = 5$) Asp-Phe. The additional OH group of Asp-Phe causes a constant addition to the values of aspartame.*

Table 1: *Relative rate constants of first H-/D-exchange (decreasing of the mother intensity signal) for cationized aspartame and Asp-Phe (best fit for the decay of the protonated / alkali metal ion attached species)*

	Aspartame			Asp-Phe			**ratio**
	Number of exchangable H-atoms (n_H)	Rate constant (k_{rel}) of first H-/D-exchange	$k_{rel, norm}$ (k_{rel}/n_H)	Number of exchangable H-atoms (n_H)	Rate constant (k_{rel}) of first H-/D-exchange	$k_{rel, norm}$ (k_{rel}/n_H)	**$k_{rel, norm}$ (Asp-Phe) / $k_{rel, norm}$ (Aspartame)**
H^+	5	1.09	0.22	6	1.40	0.23	**1.07**
Li^+	4	0.53	0.13	5	0.80	0.16	**1.20**
Na^+	4	0.21	0.05	5	0.36	0.07	**1.40**
K^+	4	0.07	0.02	5	0.19	0.04	**2.13**

5.3.2. CID investigations

All protonated, deprotonated and alkali metal ion attached species were fragmented by CID varying the fragmentation amplitude. The according fragmentation curves of the cationized species are plotted in Fig. 5.
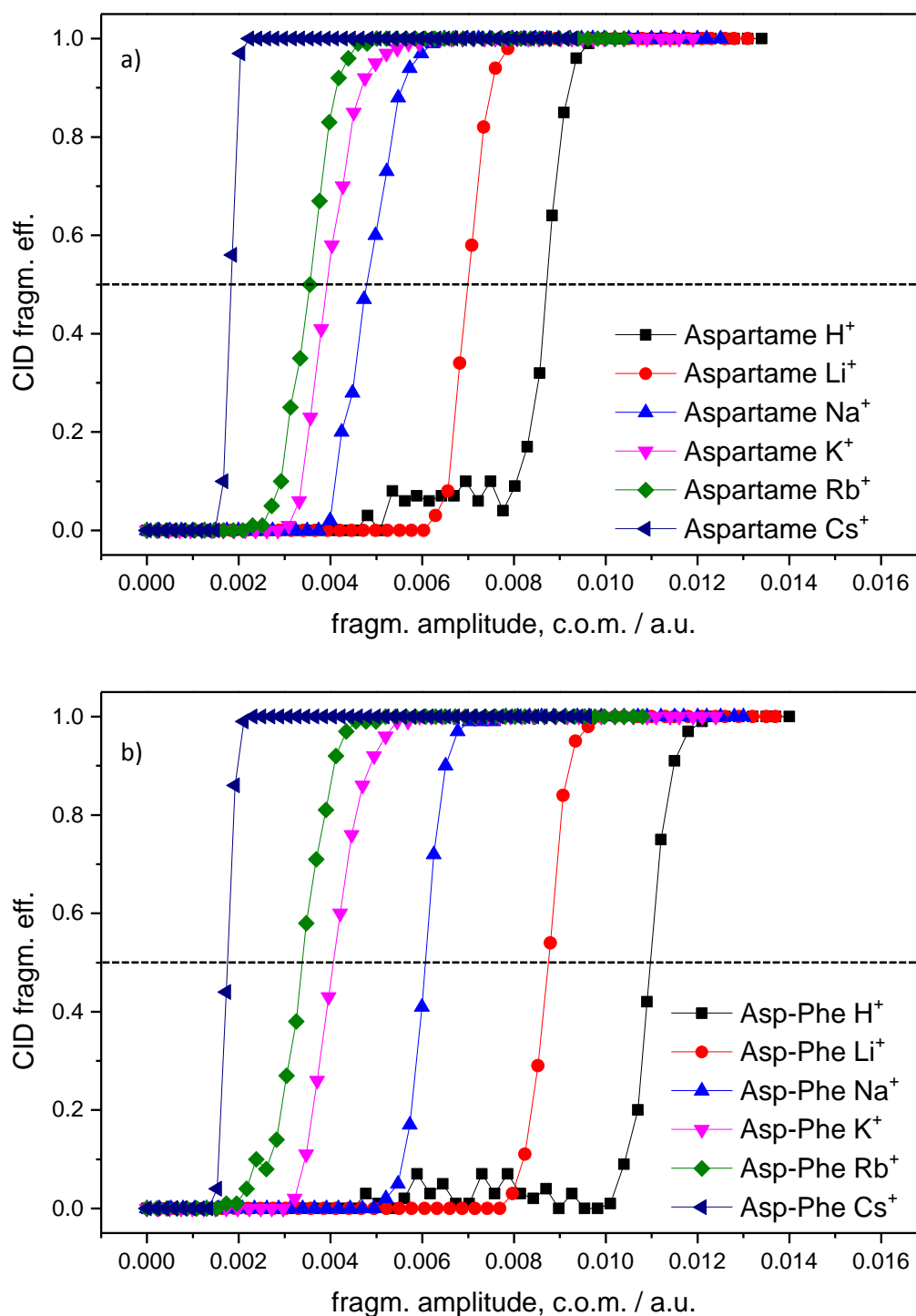
Fig. 5: *CID fragmentation curves (calculated as fragm. eff. par., see chapter 1.3.2.) of cationized aspartame and Asp-Phe. Values of fragmentation amplitude are center-of-mass-transformed collision voltages. Larger ions are bound more weakly resulting in a rise of fragmentation at lower fragmentation amplitude values.*

The values of the fragmentation amplitude at 50 % fragmentation are referred to as threshold energies $A^{50\%}_{COM} = E_{CID}$. A higher value is assigned to higher complex stability of the ion investigated (see chapter 1.3.2.). The threshold energies of both cationized aspartame and cationized Asp-Phe decrease with increasing mass of the attached ion. This might be explained by smaller binding energies of the larger alkali cations (see Fig. 6). All fragmentation efficiency values are calculated as fragmentation efficiency out of the parent, as especially for K^+ and Rb^+ the ionic fragmentation products were outside the detection range of the mass spectrometer.
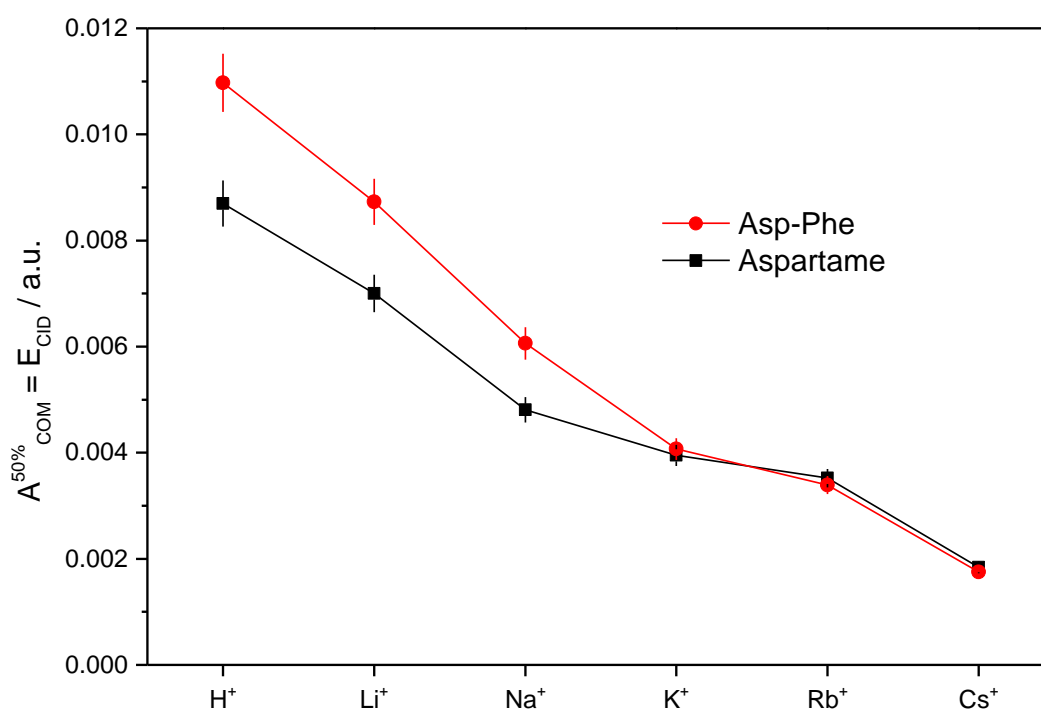
Fig. 6: *Threshold energies E_{CID} of protonated and alkalated aspartame and Asp-Phe cations. E_{CID} values are identical when K^+, Rb^+ or Cs^+ are attached. Complexes with H^+, Li^+ and Na^+ show higher E_{CID} values for Asp-Phe and thus reveal higher stability.*

Threshold energies of Asp-Phe are larger than those of aspartame when protonated or alkalated by Li^+ or Na^+. This reveals that the binding is influenced by the difference of the OH / OMe group of the Phe part of the molecule. The threshold energies E_{CID} of the complexes with K^+, Rb^+ and Cs^+ are identical for both species. Methylation of the hydroxyl group thus has no influence.

For the calculation of E_{CID} the depletion of the mother signal had been calculated neglecting the type of fragments that occur. Both for CID and for the later IR-MPD measurements the most abundant fragments are equal (see mass spectra in Fig. 7). The protonated species show the loss of water and

subsequent fragmentation out of these dehydrated ionic species. Aspartame and Asp-Phe with Li^+ or Na^+ attached both lose neutral Asp anhydride yielding $[PheOMe\ Li]^+$ / $[Phe\ Li]^+$ ionic residues. The complexes with K^+, Rb^+ and Cs^+ mainly decay into the ionic alkali metal cation and the neutral aspartame / Asp-Phe molecule (The naked K^+ and Rb^+ fragments in standard measurement are out of range of the amaZon SL mass spectrometer, and thus not visible in the graphics, but at least confirmed for Rb^+ with special mass spectrometer settings). The deprotonated species show the loss of CH_3OH in the case of aspartame and the loss of H_2O when investigating Asp-Phe. As it is quite likely that the loss of methanol originates from the methanolat of the methylester group it can be assumed that the loss of water in Asp-Phe also affects the carboxyl group of the Phe residue. A list of all detected ionic species with their assumed neutral losses is given for aspartame in Table 2 and for Asp-Phe in Table 3 with the main channels being marked in bold letters. For a suggested structural assignment of protonated Aspartame and Asp-Phe and their fragments see Ref. [62].
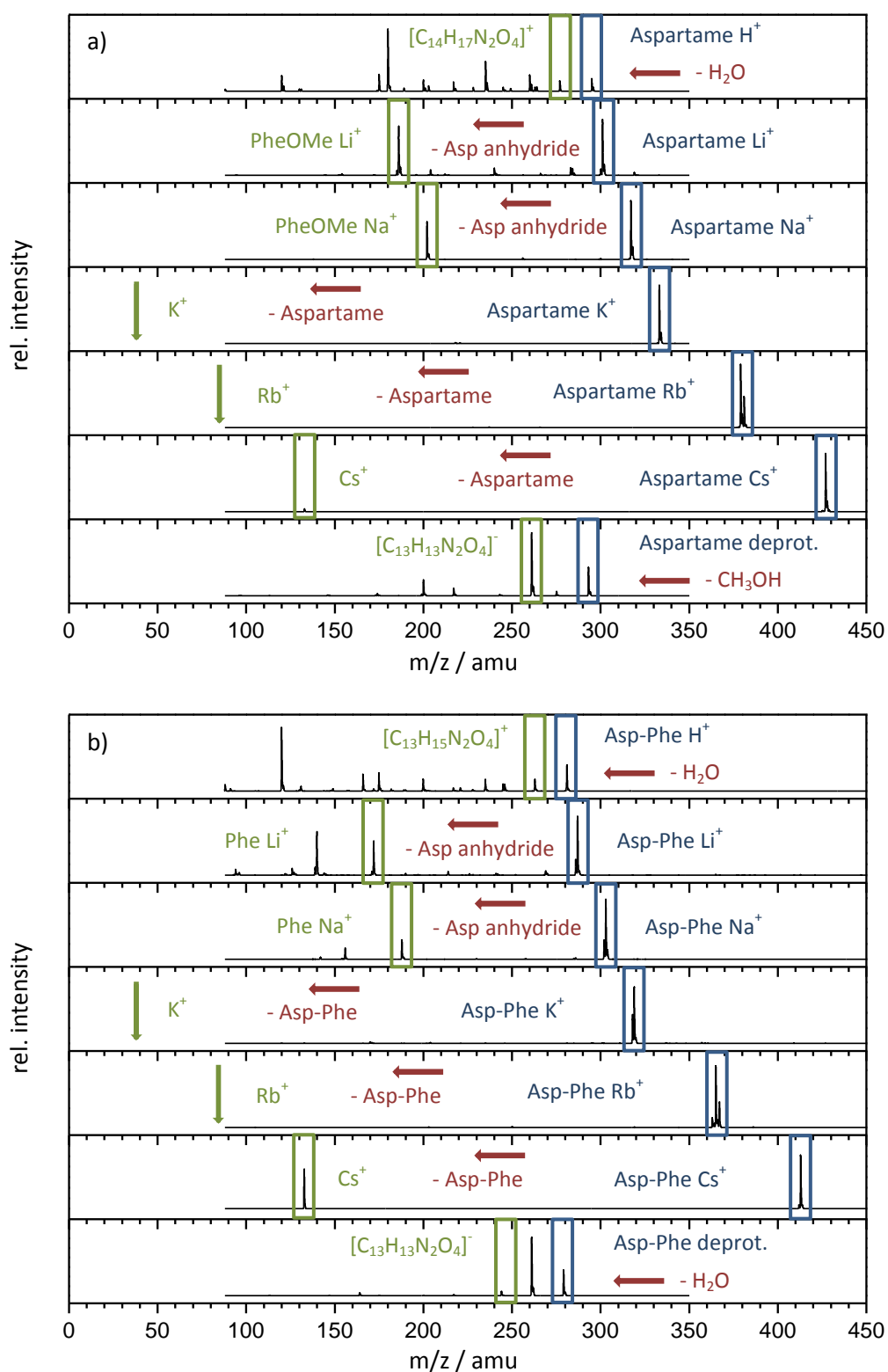
Fig. 7: *Mass spectra of maximum fragmentation. For cationized species fragmentation behavior is similar for aspartame and Asp-Phe.*

Table 2: *Fragmentation channels of aspartame (Asp-PheOMe) by CID // IR-MPD.*

	Neutral mass loss	Neutral fragment	Ionic fragm. mass	Ionic fragment
Aspartame H$^+$ (295) $[C_{14}H_{19}N_2O_5]^+$	**18**	**H$_2$O**	**277**	**$[C_{14}H_{17}N_2O_4]^+$**
	32	CH$_3$OH	263	$[C_{13}H_{15}N_2O_4]^+$
	18 + 17	H$_2$O + NH$_3$	260	$[C_{14}H_{14}N_1O_4]^+$
	46	HCOOH	249	$[C_{13}H_{17}N_2O_3]^+$
	18 + 32	H$_2$O + CH$_3$OH	245	$[C_{13}H_{13}N_2O_3]^+$
	60	CH$_3$COOH	235	$[C_{12}H_{15}N_2O_3]^+$
	18 + 32 + 17	H$_2$O + CH$_3$OH + NH$_3$	228	$[C_{13}H_{10}N_1O_3]^+$
	60 + 17	CH$_3$COOH + NH$_3$	218	$[C_{12}H_{12}N_1O_3]^+$
	18 + 60	H$_2$O + CH$_3$COOH	217	$[C_{12}H_{13}N_2O_2]^+$
	32 + 60	CH$_3$OH + CH$_3$COOH	203	$[C_{11}H_{11}N_2O_2]^+$
	18 + 17 + 60	H$_2$O + NH$_3$ + CH$_3$COOH	200	$[C_{12}H_{10}N_1O_2]^+$
	46 + 60	HCOOH + CH$_3$COOH	189	$[C_{11}H_{13}N_2O_1]^+$
	115	Asp anhyd.	180	[PheOMe H]$^+$
	60 + 60	CH$_3$COOH + CH$_3$COOH	175	$[C_{10}H_{11}N_2O_1]^+$
	115 + 60	Asp anhyd. + CH$_3$COOH	120	[Phe H - HCOOH]$^+$
	207	HCO PheOMe	88	[Asp H - HCOOH]$^+$
Aspartame Li$^+$ (301) $[C_{14}H_{18}N_2O_5Li]^+$	17	NH$_3$	284	$[C_{14}H_{15}N_1O_5Li]^+$
	18	H$_2$O	283	$[C_{14}H_{16}N_2O_4Li]^+$
	18 + 17 / 17 + 18	H$_2$O + NH$_3$ / NH$_3$ + H$_2$O	266	$[C_{14}H_{13}N_1O_4Li]^+$
	17 + 44 / 61	NH$_3$ + CO$_2$ / NH$_2$COOH	240	$[C_{13}H_{15}N_1O_3Li]^+$
	115	**Asp anhyd.**	**186**	**[PheOMe Li]$^+$**
Aspartame Na$^+$ (317) $[C_{14}H_{18}N_2O_5Na]^+$	17	NH$_3$	300	$[C_{14}H_{15}N_1O_5Na]^+$
	61	NH$_2$COOH	256	$[C_{13}H_{15}N_1O_3Na]^+$
	115	**Asp anhyd.**	**202**	**[PheOMe Na]$^+$**
Aspartame K$^+$ (333) $[C_{14}H_{18}N_2O_5K]^+$	115	Asp anhyd.	218	[PheOMe K]$^+$
	294	**Asp PheOMe**	**39**	**K$^+$**
Aspartame Rb$^+$ (379) $[C_{14}H_{18}N_2O_5Rb]^+$	**294**	**Asp PheOMe**	**85**	**Rb$^+$**
Aspartame Cs$^+$ (427) $[C_{14}H_{18}N_2O_5Cs]^+$	**294**	**Asp PheOMe**	**133**	**Cs$^+$**
Aspartame deprot. (293) $[C_{14}H_{17}N_2O_5]^-$	18	H$_2$O	275	$[C_{14}H_{15}N_2O_4]^-$
	32	**CH$_3$OH**	**261**	**$[C_{13}H_{13}N_2O_4]^-$**
	18 + 32 / 32 + 18	H$_2$O + CH$_3$OH / CH$_3$OH + H$_2$O	243	$[C_{13}H_{11}N_2O_3]^-$
	32 + 44	CH$_3$OH + CO$_2$	217	$[C_{12}H_{13}N_2O_2]^-$
	32 + 61	CH$_3$OH + NH$_2$COOH	200	$[C_{12}H_{10}N_1O_2]^-$

Table 3: *Fragmentation channels of Asp-Phe by CID // IR-MPD.*

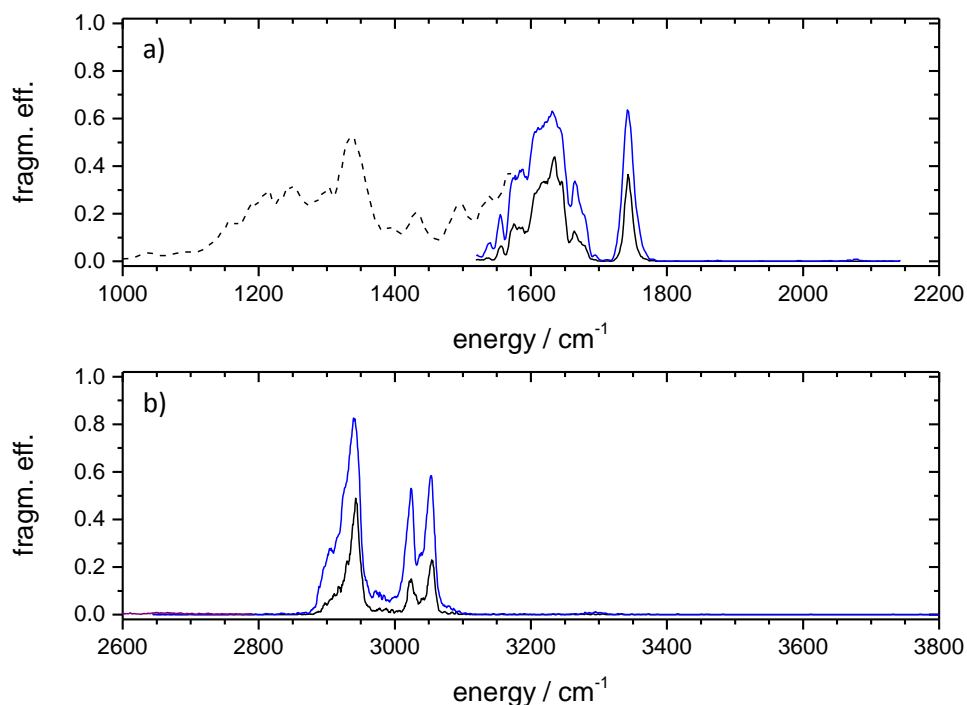|	Neutral mass loss	Neutral fragment	Ionic fragm. mass	Ionic fragment
Asp-Phe H$^+$ (281) [C$_{13}$H$_{17}$N$_2$O$_5$]$^+$	**18**	**H$_2$O**	**263**	**[C$_{13}$H$_{15}$N$_2$O$_4$]$^+$**
	18 + 17	H$_2$O + NH$_3$	246	[C$_{13}$H$_{12}$N$_1$O$_4$]$^+$
	18 + 18	H$_2$O + H$_2$O	245	[C$_{13}$H$_{13}$N$_2$O$_3$]$^+$
	60	CH$_3$COOH	221	[C$_{11}$H$_{13}$N$_2$O$_3$]$^+$
	18 + 18 + 17	H$_2$O + H$_2$O + NH$_3$	228	[C$_{13}$H$_{10}$N$_1$O$_3$]$^+$
	46 + 17	HCOOH + NH$_3$	218	[C$_{12}$H$_{12}$N$_1$O$_3$]$^+$
	18 + 46	H$_2$O + HCOOH	217	[C$_{12}$H$_{13}$N$_2$O$_2$]$^+$
	18 + 17 + 46	H$_2$O + NH$_3$ + HCOOH	200	[C$_{12}$H$_{10}$N$_1$O$_2$]$^+$
	115	Asp anhyd.	180	[Phe H]$^+$
	60 + 46	CH$_3$COOH + HCOOH	175	[C$_{10}$H$_{11}$N$_2$O$_1$]$^+$
	115 + 17 / 132	Asp anh. + NH$_3$ / Asp-OH+NH$_2$	149	[Phe H - NH$_3$]$^+$
	115 + 46	Asp anhyd. + HCOOH	120	[Phe H - HCOOH]$^+$
	207	HCO Phe	88	[C$_3$H$_6$N$_1$O$_2$]$^+$
Asp-Phe Li$^+$ (287) [C$_{13}$H$_{16}$N$_2$O$_5$Li]$^+$	17	NH$_3$	270	[C$_{13}$H$_{13}$N$_1$O$_5$Li]$^+$
	18	H$_2$O	269	[C$_{13}$H$_{14}$N$_2$O$_4$Li]$^+$
	45	NH$_2$COH	242	[C$_{12}$H$_{13}$N$_1$O$_4$Li]$^+$
	46	HCOOH	241	[C$_{12}$H$_{14}$N$_2$O$_3$Li]$^+$
	115	**Asp anhyd.**	**172**	**[Phe Li]$^+$**
	115 + 32	Asp anhyd. + CH$_3$OH	140	[Phe Li - CH$_3$OH]$^+$
	115 + 46	Asp anhyd. + HCOOH	126	[Phe Li - HCOOH]$^+$
Asp-Phe Na$^+$ (303) [C$_{13}$H$_{16}$N$_2$O$_5$Na]$^+$	17	NH$_3$	286	[C$_{13}$H$_{13}$N$_1$O$_5$Na]$^+$
	115	**Asp anhyd.**	**188**	**[Phe Na]$^+$**
	115 + 32	Asp anhyd. + CH$_3$OH	156	[Phe Na - CH$_3$OH]$^+$
	115 + 46	Asp anhyd. + HCOOH	142	[Phe Na - HCOOH]$^+$
Asp-Phe K$^+$ (319) [C$_{13}$H$_{16}$N$_2$O$_5$K]$^+$	18	H$_2$O	301	[C$_{13}$H$_{14}$N$_2$O$_4$K]$^+$
	115	Asp anhyd.	204	[Phe K]$^+$
	280	**Asp-Phe**	**39**	**K$^+$**
Asp-Phe Rb$^+$ (365) [C$_{13}$H$_{16}$N$_2$O$_5$Rb]$^+$	115	Asp anhyd.	250	[Phe Rb]$^+$
	280	**Asp-Phe**	**85**	**Rb$^+$**
Asp-Phe Cs$^+$ (413) [C$_{13}$H$_{16}$N$_2$O$_5$Cs]$^+$	**280**	**Asp-Phe**	**133**	**Cs$^+$**
Asp-Phe deprot. (279) [C$_{13}$H$_{15}$N$_2$O$_5$]$^-$	**18**	**H$_2$O**	**261**	**[C$_{13}$H$_{13}$N$_2$O$_4$]$^-$**
	18 + 17	H$_2$O + NH$_3$	244	[C$_{13}$H$_{10}$N$_1$O$_4$]$^-$
	18 + 44	H$_2$O + CO$_2$	217	[C$_{12}$H$_{13}$N$_2$O$_2$]$^-$
	18 + 61	H$_2$O + NH$_2$COOH	200	[C$_{12}$H$_{10}$N$_1$O$_2$]$^-$
	115	Asp anhyd.	164	[Phe - H]$^-$
	115 + 17	Asp anhyd. + NH$_3$	147	[Phe - H - NH$_3$]$^-$
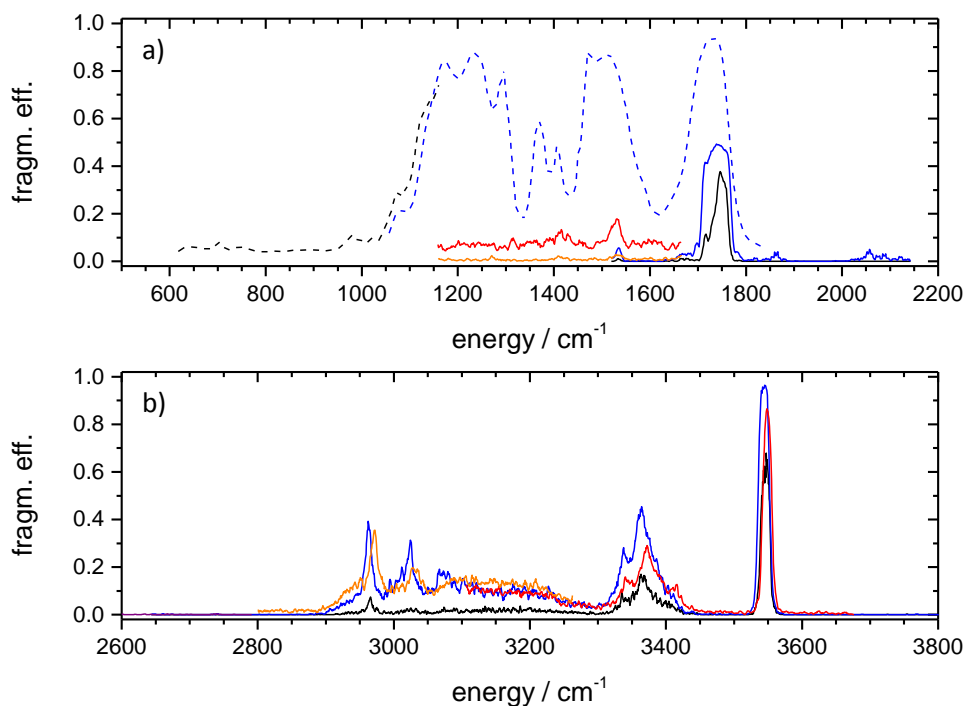
Fig. 8: IR-MPD spectra of Aspartame H⁺: *Fragmentation efficiency of IR-MPD spectra; blue and black dashed lines: one color IR-MPD spectra (FEL CLIO, Paris); blue, black and purple solid lines: one color IR-MPD spectra (blue and black at different laser intensities) (OPO/OPA, KL); red and orange solid lines: two color IR-MPD spectra (OPO/OPA, KL): a) red line probe at 3550 cm⁻¹, orange line probe at 3360 cm⁻¹; b) red and orange lines probe at 3550 cm⁻¹, different scanning laser intensities.*
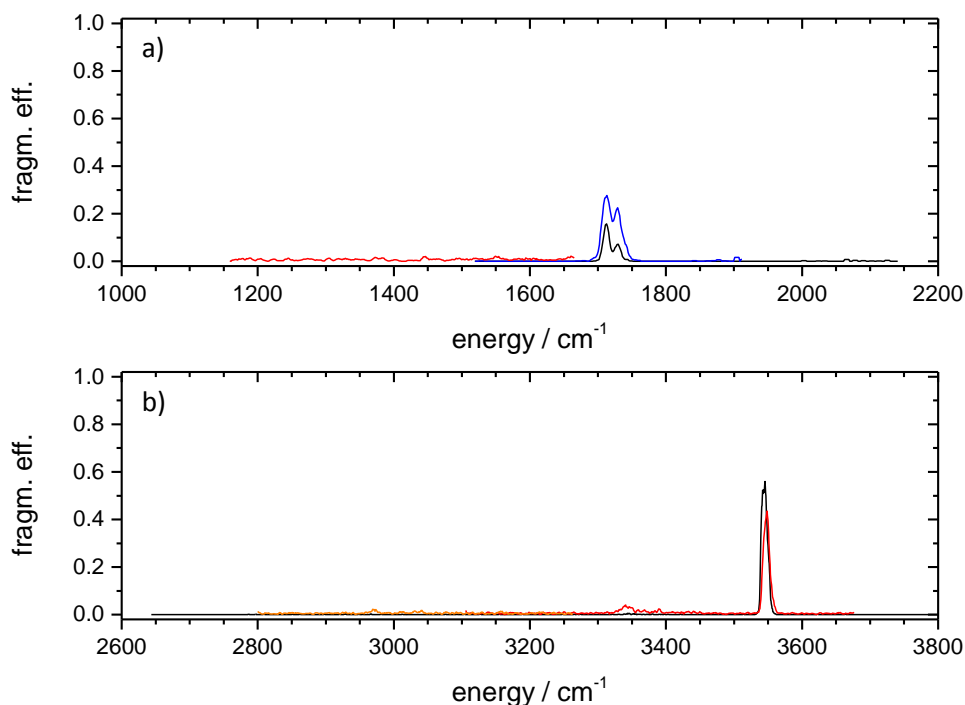
Fig. 9: IR-MPD spectra of Aspartame Li⁺: *Fragmentation efficiency of IR-MPD spectra; blue and black solid lines: one color IR-MPD spectra, different laser intensities (OPO/OPA, KL); red and orange solid lines: two color IR-MPD spectra (OPO/OPA, KL): a) red line probe at 3545 cm⁻¹; b) red and orange lines probe at 3545 cm⁻¹, different scanning laser intensities.*
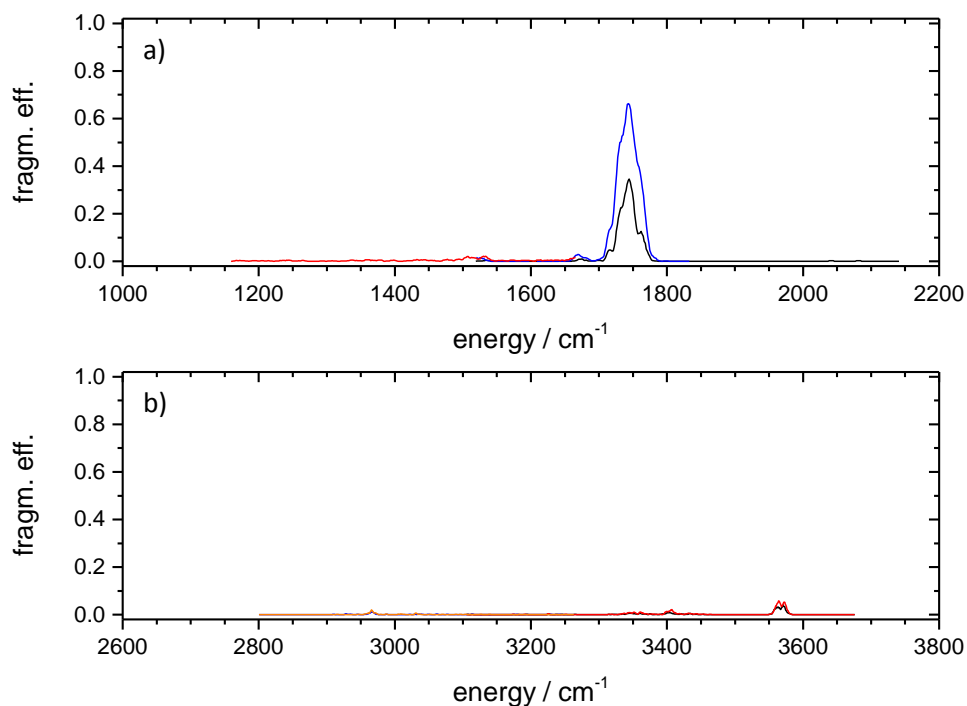
Fig. 10: IR-MPD spectra of Aspartame Cs⁺: *Fragmentation efficiency of IR-MPD spectra; blue and black solid lines: one color IR-MPD spectra, different laser intensities (OPO/OPA, KL); red and orange solid lines: two color IR-MPD spectra (OPO/OPA, KL): a) red line probe at 3565 cm⁻¹; b) red and orange lines probe at 3565 cm⁻¹, different scanning laser intensities.*

Fig. 11: IR-MPD spectra of deprotonated Aspartame: *Fragmentation efficiency of IR-MPD spectra; black dashed line: one color IR-MPD spectrum (FEL CLIO, Paris); blue, black and purple solid lines: one color IR-MPD spectra (blue and black at different laser intensities) (OPO/OPA, KL).*
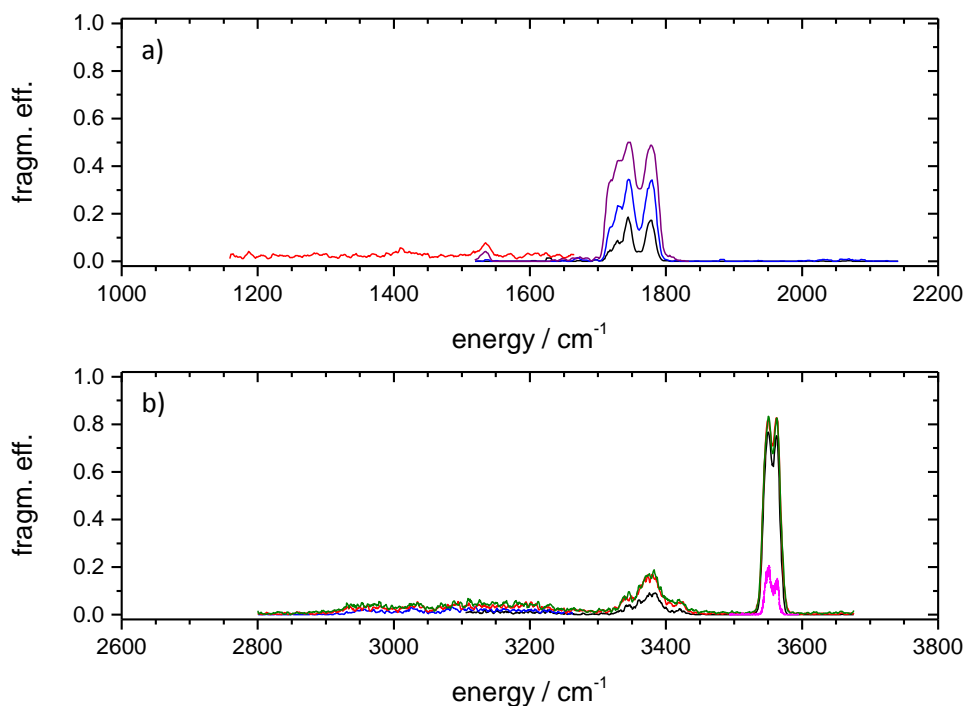
Fig. 12: IR-MPD spectra of Asp-Phe H⁺: *Fragmentation efficiency of IR-MPD spectra; blue, black and purple solid lines: one color IR-MPD spectra, different laser intensities (OPO/OPA, KL); magenta solid line: one color IR-MPD spectrum (narrow band OPO/OPA, KL); red and green solid lines: two color IR-MPD spectra (OPO/OPA, KL): a) red line probe at 3550 cm⁻¹; b) red line probe at 3565 cm⁻¹, green line probe at 3550 cm⁻¹.*
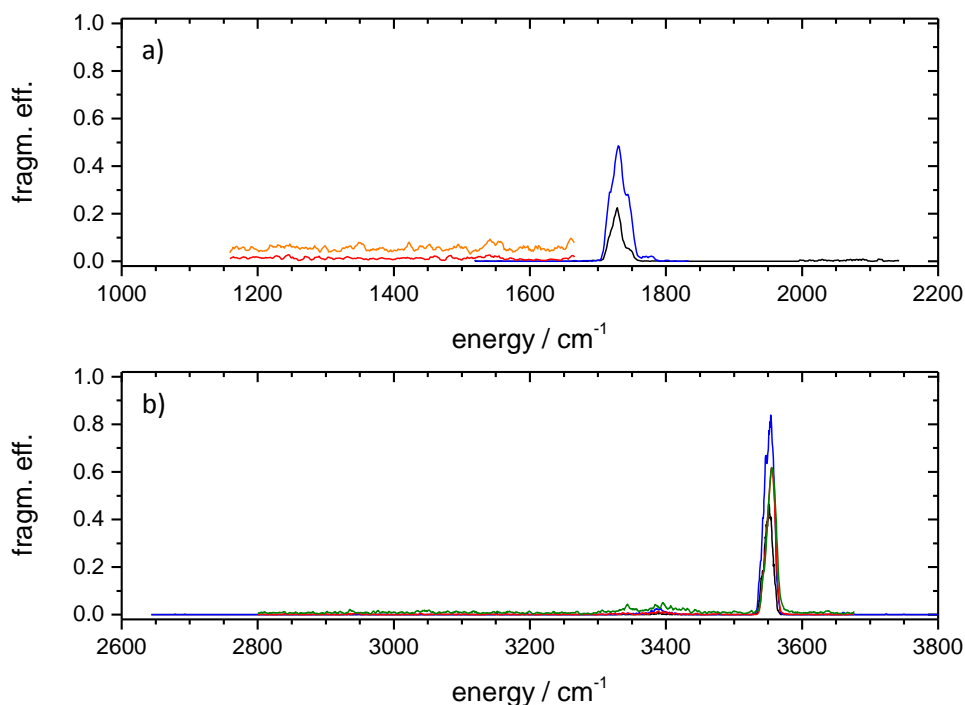
Fig. 13: IR-MPD spectra of Asp-Phe Li⁺: *Fragmentation efficiency of IR-MPD spectra; blue and black solid lines: one color IR-MPD spectra, different laser intensities (OPO/OPA, KL); red, orange and green solid lines: two color IR-MPD spectra (OPO/OPA, KL): a) red and orange lines probe at 3555 cm⁻¹, different scanning laser intensities; b) red line probe at 3565 cm⁻¹, green line probe at 3550 cm⁻¹.*
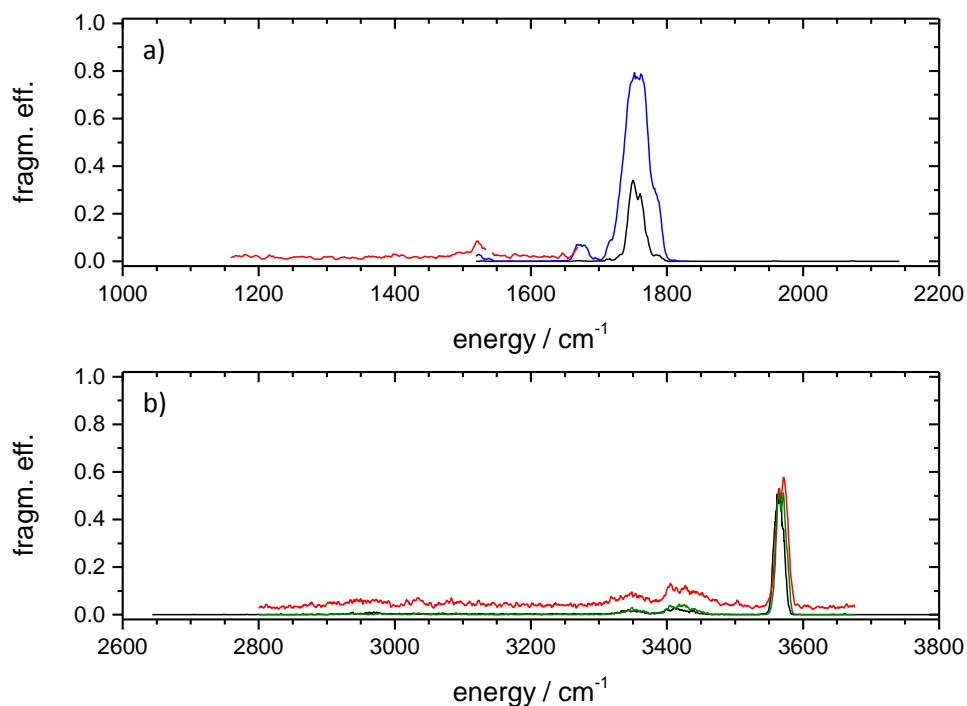
Fig. 14: IR-MPD spectra of Asp-Phe Cs⁺: *Fragmentation efficiency of IR-MPD spectra; blue and black solid lines: one color IR-MPD spectra, different laser intensities (OPO/OPA, KL); red and green solid lines: two color IR-MPD spectra (OPO/OPA, KL): a) red line probe at 3565 cm⁻¹; b) red line probe at 3565 cm⁻¹, green line probe at 3550 cm⁻¹.*
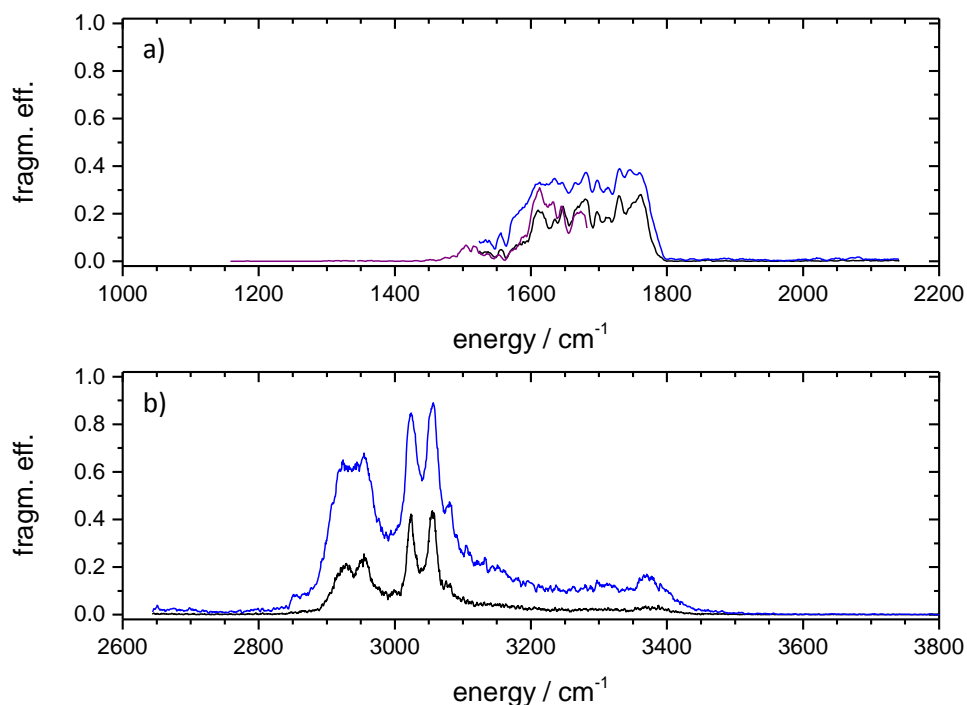
Fig. 15: IR-MPD spectra of deprotonated Asp-Phe: *Fragmentation efficiency of IR-MPD spectra; blue, black and purple solid lines: one color IR-MPD spectra, different laser intensities (OPO/OPA, KL).*

5.3.3. IR-MPD spectra of protonated, deprotonated and alkali metal ion attached species

Collision induced fragmentation patterns are similar for aspartame and Asp-Phe. Confirmation of structural differences explaining the findings of the CID threshold energies E_{CID} might arise from IR-MPD spectroscopy. We recorded IR-MPD spectra of protonated, deprotonated and alkalated species. Spectra of protonated species, species with the smallest alkali metal Li^+ and with the largest Cs^+ and deprotonated species are plotted within this chapter (see Fig. 8 to Fig. 15). The complete collection of all IR-MPD spectra is added in the supplementary material in enlarged form (see chapter 5.6., aspartame: suppl. A, Asp-Phe: suppl. C).

Each diagram shows multiple IR-MPD spectra, recorded with either one scanning OPO/OPA laser (one color spectra) or spectra with the scanning and - especially for the spectra in the frequency range of 1000 - 2200 cm^{-1} - an additional postheating fixed frequency OPO/OPA probe laser (two color spectra). The one color spectra were recorded at different laser intensities: Low intensity can improve the resolution of a broad peak structure, high energies is necessary to obtain vibrational bands which have a low IR intensity. We recorded additional FEL spectra of protonated and deprotonated aspartame.

The FEL-IR-MPD spectra of protonated aspartame (Fig. 8) show a broad peak between 1100 and 1300 cm^{-1}, two small peaks around 1400 cm^{-1} and two broad peaks between 1450 and 1550 cm^{-1} and between 1700 and 1750 cm^{-1} (probably C=O stretching vibrations). This latter feature and a small peak around 1530 cm^{-1} were also obtained with the OPO/OPA laser system. In the region with high OPO/OPA laser output (> 2500 cm^{-1}) a broad absorption between 2900 and 3450 cm^{-1} occurs, with peaks at 2960, 3020 and between 3320 and 3420 cm^{-1} (CH and NH bands). An additional high intensity peak at 3550 cm^{-1} can probably be assigned to an OH stretching vibration.

In protonated Asp-Phe (Fig. 12) we find also the small peak at 1530 cm^{-1}, a broader band between 1700 and 1750 cm^{-1} and another one around 1775 cm^{-1}. This latter one is different to the spectrum of aspartame. It can be identified as the C=O stretching vibration of the COOH pattern of the unprotected Phe part. The broad absorption between 2900 and 3450 cm^{-1} together with the peaks between 3320 and 3420 cm^{-1} is similar to the finding in aspartame. The peaks at 2960 and 3020 cm^{-1} of protonated aspartame are missing. Beneath the OH stretching band at 3550 cm^{-1}, another peak at 3570 cm^{-1} can be distinguished. This one can also be assigned to the additional OH of the COOH pattern of the Phe part.

The IR-MPD spectra of aspartame with Li$^+$ (Fig. 9) show much less spectral features. The band between 1700 and 1750 cm^{-1}, a small one around 3350 cm^{-1} and the peak at 3550 cm^{-1} are still visible but with less intensity than in the protonated case. Obviously the energy redistribution within this complex, that is necessary for fragmentation, is not as effective.

The complex of Asp-Phe with Li$^+$ (Fig. 13) shows similar shape plus the two additional features that were already seen in the protonated complex: The broadening of the peak for the C=O stretching vibrations and the one for the OH stretching vibrations into the blue, especially the latter one with higher fragmentation efficiency.

A similar finding in the range of the C=O stretching vibrations holds true for aspartame with Cs$^+$ (Fig. 10) and for Asp-Phe Cs$^+$ (Fig. 14). However, the region of the OH stretching vibration provides for different results: The OH stretching vibration of the aspartame complex has nearly completely disappeared and for the Asp-Phe complex only the peak at 3570 cm^{-1} is obtained. It likely originates from the OH of the COOH group of the Phe part. Obviously the most abundant structures of aspartame and Asp-Phe with Cs$^+$ do no longer possess a free OH motif.

Overall the spectra of cationized aspartame and Asp-Phe are quite similar, except for small changes in the spectra originating from the additional COOH feature of Asp-Phe. This leads to the assumption that the structures of the according aspartame and Asp-Phe complexes are similar.

This is different for the deprotonated spectra. Deprotonated aspartame (Fig. 11) shows a broad absorption in the OPO/OPA range from 1550 to 1670 cm^{-1} and an additional peak structure around 1740 cm^{-1}. In the high energy region we find one peak between 2900 and 2950 cm^{-1} and two peaks between 3000 and 3070 cm^{-1}. No more peaks are assigned to free OH motifs.

Deprotonated Asp-Phe (Fig. 15) shows one broad absorption band between 1500 and 1780 cm^{-1} without any resolved structure. In the high energy region, there are two peaks between 3000 and 3070 cm^{-1}. The first absorption band, ranging from 2850 to 3000 cm^{-1}, is much broader than in deprotonated aspartame. A large unstructured band on the blue side of the double peak structure indicates a much better fragmentation efficiency of deprotonated Asp-Phe, in contrast to aspartame (the laser intensity was similar in both cases).

The cationized species reveal IR-MPD spectra that show corresponding structures in the range of C=O stretching and OH stretching vibrations. A direct comparison of their spectra is given in Fig. 16.
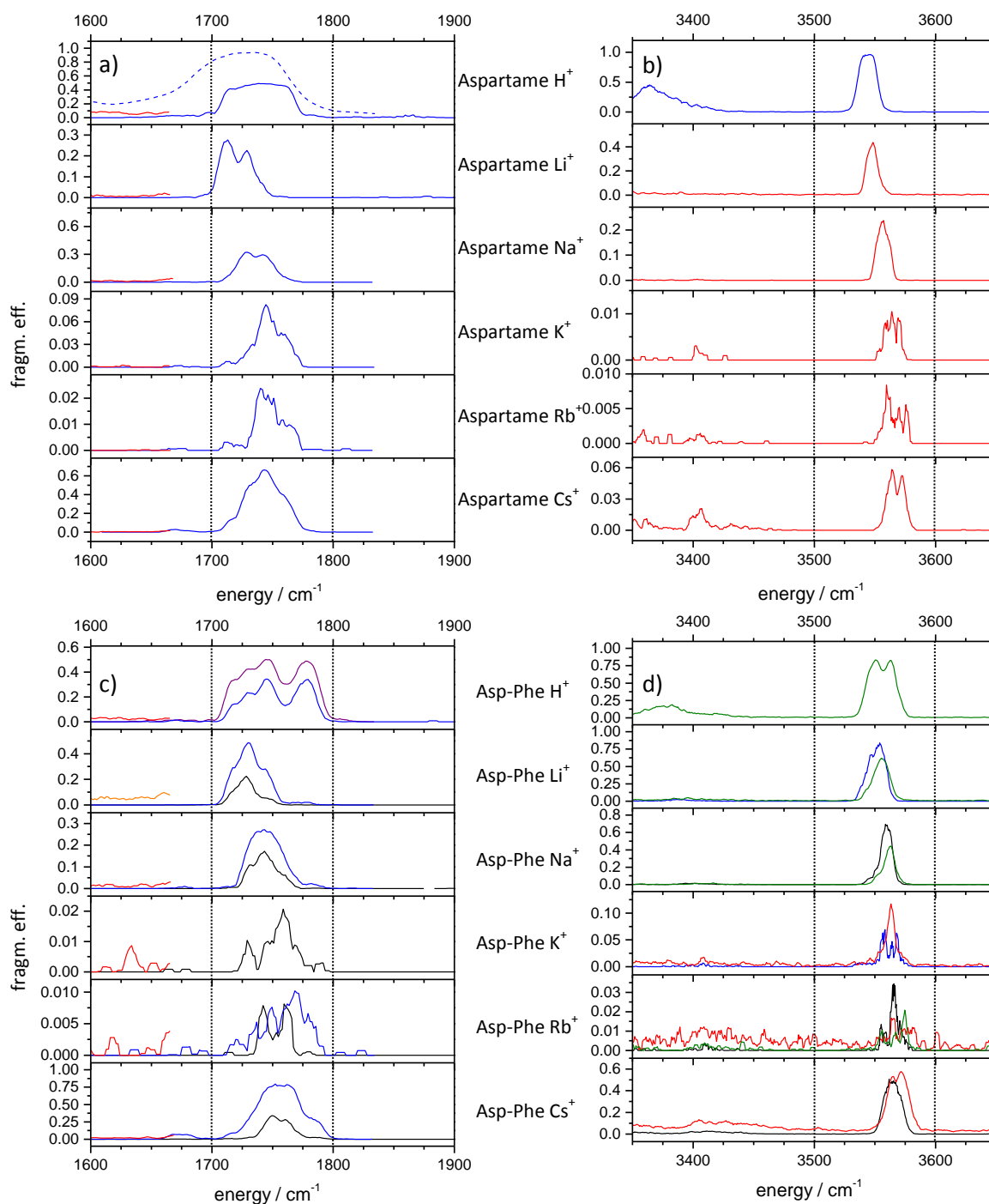
Fig. 16: *IR-MPD spectra of cationized a), b) aspartame and c), d) Asp-Phe. There is a red shift with decreasing alkali metal ion size in the regions of the C=O stretching vibration in the cases a) and c) and of the OH stretching vibration in the cases b) and d).*

The spectrum of the protonated species documents a species that is unique. It shall not be discussed further at this place. For the spectra of the alkalated species, two trends are visible: With decreasing alkali metal ion size we see a red shift (up to 25 cm^{-1}) of the peak shape around 1750 cm^{-1} (probably C=O stretching vibrations) and a red shift (up to 20 cm^{-1}) of the peak shape around 3550 cm^{-1} (probably OH stretching vibrations). This red shift could indicate that the according stretching vibrations are weakend by the influence of small alkali metal, as could be explained by the increasing Lewis acidic character of smaller alkali metal cations.

5.3.4. Correlation between IR peaks and E_{CID} values

As mentioned in Fig. 16 the two peaks around 1750 cm^{-1} and around 3550 cm^{-1} seem to have a red shift for small alkali metal ions.
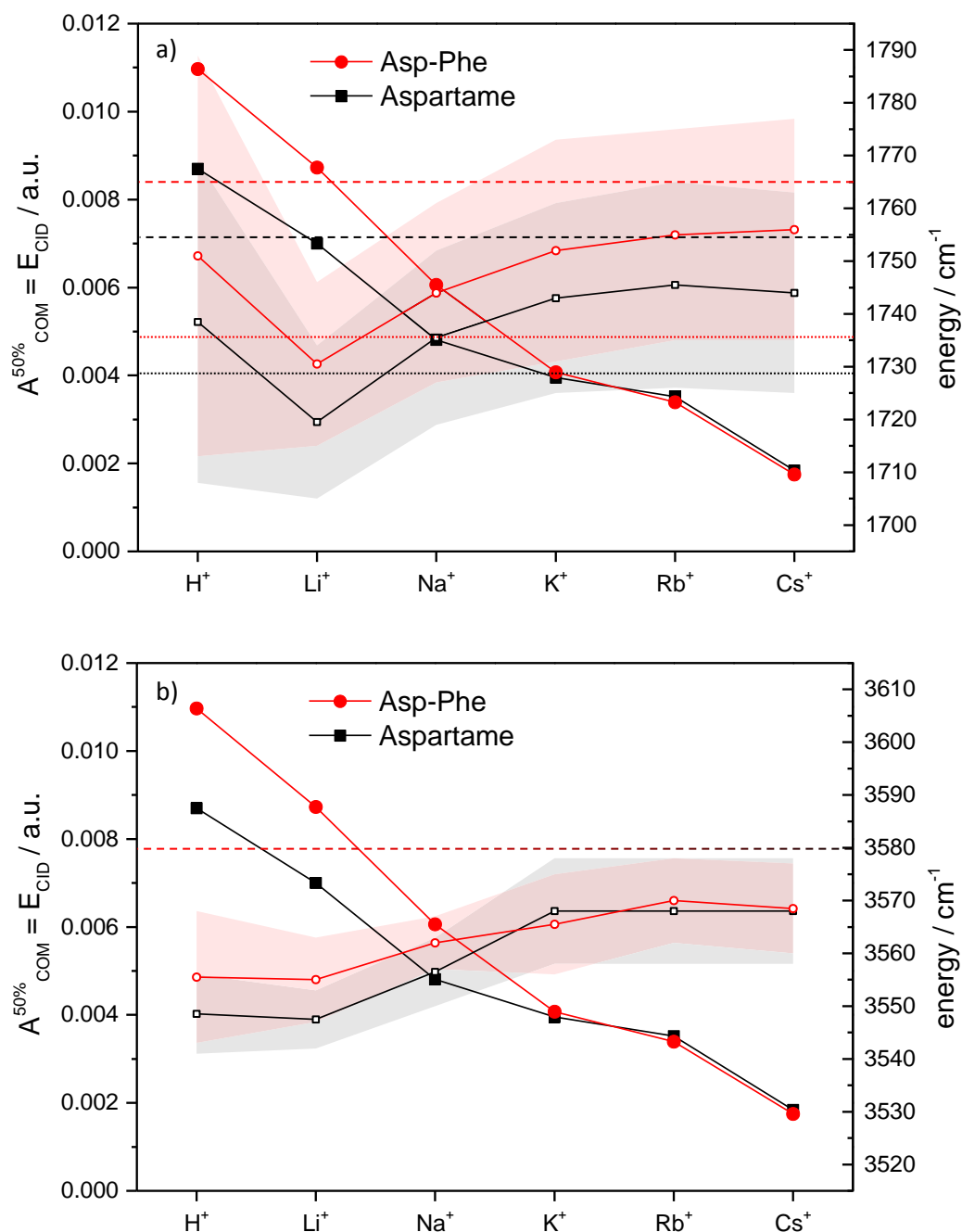
Fig. 17: *Threshold energies E_{CID} (left axis, solid symbols) and stretching vibration energies (right axis, open symbols) of cationized aspartame (black) and Asp-Phe (red). The shaded areas indicate the peak width at half maximum (fwhm); a) region of C=O stretching vibration; dashed lines indicate the average of C=O$_{Asp}$ and C=O$_{Phe}$ stretching vibrations, dotted lines the average of all C=O stretching vibrations, as calculated in neutral aspartame and Asp-Phe by cc-pVDZ/MP2 (scaled with 0.96); obviously the experimental contribution of the C=O stretching vibration of the peptide bond to the IR-MPD spectra is negligible; b) region of OH stretching vibration; dashed line indicates typical value of the OH stretching vibration in carboxyl groups.*

In Fig. 17 the centers of the stretching vibration peaks (right axis, open symbols) are plotted for all cationic aspartame species (black) and Asp-Phe species (red). The shaded areas indicate the peak width at half maximum (fwhm). For the protonated species in the region of the C=O stretching vibrations Asp-Phe has the higher center value: The C=O stretching of the COOH group of the Phe residue has a higher value than the C=O stretching of the COOMe group of aspartame. When adding Li^+ instead of a proton, the peak center shifts to the red, indicating a considerable weakening of the according C=O bonds, probably by binding of the alkali metal ion to the oxygen atom of these bonds. This red shift slowly disappears with increasing alkali metal ion size, leaving the difference between aspartame and Asp-Phe constant, indicating that the COOH / COOMe bond of the Phe residue is not involved in the bonding of the alkali metal ions. Comparing the average values of calculated $C=O_{Asp}$ and $C=O_{Phe}$ stretching vibrations (Fig. 17 a), dashed lines) or the average values of all calculated C=O stretching vibrations (Fig. 17 b), dotted lines), as calculated in neutral aspartame and Asp-Phe by cc-pVDZ/MP2 (scaled with 0.96), reveals that obviously the experimental contribution of the C=O stretching vibration of the peptide bond to the IR-MPD spectra is negligible. A comparison of the slope of the IR-MPD peak shifts with the E_{CID} values does not provide for further insights.

In the region of the OH stretching vibrations the center of the peaks for protonated Asp-Phe is higher than the one of aspartame, which originates from the additional free OH group. With decreasing alkali metal ion size these centers are red shifted, and for all alkalted complexes of alkali metal ions larger than Na^+ the difference between aspartame and Asp-Phe disappears (esp. for aspartame Cs^+ the IR-MPD is very weak, as the most abundant structure seems not to have any free OH stretching any more). Comparing these findings with the trend of E_{CID} gives an interesting finding: The difference in IR-MPD peak shifts between aspartame and Asp-Phe disappears when going from Na^+ to K^+ as observed on threshold energies in CID.

5.3.5. IR peak shift of deuterated species

We recorded IR-MPD spectra of deuterated species (species with one to species with all acidic H atoms exchanged for D) (see Fig. 18). As this H-/D-exchange can occur at several positions, we aimed to obtain information about the place of the first / second / third exchange by investigating the integral of the according peaks. In ideal behavior of uncoupled atoms a vibrational frequency ν is proportional to the square root of the ratio of force constant k and reduced mass m:

$$\nu \sim \sqrt{\frac{k}{m}}$$

For NH stretching vibrations this would mean a shift by a factor of 0.7303, and for the OH stretching vibration by a factor of 0.7276 when neglecting the rest of the molecule and assuming no changes within the force constant upon deuteration. Unfortunately only the fragmentation intensity within the OH region was high enough to make a useful analysis of the recorded IR-MPD peaks. According to the above calculation, a vibration with an experimentally observed frequency of 3550 cm^{-1} should redshift upon deuteration to 2583 cm^{-1}. The experimental value of 2620 cm^{-1} is higher by 37 cm^{-1}. Investigations of other groups have also found this kind of experimental blueshift of deuterated vibrations for ND stretches (uracil: 30 - 40 cm^{-1} [63] and keratin: approx. 45 cm^{-1} [64]) and for OD stretches (formic acid: approx. 30 cm^{-1} [65] and tropolone: 70 - 80 cm^{-1} [66]).
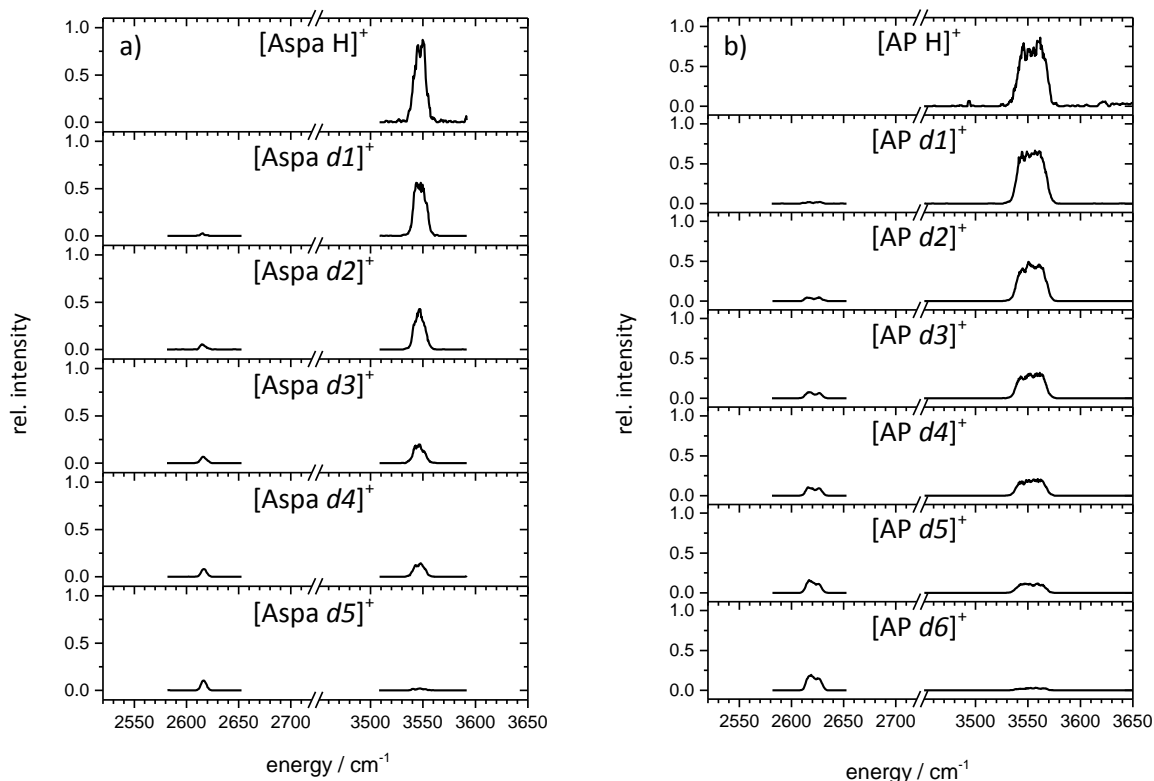
Fig. 18: *IR-MPD spectra of deuterated a) aspartame (Aspa) and b) Asp-Phe (AP). The intensity of the peaks around 3550 cm^{-1}, assigned to OH stretching vibrations decreases with an increasing number of deuterons, whilst the peak near 2620 cm^{-1} (OD stretching mode) increases.*
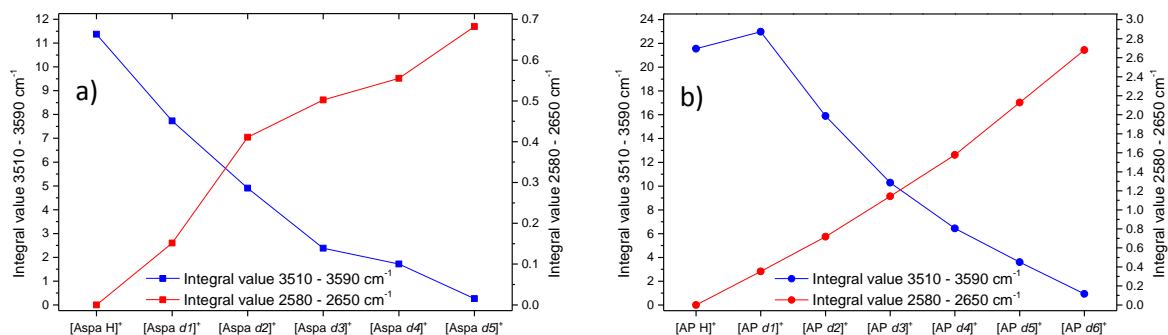
Fig. 19: *Integral values of the IR-MPD intensity of the OH stretching vibrations (left axis, blue) and OD stretching vibrations (right axis, red) of deuterated a) aspartame and b) Asp-Phe.*

The analysis of the integral values reveals an almost quantitative correspondence (see Fig. 19). The IR-MPD intensity of the peak between 3510 - 3590 cm^{-1} shows a nearly linear decay, while the peak region of 2580 - 2650 cm^{-1} reveals a nearly linear rising. There seem to be no preferred places for the single deuterations. All exchangeable positions are equally distributed.

5.3.6. The dependence on laser characteristics of a band shape

We investigated the dependence of the IR-MPD fragmentation efficiency on the band shape of the OH stretching band of protonated aspartame (see Fig. 20).
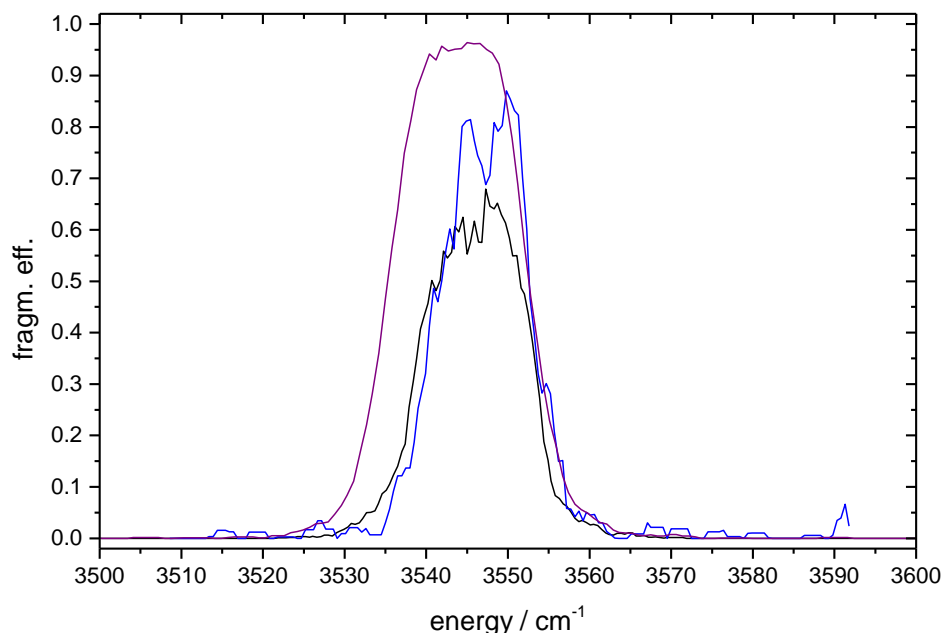
Fig. 20: *IR-MPD spectra of the OH stretching band of protonated aspartame, variation of the number of laser shots and of laser intensities: black: 2 laser shots, 28° OPA attenuator (50 % laser intensity); blue: 2 laser shots, 32° OPA attenuator (67 % laser intensity); purple: 4 laser shots, 32° OPA (67 % laser intensity). A higher laser intensity at the same number of laser shots increases the fragmentation signal, but does not influence the band shape, while more laser shots broaden the peak to the red.*

As mentioned in chapter 1.2.6. the laser intensity output of the OPO/OPA system can be varied by a variable attenuator whose opening can be tuned from 0° (0 % laser intensity) to 45° (100 % laser intensity). The black curve represents the fragmentation efficiency when two laser shots with an opening angle of 28° (50 % laser intensity) are applied before mass detection. The blue curve was recorded also with two laser shots, but with more laser intensity (an opening of 32° (67 % laser intensity)). The peak shape is similar, but the fragmentation efficiency is higher. For the purple curve the laser intensity was kept the same as for the blue one, but with applying four laser shots instead of two. This clearly broadens the peak to the red, indicating that the molecule has been heated up by the laser shots: Photons with little less energy than the original peak can then induce the fragmentation.

5.3.7. Correlation between measured and calculated IR spectra

A standard combination for calculating energy values and vibrational spectra of gas phase molecules is the use of the basis set cc-pVDZ (and for K^+, Rb^+ and Cs^+ a basis set with an effective core potential) and the DFT method with the functional B3LYP. This combination currently allows for geometry optimization and calculation of vibrational spectra of the complexes swiftly (e.g. within a few hours when combining eight processors in parallel).

The following figures show the structures and vibrational stick spectra of protonated and deprotonated aspartame and Asp-Phe and their complexes with Li^+ (smallest alkali metal ion) and Cs^+ (largest alkali metal atom investigated). All isomers with an energy difference relative to the lowest energy isomer of $\Delta E \leq 25$ kJ/mol are plotted.

For assignment of the most prominent peaks of the stick spectra to the normal modes and types of vibration (stretching, bending etc.) see chapter 5.13. (aspartame: suppl. B, Asp-Phe: suppl. D).
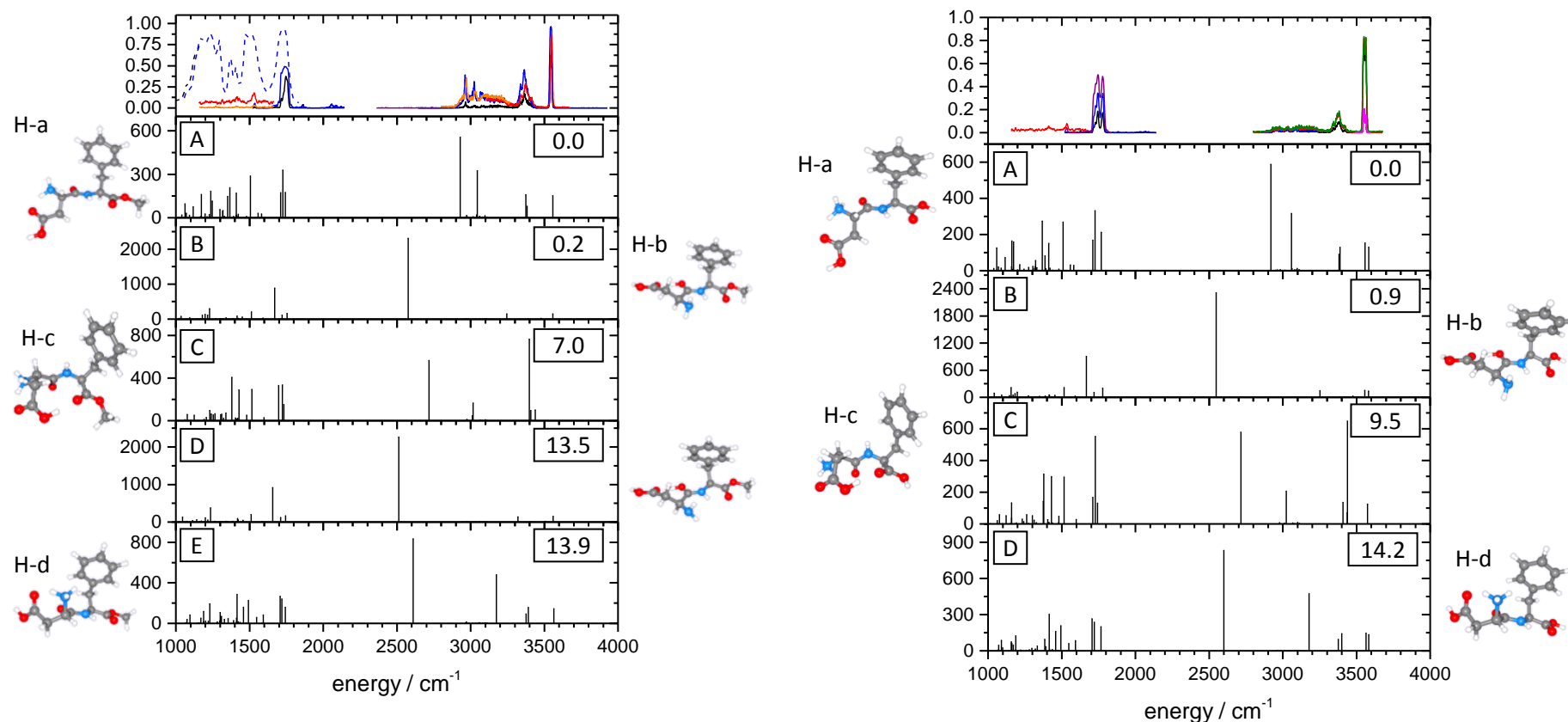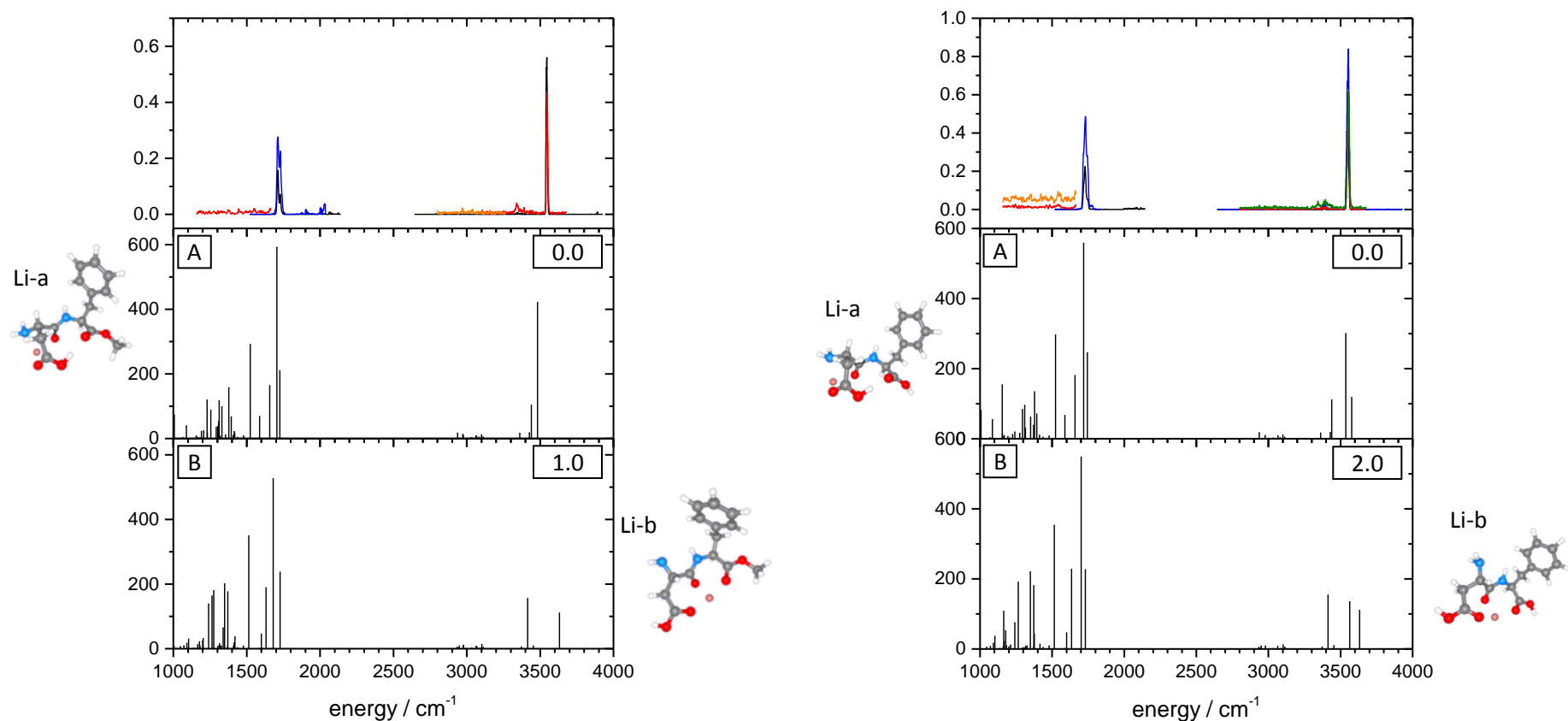
Fig. 21: a) Aspartame H⁺, b) Asp-Phe H⁺: cc-pVDZ; DFT: B3LYP:

Topmost frames: fragm. eff. of IR-MPD spectra; blue and black dashed lines: one color IR-MPD spectra (FEL CLIO, Paris); blue, black and purple solid lines: one color IR-MPD spectra (OPO/OPA, KL); magenta solid line: one color IR-MPD spectrum (narrow band OPO/OPA, KL); red, orange and green solid lines: two color IR-MPD spectra (OPO/OPA, KL): a) 1100 - 1700 cm⁻¹: red line probe at 3550 cm⁻¹, orange line probe at 3360 cm⁻¹; 2800 - 3700 cm⁻¹: red and orange lines probe at 3550 cm⁻¹, different laser intensities; b) 1100 - 1700 cm⁻¹: red line probe at 3550 cm⁻¹; 2800 - 3700 cm⁻¹: red line probe at 3565 cm⁻¹, green line probe at 3550 cm⁻¹; Lower frames: calculated IR intensities (km/mol) and structures of different isomers; values are ΔE / (kJ/mol); all identified isomers with up to ΔE ≤ 25 kJ/mol above the most stable conformer are considered; scaling factor 0.97.
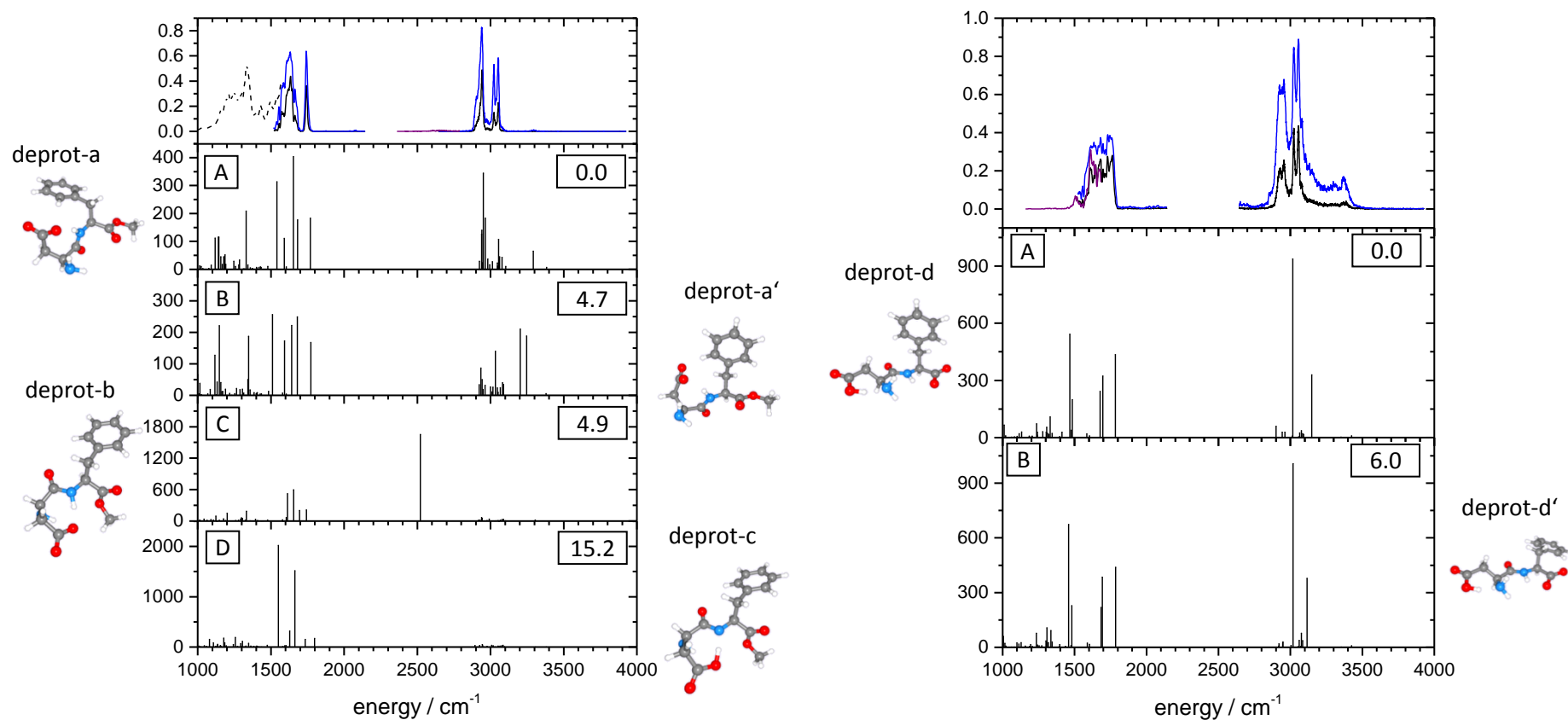
Fig. 22: a) Aspartame Li⁺, b) Asp-Phe Li⁺: cc-pVDZ; DFT: B3LYP:
Topmost frames: fragm. eff. of IR-MPD spectra; blue and black solid lines: one color IR-MPD spectra, different laser intensities (OPO/OPA, KL); red and orange solid lines: two color IR-MPD spectra (OPO/OPA, KL): a) 1100 - 1700 cm⁻¹: red line probe at 3545 cm⁻¹; 2800 - 3700 cm⁻¹: red and orange lines probe at 3545 cm⁻¹, different laser intensities; b) 1100 - 1700 cm⁻¹: red and orange lines probe at 3555 cm⁻¹, different laser intensities; 2800 - 3700 cm⁻¹: red line probe at 3565 cm⁻¹, green line probe at 3550 cm⁻¹;   Lower frames: calculated IR intensities (km/mol) and structures of different isomers; values are ΔE / (kJ/mol); all identified isomers with up to ΔE ≤ 25 kJ/mol above the most stable conformer are considered; scaling factor 0.97.

Fig. 23: a) Aspartame Cs$^+$, b) Asp-Phe Cs$^+$: cc-pVDZ (C, H, N, O), Stuttgart RSC 1997 (Cs); DFT: B3LYP:

Topmost frames: fragm. eff. of IR-MPD spectra; blue and black solid lines: one color IR-MPD spectra, different laser intensities (OPO/OPA, KL); red, orange and green solid lines: two color IR-MPD spectra (OPO/OPA, KL): 1100 - 1700 cm^{-1}: red line probe at 3565 cm^{-1}; 2800 - 3700 cm^{-1}: red and orange lines probe at 3565 cm^{-1}, different laser intensities; green line probe at 3550 cm^{-1};

Lower frames: calculated IR intensities (km/mol) and structures of different isomers; values are ΔE / (kJ/mol); all identified isomers with up to ΔE ≤ 25 kJ/mol above the most stable conformer are considered; scaling factor 0.97.

Fig. 24: Deprotonated a) Aspartame, b) Asp-Phe: cc-pVDZ; DFT: B3LYP:

Topmost frames: fragm. eff. of IR-MPD spectra; black dashed line: one color IR-MPD spectrum (FEL CLIO, Paris); blue, black and purple solid lines: one color IR-MPD spectra (blue and black at different laser intensities) (OPO/OPA, KL);

Lower frames: calculated IR intensities (km/mol) and structures of different isomers; values are ΔE / (kJ/mol); all identified isomers with up to ΔE ≤ 25 kJ/mol above the most stable conformer are considered; scaling factor 0.97.

For protonated aspartame five different structure motifs with an energy difference up to 25 kJ/mol could be identified (Fig. 21 a)). The calculated spectrum of the lowest conformer shows good agreement to the measured spectra. The band structure between 1700 and 1750 cm^{-1} originates from the three different C=O stretching vibrations (peptide C=O, C=O of $COOH_{Asp}$ and C=O of $COOMe_{Phe}$). The calculated peaks at 2930 cm^{-1} and 3050 cm^{-1} are NH stretching vibrations of the NH_3 group of the Asp part directing to the oxygen atoms forming a 6-member and a 5-member ring. The two peaks shortly below 3400 cm^{-1} are free NH stretches of the NH involved in the peptide bond and of the free NH of the NH_3 group and the peak at 3560 cm^{-1} describes the OH stretching mode of the COOH group of the Asp part. The same features appear in protonated Asp-Phe (Fig. 21 b)): three C=O stretching vibrations (peptide C=O, C=O of $COOH_{Asp}$ and C=O of $COOH_{Phe}$) and the same NH and OH stretching pattern, with an additional OH stretching vibration at 3580 cm^{-1} from the additional COOH group in the Phe part.

It is not straight forward to assign the measured IR-MPD spectrum of the aspartame Li$^+$ complex (Fig. 22 a)). For both possible structures the peak lowest in energy in the region of the C=O stretching vibration (three peaks below 1800 cm^{-1}) is assigned to the C=O of the peptide bond. The other two modes are coupled. Neither of both structures can describe the position of the OH stretching band well. Structure A is lowest and predicts the strongest vibrations correctly, it looks better than B. This is supported by the findings of Asp-Phe Li$^+$ (Fig. 22 b)). Here the corresponding structure type can describe the OH stretching vibration very well. The three NH stretching peaks between 3350 and 3450 cm^{-1} have little IR activity in both species.

The assignment of the IR spectra of the aspartame Cs$^+$ complex is hardly possible. The only feature visible in the IR spectrum is the broad, unresolved band of the C=O stretching vibrations (Fig. 23 a)). One can only exclude those structures which possess a free OH binding motif. The similar argumentation holds for Asp-Phe (Fig. 23 b)). Here all structures can be excluded who have more than the one OH bond of the COOH group of the Phe part.

In deprotonated aspartame (Fig. 24 a)) the outstanding peak at 1750 cm^{-1} is described well by the two low energy isomers. The second highest isomer also possesses a double peak feature originating from the two free NH binding motifs of the peptide bond and of the NH_2 group. According to the calculations they should appear between 3200 and 3300 cm^{-1}. In the case of deprotonated Asp-Phe, none of the two calculated spectra does obtain a double peak. In the experimental spectrum not only one, but two double peak features can be identified. The two calculated spectra have a similar shape, but slightly different positions of their highest peaks around 3000 and above 3100 cm^{-1}.This and the

fact of the very broad, seemingly unstructured, absorption in the experimental spectrum between 1500 and 1800 cm^{-1} indicates a conceivable mixture of two conformers coexisting.

We varied both the basis sets and the calculation methods systematically to see, if the combination of the basis set cc-pVDZ with the calculation method DFT: B3LYP really is sufficient for the description of the aspartame / Asp-Phe systems. Especially the influence of the dispersion interactions of the π-system of the phenyl ring in the Phe part should be figured out. The variations can be divided into four different groups: First the variation of different basis sets with the computational method of MP2 (Hartree Fock based method, including dispersion interaction), second different basis sets at DFT level of theory with the B97D functional implemented in the programme package Gaussian09 (also considering dispersion interactions), third different basis sets at DFT level with the B3LYP functional and fourth variation of DFT functionals with the basis set cc-pVDZ.

A complete list of all basis set / calculation method combinations for aspartame is given in Table 4 and for Asp-Phe in Table 5.

When considering all structure motifs whose relative energy is not larger than 25 kJ/mol (compared to the isomer with lowest energy), it turns out that there are four most prominent structures for protonated Aspartame and Asp-Phe (H-a though H-d in Table 6) and four structure types of their complexes with alkali metal ions (M-a though M-d in Table 6). For the deprotonated aspartame also four different structure motifs could be identified. In deprotonated Asp-Phe these four deprotonated structure motifs are higher than 30kJ/mol compared to two other structure motifs originating from deprotonation of the additional COOH group of the Phe part. The relative energy values of most prominent structure types for all basis set - calculation method combinations are drawn in Fig. 25 (protonated), Fig. 26 (with alkali metal ions) and Fig. 27 (deprotonated). Not only the energetic values, but also characteristic bond lengths (left axis, solid symbols) and angles (right axis, open symbols) of these most prominent structure types are compared (Fig. 28 to Fig. 36).

5. Aspartame (Asp-PheOMe) and Asp-Phe: Structural investigations on their isolated protonated, deprotonated and alkali metal ion attached species

Table 4*: Combinations of basis sets and calculation methods applied to aspartame (all structures and vibrational stick spectra see supplement part B)*

Molecule	Basis Set	Calculation Method
Aspartame H$^+$	TZVP [67]	MP2 (gaussian 03)
	cc-pVDZ [68]	MP2 (gaussian 03)
	TZVP	DFT: B97D (gaussian 09) [69]
	cc-pVTZ [68]	DFT: B97D (gaussian 09)
	aug-cc-pVDZ [68]	DFT: B97D (gaussian 09)
	cc-pVDZ	DFT: B97D (gaussian 09)
	TZVP	DFT: B3LYP (gaussian 03) [70-72]
	cc-pVQZ [68]	DFT: B3LYP (gaussian 03)
	aug-cc-pVTZ [68]	DFT: B3LYP (gaussian 03)
	cc-pVTZ	DFT: B3LYP (gaussian 03)
	aug-cc-pVDZ	DFT: B3LYP (gaussian 03)
	cc-pVDZ	DFT: B3LYP (gaussian 03)
	cc-pVDZ	DFT: BLYP (gaussian 03) [71-73]
	cc-pVDZ	DFT: BP86 (gaussian 03) [74]
	cc-pVDZ	DFT: PBE0 (gaussian 03) [75]
	cc-pVDZ	DFT: Becke97_1 (gaussian 03) [76]
	cc-pVDZ	DFT: Becke97_2 (gaussian 03) [77]
Aspartame Li$^+$	cc-pVDZ	MP2 (gaussian 03)
	cc-pVDZ	DFT: B97D (gaussian 09)
	cc-pVDZ	DFT: B3LYP (gaussian 03)
Aspartame Na$^+$	cc-pVDZ	MP2 (gaussian 03)
	cc-pVDZ	DFT: B97D (gaussian 09)
	cc-pVDZ	DFT: B3LYP (gaussian 03)
Aspartame K$^+$	cc-pVDZ / Stuttgart RSC 1997 [78-81]	MP2 (gaussian 03)
	cc-pVDZ / Stuttgart RSC 1997	DFT: B97D (gaussian 09)
	cc-pVDZ / Stuttgart RSC 1997	DFT: B3LYP (gaussian 03)
Aspartame Rb$^+$	cc-pVDZ / Stuttgart RSC 1997	MP2 (gaussian 03)
	cc-pVDZ / Stuttgart RSC 1997	DFT: B97D (gaussian 09)
	cc-pVDZ / Stuttgart RSC 1997	DFT: B3LYP (gaussian 03)
	cc-pVDZ / Stuttgart RSC 1997	DFT: Becke97_1 (gaussian 03)
	cc-pVDZ / Stuttgart RSC 1997	DFT: Becke97_2 (gaussian 03)
Aspartame Cs$^+$	cc-pVDZ / Stuttgart RSC 1997	MP2 (gaussian 03)
	cc-pVDZ / Stuttgart RSC 1997	DFT: B97D (gaussian 09)
	cc-pVDZ / Stuttgart RSC 1997	DFT: B3LYP (gaussian 03)
Aspartame deprot.	TZVP	MP2 (gaussian 03)
	cc-pVDZ	MP2 (gaussian 03)
	TZVP	DFT: B97D (gaussian 09)
	cc-pVDZ	DFT: B97D (gaussian 09)
	TZVP	DFT: B3LYP (gaussian 03)
	aug-cc-pVDZ	DFT: B3LYP (gaussian 03)
	cc-pVDZ	DFT: B3LYP (gaussian 03)

Table 5: *Combinations of basis sets and calculation methods applied to Asp-Phe (all structures and vibrational stick spectra see supplement part D)*

molecule	basis set	calculation Method
Asp-Phe H$^+$	TZVP	MP2 (gaussian 03)
	cc-pVDZ	MP2 (gaussian 03)
	TZVP	DFT: B3LYP (gaussian 03)
	cc-pVDZ	DFT: B3LYP (gaussian 03)
Asp-Phe Li$^+$	cc-pVDZ	MP2 (gaussian 03)
	cc-pVDZ	DFT: B3LYP (gaussian 03)
Asp-Phe Na$^+$	cc-pVDZ	MP2 (gaussian 03)
	cc-pVDZ	DFT: B3LYP (gaussian 03)
Asp-Phe K$^+$	cc-pVDZ / Stuttgart RSC 1997	MP2 (gaussian 03)
	cc-pVDZ / Stuttgart RSC 1997	DFT: B3LYP (gaussian 03)
Asp-Phe Rb$^+$	cc-pVDZ / Stuttgart RSC 1997	MP2 (gaussian 03)
	cc-pVDZ / Stuttgart RSC 1997	DFT: B3LYP (gaussian 03)
Asp-Phe Cs$^+$	cc-pVDZ / Stuttgart RSC 1997	MP2 (gaussian 03)
	cc-pVDZ / Stuttgart RSC 1997	DFT: B3LYP (gaussian 03)
Asp-Phe deprot.	TZVP	MP2 (gaussian 03)
	cc-pVDZ	MP2 (gaussian 03)
	TZVP	DFT: B3LYP (gaussian 03)
	aug-cc-pVDZ	DFT: B3LYP (gaussian 03)
	cc-pVDZ	DFT: B3LYP (gaussian 03)

Scaling factors according to the homepage of National Institute of Standards and Technology (NIST): Computational Chemistry Comparison and Benchmark DataBase: cccbdb.nist.gov/vibscalejust.asp

Table 6: *Most prominent structure types and their characteristics*

| structure type	description	bond lengths and angles
H-a	Protonation of aspartame and Asp-Phe at the NH_2 group of the Asp part. The molecule is bent forming a 6-member ring containing an O···H-N binding motif (C=O of the $COOH_{Asp}$ group and one N-H of the NH_2 group) and a 5-member ring also containing an O···H-N binding motif (C=O of the peptide bond and another N-H of the NH_2 group).	Fig. 28
H-b	Protonation of aspartame and Asp-Phe at the C=O peptide bond. The molecule is bent forming a 7-member ring containing an O···H-O binding motif (C=O of the $COOH_{Asp}$ group and C=O of the peptide bond).	Fig. 29
H-c	Protonation of aspartame and Asp-Phe at the NH_2 group of the Asp part. The molecule is bent forming a 6-member ring containing an O···H-N binding motif (C=O of the $COOH_{Asp}$ group and one N-H of the NH_2 group), a 5-member ring also containing an O···H-N binding motif (C=O of the peptide bond and another N-H of the NH_2 group) and a 10-member ring containing an O···H-O binding motif (OH of the $COOH_{Asp}$ group and C=O of the $COOMe/COOH_{Phe}$ group).	Fig. 30
H-d	Protonation of aspartame and Asp-Phe at the NH_2 group of the Asp part. The molecule is bent forming a 6-member ring containing an O···H-N binding motif (C=O of the $COOH_{Asp}$ group and one N-H of the NH_2 group) and pointing with another N-H bond of the NH_2 group into the direction of the phenyl ring.	Fig. 31
M-a	The metal atom is chelated by the nitrogen atom of the NH_2 group of the Asp part and the two oxygen atoms of the C=O bond of the peptide bond and the one of the C=O bond of the $COOH_{Asp}$ group. The molecule is bent forming a 10-member ring containing an O-H···O binding motif (OH of the $COOH_{Asp}$ group and C=O of the $COOMe/COOH_{Phe}$ group).	Fig. 32
M-b	The metal atom is chelated by the three oxygen atoms of the C=O bond of the $COOH_{Asp}$ group, the one of the C=O bond of the peptide bond and the one of the C=O bond of the $COOH_{Asp}$ group.	Fig. 33
M-c	The metal atom is chelated by the three oxygen atoms of the OH bond of the $COOH_{Asp}$ group, the one of the C=O bond of the $COOH_{Asp}$ group and the one of the C=O bond of the peptide bond. The molecule is bent forming a 6-member ring containing an O-H···N binding motif (C=O of the $COOH_{Asp}$ group and the nitrogen atom of the NH_2 group).	Fig. 34
M-d	The metal atom is chelated by the two oxygen atoms of the OH bond of the $COOH_{Asp}$ group and the one of the C=O bond of the $COOH_{Asp}$ group. The molecule is bent forming a 7-member ring containing an O-H···O binding motif (OH of the $COOH_{Asp}$ group and C=O of the peptide bond).	Fig. 35
dep-a	Deprotonation of aspartame at the $COOH_{Asp}$ group of the Asp part. The molecule is bent forming a 7-member ring containing an O···H-N binding motif (one C=O of the COO_{Asp} group and the N-H bond of the NH group of the peptide bond).	Fig. 36 a
dep-d	Protonation of Asp-Phe at the $COOH_{Phe}$ group of the Phe part. The molecule is bent forming a 6-member ring containing an O-H···N binding motif (OH of the $COOH_{Asp}$ group and nitrogen atom of the NH_2 group) and a 5-member ring containing an O···H-N binding motif (one C=O of the COO_{PHe} group pf the Phe part and the N-H bond of the NH group of the peptide bond).	Fig. 36 b
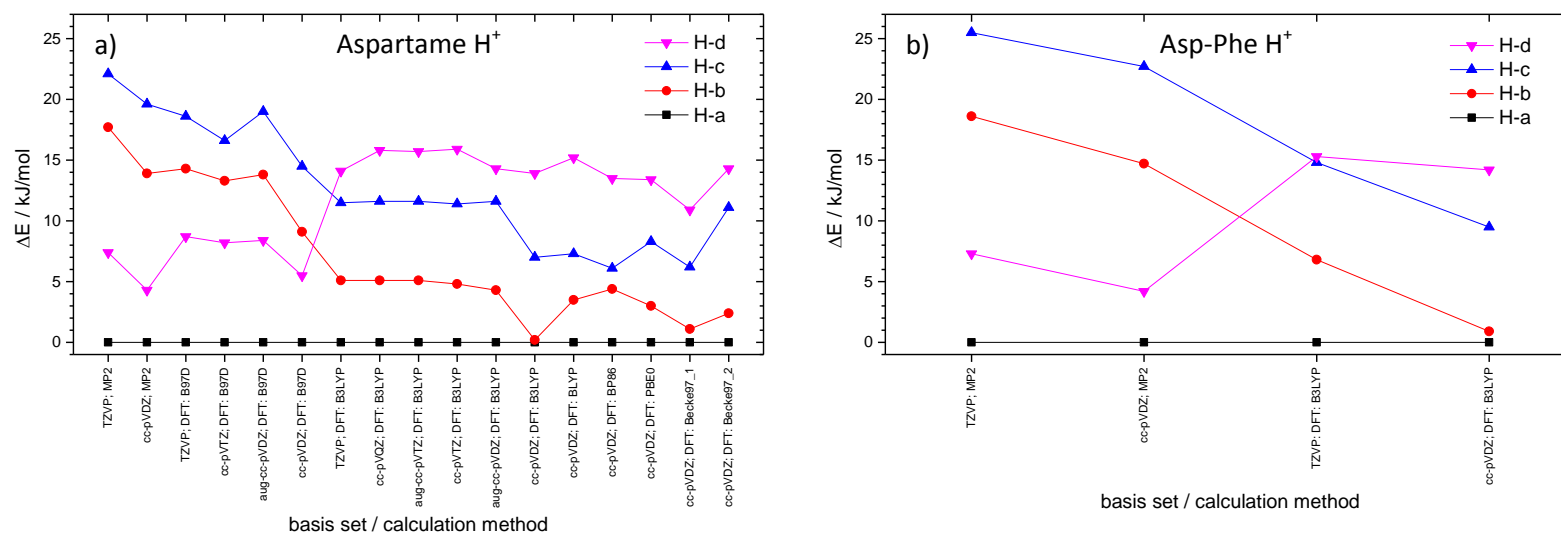
Fig. 25: *Relative total energies of the four most abundant structure types of protonated species: structure type H-a is always lowest in energy.*
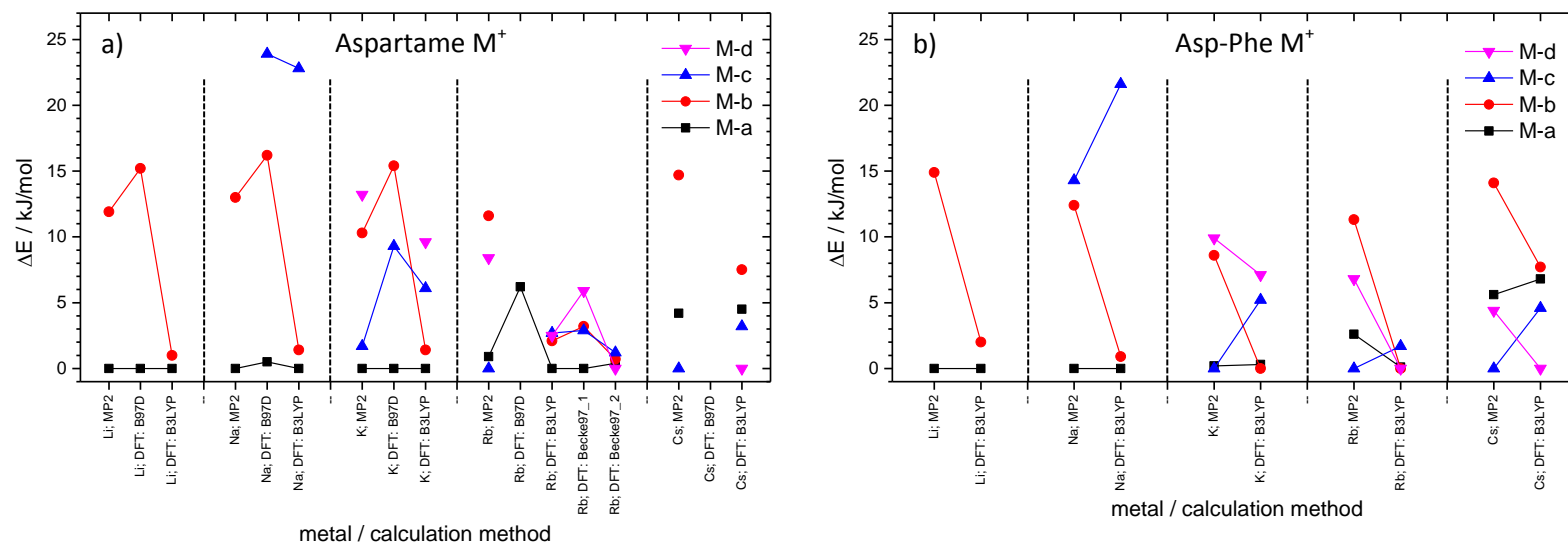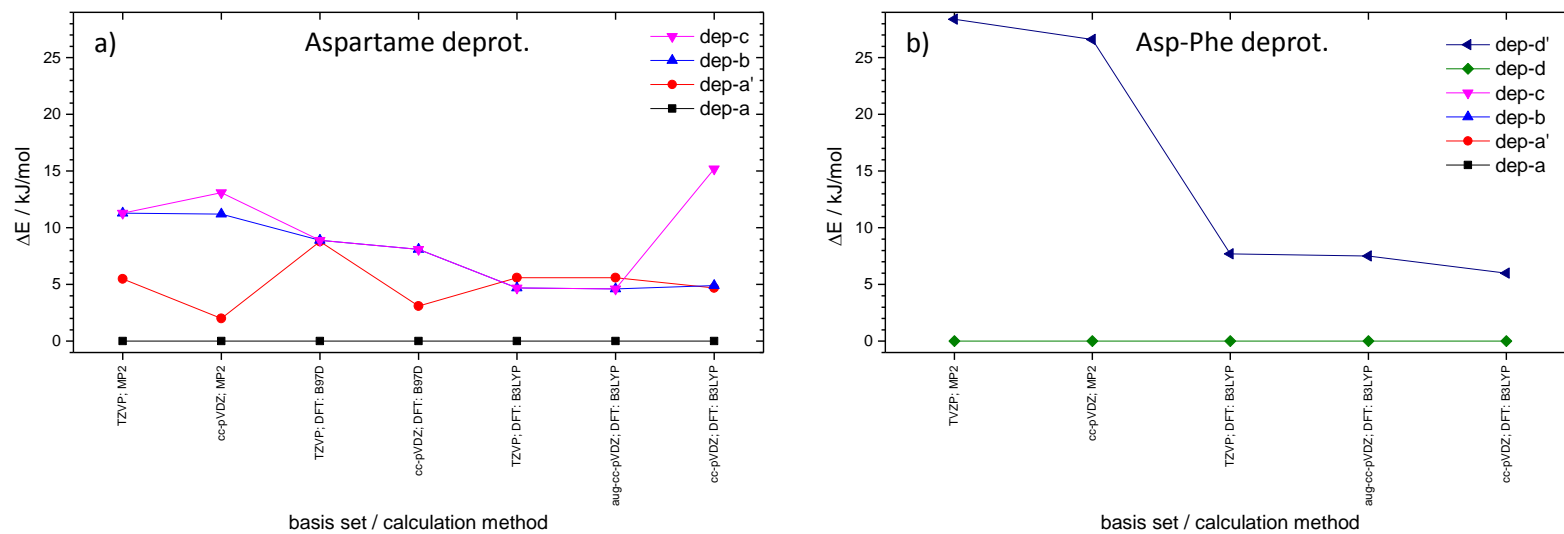

Fig. 26: *Relative total energies of the four most abundant structure types of species with alkali metal ions: structure type lowest in energy varies.*

Fig. 27: *Relative total energies of the most abundant structure types of deprotonated species: structure type dep-a is lowest in energy for aspartame and structure type dep-d for Asp-Phe (dep-d: dehydrogenation at the additional COOH group of the Phe part).*
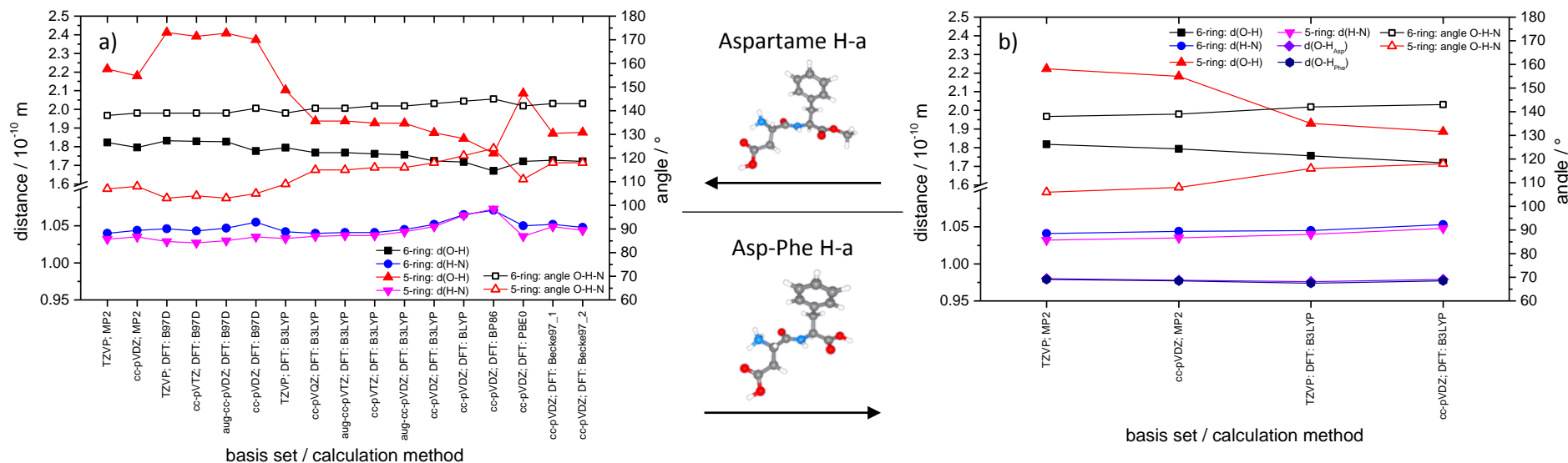
Fig. 28: *Characteristic bond lengths and angles of structure type H-a: Differences in the 5-ring O-H-N binding motif when changing calculation method.*
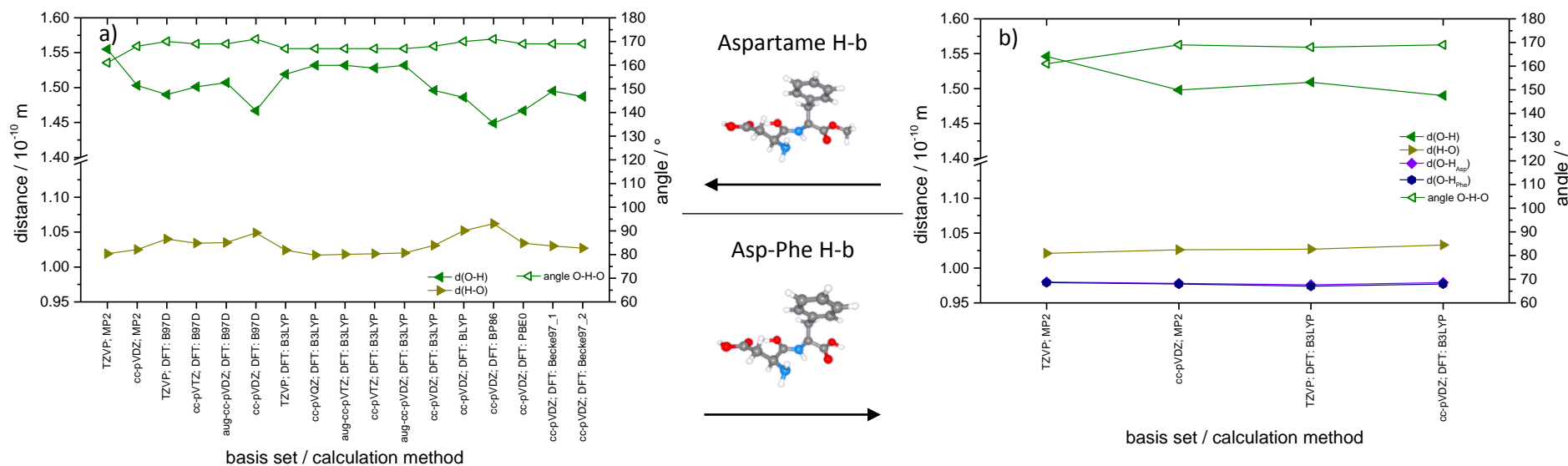
Fig. 29: *Characteristic bond lengths and angles of structure type H-b: Differences in length of the O-H-O binding motif when changing calculation method.*
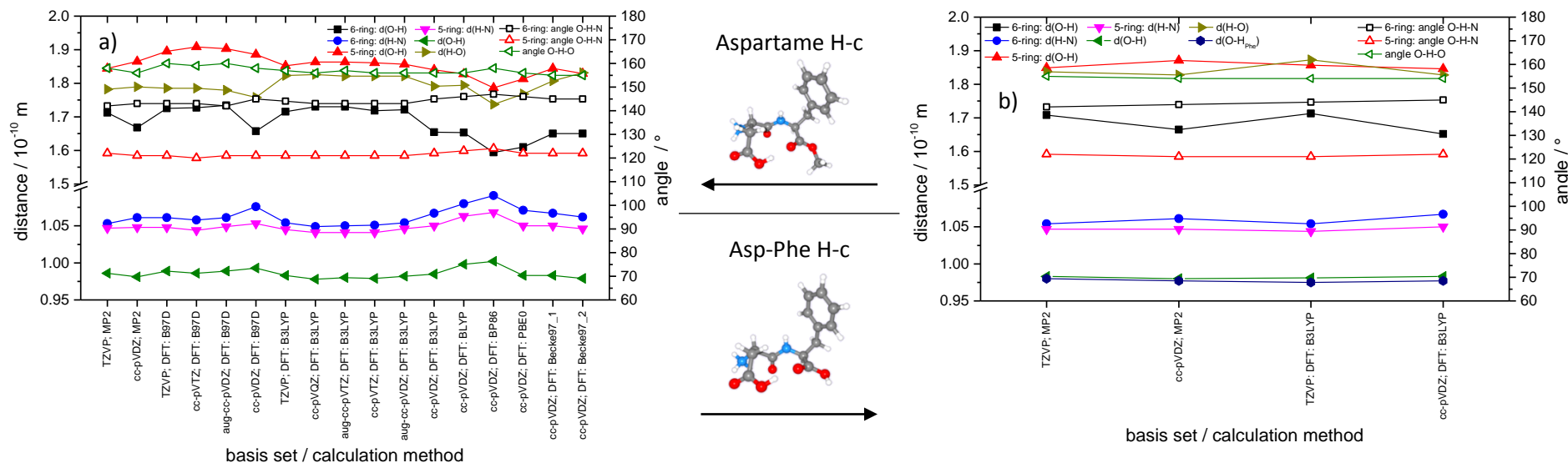
Fig. 30: *Characteristic bond lengths and angles of structure type H-c: Differences in length of the O-H-O binding motif when changing calculation method.*
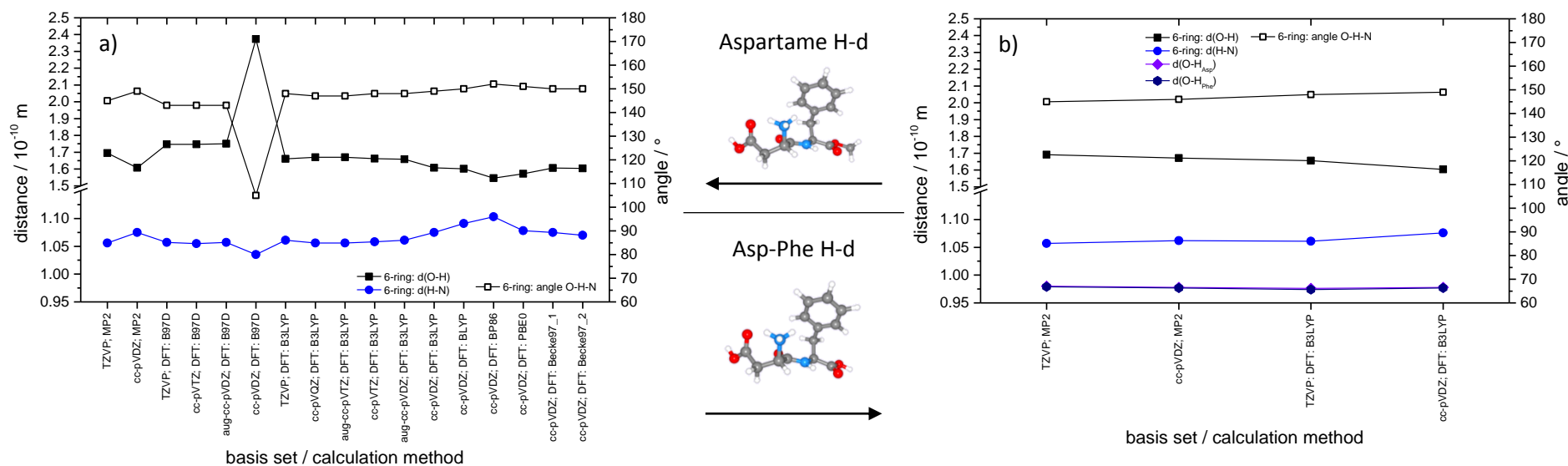
Fig. 31: *Characteristic bond lengths and angles of structure type H-d: No remarkable differences.*
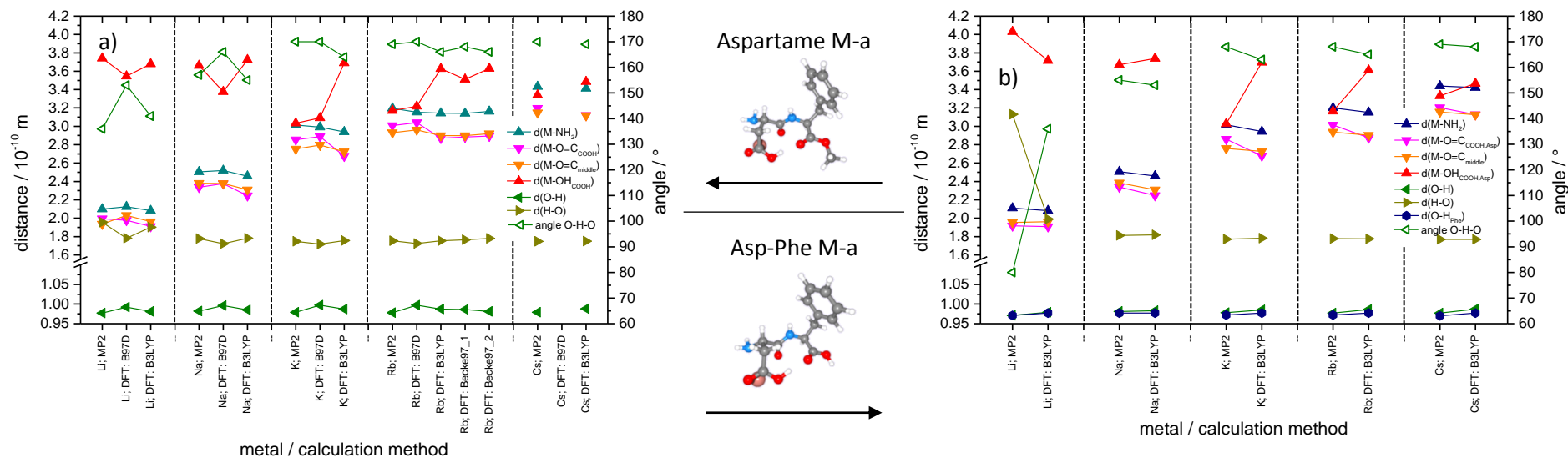
Fig. 32: *Characteristic bond lengths and angles of structure type M-a: Increasing O-H-O angle and changes in metal-atom distances with increasing metal.*
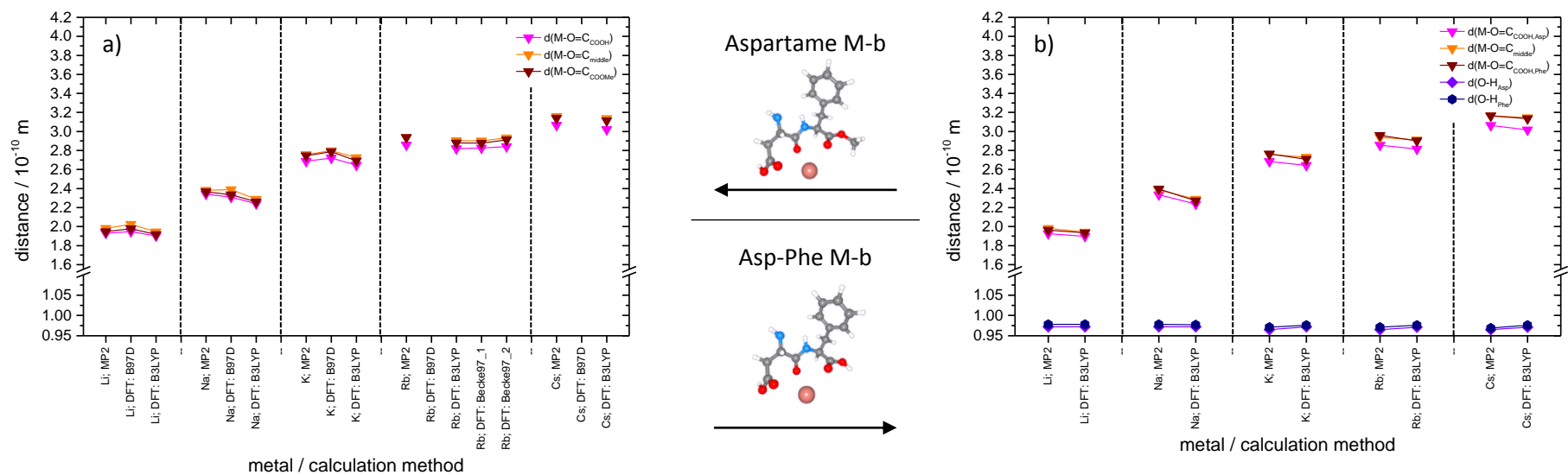
Fig. 33: *Characteristic bond lengths and angles of structure type M-b: Increasing metal-atom distances with increasing metal ion size.*
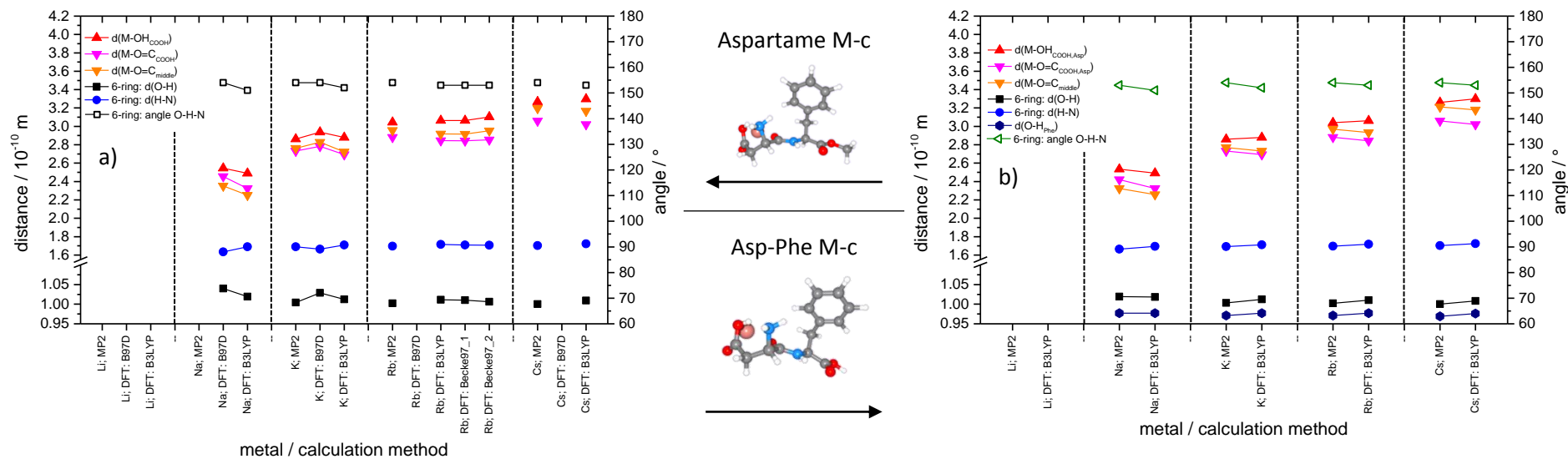
Fig. 34: *Characteristic bond lengths and angles of structure type M-c: Increasing metal-atom distances with increasing metal ion size.*
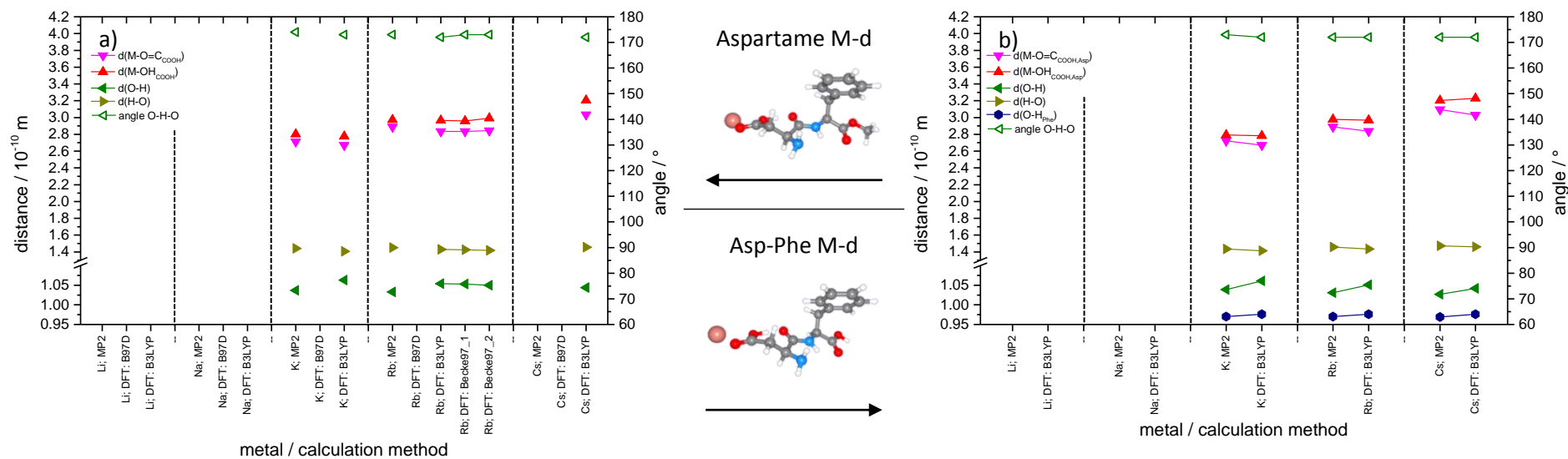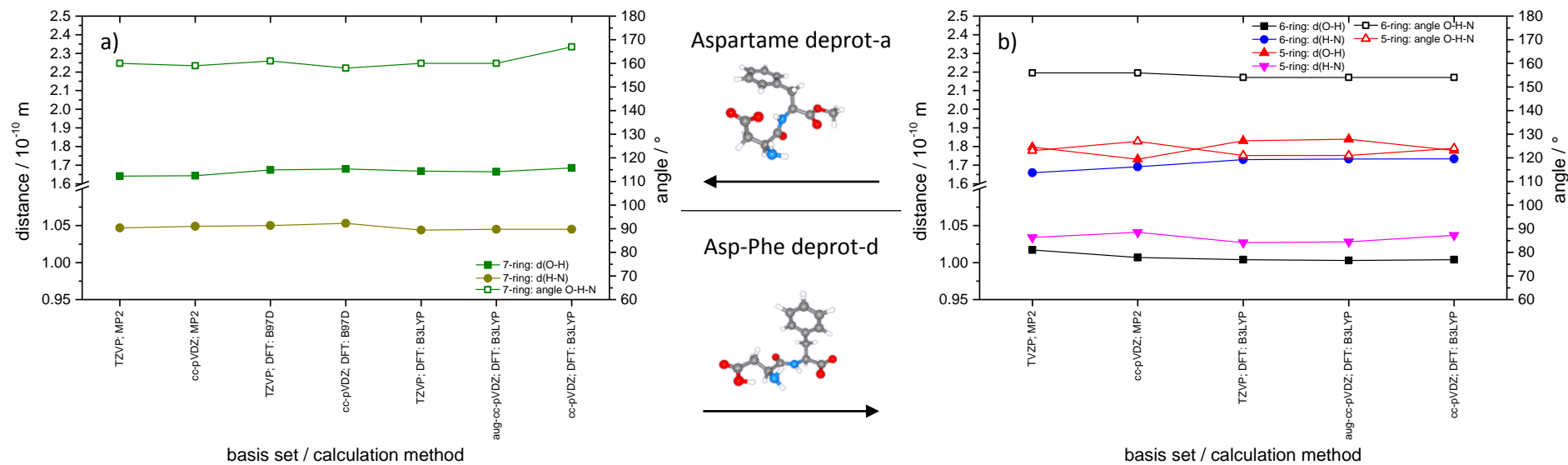

Fig. 35: *Characteristic bond lengths and angles of structure type M-d: Increasing metal-atom distances with increasing metal ion size.*

Fig. 36: *Characteristic bond lengths and angles of structure types a) Aspartame deprot-a, b) Asp-Phe deprot-d: No remarkable differences when changing basis set or calculation method.*

For both protonated aspartame and protonated Asp-Phe the energetic minimum structure is structure type H-a, independently of the basis set - calculation method combination (see Fig. 25). The relative energies by all calculations (without dispersion interactions) lead to the energetic order H-a < H-b < H-c < H-d. Methods which contain dispersion interaction (MP2 and DFT: B97D) lower the relative energy of structure H-d and extend the energy differences between structure type H-a and H-b / H-c such that the relative energies become H-a < H-d < H-b < H-c. Variation of basis sets only does not give a remarkable effect. Relative energetic values are similar for aspartame and Asp-Phe.

Aspartame and Asp-Phe with alkali metal atoms attached (see Fig. 26) do prefer structure type M-a for small ions (Li$^+$ and Na$^+$). The relative energy of other structure types decreases with increasing metal ion size, until for Cs$^+$ the type M-d is the energetically lowest one (for the DFT: B3LYP calculation method; MP2 calculates M-c to have even a bit lower energy). Relative energetic values are similar for aspartame and Asp-Phe.

The calculated structure pattern dep-a of deprotonated aspartame is the global minimum, independent of the basis set - calculation method combination (see Fig. 27 a)). Twisted benzyl residue of the Phe part (structure dep-a') and two other structure types (dep-b and dep-c) are slightly higher in energy ($\Delta E \leq 15$ kJ/mol). For deprotonated Asp-Phe the structure type dep-d is the energetic minimum structure and the twisting of the benzyl residue of the Phe part (dep-d') is second lowest in energy (see Fig. 27 b)). MP2 calculates an energy difference of approx. 30 kJ/mol between dep-d and dep-d', while DFT: B3LYP calculations remain a difference smaller than 10 kJ/mol. The structure types dep-a, dep-a', dep-b and dep-c as found in deprotonated aspartame are all more than 30 kJ/mol higher in energy in deprotonated Asp-Phe.

Structure type H-a (see Fig. 28) with its O···H-N binding motifs has a long O-H and a short N-H bond length in both the 6-member ring (angle 140 - 150 °) and the 5-member ring (angle 100 - 120°). The O-H distance and the O···H-N angle of the 5-member ring is influenced by the choice of the calculation method. The methods with dispersion interaction calculate longer O···H distances and smaller O···H-N angles than methods without. The other bond lengths or angles do not show a remarkable effect on the variation of basis set or calculation method. The 7-member ring of structure type H-b (see Fig. 29) with the O···H-O binding motif is described as hydrogen bond (angle approx. 170°), where calculations assign the hydrogen atom to the oxygen atom of the C=O bond of the peptide bond. Structure type H-c (see Fig. 30) contains two O···H-N binding motifs with long O-H and short N-H bond lengths in both a 6-member (angle 140 - 150 °) and a 5-member ring (approx. 120°) and an O-H···O binding motif. In contrast to structure type H-b it is not a linear, short hydrogen bond.

Instead, its angle (< 160°) and longer H···O distance are evidence for some strain. The findings are independent of basis set or calculation method. The bond lengths and angles of the O···H-N binding motif in the 6-member ring of structure type H-d (see Fig. 31) with a short N-H bond and a long O···H distance do not show any remarkable dependence on basis set or calculation method variation. None of the protonated structure types does show significant differences between aspartame and Asp-Phe.

In all alkalated complexes the distances between alkali metal atoms and their chelating atoms increase with increasing size of the metal atom. The distances are similar independent of the basis sets or calculation methods. Structure type M-a (see Fig. 32) contains a hydrogen bond. The O-H and H···O distances are independent of the alkali metal atom size, but the angle changes from lower than 150° for complexes with Li^+ to a nearly linear hydrogen bond with an angle of approx. 170° in the complexes with Cs^+. The O-H···N motif in structure type M-c (see Fig. 34) assigns the hydrogen atom not to the nitrogen (as in the similar protonated structure type H-d) but to the oxygen atom. This can be explained by the fact that the oxygen atom is also involved in the binding of the metal (polarization effect of the metal ion). An equivalent finding of the influence of the metal holds true for structure type M-d (see Fig. 35). The binding motif O-H···O (similar to structure type H-b) with an angle of larger than 170° assigns the hydrogen atom to the oxygen atom which is contributing to the metal binding. None of the structure types with alkali metal ions attached does show significant differences between aspartame and Asp-Phe.

There are two favorable structure types of deprotonated aspartame and Asp-Phe. No significant influence on characteristic bond lengths or angles on the basis set or calculation method is found.

We conclude as follows on the influence of the basis set or calculation method on the relative energy values or the bond lengths and angles of characteristic hydrogen atom containing bonds: For protonated species differences in energetic values occur when using calculation methods containing dispersion interaction. None of their vibrational spectra matches the experimentally obtained (see chapter 5.13., suppl. material, Fig. S B1 to Fig. S B6). Therefore, the use of these methods can be considered unsuitable. The use of larger basis sets does neither provide large differences in relative energy values nor in characteristic bond lengths or angles. We therefore conclude that the use of the cc-pVDZ basis set in combination with the DFT: B3LYP functional is appropriate for the investigations on aspartame and Asp-Phe. In particular, double zeta quality basis sets seem to suffice. The use of triple zeta does not seem mandatory.

5.3.8. Correlation between calculated energies and E_{CID} values

The CID investigations have revealed information on the relative stability of cationized aspartame and Asp-Phe complexes (see chapter 5.4.). We calculated dissociation energies to verify a conceivable correlation between calculated fragmentation energies and experimental E_{CID} values.
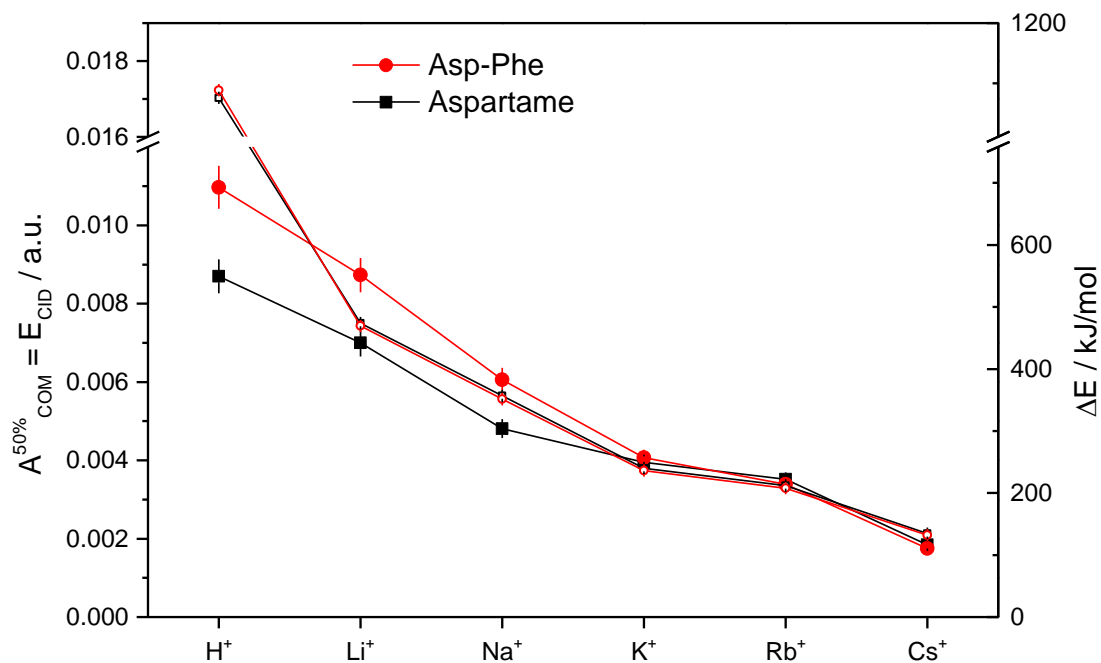

Fig. 37: *E_{CID} values (left axis, solid symbols) and calculated dissociation energies (right axis, open symbols) for cationized aspartame (black) and Asp-Phe (red). Energy value calculated as sum of energy of alkali metal ion plus single point calculation of lowest energy structure type after removal of the ion (no relaxation, vertical ion detachment).*
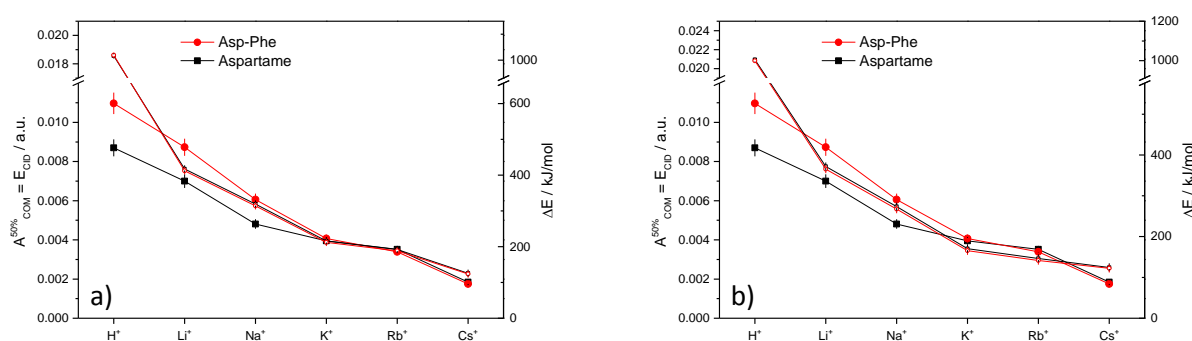

Fig. 38: *E_{CID} values (left axis, solid symbols) and alternatively calculated dissociation energies (right axis, open symbols) for cationized aspartame (black) and Asp-Phe (red). a) Energy value calculated as sum of energy of alkali metal ion plus geometry optimized calculation of lowest energy structure type after removal of the ion (local relaxation, adiabatic ion detachment). b) Energy value calculated as sum of energy of alkali metal ion plus globally geometry optimized calculation of neutral aspartame / Asp-Phe with lowest energy (global relaxation). Note: locally relaxed structures in a) are different from globally relaxed structures in b).*

The fragmentation energy was calculated as the energy difference between the energy of the minimum structure of the according aspartame / Asp-Phe - cation complex and the sum of the energies of the cation plus the energy of the neutral molecule.

This energy of the neutral molecule was calculated in three different ways:

1) No relaxation, vertical ion detachment: Energy obtained from single point calculation of the remaining neutral molecule residue after removal of the cation from the molecule - cation complex (see Fig. 37).

2) Local relaxation, adiabatic ion detachment: Energy obtained after geometry optimization of the neutral molecule residue after removal of the cation from the molecule - cation complex (see Fig. 38 a)).

3) Global relaxation: Energy is global minimum energy of aspartame / Asp-Phe (see Fig. 38 b)).

Neglecting the protonated case, in which the main fragment is the loss of a water molecule, the best match for a relation between fragmentation energy and the E_{CID} values is given for number one. This is obvious for the alkali metal atoms K^+, Rb^+ and Cs^+, as the fragmentation of their complexes leads to the two fragments of the naked alkali metal ion and neutral aspartame or Asp-Phe.

The E_{CID} values of the Li^+ and Na^+ complexes also match to the calculated fragmentation energies, although their fragmentation channel is not the loss of the alkali metal atom, but the division of the molecule metal complexes into neutral Asp anhydride and the $[Phe\ M]^+$ / $[PheOMe\ M]^+$ complex. Nevertheless the bond breaking of the metal molecule bonds within the transition state is necessary to form the new complexes.

Possible reaction pathways taking this type of transition state into account are given in Fig. 39. The energy values of the according minimum energy structures of the molecule metal complexes are set to 0.

The calculated minimum energy structures of the aspartame and Asp-Phe complexes do not differ much. Thus their fragmentation energies are nearly identical.
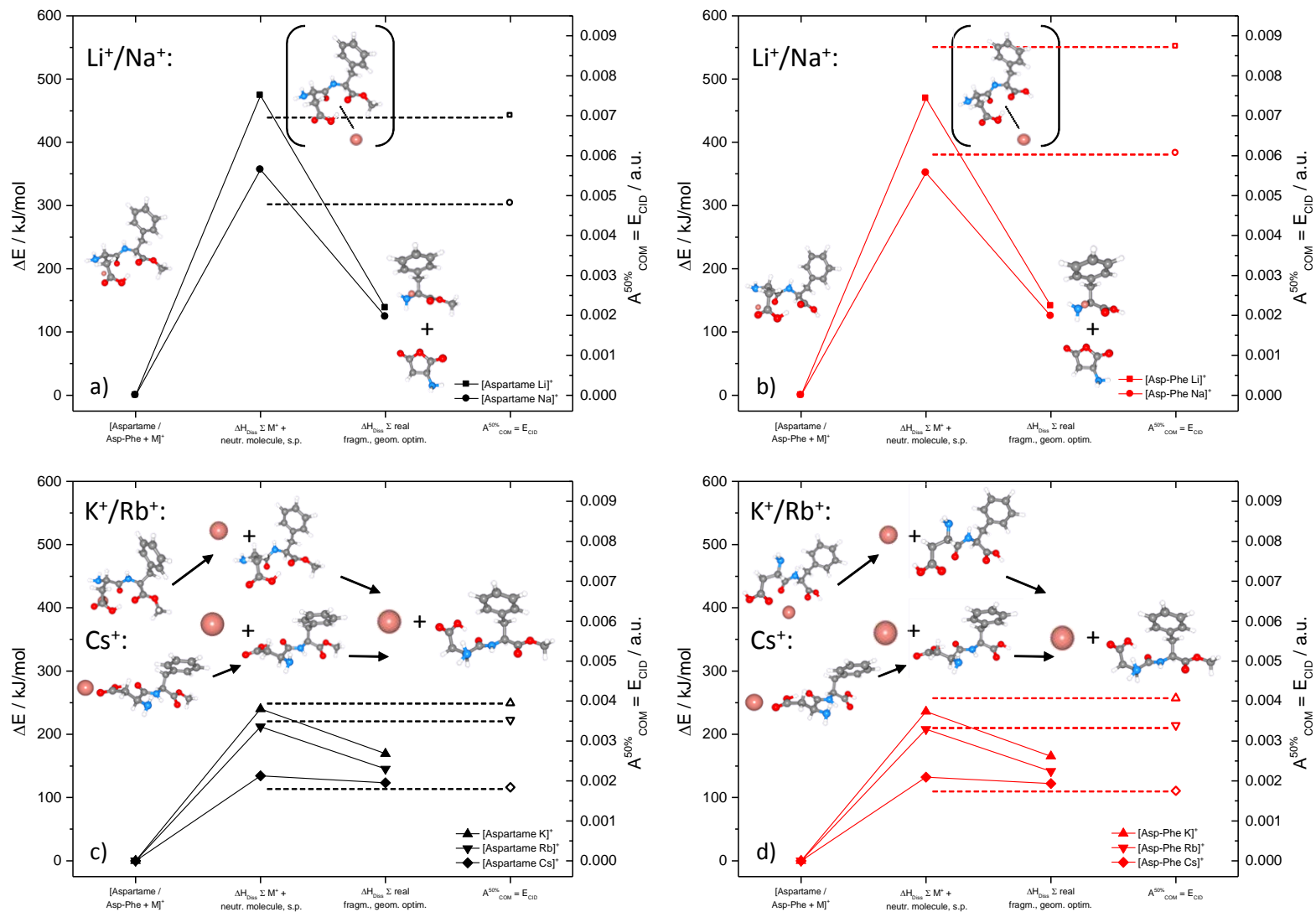
Fig. 39: *Suggested fragmentation pathways (energy values, left axis, solid symbols) and E_{CID} values (right axis, open symbols). For all alkali metal ion attached structure types the transition state is the complete releasing of the alkali metal ion.*

As already mentioned in Fig. 6 less CID energy is needed to introduce fragmentation in aspartame H^+, Li^+ or Na^+ than in the according complexes of Asp-Phe whereupon it is equal for the complexes with K^+, Rb^+ and Cs^+. This finding may be rationalized in terms of the internal energy of the involved molecules as follows:

The molecule metal complexes are sprayed at room temperature and trapped inside the Paul traps with the help of helium atoms as collision gas. They are thermalized to temperatures slightly above room temperature and possess a molar internal energy U, that estimates in the high temperature limit easily by the equipartition theorem to ½·R·T per quadratic degree of freedom, vibrations counting twice. This makes

$$U_{tot,molar} = 3NRT$$

and

$$U_{vib,molar} = (3N - 6)RT$$

with

N: number of atoms in the molecule
R: gas constant
T: temperature

In effect, the complexes provide for heat baths that scale by their size. Aspartame is the larger molecule and thus stores a higher internal energy than Asp-Phe (at equal T). When transferring energy into the molecule by CID, thermal heating / statistical redistribution within the complex ($\cong$ its heat bath) arises first, concomitant T_{vib} rise scaling by the size. Subsequent activated fragmentation scales exponentially by this internal temperature according to Arrhenius. Thus less energy input would be needed to overcome equal activation barriers of fragmentation in "small" Asp-Phe as compared to "large" aspartame. The experimentally observed substitution effect in protonated or alkalated (Li^+, Na^+) complexes goes the other way around, however. One may speculate about possible reasoning:

a) A smaller molecular heat bath initially provides less energy in total and takes more additional activation energy input to reach equal available energies eventually (see Fig. 40 and Fig. 41). This argumentation seems somewhat arbitrary and would take explicit verification by dynamical modeling.

b) Small size complexes (Asp-Phe) of small alkalis (Li^+, Na^+) or when protonated are "hard" or "stiff". Low energy collective vibrational modes tend to blueshift as compared to larger sized complexes (aspartame) and/or to alkalated complexes of larger alkali metal ions (K^+, Rb^+ and Cs^+). Therefore, the density of states is sparse in stiff complexes and higher in soft/floppy complexes. OMe substitution (Asp-Phe $\rightarrow$ aspartame) helps "somewhat" to switch from stiff to floppy. In stiff complexes the energy uptake through CID is anticipated smaller (at equal
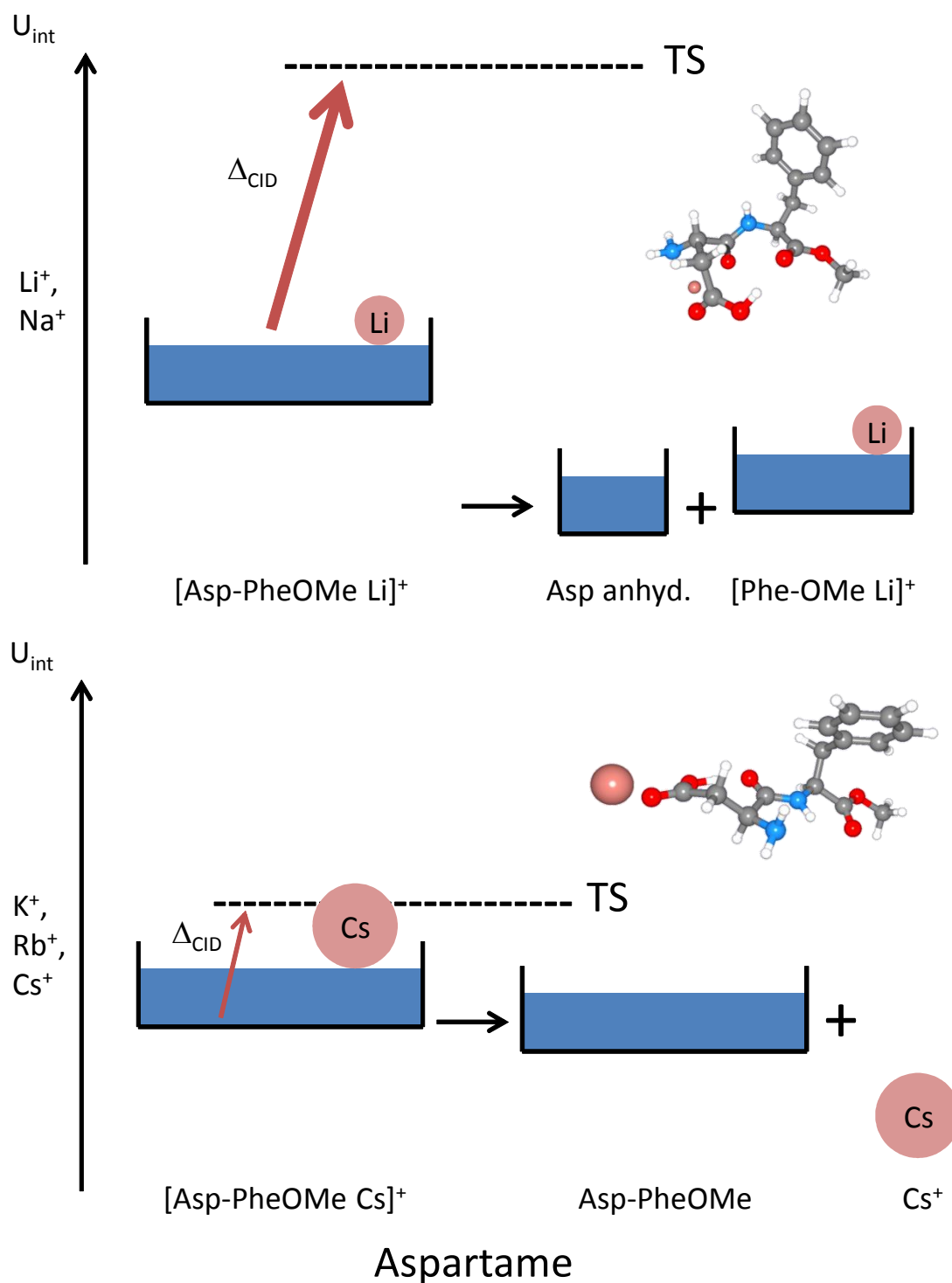
Fig. 40: *Schematic drawing of the "heat bath concept": Internal energy progression during fragmentation reaction of cationized aspartame: For Li+ and Na+ much energy is needed to reach the transition state (TS) and break the aspartame molecule leaving two molecules one of them carrying the metal ion. For the larger alkali metal ions less energy is needed to split off the alkali metal atom.*
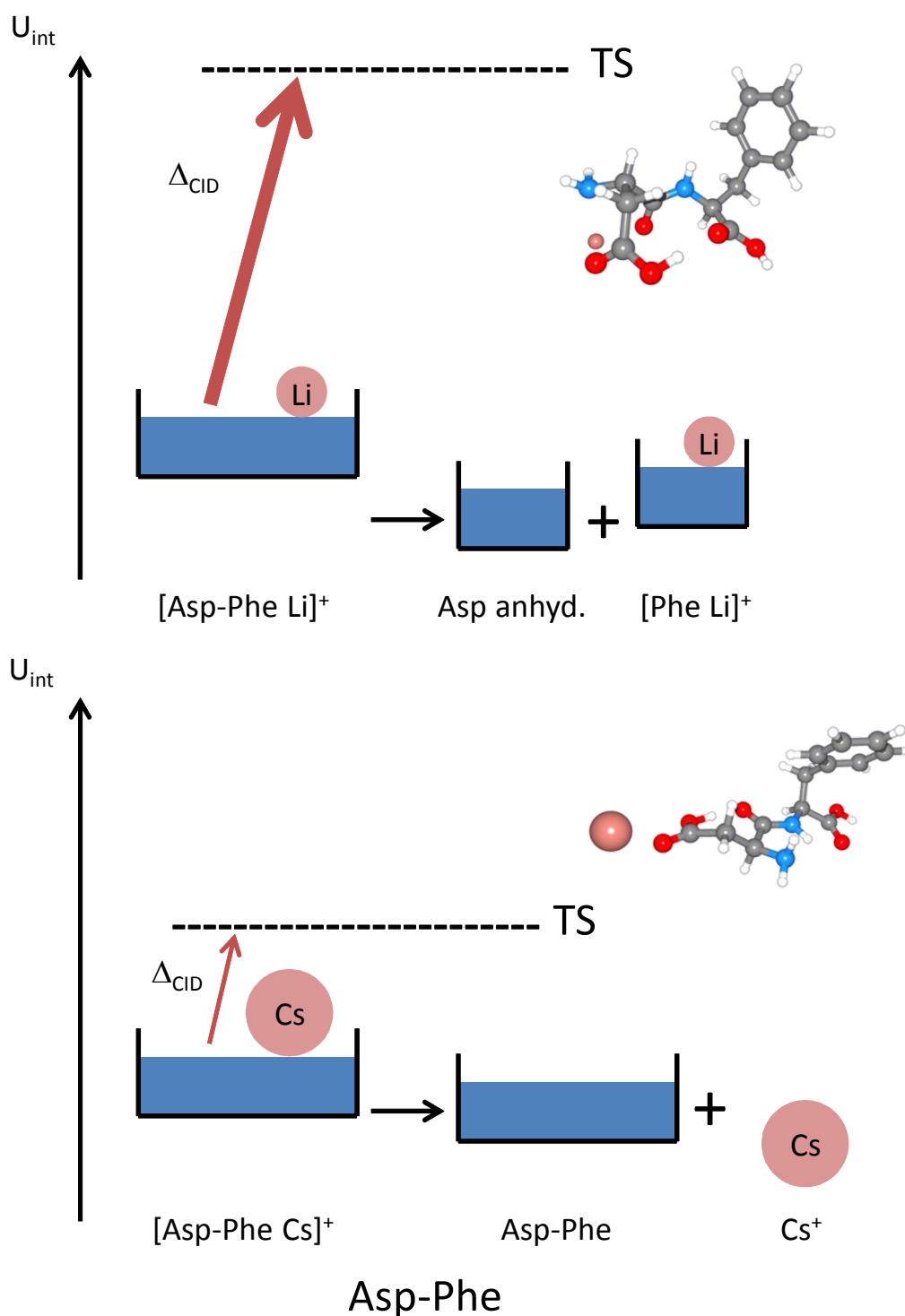
Fig. 41: *Schematic drawing of the "heat bath concept": Internal energy progression during fragmentation reaction of cationized aspartame: For Li⁺ and Na⁺ much energy is needed to reach the transition state (TS) and break the aspartame molecule leaving two molecules one of them carrying the metal ion. The amount of energy needed is even higher compared to the value for aspartame, as the internal energy of aspartame is higher from the beginning (added by the additional methylester group). For the larger alkali metal ions less energy is needed to split off the alkali metal atom. The amount of this energy equals the one needed for aspartame, as in this case the additional "internal energy modes" of the methylester group are not involved in the fragmentation / rearrangement process.*

excitation amplitude) than in floppy complexes, formal E_{CID} seemingly increasing in small/stiff complexes. Complexation with large alkali ions may level off this effect somewhat or totally. As before, this speculation would need verification by according model calculations.

In the complexes with Li^+ and Na^+ fragmentation leads to a neutral Asp anhydride molecule and a residue of Phe / Phe-OMe carrying the alkali metal ion. According to quantum mechanical calculations the small alkali metal ions prefer to establish a charge-solvated tridentate structure (see structures of Li^+ complexes in Fig. 40 and Fig. 41). The additional atoms of aspartame that cause the higher internal energy are directly involved in the fragmentation reaction. Large complexes prefer to form a salt-bridge type complex where the alkali metal atom is weakly bound e.g. to the two oxygen atoms of the Asp residue of the molecule (see structures of Cs^+ complexes in Fig. 40 and Fig. 41). During fragmentation the alkali metal atom is split off from the molecule, the fragmentation process not being affected by the additional "internal energy modes" of the Phe-OMe residue far away from the place of fragmentation. Thus the E_{CID} values are the same for aspartame and Asp-Phe complexes of K^+, Rb^+ and Cs^+.

5.4. Summary and conclusions

We have explored the influence of the methylester group in the molecules aspartame (Asp-PheOMe) and Asp-Phe by investigation of their protonated and deprotonated species and their complexes with alkali metal ions attached utilizing various mass spectrometry based techniques.

Gas phase H-/D-exchange with ND_3 has proven that in both molecules all acidic NH and OH sites do exchange their hydrogen atom and that simultaneous multi exchange is evident. Kinetic studies revealed that with alkali metal ions attached the speed of the first exchange step decreases with increasing ion size. The additional OH of the carboxylic $COOH_{Phe}$ group in Asp-Phe increases the exchange speed by a constant value.

CID experiments yielded water and the ionic Asp-Phe anhydride as main fragments out of the protonated molecules, neutral Asp anhydride and $[Phe \ M]^+$ / $[PheOMe \ M]^+$ out of Li^+ and Na^+ complexes, and neutral aspartame / Asp-Phe and ionic M^+ out of K^+, Rb^+ and Cs^+ complexes. The E_{CID} value, relating to the complex stability, decreases with increasing ion size. Aspartame fragmentation occurs at lower E_{CID} values in complexes of H^+, Li^+ and Na^+ than for the Asp-Phe analoga. Fragmentation of complexes of K^+, Rb^+ and Cs^+ with aspartame and Asp-Phe give the same E_{CID} value.

IR-MPD investigations provide for the same fragments as the CID experiments. Quantum mechanical calculations confirm a change in the preferred structure from charge-solvated, tridentate type in complexes of small alkali metal ions (Li^+) to salt-bridge type structure in complexes of large alkali metal ions (Cs^+). Calculations of cationized species reveal nearly no structural differences between complexes with aspartame and Asp-Phe. The deprotonation of the additional $COOH_{Phe}$ group in Asp-Phe is preferred against that of other acidic positions. A better experimental distinction between possible (calculated) structure types would arise from additional FEL IR-MPD measurements in the energy range of 600 to 1800 cm^{-1}.

The comparison of the E_{CID} values with calculated fragmentation energy values proved that not only for alkali metal complexes with K^+, Rb^+ and Cs^+, but also for Li^+ and Na^+ the bond breaking of all metal atom bonds is part of the transition state.

The lower E_{CID} values for complexes of small cations with aspartame may be explained in terms of internal energy. Aspartame is a larger molecule, possesses more internal energy and can be recognized as the larger heat bath. Less energy may be needed for fragmentation, if the Phe part with the additional methylester group is involved in the fragmentation process.

5.5. References

[1]   E.G. Robertson, J.P. Simons, *Getting into shape: Conformational and supramolecular landscapes in small biomolecules and their hydrated clusters*, Physical Chemistry Chemical Physics, **3** (2001) 1-18.

[2]   M.K. Green, C.B. Lebrilla, *Ion-molecule reactions as probes of gas-phase structures of peptides and proteins*, Mass Spectrometry Reviews, **16** (1997) 53-71.

[3]   C. Lifshitz, *A review of gas-phase H/D exchange experiments: The protonated arginine dimer and bradykinin nonapeptide systems*, International Journal of Mass Spectrometry, **234** (2004) 63-70.

[4]   L. Konermann, J. Pan, Y.-H. Liu, *Hydrogen exchange mass spectrometry for studying protein structure and dynamics*, Chemical Society Reviews, **40** (2011) 1224-1234.

[5]   S. Campbell, M.T. Rodgers, E.M. Marzluff, J.L. Beauchamp, *Deuterium exchange reactions as a probe of biomolecule structure. Fundamental studies of cas phase H/D exchange reactions of protonated glycine oligomers with D2O, CD3OD, CD3CO2D, and ND3*, Journal of the American Chemical Society, **117** (1995) 12840-12854.

[6]   G. Koster, C. Lifshitz, *H/D exchange reactions of protonated diglycine; an electrospray ionization-flow tube reactor experiment*, International Journal of Mass Spectrometry, **182** (1999) 213-220.

[7]   F. He, A.G. Marshall, *Weighted quasi-Newton and variable-order, variable-step Adams algorithm for determining site-specific reaction rate constants*, Journal of Physical Chemistry A, **104** (2000) 562-567.

[8]   M. Rozman, *Aspartic acid side chain effect - Experimental and theoretical insight*, Journal of the American Society for Mass Spectrometry, **18** (2007) 121-127.

[9]   M. Rozman, *The gas-phase H/D exchange mechanism of protonated amino acids*, Journal of the American Society for Mass Spectrometry, **16** (2005) 1846-1852.

[10]   M. Rozman, S. Kazazic, L. Klasinc, D. Srzic, *Kinetics of gas-phase hydrogen/deuterium exchange and gas-phase structure of protonated phenylalanine, proline, tyrosine and tryptophan*, Rapid Communications in Mass Spectrometry, **17** (2003) 2769-2772.

[11]   B.E. Ziegler, T.B. McMahon, *Energetics and structural elucidation of mechanisms for gas phase H/D exchange of protonated peptides*, Journal of Physical Chemistry A, **114** (2010) 11953-11963.

[12]   M. Rozman, B. Bertosa, L. Klasinc, D. Srzic, *Gas phase H/D exchange of sodiated amino acids: Why do we see zwitterions?*, Journal of the American Society for Mass Spectrometry, **17** (2006) 29-36.

[13]   K.B. Green-Church, P.A. Limbach, M.A. Freitas, A.G. Marshall, *Gas-phase hydrogen/deuterium exchange of positively charged mononucleotides by use of Fourier-transform ion cyclotron resonance mass spectrometry*, Journal of the American Society for Mass Spectrometry, **12** (2001) 268-277.

[14]   L.A. Mertens, E.M. Marzluff, *Gas phase hydrogen/deuterium exchange of Arginine and Arginine dipeptides complexed with alkali metals*, Journal of Physical Chemistry A, **115** (2011) 9180-9187.

[15]   B. Balta, M. Basma, V. Aviyente, C.B. Zhu, C. Lifshitz, *Structures and reactivity of gaseous glycine and its derivatives*, International Journal of Mass Spectrometry, **201** (2000) 69-85.

[16]   E.R. Talaty, B.A. Perera, A.L. Gallardo, J.M. Barr, M.J. Van Stipdonk, *Elucidation of fragmentation pathways for the collision-induced dissociation of the binary Ag(I) complex with phenylalanine*, Journal of Physical Chemistry A, **105** (2001) 8059-8068.

[17]   R.M. Moision, P.B. Armentrout, *Experimental and theoretical dissection of sodium cation/glycine interactions*, Journal of Physical Chemistry A, **106** (2002) 10350-10362.

[18]   P.B. Armentrout, E.I. Armentrout, A.A. Clark, T.E. Cooper, E.M.S. Stennett, D.R. Carl, *An experimental and theoretical study of alkali metal cation interactions with Cysteine*, Journal of Physical Chemistry B, **114** (2010) 3927-3937.

[19]   M. Rozman, S.J. Gaskell, *Non-covalent interactions of alkali metal cations with singly charged tryptic peptides*, Journal of Mass Spectrometry, **45** (2010) 1409-1415.

[20]   M.J. Tomlinson, J.R. Scott, C.L. Wilkins, J.B. Wright, W.E. White, *Fragmentation of an alkali metal-attached peptide probed by collision-induced dissociation Fourier transform mass spectrometry and computational methodology*, Journal of Mass Spectrometry, **34** (1999) 958-968.

[21]   S.W. Lee, H.S. Kim, J.L. Beauchamp, *Salt bridge chemistry applied to gas-phase peptide sequencing: Selective fragmentation of sodiated gas-phase peptide ions adjacent to aspartic acid residues*, Journal of the American Chemical Society, **120** (1998) 3188-3195.

[22]   F. Menges, C. Riehn, G. Niedner-Schatteburg, *The interaction of the dipeptide Carnosine with alkali metal ions studied by ion trap mass spectrometry*, Zeitschrift Fur Physikalische Chemie-International Journal of Research in Physical Chemistry & Chemical Physics, **225** (2011) 595-609.

[23]   M.J. Van Stipdonk, D.R. Kerstetter, C.M. Leavitt, G.S. Groenewold, J. Steill, J. Oomens, *Spectroscopic investigation of H atom transfer in a gas-phase dissociation reaction: McLafferty rearrangement of model gas-phase peptide ions*, Physical Chemistry Chemical Physics, **10** (2008) 3209-3221.

[24]   C.S. Contreras, N.C. Polfer, A.C. Chung, J. Oomens, J.R. Eyler, *Hydrogen/deuterium exchange of phenylalanine analogs studied with infrared multiple photon dissociation*, International Journal of Mass Spectrometry, **297** (2010) 162-169.

[25]   S. Hoyau, G. Ohanessian, *Interaction of alkali metal cations (Li+-Cs+) with glycine in the gas phase: A theoretical study*, Chemistry-a European Journal, **4** (1998) 1561-1569.

[26]   C. Kapota, J. Lemaire, P. Maitre, G. Ohanessian, *Vibrational signature of charge solvation vs salt bridge isomers of sodiated amino acids in the gas phase*, Journal of the American Chemical Society, **126** (2004) 1836-1842.

[27]   N.C. Polfer, B. Paizs, L.C. Snoek, I. Compagnon, S. Suhai, G. Meijer, G. von Helden, J. Oomens, *Infrared fingerprint spectroscopy and theoretical studies of potassium ion tagged amino acids and peptides in the gas phase*, Journal of the American Chemical Society, **127** (2005) 8571-8579.

[28]   M.W. Forbes, M.F. Bush, N.C. Polfer, J. Oomens, R.C. Dunbar, E.R. Williams, R.A. Jockusch, *Infrared spectroscopy of arginine cation complexes: Direct observation of gas-phase zwitterions*, Journal of Physical Chemistry A, **111** (2007) 11759-11770.

[29]   M.F. Bush, J.T. O'Brien, J.S. Prell, R.J. Saykally, E.R. Williams, *Infrared spectroscopy of cationized arginine in the gas phase: Direct evidence for the transition from nonzwitterionic to zwitterionic structure*, Journal of the American Chemical Society, **129** (2007) 1612-1622.

[30]   M.F. Bush, M.W. Forbes, R.A. Jockusch, J. Oomens, N.C. Polfer, R.J. Saykally, E.R. Williams, *Infrared spectroscopy of cationized lysine and epsilon-N-methyllysine in the gas phase: Effects of alkali-metal ion size and proton affinity on zwitterion stability*, Journal of Physical Chemistry A, **111** (2007) 7753-7760.

[31]   M.F. Bush, J. Oomens, E.R. Williams, *Proton Affinity and Zwitterion Stability: New Results from Infrared Spectroscopy and Theory of Cationized Lysine and Analogues in the Gas Phase*, Journal of Physical Chemistry A, **113** (2009) 431-438.

[32]   M.K. Drayss, D. Blunk, J. Oomens, M. Schaefer, *Infrared Multiple Photon Dissociation Spectroscopy of Potassiated Proline*, Journal of Physical Chemistry A, **112** (2008) 11972-11974.

[33]   P.B. Armentrout, M.T. Rodgers, J. Oomens, J.D. Steill, *Infrared multiphoton dissociation spectroscopy of cationized serine: Effects of alkali-metal cation size on gas-phase conformation*, Journal of Physical Chemistry A, **112** (2008) 2248-2257.

[34]   M.F. Bush, J. Oomens, R.J. Saykally, E.R. Williams, *Alkali metal ion binding to glutamine and glutamine derivatives investigated by infrared action spectroscopy and theory*, Journal of Physical Chemistry A, **112** (2008) 8578-8584.

[35]   M.T. Rodgers, P.B. Armentrout, J. Oomens, J.D. Steill, *Infrared multiphoton dissociation spectroscopy of cationized threonine: Effects of alkali-metal cation size on gas-phase conformation*, Journal of Physical Chemistry A, **112** (2008) 2258-2267.

[36]   A.L. Heaton, V.N. Bowman, J. Oomens, J.D. Steill, P.B. Armentrout, *Infrared Multiple Photon Dissociation Spectroscopy of Cationized Asparagine: Effects of Metal Cation Size on Gas-Phase Conformation*, Journal of Physical Chemistry A, **113** (2009) 5519-5530.

[37]   M.K. Drayss, P.B. Armentrout, J. Oomens, M. Schaefer, *IR spectroscopy of cationized aliphatic amino acids: Stability of charge-solvated structure increases with metal cation size*, International Journal of Mass Spectrometry, **297** (2010) 18-27.

[38]   D.R. Carl, T.E. Cooper, J. Oomens, J.D. Steill, P.B. Armentrout, *Infrared multiple photon dissociation spectroscopy of cationized methionine: effects of alkali-metal cation size on gas-phase conformation*, Physical Chemistry Chemical Physics, **12** (2010) 3384-3398.

[39]   M. Citir, E.M.S. Stennett, J. Oomens, J.D. Steill, M.T. Rodgers, P.B. Armentrout, *Infrared multiple photon dissociation spectroscopy of cationized cysteine: Effects of metal cation size on gas-phase conformation*, International Journal of Mass Spectrometry, **297** (2010) 9-17.

[40]   R.C. Dunbar, J.D. Steill, J. Oomens, *Cationized phenylalanine conformations characterized by IRMPD and computation for singly and doubly charged ions*, Physical Chemistry Chemical Physics, **12** (2010) 13383-13393.

[41]   M. Citir, C.S. Hinton, J. Oomens, J.D. Steill, P.B. Armentrout, *Infrared Multiple Photon Dissociation Spectroscopy of Cationized Histidine: Effects of Metal Cation Size on Gas-Phase Conformation*, Journal of Physical Chemistry A, **116** (2012) 1532-1541.

[42]   J.T. O'Brien, J.S. Prell, J.D. Steill, J. Oomens, E.R. Williams, *Interactions of mono- and divalent metal ions with Aspartic and Glutamic acid investigated with IR photodissociation spectroscopy and theory*, Journal of Physical Chemistry A, **112** (2008) 10823-10830.

[43]   R.A. Jockusch, W.D. Price, E.R. Williams, *Structure of cationized arginine (Arg center dot M+, M = H, Li, Na, K, Rb, and Cs) in the gas phase: Further evidence for zwitterionic arginine*, Journal of Physical Chemistry A, **103** (1999) 9266-9274.

[44]   D.T. Moore, J. Oomens, L. van der Meer, G. von Helden, G. Meijer, J. Valle, A.G. Marshall, J.R. Eyler, *Probing the vibrations of shared, OH+O-bound protons in the gas phase*, ChemPhysChem, **5** (2004) 740-743.

[45]   J. Oomens, J.D. Steill, B. Redlich, *Gas-phase IR spectroscopy of deprotonated amino acids*, Journal of the American Chemical Society, **131** (2009) 4310-4319.

[46]   C.M. Leavitt, A.B. Wolk, J.A. Fournier, M.Z. Kamrath, E. Garand, M.J. Van Stipdonk, M.A. Johnson, *Isomer-Specific IR-IR Double. Resonance Spectroscopy of D-2-Tagged Protonated Dipeptides Prepared in a Cryogenic Ion Trap*, Journal of Physical Chemistry Letters, **3** (2012) 1099-1105.

[47]   R.C. Dunbar, J.D. Steill, N.C. Polfer, J. Oomens, *Gas-phase infrared spectroscopy of the protonated dipeptides H(+)PheAla and H(+)AlaPhe compared to condensed-phase results*, International Journal of Mass Spectrometry, **283** (2009) 77-84.

[48]   H. Fricke, K. Schwing, A. Gerlach, C. Unterberg, M. Gerhards, *Investigations of the water clusters of the protected amino acid Ac-Phe-OMe by applying IR/UV double resonance spectroscopy: microsolvation of the backbone*, Physical Chemistry Chemical Physics, **12** (2010) 3511-3521.

[49]   H. Fricke, A. Gerlach, M. Gerhards, *Structure of a [small beta]-sheet model system in the gas phase: Analysis of the fingerprint region up to 10 [small mu]m*, Physical Chemistry Chemical Physics, **8** (2006) 1660-1662.

[50]   M. Gerhards, C. Unterberg, *Structures of the protected amino acid Ac-Phe-OMe and its dimer: A [small beta]-sheet model system in the gas phase*, Physical Chemistry Chemical Physics, **4** (2002) 1760-1765.

[51]   M. Gerhards, C. Unterberg, A. Gerlach, *Structure of a [small beta]-sheet model system in the gas phase: Analysis of the C[double bond, length half m-dash]O stretching vibrations*, Physical Chemistry Chemical Physics, **4** (2002) 5563-5565.

[52]   O.M. Cabarcos, C.J. Weinheimer, J.M. Lisy, *Size selectivity by cation-pi interactions: Solvation of K+ and Na+ by benzene and water*, Journal of Chemical Physics, **110** (1999) 8429-8435.

[53]   D.A. Dougherty, *Cation-pi interactions in chemistry and biology: A new view of benzene, Phe, Tyr, and Trp*, Science, **271** (1996) 163-168.

[54]   V. Ryzhov, R.C. Dunbar, B. Cerda, C. Wesdemiotis, *Cation-pi effects in the complexation of Na+ and K+ with Phe, Tyr, and Trp in the gas phase*, Journal of the American Society for Mass Spectrometry, **11** (2000) 1037-1046.

[55]   J.C. Ma, D.A. Dougherty, *The cation-pi interaction*, Chemical Reviews, **97** (1997) 1303-1324.

[56]   G.W. Gokel, S.L. De Wall, E.S. Meadows, *Experimental evidence for alkali metal cation-pi interactions*, European Journal of Organic Chemistry, (2000) 2967-2978.

[57]   A. Gapeev, R.C. Dunbar, *Cation-pi interactions and the gas-phase thermochemistry of the Na+/phenylalanine complex*, Journal of the American Chemical Society, **123** (2001) 8360-8365.

[58]   C.H. Ruan, M.T. Rodgers, *Cation-pi interactions: Structures and energetics of complexation of Na+ and K+ with the aromatic amino acids, phenylalanine, tyrosine, and tryptophan*, Journal of the American Chemical Society, **126** (2004) 14600-14610.

[59]   N.C. Polfer, J. Oomens, R.C. Dunbar, *IRMPD spectroscopy of metal-ion/tryptophan complexes*, Physical Chemistry Chemical Physics, **8** (2006) 2744-2751.

[60]   T.D. Vaden, T.S.J.A. de Boer, J.P. Simons, L.C. Snoek, *Intramolecular interactions in protonated peptides: H+ PheGlyGly and H+ GlyGlyPhe*, Physical Chemistry Chemical Physics, **10** (2008) 1443-1447.

[61]   http://www.efsa.europa.eu/de/faqs/faqaspartame.htm, *Häufig gestellte Fragen zu Aspartam*, in, Europäische Behörde für Lebensmittelsicherheit.

[62]   X.Z. Qin, *Atmospheric pressure chemical ionization tandem mass spectra of alpha- and beta-aspartame*, Journal of Mass Spectrometry, **33** (1998) 55-63.

[63]   A.J. Barnes, M.A. Stuckey, L. Legall, *NUCLEIC-ACID BASES STUDIED BY MATRIX-ISOLATION VIBRATIONAL SPECTROSCOPY - URACIL AND DEUTERATED URACILS*, Spectrochimica Acta Part a-Molecular and Biomolecular Spectroscopy, **40** (1984) 419-431.

[64]   E.G. Bendit, *Infrared absorption spectrum of keratin .2. Deuteration studies*, Biopolymers, **4** (1966) 561-&.

[65]   Y. Marechal, *IR-spectra of carboxylic-acids in the gas-phase - a quantitative reinvestigation*, Journal of Chemical Physics, **87** (1987) 6344-6353.

[66]   R.L. Redington, T.E. Redington, J.M. Montgomery, *IR spectra of tropolone(OH) and tropolone(OD)*, Journal of Chemical Physics, **113** (2000) 2304-2318.

[67]   N. Godbout, D.R. Salahub, J. Andzelm, E. Wimmer, *Optimization of Gaussian-type basis-sets for local spin-density functional calculations .1. Boron through neon, optimization technique and validation*, Canadian Journal of Chemistry-Revue Canadienne De Chimie, **70** (1992) 560-571.

[68]   T.H. Dunning, *Gaussian-basis sets for use in correlated molecular calculations .1. The atoms boron through neon and hydrogen*, Journal of Chemical Physics, **90** (1989) 1007-1023.

[69]   S. Grimme, *Semiempirical GGA-type density functional constructed with a long-range dispersion correction*, Journal of Computational Chemistry, **27** (2006) 1787-1799.

[70]   S.H. Vosko, L. Wilk, M. Nusair, *Accurate spin-dependent electron liquid correlation energies for local spin-density calculations - a critical analysis*, Canadian Journal of Physics, **58** (1980) 1200-1211.

[71]   C.T. Lee, W.T. Yang, R.G. Parr, *Development of the Colle-Salvetti correlation-energy formula into a functional of the electron-density*, Physical Review B, **37** (1988) 785-789.

[72]   B. Miehlich, A. Savin, H. Stoll, H. Preuss, *Rseults obtained with the correlation-energy density functionals of Becke and Lee, Yang and Parr*, Chemical Physics Letters, **157** (1989) 200-206.

[73]   A.D. Becke, *Density-functional exchange-energy approximation with correct asymptotic-behavior*, Physical Review A, **38** (1988) 3098-3100.

[74]   J.P. Perdew, *Density-functional approximation for the correlation-energy of the inhomogeneous electron-gas*, Physical Review B, **33** (1986) 8822-8824.

[75]   C. Adamo, V. Barone, *Toward reliable density functional methods without adjustable parameters: The PBE0 model*, Journal of Chemical Physics, **110** (1999) 6158-6170.

[76]   F.A. Hamprecht, A.J. Cohen, D.J. Tozer, N.C. Handy, *Development and assessment of new exchange-correlation functionals*, Journal of Chemical Physics, **109** (1998) 6264-6271.

[77]   P.J. Wilson, T.J. Bradley, D.J. Tozer, *Hybrid exchange-correlation functional determined from thermochemical data and ab initio potentials*, Journal of Chemical Physics, **115** (2001) 9233-9242.

[78]   A. Bergner, M. Dolg, W. Kuchle, H. Stoll, H. Preuss, *Ab-initio energy-adjusted pseudopotentials for elements of groups 13-17*, Molecular Physics, **80** (1993) 1431-1441.

[79]   M. Dolg, H. Stoll, H. Preuss, R.M. Pitzer, *Relativistic and correlation-effects for element 105 (Hahnium, Ha) - a comparative-study of M and MO (M=Nb, Ta, Ha) using energy-adjusted abinitio pseudopotentials*, Journal of Physical Chemistry, **97** (1993) 5852-5859.

[80]   M. Kaupp, P.V. Schleyer, H. Stoll, H. Preuss, *Pseudopotential approaches to Ca, Sr, and Ba hydrides - why are some alkaline-earth MX2 compounds bent*, Journal of Chemical Physics, **94** (1991) 1360-1366.

[81]   M. Dolg, U. Wedig, H. Stoll, H. Preuss, *Energy-adjusted abinitio pseudopotentials for the 1st-row transition-elements*, Journal of Chemical Physics, **86** (1987) 866-872.
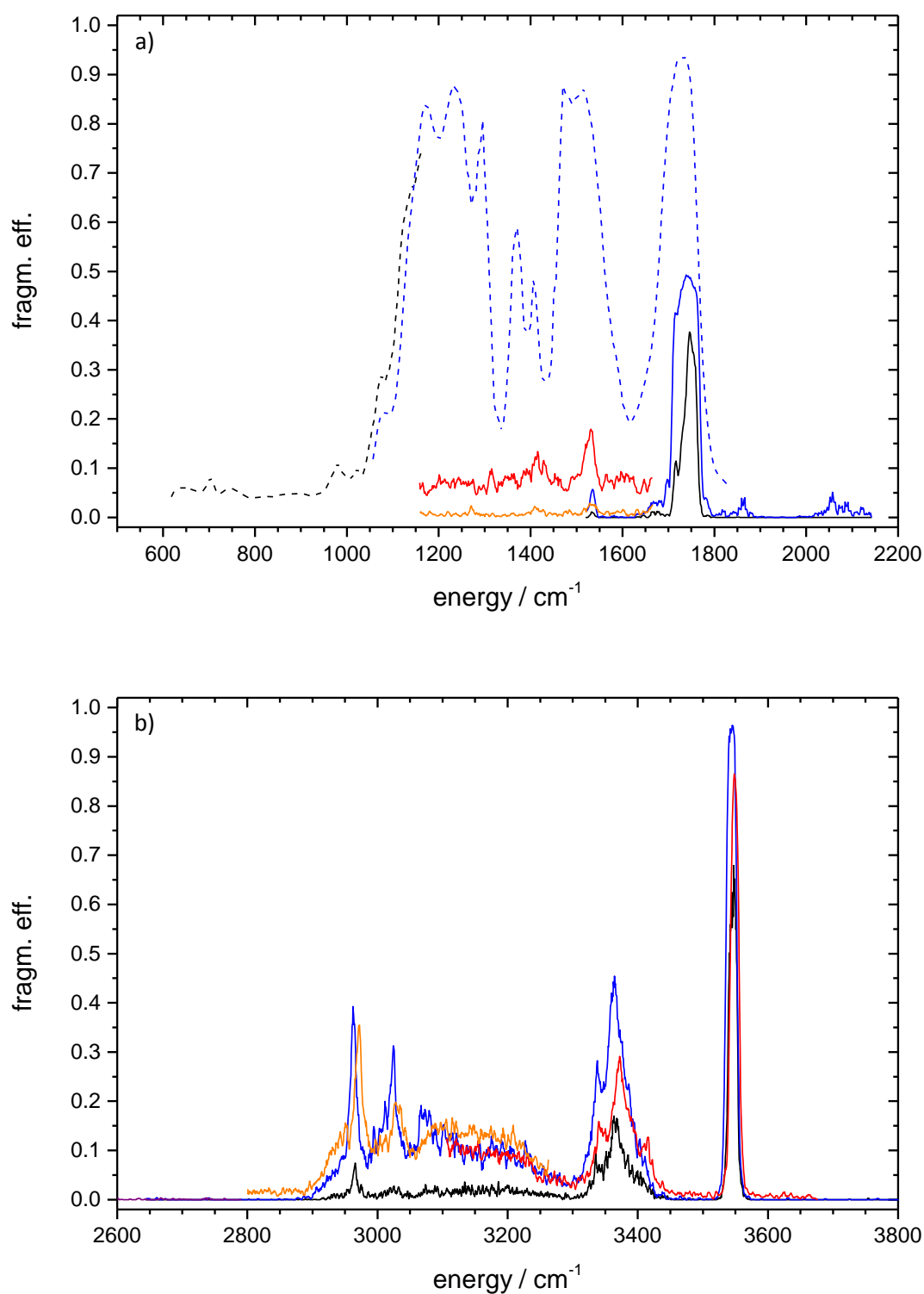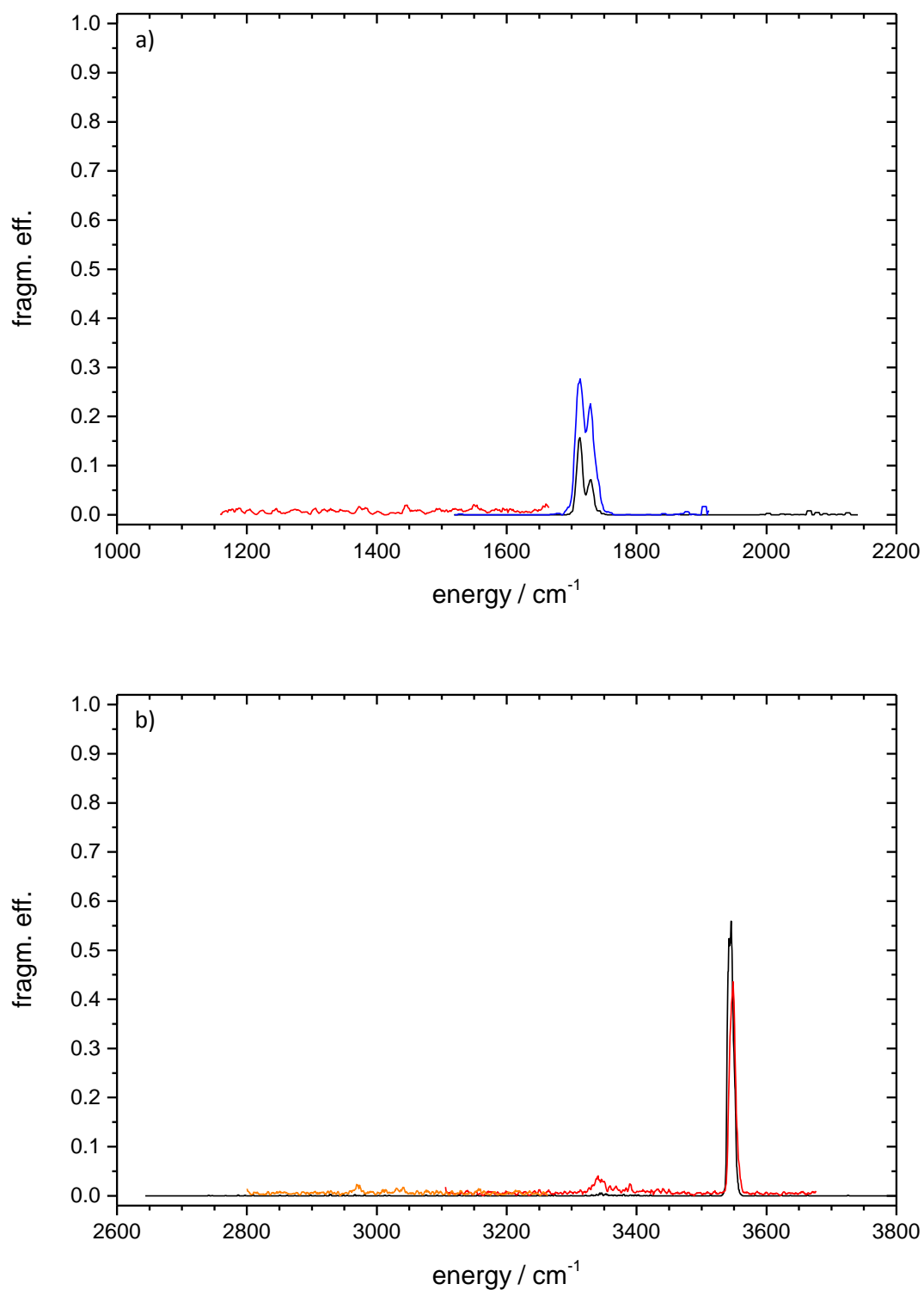
Measured IR-MPD spectra of Aspartame H⁺

Fig. S A1: Aspartame H⁺:
Fragmentation efficiency of IR-MPD spectra; blue and black dashed lines: one color IR-MPD spectra (FEL CLIO, Paris); blue, black and purple solid lines: one color IR-MPD spectra (blue and black at different laser intensities) (OPO/OPA, KL); red and orange solid lines: two color IR-MPD spectra (OPO/OPA, KL): a) red line probe at 3550 cm⁻¹, orange line probe at 3360 cm⁻¹; b) red and orange lines probe at 3550 cm⁻¹, different scanning laser intensities.
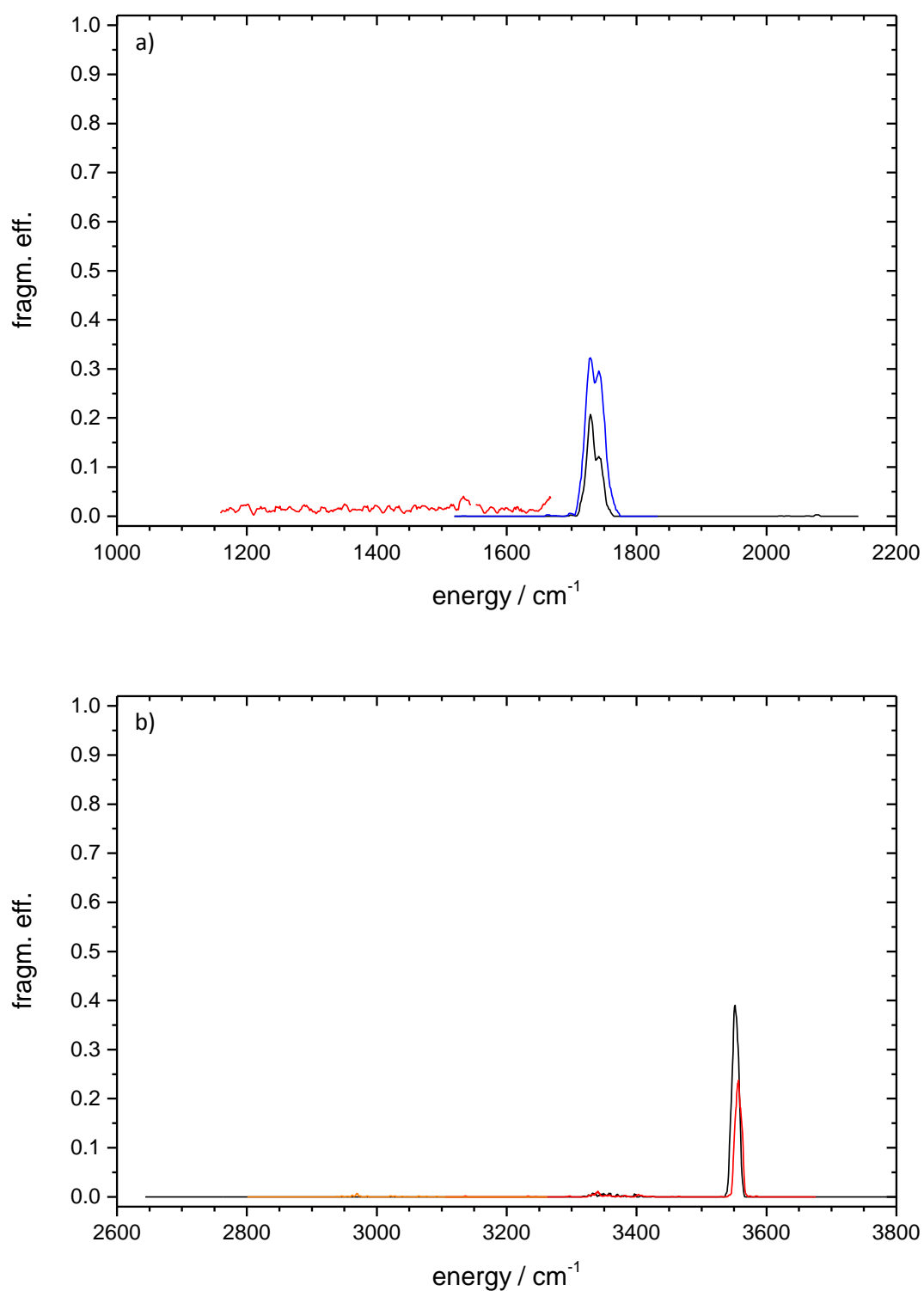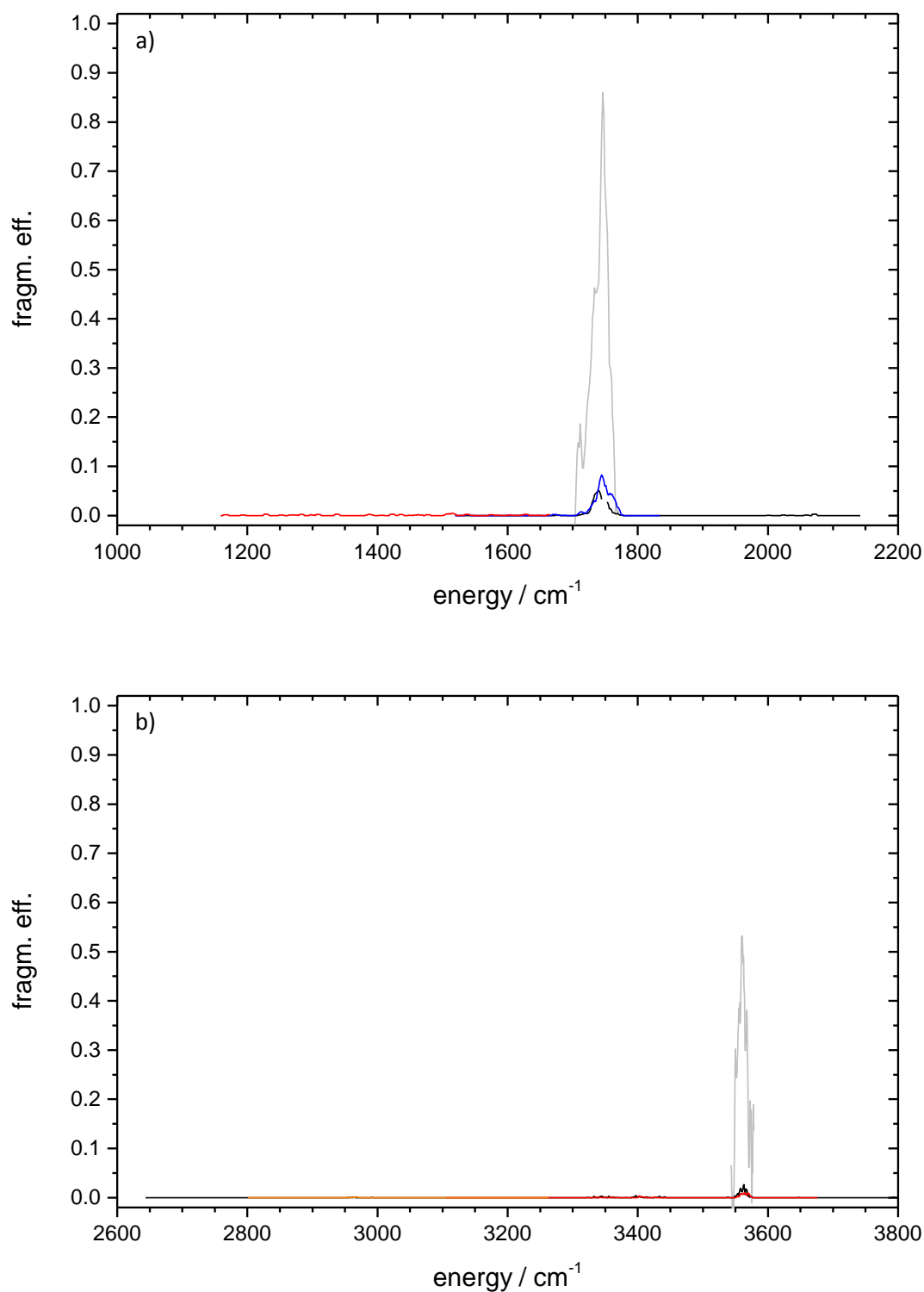
Measured IR-MPD spectra of Aspartame Li⁺

Fig. S A2: Aspartame Li⁺:
Fragmentation efficiency of IR-MPD spectra; blue and black solid lines: one color IR-MPD spectra, different laser intensities (OPO/OPA, KL); red and orange solid lines: two color IR-MPD spectra (OPO/OPA, KL): a) red line probe at 3545 cm⁻¹; b) red and orange lines probe at 3545 cm⁻¹, different scanning laser intensities.

Measured IR-MPD spectra of Aspartame Na$^+$

Fig. S A3: Aspartame Na$^+$:
Fragmentation efficiency of IR-MPD spectra; blue and black solid lines: one color IR-MPD spectra, different laser intensities (OPO/OPA, KL); red and orange solid lines: two color IR-MPD spectra (OPO/OPA, KL): a) red line probe at 3550 cm^{-1}; b) red and orange lines probe at 3550 cm^{-1}, different scanning laser intensities.

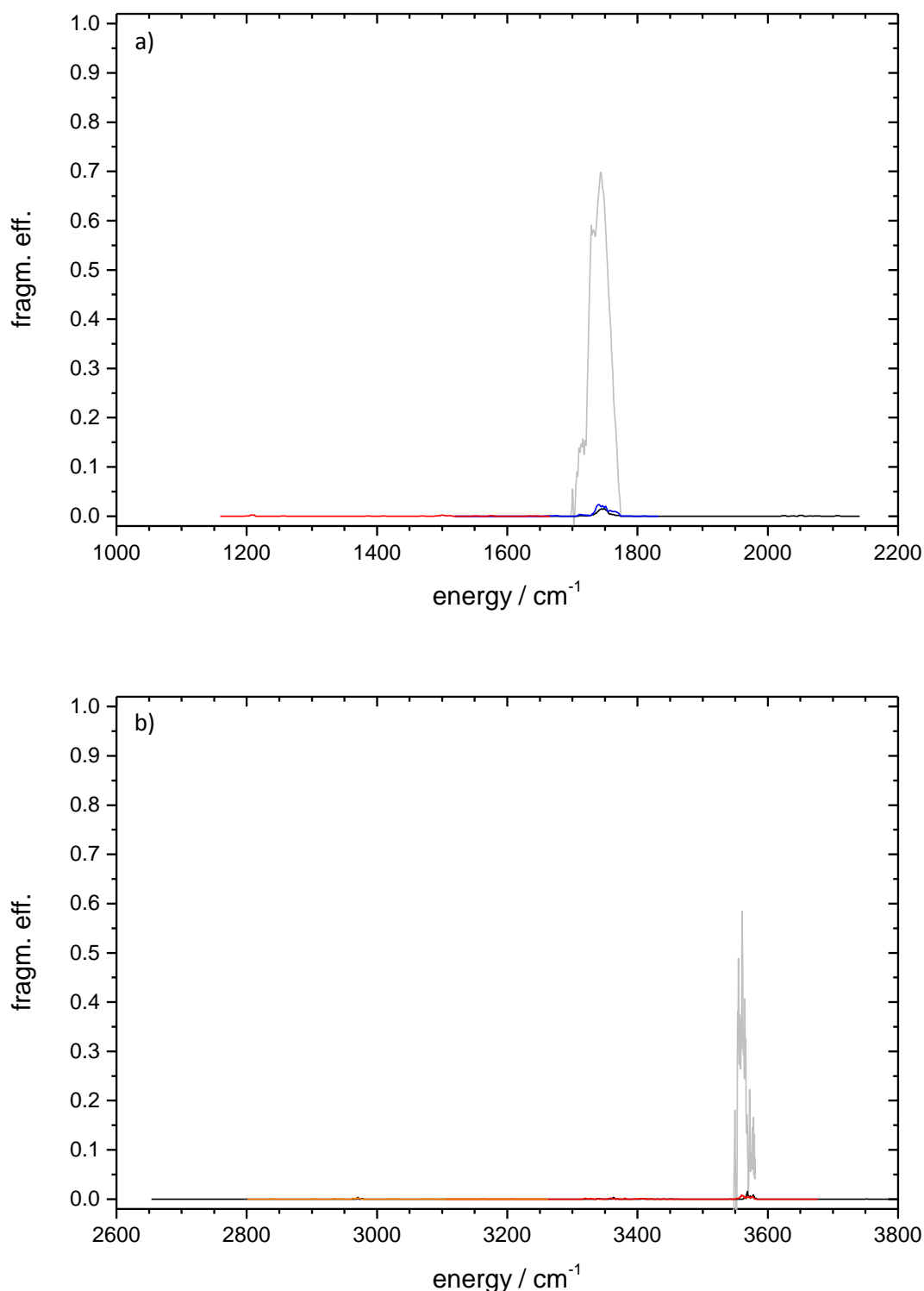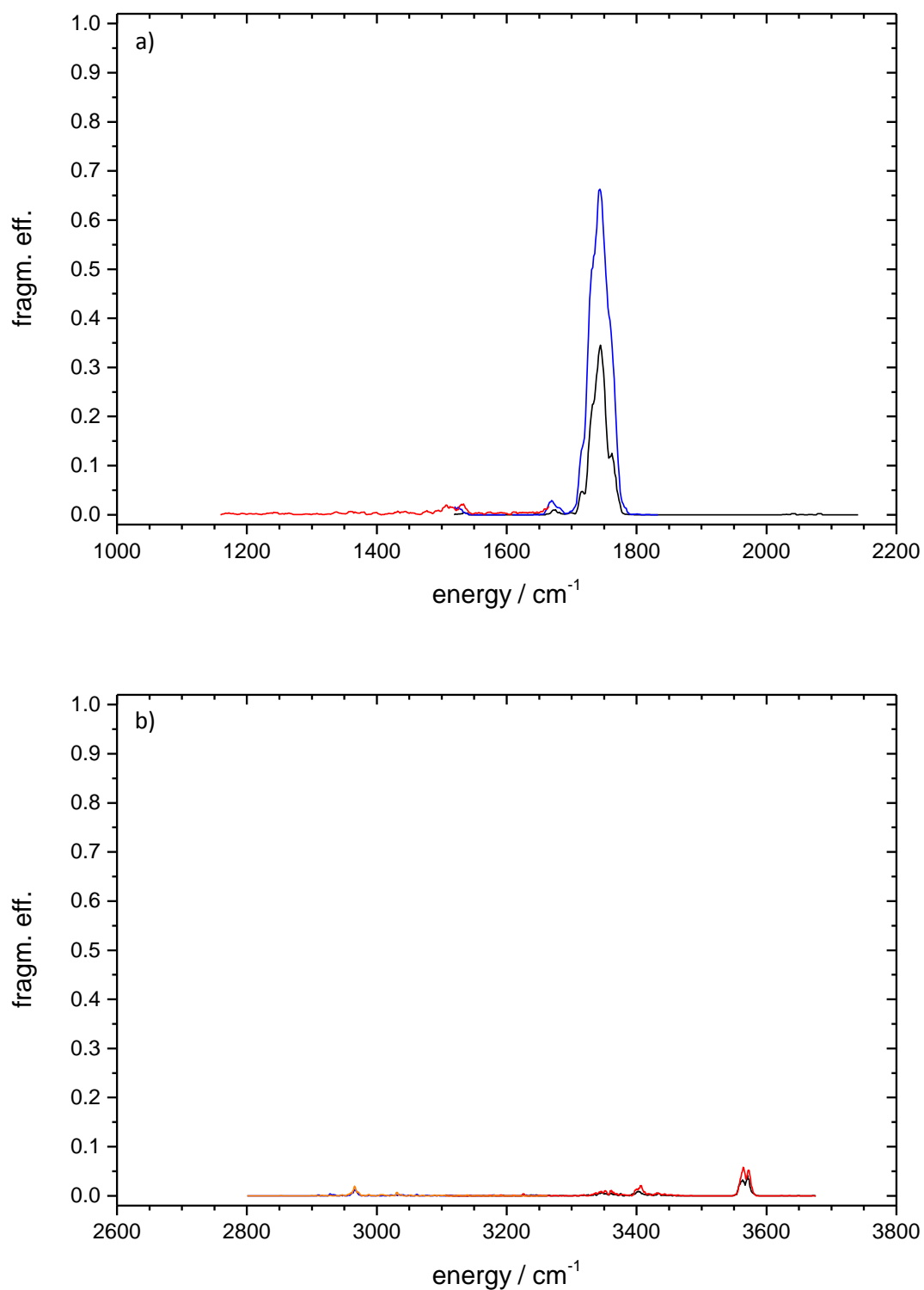**Measured IR-MPD spectra of Aspartame K$^+$**

Fig. S A4: Aspartame K$^+$:
Fragmentation efficiency of IR-MPD spectra; blue and black solid lines: one color IR-MPD spectra, different laser intensities (OPO/OPA, KL); red and orange solid lines: two color IR-MPD spectra (OPO/OPA, KL): a) red line probe at 3560 cm^{-1}; b) red and orange lines probe at 3560 cm^{-1}, different scanning laser intensities;
grey solid lines: one color IR-MPD spectra, fragmentation efficiency calculated as depletion of Aspartame K$^+$ intensity (fragm. eff. par., see chapter 1.3.2.).

Measured IR-MPD spectra of Aspartame Rb$^+$

Fig. S A5: Aspartame Rb$^+$:
Fragmentation efficiency of IR-MPD spectra; blue and black solid lines: one color IR-MPD spectra, different laser intensities (OPO/OPA, KL); red and orange solid lines: two color IR-MPD spectra (OPO/OPA, KL): a) red line probe at 3560 cm^{-1}; b) red and orange lines probe at 3560 cm^{-1}, different scanning laser intensities;
grey solid lines: one color IR-MPD spectra, fragmentation efficiency calculated as depletion of Aspartame Rb$^+$ intensity (fragm. eff. par., see chapter 1.3.2.).

Measured IR-MPD spectra of Aspartame Cs⁺

Fig. S A6: Aspartame Cs⁺:
Fragmentation efficiency of IR-MPD spectra; blue and black solid lines: one color IR-MPD spectra, different laser intensities (OPO/OPA, KL); red and orange solid lines: two color IR-MPD spectra (OPO/OPA, KL): a) red line probe at 3565 cm⁻¹; b) red and orange lines probe at 3565 cm⁻¹, different scanning laser intensities.

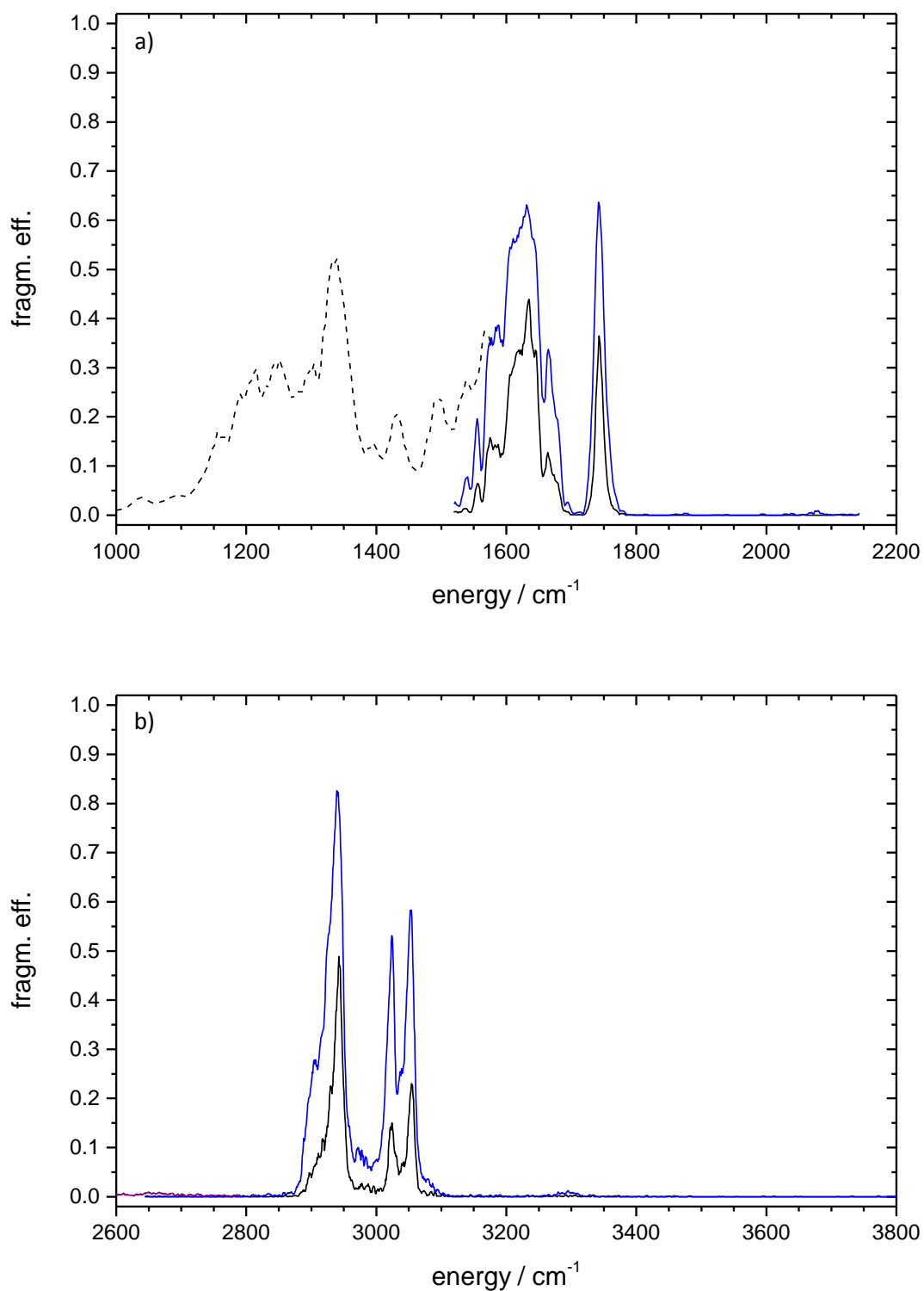**Measured IR-MPD spectra of deprotonated Aspartame**

Fig. S A7: Deprotonated Aspartame:
Fragmentation efficiency of IR-MPD spectra; black dashed line: one color IR-MPD spectrum (FEL CLIO, Paris); blue, black and purple solid lines: one color IR-MPD spectra (blue and black at different laser intensities) (OPO/OPA, KL).

IR-MPD spectra and calculated IR intensities of Aspartame H$^+$; TZVP; MP2 (g03)
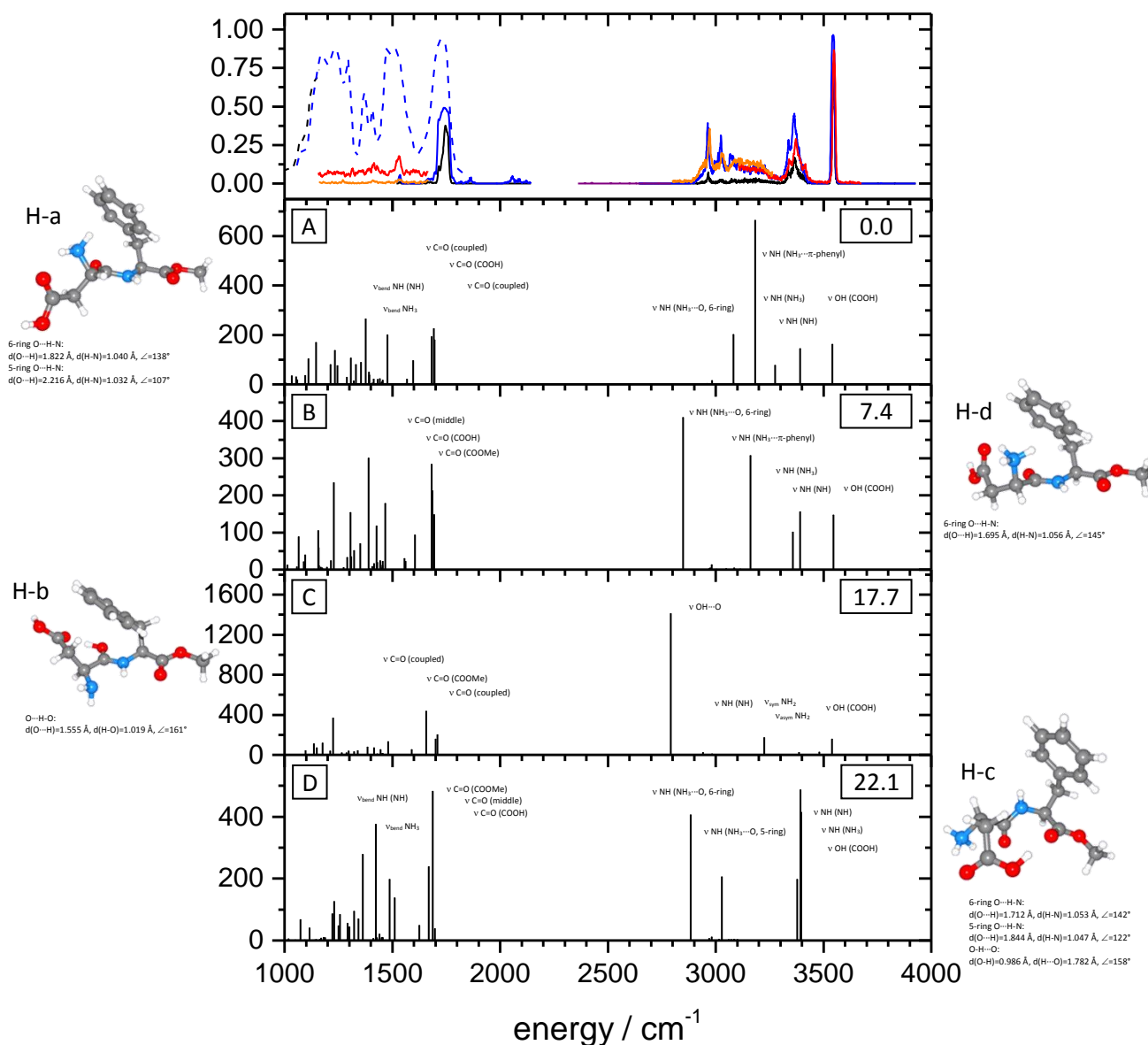
Fig. S B1: Aspartame H$^+$; TZVP; MP2:

Topmost frame: Fragmentation efficiency of IR-MPD spectra; blue and black dashed lines: one color IR-MPD spectra (FEL CLIO, Paris); blue, black and purple solid lines: one color IR-MPD spectra (blue and black at different laser intensities) (OPO/OPA, KL); red and orange solid lines: two color IR-MPD spectra (OPO/OPA, KL): 1100 - 1700 cm^{-1}: red line probe at 3550 cm^{-1}, orange line probe at 3360 cm^{-1}; 2800 - 3700 cm^{-1}: red and orange lines probe at 3550 cm^{-1}, different scanning laser intensities;

Lower frame: calculated IR intensities (km/mol) and structure of the lowest energy isomer; value is ∆E / (kJ/mol); all identified isomers with up to ∆E ≤ 25 kJ/mol above the most stable conformer are considered; scaling factor 0.96.

The calculated pattern of structure B shows best agreement, but also structure A could be conducive to the experimental spectrum. A distinction between the two structures in the area of the C=O stretching vibration is challenging, as the laser intensity of the OPO/OPA is rather low below 1700 cm^{-1}.

IR-MPD spectra and calculated IR intensities of Aspartame H^{+}; cc-pVDZ; MP2 (g03)
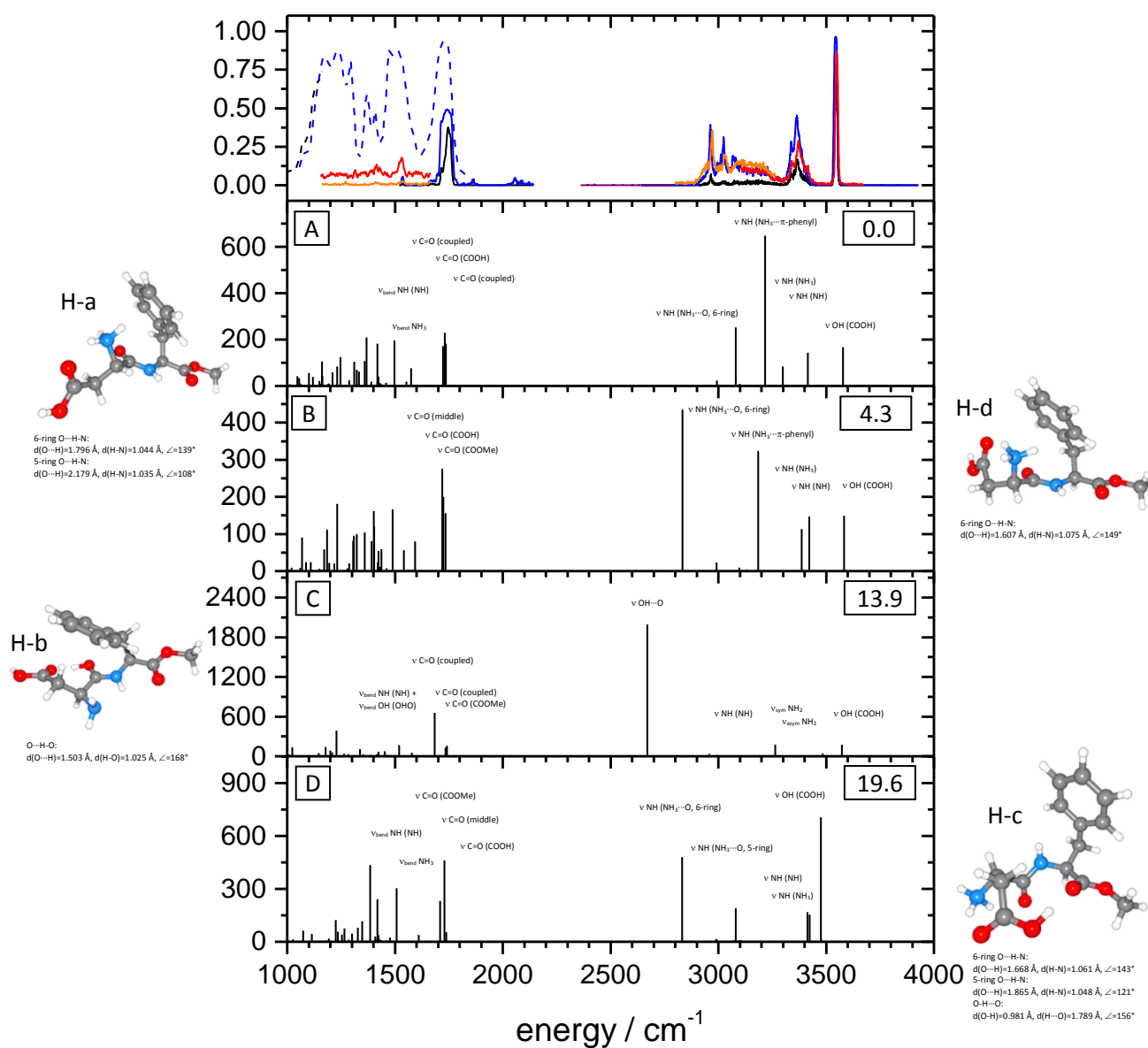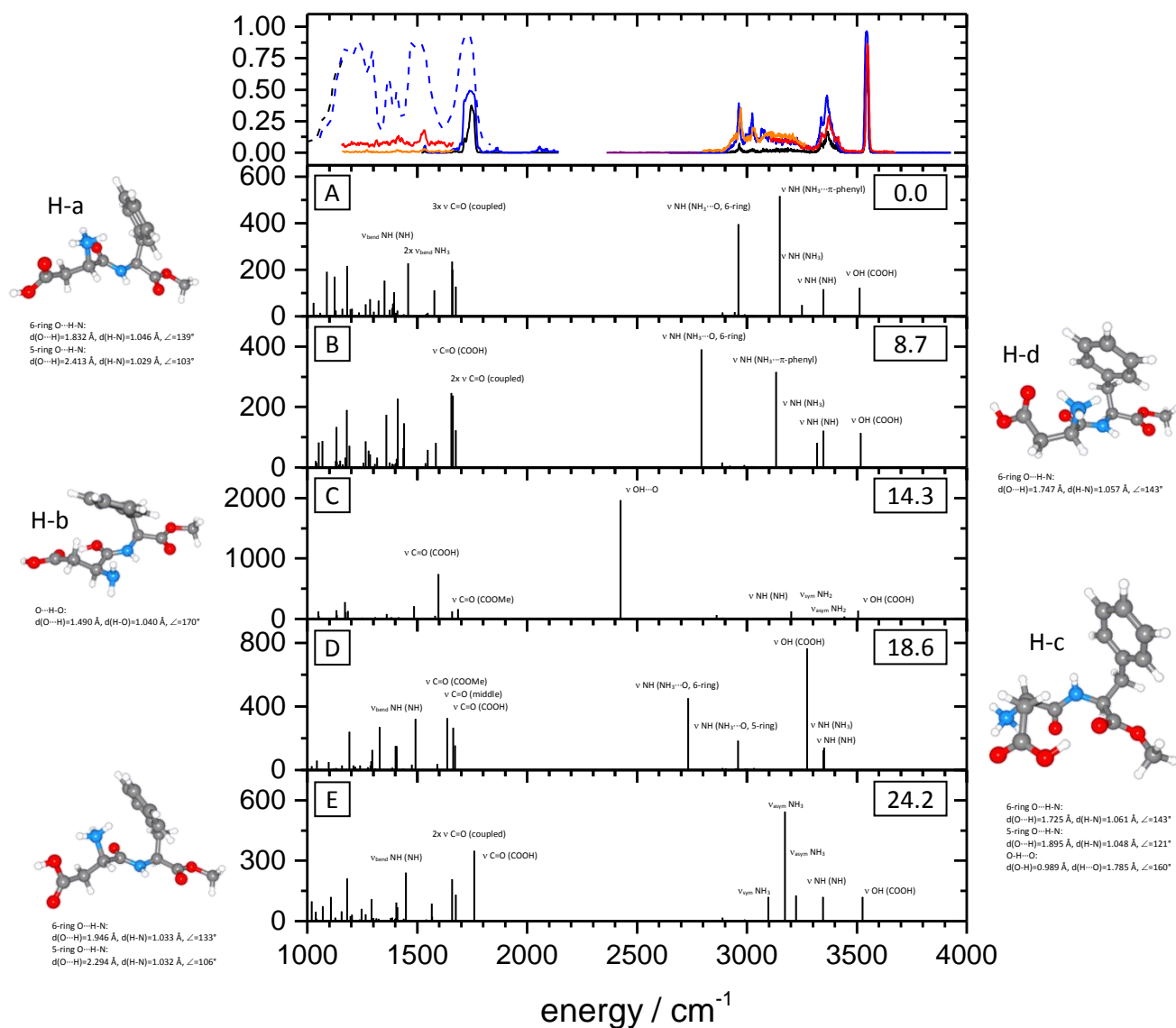

Fig. S B2: Aspartame H^{+}; cc-pVDZ; MP2:
Topmost frame: Fragmentation efficiency of IR-MPD spectra; blue and black dashed lines: one color IR-MPD spectra (FEL CLIO, Paris); blue, black and purple solid lines: one color IR-MPD spectra (blue and black at different laser intensities) (OPO/OPA, KL); red and orange solid lines: two color IR-MPD spectra (OPO/OPA, KL): 1100 - 1700 cm^{-1}: red line probe at 3550 cm^{-1}, orange line probe at 3360 cm^{-1}; 2800 - 3700 cm^{-1}: red and orange lines probe at 3550 cm^{-1}, different scanning laser intensities;
Lower frames: calculated IR intensities (km/mol) and structures of different isomers; values are ΔE / (kJ/mol); all identified isomers with up to ΔE ≤ 25 kJ/mol above the most stable conformer are considered; scaling factor 0.96.
The calculated pattern of structure B shows best agreement, but also structure A could be conducive to the experimental spectrum. A distinction between the two structures in the area of the C=O stretching vibration is challenging, as the laser intensity of the OPO/OPA is rather low below 1700 cm^{-1}.

IR-MPD spectra and calculated IR intensities of Aspartame H⁺; TZVP; DFT: B97D (g09)

Fig. S B3: Aspartame H⁺; TZVP; DFT: B97D:

Topmost frame: Fragmentation efficiency of IR-MPD spectra; blue and black dashed lines: one color IR-MPD spectra (FEL CLIO, Paris); blue, black and purple solid lines: one color IR-MPD spectra (blue and black at different laser intensities) (OPO/OPA, KL); red and orange solid lines: two color IR-MPD spectra (OPO/OPA, KL): 1100 - 1700 cm⁻¹: red line probe at 3550 cm⁻¹, orange line probe at 3360 cm⁻¹; 2800 - 3700 cm⁻¹: red and orange lines probe at 3550 cm⁻¹, different scanning laser intensities;

Lower frames: calculated IR intensities (km/mol) and structures of different isomers; values are ΔE / (kJ/mol); all identified isomers with up to ΔE ≤ 25 kJ/mol above the most stable conformer are considered; scaling factor 0.97.

The calculated patterns of structures A and B show some agreement to the experiment, but fail in the prediction of some of the NH stretching bands. A distinction between the two structures in the area of the C=O stretching vibration is challenging, as the laser intensity of the OPO/OPA is rather low below 1700 cm⁻¹.

IR-MPD spectra and calculated IR intensities of Aspartame H⁺; cc-pVTZ; DFT: B97D (g09)
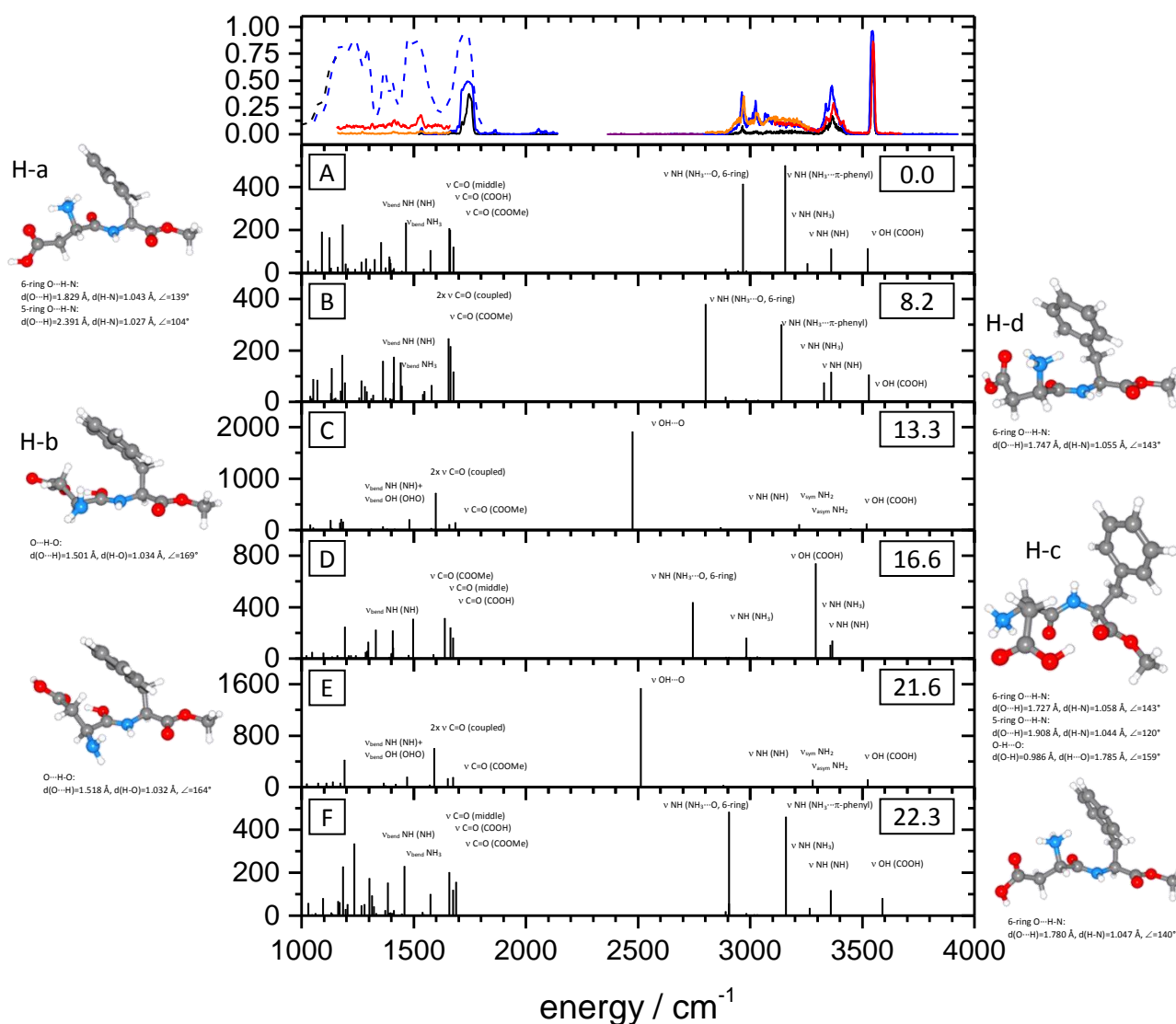

Fig. S B4: Aspartame H⁺; cc-pVTZ; DFT: B97D:

Topmost frame: Fragmentation efficiency of IR-MPD spectra; blue and black dashed lines: one color IR-MPD spectra (FEL CLIO, Paris); blue, black and purple solid lines: one color IR-MPD spectra (blue and black at different laser intensities) (OPO/OPA, KL); red and orange solid lines: two color IR-MPD spectra (OPO/OPA, KL): 1100 - 1700 cm⁻¹: red line probe at 3550 cm⁻¹, orange line probe at 3360 cm⁻¹; 2800 - 3700 cm⁻¹: red and orange lines probe at 3550 cm⁻¹, different scanning laser intensities;

Lower frames: calculated IR intensities (km/mol) and structures of different isomers; values are ΔE / (kJ/mol); all identified isomers with up to ΔE ≤ 25 kJ/mol above the most stable conformer are considered; scaling factor 0.97.

The calculated patterns of structures A and B show some agreement to the experiment, but fail in the prediction of some of the NH stretching bands. A distinction between the two structures in the area of the C=O stretching vibration is challenging, as the laser intensity of the OPO/OPA is rather low below 1700 cm⁻¹.

IR-MPD spectra and calculated IR intensities of Aspartame H^{+}; aug-cc-pVDZ; DFT: B97D (g09)

Fig. S B5: Aspartame H^{+}; aug-cc-pVDZ; DFT: B97D:

Topmost frame: Fragmentation efficiency of IR-MPD spectra; blue and black dashed lines: one color IR-MPD spectra (FEL CLIO, Paris); blue, black and purple solid lines: one color IR-MPD spectra (blue and black at different laser intensities) (OPO/OPA, KL); red and orange solid lines: two color IR-MPD spectra (OPO/OPA, KL): 1100 - 1700 cm^{-1}: red line probe at 3550 cm^{-1}, orange line probe at 3360 cm^{-1}; 2800 - 3700 cm^{-1}: red and orange lines probe at 3550 cm^{-1}, different scanning laser intensities;

Lower frames: calculated IR intensities (km/mol) and structures of different isomers; values are ΔE / (kJ/mol); all identified isomers with up to ΔE ≤ 25 kJ/mol above the most stable conformer are considered; scaling factor 0.97.

The calculated patterns of structures A and B show some agreement to the experiment, but fail in the prediction of some of the NH stretching bands. A distinction between the two structures in the area of the C=O stretching vibration is challenging, as the laser intensity of the OPO/OPA is rather low below 1700 cm^{-1}.
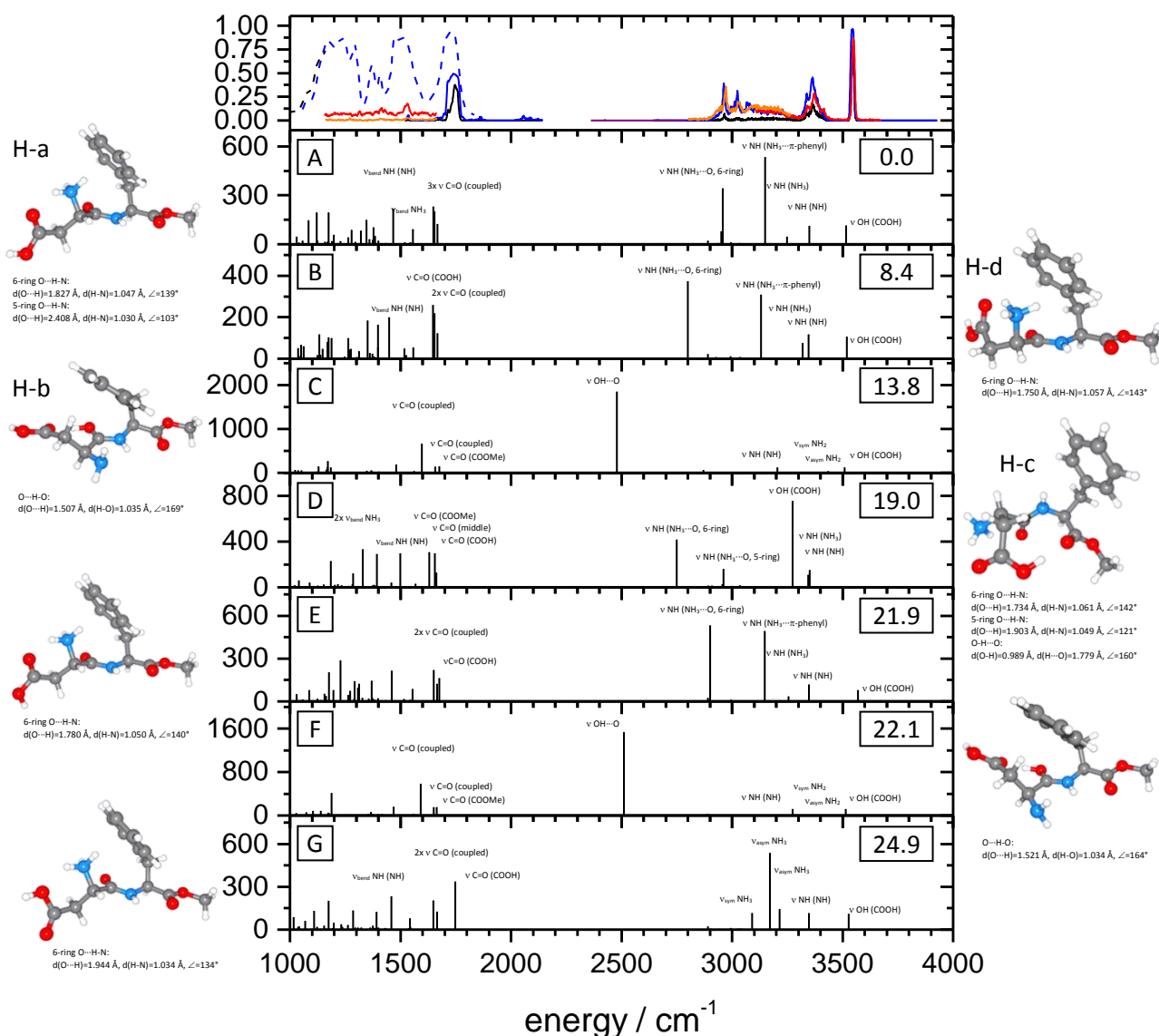
IR-MPD spectra and calculated IR intensities of Aspartame H$^+$; cc-pVDZ; DFT: B97D (g09)

Fig. S B6: Aspartame H$^+$; cc-pVDZ; DFT: B97D:

Topmost frame: Fragmentation efficiency of IR-MPD spectra; blue and black dashed lines: one color IR-MPD spectra (FEL CLIO, Paris); blue, black and purple solid lines: one color IR-MPD spectra (blue and black at different laser intensities) (OPO/OPA, KL); red and orange solid lines: two color IR-MPD spectra (OPO/OPA, KL): 1100 - 1700 cm^{-1}: red line probe at 3550 cm^{-1}, orange line probe at 3360 cm^{-1}; 2800 - 3700 cm^{-1}: red and orange lines probe at 3550 cm^{-1}, different scanning laser intensities;

Lower frames: calculated IR intensities (km/mol) and structures of different isomers; values are ΔE / (kJ/mol); all identified isomers with up to ΔE ≤ 25 kJ/mol above the most stable conformer are considered; scaling factor 0.97.

The calculated pattern of structure B shows best agreement, but also structure A could be conducive to the experimental spectrum. A distinction between the two structures in the area of the C=O stretching vibration is challenging, as the laser intensity of the OPO/OPA is rather low below 1700 cm^{-1}.

IR-MPD spectra and calculated IR intensities of Aspartame H⁺; TZVP; DFT: B3LYP (g03)
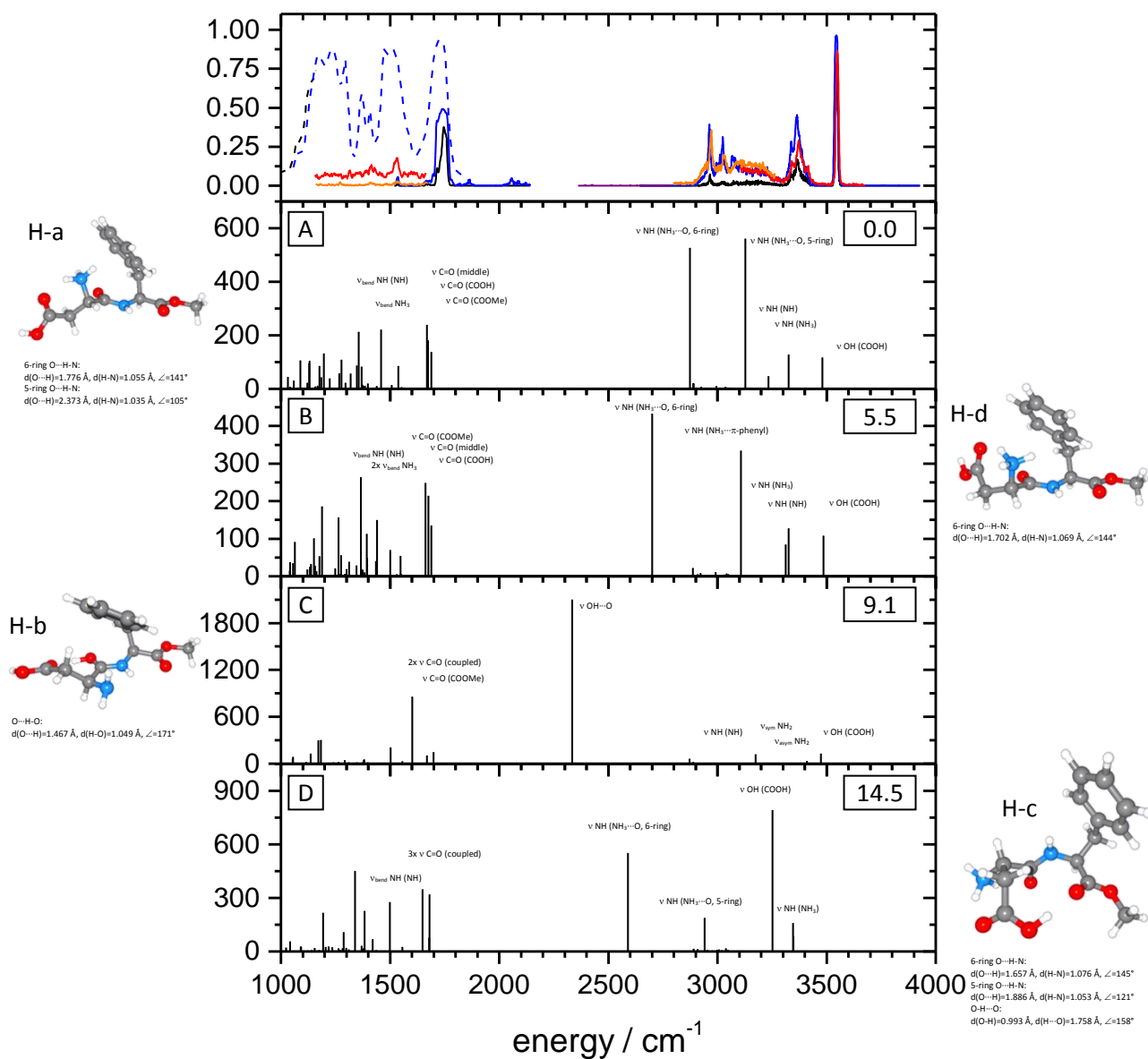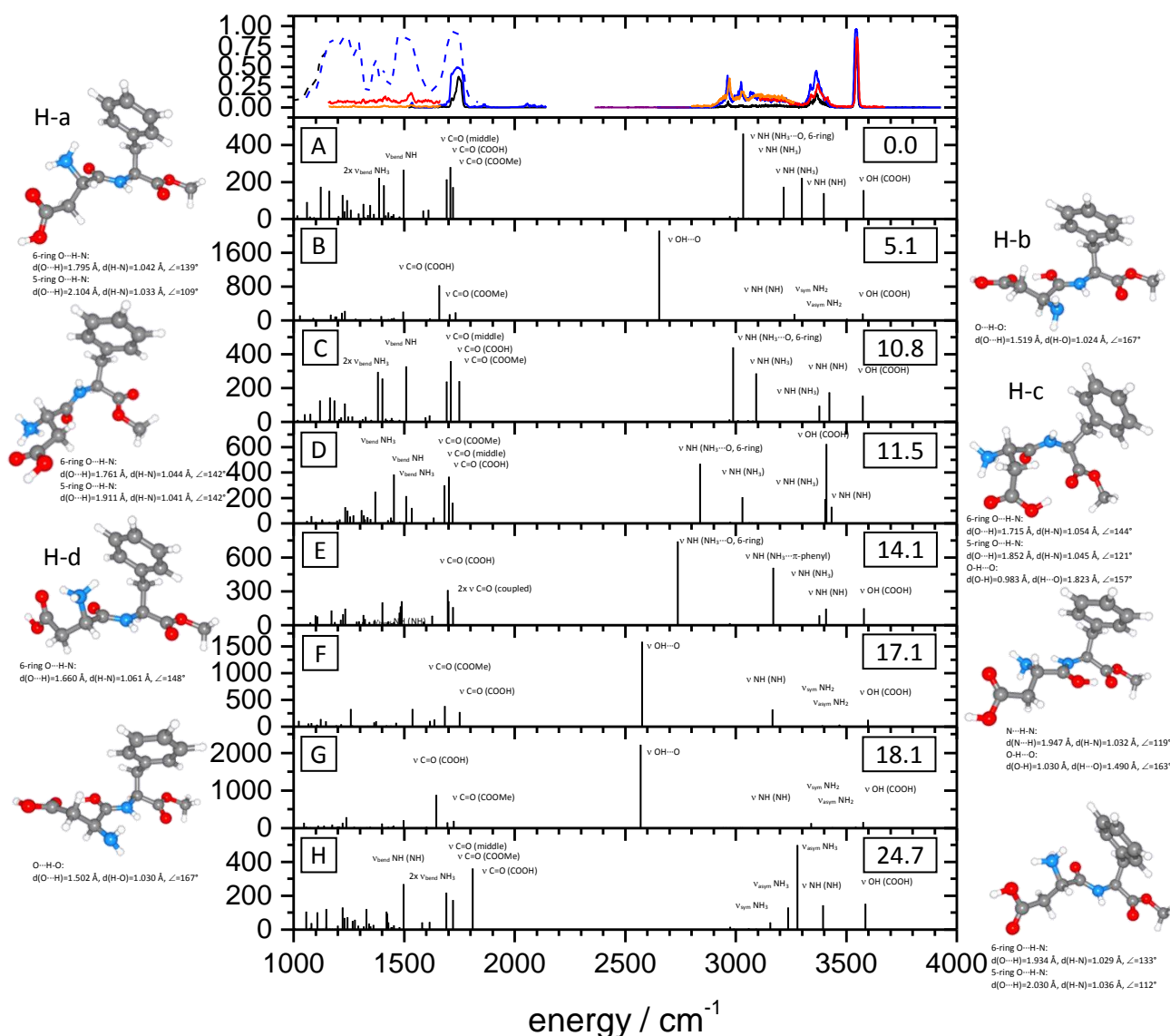

Fig. S B7: Aspartame H⁺; TZVP; DFT: B3LYP:

Topmost frame: Fragmentation efficiency of IR-MPD spectra; blue and black dashed lines: one color IR-MPD spectra (FEL CLIO, Paris); blue, black and purple solid lines: one color IR-MPD spectra (blue and black at different laser intensities) (OPO/OPA, KL); red and orange solid lines: two color IR-MPD spectra (OPO/OPA, KL): 1100 - 1700 cm⁻¹: red line probe at 3550 cm⁻¹, orange line probe at 3360 cm⁻¹; 2800 - 3700 cm⁻¹: red and orange lines probe at 3550 cm⁻¹, different scanning laser intensities;

Lower frames: calculated IR intensities (km/mol) and structures of different isomers; values are ΔE / (kJ/mol); all identified isomers with up to ΔE ≤ 25 kJ/mol above the most stable conformer are considered; scaling factor 0.97.

The calculated pattern of structure C shows best agreement, but also structures A and E could be conducive to the experimental spectrum. A distinction between the three structures in the area of the C=O stretching vibration is challenging, as the laser intensity of the OPO/OPA is rather low below 1700 cm⁻¹.

IR-MPD spectra and calculated IR intensities of Aspartame H$^+$; cc-pVQZ; DFT: B3LYP (g03)

Fig. S B8: Aspartame H$^+$; cc-pVQZ; DFT: B3LYP:

Topmost frame: Fragmentation efficiency of IR-MPD spectra; blue and black dashed lines: one color IR-MPD spectra (FEL CLIO, Paris); blue, black and purple solid lines: one color IR-MPD spectra (blue and black at different laser intensities) (OPO/OPA, KL); red and orange solid lines: two color IR-MPD spectra (OPO/OPA, KL): 1100 - 1700 cm^{-1}: red line probe at 3550 cm^{-1}, orange line probe at 3360 cm^{-1}; 2800 - 3700 cm^{-1}: red and orange lines probe at 3550 cm^{-1}, different scanning laser intensities;

Lower frames: calculated IR intensities (km/mol) and structures of different isomers; values are ΔE / (kJ/mol); all identified isomers with up to ΔE ≤ 25 kJ/mol above the most stable conformer are considered; scaling factor 0.97.

The calculated pattern of structure A shows best agreement.

IR-MPD spectra and calculated IR intensities of Aspartame H^{+}; aug-cc-pVTZ; DFT: B3LYP (g03)
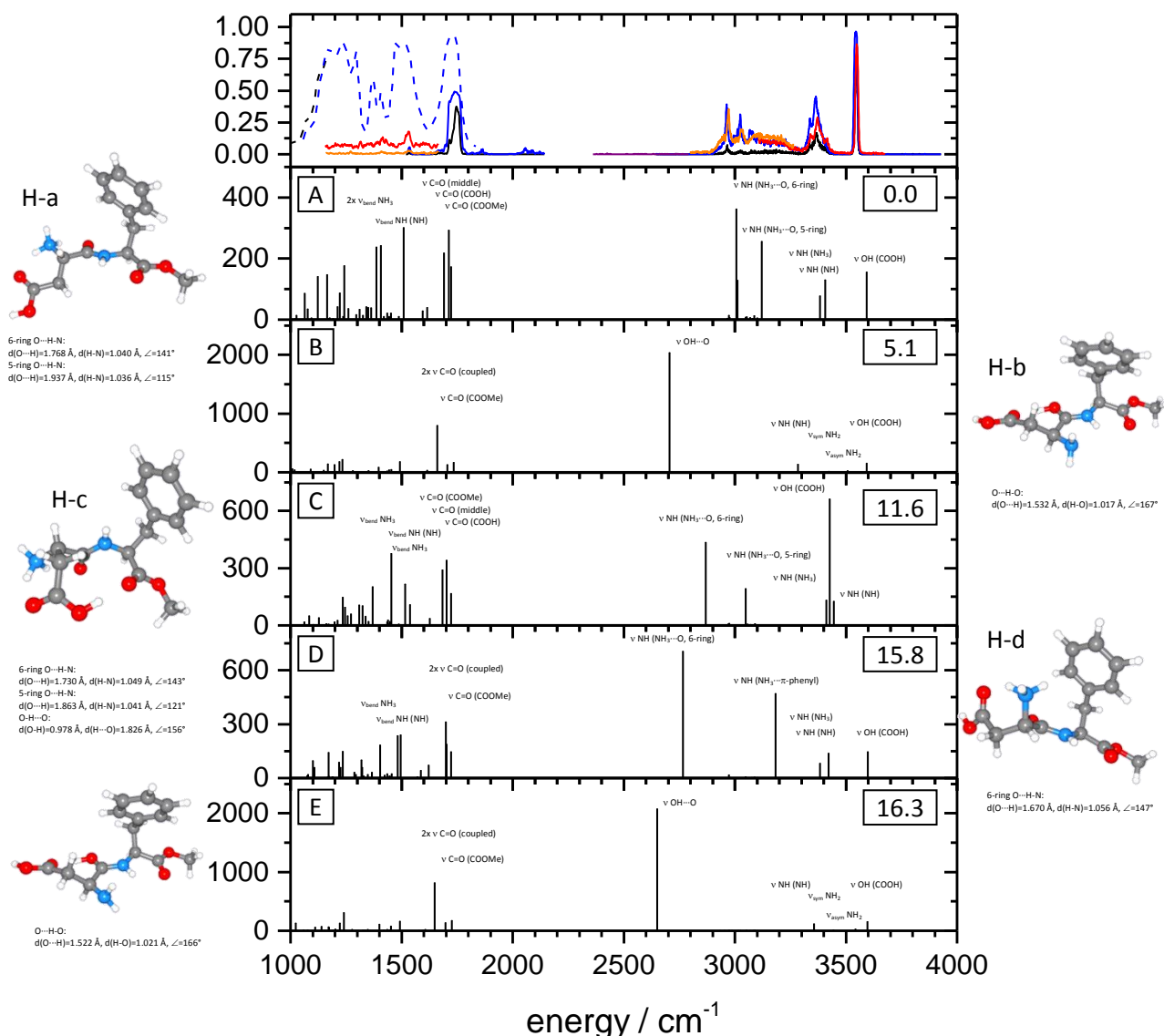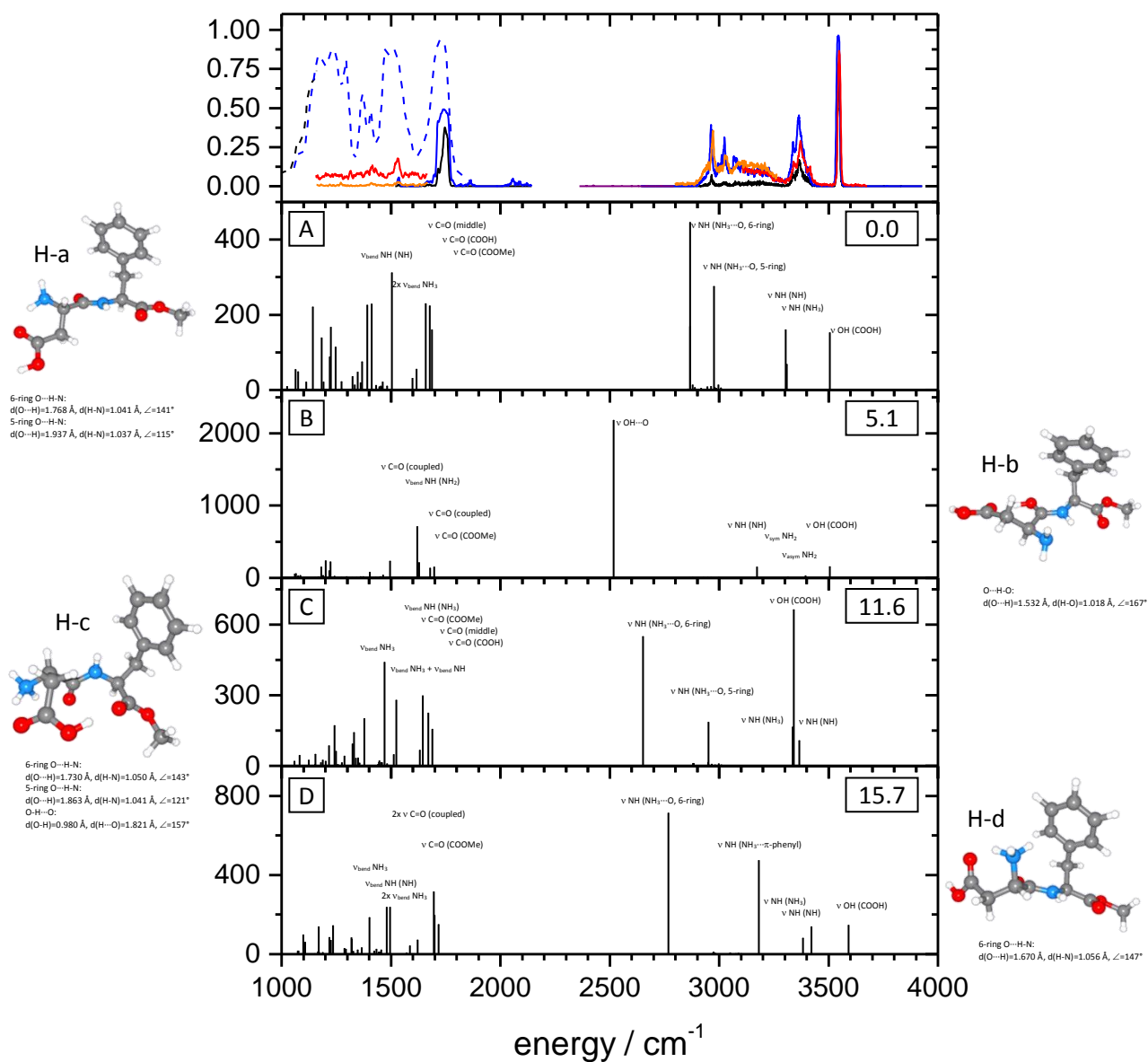

Fig. S B9: Aspartame H^{+}; aug-cc-pVTZ; DFT: B3LYP:
Topmost frame: Fragmentation efficiency of IR-MPD spectra; blue and black dashed lines: one color IR-MPD spectra (FEL CLIO, Paris); blue, black and purple solid lines: one color IR-MPD spectra (blue and black at different laser intensities) (OPO/OPA, KL); red and orange solid lines: two color IR-MPD spectra (OPO/OPA, KL): 1100 - 1700 cm^{-1}: red line probe at 3550 cm^{-1}, orange line probe at 3360 cm^{-1}; 2800 - 3700 cm^{-1}: red and orange lines probe at 3550 cm^{-1}, different scanning laser intensities;
Lower frames: calculated IR intensities (km/mol) and structures of different isomers; values are ΔE / (kJ/mol); all identified isomers with up to ΔE ≤ 25 kJ/mol above the most stable conformer are considered; scaling factor 0.97.
The calculated pattern of structure A shows best agreement.

IR-MPD spectra and calculated IR intensities of Aspartame H$^+$; cc-pVTZ; DFT: B3LYP (g03)

H-a

6-ring O···H-N:
d(O···H)=1.762 Å, d(H-N)=1.041 Å, ∠=142°
5-ring O···H-N:
d(O···H)=1.927 Å, d(H-N)=1.037 Å, ∠=116°

H-c

6-ring O···H-N:
d(O···H)=1.718 Å, d(H-N)=1.051 Å, ∠=143°
5-ring O···H-N:
d(O···H)=1.861 Å, d(H-N)=1.041 Å, ∠=121°
O-H···O:
d(O-H)=0.979 Å, d(H···O)=1.821 Å, ∠=156°

O···H-O:
d(O···H)=1.518 Å, d(H-O)=1.023 Å, ∠=166°

H-b

O···H-O:
d(O···H)=1.528 Å, d(H-O)=1.019 Å, ∠=167°

H-d

6-ring O···H-N:
d(O···H)=1.662 Å, d(H-N)=1.058 Å, ∠=148°

Fig. S B10: Aspartame H$^+$; cc-pVTZ; DFT: B3LYP:
Topmost frame: Fragmentation efficiency of IR-MPD spectra; blue and black dashed lines: one color IR-MPD spectra (FEL CLIO, Paris); blue, black and purple solid lines: one color IR-MPD spectra (blue and black at different laser intensities) (OPO/OPA, KL); red and orange solid lines: two color IR-MPD spectra (OPO/OPA, KL): 1100 - 1700 cm^{-1}: red line probe at 3550 cm^{-1}, orange line probe at 3360 cm^{-1}; 2800 - 3700 cm^{-1}: red and orange lines probe at 3550 cm^{-1}, different scanning laser intensities;
Lower frames: calculated IR intensities (km/mol) and structures of different isomers; values are ΔE / (kJ/mol); all identified isomers with up to ΔE ≤ 25 kJ/mol above the most stable conformer are considered; scaling factor 0.97.
The calculated pattern of structure A shows best agreement.

IR-MPD spectra and calculated IR intensities of Aspartame H$^+$; aug-cc-pVDZ; DFT: B3LYP (g03)
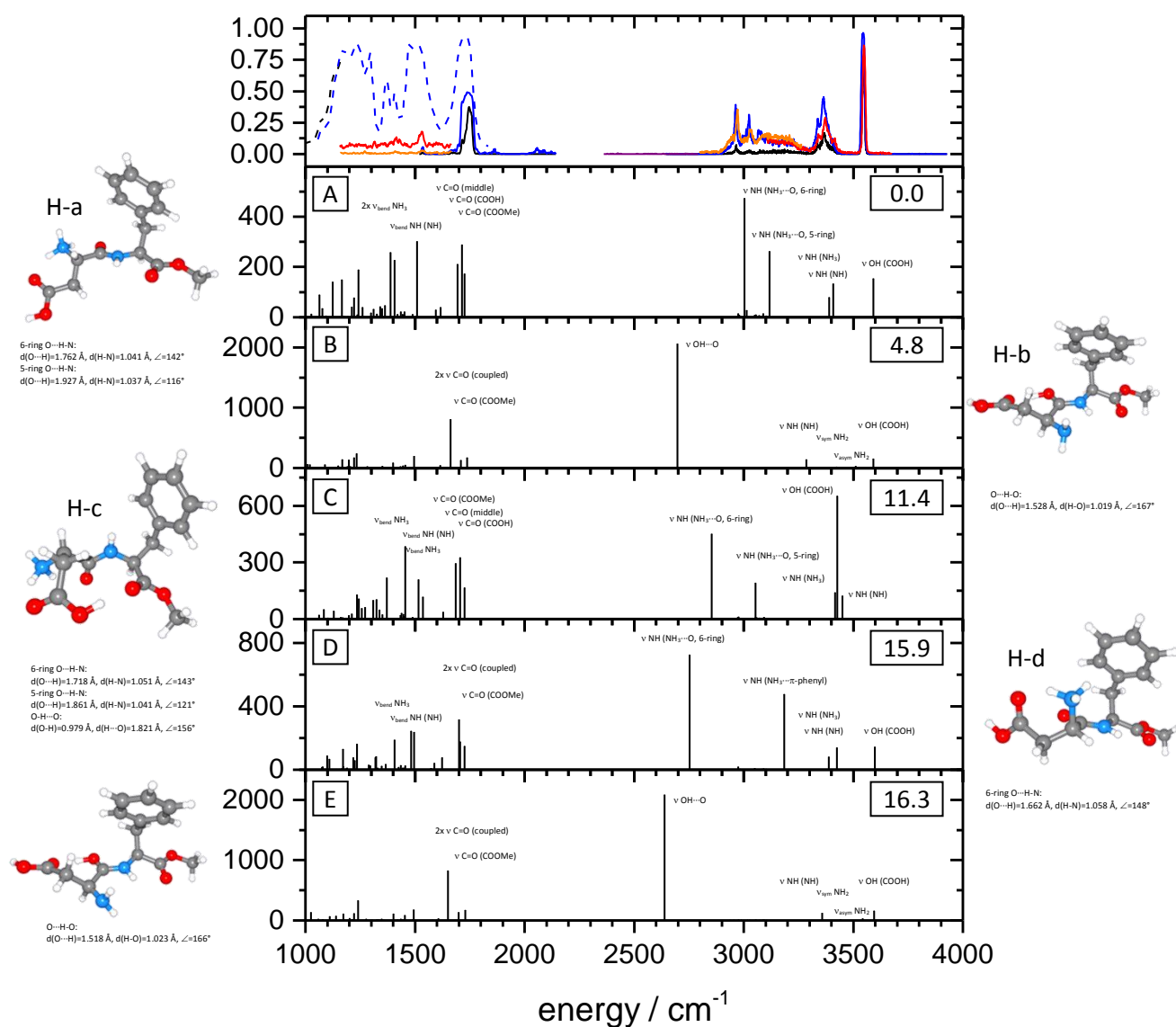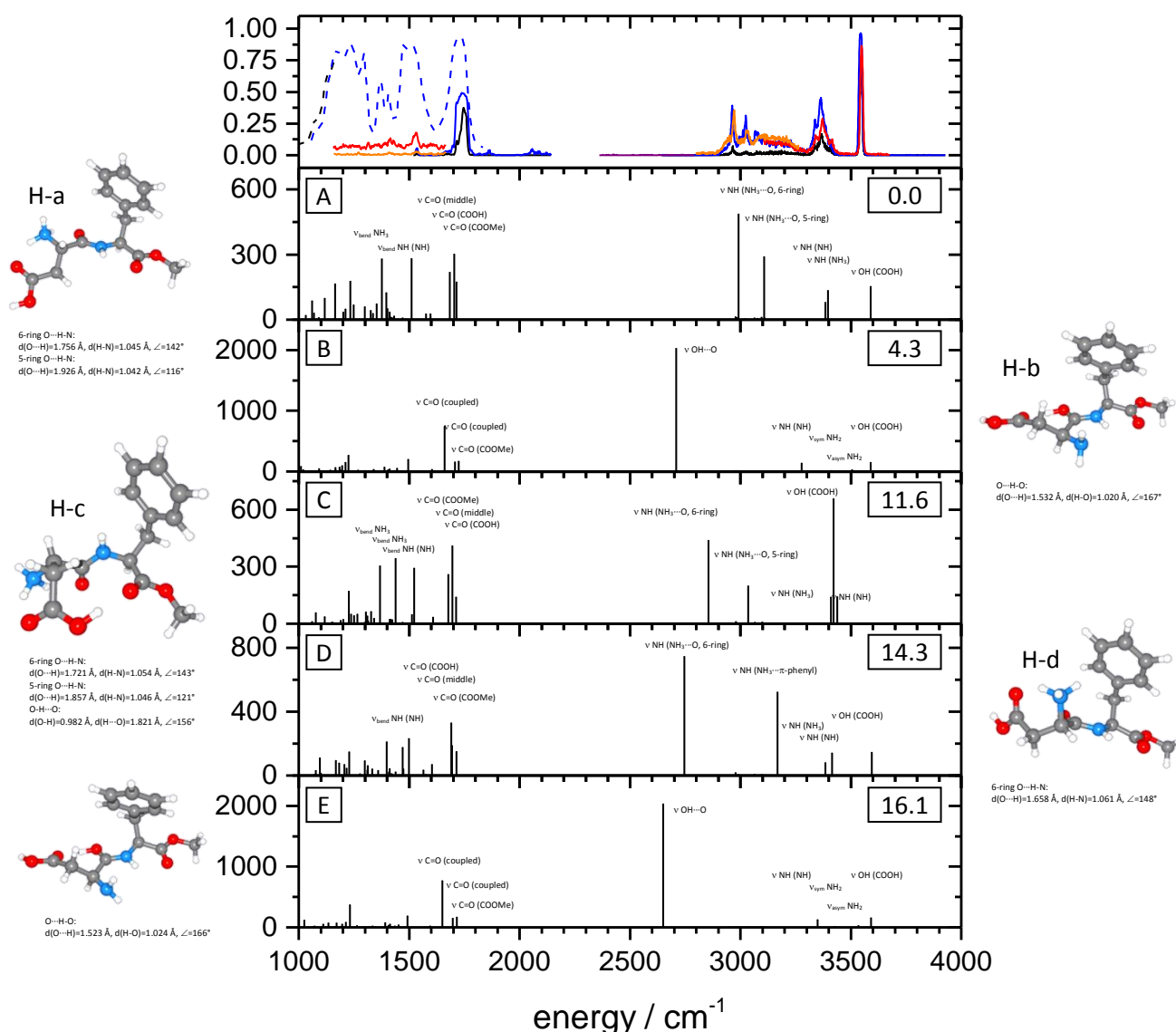

Fig. S B11: Aspartame H$^+$; aug-cc-pVDZ; DFT: B3LYP:
Topmost frame: Fragmentation efficiency of IR-MPD spectra; blue and black dashed lines: one color IR-MPD spectra (FEL CLIO, Paris); blue, black and purple solid lines: one color IR-MPD spectra (blue and black at different laser intensities) (OPO/OPA, KL); red and orange solid lines: two color IR-MPD spectra (OPO/OPA, KL): 1100 - 1700 cm^{-1}: red line probe at 3550 cm^{-1}, orange line probe at 3360 cm^{-1}; 2800 - 3700 cm^{-1}: red and orange lines probe at 3550 cm^{-1}, different scanning laser intensities;
Lower frames: calculated IR intensities (km/mol) and structures of different isomers; values are ΔE / (kJ/mol); all identified isomers with up to ΔE ≤ 25 kJ/mol above the most stable conformer are considered; scaling factor 0.97.
The calculated pattern of structure A shows best agreement.

IR-MPD spectra and calculated IR intensities of Aspartame H⁺; cc-pVDZ; DFT: B3LYP (g03)

H-a

6-ring O···H-N:
d(O···H)=1.723 Å, d(H-N)=1.052 Å, ∠=143°
5-ring O···H-N:
d(O···H)=1.874 Å, d(H-N)=1.049 Å, ∠=118°

H-b

O···H-O:
d(O···H)=1.496 Å, d(H-O)=1.031 Å, ∠=168°

H-c

6-ring O···H-N:
d(O···H)=1.654 Å, d(H-N)=1.067 Å, ∠=145°
5-ring O···H-N:
d(O···H)=1.840 Å, d(H-N)=1.050 Å, ∠=122°
O-H···O:
d(O-H)=0.985 Å, d(H···O)=1.791 Å, ∠=156°

O···H-O:
d(O···H)=1.487 Å, d(H-O)=1.036 Å, ∠=167°

H-d

6-ring O···H-N:
d(O···H)=1.607 Å, d(H-N)=1.075 Å, ∠=149°

Fig. S B12: Aspartame H⁺; cc-pVDZ; DFT: B3LYP:

Topmost frame: Fragmentation efficiency of IR-MPD spectra; blue and black dashed lines: one color IR-MPD spectra (FEL CLIO, Paris); blue, black and purple solid lines: one color IR-MPD spectra (blue and black at different laser intensities) (OPO/OPA, KL); red and orange solid lines: two color IR-MPD spectra (OPO/OPA, KL): 1100 - 1700 cm⁻¹: red line probe at 3550 cm⁻¹, orange line probe at 3360 cm⁻¹; 2800 - 3700 cm⁻¹: red and orange lines probe at 3550 cm⁻¹, different scanning laser intensities;
Lower frames: calculated IR intensities (km/mol) and structures of different isomers; values are ΔE / (kJ/mol); all identified isomers with up to ΔE ≤ 25 kJ/mol above the most stable conformer are considered; scaling factor 0.97.
The calculated pattern of structure A shows best agreement.

IR-MPD spectra and calculated IR intensities of Aspartame H⁺; cc-pVDZ; DFT: BLYP (g03)
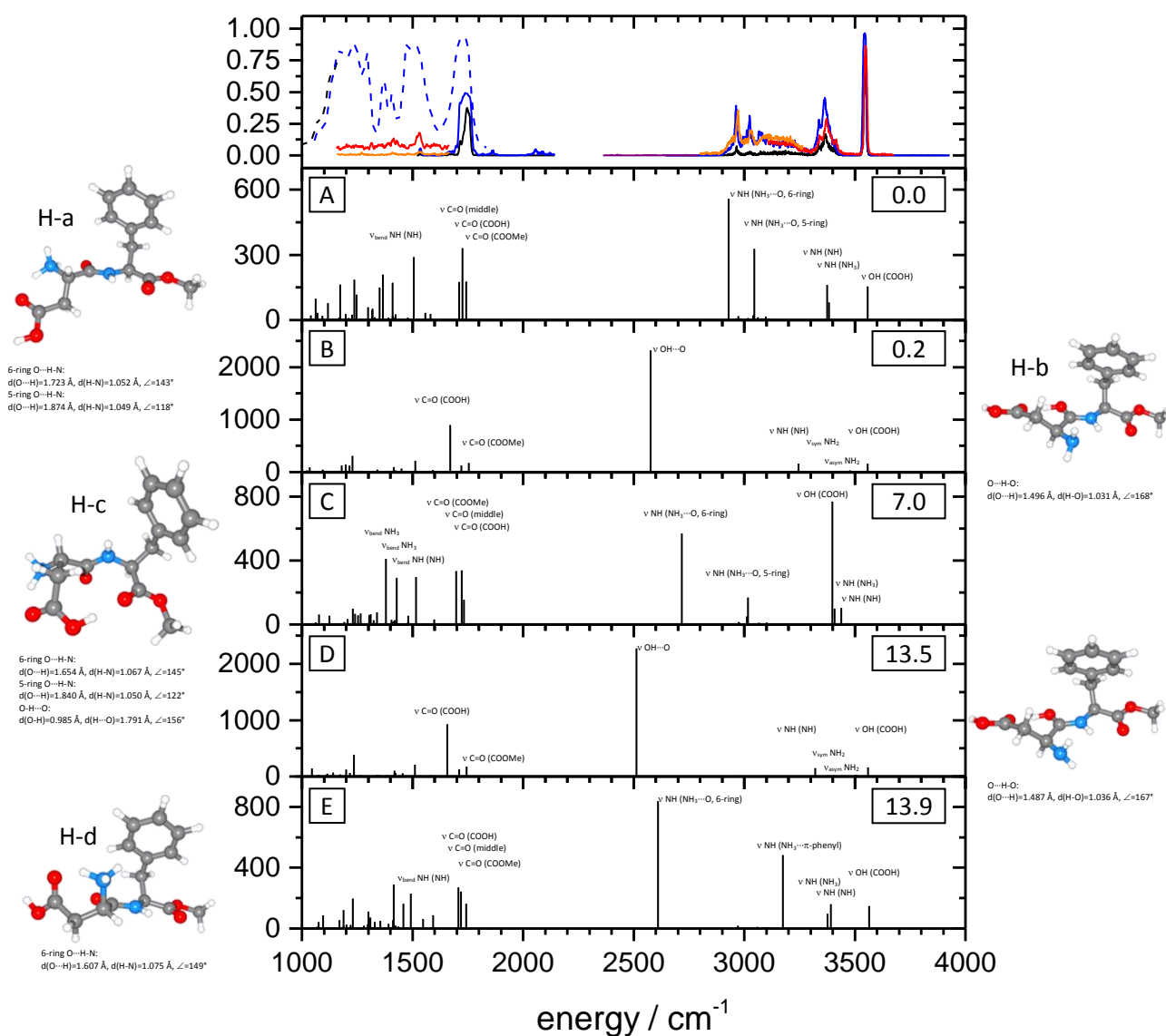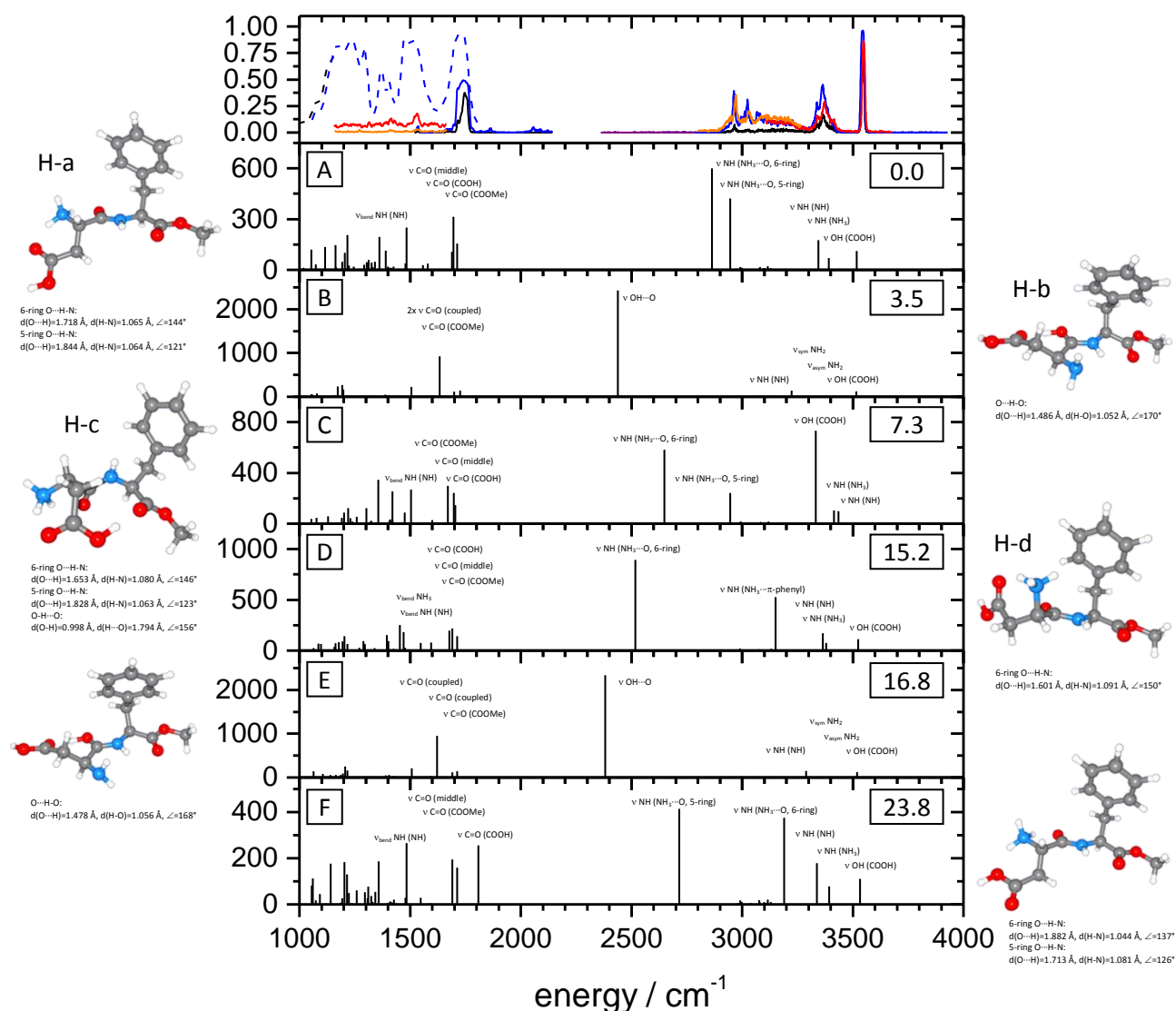

Fig. S B13: Aspartame H⁺; cc-pVDZ; DFT: BLYP:

Topmost frame: Fragmentation efficiency of IR-MPD spectra; blue and black dashed lines: one color IR-MPD spectra (FEL CLIO, Paris); blue, black and purple solid lines: one color IR-MPD spectra (blue and black at different laser intensities) (OPO/OPA, KL); red and orange solid lines: two color IR-MPD spectra (OPO/OPA, KL): 1100 - 1700 cm⁻¹: red line probe at 3550 cm⁻¹, orange line probe at 3360 cm⁻¹; 2800 - 3700 cm⁻¹: red and orange lines probe at 3550 cm⁻¹, different scanning laser intensities;

Lower frames: calculated IR intensities (km/mol) and structures of different isomers; values are ΔE / (kJ/mol); all identified isomers with up to ΔE ≤ 25 kJ/mol above the most stable conformer are considered; scaling factor 1.002.

The calculated pattern of structure A shows best agreement.

IR-MPD spectra and calculated IR intensities of Aspartame H$^+$; cc-pVDZ; DFT: BP86 (g03)
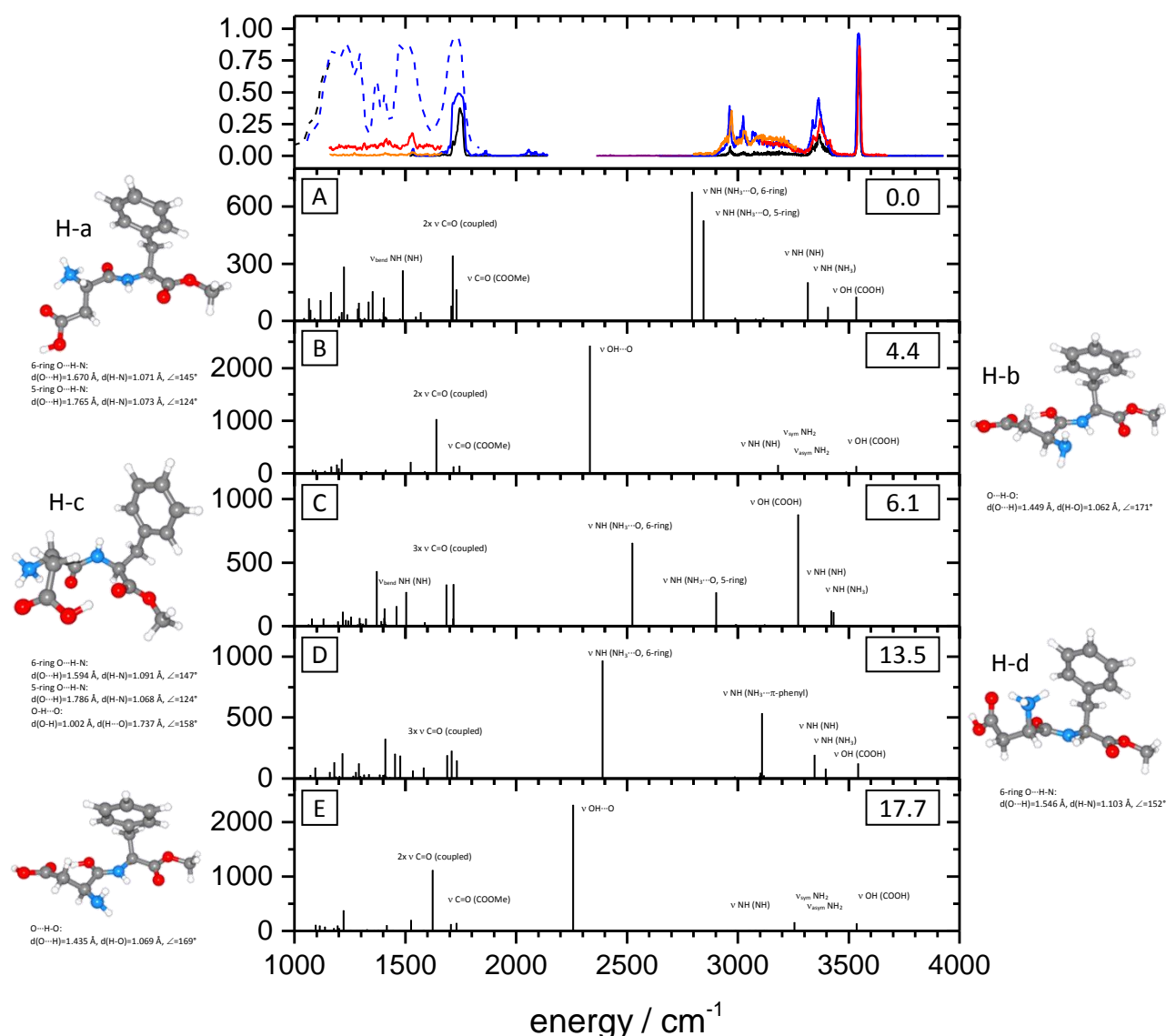

Fig. S B14: Aspartame H$^+$; cc-pVDZ; DFT: BP86:

Topmost frame: Fragmentation efficiency of IR-MPD spectra; blue and black dashed lines: one color IR-MPD spectra (FEL CLIO, Paris); blue, black and purple solid lines: one color IR-MPD spectra (blue and black at different laser intensities) (OPO/OPA, KL); red and orange solid lines: two color IR-MPD spectra (OPO/OPA, KL): 1100 - 1700 cm^{-1}: red line probe at 3550 cm^{-1}, orange line probe at 3360 cm^{-1}; 2800 - 3700 cm^{-1}: red and orange lines probe at 3550 cm^{-1}, different scanning laser intensities;

Lower frames: calculated IR intensities (km/mol) and structures of different isomers; values are ΔE / (kJ/mol); all identified isomers with up to $\Delta E \leq 25$ kJ/mol above the most stable conformer are considered; scaling factor 1.00.

The calculated pattern of structure A shows some agreement to the experiment, but fails in the prediction of some of the NH stretching bands.

IR-MPD spectra and calculated IR intensities of Aspartame H$^+$; cc-pVDZ; DFT: PBE0 (g03)

H-a

6-ring O···H-N:
d(O···H)=1.721 Å, d(H-N)=1.050 Å, ∠=142°
5-ring O···H-N:
d(O···H)=2.087 Å, d(H-N)=1.036 Å, ∠=111°

H-b

O···H-O:
d(O···H)=1.467 Å, d(H-O)=1.034 Å, ∠=169°

H-d

6-ring O···H-N:
d(O···H)=1.572 Å, d(H-N)=1.078 Å, ∠=151°

6-ring O···H-N:
d(O···H)=1.692 Å, d(H-N)=1.053 Å, ∠=143°
5-ring O···H-N:
d(O···H)=1.832 Å, d(H-N)=1.050 Å, ∠=119°

H-c

6-ring O···H-N:
d(O···H)=1.610 Å, d(H-N)=1.071 Å, ∠=146°
5-ring O···H-N:
d(O···H)=1.813 Å, d(H-N)=1.050 Å, ∠=122°
O-H···O:
d(O-H)=0.983 Å, d(H···O)=1.768 Å, ∠=156°

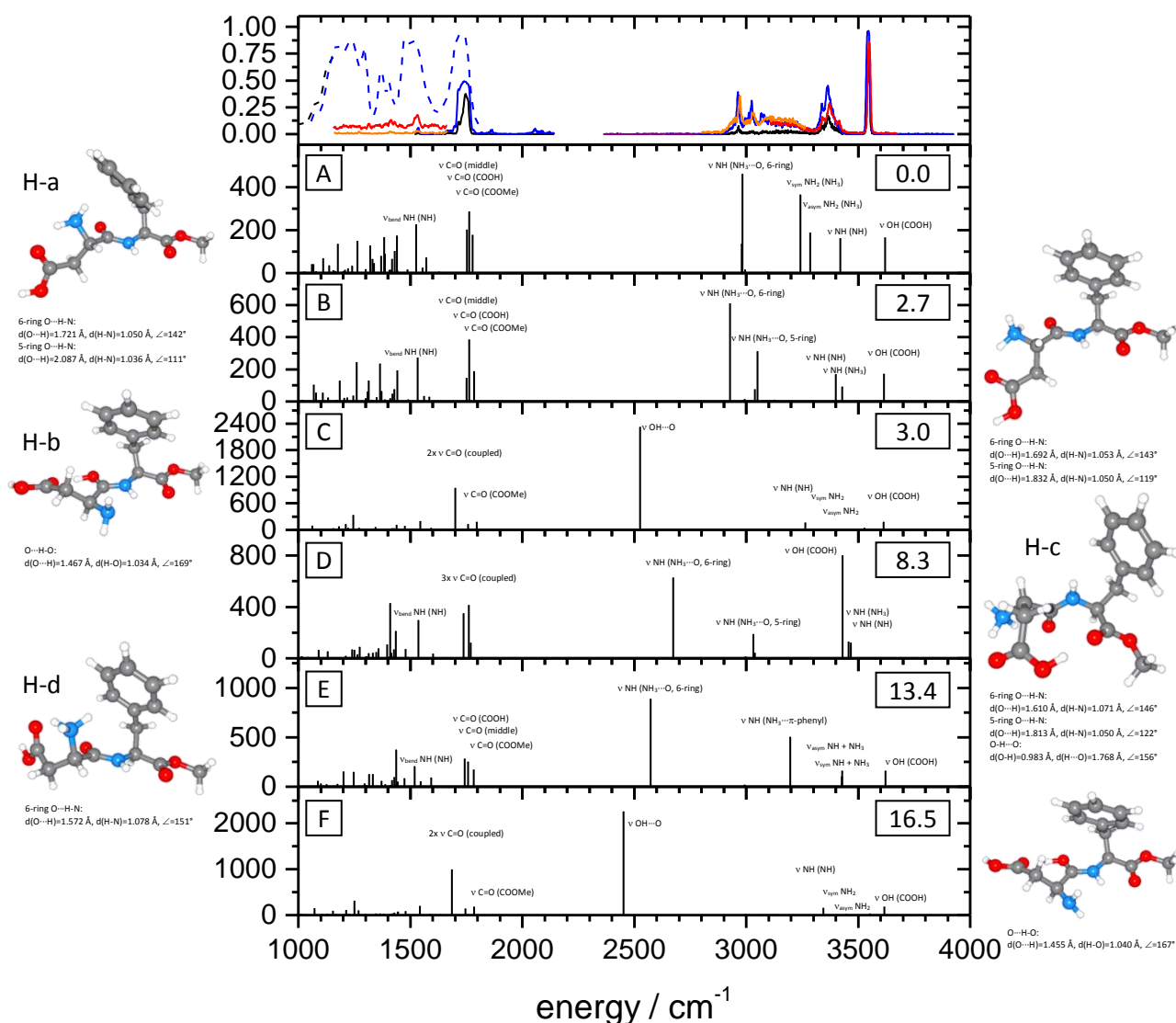O···H-O:
d(O···H)=1.455 Å, d(H-O)=1.040 Å, ∠=167°

Fig. S B15: Aspartame H$^+$; cc-pVDZ; DFT: PBE0:

Topmost frame: Fragmentation efficiency of IR-MPD spectra; blue and black dashed lines: one color IR-MPD spectra (FEL CLIO, Paris); blue, black and purple solid lines: one color IR-MPD spectra (blue and black at different laser intensities) (OPO/OPA, KL); red and orange solid lines: two color IR-MPD spectra (OPO/OPA, KL): 1100 - 1700 cm^{-1}: red line probe at 3550 cm^{-1}, orange line probe at 3360 cm^{-1}; 2800 - 3700 cm^{-1}: red and orange lines probe at 3550 cm^{-1}, different scanning laser intensities;

Lower frames: calculated IR intensities (km/mol) and structures of different isomers; values are ΔE / (kJ/mol); all identified isomers with up to ΔE ≤ 25 kJ/mol above the most stable conformer are considered; scaling factor 0.97.

The calculated pattern of structure B shows best agreement, but also structure A could be conducive to the experimental spectrum. A distinction between the two structures in the area of the C=O stretching vibration is challenging, as the laser intensity of the OPO/OPA is rather low below 1700 cm^{-1}.

IR-MPD spectra and calculated IR intensities of Aspartame H$^+$; cc-pVDZ; DFT: Becke97_1 (g03)

Fig. S B16: Aspartame H$^+$; cc-pVDZ; DFT: Becke97_1:

Topmost frame: Fragmentation efficiency of IR-MPD spectra; blue and black dashed lines: one color IR-MPD spectra (FEL CLIO, Paris); blue, black and purple solid lines: one color IR-MPD spectra (blue and black at different laser intensities) (OPO/OPA, KL); red and orange solid lines: two color IR-MPD spectra (OPO/OPA, KL): 1100 - 1700 cm^{-1}: red line probe at 3550 cm^{-1}, orange line probe at 3360 cm^{-1}; 2800 - 3700 cm^{-1}: red and orange lines probe at 3550 cm^{-1}, different scanning laser intensities;

Lower frames: calculated IR intensities (km/mol) and structures of different isomers; values are ΔE / (kJ/mol); all identified isomers with up to ΔE ≤ 25 kJ/mol above the most stable conformer are considered; scaling factor 0.97.

The calculated pattern of structure A shows best agreement.

IR-MPD spectra and calculated IR intensities of Aspartame H$^+$; cc-pVDZ; DFT: Becke97_2 (g03)
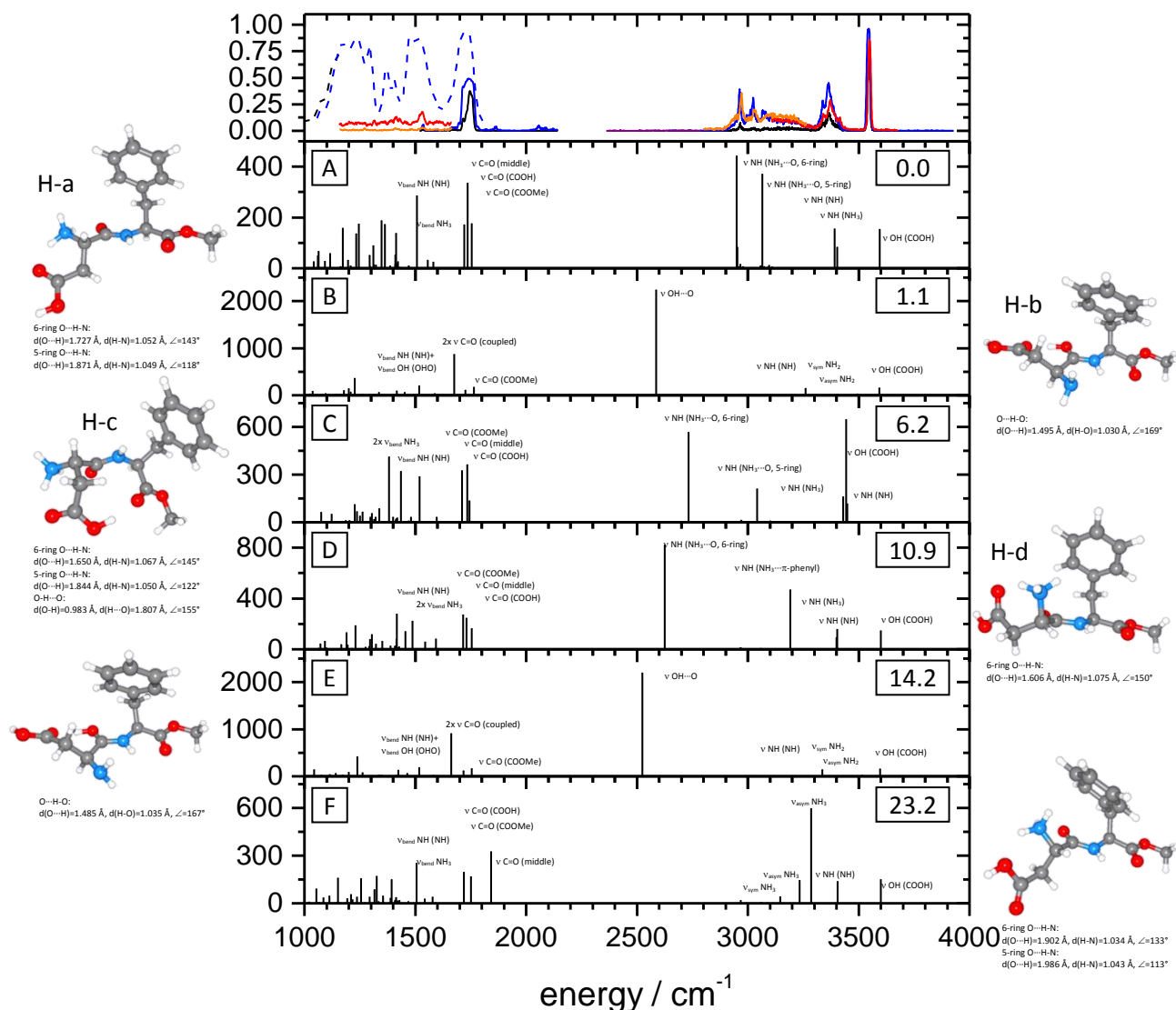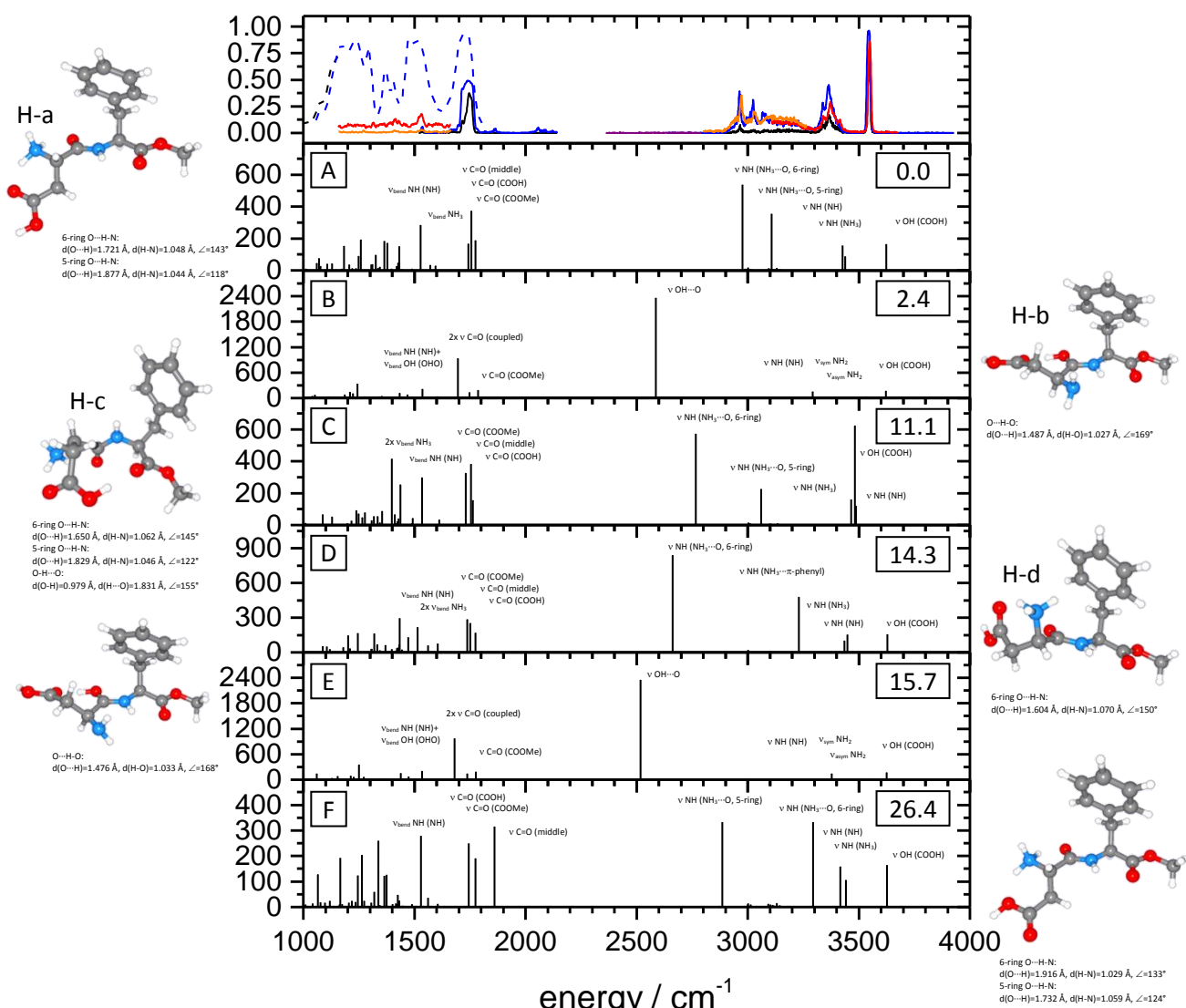

Fig. S B17: Aspartame H$^+$; cc-pVDZ; DFT: Becke97_2:

Topmost frame: Fragmentation efficiency of IR-MPD spectra; blue and black dashed lines: one color IR-MPD spectra (FEL CLIO, Paris); blue, black and purple solid lines: one color IR-MPD spectra (blue and black at different laser intensities) (OPO/OPA, KL); red and orange solid lines: two color IR-MPD spectra (OPO/OPA, KL): 1100 - 1700 cm^{-1}: red line probe at 3550 cm^{-1}, orange line probe at 3360 cm^{-1}; 2800 - 3700 cm^{-1}: red and orange lines probe at 3550 cm^{-1}, different scanning laser intensities;

Lower frames: calculated IR intensities (km/mol) and structures of different isomers; values are ΔE / (kJ/mol); all identified isomers with up to ΔE ≤ 26.4 kJ/mol above the most stable conformer are considered; scaling factor 0.97.

The calculated pattern of structure A shows best agreement.

IR-MPD spectra and calculated IR intensities of Aspartame Li$^+$; cc-pVDZ; MP2 (g03)

Li-a

Li:
d(Li···NH$_2$)=2.100 Å, d(Li···O=C$_{COOH}$)=1.995 Å,
d(Li···O=C$_{middle}$)=1.936 Å, d(Li···OH$_{COOH}$)=3.741 Å
O-H···O:
d(O-H)=0.977 Å, d(H···O)=1.955 Å, ∠=136°

Li-b

Li:
d(Li···O=C$_{COOH}$)=1.929 Å, d(Li···O=C$_{middle}$)=1.982 Å,
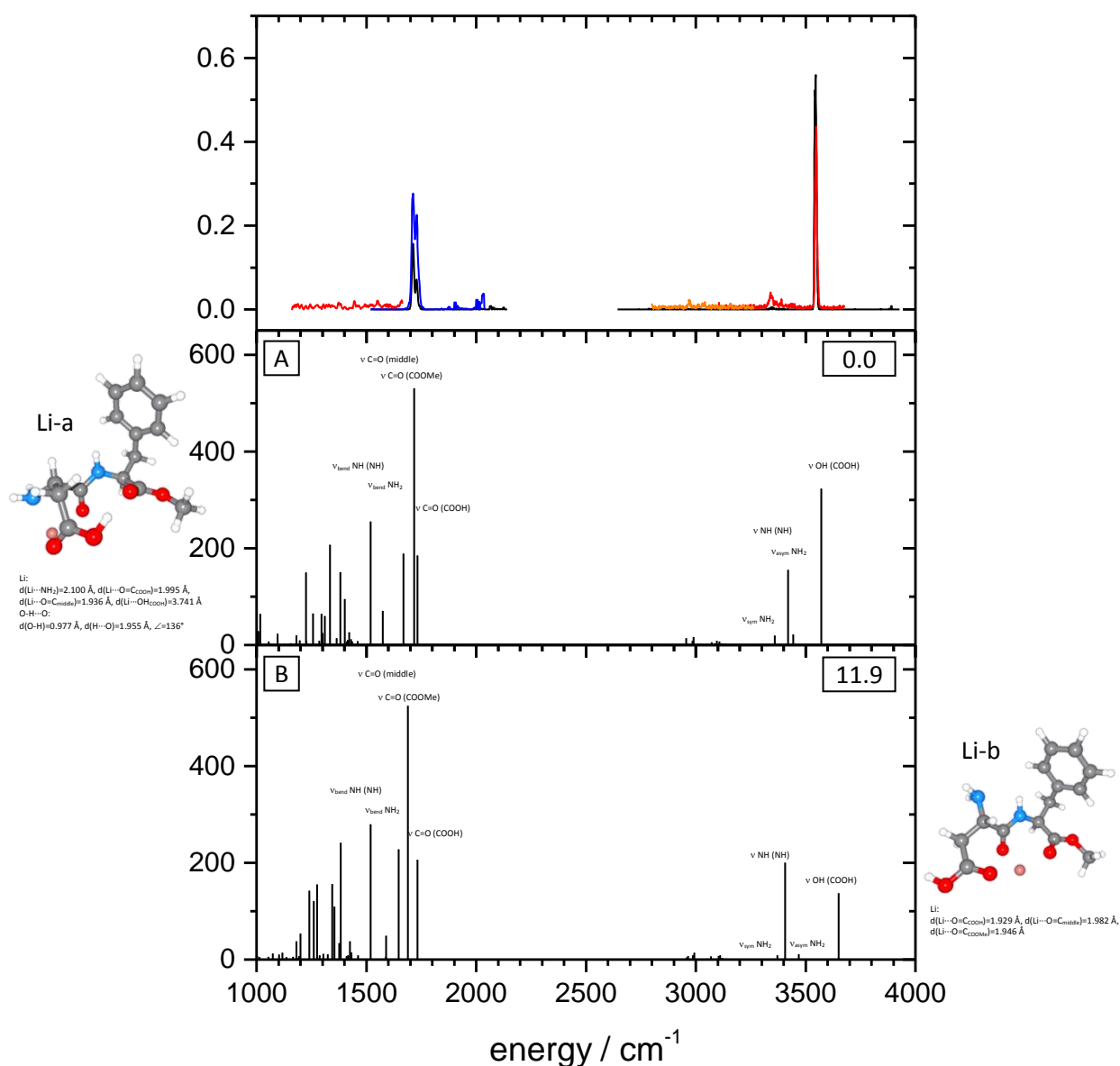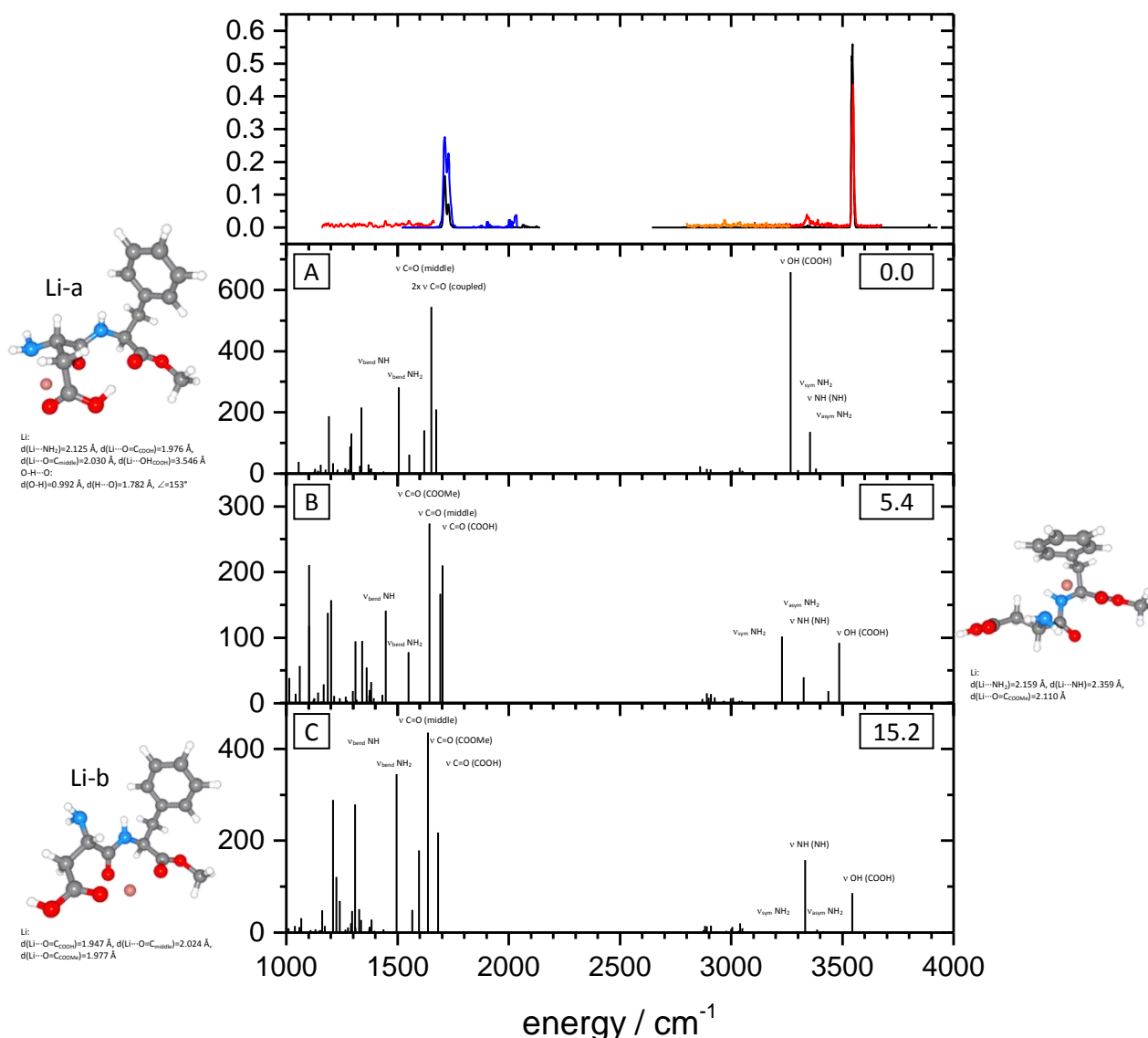d(Li···O=C$_{COOMe}$)=1.946 Å

Fig. S B18: Aspartame Li$^+$; cc-pVDZ; MP2:

Topmost frame: Fragmentation efficiency of IR-MPD spectra; blue and black solid lines: one color IR-MPD spectra, different laser intensities (OPO/OPA, KL); red and orange solid lines: two color IR-MPD spectra (OPO/OPA, KL): 1100 - 1700 cm^{-1}: red line probe at 3545 cm^{-1}; 2800 - 3700 cm^{-1}: red and orange lines probe at 3545 cm^{-1}, different scanning laser intensities;

Lower frames: calculated IR intensities (km/mol) and structures of different isomers; values are ΔE / (kJ/mol); all identified isomers with up to ΔE ≤ 25 kJ/mol above the most stable conformer are considered; scaling factor 0.96.

The calculated pattern of structure A shows best agreement, but also structure B could be conducive to the experimental spectrum. A distinction between the two structures in the area of the C=O stretching vibration is challenging, as the laser intensity of the OPO/OPA is rather low below 1700 cm^{-1}. In both assignments the experimental fragmentation efficiency of the OH stretching vibration is much higher than the one of the NH stretching vibrations.

IR-MPD spectra and calculated IR intensities of Aspartame Li$^+$; cc-pVDZ; DFT: B97D (g09)

Fig. S B19: Aspartame Li$^+$; cc-pVDZ; DFT: B97D:

Topmost frame: Fragmentation efficiency of IR-MPD spectra; blue and black solid lines: one color IR-MPD spectra, different laser intensities (OPO/OPA, KL); red and orange solid lines: two color IR-MPD spectra (OPO/OPA, KL): 1100 - 1700 cm^{-1}: red line probe at 3545 cm^{-1}; 2800 - 3700 cm^{-1}: red and orange lines probe at 3545 cm^{-1}, different scanning laser intensities;

Lower frames: calculated IR intensities (km/mol) and structures of different isomers; values are ΔE / (kJ/mol); all identified isomers with up to $\Delta E \leq 25$ kJ/mol above the most stable conformer are considered; scaling factor 0.97.

The calculated pattern of structure C shows best agreement. In that assignment the experimental fragmentation efficiency of the OH stretching vibration is much higher than the one of the NH stretching vibrations.

IR-MPD spectra and calculated IR intensities of Aspartame Li$^+$; cc-pVDZ; DFT: B3LYP (g03)
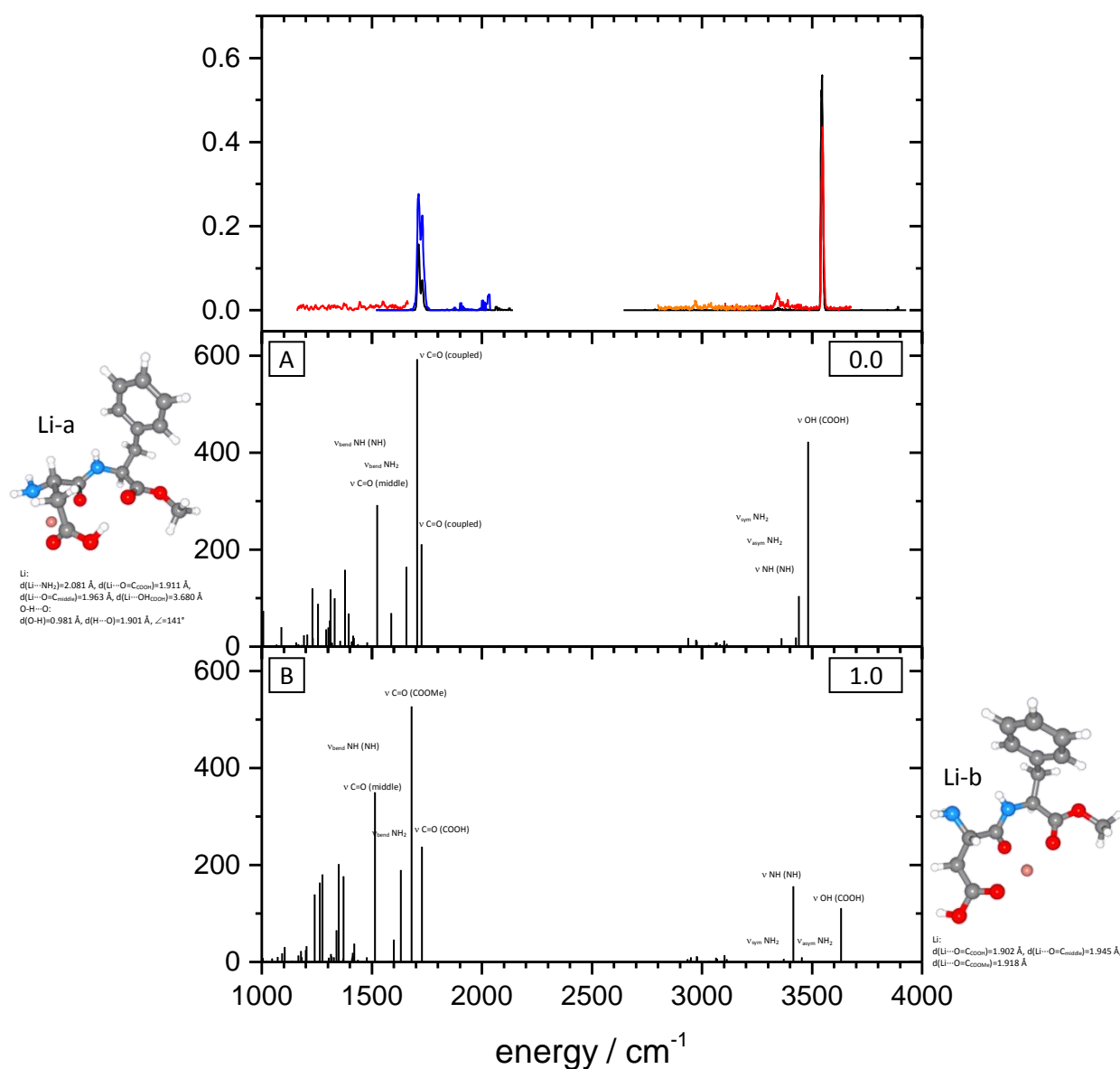

Fig. S B20: Aspartame Li$^+$; cc-pVDZ; DFT: B3LYP:

Topmost frame: Fragmentation efficiency of IR-MPD spectra; blue and black solid lines: one color IR-MPD spectra, different laser intensities (OPO/OPA, KL); red and orange solid lines: two color IR-MPD spectra (OPO/OPA, KL): 1100 - 1700 cm^{-1}: red line probe at 3545 cm^{-1}; 2800 - 3700 cm^{-1}: red and orange lines probe at 3545 cm^{-1}, different scanning laser intensities;

Lower frames: calculated IR intensities (km/mol) and structures of different isomers; values are ΔE / (kJ/mol); all identified isomers with up to ΔE ≤ 25 kJ/mol above the most stable conformer are considered; scaling factor 0.97.

The calculated pattern of structure B shows best agreement, although the calculated OH and NH stretching vibrations are blue shifted, but also structure A could be conducive to the experimental spectrum. A distinction between the two structures in the area of the C=O stretching vibration is challenging, as the laser intensity of the OPO/OPA is rather low below 1700 cm^{-1}. In both assignments the experimental fragmentation efficiency of the OH stretching vibration is much higher than the one of the NH stretching vibrations.

IR-MPD spectra and calculated IR intensities of Aspartame Na$^+$; cc-pVDZ; MP2 (g03)

Fig. S B21: Aspartame Na$^+$; cc-pVDZ; MP2:

Topmost frame: Fragmentation efficiency of IR-MPD spectra; blue and black solid lines: one color IR-MPD spectra, different laser intensities (OPO/OPA, KL); red and orange solid lines: two color IR-MPD spectra (OPO/OPA, KL): 1100 - 1700 cm^{-1}: red line probe at 3550 cm^{-1}; 2800 - 3700 cm^{-1}: red and orange lines probe at 3550 cm^{-1}, different scanning laser intensities;

Lower frames: calculated IR intensities (km/mol) and structures of different isomers; values are ΔE / (kJ/mol); all identified isomers with up to $\Delta E \leq 25$ kJ/mol above the most stable conformer are considered; scaling factor 0.96.

The calculated pattern of structure B shows best agreement, although the calculated OH and NH stretching vibrations are blue shifted. In that assignment the experimental fragmentation efficiency of the OH stretching vibration is much higher than the one of the NH stretching vibrations.
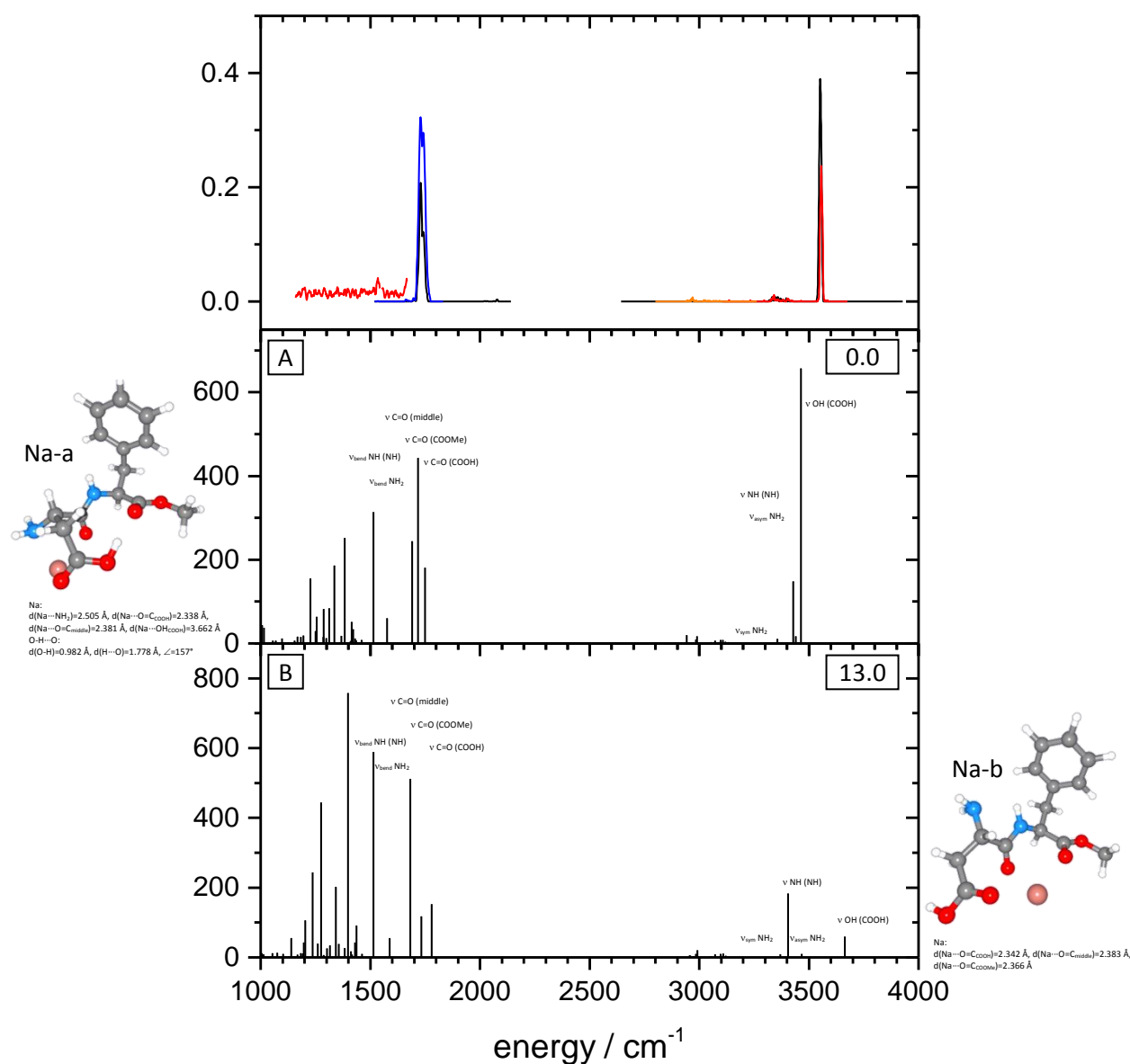
IR-MPD spectra and calculated IR intensities of Aspartame Na^{+}; cc-pVDZ; DFT: B97D (g09)
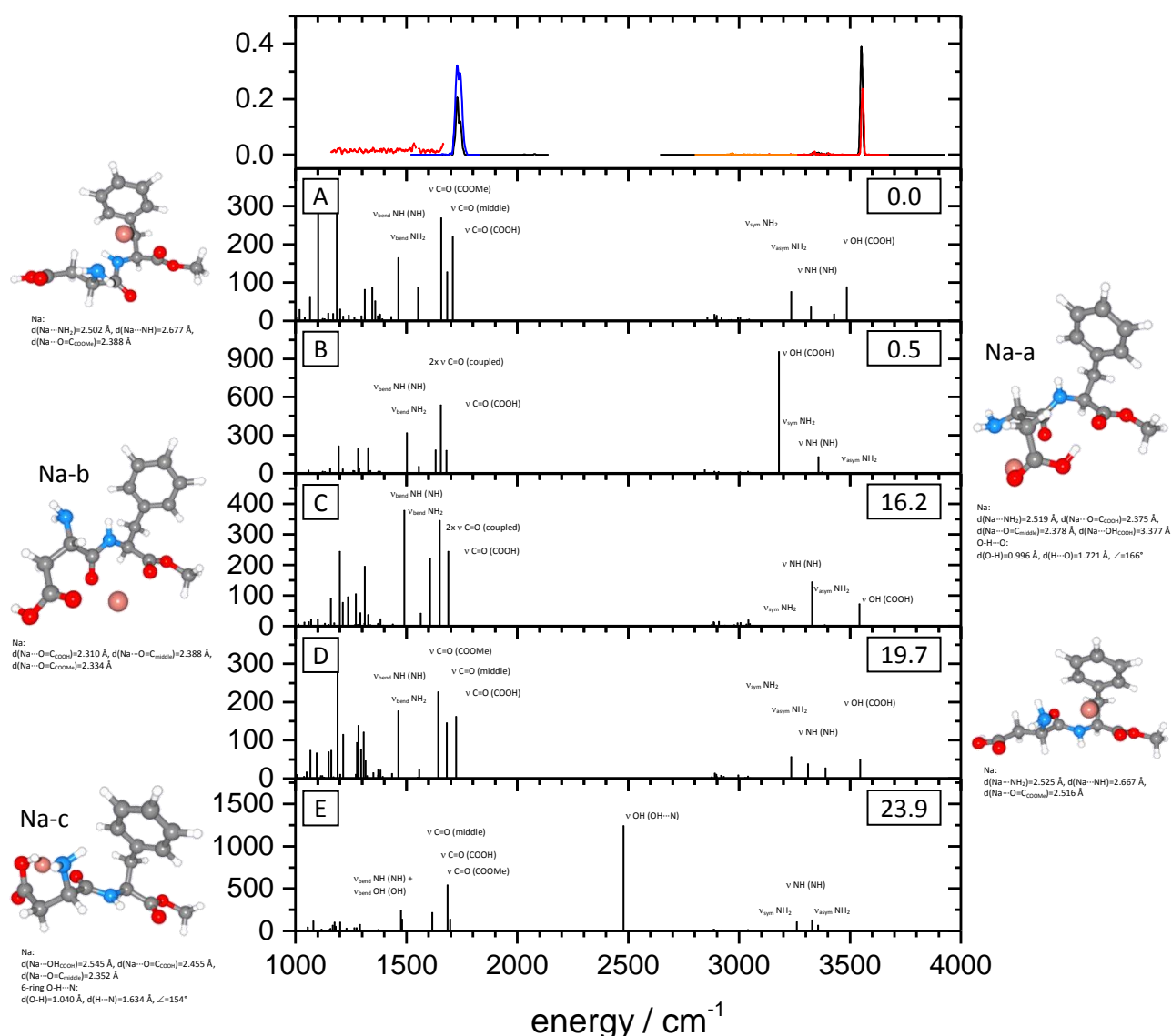

Fig. S B22: Aspartame Na^{+}; cc-pVDZ; DFT: B97D:

Topmost frame: Fragmentation efficiency of IR-MPD spectra; blue and black solid lines: one color IR-MPD spectra, different laser intensities (OPO/OPA, KL); red and orange solid lines: two color IR-MPD spectra (OPO/OPA, KL): 1100 - 1700 cm^{-1}: red line probe at 3550 cm^{-1}; 2800 - 3700 cm^{-1}: red and orange lines probe at 3550 cm^{-1}, different scanning laser intensities;

Lower frames: calculated IR intensities (km/mol) and structures of different isomers; values are ΔE / (kJ/mol); all identified isomers with up to ΔE ≤ 25 kJ/mol above the most stable conformer are considered; scaling factor 0.97.

The calculated pattern of structure C shows best agreement, but also structure D could be conducive to the experimental spectrum. A distinction between the two structures in the area of the C=O stretching vibration is challenging, as the laser intensity of the OPO/OPA is rather low below 1700 cm^{-1}. In both assignments the experimental fragmentation efficiency of the OH stretching vibration is much higher than the one of the NH stretching vibrations.

IR-MPD spectra and calculated IR intensities of Aspartame Na^{+}; cc-pVDZ; DFT: B3LYP (g03)

Na-a

Na:
d(Na···NH₂)=2.457 Å, d(Na···O=C_COOH)=2.245 Å,
d(Na···O=C_middle)=2.309 Å, d(Na···OH_COOH)=3.725 Å
O-H···O:
d(O-H)=0.985 Å, d(H···O)=1.782 Å, ∠=155°

Na-b

Na:
d(Na···O=C_COOH)=2.240 Å, d(Na···O=C_middle)=2.287 Å,
d(Na···O=C_COOMe)=2.259 Å

Na:
d(Na···NH₂)=2.467 Å, d(Na···O=C_COOH)=2.228 Å,
d(Na···O=C_middle)=2.235 Å

Na-c

Na:
d(Na···OH_COOH)=2.490 Å, d(Na···O=C_COOH)=2.325 Å,
d(Na···O=C_middle)=2.252 Å
6-ring O-H···N:
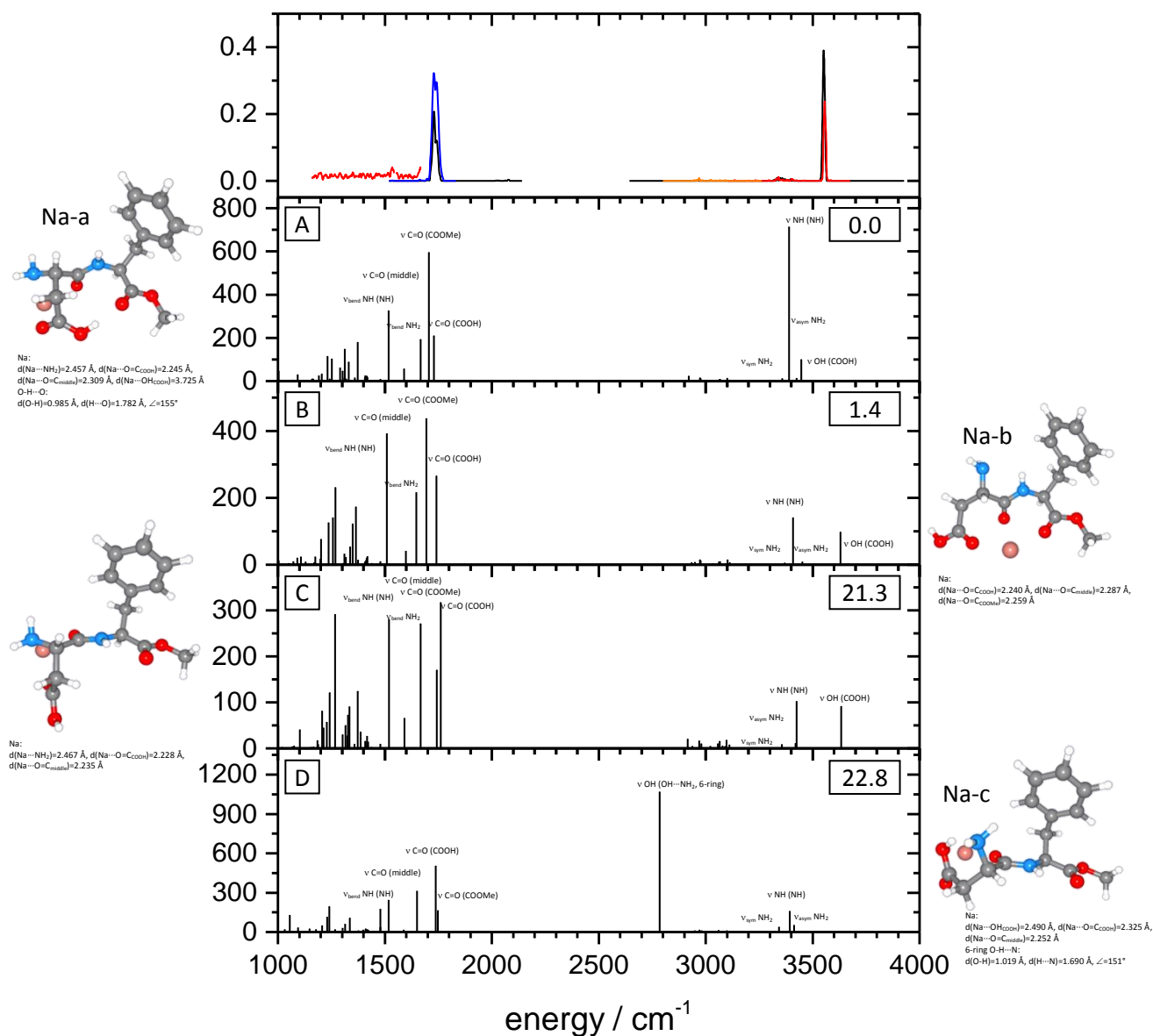d(O-H)=1.019 Å, d(H···N)=1.690 Å, ∠=151°

Fig. S B23: Aspartame Na^{+}; cc-pVDZ; DFT: B3LYP:

Topmost frame: Fragmentation efficiency of IR-MPD spectra; blue and black solid lines: one color IR-MPD spectra, different laser intensities (OPO/OPA, KL); red and orange solid lines: two color IR-MPD spectra (OPO/OPA, KL): 1100 - 1700 cm^{-1}: red line probe at 3550 cm^{-1}; 2800 - 3700 cm^{-1}: red and orange lines probe at 3550 cm^{-1}, different scanning laser intensities;

Lower frames: calculated IR intensities (km/mol) and structures of different isomers; values are ΔE / (kJ/mol); all identified isomers with up to ΔE ≤ 25 kJ/mol above the most stable conformer are considered; scaling factor 0.97.

The calculated patterns of structures B and C show best agreement, although the calculated OH and NH stretching vibrations are blue shifted. A distinction between the two structures in the area of the C=O stretching vibration is challenging, as the laser intensity of the OPO/OPA is rather low below 1700 cm^{-1}. In both assignments the experimental fragmentation efficiency of the OH stretching vibration is much higher than the one of the NH stretching vibrations.

IR-MPD spectra and calculated IR intensities of Aspartame K⁺;
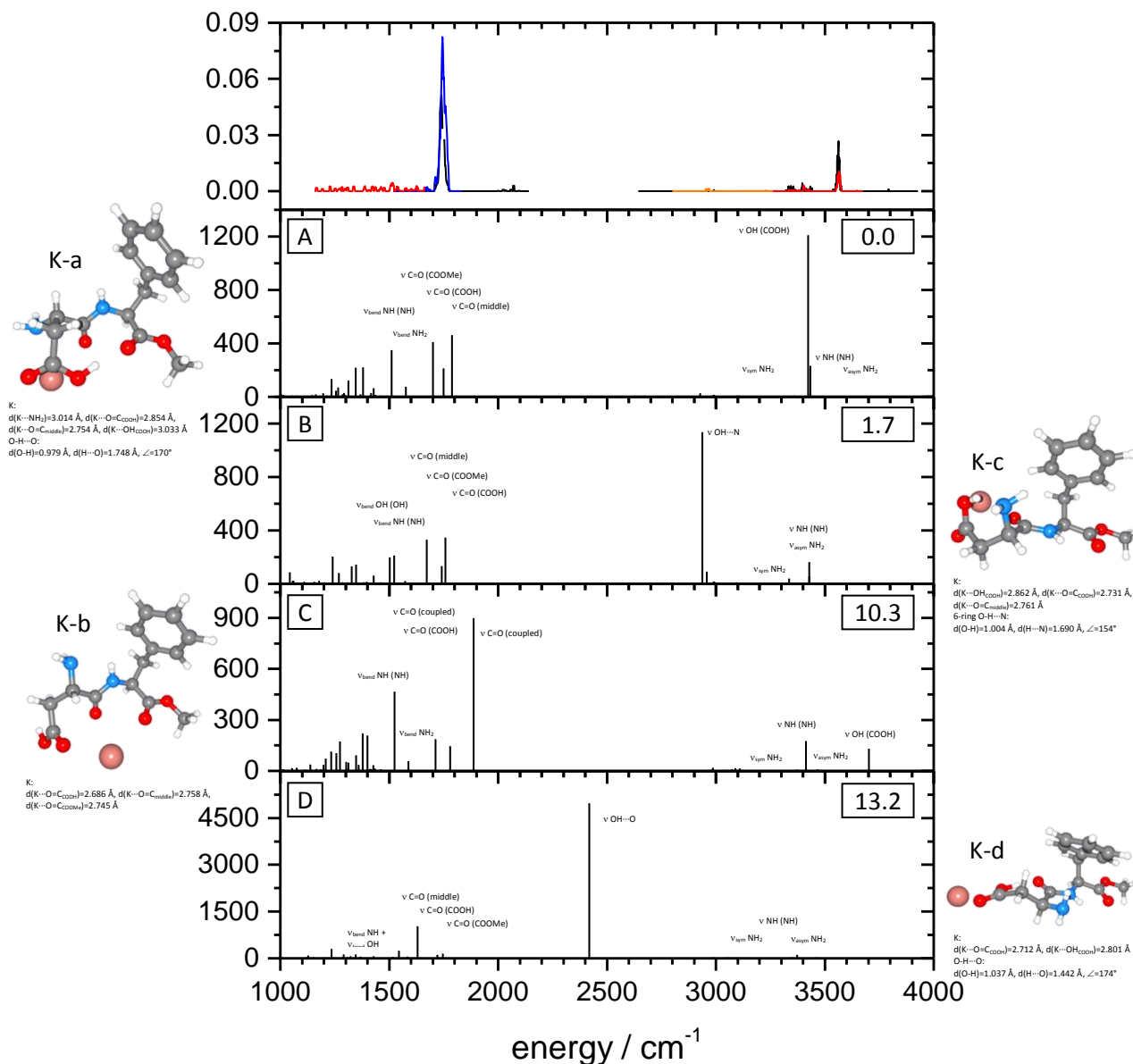**cc-pVDZ / Stuttgart RSC 1997; MP2 (g03)**

Fig. S B24: Aspartame K⁺; cc-pVDZ (C, H, N, O), Stuttgart RSC 1997 (K); MP2:

Topmost frame: Fragmentation efficiency of IR-MPD spectra; blue and black solid lines: one color IR-MPD spectra, different laser intensities (OPO/OPA, KL); red and orange solid lines: two color IR-MPD spectra (OPO/OPA, KL): 1100 - 1700 cm⁻¹: red line probe at 3560 cm⁻¹; 2800 - 3700 cm⁻¹: red and orange lines probe at 3560 cm⁻¹, different scanning laser intensities;

Lower frames: calculated IR intensities (km/mol) and structures of different isomers; values are ΔE / (kJ/mol); all identified isomers with up to ΔE ≤ 25 kJ/mol above the most stable conformer are considered; scaling factor 0.96.

The calculated pattern of structure C shows best agreement, although the calculated OH and NH stretching vibrations are blue shifted. In that assignment the experimental fragmentation efficiency of the OH stretching vibration is much higher than the one of the NH stretching vibrations.

IR-MPD spectra and calculated IR intensities of Aspartame K$^+$;
cc-pVDZ / Stuttgart RSC 1997; DFT: B97D (g09)

Fig. S B25: Aspartame K$^+$; cc-pVDZ (C, H, N, O), Stuttgart RSC 1997 (K); DFT: B97D:

Topmost frame: Fragmentation efficiency of IR-MPD spectra; blue and black solid lines: one color IR-MPD spectra, different laser intensities (OPO/OPA, KL); red and orange solid lines: two color IR-MPD spectra (OPO/OPA, KL): 1100 - 1700 cm^{-1}: red line probe at 3560 cm^{-1}; 2800 - 3700 cm^{-1}: red and orange lines probe at 3560 cm^{-1}, different scanning laser intensities;

Lower frames: calculated IR intensities (km/mol) and structures of different isomers; values are ΔE / (kJ/mol); all identified isomers with up to $\Delta E \leq 25$ kJ/mol above the most stable conformer are considered; scaling factor 0.97.

The calculated pattern of structure C shows best agreement, but also structure B could be conducive to the experimental spectrum. A distinction between the two structures in the area of the C=O stretching vibration is challenging, as the laser intensity of the OPO/OPA is rather low below 1700 cm^{-1}. In both assignments the experimental fragmentation efficiency of the OH stretching vibration is much higher than the one of the NH stretching vibrations.

**IR-MPD spectra and calculated IR intensities of Aspartame K⁺;
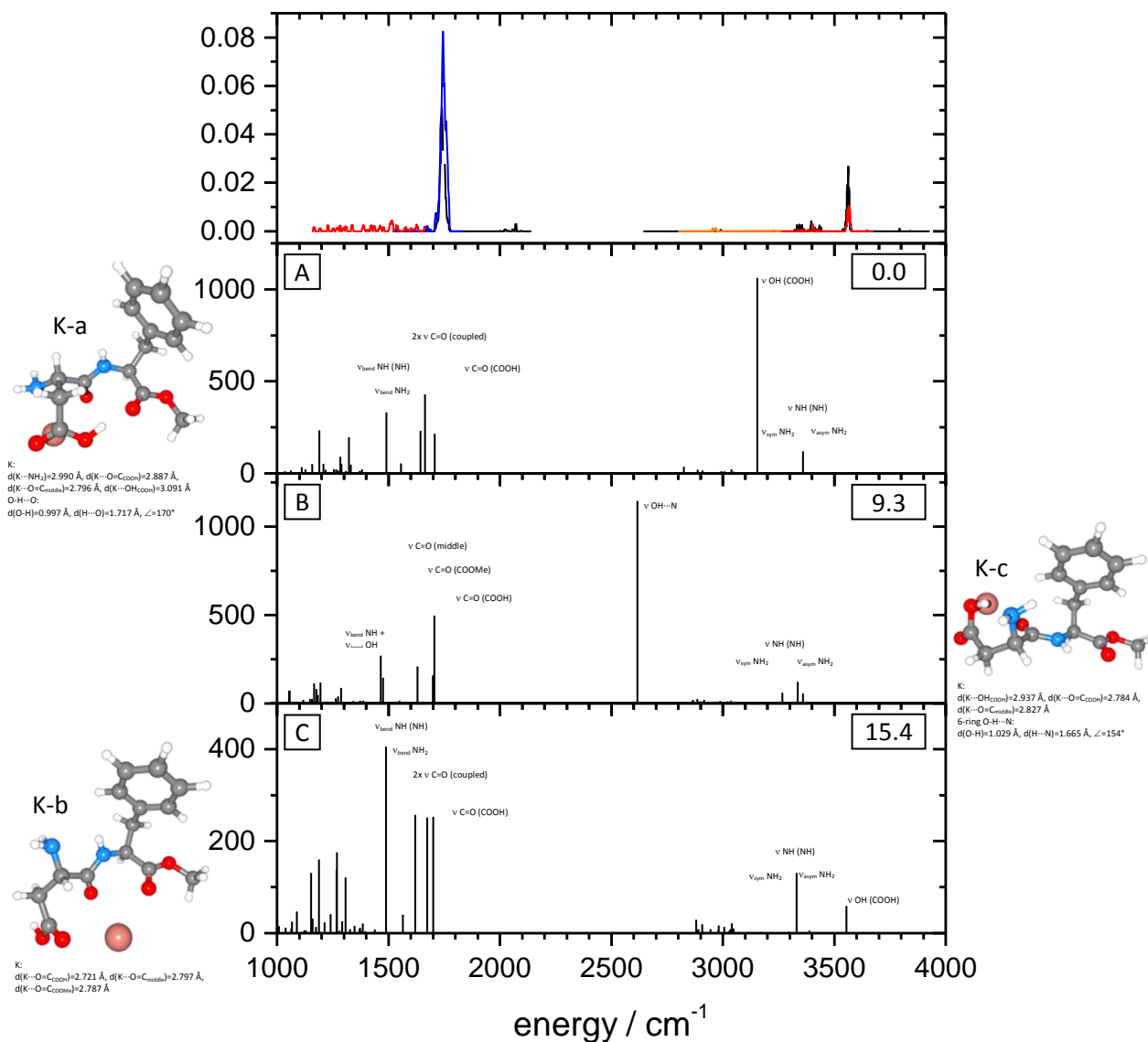cc-pVDZ / Stuttgart RSC 1997; DFT: B3LYP (g03)**

Fig. S B26: Aspartame K⁺; cc-pVDZ (C, H, N, O), Stuttgart RSC 1997 (K); DFT: B3LYP:

Topmost frame: Fragmentation efficiency of IR-MPD spectra; blue and black solid lines: one color IR-MPD spectra, different laser intensities (OPO/OPA, KL); red and orange solid lines: two color IR-MPD spectra (OPO/OPA, KL): 1100 - 1700 cm⁻¹: red line probe at 3560 cm⁻¹; 2800 - 3700 cm⁻¹: red and orange lines probe at 3560 cm⁻¹, different scanning laser intensities;

Lower frames: calculated IR intensities (km/mol) and structures of different isomers; values are ΔE / (kJ/mol); all identified isomers with up to ΔE ≤ 25 kJ/mol above the most stable conformer are considered; scaling factor 0.97.

The calculated pattern of structure B shows best agreement, although the calculated OH and NH stretching vibrations are blue shifted. In that assignment the experimental fragmentation efficiency of the OH stretching vibration is much higher than the one of the NH stretching vibrations.

IR-MPD spectra and calculated IR intensities of Aspartame Rb^{+};
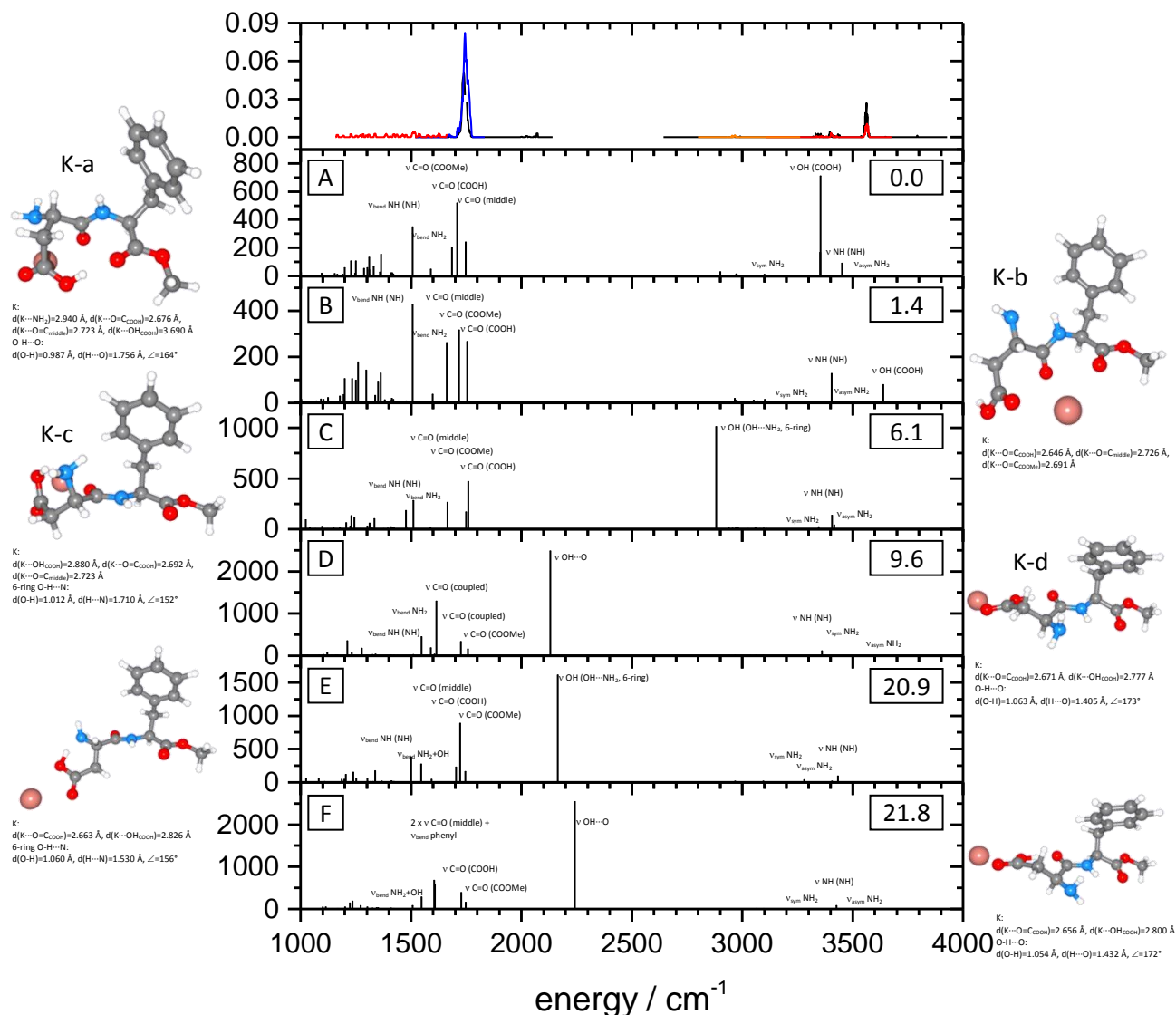**cc-pVDZ / Stuttgart RSC 1997; MP2 (g03)**

Fig. S B27: Aspartame Rb^{+}; cc-pVDZ (C, H, N, O), Stuttgart RSC 1997 (Rb); MP2:
Topmost frame: Fragmentation efficiency of IR-MPD spectra; blue and black solid lines: one color IR-MPD spectra, different laser intensities (OPO/OPA, KL); red and orange solid lines: two color IR-MPD spectra (OPO/OPA, KL): 1100 - 1700 cm^{-1}: red line probe at 3560 cm^{-1}; 2800 - 3700 cm^{-1}: red and orange lines probe at 3560 cm^{-1}, different scanning laser intensities;

Lower frames: calculated IR intensities (km/mol) and structures of different isomers; values are ΔE / (kJ/mol); all identified isomers with up to ΔE ≤ 25 kJ/mol above the most stable conformer are considered; scaling factor 0.96.

The calculated pattern of structure E shows best agreement, although the calculated OH and NH stretching vibrations are blue shifted, but also structures A and D could be conducive to the experimental spectrum. A distinction between the two structures in the area of the C=O stretching vibration is challenging, as the laser intensity of the OPO/OPA is rather low below 1700 cm^{-1}. In all assignments the experimental fragmentation efficiency of the OH stretching vibration is much higher than the one of the NH stretching vibrations.

IR-MPD spectra and calculated IR intensities of Aspartame Rb^{+};
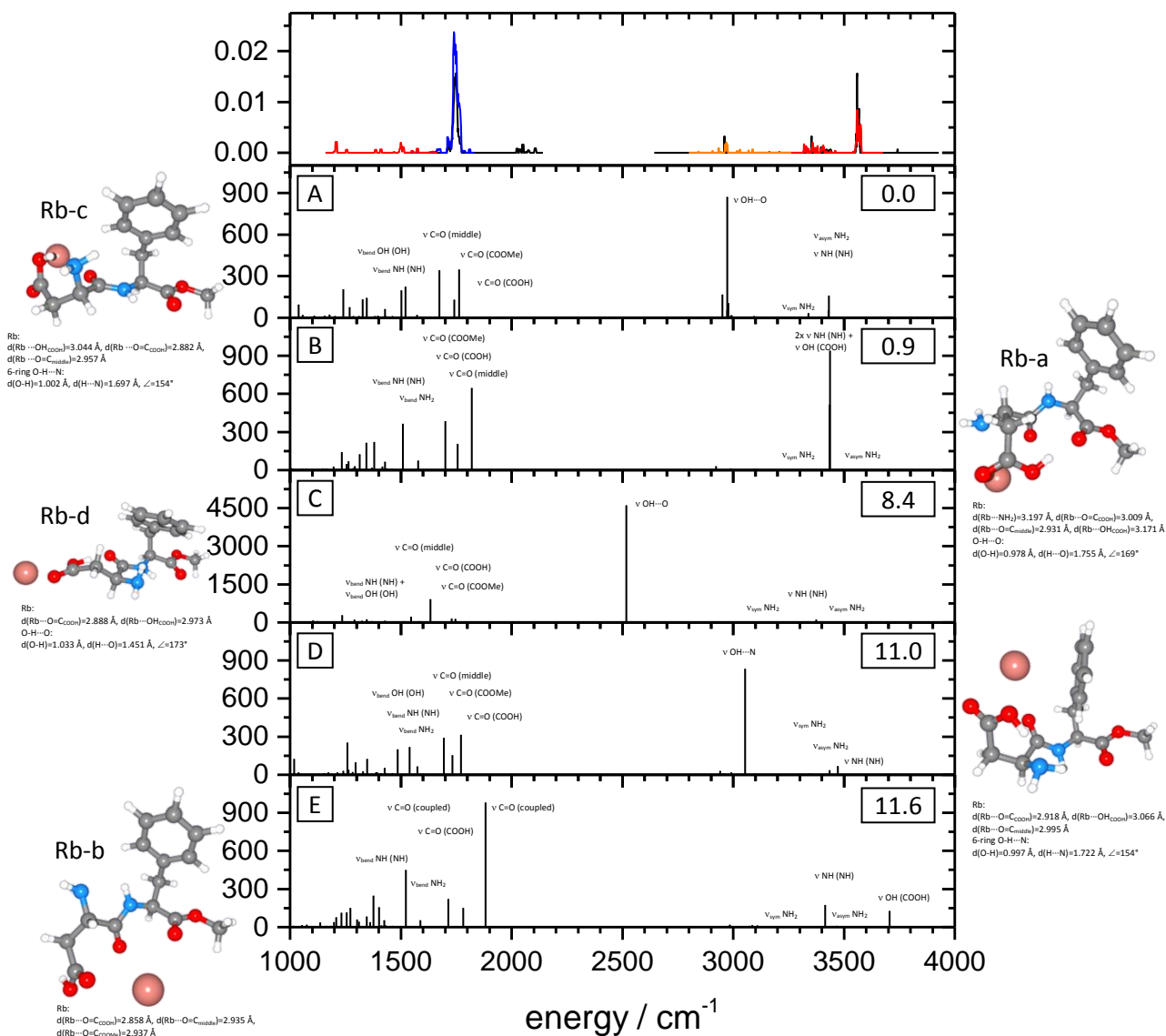**cc-pVDZ / Stuttgart RSC 1997; DFT: B97D (g09)**

Fig. S B28: Aspartame Rb^{+}; cc-pVDZ (C, H, N, O), Stuttgart RSC 1997 (Rb); DFT: B97D:

Topmost frame: Fragmentation efficiency of IR-MPD spectra; blue and black solid lines: one color IR-MPD spectra, different laser intensities (OPO/OPA, KL); red and orange solid lines: two color IR-MPD spectra (OPO/OPA, KL): 1100 - 1700 cm^{-1}: red line probe at 3560 cm^{-1}; 2800 - 3700 cm^{-1}: red and orange lines probe at 3560 cm^{-1}, different scanning laser intensities;

Lower frames: calculated IR intensities (km/mol) and structures of different isomers; values are ΔE / (kJ/mol); all identified isomers with up to $\Delta E \leq 25$ kJ/mol above the most stable conformer are considered; scaling factor 0.97.

The calculated pattern of structure C shows best agreement, but also structure A could be conducive to the experimental spectrum. A distinction between the two structures in the area of the C=O stretching vibration is challenging, as the laser intensity of the OPO/OPA is rather low below 1700 cm^{-1}. In both assignments the experimental fragmentation efficiency of the OH stretching vibration is much higher than the one of the NH stretching vibrations.

IR-MPD spectra and calculated IR intensities of Aspartame Rb^{+};
cc-pVDZ / Stuttgart RSC 1997; DFT: B3LYP (g03)

Rb-a

Rb:
d(Rb···NH₂)=3.143 Å, d(Rb···O=C_COOH)=2.871 Å,
d(Rb···O=C_middle)=2.899 Å, d(Rb···OH_COOH)=3.627 Å
O-H···O:
d(O-H)=0.987 Å, d(H···O)=1.753 Å, ∠=166°

Rb-d

Rb:
d(Rb···O=C_COOH)=2.834 Å, d(Rb···OH_COOH)=2.965 Å
O-H···O:
d(O-H)=1.054 Å, d(H···O)=1.429 Å, ∠=172°

Rb:
d(Rb···O=C_COOH)=2.824 Å, d(Rb···OH_COOH)=3.027 Å
6-ring O-H···N:
d(O-H)=1.051 Å, d(H···N)=1.555 Å, ∠=156°

Rb:
d(Rb···NH₂)=3.034 Å, d(Rb···O=C_middle)=2.961 Å,
d(Rb···O=C_COOMe)=2.925 Å

Rb-b

Rb:
d(Rb···O=C_COOH)=2.820 Å, d(Rb···O=C_middle)=2.902 Å,
d(Rb···O=C_COOMe)=2.880 Å

Rb-c

Rb:
d(Rb···OH_COOH)=3.063 Å, d(Rb···O=C_COOH)=2.845 Å,
d(Rb···O=C_middle)=2.919 Å
6-ring O-H···N:
d(O-H)=1.011 Å, d(H···N)=1.715 Å, ∠=153°

Rb:
d(Rb···O=C_COOH)=2.822 Å, d(Rb···OH_COOH)=2.987 Å
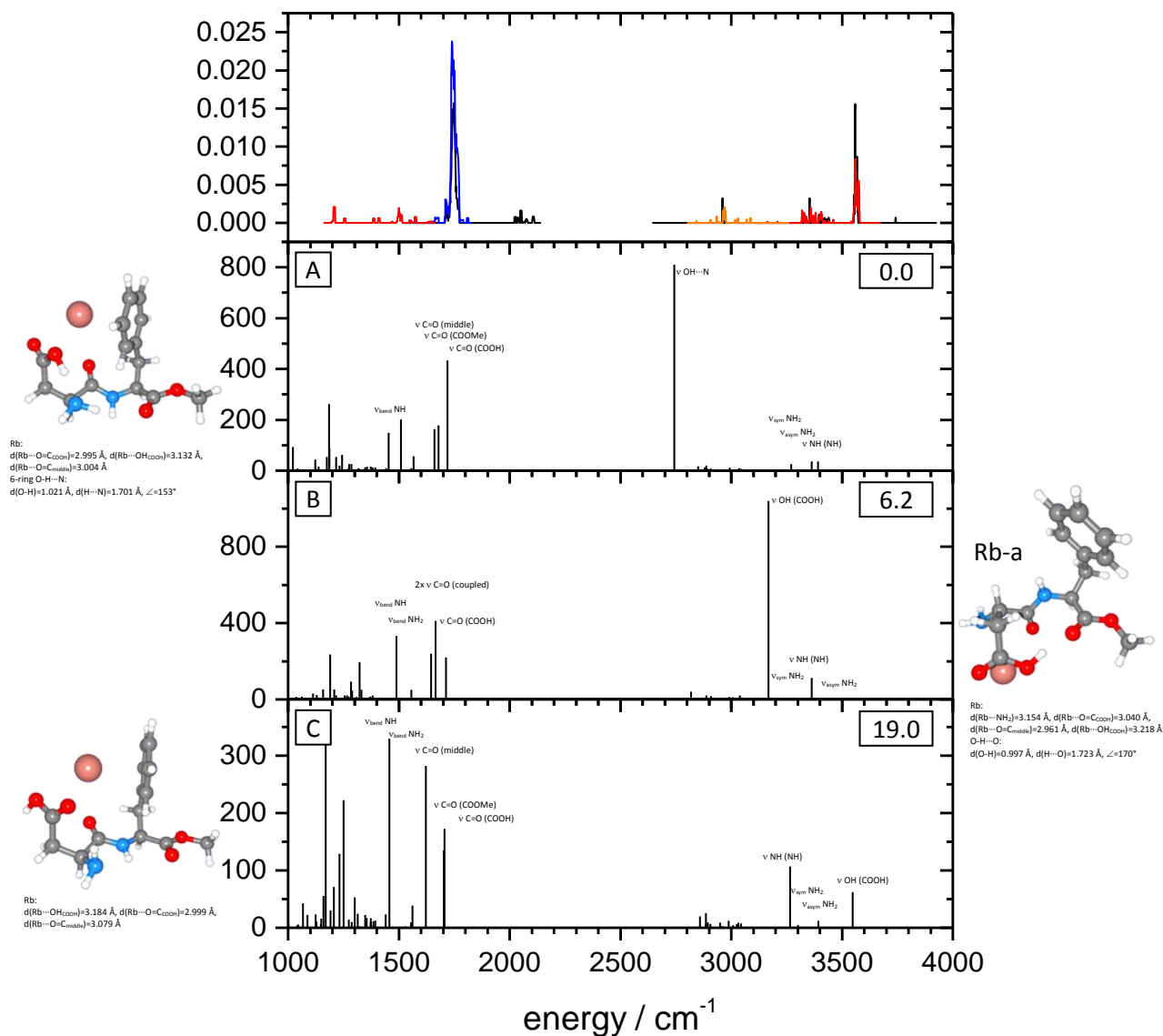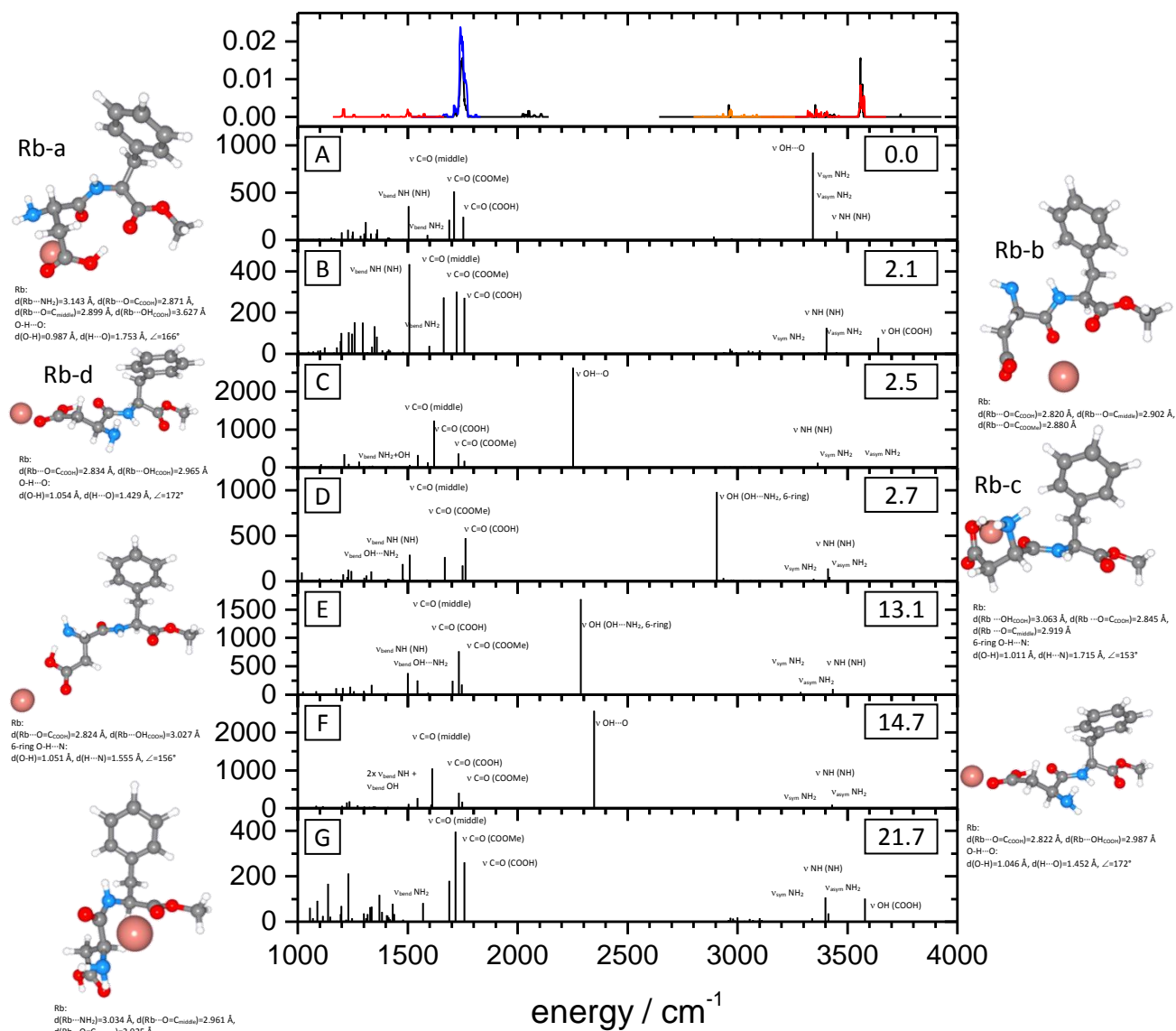O-H···O:
d(O-H)=1.046 Å, d(H···O)=1.452 Å, ∠=172°

Fig. S B29: Aspartame Rb^{+}; cc-pVDZ (C, H, N, O), Stuttgart RSC 1997 (Rb); DFT: B3LYP:
Topmost frame: Fragmentation efficiency of IR-MPD spectra; blue and black solid lines: one color IR-MPD spectra, different laser intensities (OPO/OPA, KL); red and orange solid lines: two color IR-MPD spectra (OPO/OPA, KL): 1100 - 1700 cm⁻¹: red line probe at 3560 cm⁻¹; 2800 - 3700 cm⁻¹: red and orange lines probe at 3560 cm⁻¹, different scanning laser intensities;
Lower frames: calculated IR intensities (km/mol) and structures of different isomers; values are ΔE / (kJ/mol); all identified isomers with up to ΔE ≤ 25 kJ/mol above the most stable conformer are considered; scaling factor 0.97.
The calculated patterns of structures B and G show best agreement, although the calculated OH and NH stretching vibrations of structure B are blue shifted, but also structures A and D could be conducive to the experimental spectrum. A distinction between the four structures in the area of the C=O stretching vibration is challenging, as the laser intensity of the OPO/OPA is rather low below 1700 cm⁻¹. In all assignments the experimental fragmentation efficiency of the OH stretching vibration is much higher than the one of the NH stretching vibrations.

**IR-MPD spectra and calculated IR intensities of Aspartame Rb⁺;
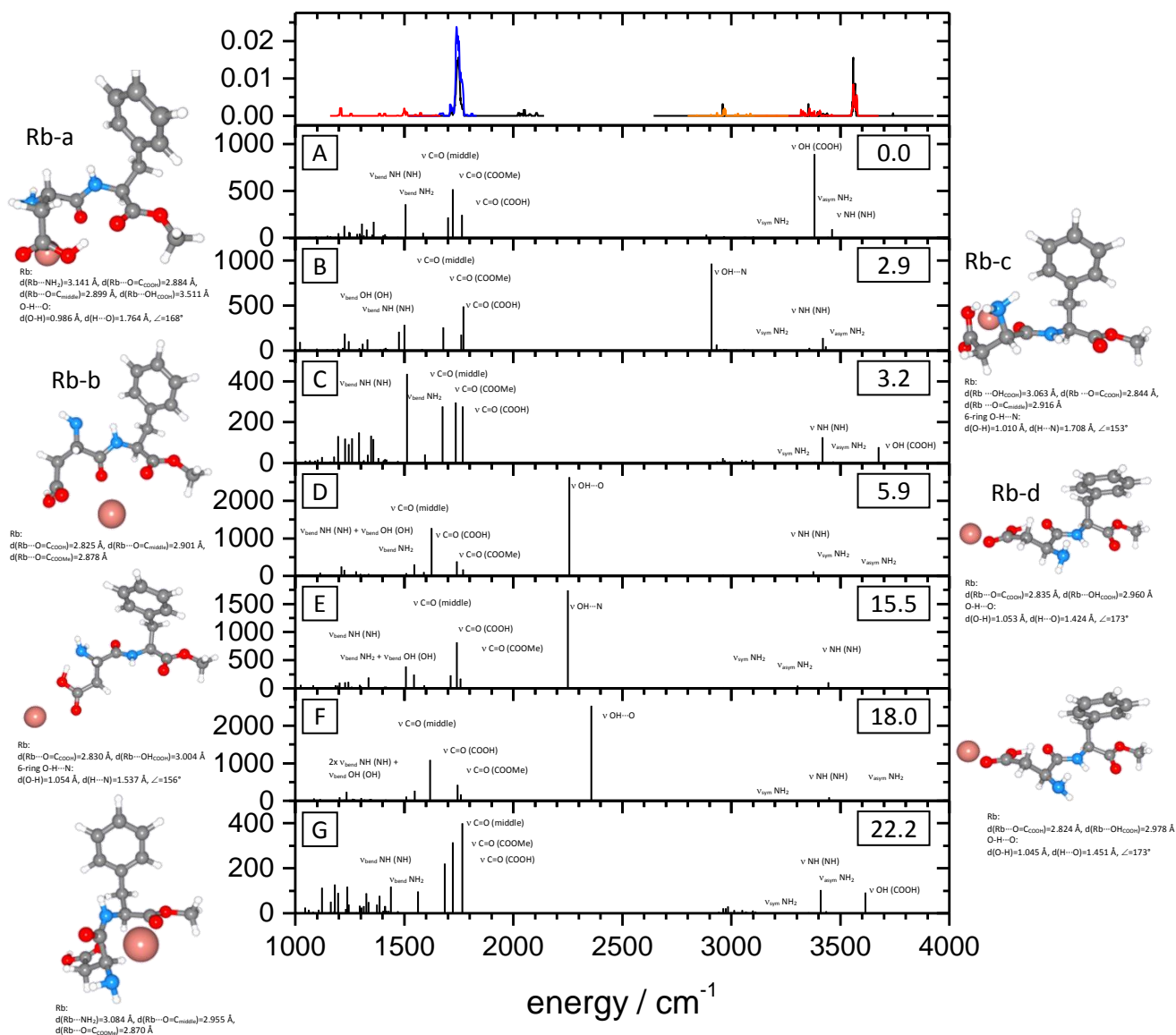cc-pVDZ / Stuttgart RSC 1997; DFT: Becke97_1 (g03)**

Fig. S B30: Aspartame Rb⁺; cc-pVDZ (C, H, N, O), Stuttgart RSC 1997 (Rb); DFT: Becke97_1:
Topmost frame: Fragmentation efficiency of IR-MPD spectra; blue and black solid lines: one color IR-MPD spectra, different laser intensities (OPO/OPA, KL); red and orange solid lines: two color IR-MPD spectra (OPO/OPA, KL): 1100 - 1700 cm⁻¹: red line probe at 3560 cm⁻¹; 2800 - 3700 cm⁻¹: red and orange lines probe at 3560 cm⁻¹, different scanning laser intensities;
Lower frames: calculated IR intensities (km/mol) and structures of different isomers; values are ΔE / (kJ/mol); all identified isomers with up to ΔE ≤ 25 kJ/mol above the most stable conformer are considered; scaling factor 0.97.
The calculated patterns of structures C and G show best agreement, although the calculated OH and NH stretching vibrations are blue shifted, but also structures A and B could be conducive to the experimental spectrum. A distinction between the four structures in the area of the C=O stretching vibration is challenging, as the laser intensity of the OPO/OPA is rather low below 1700 cm⁻¹. In all assignments the experimental fragmentation efficiency of the OH stretching vibration is much higher than the one of the NH stretching vibrations.

IR-MPD spectra and calculated IR intensities of Aspartame Rb⁺;
cc-pVDZ / Stuttgart RSC 1997; DFT: Becke97_2 (g03)

Rb-d

Rb:
d(Rb···O=C_COOH)=2.844 Å, d(Rb···OH_COOH)=2.992 Å
O-H···O:
d(O-H)=1.050 Å, d(H···O)=1.418 Å, ∠=173°

Rb-b

Rb:
d(Rb···O=C_COOH)=2.840 Å, d(Rb···O=C_middle)=2.934 Å,
d(Rb···O=C_COOMe)=2.911 Å

Rb:
d(Rb···O=C_COOH)=2.834 Å, d(Rb···OH_COOH)=3.070 Å
6-ring O-H···N:
d(O-H)=1.048 Å, d(H···N)=1.541 Å, ∠=156°

Rb:
d(Rb···NH₂)=3.055 Å, d(Rb···O=C_middle)=2.978 Å,
d(Rb···O=C_COOMe)=2.953 Å

Rb-a

Rb:
d(Rb···NH₂)=3.163 Å, d(Rb···O=C_COOH)=2.894 Å,
d(Rb···O=C_middle)=2.920 Å, d(Rb···OH_COOH)=3.630 Å
O-H···O:
d(O-H)=0.981 Å, d(H···O)=1.780 Å, ∠=166°

Rb-c

Rb:
d(Rb···OH_COOH)=3.102 Å, d(Rb···O=C_COOH)=2.854 Å,
d(Rb···O=C_middle)=2.952 Å
6-ring O-H···N:
d(O-H)=1.006 Å, d(H···N)=1.706 Å, ∠=153°

Rb:
d(Rb···O=C_COOH)=2.832 Å, d(Rb···OH_COOH)=3.023 Å
O-H···O:
d(O-H)=1.041 Å, d(H···O)=1.446 Å, ∠=173°

Rb:
d(Rb···O=C_COOH)=2.821 Å, d(Rb···OH_COOH)=2.978 Å
6-ring O-H···N:
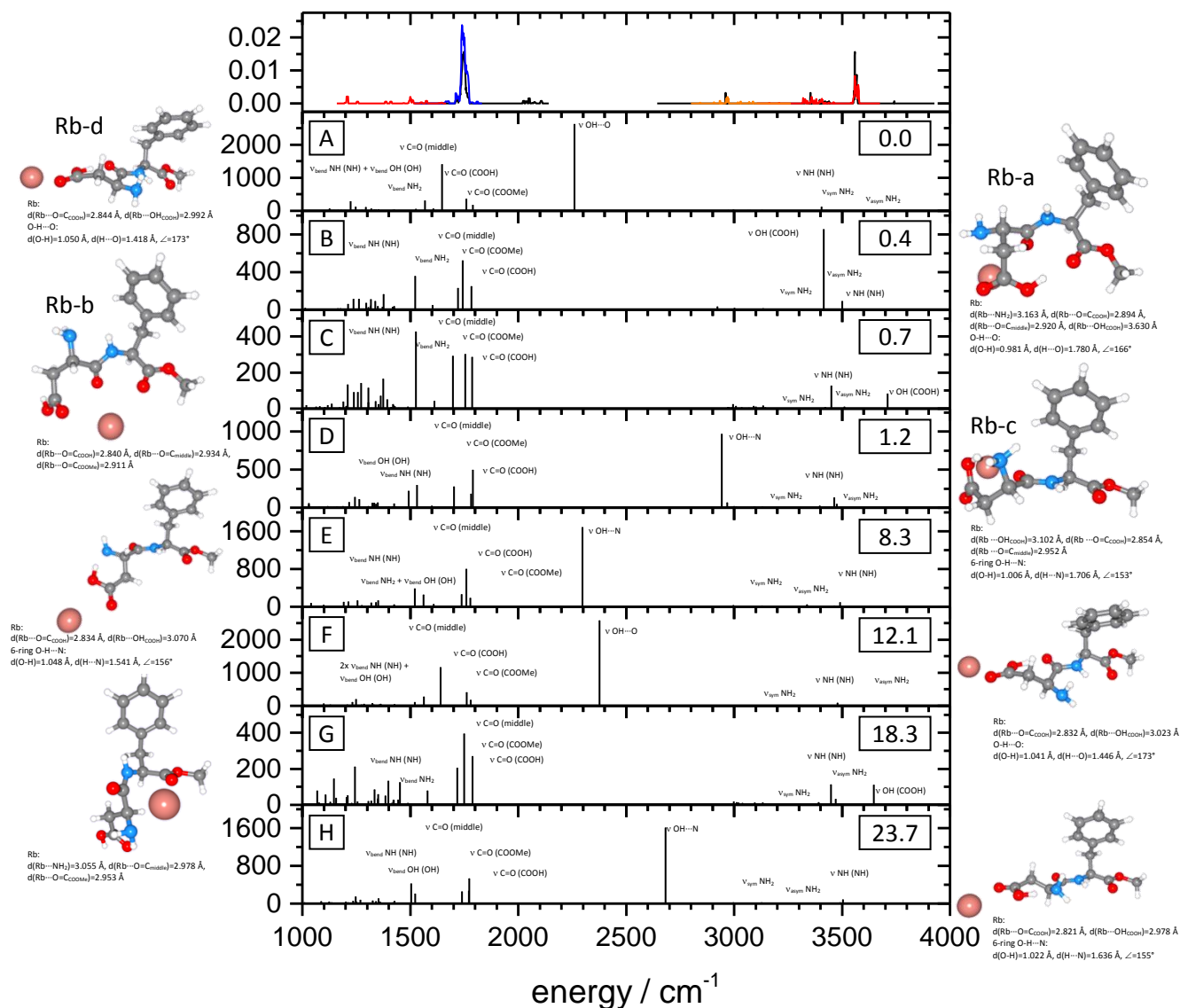d(O-H)=1.022 Å, d(H···N)=1.636 Å, ∠=155°

Fig. S B31: Aspartame Rb⁺; cc-pVDZ (C, H, N, O), Stuttgart RSC 1997 (Rb); DFT: Becke97_2:
Topmost frame: Fragmentation efficiency of IR-MPD spectra; blue and black solid lines: one color IR-MPD spectra, different laser intensities (OPO/OPA, KL); red and orange solid lines: two color IR-MPD spectra (OPO/OPA, KL): 1100 - 1700 cm⁻¹: red line probe at 3560 cm⁻¹; 2800 - 3700 cm⁻¹: red and orange lines probe at 3560 cm⁻¹, different scanning laser intensities;
Lower frames: calculated IR intensities (km/mol) and structures of different isomers; values are ΔE / (kJ/mol); all identified isomers with up to ΔE ≤ 25 kJ/mol above the most stable conformer are considered; scaling factor 0.97.
The calculated patterns of structures C and G show best agreement, although the calculated OH and NH stretching vibrations are blue shifted, but also structures B and D could be conducive to the experimental spectrum. A distinction between the four structures in the area of the C=O stretching vibration is challenging, as the laser intensity of the OPO/OPA is rather low below 1700 cm⁻¹. In all assignments the experimental fragmentation efficiency of the OH stretching vibration is much higher than the one of the NH stretching vibrations.

IR-MPD spectra and calculated IR intensities of Aspartame Cs⁺;
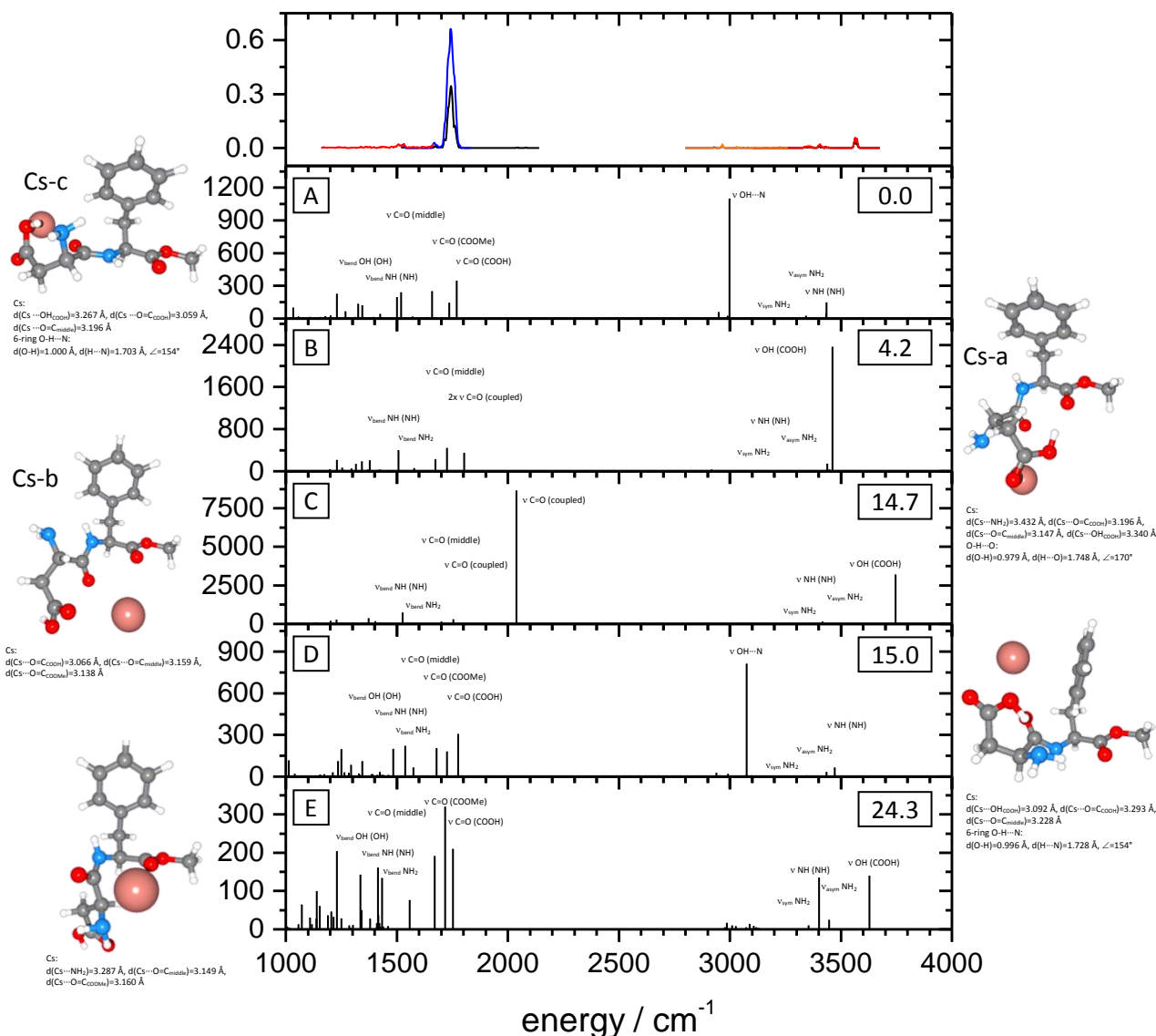**cc-pVDZ / Stuttgart RSC 1997; MP2 (g03)**

Fig. S B32: Aspartame Cs⁺; cc-pVDZ (C, H, N, O), Stuttgart RSC 1997 (Cs); MP2:

Topmost frame: Fragmentation efficiency of IR-MPD spectra; blue and black solid lines: one color IR-MPD spectra, different laser intensities (OPO/OPA, KL); red and orange solid lines: two color IR-MPD spectra (OPO/OPA, KL): 1100 - 1700 cm⁻¹: red line probe at 3565 cm⁻¹; 2800 - 3700 cm⁻¹: red and orange lines probe at 3565 cm⁻¹, different scanning laser intensities;

Lower frames: calculated IR intensities (km/mol) and structures of different isomers; values are ΔE / (kJ/mol); all identified isomers with up to ΔE ≤ 25 kJ/mol above the most stable conformer are considered; scaling factor 0.96.

Experimental fragmentation efficiency does not show significant features between 2800 and 3700 cm⁻¹. A distinction between the structures in the area of the C=O stretching vibration is challenging, as the laser intensity of the OPO/OPA is rather low below 1700 cm⁻¹.

IR-MPD spectra and calculated IR intensities of Aspartame Cs$^+$;
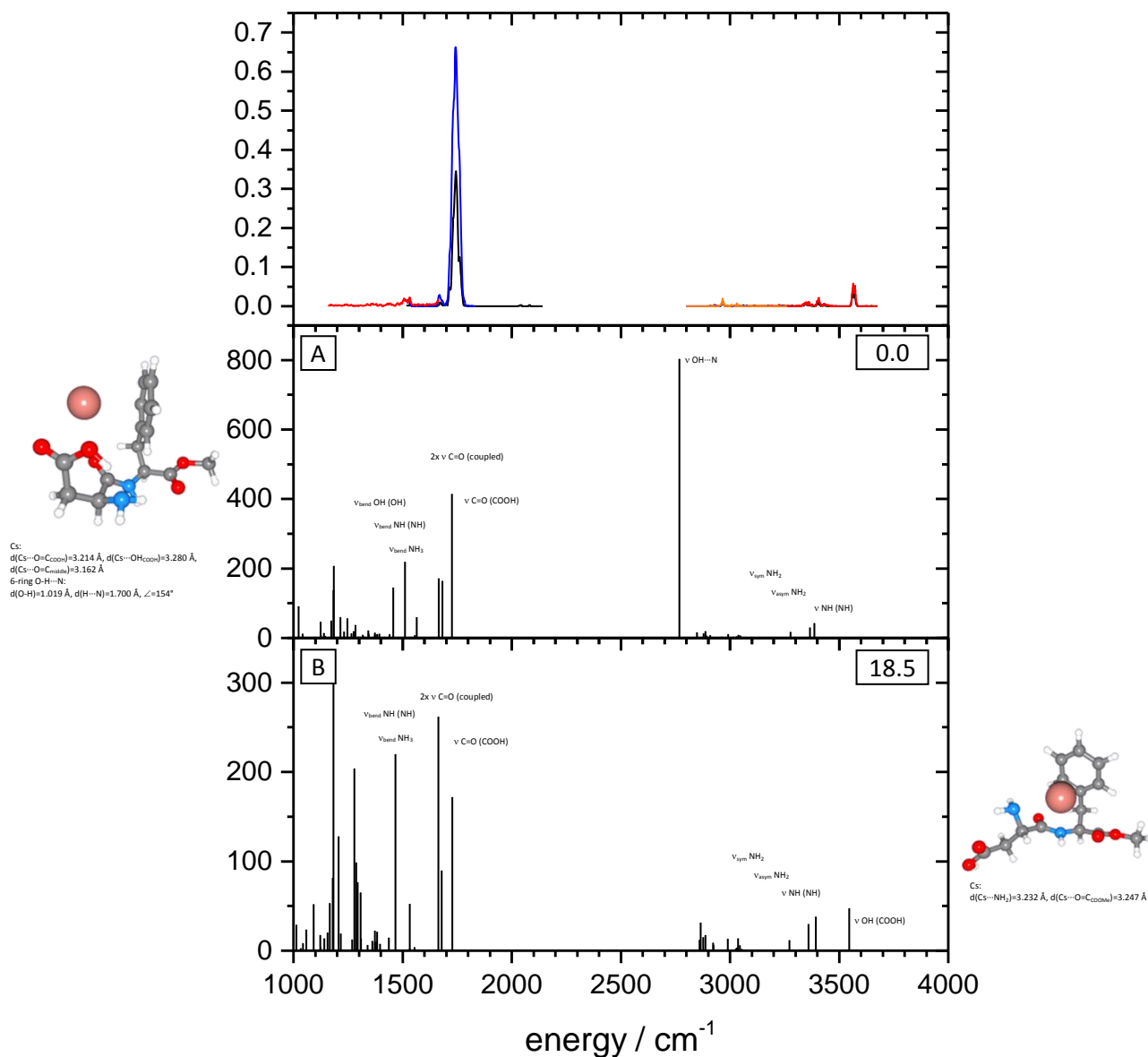**cc-pVDZ / Stuttgart RSC 1997; B97D (g09)**

Fig. S B33: Aspartame Cs$^+$; cc-pVDZ (C, H, N, O), Stuttgart RSC 1997 (Cs); DFT: B97D:

Topmost frame: Fragmentation efficiency of IR-MPD spectra; blue and black solid lines: one color IR-MPD spectra, different laser intensities (OPO/OPA, KL); red and orange solid lines: two color IR-MPD spectra (OPO/OPA, KL): 1100 - 1700 cm^{-1}: red line probe at 3565 cm^{-1}; 2800 - 3700 cm^{-1}: red and orange lines probe at 3565 cm^{-1}, different scanning laser intensities;

Lower frames: calculated IR intensities (km/mol) and structures of different isomers; values are ΔE / (kJ/mol); all identified isomers with up to $\Delta E \leq 25$ kJ/mol above the most stable conformer are considered; scaling factor 0.97.

Experimental fragmentation efficiency does not show significant features between 2800 and 3700 cm^{-1}. A distinction between the structures in the area of the C=O stretching vibration is challenging, as the laser intensity of the OPO/OPA is rather low below 1700 cm^{-1}.

IR-MPD spectra and calculated IR intensities of Aspartame Cs⁺;
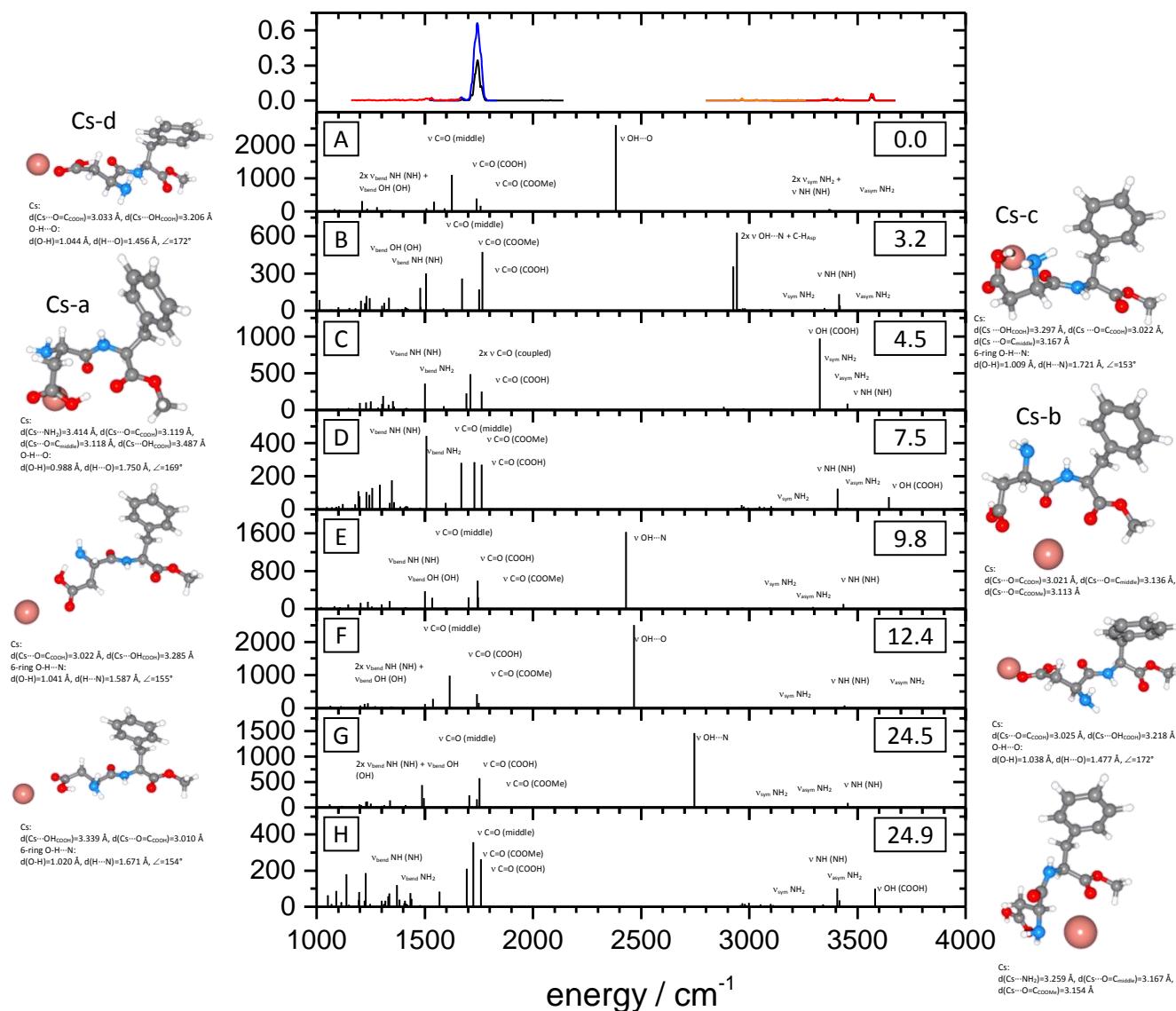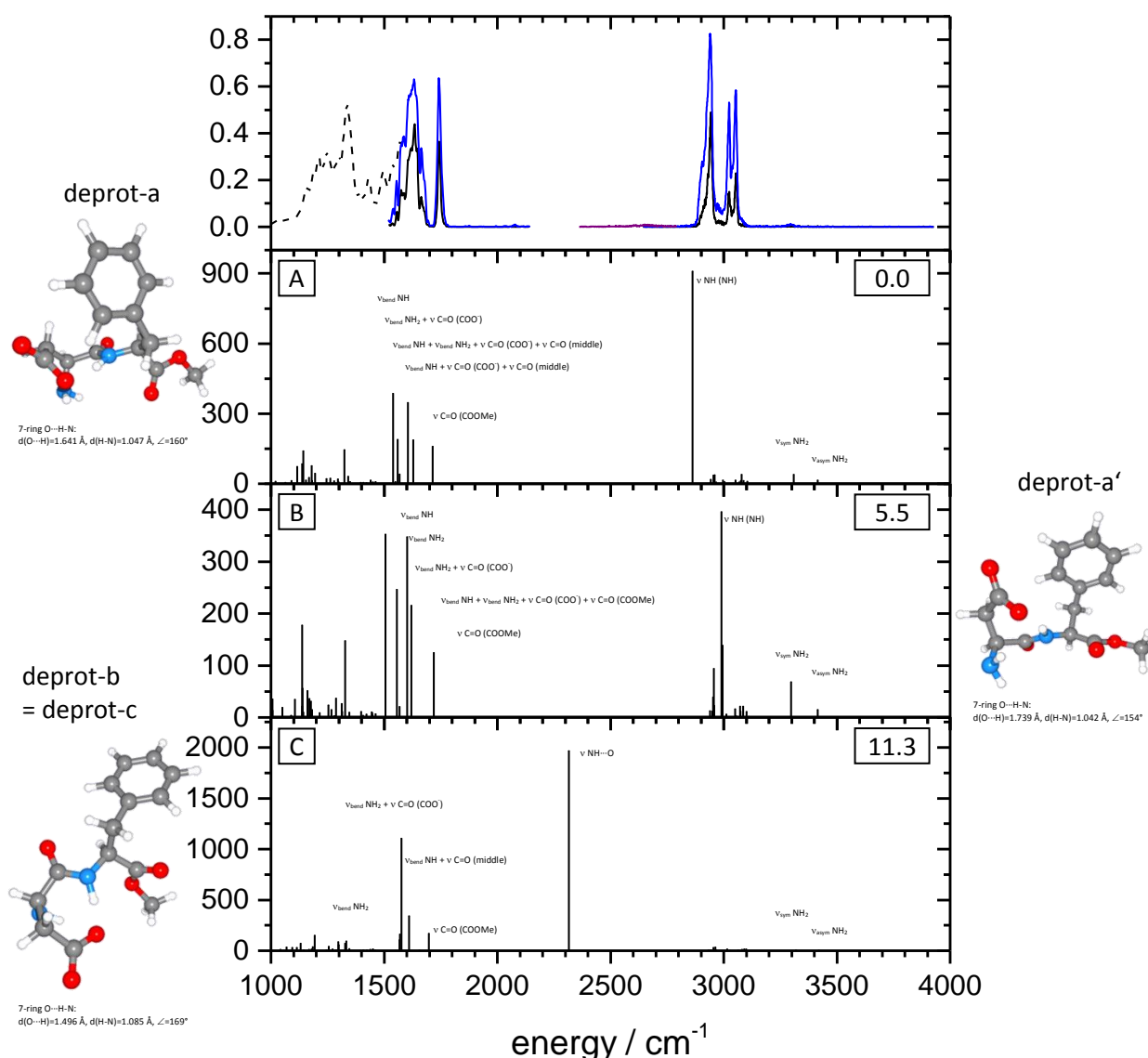**cc-pVDZ / Stuttgart RSC 1997; DFT: B3LYP (g03)**

Fig. S B34: Aspartame Cs⁺; cc-pVDZ (C, H, N, O), Stuttgart RSC 1997 (Cs); DFT: B3LYP:

Topmost frame: Fragmentation efficiency of IR-MPD spectra; blue and black solid lines: one color IR-MPD spectra, different laser intensities (OPO/OPA, KL); red and orange solid lines: two color IR-MPD spectra (OPO/OPA, KL): 1100 - 1700 cm⁻¹: red line probe at 3565 cm⁻¹; 2800 - 3700 cm⁻¹: red and orange lines probe at 3565 cm⁻¹, different scanning laser intensities;

Lower frames: calculated IR intensities (km/mol) and structures of different isomers; values are ΔE / (kJ/mol); all identified isomers with up to ΔE ≤ 25 kJ/mol above the most stable conformer are considered; scaling factor 0.97.

Experimental fragmentation efficiency does not show significant features between 2800 and 3700 cm⁻¹. A distinction between the structures in the area of the C=O stretching vibration is challenging, as the laser intensity of the OPO/OPA is rather low below 1700 cm⁻¹.

IR-MPD spectra and calculated IR intensities of deprotonated Aspartame; TZVP; MP2 (g03)

deprot-a

7-ring O···H-N:
d(O···H)=1.641 Å, d(H-N)=1.047 Å, ∠=160°

deprot-a'

7-ring O···H-N:
d(O···H)=1.739 Å, d(H-N)=1.042 Å, ∠=154°

deprot-b
= deprot-c

7-ring O···H-N:
d(O···H)=1.496 Å, d(H-N)=1.085 Å, ∠=169°

Fig. S B35: Deprotonated Aspartame; TZVP; MP2:

Topmost frame: Fragmentation efficiency of IR-MPD spectra; black dashed line: one color IR-MPD spectrum (FEL CLIO, Paris); blue, black and purple solid lines: one color IR-MPD spectra (blue and black at different laser intensities) (OPO/OPA, KL);

Lower frames: calculated IR intensities (km/mol) and structures of different isomers; values are ΔE / (kJ/mol); all identified isomers with up to ΔE ≤ 25 kJ/mol above the most stable conformer are considered; scaling factor 0.96.

The calculated pattern of structure B shows best agreement, although the intensity of the experimentally visible double peak between 3000 and 3100 cm^{-1} is not described well. Also structure A could be conducive to the experimental spectrum.

IR-MPD spectra and calculated IR intensities of deprotonated Aspartame; cc-pVDZ; MP2 (g03)
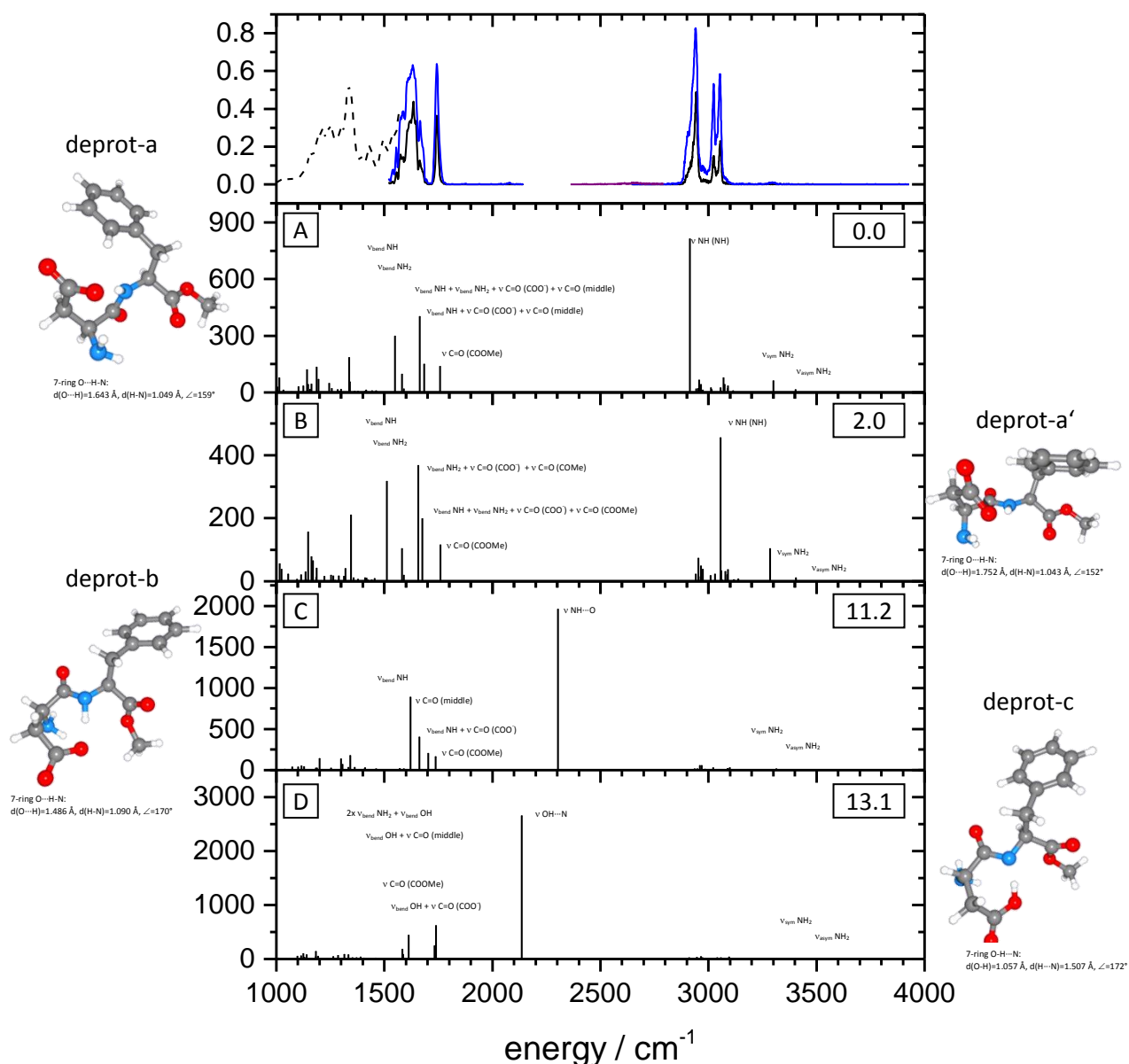

Fig. S B36: Deprotonated Aspartame; cc-pVDZ; MP2:

Topmost frame: Fragmentation efficiency of IR-MPD spectra; black dashed line: one color IR-MPD spectrum (FEL CLIO, Paris); blue, black and purple solid lines: one color IR-MPD spectra (blue and black at different laser intensities) (OPO/OPA, KL);

Lower frames: calculated IR intensities (km/mol) and structures of different isomers; values are ΔE / (kJ/mol); all identified isomers with up to ΔE ≤ 25 kJ/mol above the most stable conformer are considered; scaling factor 0.96.

The combination of the calculated patterns of structures A and B show best agreement, although the appearance of the experimentally visible double peak between 3000 and 3100 cm^{-1} is not described well.

IR-MPD spectra and calculated IR intensities of deprotonated Aspartame; TZVP; B97D (g09)

deprot-a

7-ring O···H-N:
d(O···H)=1.674 Å, d(H-N)=1.050 Å, ∠=161°

deprot-a′

7-ring O···H-N:
d(O···H)=1.763 Å, d(H-N)=1.045 Å, ∠=156°

deprot-b
(= deprot-c)

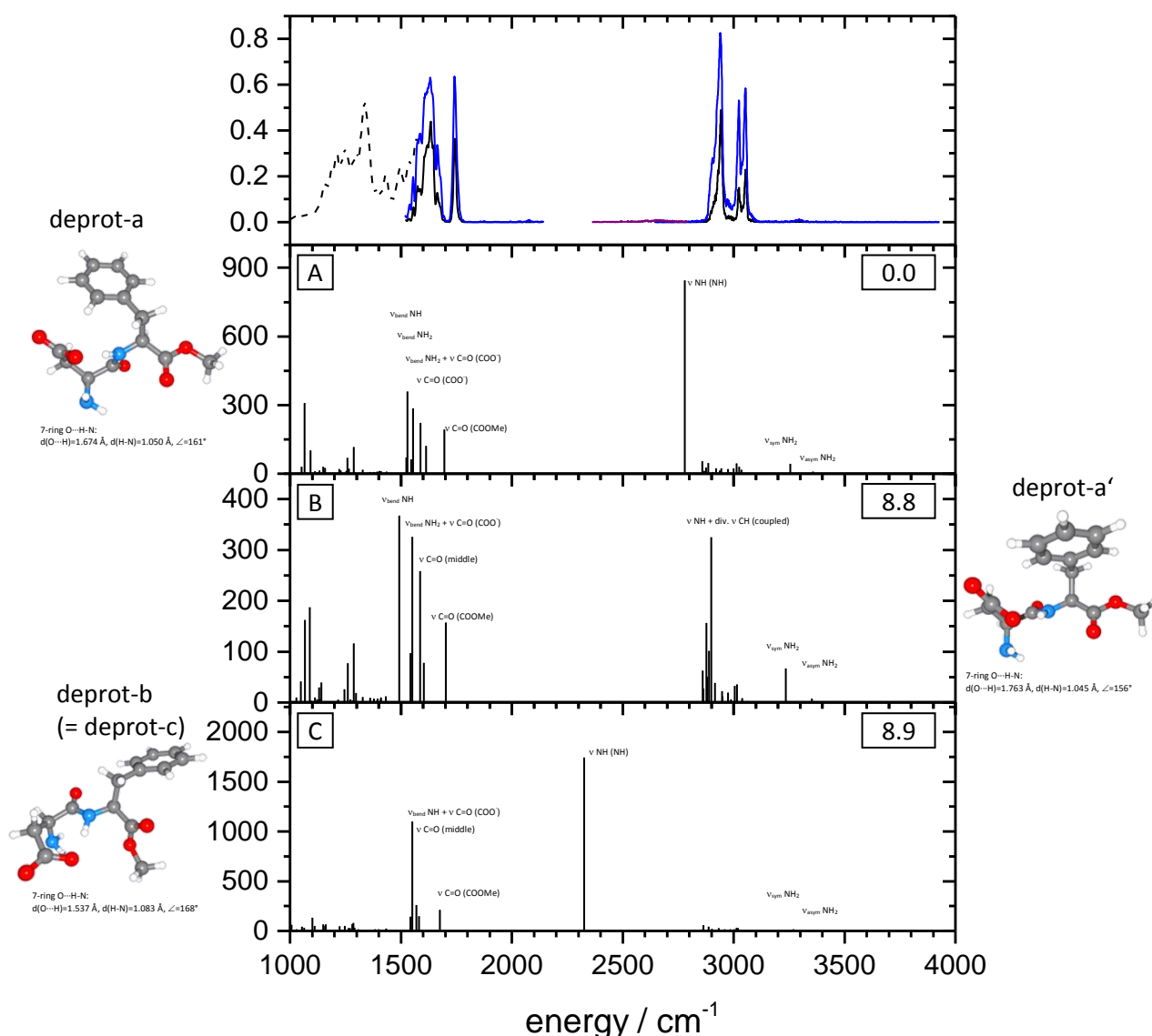7-ring O···H-N:
d(O···H)=1.537 Å, d(H-N)=1.083 Å, ∠=168°

Fig. S B37: Deprotonated Aspartame; TZVP; DFT: B97D:

Topmost frame: Fragmentation efficiency of IR-MPD spectra; black dashed line: one color IR-MPD spectrum (FEL CLIO, Paris); blue, black and purple solid lines: one color IR-MPD spectra (blue and black at different laser intensities) (OPO/OPA, KL);

Lower frames: calculated IR intensities (km/mol) and structures of different isomers; values are ΔE / (kJ/mol); all identified isomers with up to ΔE ≤ 25 kJ/mol above the most stable conformer are considered; scaling factor 0.97.

The calculated pattern of structure B shows best agreement, although the intensity of the experimentally visible double peak between 3000 and 3100 cm⁻¹ is not described well.

IR-MPD spectra and calculated IR intensities of deprotonated Aspartame; cc-pVDZ; B97D (g09)

Fig. S B38: Deprotonated Aspartame; cc-pVDZ; DFT: B97D:

Topmost frame: Fragmentation efficiency of IR-MPD spectra; black dashed line: one color IR-MPD spectrum (FEL CLIO, Paris); blue, black and purple solid lines: one color IR-MPD spectra (blue and black at different laser intensities) (OPO/OPA, KL);

Lower frames: calculated IR intensities (km/mol) and structures of different isomers; values are ΔE / (kJ/mol); all identified isomers with up to ΔE ≤ 25 kJ/mol above the most stable conformer are considered; scaling factor 0.97.

The calculated pattern of structure B shows best agreement, although the intensity of the experimentally visible double peak between 3000 and 3100 cm^{-1} is not described well. Also structure A could be conducive to the experimental spectrum.

IR-MPD spectra and calculated IR intensities of deprotonated Aspartame; TZVP; B3LYP (g03)
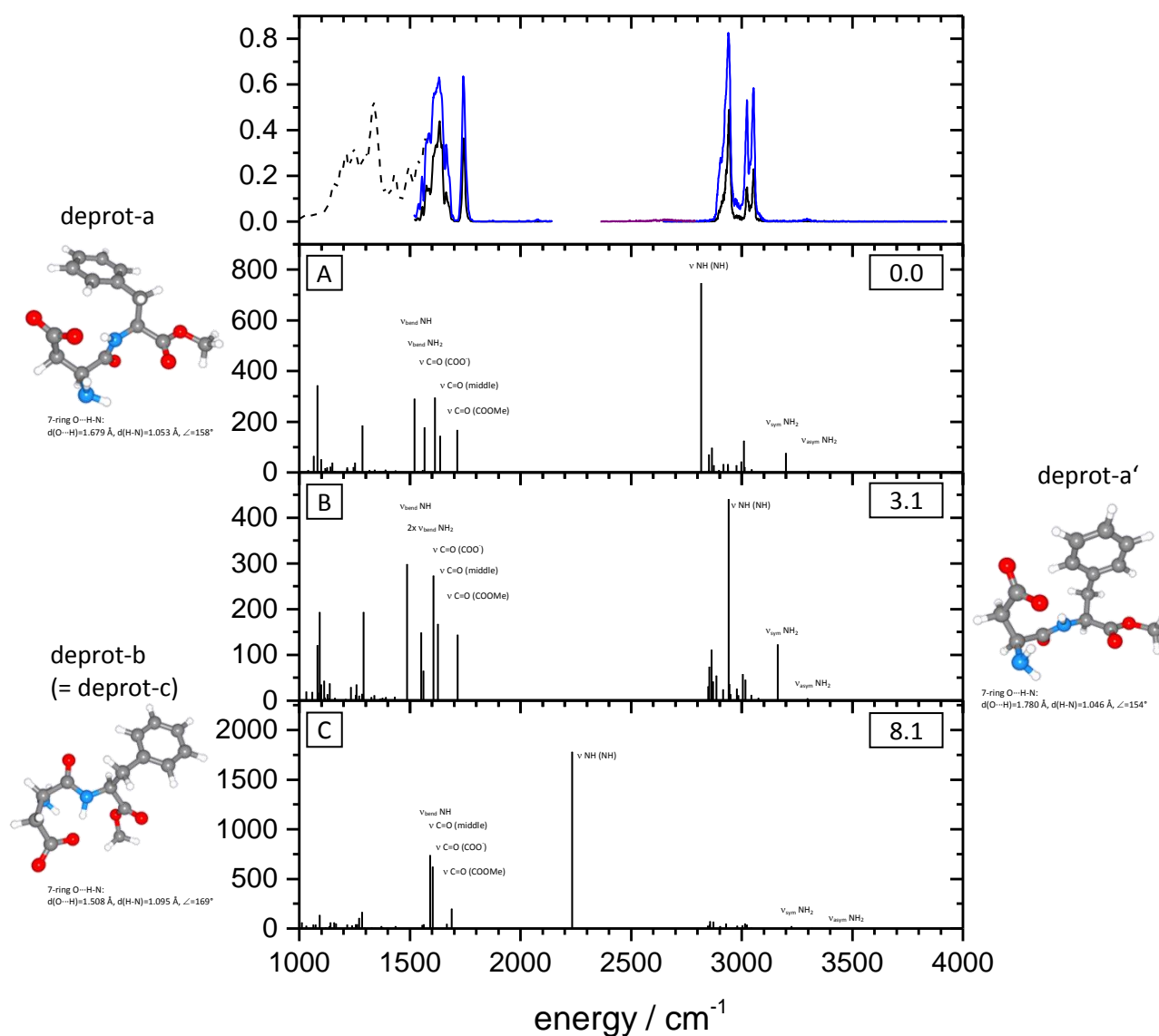

Fig. S B39: Deprotonated Aspartame; TZVP; DFT: B3LYP:

Topmost frame: Fragmentation efficiency of IR-MPD spectra; black dashed line: one color IR-MPD spectrum (FEL CLIO, Paris); blue, black and purple solid lines: one color IR-MPD spectra (blue and black at different laser intensities) (OPO/OPA, KL);

Lower frames: calculated IR intensities (km/mol) and structures of different isomers; values are ΔE / (kJ/mol); all identified isomers with up to ΔE ≤ 25 kJ/mol above the most stable conformer are considered; scaling factor 0.97.

The calculated patterns of structures A and D show best agreement, including the peak at 3400 cm⁻¹, although the experimentally visible double peak between 3000 and 3100 cm⁻¹ is not described.

IR-MPD spectra and calculated IR intensities of deprotonated Aspartame; aug-cc-pVDZ; B3LYP (g03)
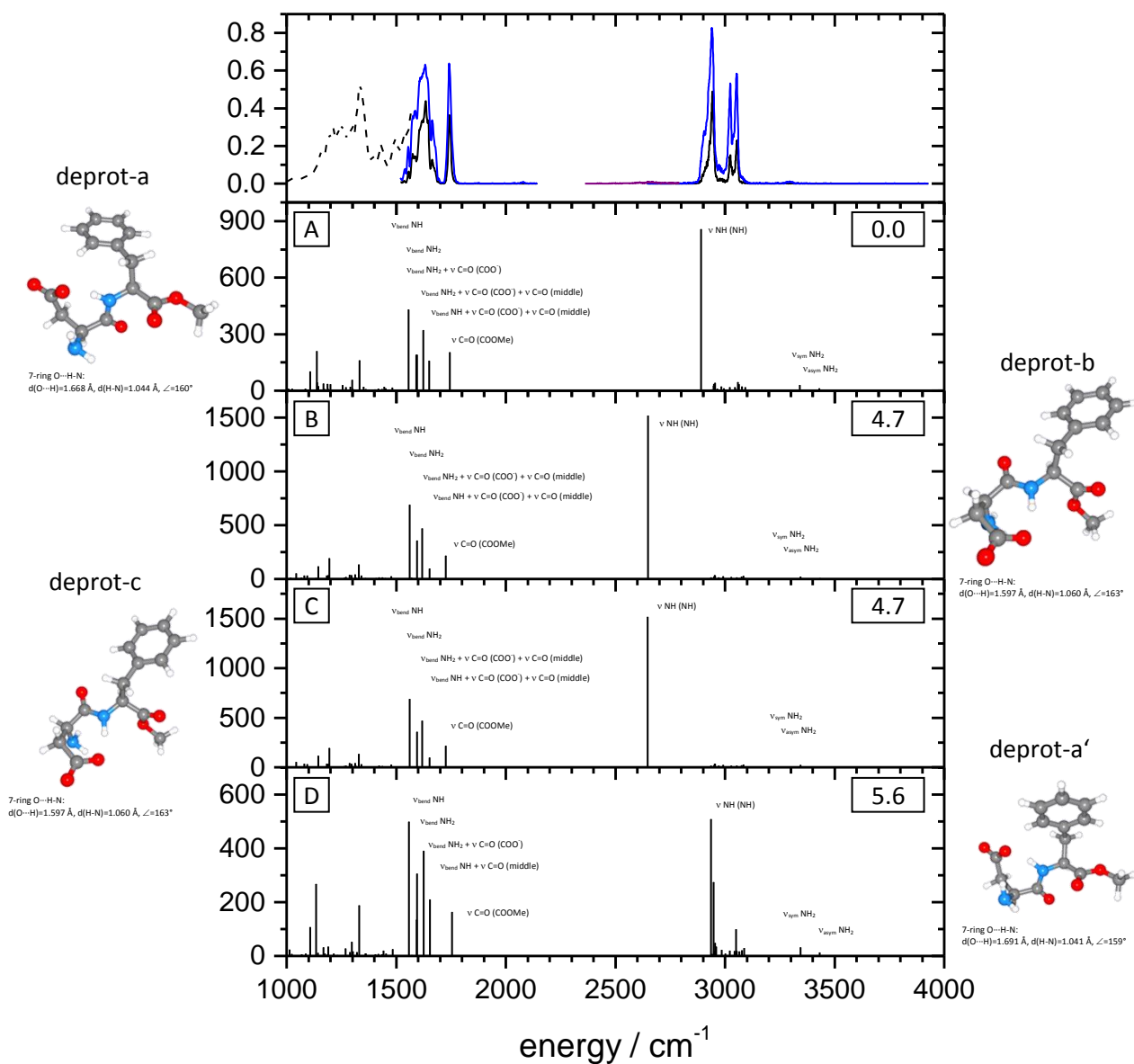

Fig. S B40: Deprotonated Aspartame; aug-cc-pVDZ; DFT: B3LYP:

Topmost frame: Fragmentation efficiency of IR-MPD spectra; black dashed line: one color IR-MPD spectrum (FEL CLIO, Paris); blue, black and purple solid lines: one color IR-MPD spectra (blue and black at different laser intensities) (OPO/OPA, KL);

Lower frames: calculated IR intensities (km/mol) and structures of different isomers; values are $\Delta E / (kJ/mol)$; all identified isomers with up to $\Delta E \leq 25$ kJ/mol above the most stable conformer are considered; scaling factor 0.97.

The calculated patterns of structures A and C show best agreement, although the intensity of the experimentally visible double peak between 3000 and 3100 cm^{-1} is not described well.

IR-MPD spectra and calculated IR intensities of deprotonated Aspartame; cc-pVDZ; B3LYP (g03)

deprot-a

7-ring O···H-N:
d(O···H)=1.685 Å, d(H-N)=1.045 Å, ∠=167°

deprot-a'

7-ring O···H-N:
d(O···H)=1.894 Å, d(H-N)=1.031 Å, ∠=148°

deprot-b

7-ring O-H···N:
d(O-H)=1.553 Å, d(H···N)=1.073 Å, ∠=167°

deprot-c

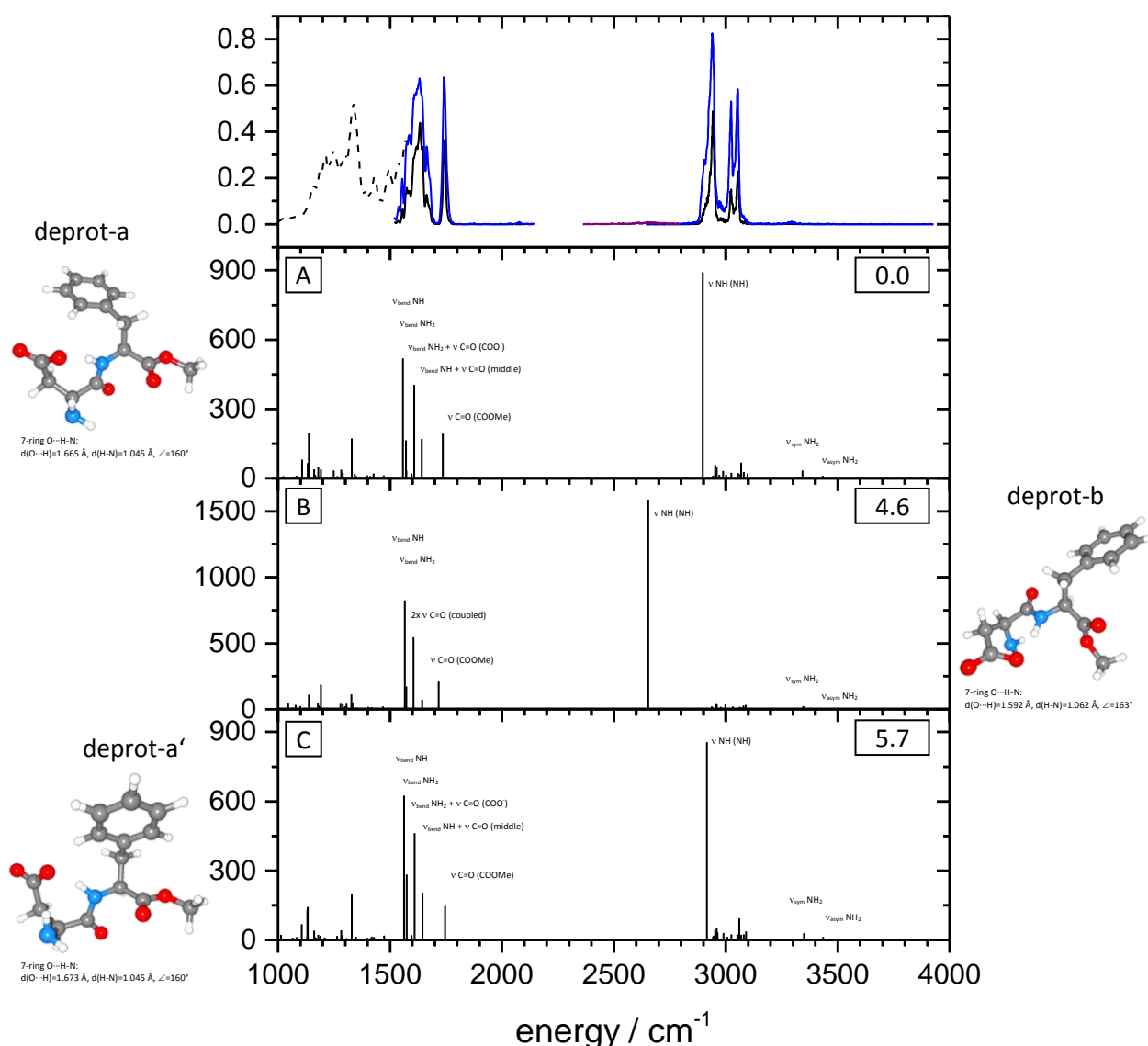7-ring O-H···N:
d(O-H)=1.092 Å, d(H···N)=1.443 Å, ∠=172°
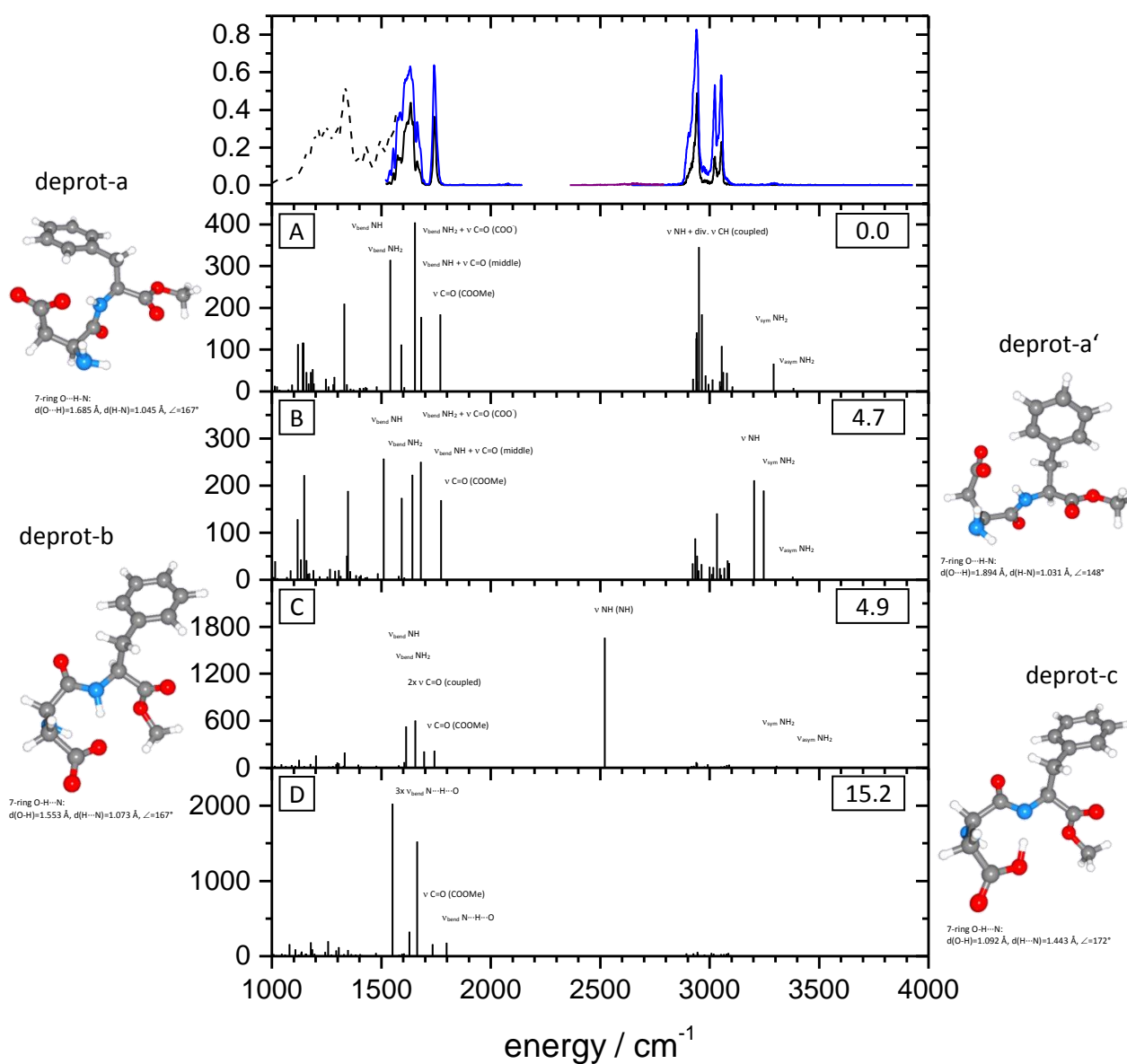
Fig. S B41: Deprotonated Aspartame; cc-pVDZ; DFT: B3LYP:

Topmost frame: Fragmentation efficiency of IR-MPD spectra; black dashed line: one color IR-MPD spectrum (FEL CLIO, Paris); blue, black and purple solid lines: one color IR-MPD spectra (blue and black at different laser intensities) (OPO/OPA, KL);

Lower frames: calculated IR intensities (km/mol) and structures of different isomers; values are ΔE / (kJ/mol); all identified isomers with up to ΔE ≤ 25 kJ/mol above the most stable conformer are considered; scaling factor 0.97.

The calculated pattern of structure A shows best agreement with the peak around 2900 cm⁻¹, although the intensity of the experimentally visible double peak between 3000 and 3100 cm⁻¹ is not described well. Pattern B includes a double peak, but this pattern shows a blue-shift of approx. 200 cm⁻¹ compared to the experiment.

Measured IR-MPD spectra of Asp-Phe H⁺

Fig. S C1: Asp-Phe H⁺:
Fragmentation efficiency of IR-MPD spectra; blue, black and purple solid lines: one color IR-MPD spectra, different laser intensities (OPO/OPA, KL); magenta solid line: one color IR-MPD spectrum (narrow band OPO/OPA, KL); red and green solid lines: two color IR-MPD spectra (OPO/OPA, KL): a) red line probe at 3550 cm^{-1}; b) red line probe at 3565 cm^{-1}, green line probe at 3550 cm^{-1}.

Measured IR-MPD spectra of Asp-Phe Li$^+$

Fig. S C2: Asp-Phe Li$^+$:
Fragmentation efficiency of IR-MPD spectra; blue and black solid lines: one color IR-MPD spectra, different laser intensities (OPO/OPA, KL); red, orange and green solid lines: two color IR-MPD spectra (OPO/OPA, KL): a) red and orange lines probe at 3555 cm^{-1}, different scanning laser intensities; b) red line probe at 3565 cm^{-1}, green line probe at 3550 cm^{-1}.

Measured IR-MPD spectra of Asp-Phe Na$^+$

Fig. S C3: Asp-Phe Na$^+$:

Fragmentation efficiency of IR-MPD spectra; blue and black solid lines: one color IR-MPD spectra, different laser intensities (OPO/OPA, KL); red and green solid lines: two color IR-MPD spectra (OPO/OPA, KL): a) red line probe at 3560 cm^{-1}; b) red line probe at 3565 cm^{-1}, green line probe at 3550 cm^{-1}.
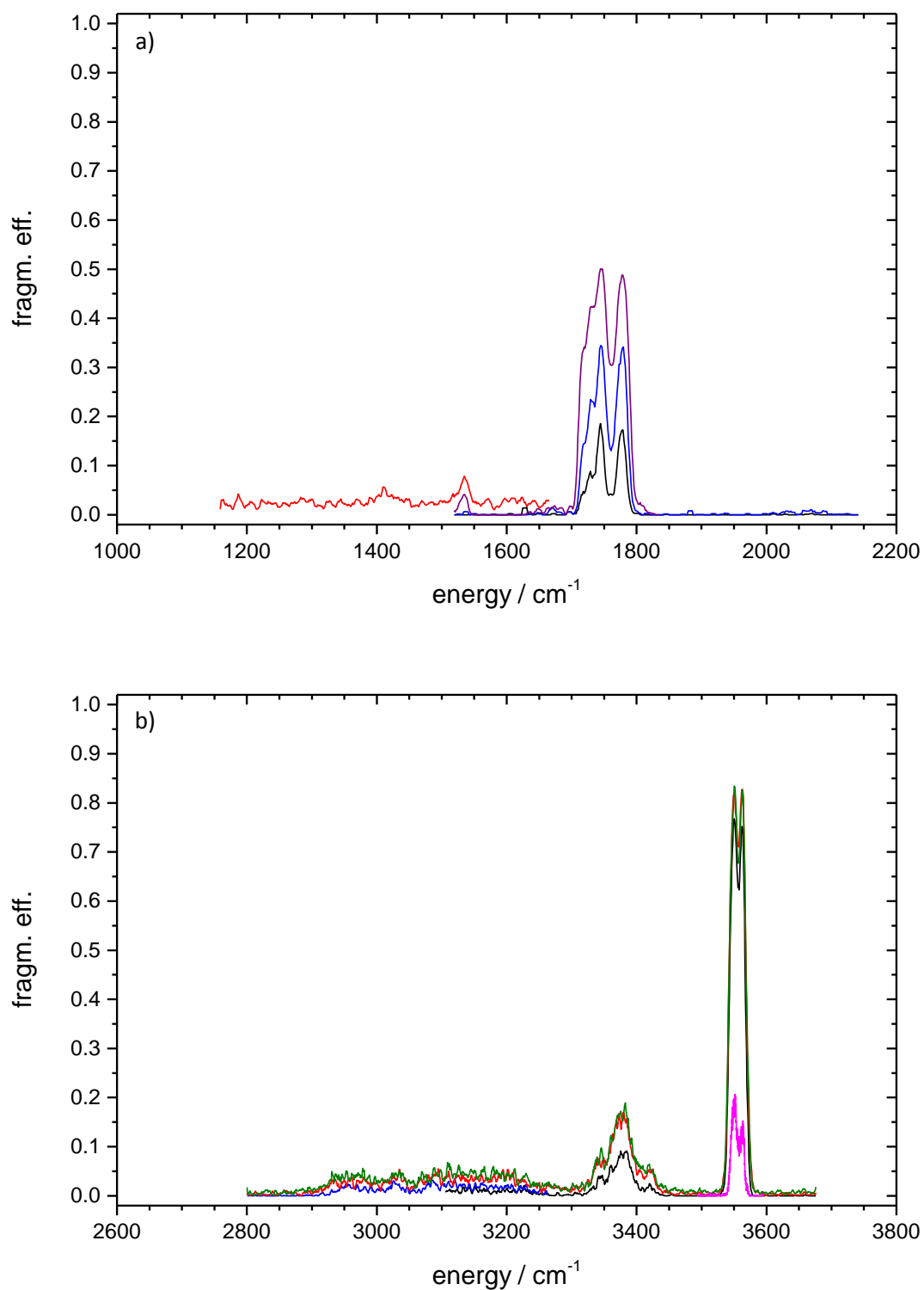
Measured IR-MPD spectra of Asp-Phe K$^+$

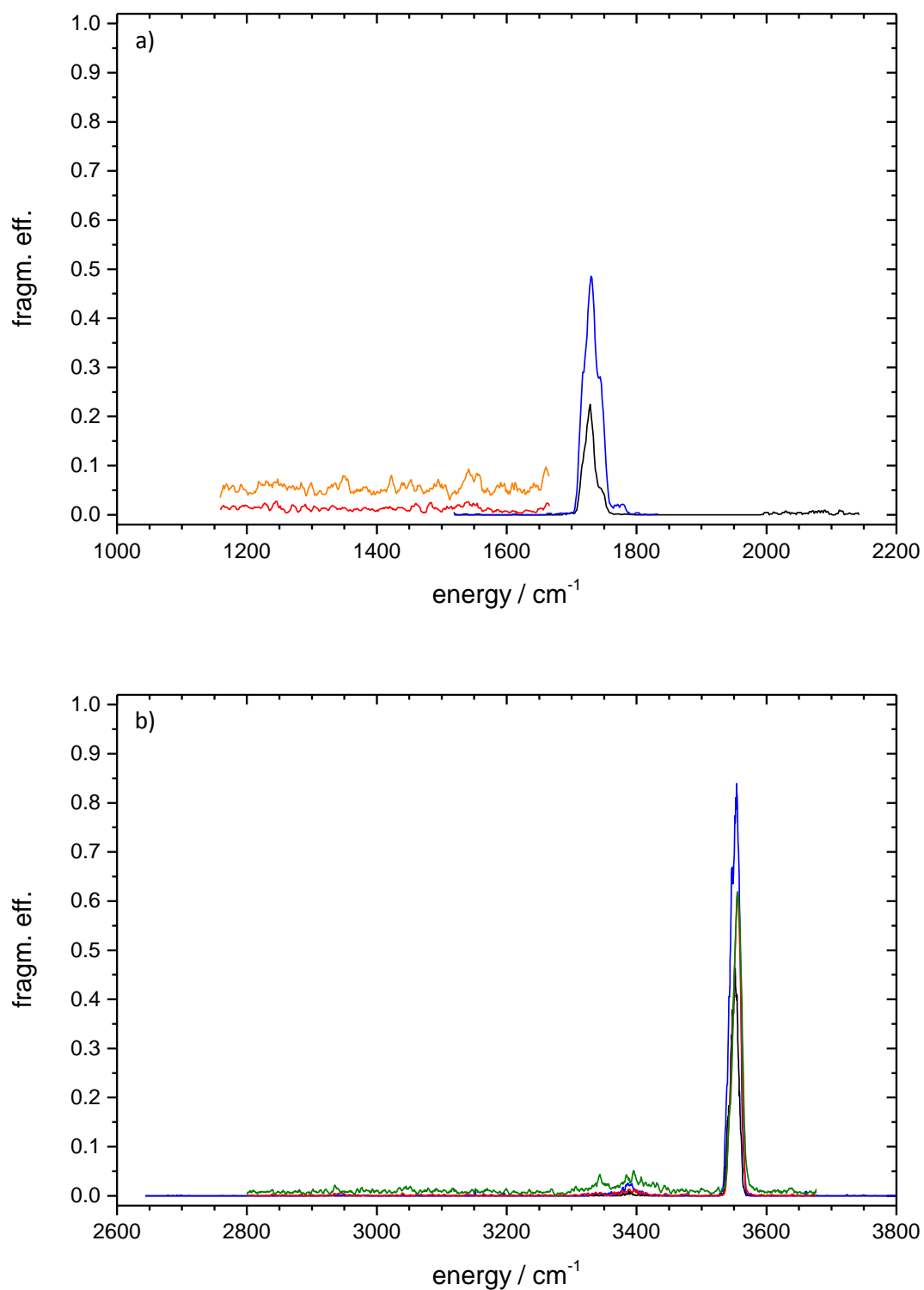**Fig. S C4: Asp-Phe K$^+$:**
Fragmentation efficiency of IR-MPD spectra; blue and black solid lines: one color IR-MPD spectra, different laser intensities (OPO/OPA, KL); red and green solid lines: two color IR-MPD spectra (OPO/OPA, KL): a) red line probe at 3565 cm^{-1}; b) red line probe at 3565 cm^{-1}, green line probe at 3550 cm^{-1};
grey solid lines: one color IR-MPD spectra, fragmentation efficiency calculated as depletion of Asp-Phe K$^+$ intensity (fragm. eff. par., see chapter 1.3.2.).

Measured IR-MPD spectra of Asp-Phe Rb⁺

Fig. S C5: Asp-Phe Rb^{+}:
Fragmentation efficiency of IR-MPD spectra; blue and black solid lines: one color IR-MPD spectra, different laser intensities (OPO/OPA, KL); red and green solid lines: two color IR-MPD spectra (OPO/OPA, KL): a) red line probe at 3565 cm^{-1}; b) red line probe at 3565 cm^{-1}, green line probe at 3550 cm^{-1};
grey solid lines: one color IR-MPD spectra, fragmentation efficiency calculated as depletion of Asp-Phe Rb^{+} intensity (fragm. eff. par., see chapter 1.3.2.).

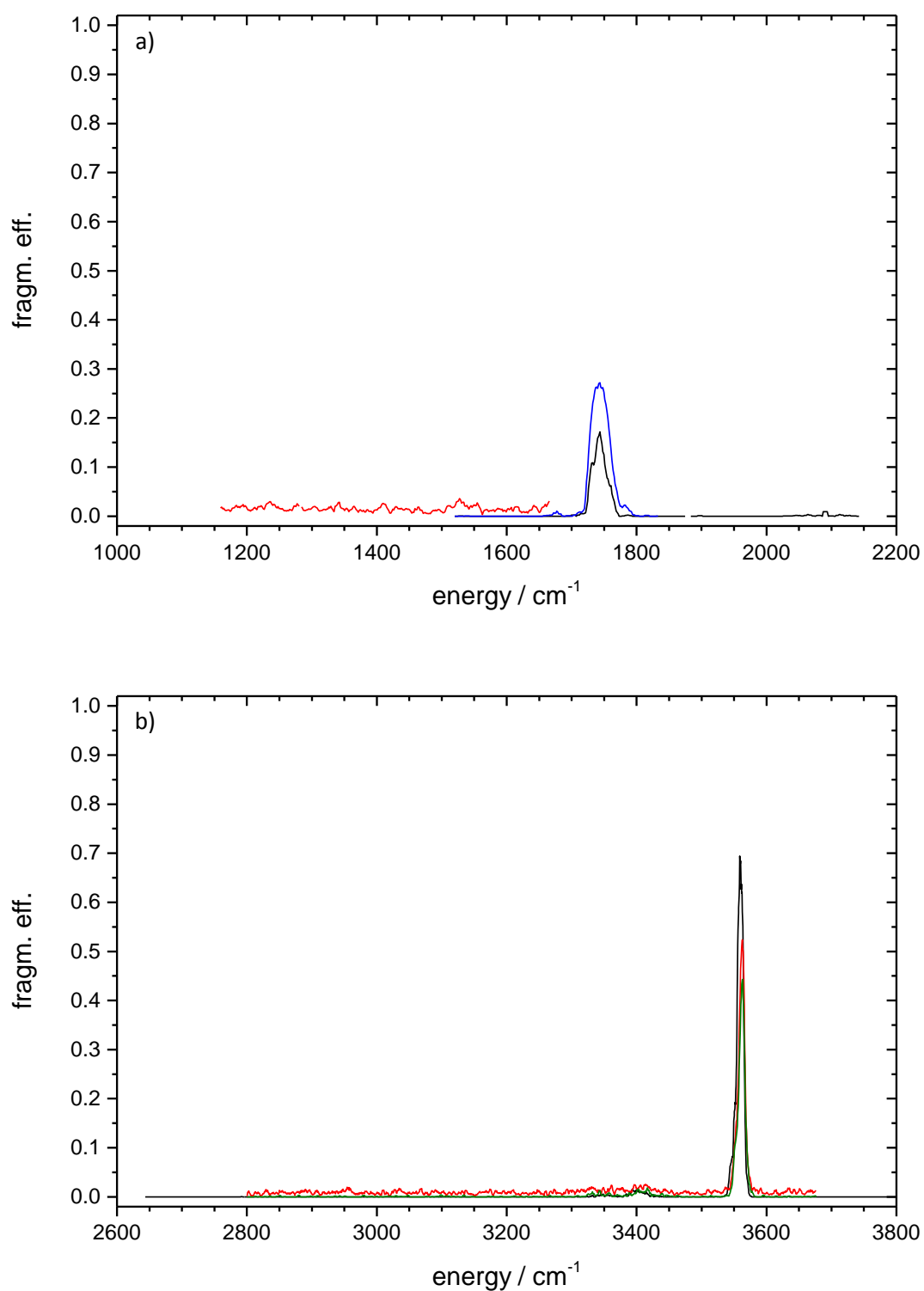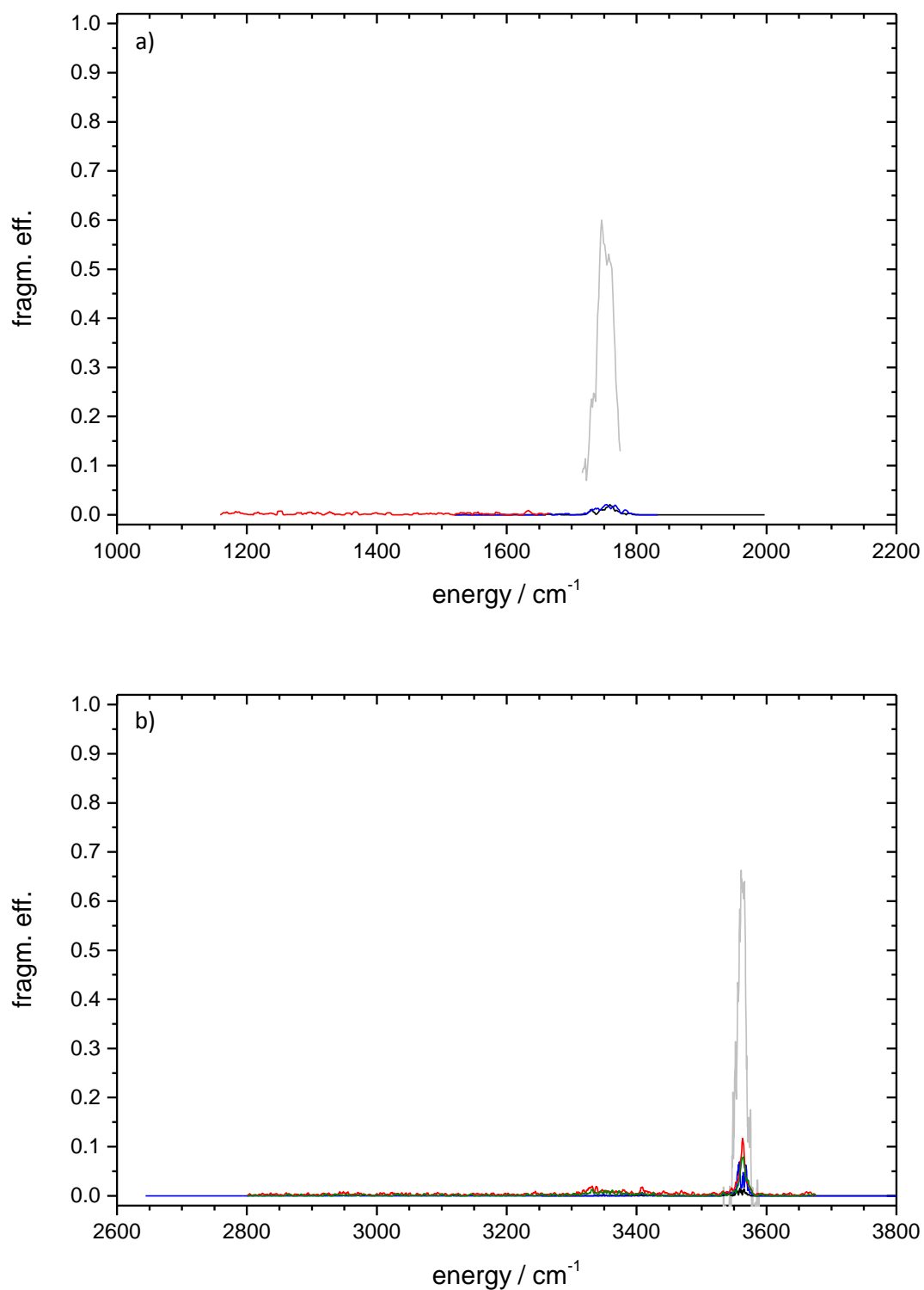**Measured IR-MPD spectra of Asp-Phe Cs$^+$**

Fig. S C6: Asp-Phe Cs$^+$:
Fragmentation efficiency of IR-MPD spectra; blue and black solid lines: one color IR-MPD spectra, different laser intensities (OPO/OPA, KL); red and green solid lines: two color IR-MPD spectra (OPO/OPA, KL): a) red line probe at 3565 cm^{-1}; b) red line probe at 3565 cm^{-1}, green line probe at 3550 cm^{-1}

Measured IR-MPD spectra of deprotonated Asp-Phe

Fig. S C7: Deprotonated Asp-Phe:
Fragmentation efficiency of IR-MPD spectra; blue, black and purple solid lines: one color IR-MPD spectra, different laser intensities (OPO/OPA, KL).

IR-MPD spectra and calculated IR intensities of Asp-Phe H$^+$; TZVP; MP2 (g03)

H-a

6-ring O···H-N:
d(O···H)=1.818 Å, d(H-N)=1.041 Å, ∠=138°
5-ring O···H-N:
d(O···H)=2.223 Å, d(H-N)=1.032 Å, ∠=106°

d(O-H$_{Asp}$)=0.980 Å
d(O-H$_{Phe}$)=0.979 Å

H-b

O···H-O:
d(O···H)=1.546 Å, d(H-O)=1.021 Å, ∠=161°

d(O-H$_{Asp}$)=0.980 Å
d(O-H$_{Phe}$)=0.979 Å

H-d

6-ring O···H-N:
d(O···H)=1.691 Å, d(H-N)=1.057 Å, ∠=145°

d(O-H$_{Asp}$)=0.980 Å
d(O-H$_{Phe}$)=0.979 Å

H-c

6-ring O···H-N:
d(O···H)=1.708 Å, d(H-N)=1.054 Å, ∠=142°
5-ring O···H-N:
d(O···H)=1.849 Å, d(H-N)=1.047 Å, ∠=122°
O-H···O:
d(O-H)=0.983 Å, d(H···O)=1.837 Å, ∠=155°

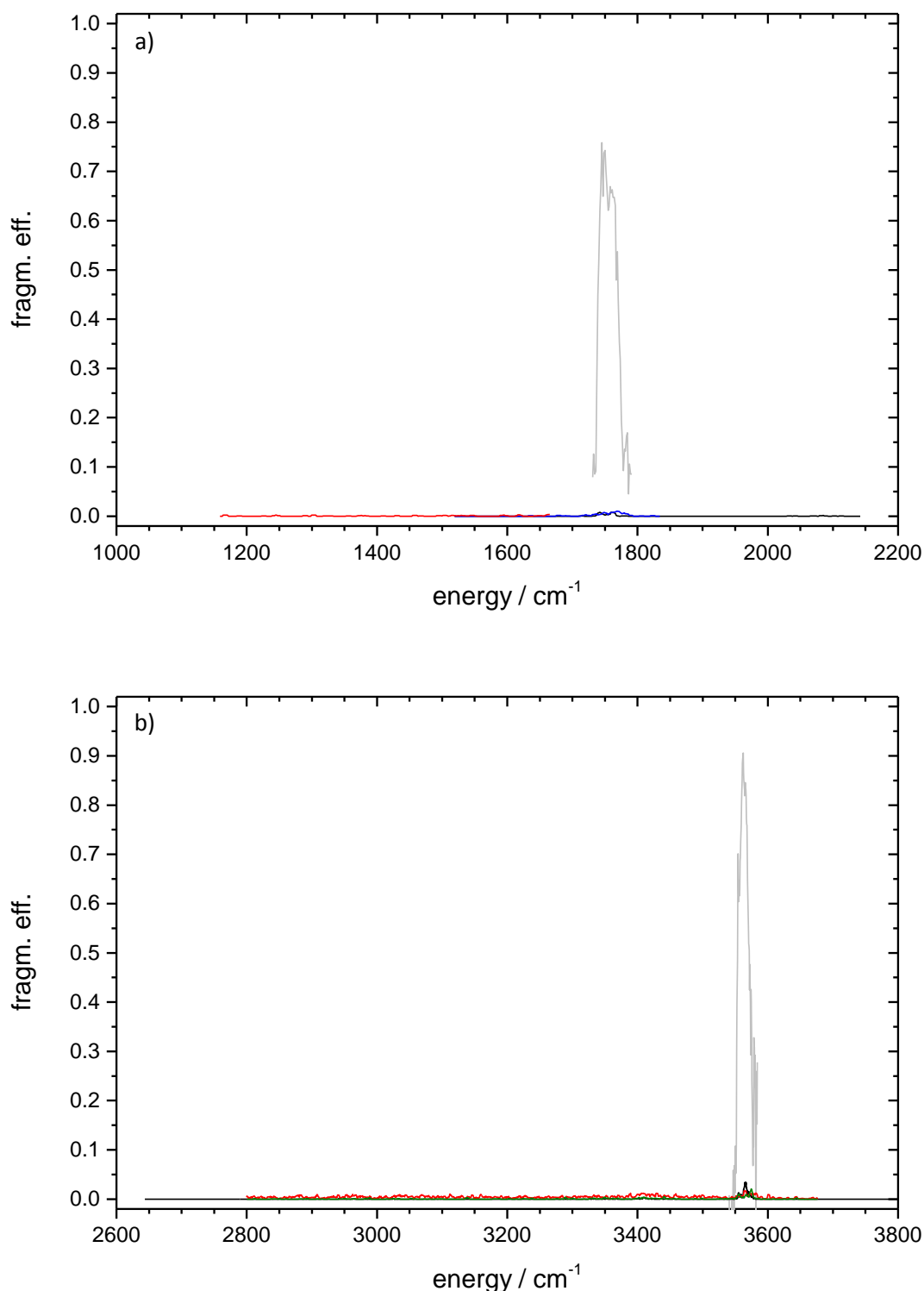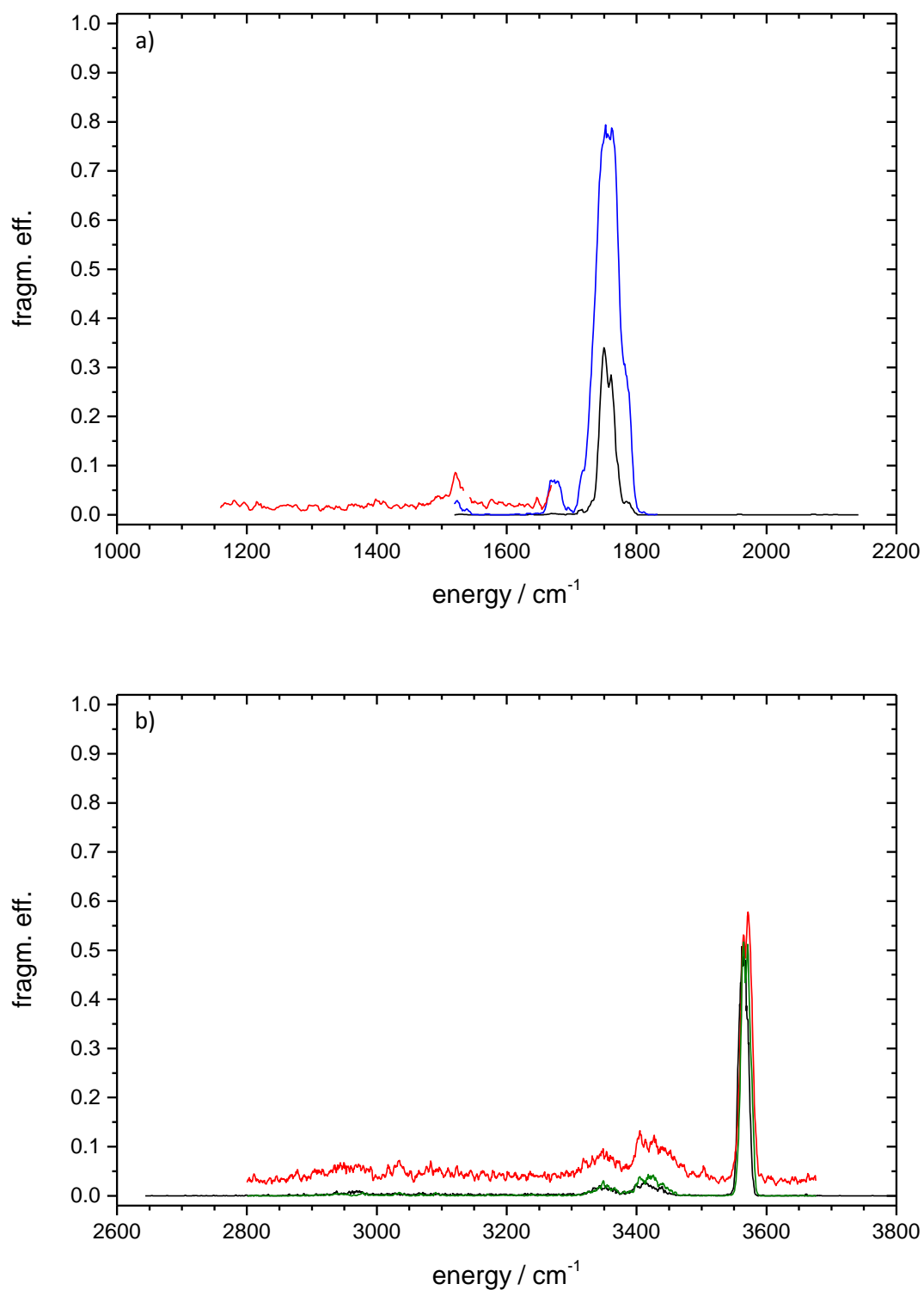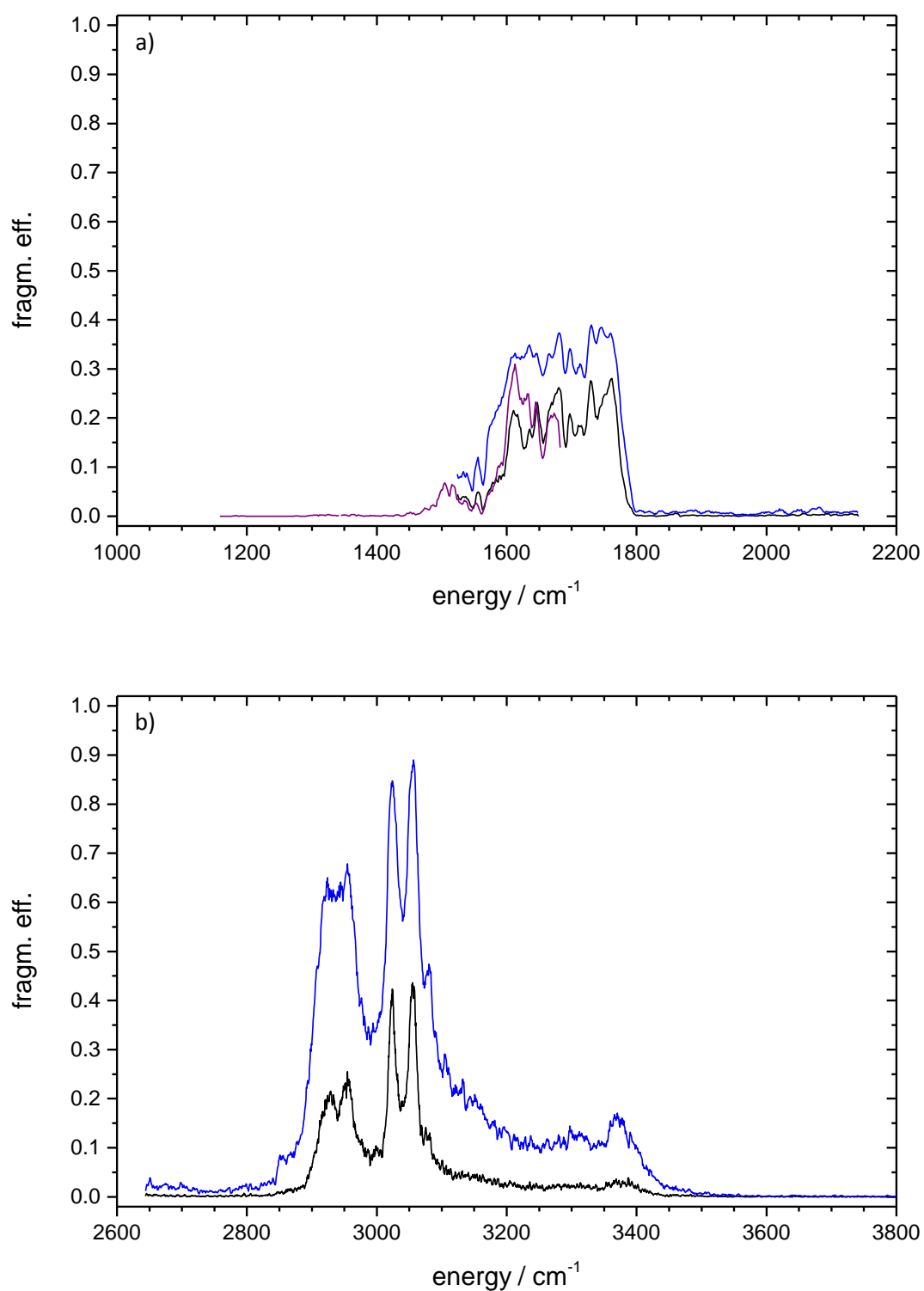d(O-H$_{Phe}$)=0.980 Å

Fig. S D1: Asp-Phe H$^+$; TZVP; MP2:

Topmost frame: Fragmentation efficiency of IR-MPD spectra; blue, black and purple solid lines: one color IR-MPD spectra, different laser intensities (OPO/OPA, KL); magenta solid line: one color IR-MPD spectrum (narrow band OPO/OPA, KL); red and green solid lines: two color IR-MPD spectra (OPO/OPA, KL): 1100 - 1700 cm^{-1}: red line probe at 3550 cm^{-1}; 2800 - 3700 cm^{-1}: red line probe at 3565 cm^{-1}, green line probe at 3550 cm^{-1};

Lower frames: calculated IR intensities (km/mol) and structures of different isomers; values are ΔE / (kJ/mol); all identified isomers with up to ΔE ≤ 25.5 kJ/mol above the most stable conformer are considered; scaling factor 0.96.

The calculated pattern of structure B shows best agreement, but also structures A and C could be conducive to the experimental spectrum. A distinction between the three structures in the area of the C=O stretching vibration is challenging, as the laser intensity of the OPO/OPA is rather low below 1700 cm^{-1}.

IR-MPD spectra and calculated IR intensities of Asp-Phe H$^+$; cc-pVDZ; MP2 (g03)

Fig. S D2: Asp-Phe H$^+$; cc-pVDZ; MP2:

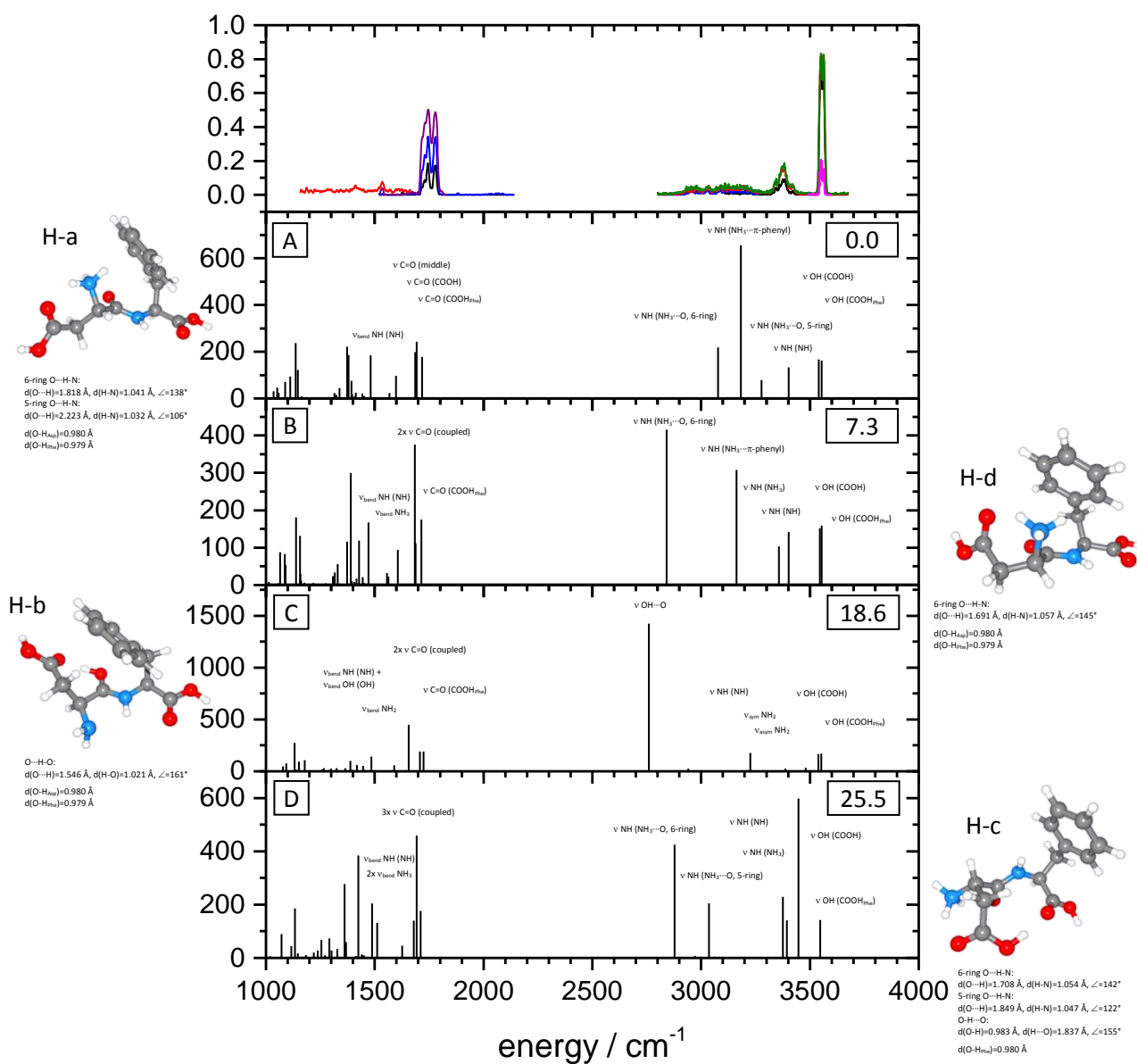*Topmost frame: Fragmentation efficiency of IR-MPD spectra; blue, black and purple solid lines: one color IR-MPD spectra, different laser intensities (OPO/OPA, KL); magenta solid line: one color IR-MPD spectrum (narrow band OPO/OPA, KL); red and green solid lines: two color IR-MPD spectra (OPO/OPA, KL): 1100 - 1700 cm^{-1}: red line probe at 3550 cm^{-1}; 2800 - 3700 cm^{-1}: red line probe at 3565 cm^{-1}, green line probe at 3550 cm^{-1};*

Lower frames: calculated IR intensities (km/mol) and structures of different isomers; values are ΔE / (kJ/mol); all identified isomers with up to ΔE ≤ 25 kJ/mol above the most stable conformer are considered; scaling factor 0.96.

The calculated patterns of structures A and B show best agreement, although the experimental fragmentation efficiency of the OH stretching vibrations is much higher than the one of the NH stretching vibrations. A distinction between the two structures in the area of the C=O stretching vibration is challenging, as the laser intensity of the OPO/OPA is rather low below 1700 cm^{-1}.

IR-MPD spectra and calculated IR intensities of Asp-Phe H$^+$; TZVP; DFT: B3LYP (g03)
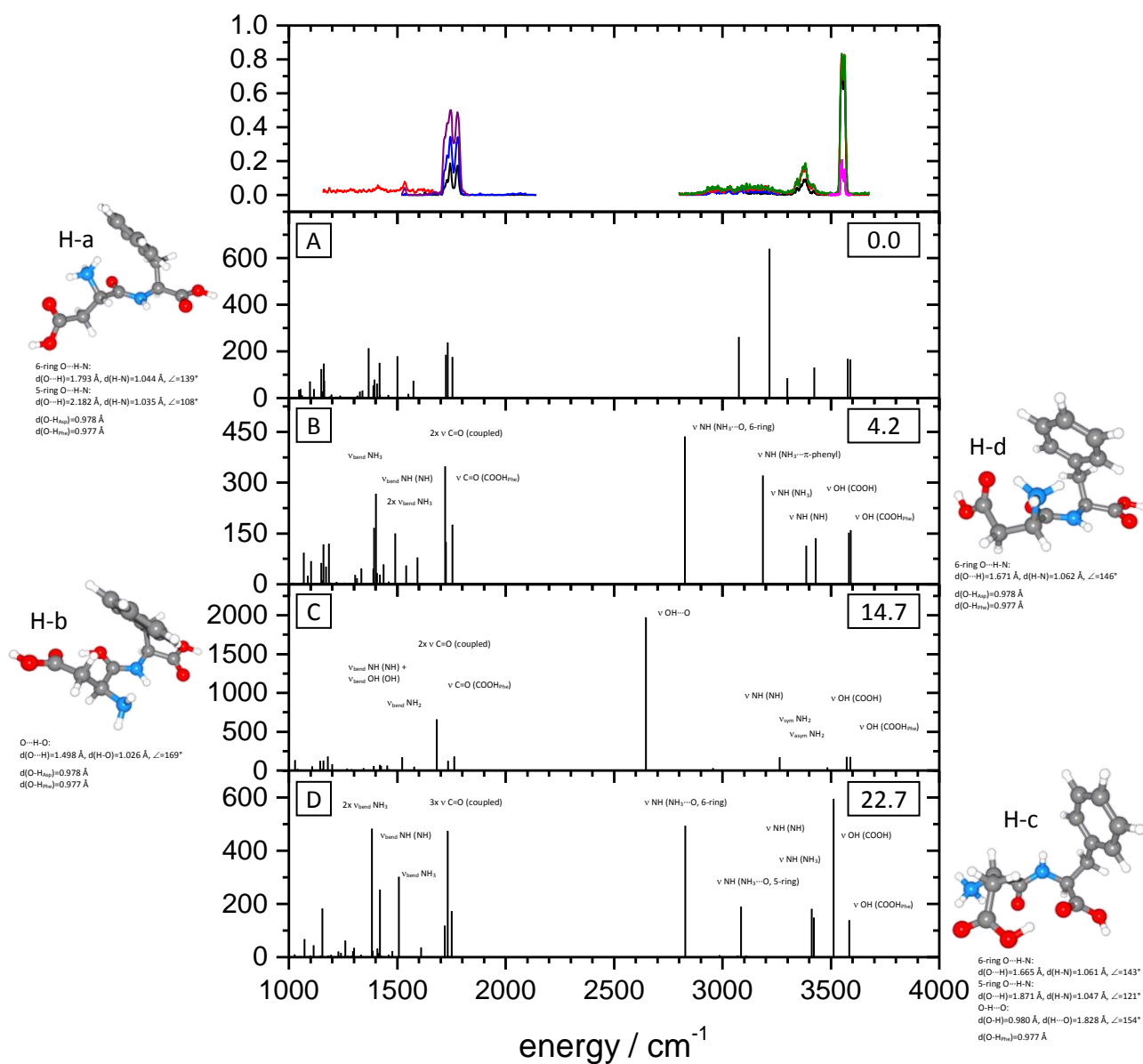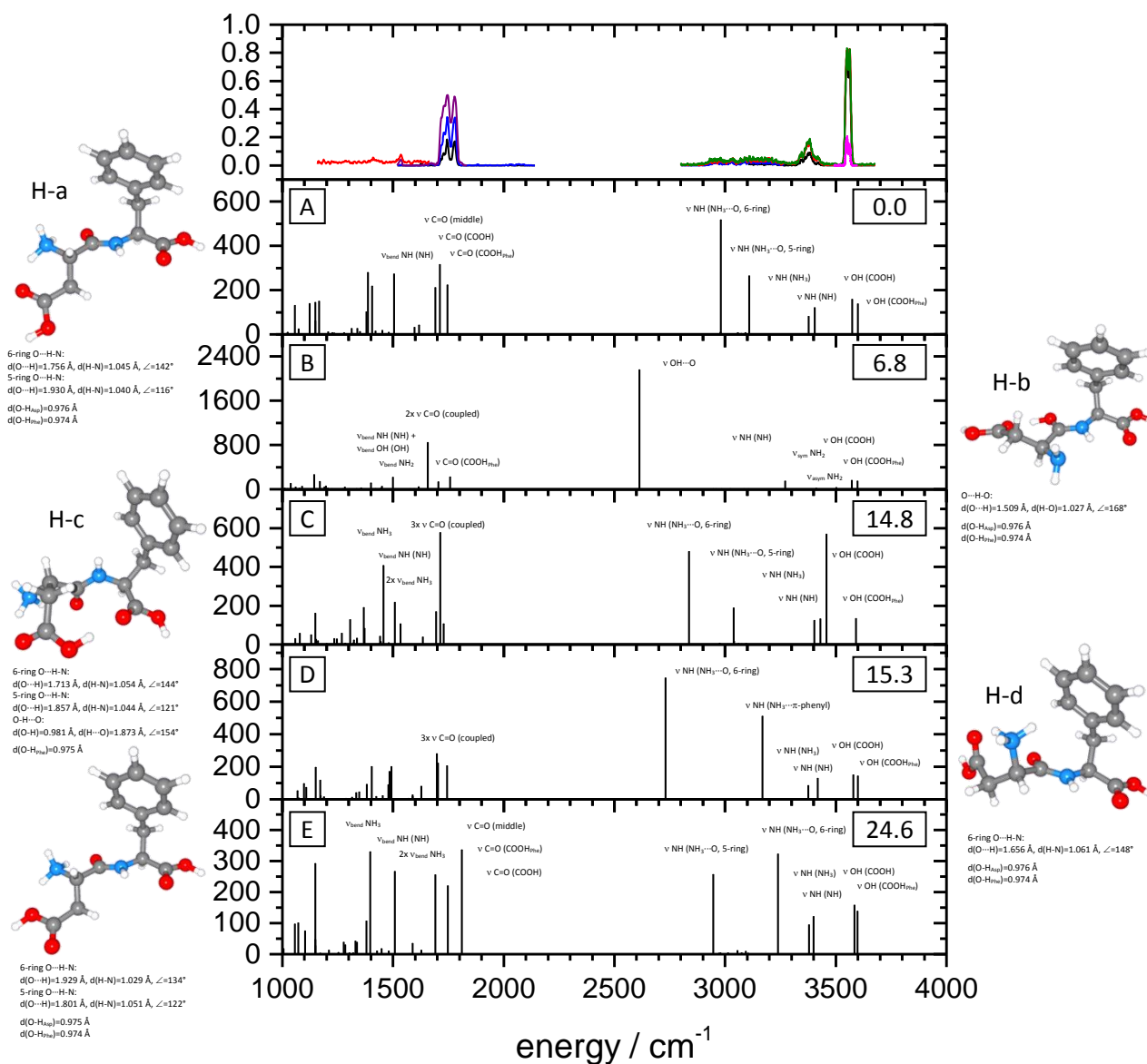

Fig. S D3: Asp-Phe H$^+$; TZVP; DFT: B3LYP:

Topmost frame: Fragmentation efficiency of IR-MPD spectra; blue, black and purple solid lines: one color IR-MPD spectra, different laser intensities (OPO/OPA, KL); magenta solid line: one color IR-MPD spectrum (narrow band OPO/OPA, KL); red and green solid lines: two color IR-MPD spectra (OPO/OPA, KL): 1100 - 1700 cm^{-1}: red line probe at 3550 cm^{-1}; 2800 - 3700 cm^{-1}: red line probe at 3565 cm^{-1}, green line probe at 3550 cm^{-1};

Lower frames: calculated IR intensities (km/mol) and structures of different isomers; values are ΔE / (kJ/mol); all identified isomers with up to $\Delta E \leq 25$ kJ/mol above the most stable conformer are considered; scaling factor 0.97.

The calculated pattern of structure A shows best agreement, but also structures D and E could be conducive to the experimental spectrum. A distinction between the three structures in the area of the C=O stretching vibration is challenging, as the laser intensity of the OPO/OPA is rather low below 1700 cm^{-1}.

IR-MPD spectra and calculated IR intensities of Asp-Phe H$^+$; cc-pVDZ; DFT: B3LYP (g03)

H-a

6-ring O···H-N:
d(O···H)=1.719 Å, d(H-N)=1.053 Å, ∠=143°
5-ring O···H-N:
d(O···H)=1.886 Å, d(H-N)=1.048 Å, ∠=118°
d(O-H$_{Asp}$)=0.979 Å
d(O-H$_{Phe}$)=0.977 Å

H-b

O···H-O:
d(O···H)=1.490 Å, d(H-O)=1.033 Å, ∠=169°
d(O-H$_{Asp}$)=0.979 Å
d(O-H$_{Phe}$)=0.977 Å

H-c

6-ring O···H-N:
d(O···H)=1.652 Å, d(H-N)=1.067 Å, ∠=145°
5-ring O···H-N:
d(O···H)=1.846 Å, d(H-N)=1.050 Å, ∠=122°
O···H···O:
d(O-H)=0.983 Å, d(H···O)=1.828 Å, ∠=154°
d(O-H$_{Phe}$)=0.977 Å

H-d

6-ring O···H-N:
d(O···H)=1.604 Å, d(H-N)=1.076 Å, ∠=149°
d(O-H$_{Asp}$)=0.978 Å
d(O-H$_{Phe}$)=0.977 Å

Fig. S D4: Asp-Phe H$^+$; cc-pVDZ; DFT: B3LYP:
Topmost frame: Fragmentation efficiency of IR-MPD spectra; blue, black and purple solid lines: one color IR-MPD spectra, different laser intensities (OPO/OPA, KL); magenta solid line: one color IR-MPD spectrum (narrow band OPO/OPA, KL); red and green solid lines: two color IR-MPD spectra (OPO/OPA, KL): 1100 - 1700 cm^{-1}: red line probe at 3550 cm^{-1}; 2800 - 3700 cm^{-1}: red line probe at 3565 cm^{-1}, green line probe at 3550 cm^{-1};
Lower frames: calculated IR intensities (km/mol) and structures of different isomers; values are ΔE / (kJ/mol); all identified isomers with up to ΔE ≤ 25 kJ/mol above the most stable conformer are considered; scaling factor 0.97.
The calculated pattern of structure A and B show best agreement. A distinction between the two structures in the area of the C=O stretching vibration is challenging, as the laser intensity of the OPO/OPA is rather low below 1700 cm^{-1}.

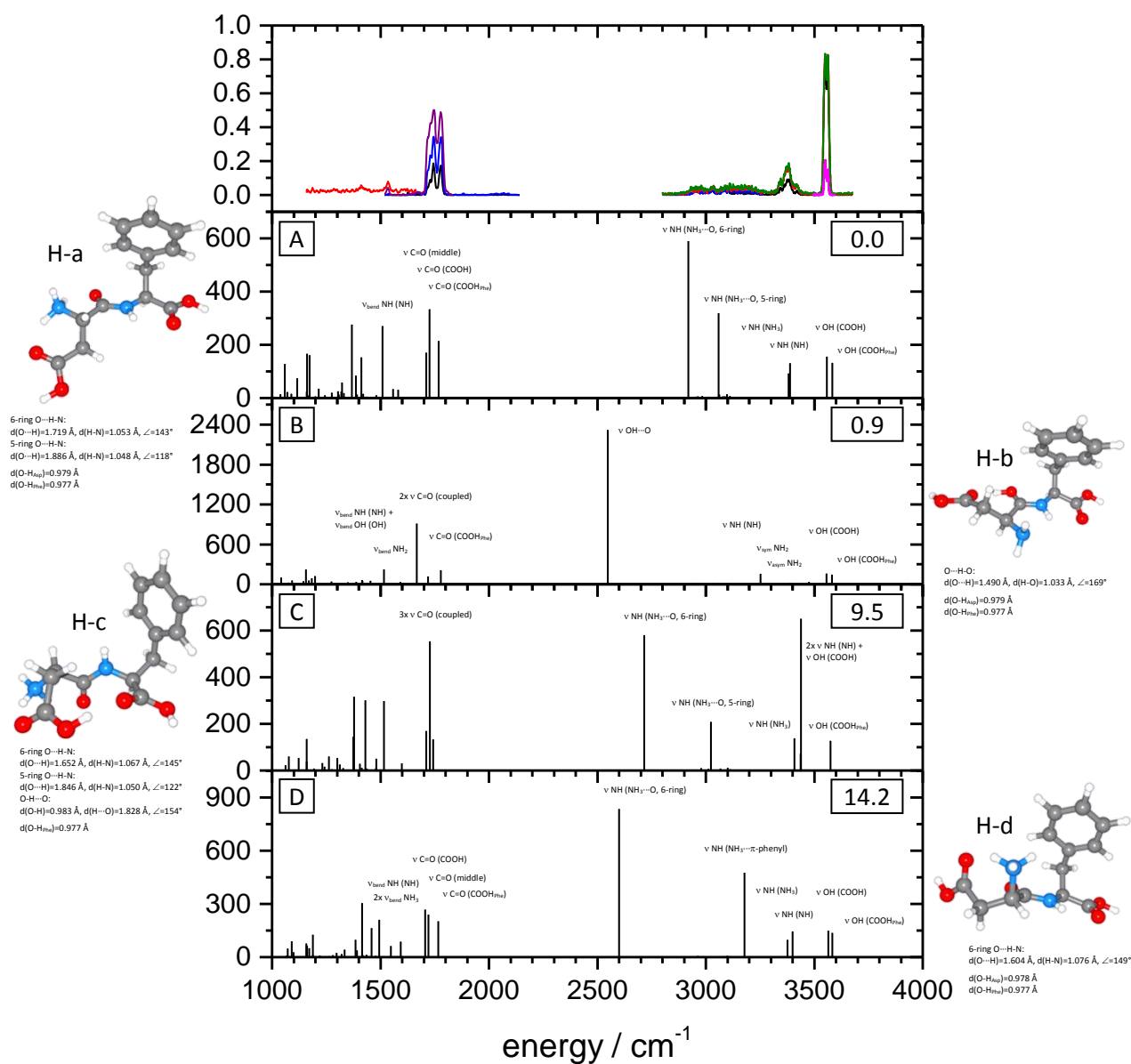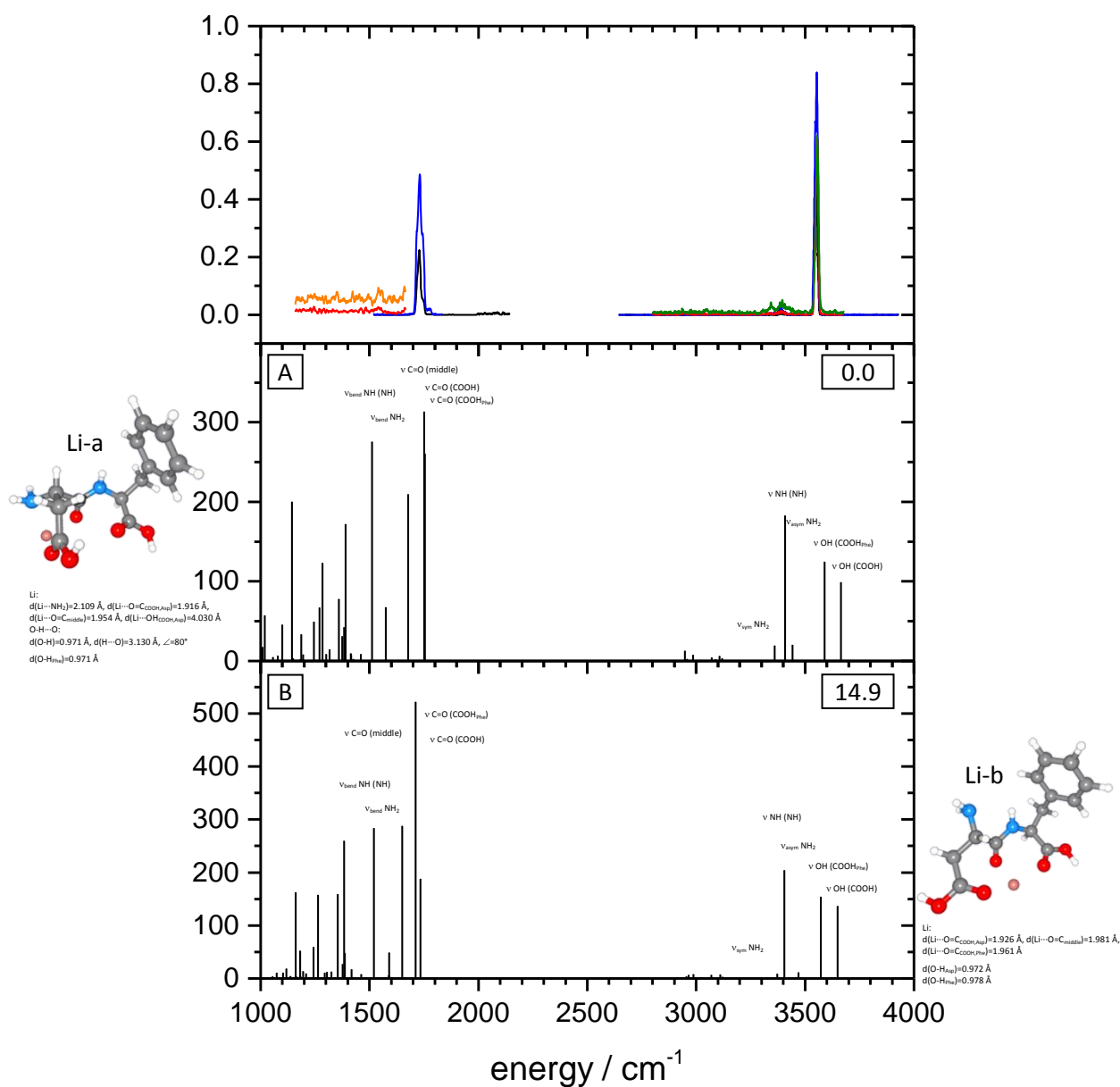**IR-MPD spectra and calculated IR intensities of Asp-Phe Li⁺; cc-pVDZ; MP2 (g03)**

Fig. S D5: Asp-Phe Li⁺; cc-pVDZ; MP2:

Topmost frame: Fragmentation efficiency of IR-MPD spectra; blue and black solid lines: one color IR-MPD spectra, different laser intensities (OPO/OPA, KL); red, orange and green solid lines: two color IR-MPD spectra (OPO/OPA, KL): 1100 - 1700 cm⁻¹: red and orange lines probe at 3555 cm⁻¹, different laser intensities; 2800 - 3700 cm⁻¹: red line probe at 3565 cm⁻¹, green line probe at 3550 cm⁻¹;

Lower frames: calculated IR intensities (km/mol) and structures of different isomers; values are ΔE / (kJ/mol); all identified isomers with up to ΔE ≤ 25 kJ/mol above the most stable conformer are considered; scaling factor 0.96.

For both calculated structures the distance between the two OH stretching vibrations is much higher than the experimentally observed one.

IR-MPD spectra and calculated IR intensities of Asp-Phe Li$^+$; cc-pVDZ; DFT: B3LYP (g03)

Fig. S D6: Asp-Phe Li$^+$; cc-pVDZ; DFT: B3LYP:

Topmost frame: Fragmentation efficiency of IR-MPD spectra; blue and black solid lines: one color IR-MPD spectra, different laser intensities (OPO/OPA, KL); red, orange and green solid lines: two color IR-MPD spectra (OPO/OPA, KL): 1100 - 1700 cm^{-1}: red and orange lines probe at 3555 cm^{-1}, different laser intensities; 2800 - 3700 cm^{-1}: red line probe at 3565 cm^{-1}, green line probe at 3550 cm^{-1};

Lower frames: calculated IR intensities (km/mol) and structures of different isomers; values are ΔE / (kJ/mol); all identified isomers with up to $\Delta E \leq 25$ kJ/mol above the most stable conformer are considered; scaling factor 0.97.

The calculated pattern of structure A shows best agreement.

IR-MPD spectra and calculated IR intensities of Asp-Phe Na⁺; cc-pVDZ; MP2 (g03)

Fig. S D7: Asp-Phe Na⁺; cc-pVDZ; MP2:

Topmost frame: Fragmentation efficiency of IR-MPD spectra; blue and black solid lines: one color IR-MPD spectra, different laser intensities (OPO/OPA, KL); red and green solid lines: two color IR-MPD spectra (OPO/OPA, KL): 1100 - 1700 cm⁻¹: red line probe at 3560 cm⁻¹; 2800 - 3700 cm⁻¹: red line probe at 3565 cm⁻¹, green line probe at 3550 cm⁻¹;

Lower frames: calculated IR intensities (km/mol) and structures of different isomers; values are ΔE / (kJ/mol); all identified isomers with up to ΔE ≤ 25 kJ/mol above the most stable conformer are considered; scaling factor 0.96.

The calculated pattern of structure B shows best agreement, although the predicted C=O (middle) stretching vibration was not obtained experimentally.

IR-MPD spectra and calculated IR intensities of Asp-Phe Na$^+$; cc-pVDZ; DFT: B3LYP (g03)
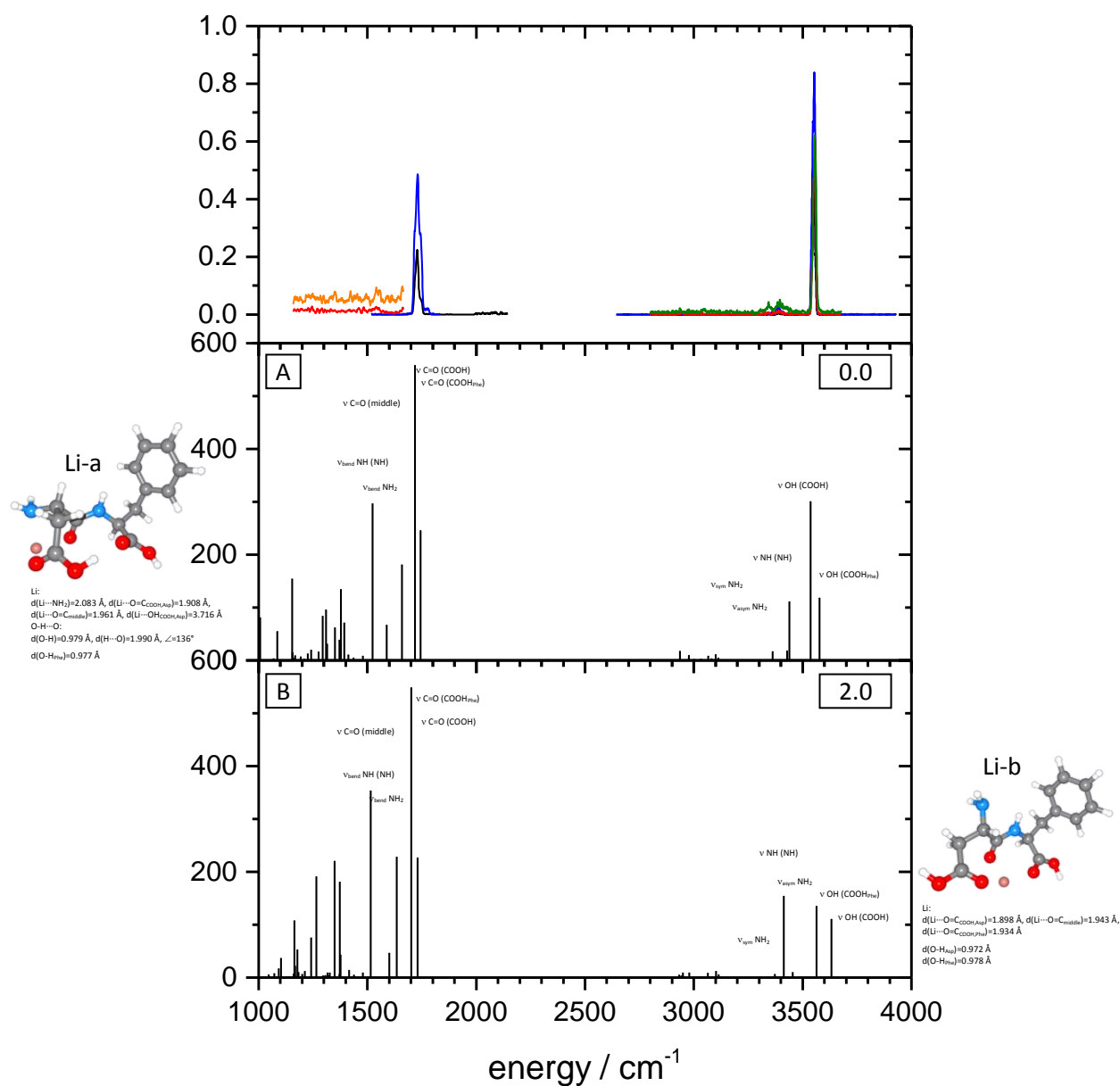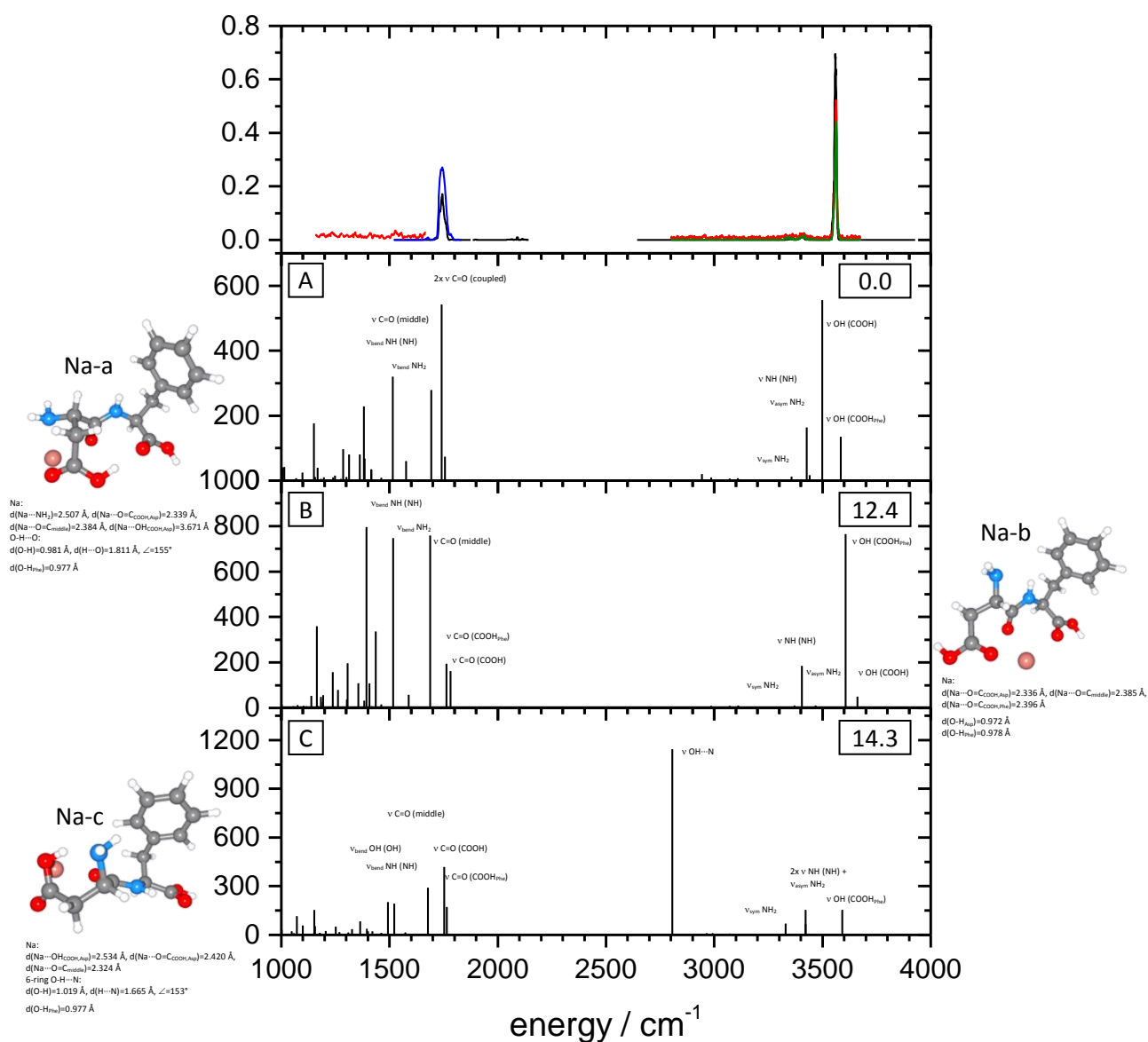

Fig. S D8: Asp-Phe Na$^+$; cc-pVDZ; DFT: B3LYP:

Topmost frame: Fragmentation efficiency of IR-MPD spectra; blue and black solid lines: one color IR-MPD spectra, different laser intensities (OPO/OPA, KL); red and green solid lines: two color IR-MPD spectra (OPO/OPA, KL): 1100 - 1700 cm^{-1}: red line probe at 3560 cm^{-1}; 2800 - 3700 cm^{-1}: red line probe at 3565 cm^{-1}, green line probe at 3550 cm^{-1};

Lower frames: calculated IR intensities (km/mol) and structures of different isomers; values are ΔE / (kJ/mol); all identified isomers with up to ΔE ≤ 25 kJ/mol above the most stable conformer are considered; scaling factor 0.97.

The calculated pattern of structure B shows best agreement, although the predicted C=O (middle) stretching vibration was not obtained experimentally.

IR-MPD spectra and calculated IR intensities of Asp-Phe K⁺;
cc-pVDZ / Stuttgart RSC 1997; MP2 (g03)

Fig. S D9: Asp-Phe K⁺; cc-pVDZ (C, H, N, O), Stuttgart RSC 1997 (K); MP2:

Topmost frame: Fragmentation efficiency of IR-MPD spectra; blue and black solid lines: one color IR-MPD spectra, different laser intensities (OPO/OPA, KL); red and green solid lines: two color IR-MPD spectra (OPO/OPA, KL): 1100 - 1700 cm⁻¹: red line probe at 3565 cm⁻¹; 2800 - 3700 cm⁻¹: red line probe at 3565 cm⁻¹, green line probe at 3550 cm⁻¹;

Lower frames: calculated IR intensities (km/mol) and structures of different isomers; values are ΔE / (kJ/mol); all identified isomers with up to ΔE ≤ 25 kJ/mol above the most stable conformer are considered; scaling factor 0.96.

The calculated pattern of structure A shows best agreement, although the predicted C=O (middle) stretching vibration and the harmonically calculated OH···N stretching vibration were not obtained experimentally.

IR-MPD spectra and calculated IR intensities of Asp-Phe K$^+$; cc-pVDZ / Stuttgart RSC 1997; DFT: B3LYP (g03)

K-b

K:
d(K···O=C$_{COOH,Asp}$)=2.644 Å, d(K···O=C$_{middle}$)=2.729 Å,
d(K···O=C$_{COOH,Phe}$)=2.707 Å

d(O-H$_{Asp}$)=0.972 Å
d(O-H$_{Phe}$)=0.976 Å

K-a

K:
d(K···NH$_2$)=2.944 Å, d(K···O=C$_{COOH,Asp}$)=2.677 Å,
d(K···O=C$_{middle}$)=2.727 Å, d(K···OH$_{COOH,Asp}$)=3.696 Å
O-H···O:
d(O-H)=0.985 Å, d(H···O)=1.782 Å, ∠=163°
d(O-H$_{Phe}$)=0.977 Å

K-c

K:
d(K···OH$_{COOH,Asp}$)=2.880 Å, d(K···O=C$_{COOH,Asp}$)=2.692 Å,
d(K···O=C$_{middle}$)=2.732 Å
6-ring O-H···N:
d(O-H)=1.012 Å, d(H···N)=1.711 Å, ∠=152°
d(O-H$_{Phe}$)=0.977 Å

K-d

K:
d(K···O=C$_{COOH,Asp}$)=2.671 Å, d(K···OH$_{COOH,Asp}$)=2.782 Å
O-H···O:
d(O-H)=1.061 Å, d(H···O)=1.412 Å, ∠=172°
d(O-H$_{Phe}$)=0.976 Å

K:
d(K···O=C$_{COOH,Asp}$)=2.663 Å, d(K···OH$_{COOH,Asp}$)=2.831 Å
6-ring O-H···N:
d(O-H)=1.060 Å, d(H···N)=1.532 Å, ∠=156°
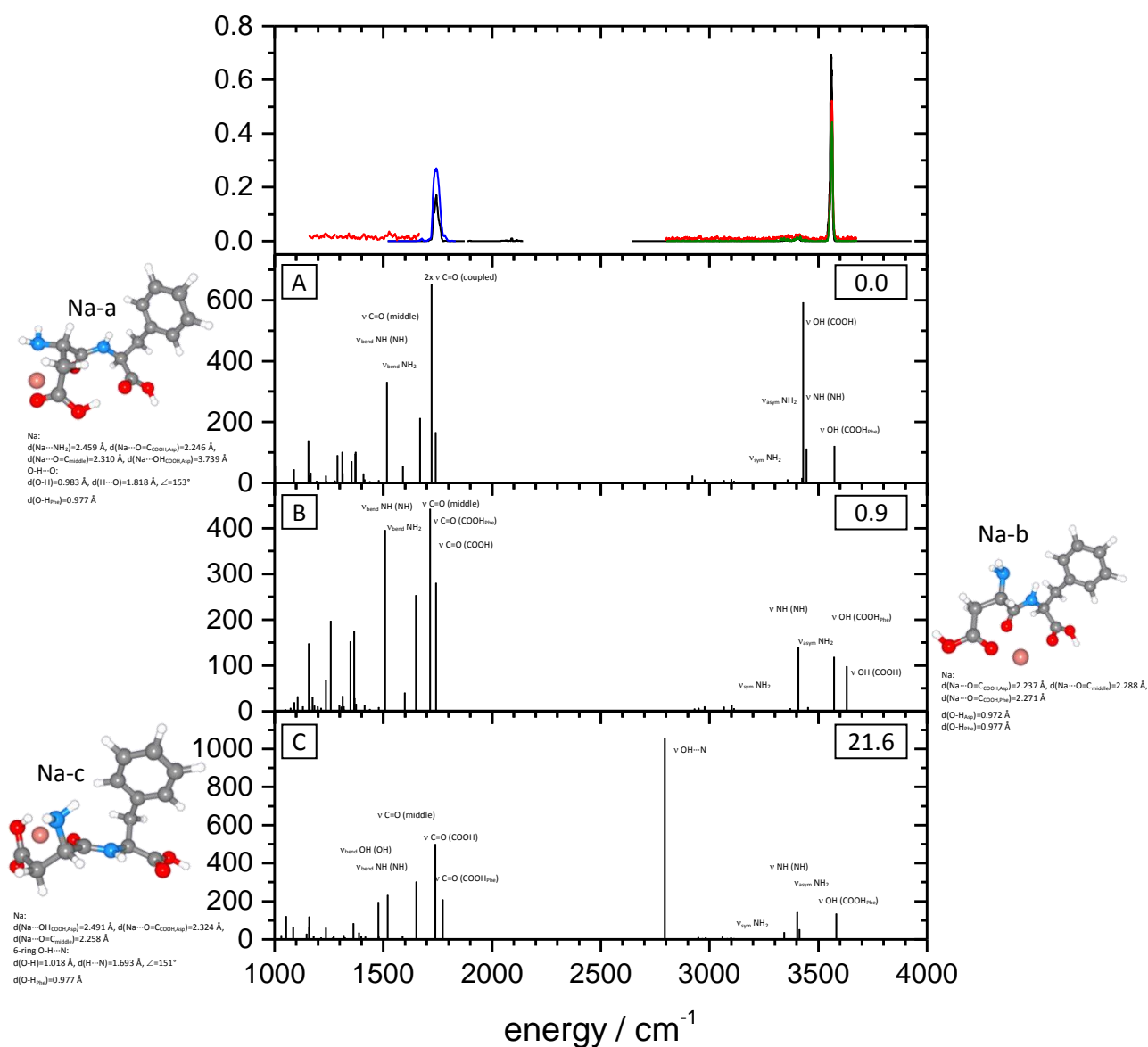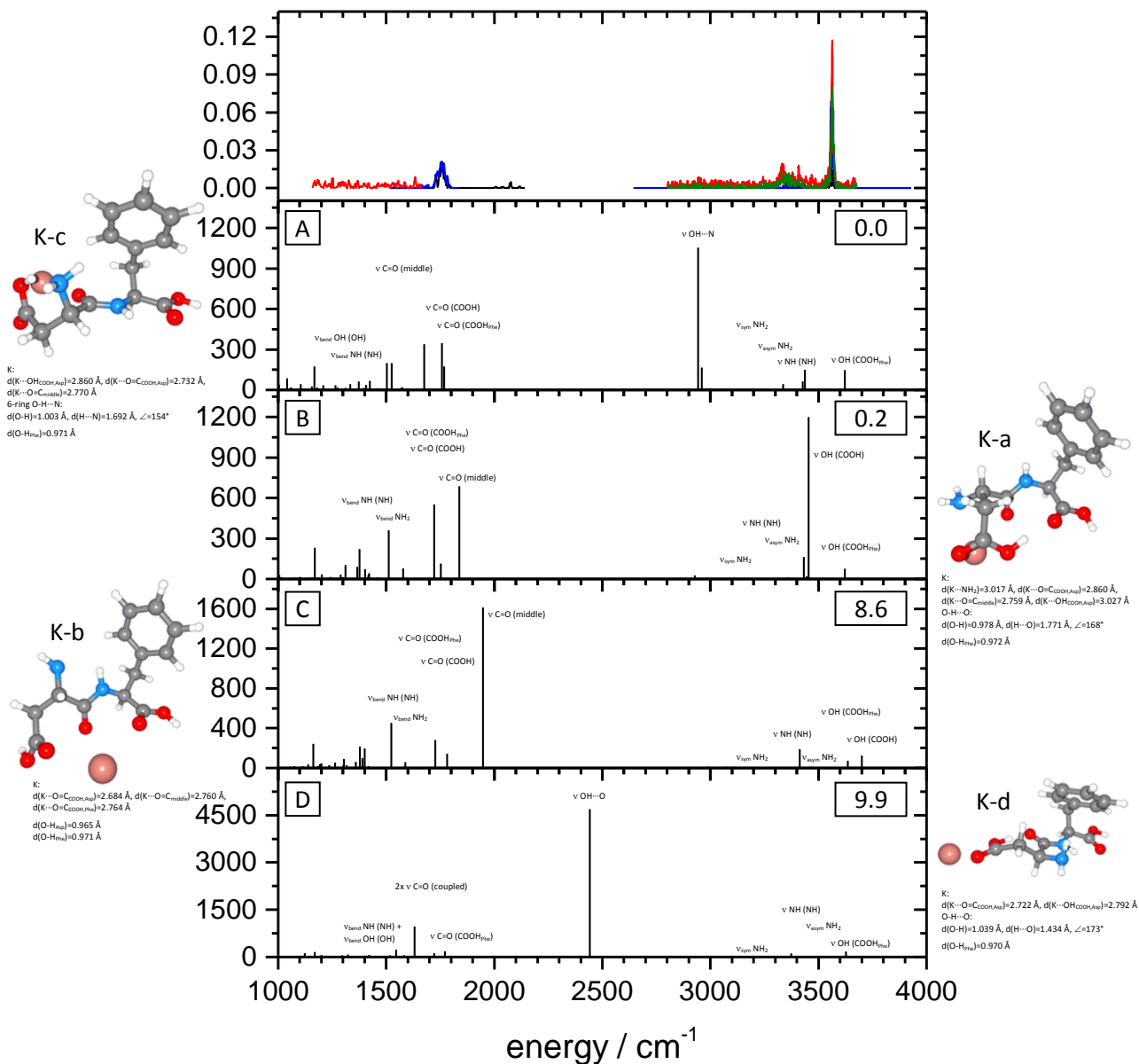d(O-H$_{Phe}$)=0.976 Å

Fig. S D10: Asp-Phe K$^+$; cc-pVDZ (C, H, N, O), Stuttgart RSC 1997 (K); DFT: B3LYP:

Topmost frame: Fragmentation efficiency of IR-MPD spectra; blue and black solid lines: one color IR-MPD spectra, different laser intensities (OPO/OPA, KL); red and green solid lines: two color IR-MPD spectra (OPO/OPA, KL): 1100 - 1700 cm^{-1}: red line probe at 3565 cm^{-1}; 2800 - 3700 cm^{-1}: red line probe at 3565 cm^{-1}, green line probe at 3550 cm^{-1};

Lower frames: calculated IR intensities (km/mol) and structures of different isomers; values are ΔE / (kJ/mol); all identified isomers with up to ΔE ≤ 25 kJ/mol above the most stable conformer are considered; scaling factor 0.97.

The calculated patterns of structures B and C show best agreement, although the predicted C=O (middle) stretching vibration and the harmonically calculated OH···N stretching vibration were not obtained experimentally. A distinction between the four structures in the area of the C=O stretching vibration is challenging, as the laser intensity of the OPO/OPA is rather low below 1700 cm^{-1}.

IR-MPD spectra and calculated IR intensities of Asp-Phe Rb$^+$;
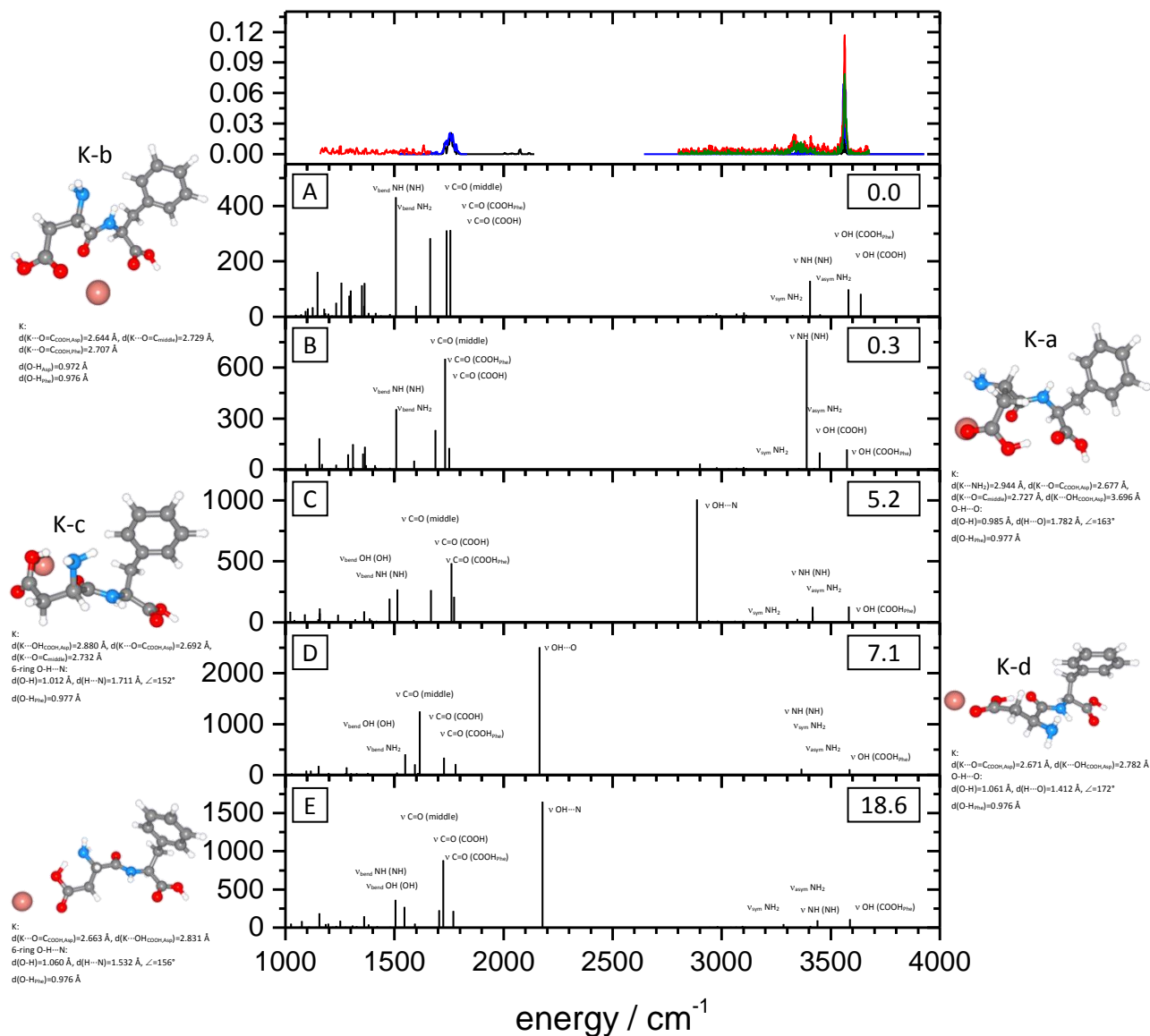**cc-pVDZ / Stuttgart RSC 1997; MP2 (g03)**

Fig. S D11: Asp-Phe Rb$^+$; cc-pVDZ (C, H, N, O), Stuttgart RSC 1997 (Rb); MP2:

Topmost frame: Fragmentation efficiency of IR-MPD spectra; blue and black solid lines: one color IR-MPD spectra, different laser intensities (OPO/OPA, KL); red and green solid lines: two color IR-MPD spectra (OPO/OPA, KL): 1100 - 1700 cm^{-1}: red line probe at 3565 cm^{-1}; 2800 - 3700 cm^{-1}: red line probe at 3565 cm^{-1}, green line probe at 3550 cm^{-1};

Lower frames: calculated IR intensities (km/mol) and structures of different isomers; values are ΔE / (kJ/mol); all identified isomers with up to $\Delta E \leq 25$ kJ/mol above the most stable conformer are considered; scaling factor 0.96.

The calculated pattern of structure A shows best agreement, although the predicted C=O (middle) stretching vibration and the harmonically calculated OH + div. C-H stretching vibrations were not obtained experimentally.

IR-MPD spectra and calculated IR intensities of Asp-Phe Rb^{+};
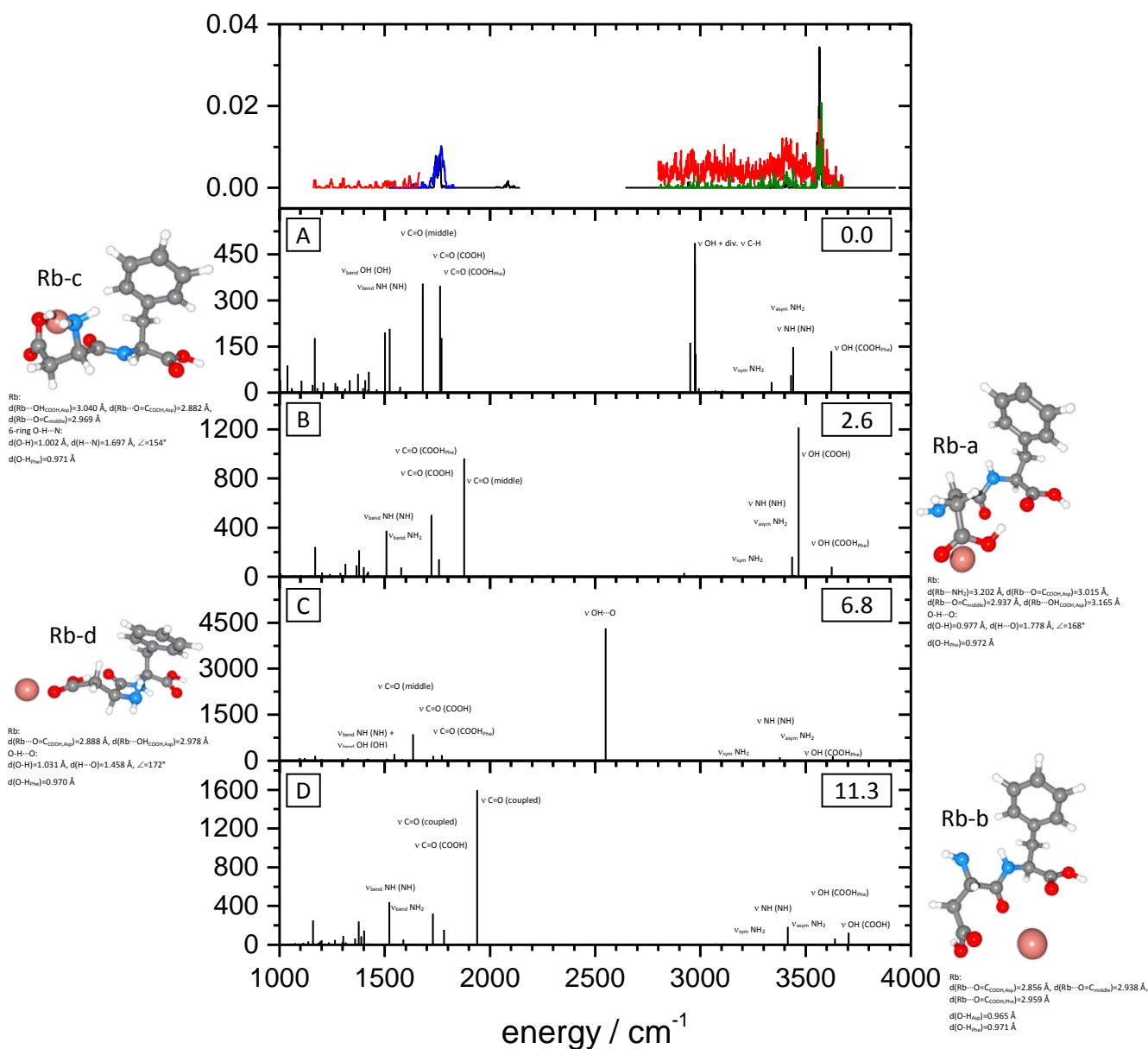**cc-pVDZ / Stuttgart RSC 1997; DFT: B3LYP (g03)**

Fig. S D12: Asp-Phe Rb^{+}; cc-pVDZ (C, H, N, O), Stuttgart RSC 1997 (Rb); DFT: B3LYP:

Topmost frame: Fragmentation efficiency of IR-MPD spectra; blue and black solid lines: one color IR-MPD spectra, different laser intensities (OPO/OPA, KL); red and green solid lines: two color IR-MPD spectra (OPO/OPA, KL): 1100 - 1700 cm^{-1}: red line probe at 3565 cm^{-1}; 2800 - 3700 cm^{-1}: red line probe at 3565 cm^{-1}, green line probe at 3550 cm^{-1};

Lower frames: calculated IR intensities (km/mol) and structures of different isomers; values are ΔE / (kJ/mol); all identified isomers with up to ΔE ≤ 25 kJ/mol above the most stable conformer are considered; scaling factor 0.97.

The calculated pattern of structure D shows best agreement, although the predicted C=O (middle) stretching vibration and the harmonically calculated OH + div. C-H stretching vibrations were not obtained experimentally.

IR-MPD spectra and calculated IR intensities of Asp-Phe Cs$^+$;
cc-pVDZ / Stuttgart RSC 1997; MP2 (g03)

Cs-c

Cs:
d(Cs···OH$_{COOH,Asp}$)=3.262 Å, d(Cs···O=C$_{COOH,Asp}$)=3.059 Å,
d(Cs···O=C$_{middle}$)=3.212 Å
6-ring O-H···N:
d(O-H)=1.000 Å, d(H···N)=1.703 Å, ∠=154°
d(O-H$_{Phe}$)=0.969 Å

Cs-d

Cs:
d(Cs···O=C$_{COOH,Asp}$)=3.094 Å, d(Cs···OH$_{COOH,Asp}$)=3.204 Å
O-H···O:
d(O-H)=1.027 Å, d(H···O)=1.471 Å, ∠=172°
d(O-H$_{Phe}$)=0.969 Å

Cs-a

Cs:
d(Cs···NH$_2$)=3.439 Å, d(Cs···O=C$_{COOH,Asp}$)=3.203 Å,
d(Cs···O=C$_{middle}$)=3.155 Å, d(Cs···OH$_{COOH,Asp}$)=3.332 Å
O-H···O:
d(O-H)=0.977 Å, d(H···O)=1.770 Å, ∠=169°
d(O-H$_{Phe}$)=0.970 Å

Cs-b

Cs:
d(Cs···O=C$_{COOH,Asp}$)=3.063 Å, d(Cs···O=C$_{middle}$)=3.164 Å,
d(Cs···O=C$_{COOH,Phe}$)=3.165 Å
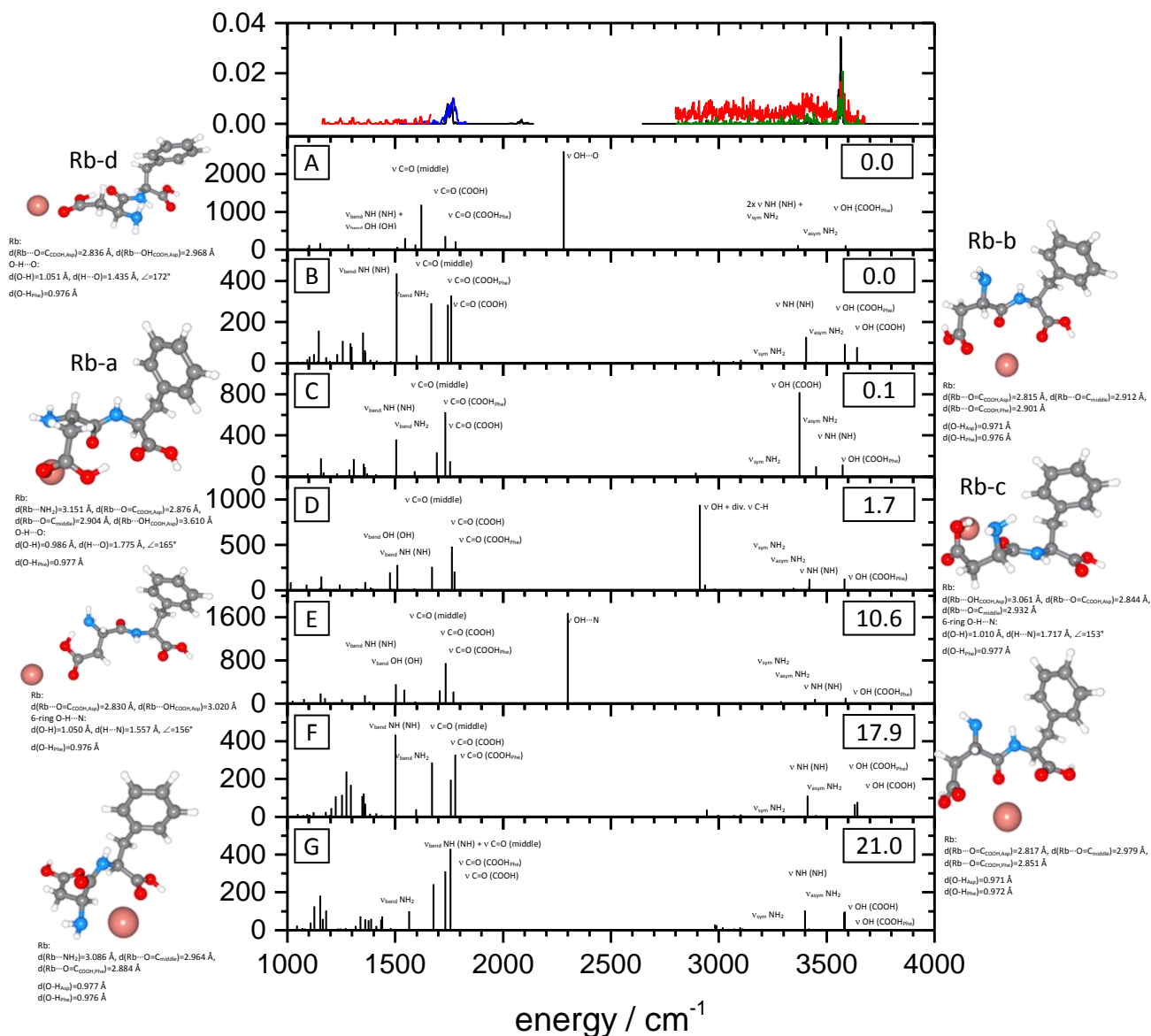
d(O-H$_{Asp}$)=0.965 Å
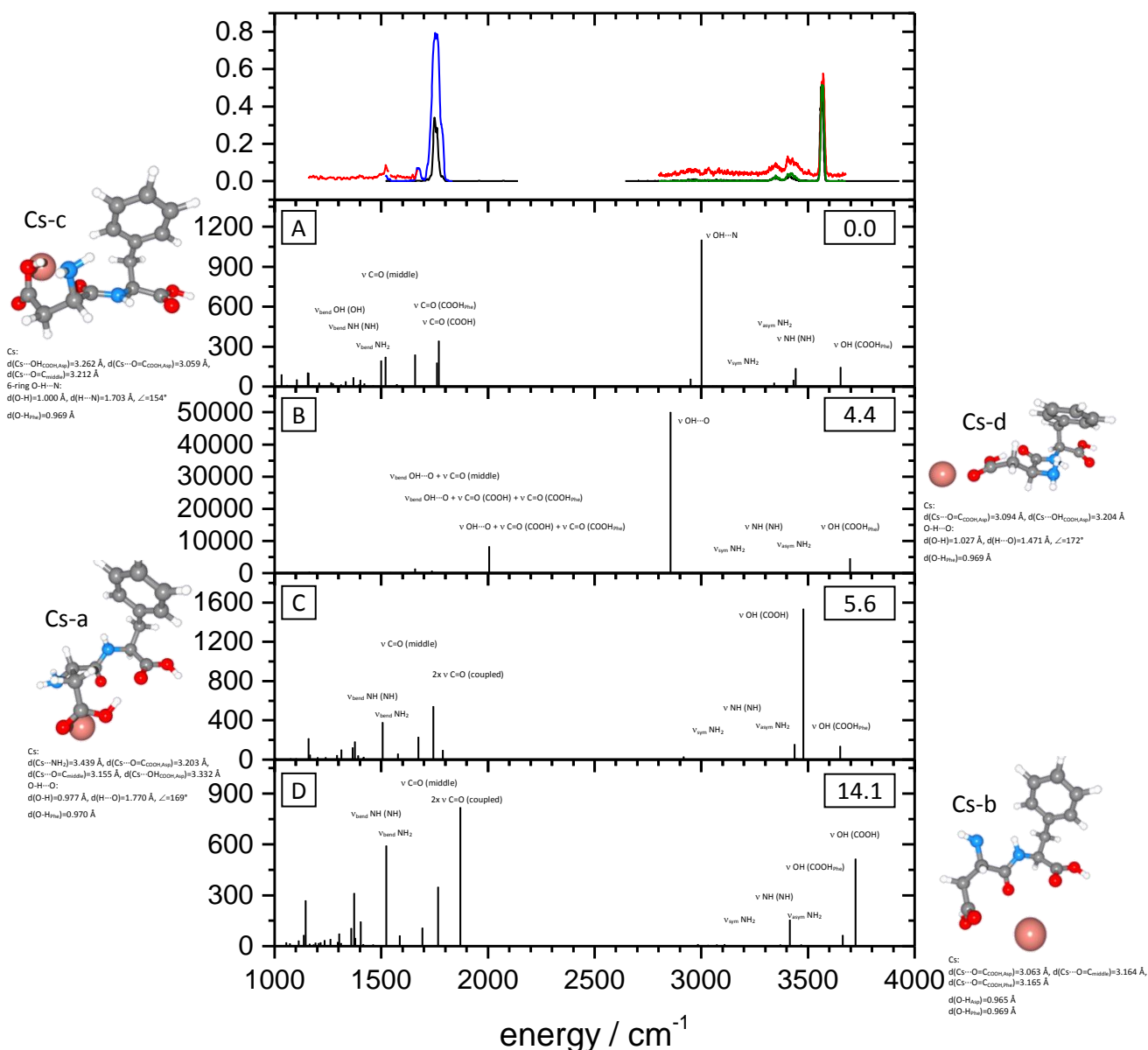d(O-H$_{Phe}$)=0.969 Å

Fig. S D13: Asp-Phe Cs$^+$; cc-pVDZ (C, H, N, O), Stuttgart RSC 1997 (Cs); MP2:

Topmost frame: Fragmentation efficiency of IR-MPD spectra; blue and black solid lines: one color IR-MPD spectra, different laser intensities (OPO/OPA, KL); red and green solid lines: two color IR-MPD spectra (OPO/OPA, KL): 1100 - 1700 cm^{-1}: red line probe at 3565 cm^{-1}; 2800 - 3700 cm^{-1}: red line probe at 3565 cm^{-1}, green line probe at 3550 cm^{-1};

Lower frames: calculated IR intensities (km/mol) and structures of different isomers; values are ΔE / (kJ/mol); all identified isomers with up to ΔE ≤ 25 kJ/mol above the most stable conformer are considered; scaling factor 0.96.

The calculated pattern of structure A shows best agreement, although the calculated OH$_{Phe}$ stretching vibration is blue shifted and the predicted C=O (middle) stretching vibration and the harmonically calculated OH···N stretching vibration were not obtained experimentally.

IR-MPD spectra and calculated IR intensities of Asp-Phe Cs$^+$;
cc-pVDZ / Stuttgart RSC 1997; DFT: B3LYP (g03)
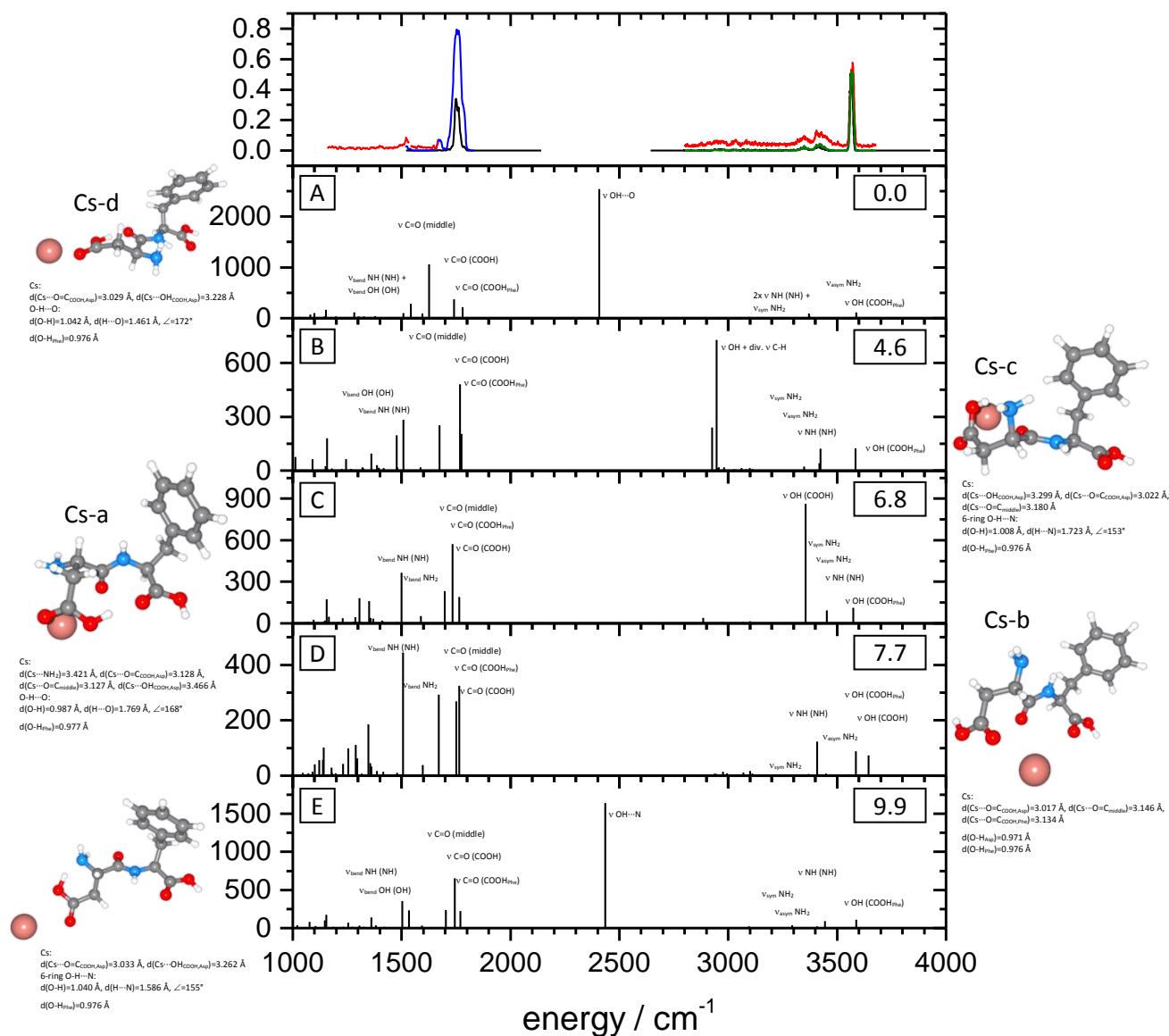
Fig. S D14: Asp-Phe Cs$^+$; cc-pVDZ (C, H, N, O), Stuttgart RSC 1997 (Cs); DFT: B3LYP:

Topmost frame: Fragmentation efficiency of IR-MPD spectra; blue and black solid lines: one color IR-MPD spectra, different laser intensities (OPO/OPA, KL); red and green solid lines: two color IR-MPD spectra (OPO/OPA, KL): 1100 - 1700 cm^{-1}: red line probe at 3565 cm^{-1}; 2800 - 3700 cm^{-1}: red line probe at 3565 cm^{-1}, green line probe at 3550 cm^{-1};

Lower frames: calculated IR intensities (km/mol) and structures of different isomers; values are ΔE / (kJ/mol); all identified isomers with up to ΔE ≤ 25 kJ/mol above the most stable conformer are considered; scaling factor 0.97.

The calculated pattern of structure B shows best agreement, although the predicted C=O (middle) stretching vibration and the harmonically calculated OH + div. C-H stretching vibrations were not obtained experimentally.

IR-MPD spectra and calculated IR intensities of deprotonated Asp-Phe; TZVP; MP2 (g03)

deprot-d

6-ring O-H···N:
d(O-H)=1.017 Å, d(H···N)=1.659 Å, ∠=156°
5-ring O···H-N:
d(O···H)=1.797 Å, d(H-N)=1.034 Å, ∠=123°

deprot-d'

6-ring O-H···N:
d(O-H)=1.009 Å, d(H···N)=1.696 Å, ∠=156°
5-ring O···H-N:
d(O···H)=1.765 Å, d(H-N)=1.036 Å, ∠=124°

Fig. S D15: Deprotonated Asp-Phe; TZVP; MP2:

Topmost frame: Fragmentation efficiency of IR-MPD spectra; blue, black and purple solid lines: one color IR-MPD spectra, different laser intensities (OPO/OPA, KL);

Lower frames: calculated IR intensities (km/mol) and structures of different isomers; values are ΔE / (kJ/mol); all identified isomers with up to $\Delta E \leq 30$ kJ/mol above the most stable conformer are considered; scaling factor 0.96.

The calculated patterns of both structures show some agreement, although the intensity of the experimentally visible double peak between 3000 and 3100 cm^{-1} is not described well. An experimental distinction between the two structures would only be possible at very high IR laser resolution.

IR-MPD spectra and calculated IR intensities of deprotonated Asp-Phe; cc-pVDZ; MP2 (g03)

Fig. S D16: Deprotonated Asp-Phe; cc-pVDZ; MP2:

Topmost frame: Fragmentation efficiency of IR-MPD spectra; blue, black and purple solid lines: one color IR-MPD spectra, different laser intensities (OPO/OPA, KL);

Lower frame: calculated IR intensities (km/mol) and structure of the lowest energy isomer; value is ΔE / (kJ/mol); all identified isomers with up to $\Delta E \leq 30$ kJ/mol above the most stable conformer are considered; scaling factor 0.96.

The calculated patterns of both structures show some agreement, although the intensity of the experimentally visible double peak between 3000 and 3100 cm^{-1} is not described well. An experimental distinction between the two structures would only be possible at very high IR laser resolution.

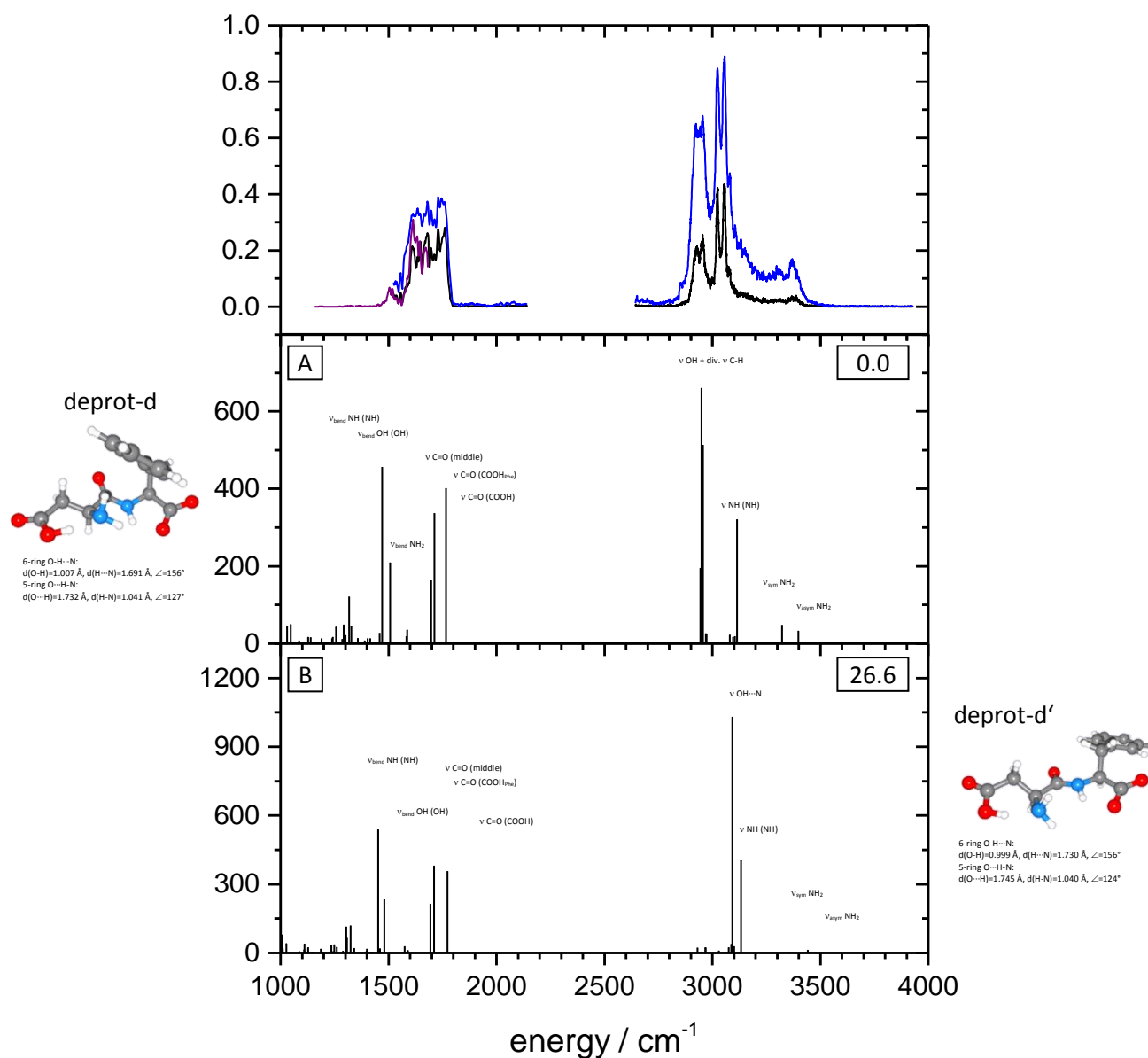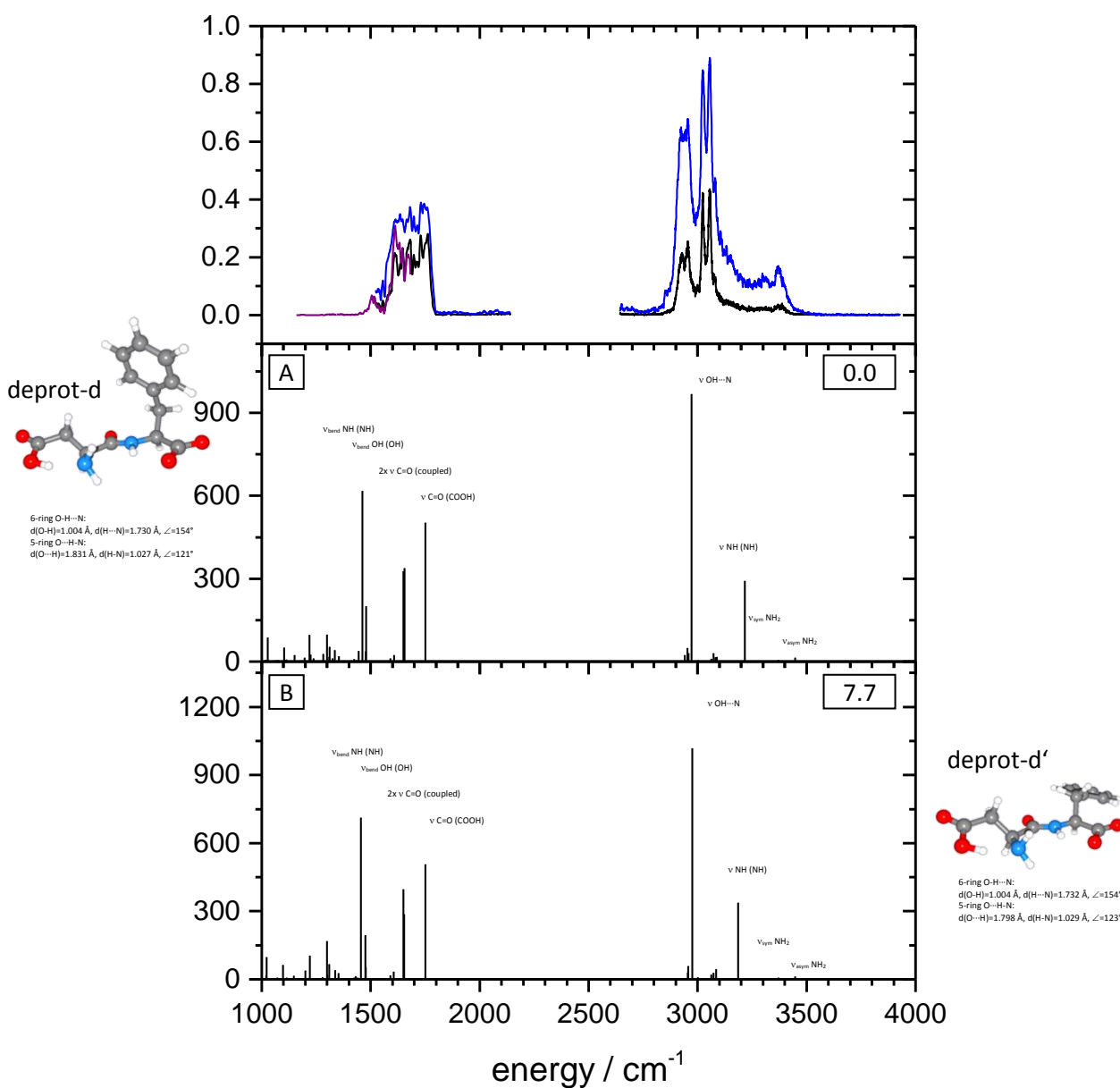**IR-MPD spectra and calculated IR intensities of deprotonated Asp-Phe; TZVP; DFT: B3LYP (g03)**

deprot-d

6-ring O-H···N:
d(O-H)=1.004 Å, d(H···N)=1.730 Å, ∠=154°
5-ring O···H-N:
d(O···H)=1.831 Å, d(H-N)=1.027 Å, ∠=121°

deprot-d'

6-ring O-H···N:
d(O-H)=1.004 Å, d(H···N)=1.732 Å, ∠=154°
5-ring O···H-N:
d(O···H)=1.798 Å, d(H-N)=1.029 Å, ∠=123°

Fig. S D17: Deprotonated Asp-Phe; TZVP; DFT: B3LYP:

Topmost frame: Fragmentation efficiency of IR-MPD spectra; blue, black and purple solid lines: one color IR-MPD spectra, different laser intensities (OPO/OPA, KL);

Lower frames: calculated IR intensities (km/mol) and structures of different isomers; values are ΔE / (kJ/mol); all identified isomers with up to ΔE ≤ 25 kJ/mol above the most stable conformer are considered; scaling factor 0.97.

The calculated patterns of both structures show some agreement, although the intensity of the experimentally visible double peak between 3000 and 3100 cm^{-1} is not described well. An experimental distinction between the two structures would only be possible at very high IR laser resolution.

IR-MPD spectra and calculated IR intensities of deprotonated Asp-Phe;
aug-cc-pVDZ; DFT: B3LYP (g03)

Fig. S D18: Deprotonated Asp-Phe; aug-cc-pVDZ; DFT: B3LYP:

Topmost frame: Fragmentation efficiency of IR-MPD spectra; blue, black and purple solid lines: one color IR-MPD spectra, different laser intensities (OPO/OPA, KL);

Lower frames: calculated IR intensities (km/mol) and structures of different isomers; values are ΔE / (kJ/mol); all identified isomers with up to $\Delta E \leq 25$ kJ/mol above the most stable conformer are considered; scaling factor 0.97.

The calculated patterns of both structures show some agreement, although the intensity of the experimentally visible double peak between 3000 and 3100 cm^{-1} is not described well. An experimental distinction between the two structures would only be possible at very high IR laser resolution.

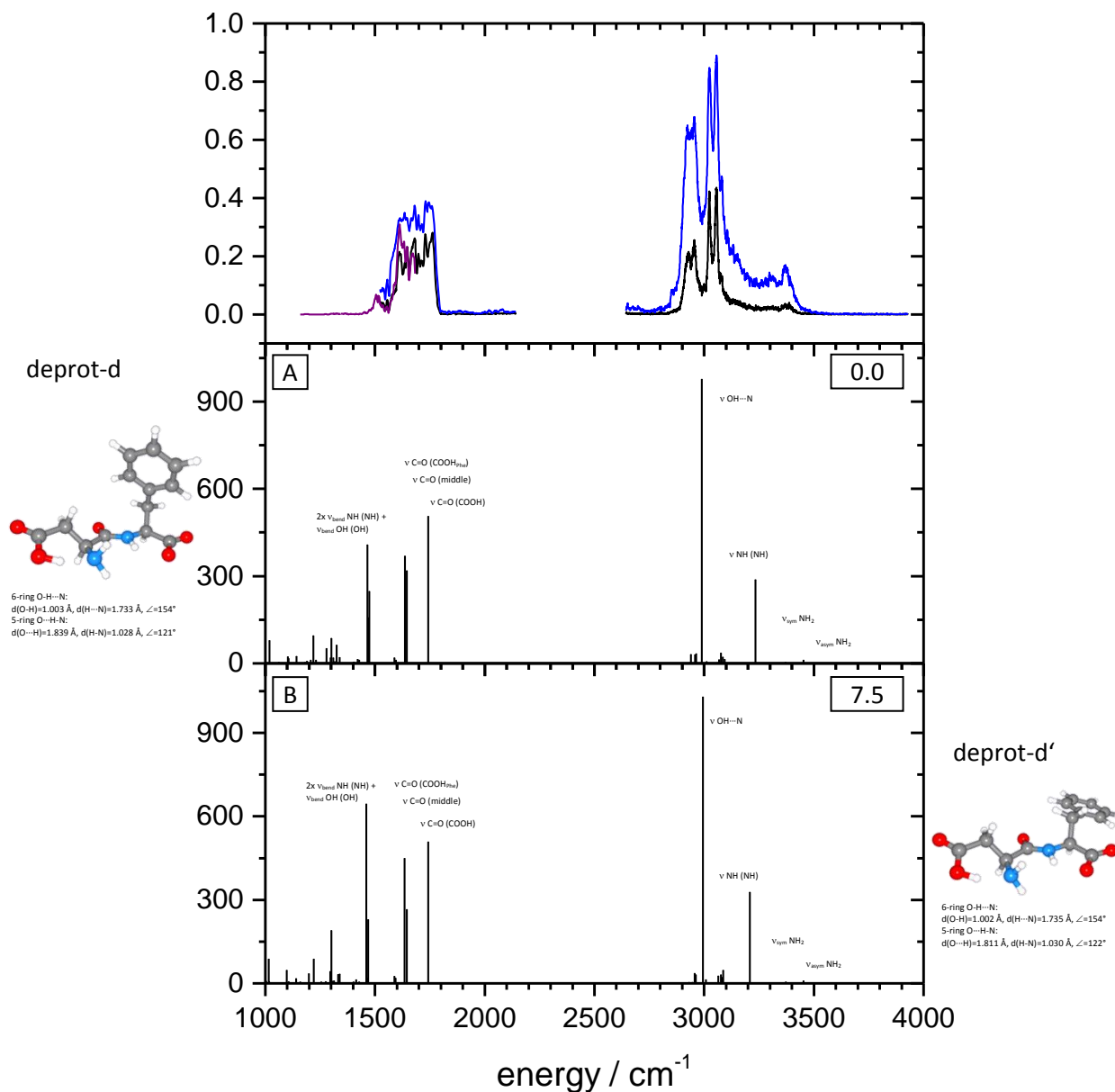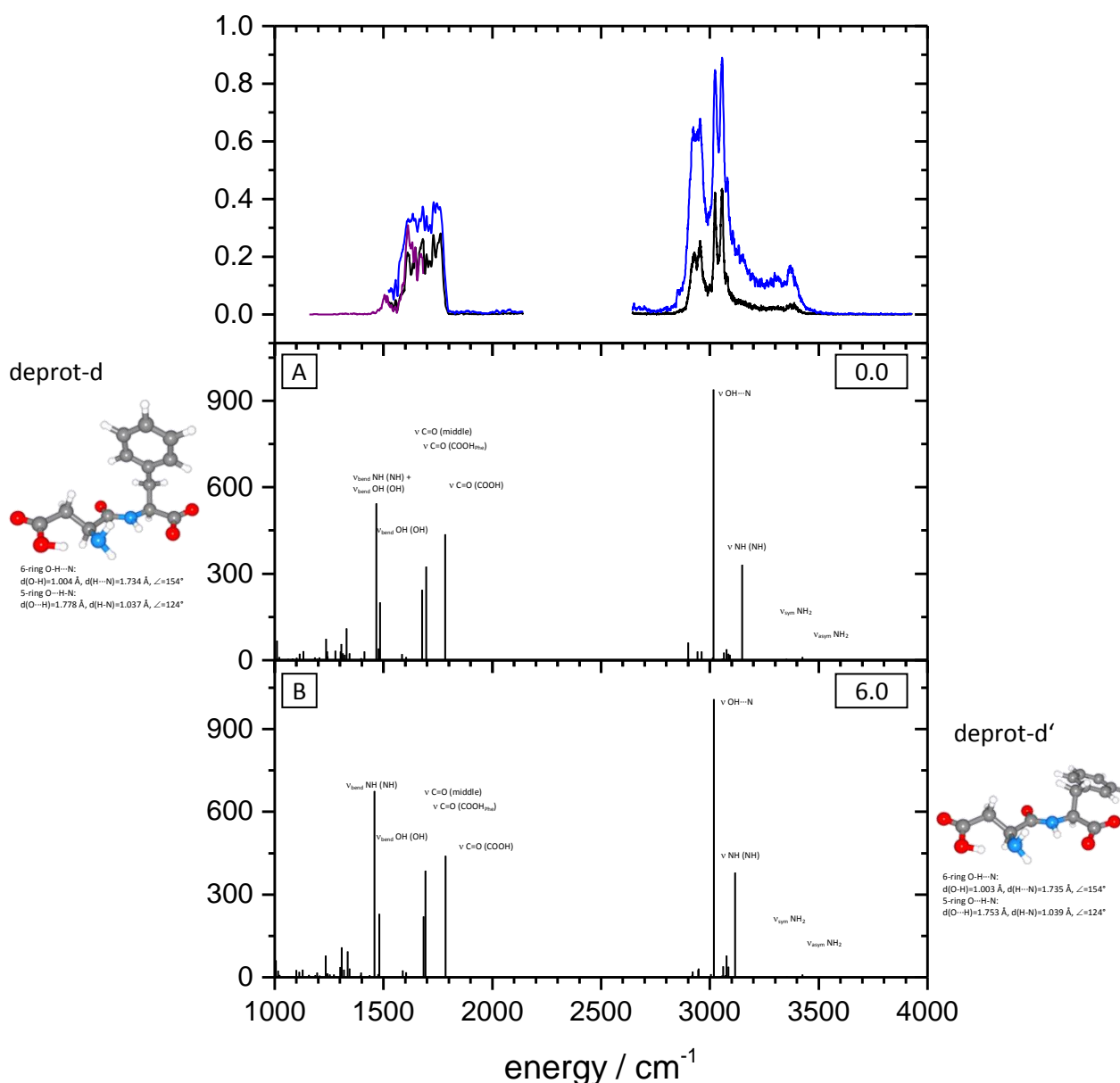**IR-MPD spectra and calculated IR intensities of deprotonated Asp-Phe; cc-pVDZ; DFT: B3LYP (g03)**

Fig. S D19: Deprotonated Asp-Phe; cc-pVDZ; DFT: B3LYP:

Topmost frame: Fragmentation efficiency of IR-MPD spectra; blue, black and purple solid lines: one color IR-MPD spectra, different laser intensities (OPO/OPA, KL);

Lower frames: calculated IR intensities (km/mol) and structures of different isomers; values are ΔE / (kJ/mol); all identified isomers with up to $\Delta E \leq 25$ kJ/mol above the most stable conformer are considered; scaling factor 0.97.

The calculated patterns of both structures show some agreement, although the intensity of the experimentally visible double peak between 3000 and 3100 cm^{-1} is not described well. An experimental distinction between the two structures would only be possible at very high IR laser resolution.

6.1. Summary

This thesis combined gas phase mass spectrometric investigations of ionic transition metal clusters that are either homogeneous ($Nb_n^{+/-}$, $Co_n^{+/-}$) or heterogeneous ($[Co_nPt_m]^{+/-}$), of their organo metallic reaction products, and of organic molecules (aspartame and Asp-Phe) and their alkali metal ion adducts.

At the Paris FEL facility CLIO a newly installed FT-ICR mass spectrometer has been modified by inclusion of an ion bender that allows for the usage of additional ion sources beyond the installed ESI source. The installation of an LVAP metal cluster source served to produce metal cluster adsorbate complex ions of the type $[Nb_n(C_6H_6)]^{+/-}$. IR-MPD of the complexes $[Nb_nC_6H_6]^{+/-}$ (n = 18, 19) resulted in $[Nb_nC_6]^{+/-}$ (n = 18, 19) fragments. Spectra are broad, possibly because of vibronic / electronic transitions. In Kaiserslautern the capabilities of the LVAP source were extended by adding a gas pick up unit. Complex gases containing C-H bonds otherwise break within the cluster forming plasma. More stable gases like CO seem to attach at least partially intact. Metal cluster production with argon tagged onto the cluster failed when introducing argon through the pick up source, but succeeded when using argon as expansion gas. A new mass spectrometer concept of an additional multipole collision cell for metal cluster adsorbate formation is currently under construction. Subsequent cooling shall achieve high resolution IR-MPD spectra of transition metal cluster adsorbate complexes.

Prior work on reaction of transition metal clusters with benzene was extended by investigating the reaction with benzene and benzene-d_6 of size selected cationic cobalt clusters Co_n^+ and of anionic cobalt clusters Co_n^- in the size range n = 3 - 28 and of bimetallic cobalt platinum clusters $[Co_nPt_m]^{+/-}$ in the size range n + m ≤ 8. Dehydrogenation by cationic cobalt clusters Co_n^+ is sparse, it is effective in small bimetallic clusters $[Co_nPt_m]^+$, n + m ≤ 3. Thus single platinum atoms promote benzene dehydrogenation while further cobalt atoms quench it. Dehydrogenation is ubiquitous in reactions of anionic cobalt clusters. Mixed triatomic clusters $[Co_2Pt_1]^-$ and $[Co_1Pt_2]^-$ are special in causing effective reactions and single dehydrogenation through some kind of cooperativity while $[Co_nPt_{1,2}]^-$, n ≥ 3 do not react at all. Kinetic isotope effects KIE(n) in total reaction rates are inverse and - in part - large, dehydrogenation isotope effects DIE(n) are normal. A multistep model of adsorption and stepwise dehydrogenation from the precursor adsorbate proves suitable to rationalize the found KIEs and DIEs in principle. Particular insights into the effects of charge and of cluster size are largely beyond this model. Some DFT calculations - though preliminary - lend strong support to the otherwise assumed structures and enthalpies. More insights into the cause of the found effects of charge, size and composition of both pure and mixed clusters shall arise from ongoing high level ab initio modeling (of especially the n + m = 3 case for mixed clusters).

The influence of the methylester group in the molecules aspartame (Asp-PheOMe) and Asp-Phe has been explored. Therefore, their protonated and deprotonated species and their complexes with alkali metal ions attached were investigated with different techniques utilizing mass spectrometry. Gas phase H-/D-exchange with ND_3 has proven that in both molecules all acidic NH and OH binding motifs do exchange their hydrogen atom and that simultaneous multi exchange is present. Kinetic studies revealed that with alkali metal ions attached the speed of the first exchange step decreases with increasing ion size. The additional OH of the carboxylic $COOH_{Phe}$ group in Asp-Phe increases the exchange speed by a constant value. CID experiments yielded water and the protonated Asp-Phe anhydride as main fragments out of the protonated molecules, neutral Asp anhydride and $[Phe M]^+$ / $[PheOMe M]^+$ for Li^+ and Na^+ attached, and neutral aspartame / Asp-Phe and ionic M^+ for K^+, Rb^+ and Cs^+ attached. The threshold energy E_{CID}, indicating ion stability, decreases with increasing ion size. For aspartame fragmentation occurs at lower E_{CID} values for complexes with H^+, Li^+ and Na^+ than for the Asp-Phe analoga. Complexes with K^+, Rb^+ and Cs^+ give the same E_{CID} value for aspartame and Asp-Phe. IR-MPD investigations lead to the same fragments as the CID experiments. In combination with quantum mechanical calculations a change in the preferred structure from charge-solvated, tridentate type for complexes with small alkali metal ions (Li^+) to salt-bridge type structure for large alkali metal ions (Cs^+) could be confirmed. Calculations thereby reveal nearly no structural differences between aspartame and Asp-Phe for cationized species. The deprotonation of the additional $COOH_{Phe}$ group in Asp-Phe is preferred against other acidic positions. A better experimental distinction between possible (calculated) structure types would arise from additional FEL IR-MPD measurements in the energy range of 600 to 1800 cm^{-1}. The comparison of the E_{CID} values with calculated fragmentation energy values proves that not only for alkali metal complexes with K^+, Rb^+ and Cs^+, but also for Li^+ and Na^+ the bond breaking of all metal atom bonds is part of the transition state. The lower E_{CID} values for aspartame with small cations may be explained in terms of internal energy. Aspartame is a larger molecule, possesses more internal energy and can be recognized as the larger heat bath. Less energy is needed for fragmentation, if the Phe part with the additional methylester group is involved in the fragmentation process.

During the last six years we have obtained very first IR-MPD spectra of large niobium cluster adsorbate complexes (up to clusters with 19 atoms) after modifications on a new FT-ICR mass spectrometer system at the FEL-facility CLIO in Paris. The installation of an additional collision cell setup with cryostat at the FT-ICR mass spectrometer in Kaiserslautern will simplify the production of any kind of metal cluster adsorbate complexes. In addition, they can be cooled to obtain better resolved spectra. Remarkable effects of cluster charge, size and constitution on Kinetic and

Dehydrogenation Isotope Effects were found by kinetic investigations of the gas phase reactions of cobalt and cobalt platinum clusters with normal and deuterated benzene. These investigations have already been extended to other transition metals and alloys by other group members and will be continued by the use of other adsorbate molecules. For protonated, deprotonated and alkalated complexes of the dipeptides aspartame (Asp-PheOMe) and Asp-Phe the assignment of gas phase structures was achieved by a combination of H-/D-exchange, CID and IR-MPD experiments with quantum mechanical calculations. An influence of the additional methylester group of aspartame is visible in threshold energy E_{CID} values. Within most of the investigations presented in this thesis, the ions still possess at least room temperature. The modifications on the FT-ICR setup will shortly allow the investigation of cold ions (T < 20 K).

6.2. Zusammenfassung

Die vorliegende Arbeit umfasst Gasphasen-massenspektrometrische Untersuchungen ionischer Übergangsmetallcluster entweder homogener ($Nb_n^{+/-}$, $Co_n^{+/-}$) oder heterogener ($[Co_nPt_m]^{+/-}$) Zusammensetzung, ihrer organo-metallischen Reaktionsprodukte, und organischer Moleküle (Aspartam und Asp-Phe) und ihrer Alkalimetallionen-Addukte.

In der Freie-Elektronen-Laser-Einrichtung CLIO in Paris wurde ein neu installiertes FT-ICR Massenspektrometer durch Einbau eines Ionenbiegers modifiziert. Dieser ermöglicht zusätzlich zur Nutzung der durch den Hersteller angebauten Elektrospray-Ionisationsquelle (ESI) auch den Anbau und die Verwendung anderer Ionenquellen. Die Installation einer Laserverdampfungs-Metallclusterquelle (LVAP) diente uns dazu, Metallcluster-Adsorbat-Komplexionen des Typs $[Nb_n(C_6H_6)]^{+/-}$ herzustellen. Es gelang, Infrarot-Multiphotonen-Dissoziations(IR-MPD)-spektren der Komplexe $[Nb_n(C_6H_6)]^{+/-}$ (n = 18, 19) unter $[Nb_n(C_6)]^{+/-}$ (n = 18, 19) Fragmentbildung aufzunehmen. Die Spektren sind breit, möglicherweise aufgrund von vibronischen / elektronischen Übergängen. In Kaiserslautern wurden die Möglichkeiten der LVAP-Quelle durch Einbau einer Pick up-Einheit erweitert. Komplexe Moleküle, die C-H-Bindungen enthalten, zerbrechen teilweise im Plasma der Cluster-Erzeugung. Stabilere Gase wie CO scheinen zumindest teilweise intakt an die Metallcluster anzulagern. Die Darstellung von Metallclustern mit angelagerten Argon-Atomen scheitert, wenn das Gas über die Pick up-Einheit zugegeben wird, aber gelingt durch Verwendung von Argon als Expansionsgas. Ein neues Massenspektrometer-Konzept, das die Nutzung einer zusätzlichen, kühlbaren Multipol-Kollisions-Zelle vorsieht, befindet sich derzeit im Einbau. Durch Cluster-Adsorbat-Bildung und Abkühlung der Ionen soll die spektrale Auflösung der IR-MPD-Spektren von Übergangsmetallcluster-Adsorbat-Komplexen erhöht werden.

Frühere Arbeiten an Reaktionen von Übergangsmetallclustern mit Benzol wurden um Untersuchungen der Reaktion von größen-selektierten kationischen und anionischen Kobaltclustern $Co_n^{+/-}$ (n = 3 - 28) und von bimetallischen Kobalt-Platin-Clustern $[Co_nPt_m]^{+/-}$ (n + m ≤ 8) mit Benzol und Benzol-d6 erweitert. Dehydrierung durch kationische Kobaltcluster Co_n^+ ist schwach ausgeprägt, aber effektiv in kleinen bimetallischen Clustern $[Co_nPt_m]^+$ (n + m ≤ 3). Demnach fördern einzelne Platinatome die Dehydrierung von Benzol, wohingegen zusätzliche Kobaltatome diese verringern. Dehydrierung ist allgegenwärtig durch anionische Kobaltcluster. Die gemischten dreiatomigen Cluster $[Co_2Pt_1]^-$ und $[Co_1Pt_2]^-$ reagieren aufgrund einer speziellen Kooperativität besonders effektiv unter einfacher Dehydrierung, während Cluster der Zusammensetzung $[Co_nPt_{1,2}]^-$ (n ≥ 3) keinerlei Reaktion zeigen. Kinetische-Isotopeneffekte KIE(n) der totalen Geschwindigkeitskonstanten sind invers und - teilweise - groß, Dehydrierungs-Isotopeneffekte DIE(n) sind normal. Mithilfe eines Mehrstufen-

Modells von Absorption und schrittweiser Dehydrierung aus dem vorgeformten Adsorbat können die gefundenen KIEs und DIEs erklärt werden. Detailliertere Unterscheidungen der durch Ladung und Clustergröße induzierten Effekte liegen weit außerhalb dieses Modells. Einige vorbereitende DFT Berechnungen unterstützen die ansonsten nur abgeschätzten Strukturen und Enthalpien. Tiefere Einblicke in die Ursachen der gefundenen Effekte von Ladung, Größe und Zusammensetzung sowohl reiner als auch gemischter Cluster sollen durch noch andauernde Modellierung auf ab initio Level erfolgen (besonders für n + m = 3 für gemischte Cluster). Vergleiche zu Experimenten mit anderen reinen und gemischten Übergangsmetallclustern sind ebenfalls im Gange.

In den Molekülen Aspartam (Asp-PheOMe) und Asp-Phe wurde der Einfluss der Methylestergruppe erforscht. Dazu wurden sowohl ihre protonierten und deprotonierten Formen als auch ihre Komplexe mit Alkalimetallionen (alkalierte Komplexe) mittels verschiedener massenspektrometrischer Techniken untersucht. H-/D-Austausch mit ND_3 in der Gasphase zeigte in allen untersuchten kationischen und alkalierten Spezies, dass alle H-Atome der aziden NH und OH Bindungsmotive austauschen und dass gleichzeitiger Mehrfachaustausch auftritt. Kinetische Studien des H-/D-Austauschs machen deutlich, dass, je größer das angelagerte Alkalimetallion ist, desto langsamer ist der erste H-/D-Austauschschritt. Die zusätzliche OH Gruppe der Carboxylgruppe des Phe-Restes in Asp-Phe erhöht die Geschwindigkeitskonstante für alle untersuchten kationischen Spezies um einen konstanten Wert. Kollisionsinduzierte Dissoziations-(CID)experimente ergeben Wasser und protoniertes Asp-Phe anhydrid als Hauptfragmente aus den protonierten Spezies, neutrales Asp anhydrid und $[Phe\ M]^+$ / $[PheOMe\ M]^+$ für Spezies mit angelagertem Li^+ und Na^+, und neutrales Aspartam / Asp-Phe und ionisches M^+ für angelagertes K^+, Rb^+ und Cs^+. Die Schwellenenergie E_{CID}, die die Stabilität von Ionen anzeigt, sinkt mit zunehmender Alkalimetallionen-Größe. Für protoniertes Aspartam und für die Anlagerung von Li^+ und Na^+ finden sich niedrigere E_{CID}-Werte als für die analogen Asp-Phe-Komplexe. Keine Unterschiede gibt es hingegen zwischen den jeweiligen Komplexen mit K^+, Rb^+ und Cs^+. IR-MPD-Untersuchungen ergeben die gleichen Fragmente wie CID-Untersuchungen. In Kombination mit quantenmechanischen Rechnungen konnte ein Wechsel im bevorzugten Strukturtyp vom *charge-solvated, tridentate* Typ für Komplexe mit kleinen Alkalimetallionen (Li^+) zum *salt-bridge* Typ für Komplexe mit großen Alkalimetallionen (Cs^+) bestätigt werden. Die Rechnungen zeigen dabei annähernd keine strukturellen Unterschiede zwischen den Aspartam-Komplexen und den analogen Asp-Phe-Komplexen auf. Im Strukturvergleich der deprotonierten Spezies ist im Asp-Phe die Deprotonierung der COOH-Gruppe des Phe-Restes gegenüber den anderen Stellen bevorzugt. Zusätzliche IR-MPD-Messungen an einem Frei-Elektronen-Laser im IR-Laser-Energiebereich zwischen 600 und 1800 cm^{-1} können eine bessere experimentelle Unterscheidung zwischen möglichen, kalkulierten Strukturtypen ermöglichen. Der Vergleich der

Schwellenenergie E_{CID} mit berechneten Fragmentationsenergien beweist, dass nicht nur für Komplexe mit K$^+$, Rb$^+$ und Cs$^+$, die nackte Metall-Ionen als Fragmente aufweisen, sondern auch für Komplexe mit Li$^+$ und Na$^+$ der Bindungsbruch aller Metall-Molekül-Bindungen zur Fragmentierung nötig ist. Die niedrigeren E_{CID}-Werte für Komplexe mit kleineren Alkalimetallionen des Aspartam im Vergleich zu denen des Asp-Phe kann mittels Unterschieden in der inneren Energie der Moleküle erklärt werden: Aspartam ist das größere Molekül, besitzt somit mehr Freiheitsgrade und kann somit als das größere Wärmebad angesehen werden. Zur Fragmentierung ist somit weniger zusätzliche Energie nötig, wenn der Phe-Rest mit der zusätzlichen Methylestergruppe am Fragmentationsprozess beteiligt ist.

Während der letzten sechs Jahre konnten nach Modifikationen eines neuen FT-ICR Massenspek-trometers am Frei-Elektronen-Laser CLIO in Paris allererste IR-MPD Spektren großer Niobcluster-Adsorbat-Komplexe (bis zu 19 Atome pro Cluster) erhalten werden. Der Einbau einer zusätzlichen Kollisionszelle mit Kryostat am FT-ICR Massenspektrometer in Kaiserslautern wird die Darstellung jeglicher Art von Metallcluster-Adsorbat-Komplexen vereinfachen. Zusätzlich können diese gekühlt werden, um besser aufgelöste IR-MPD-Spektren zu erhalten. Bemerkenswerte Effekte abhängig von Clusterladung, -größe und -zusammensetzung auf Kinetische- und Dehydrierungsisotopeneffekte wurden bei kinetischen Untersuchungen der Gasphasenreaktionen von Kobalt und Kobalt-Platin-Clustern mit normalem und deuteriertem Benzol gefunden. Diese Untersuchungen wurden bereits durch andere Gruppenmitglieder auf andere Metalle und Legierungen ausgeweitet und werden unter Verwendung anderer Adsorbat-Moleküle fortgesetzt werden. Für protonierte, deprotonierte und alkalierte Komplexe der Dipeptide Aspartam (Asp-PheOMe) und Asp-Phe konnten durch Kombination von H-/D-Austausch-, CID- und IR-MPD-Experimenten mit quantenmechanischen Rechnungen Gasphasenstrukturen zugeordnet werden. Ein Einfluss der zusätzlichen Methylestergruppe des Aspartam wird in der Betrachtung der E_{CID}-Werte bemerkbar. In den meisten Untersuchungen, die in dieser Arbeit gezeigt werden, besitzen die Ionen noch mindestens Raumtemperatur. Die Modifikationen am FT-ICR-Setup werden bald die Untersuchung kalter Ionen (T < 20 K) ermöglichen.

6.3. Publications and contributions to conferences / Publikationen und Konferenzbeiträge

Publications / Publikationen

published / veröffentlicht:

L. Barzen, M. Tombers, C. Merkert, J. Hewer, G. Niedner-Schatteburg, Benzene activation and H/D isotope effects in reactions of mixed cobalt platinum clusters: the influence of charge and of composition, International Journal of Mass Spectrometry, 330–332 (2012) 271–276.

M. Tombers, L. Barzen, G. Niedner-Schatteburg, Inverse H/D isotope effects in benzene activation by cationic and anionic cobalt clusters, Journal of Physical Chemistry A, 117 (2013) 1197-1203.

in preparation / in Vorbereitung:

L. Barzen, F. Menges, C. Merkert, G. Niedner-Schatteburg, "Aspartame (Asp-PheOMe) and Asp-Phe: Structural investigations on their isolated protonated, deprotonated and alkali metal ion attached species"; *manuscript in preparation.*

Christine Merkert, Anita Röthke, Lars Barzen, Gereon Niedner-Schatteburg, Philippe Maître; "Spectral fingerprints of proton delocalization in isolated dicarboxylic ions"; *manuscript in preparation.*

Contributions to conferences / Konferenzbeiträge:

Talks / Vorträge:

M. Tombers, C. Merkert, L. Barzen, Gereon Niedner-Schatteburg, C-H bond activation at the surface of isolated homo- and heteronuclear transition metal clusters, Tagung der Deutschen Physikalischen Gesellschaft, Dresden, 2011.

L. Barzen, C. Merkert, F. Menges, Y. Nosenko, G. Niedner-Schatteburg, P. Maitre, J.-M. Ortega, IR-MPD and H-/D-exchange studies on aspartame (Asp-PheOMe) and Asp-Phe, Tagung der Deutschen Physikalischen Gesellschaft, Stuttgart, 2012.

L. Barzen, F. Menges, M. Gaffga, Y. Nosenko, C. Riehn, G. Niedner-Schatteburg, Untersuchungen zu Kinetik / Reaktivität / Katalyse in Paul- und Penningfallen, Gasphasentreffen im Rahmen des Sonderforschungsbereichs SFB/TRR88 "3MET"; Karlsruhe, 2012.

Posters / Poster:

S. Jaberg, B. Pfeffer, L. Barzen, G. Niedner-Schatteburg, C-H bond activation at the surface of isolated transition metal clusters, Tagung der Deutschen Bunsengesellschaft, Saarbrücken, 2008.

L. Barzen, B. Hofferberth, H. Kampschulte, C. Merkert, Philippe Maître, Gereon Niedner-Schatteburg, EPITOPES: Electrons Plus Infrared TO Probe and Elucidate Structures, Tagung der Deutschen Gesellschaft für Massenspektrometrie, Gießen, 2008.

L. Barzen, B. Hofferberth, H. Kampschulte, C. Merkert, P. Maître, G. Niedner-Schatteburg, EPITOPES: Electrons Plus Infrared TO Probe and Elucidate Structures, Deutsch-Französisches Kooperationstreffen, Berlin, 2010.

M. Tombers, L. Barzen, C. Merkert, G. Niedner-Schatteburg, Charge, size and isotope effects within the reaction of ionic size selected cobalt-platinum clusters with C_6H_6/C_6D_6 in the gas phase, Erste Gesamtkonferenz des Sonderforschungsbereichs SFB/TRR88 "3MET", Bad Bergzabern, 2011.

A. Lagutschenkov, C. Merkert, F. Menges, L. Barzen, G. Niedner-Schatteburg, IR-MPD probing of dicarboxylic acids, Tagung der Deutschen Bunsengesellschaft, Berlin, 2011.

L. Barzen, M. Tombers, C. Merkert, J. Hewer, J. Mohrbach, G. Niedner-Schatteburg, Benzene activation and H/D isotope effects in reactions of mixed cobalt-platinum and cobalt-rhodium clusters, Zweite Gesamtkonferenz des Sonderforschungsbereichs SFB/TRR88 "3MET", Kaiserslautern, 2012.

Mein **DANKESCHÖN** gilt …

… Prof. Gereon Niedner-Schatteburg für seine freundliche Betreuung, die gute Zusammenarbeit, die stete Diskussionsbereitschaft und den mir eingeräumten Freiraum. Seine physikalisch geprägte Herangehensweise an Probleme hat mein Wissen und meine Sichtweise als Chemiker erweitert. Seine gelegentlichen Erinnerungen, mich nicht durch vielfältige andere Aufgaben von meiner eigentlichen Promotionsarbeit ablenken zu lassen, werden mir in Erinnerung bleiben.

… Prof. Markus Gerhards für die Übernahme des Zweitgutachtens und Prof. Werner Thiel für die Übernahme des Prüfungsvorsitzes.

… Prof. Christoph vanWüllen und Dr. Markus Mang aus der theoretischen Chemie für alle Fragen rund um Linux und die Betreuung der Rechencluster.

… den aktuellen Rudelmitgliedern unseres kuscheligen Doppelbüro-Clusters Maximilian Gaffga, Joachim Hewer, Dr. Thomas Kolling, Johannes Lang, Jennifer Mohrbach, Matthias Tombers. Es war nie langweilig mit Euch.

… auch allen anderen aktuellen Arbeitskreis-Kollegen, die zur immer netten, hilfsbereiten und freundschaftlichen Atmosphäre des Arbeitskreises beitragen: Dimitri Imanbaew, Hans-Peter Mayer, Fabian Menges, Christine Merkert, Jennifer Meyer, Jonathan Meyer, Dr. Yevgeniy Nosenko, PD Dr. Christoph Riehn.

… allen ehemaligen Arbeitskreis-Kollegen für ihre Aufnahme und die Einführung im Arbeitskreis, sowie die Weitergabe ihres Wissens: Bernd Hofferberth, Stephanie Jaberg, Heinrich Kampschulte, Anita Röthke und Britta Pfeffer.

… besonders allen, die im Abenteuer „Paris" mit unterwegs waren.

… Markus Becherer, Lukas Burkhardt, Sebastian Dillinger, Maximilian Gaffga, Joachim Hewer, Jennifer Meyer, Jennifer Mohrbach und Matthias Tombers für ihre Forschungsarbeiten im Rahmen von Schwerpunktpraktika und Diplomarbeiten und ihre Unterstützung als wissenschaftliche Hilfskräfte.

… allen weiteren aktuellen und ehemaligen Mitgliedern der physikalischen und theoretischen Chemie für viele unterhaltsame Stunden und leckeren Kuchen im Kaffeezimmer.

… unseren guten Seelen Hilde Seelos, Sibylle Heieck und Inge Krull im Sekretariat der physikalischen und theoretischen Chemie und allen übrigen guten Seelen, die fast immer alles möglich machen.

… den Mitarbeitern der zentralen Metall- und Elektronikwerkstätten für viele beratende Gespräche und die Unterstützung, wenn's mal wieder eilig sein musste.

… der EU für die Finanzierung des Forschungsprojektes EPITOPES und der DFG für die Einrichtung des Sonderforschungsbereichs SFB/TRR 88 „3MET" und die damit verbundene Finanzierung meiner Anstellung.

… allen Freunden in besonderer Weise für viele nette Fernseh-, Kino-, Spiele-, Grill- oder „einfach nur so"-abende. Danke für viele lustige und abwechslungsreiche Stunden!

… allen, die zum Kreis meiner Familie gehören. Im Besonderen meinen Eltern für Ihre Unterstützung und den Rückhalt während meines Studiums und der Promotionszeit in vielfältigster Weise.

… meiner Ehefrau Jessy dafür, dass es sie gibt!

Lebenslauf

zur Person Lars Barzen Tel.: +49-631-3039340
Casimirring 67 email: LarsBarzen@web.de
D-67663 Kaiserslautern

Schule
06/1999 Allgemeine Hochschulreife: Martin-von-Cochem-Gymnasium, Cochem / Mosel

Militärdienst
07/1999 - 07/2000 Truppengattung Heer, Falckenstein-Kaserne Koblenz; Aufgabengebiet: Kraftfahrer BCE und Ausbilder Wachausbildung und Fernsprechbau

Studium
Studienrichtung: Chemie
Schwerpunkt: Physikalische Chemie
Erreichter Abschluss: Diplom; Titel der Diplomarbeit: „Erste Messungen an einem Flugzeit-Massenspektrometer mit einer neuen Elektrosprayquelle und einer Laserverdampfungsquelle"
Abschlussjahr: 2006

Promotion
seit 12/2006 Doktorarbeit in Physikalischer Chemie: Wissenschaftlicher Mitarbeiter, TU Kaiserslautern: „Metal cluster aggregates of the composition $Nb_n^{+/-}$, $Co_n^{+/-}$ and $[Co_nPt_m]^{+/-}$ as model systems for catalytic C-H activation and structural determination of selected metal peptide complexes of the molecules aspartame (Asp-PheOMe) and Asp-Phe";
Mdl. Abschlussprüfung: 11. Juni 2013

Vakuumtechnik, Massenspektrometrie, Infrarotspektroskopie, Aufbau/ Modifikationen/ Programmierung von wissenschaftlichen Geräten; Betreuung/ Anleiten von wissenschaftlichen Hilfskräften, Betreuung von studentischen Experimenten, Leitung von Übungsgruppen; Computeradministration (Clients: Windows, Server: Linux)

Praktika
10/2004 - 01/2005 im Rahmen des Studiums: Forschungspraktikum, Lebensmittelchemie/ Umwelttoxikologie, TU Kaiserslautern: „Etablierung des TAC-Assays zur Bestimmung der antioxidativen Kapazität von Reinsubstanzen und Blutplasma"

07/2004 - 10/2004 im Rahmen des Studiums: Forschungspraktikum Physikalische Chemie, TU Kaiserslautern: „Massenspektrometrische Untersuchungen an Cisplatin, Transplatin und Transpalladium"

03/2004 - 06/2004 im Rahmen des Studiums: Forschungspraktikum Anorganische Chemie, Universität Barcelona, Spanien: „Untersuchungen an Substanzen mit Perovskit-Struktur"

07/1998 Schüler-Praktikant, Hans-Knöll-Institut für Naturstoffforschung, Jena

Chemisch-Biologisches Screening

Zusatzqualifikationen Eingeschränkte Sachkunde nach § 5 Chemikalien-Verbotsverordnung

Sonstige studienbegleitende Aktivitäten Vielseitige, langjährige Erfahrung als studentisches Mitglied in Universitäts-Gremien: Fachschaftsrat (Kassenwart), Fachausschuss für Studium und Lehre (Mitgestaltung des reformierten Diplomchemie-Studienganges), professorale Berufungskommissionen; Regionalsprecher des Jungchemikerforums der Gesellschaft Deutscher Chemiker, Ortsgruppe Kaiserslautern

Eidesstattliche Erklärung

Hiermit bestätige ich, Lars Barzen, dass die vorliegende Arbeit gemäß der Promotionsordnung des Fachbereichs Chemie der Technischen Universität Kaiserslautern selbständig und nur unter Verwendung der angegebenen Quellen und Hilfsmittel angefertigt wurde.

Kaiserslautern, im Juni 2013